GEOPHYSICAL STUDIES

OF THE SERPENT MOUND STRUCTURE

ADAMS COUNTY, OHIO, U.S.A.

BY

BELGASEM M. B. EL-SAITI

B.Sc. (Faculty of Petroleum and Mining Engineering, Tripoli)

M.Sc. (Colorado School of Mines, Golden, Colorado, U.S.A.)

Thesis Submitted for the degree of Doctor of Philosophy at the Department of

Geology & Applied Geology, University of Glasgow

(May, 1998)

DEDICATION

This thesis is dedicated to those who helped me find the way, but are no longer with me. To the memories of my Father (**Mohammud**), and my uncle (**Ibrahim**).

Abstract

Integrated geophysical study of the Serpent Mound Structure provides significant new findings and confirms the previously reported findings. These findings are based on newly processed and interpreted seismic reflection data, gravity, magnetic, palaeomagnetic, the availability of deep continuous cores and well data.

The purpose of this investigation is to resolve the controversy regarding the origin of the Serpent Mound Structure and its age. The reprocessing of seismic data shows a significant improvement when compared to earlier processing carried out by industry.

The processed seismic data indicate a highly faulted, structurally complex depression extending downward to about 700 feet into the Precambrian basement beneath the central uplift area of the structure. These findings are supported by the analysis of two deep cores. The seismic data as well as the core data indicate a decrease in structural complexity and intensity with depth, and away from the central uplift area of the structure. The relative degree of structure complexity is related to the structural zone within the disturbance, ranging from the most complex in the central uplift to least complex in the ring graben. Seismic data also indicate a ring anticline associated with the ring graben of the structure and the presence of an anomalous lens-shaped volume of chaotic reflections occurs within the depression beneath the central uplift.

The microgravity survey of the Serpent Mound Structure reveals a residual negative gravity anomaly associated with the central uplift area of the structure. The gravity anomaly reflects the lower density, fractured and brecciated target rocks at the centre of the structure. The modelling of the structure indicates a central uplift composed of brecciated and fractured lens surrounded by less deformed country rock. The brecciated lens extends to the top of the Gull River, about 2000 feet (610 m) below surface and has a density contrast of –0.06 gm/cc. The position and the diameter of the low-density region mimic the depression seen on the seismic section.

The ground magnetic survey of the Serpent Mound Structure shows a well-defined magnetic anomaly indicated by its trend, width, and high amplitude. Our magnetic survey shows a significant revision of the previous map of the area.

The Serpent Mound Structure is located near a north-south regional anomaly trend. The modelling of the magnetic data shows it is possible that a volume of rocks beneath the structure was magnetised by the passage of shock waves caused by the impact.

Palaeomagnetic analysis of some oriented samples collected from deep cores within and outside the structure revealed a secondary magnetisation in both cores. The analysis shows the magnetisation was probably acquired during Late Permian (250±15 my). Better data based on radiometric methods are unlikely, this represents the best constraint of the upper age of the Serpent Mound Structure to date.

Core DGS3274 drilled in the central uplift area of the structure shows abundant macroscopic evidence for shock metamorphism in the form of intense deformation, brecciation, and shatter cones. Microscopic evidence for shock is found as a set of planar deformation features (PDFs) in quartz grains.

Based on the findings of geophysical studies including seismic, gravity, magnetic, and palaeomagnetic and petrographic and geochemical studies of the cores, the interpretation of the origin of the Serpent Mound Structure is of an impact which occurred during the Late Palaeozoic.

DECLARATION

The material presented herein is a result of my research undertaken between April 1994 and April 1998 in the Department of Geology and Applied Geology, University of Glasgow, under the supervision of Dr. Doyle R. Watts.
Any published or unpublished material used by me has been given full acknowledgement in the text.

Belgasem M. El-Saiti
May 1998

ACKNOWLEDGEMENT

I would like to express my sincere appreciation to many people who assisted or contributed to this study. This research project was devised and supervised by Dr. Doyle R. Watts of the Department of Geology & Applied Geology, University of Glasgow- the friend whose door is always open and always ready to spend as much time as needed for the progress of this study. His encouragement, fruitful discussions, comments, and endless patience has been more than invaluable. I gratefully acknowledge his assistance during the fieldwork.

I am very grateful to the Geophysics group of the Department represented by Prof. Dave K. Smythe and Dr. Ben Doody for the assistance I have received from their valuable suggestions and comments and making available to me all of the facilities of the group including the personal computers.

Thanks go to Dr. Colin Gribble (Head of the Department) and to the faculty members for allowing me the use of the facilities during this research. Dr. Allan Hall helped in the mineralogical analysis. Thanks to Prof. Mike Russell for encouragement.

Thanks are due to the technical staff of the department, among whom special mention must be made of Bob Cumberland for rescuing my files and making backups, George Gordon for building my PC, Douglas Maclean who produced numbers of slides for my seminar, Kenny Roberts for providing computer support. Roddy Morrison rapidly and efficiently provided whatever materials were needed. Eddie Speirs for giving the right advice.

In the course of my travel to Ohio, USA. For the fieldwork, Mr. and Mrs. Poter Watts provided lodging at their home (Brookville, Ohio), and were very kind and truly generous. Many thanks to them and to their daughter Mrs Shirley Kinsey and her family. Thanks are due to Mr. Gary C. Watts who assisted in the magnetic survey on one weekend.

My sincere appreciation is extended to many geologists at the Ohio Department of Natural Resources (ODNR), particularly Mark T. Baranoski, Gregory A. Schumacher, and Dr. Richard W. Carlton. For providing us with the data, for their contribution and finding the time to visit the core depository in Columbus and examine the two cores.

I thank the many landowners whose co-operation resulted in the successful completion of our magnetic and gravity surveys of the Serpent Mound Structure.

The Department of Geological Sciences at Wright State University, Dayton, Ohio provided equipment (gravity meters, GPS equipment, magnetometers, survey equipment, field computer) and other facilities to support our geophysical field work. I am grateful to Prof. Ben Richard, Prof. Paul Wolfe, Dr. Ernest Hauser, and Dr. Byron Kulander of Wright State for their advice and discussions. The Royal Society of London provided financial support for the geophysical fieldwork and seismic data processing.

Thanks to many research students at this Department, namely Emhemed Elhamali, Zuhar Harith, Ahmed Mohammed, Andrew Deighan, Carsten Riedel, Alisdair Fitch, Kejian Wu, Joan Walsh, and Andrew Cavana.

My thanks are due to my friends and colleagues at the Department of Geosciences, Gar-Yonis University, Benghazi, Libya. Prof. Ali Alarnauti, Prof. Ahmed Alhawat, Dr. Rajab Al-kazmi, Dr. Ashur Al-Zouki, Dr. Abdulla Ben-Surati, Dr. Mohammud Abdulmalik, Mr. Fathi Salloum, and Mr. Isam Abdul-Sammad.

Last but not least I would like express my thanks to my family, my dear Mother my brothers and sisters, my children and my wife Shamisa A. Hammad for her patience, understanding, encouragement and continuous backing during the ups and downs.

Table of Contents

LIST OF FIGURES

Chapter 3

Chapter 4

Chapter 7

Chapter 8

Chapter 9

LIST OF TABLES

Chapter-1 INTRODUCTION

1.1- Introduction

The Serpent Mound Structure of southwestern Ohio has a characteristic circular morphological outline, and closely resembles many other highly deformed circular cryptoexplosion structures throughout the world, displaying evidence of violent disruption during its formation. This significant surface structural geological anomaly lies in a generally undeformed region of Ohio at the western edge of the Appalachian escarpment. The geology of this part of Ohio consists of Precambrian basement completely covered by thin sequences of relatively undisturbed Palaeozoic sedimentary rocks, which dip slightly to the southeast. In much of Ohio, Pleistocene glacial deposits overlie the Palaeozoic rocks.

The structure itself is a circular area 7 to 8 km (4 to 5 miles) in diameter of intensely faulted and folded Ordovician to Mississippian age rocks exposed at the surface. Stephen P. Reidel (1975) remapped the Serpent Mound Structure and produced its first detailed geologic map. The structure can be divided into three zones, these are the central uplift area, the transition zone (inner ring), and the outer ring graben zone. The zones are defined by rock units and their relative stratigraphic positions, and by structural characteristics based on the surface geology mapping and the sampling of the structural framework. The intensity of deformation increases toward the centre of the structure. The centre of the structure (the central uplift area) consists of Ordovician and Silurian age rocks that have been uplifted above their normal stratigraphic position. These rocks have been faulted and folded into seven radiating anticlines, some of which are overturned. The anticlines exhibit the most intense deformation in the structure in the form of vertical to overturned beds, also show shock features known as shatter cones.

The transition zone (inner ring) surrounds the central uplift area and represents a transitional area between the radial structures of the central uplift and the concentric structures of the outer ring graben. The rocks in this zone are mostly Silurian carbonates at or near their normal stratigraphic positions. The outer ring-graben area is characterised by fault-bounded strata which have been displaced below their undisturbed structural position by as much as 250m (850ft) (Reidel et al, 1982). The topographic expression of the Serpent Mound Structure clearly defines the configuration of the feature and delineates the major structural zones. It appears that this expression is a function of the structural arrangement of the rocks in each zone and the resistance of these rocks to erosion. The erosion during the Mesozoic and Tertiary removed rocks, and continued erosion has exposed the resistant Mississippian and Devonian rocks that cover the down-dropped ring graben. The perimeter of the structure is sharply defined by nearly continuous concentric faults. The wooded hills on the outer ring graben now define the outer margin of the structure. The rocks in the ring graben are structurally lower than the rocks of the other two zones and the surrounding undisturbed Silurian rocks outside the structure. The transition zone (inner ring) is topographically lower than both the ring-graben and the central uplift area. The central uplift area composed of Ordovician shales and limestones, stands as a topographic high area. These three zones are clearly visible from the ground a short distance from the structure.

The exact origin of the Serpent Mound Structure was a controversial problem for many geologists in the past. In general there are two conflicting theories regarding the origin of the Serpent Mound Structure. The first theory, proposed by Bucher (1921b), suggested the structure is of endogenic origin (violent gas explosion), and the second theory, proposed by Dietz (1960), interpreted the structure as of exogenic origin (meteorite impact). The origin of the Serpent Mound Structure would be difficult to establish without subsurface geological data to support the findings of surface measurements.

1.2 - Location

The Serpent Mound Structure is located in the south-western quadrant of Ohio (Figure 1.1). It occupies the north-eastern part of Adams County, the south-eastern part of Highland County, and the south-western part of Pike County. The structure was named by Bucher (1921) after the most spectacular American Indian effigy mound that depicts a serpent. This is the largest known effigy in the United States (Figure 1.2) and lies on the western flank of the structure. The serpent effigy is 1348 ft long, 2 to 6 ft high and the average width of the serpent's body is about 20 ft. Ohio Historical Society archaeologist, Dr. Bradley T. Lepper, dated the effigy mound to about 1070 AD. He suggested that the Native American Indians may have been inspired by the brightest and most spectacular recorded display of Halley's comet in 1066 AD, which they interpreted as a celestial serpent.

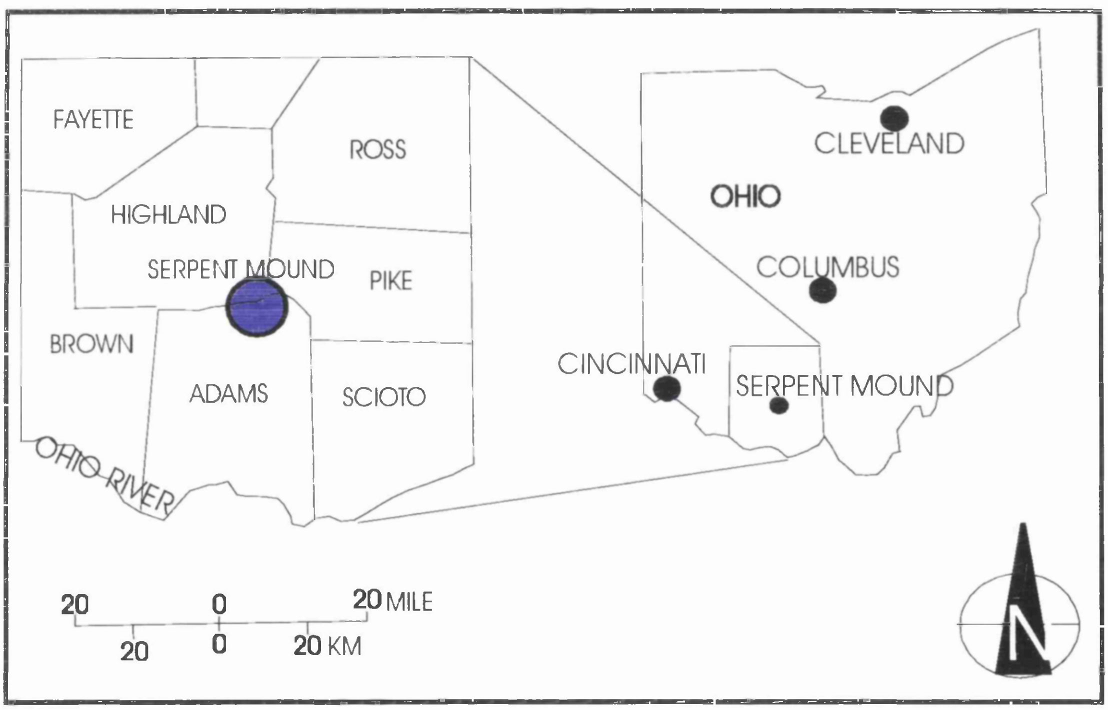

Figure 1.1- Map showing the location of the Serpent Mound Structure in Ohio

Figure 1.2- Air photo of the American Indian effigy mound Serpent Mound, Adams Co., Ohio

1.3- Origin Controversy and Age of the Structure

Determining exactly what formed the Serpent Mound Structure and similar features is a problem that geologists continue to debate. Two major hypotheses have been proposed for the origin of the structure. The first theory was presented by Bucher (1921,1936), who proposed that the structure is due to forces inside the earth, that is a sudden liberation of volcanic (explosive eruption) gas from a deep seated magma source in the basement rock. The explosion forced the Palaeozoic layers above the basement upward, shattering and cracking these rocks, and throwing some outward. Bucher (1921, 1936) postulated the endogenic origin of the structure based on similarities to the Steinheim Basin in Germany. Both structures are generally circular with a central uplifted areas of highly brecciated, intensely folded and faulted rocks, surrounded by less deformed rocks.

Branca and Fraas (1905) concluded that the Steinheim Basin was caused by an explosion of volcanic gases. They coined the term cryptovolcanic to describe these types of structures. Bucher (1936) concluded that the Serpent Mound Structure and five similar structures in the United States were also cryptovolcanic structures.

Robert Dietz (1947, 1959, 1960 and 1961) proposed the second theory, that shatter cones in rocks were formed only by the high-velocity shock waves of meteorite impact. Dietz (1960), proposed an exogenic origin (meteorite impact) for the Serpent Mound Structure, after finding shatter cones in the Ordovician limestone in the central uplift area. Dietz introduced the term cryptoexplosion instead of cryptovolcanic, which implies a known origin. He argued that any known volcanic processes or other terrestrial phenomenon could not produce the ultra high pressures associated with the impact of a meteorite.

Cohen and others (1961) discovered the high-pressure silica mineral, coesite, which is unequivocal evidence for the impact origin of the structure. In the laboratory, coesite forms by the recrystallization of solid forms of silica and quartz under extremely high pressures and temperatures (Coes, 1953). Thus the discovery of the mineral coesite would have provided unquestionable prove of impact origin.

Reidel and others (1982) discounted Cohen's coesite discovery as a probable misidentification of a diffuse X-ray line. They concluded that neither a meteorite impact nor a gas explosion hypothesis can completely explains all of the evidence observed, and suggested that some poorly understood form of volcanic activity or tectonic process (an endogenic process) created the Serpent Mound Structure.

It is difficult to assign an exact age for the structure because of the absence of igneous rocks for radiometric dating. It is certain that the Serpent Mound Structure occurred after early Mississippian time (about 345 million years ago), because rocks of this age are involved in the structure. The structure can be no younger than the age of undisturbed Illinoian glacier deposits (about 125 thousand years) in the northern part of the structure. There is therefore considerable uncertainty as to when the structure formed in this immense span of time, when the State of Ohio experienced its worst natural catastrophe. Palaeomagnetic study of some samples of zinc minerals (Istok, 1978) in Silurian rocks in the structure recorded a Late Triassic pole position. This may indicate the approximate age of the structure or perhaps a later phase of hydrothermal mineralization.

1.4- Previous Work

The first geologist to observe the Serpent Mound geologic structure was Dr. John Locke (1838) during the first geological survey of Ohio. Locke visited Massie's Spring located about two miles to the northwest of Locust Grove, he noted he was travelling on rocks of the Silurian Cliff Limestone (Bisher, Lilley, and Pebbles Dolomite) and expected to encounter the Great Marl Stratum (Estill Shale) as they descended into the valley of Crooked Creek. Locke noticed a region of no small extent had sunk down several hundred of ft, producing faults, dislocations and upturnings of the layers of the rocks. John Locke named this region of Adams County the Sunken Mountain because of the downward displacement of the strata in this region. Edward Orton, in his report on the geology of the Highland County (1871), mentioned Locke's observations in neighbouring Adams County to the south of Highland County. He added that the Mississippian Waverly Sandstone (Berea Sandstone), and the various slates, and limestones in the north-east corner of Adams County and adjacent territory are much dislocated and involved in inextricable confusion.

Professor Walter H. Bucher (1921) mapped the geology of the Serpent Mound Structure and instead of using Locke's appellation of Sunken Mountain, he used the name of the serpent-shaped effigy mound for the geologic structure. Bucher interpreted the structure to have been formed by the explosion of gases derived from a deep-seated intrusion of molten rocks escaped to the surface with violent force disrupted considerable volume of rocks. Galbraith (1968) investigated the regional structural geology of Adams, Highland, and Pike Counties, Ohio. Galbraith (1968) and Galbraith and Koucky (1969) concluded that the deformation extends beyond Bucher's outer boundary 1 to 2 miles to the southeast. The amount of deformation increases toward the centre of the structure with the stratigraphic units displaced vertically by several hundreds of ft (Bucher, 1936).

Reidel (1975) remapped the structure and produced the first detailed geologic map of the structure, showing it can be divided into three zones (Figure1.3). These are the central uplift area, the transition zone (inner-ring), and the outer ring-graben zone. These are defined by rock units and their relative stratigraphic positions, and by structural characteristics. In particular Reidel defined the components of the structure as follows:

1- Central uplift area:

The centre of the structure consists of Ordovician and Silurian rocks that have been uplifted several hundred feet above their normal stratigraphic position. These rocks have been faulted and folded into seven radiating anticlines (Figure 1.3), some of which are overturned. The anticlines exhibit the most intense deformation in the structure in the form of vertical to overturned beds, and also show shock features known as shatter cones. The central uplift area forms a topographic high.

2- Transition zone (inner-ring):

The transition zone surrounds the central uplift and represents a transitional area between the radial structures of the central uplift and the concentric structures of the outer ring graben. The rocks in this zone are mostly Silurian carbonates at or near their normal stratigraphic positions. The transition area is topographically low relatively to both the central uplift area and the outer ring graben.

3- Outer ring graben:

The perimeter of the structure is sharply defined by nearly continuous concentric faults. The rocks of the ring graben zone are mostly of younger strata of Devonian and Mississippian age and are structurally lower than the rocks of the other two zones and of the surrounding undisturbed Silurian rocks. The ring-graben zone is topographically higher than the transition zone In general the topographic expression of the Serpent Mound Structure clearly defines the configuration of the feature and delineates the major structural zones (Figure 1.4). It appears that this expression is a function of the structural arrangement of the rocks in each zone and the resistance of these rocks to erosion.

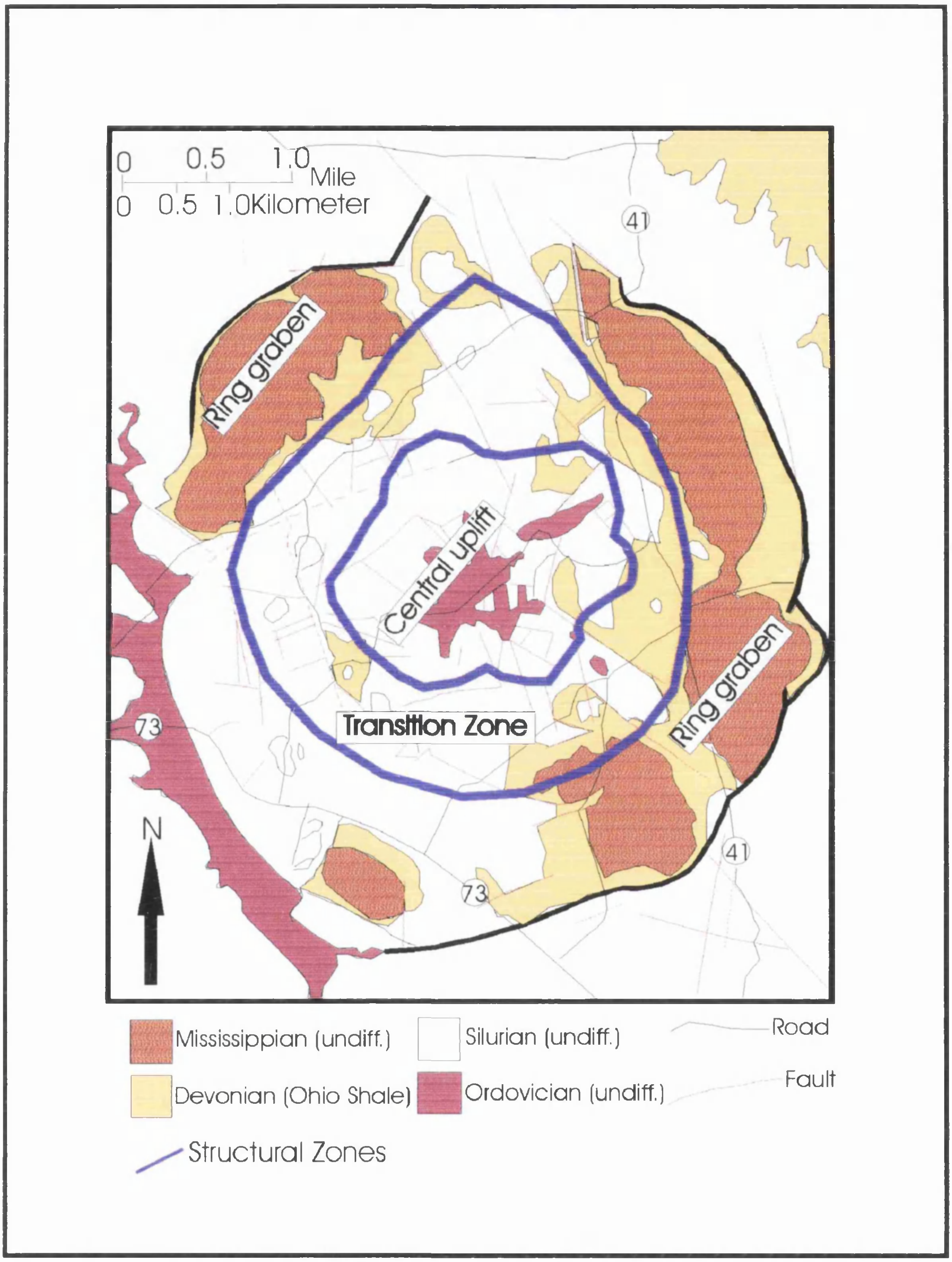

Figure 1.3- Generalised Geologic Map of the Serpent Mound Structure (modified from Reidel et al. 1982)

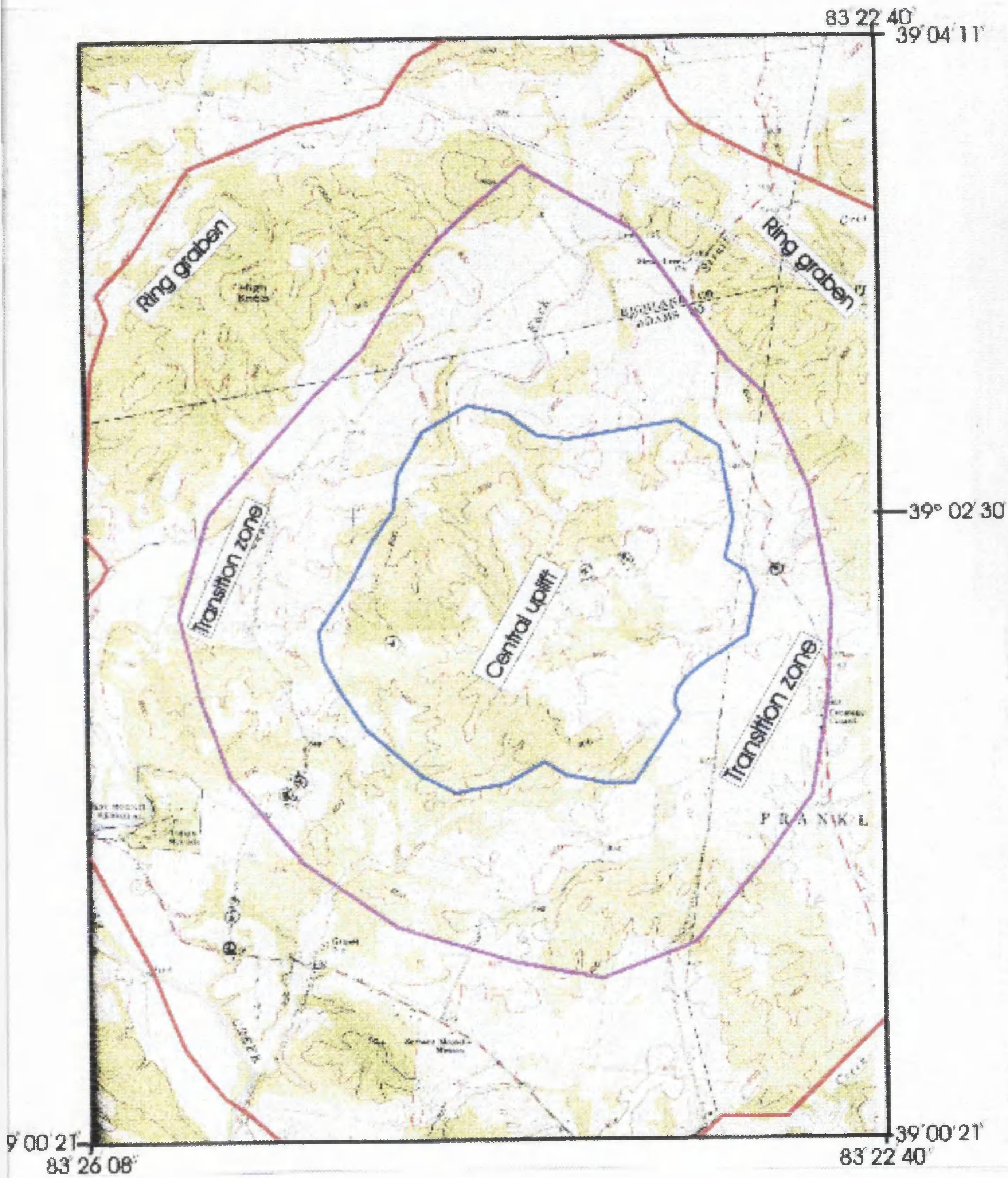

Figure 1.4- Topographic expression of the Serpent Mound Structure

The structural and topographic development of the Serpent Mound Structure is illustrated by Figure 1.5 (Hansen, 1994). There is no direct evidence that Pennsylvanian and Permian rocks covered the area, but it is reasonable to assume their presence. The disturbing force elevated the central uplift and depressed the outer ring graben. Erosion during the Mesozoic and Tertiary removed rocks, and continued erosion exposed the resistant Mississippian and Devonian rocks that are found in the down-dropped ring graben. The outer ring graben now defines the outer margin of the structure as wooded hills. These zones are clearly visible from the ground a short distance from the structure.

The Serpent Mound Structure has been the subject of a number of geophysical investigations, which include magnetic and gravity surveys. Sappenfield (1951) conducted a ground magnetic survey of approximately 400 square km of north-eastern Adams, south-eastern Highland, and south-western Pike Counties including the Serpent Mound Structure. The vertical intensity magnetic map (Figure 1.6) shows an elongated magnetic anomaly with its axis trending N 25 W. Sappenfield (1951) suggested that this anomaly was a result of an intrusion of a basic magma into the upper part of the siliceous basement.

Zahn (1965), Flaugher (1973), and Langford (1984) conducted gravity surveys in the region of the Serpent Mound Structure. Their studies show no relationship between the surface expression of the structure and the regional gravity anomaly. The full extent of their studies, used with the state-wide regional gravity surveys of Heiskanen and Uotila (1956), and Hildenbrand and Kucks (1984), recognise a linear regional anomaly oriented northwest-southeast extending from extreme north-eastern Kentucky through Scioto, Adams, Highland, and into Indiana east of Fort Wayne (Figure 1.7).

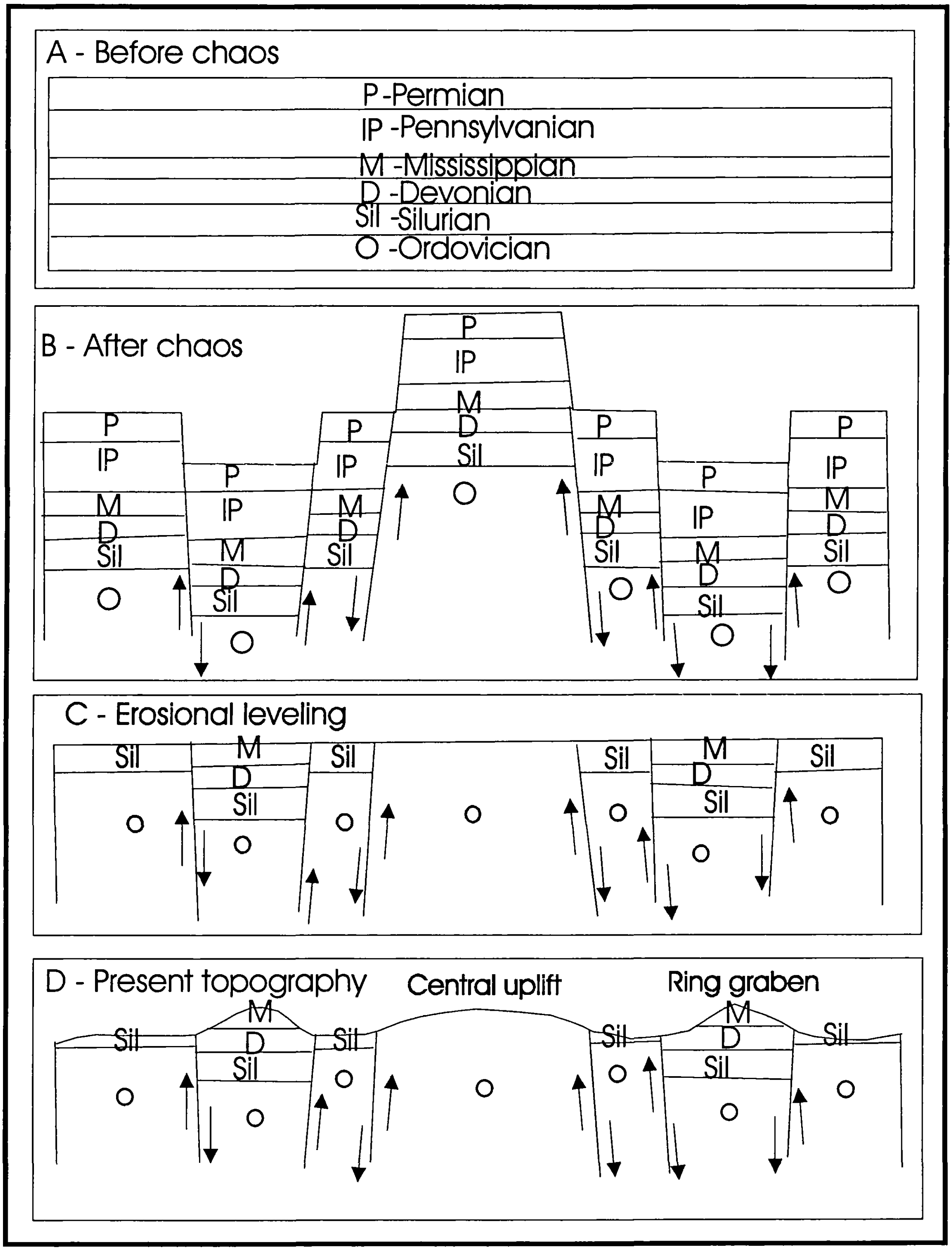

Figure 1.5- Diagram illustrating the structural and the topographic development of the Serpent Mound Structure (after Hansen, 1994)

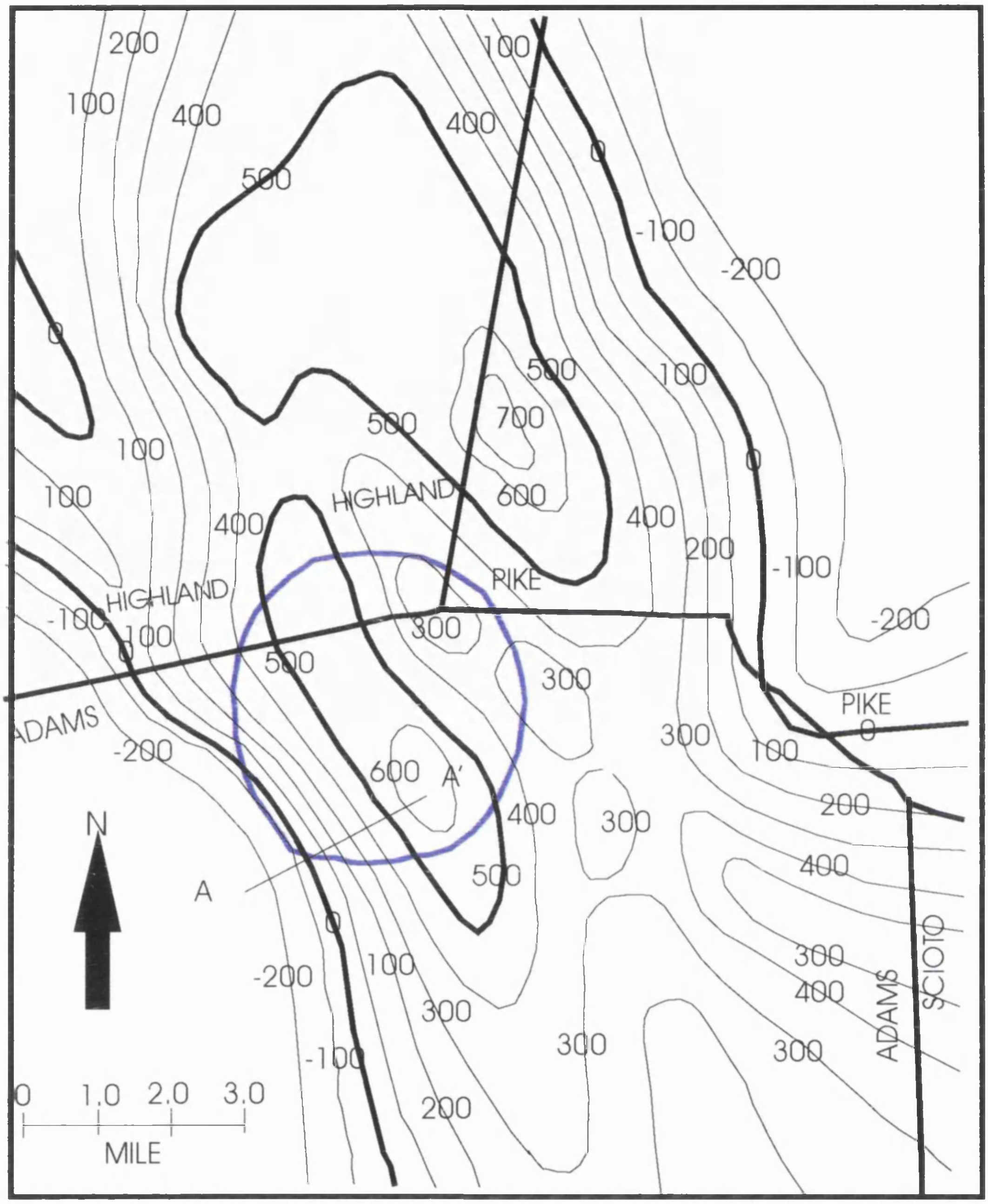

Figure 1.6- Vertical Intensity Magnetic Map (n.T.) of the Serpent Mound area (the blue line represents the outer boundary of the Serpent Mound Structure, and the line A-A' shows the falls off of the anomaly to the west) (Sappenfield, 1951)

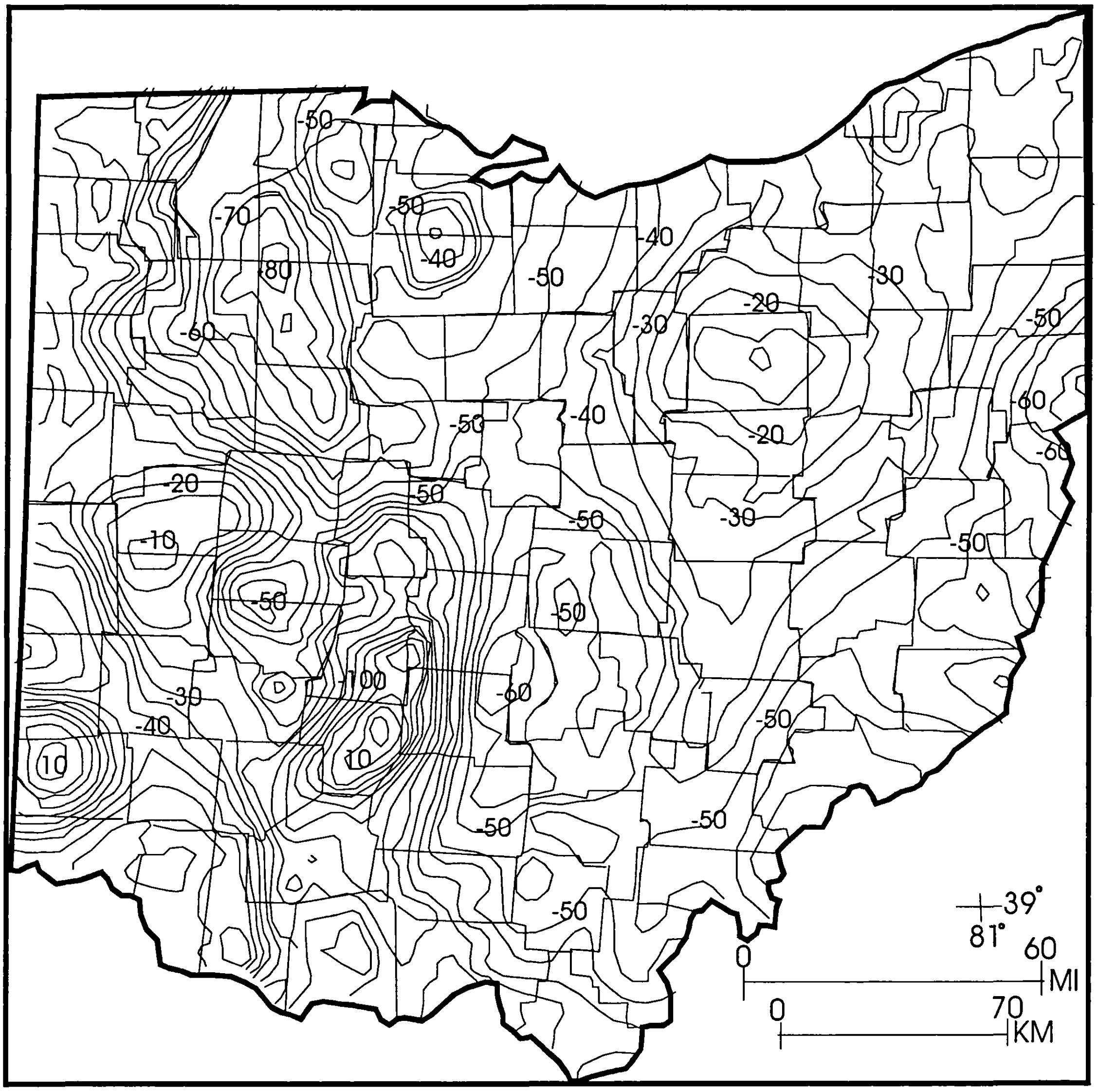

Figure 1.7- Bouguer Gravity Anomaly Map of Ohio

(Elevation Mean Sea Level C.I. 5 mGals)

Istok (1978) studied the palaeomagnetism of eight hand samples from the Brassfield Formation and the Tymochette Dolomite collected from core and flanks of the Serpent Mound Structure. He concluded that the structure was at least as old as the Late Triassic and the magnetisation was associated with mineralization.

Heyl and Brock (1962) reported zinc mineralization associated with brecciated rocks within the Serpent Mound Structure. The zinc minerals present occur in the Peebles and Greenfield Dolomites and consist of sphalerite that partly weathers to smithsonite and hydrozinite. They observed that several stages of fracturing and mineralization of sphalerite indicates that several episodes of zinc mineralization occurred over the long history of the structure. They concluded that the zinc occurrence was small and was likely not to be an economic deposit. Reidel (1975), Reidel and others (1982), and Stryker (1971) studied the zinc mineralization and asphalt coating mineralization which occurs along fault planes and the intersection of several faults. Economic deposits of zinc minerals and petroleum were not located as a result of their mapping. These studies agree with Heyl and Brock (1962) that at least two episodes of mineralization and deformation occurred in the Serpent Mound Structure. Carlson (1991) reported that the Serpent Mound Structure occurs within one of the major mineralised areas of Ohio, called the Serpent Mound Zinc District. This district is about 32 km wide and 64 km along a north-south axis, lying on the eastern flank of the Cincinnati Arch, and extending from southern Fayette County through Highland County into west-central Adams County. McFarland and others (1993), McFarland and Carlson (1994), McFarland and others (1994), McFarland and Carlson (1995, 1995b), McFarland and Carlson (1996) conducted further studies of the mineralization associated with the Serpent Mound Structure. They proposed a model of renewed inflow of zinc minerals inside and adjacent to the structure based on the mineralogy, sulphur isotopes, and trace element geochemistry.

1.5- Purpose and Objective of This Study

Clearly more data are needed to resolve the controversy and the confusion concerning the origin and subsurface nature of the Serpent Mound Structure. This is the objective of this research, which provides new geophysical data for this purpose. These new data include reprocessed seismic reflection data, modelling of geophysical well logs, a micro-gravity profile, a detailed magnetic survey, and a palaeomagnetic investigation. Our colleagues at the Ohio Department of Natural Resources supplied descriptions of cores with petrographic analysis.

Until this study most of the geophysical investigations of the Serpent Mound Structure were either conducted on a regional scale or one of the potential field methods (gravity and magnetic) were used. In this study we combine the results of potential field methods with the results of seismic investigation, and data from deep cores. Because different geophysical methods are sensitive to different physical properties they complement each other to provide an integrated view of the structure.

Two seismic lines were made available for this research, by the Ohio Department of Natural Resources (ODNR) for reprocessing and interpretation. The first seismic line crossed the transition zone through the eastern portion of the structure. The second seismic line traversed southwest-northeast along across the central uplift area of the structure. For the interpretation of the seismic lines, the ODNR made available geophysical well logs from nearby oils wells drilled to basement. These logs enabled us to model the seismic response of the stratigraphic units in the vicinity of the Serpent Mound Structure and to interpret the seismic data.

Mapping of the subsurface structure is the most important use of the seismic reflection data gathered across the structure. Without subsurface geological data or well log information it would be difficult to establish the origin of the structure based on seismic sections alone. However, observed morphological, structural and tectonic features, change in intensity of deformation with the depth, and the local fault patterns, may provide compelling evidence for the origin of the structure. Geological data (surface and subsurface) remain very important to constrain the interpretation of geophysical data, in the same way it is important that geophysical observations place stringent restrictions on the proposed geological interpretation for the origin of the structure. In this regard, two small-diameter continuous cores drilled in 1979 by John L. Carrol Minerals Exploration Company, New York City, were made available for investigation. These two continuous cores, one drilled in the transition zone DGS 3275 (Ohio Department of Geological survey well # 3275) and one drilled in the central uplift area (DGS 3274) of the Serpent Mound Structure, both penetrated the Knox Dolomite and reached 630m (2065ft) and 903m (2962ft) total depth respectively. Three shallow cores from the northern part of the structure were also available for study, as were deep cores from undisturbed areas near the structure.

The new potential field data include a detailed ground magnetic survey over the structure and beyond, covering hundreds of square km using two Geometrics 856 recording proton precession magnetometers. A micro-gravity survey profile was carried out across the centre of the structure, to search for a local gravity anomaly of the structure not related to regional gravity trends. Differential global positioning methods were used to locate stations for the gravity and magnetic work.

Palaeomagnetic analysis of samples collected from the well cores, allow us to assign an approximate age of the structure. This was done using cores that were not oriented in declination but the vertical direction was known.

The geophysical study, combined the descriptions and the petrographic analysis of the cores carried out by colleagues at the ODNR provide new information regarding the distribution, geometry, and physical properties of the subsurface of the structure. We believe we have sufficient information for the proper interpretation regarding the origin and the geophysical signatures of the Serpent Mound Structure.

Chapter- 2 REGIONAL SETTING AND STRATIGRAPHY

2.1- Regional Structural Geology

2.1.1- Introduction

Ohio is a part of a central stable region (craton) characterised by broad sedimentary basins and arches near the eastern edge of the mid-continent United States (Figure 2.1). This portion of the craton consists of three regional sedimentary and structural basins, unconformably lying on the Precambrian basement complex. These are, the Appalachian Basin to the east, the Illinois Basin to the southwest, and the Michigan Basin to the north. The three basins are separated by the Cincinnati-Kankakee Arch system, and the Findlay Arch and Indiana-Ohio Platform (Figure 2.1), which are considered regional structural positive features (Green, 1957). The Michigan Basin and Illinois Basin, are separated by the Kankakee Arch that intersects the Findlay Arch in western Ohio. The Appalachian Basin is separated from the Michigan Basin and Illinois Basin by the Findlay Arch to the north and the Cincinnati Arch to the south, respectively. These basins developed during the Palaeozoic Era because of periodic faulting and structural adjustment in the Precambrian basement complex along plate tectonic boundaries. The eastern part of Ohio rests on the western flank of the Appalachian Basin while the western part of the state straddles the Cincinnati Arch and the Findlay Arch (Figure 2.1). The geology of Ohio consists of a Precambrian basement made up of predominantly igneous and metamorphic rocks, overlain by platform and basin deposits. The Precambrian basement has been subdivided into different provinces based on age, lithological, and structural characteristics.

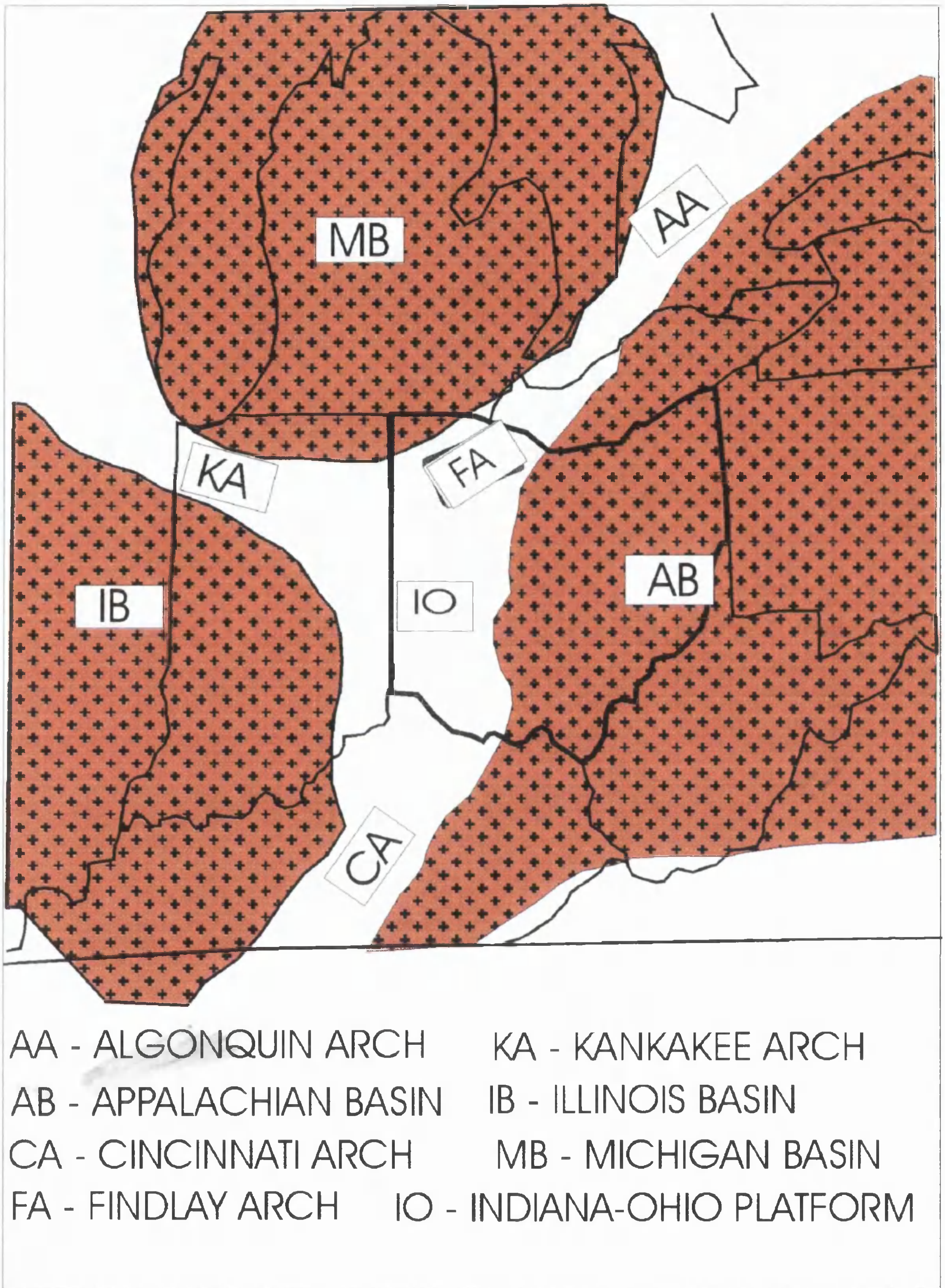

Figure 2.1- Diagram of Regional Structural Features

In Ohio, the Precambrian basement is completely covered by thick sequences of relatively undisturbed Palaeozoic sedimentary rocks, which dip slightly to the southeast. The Precambrian provinces which occur beneath the Palaeozoic sedimentary rocks in Ohio are: the Grenville Province (Bass, 1960; Keller et al. 1983; Black, 1986; Lucius and Von Frese, 1988) in eastern Ohio, the Granite-Rhyolite Province (Dension, et al. 1968; Bickford, et al. 1986) and the East Continent Rift (Drahovzal, et al. 1992) in Western Ohio. Figure (2.2) shows the major tectonic provinces and features of the mid-continent United States and southern Canada.

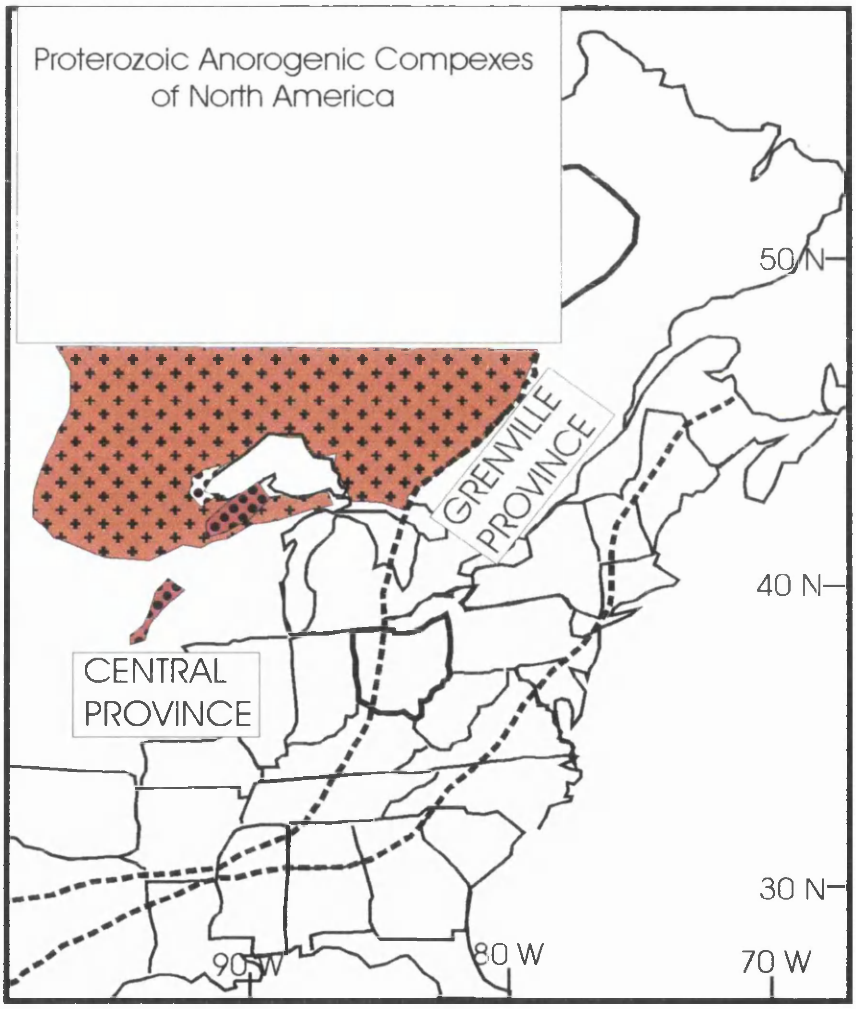

Figure 2.2- Major Tectonic Provinces and Features of Mid-continental United States (adapted from Anderson, 1983)

The regional Bouguer gravity map of Ohio (Heiskanen and Uotila (1956) can be divided into two regions. Figure (2.3) is a Bouguer gravity map of Ohio showing the boundary between these two regions. To the west of this boundary the Bouguer anomalies in Ohio are greater in magnitude and form a more complex pattern than anomalies to the east of the boundary. This boundary corresponds to the division between two major structural provinces, the Ohio-Indiana Platform to the west and the Appalachian Basin to the east.

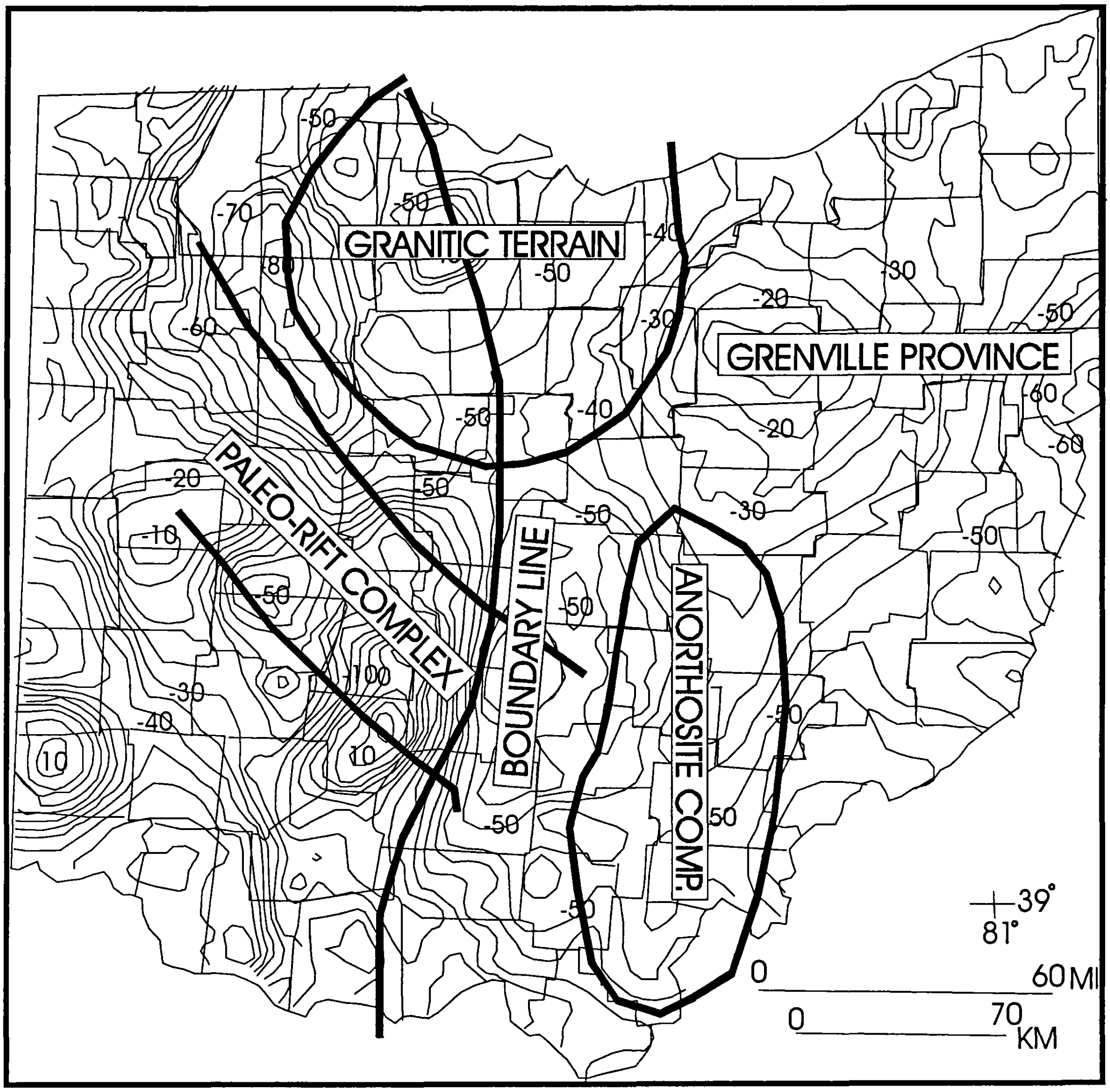

Figure 2.3- Schematic Diagram of the Crustal Features on the Gravity Anomaly Map of Ohio, C.I. mGal.

The Palaeozoic sedimentary rock sequence above the crystalline basement varies in thickness from less than 2500 ft (760 m) in northwestern Ohio to over 13,000 ft (4000 m) in southeastern Ohio. Figure 2.4 shows a basement configuration map constructed from scattered deep wells (Figure 2.5) in Ohio and surrounding regions (Lucius, 1985). One of the dominant topographic features in the basement map (Figure 2.4) is the Ohio-Indiana Platform. This area is roughly outlined by the -3000 ft (914 m) contour in the western half of Ohio.

This map also shows the depth to the basement in the area near the Serpent Mound Structure is in the range of -3000 ft.(914 m). The Palaeozoic sediments are overlain by Pleistocene glacial deposits in much of Ohio. Figure 2.6 shows the approximate edge of the glacial zone in western Ohio. Topographically the western region and part of northeastern Ohio are part of the Central Lowlands physiographic province, which is characterised by low relief. The southeastern and eastern parts of Ohio are part of the physiographic Appalachian Plateau, which consists of a resistant highland that continues southeastward to the Appalachian Mountains.

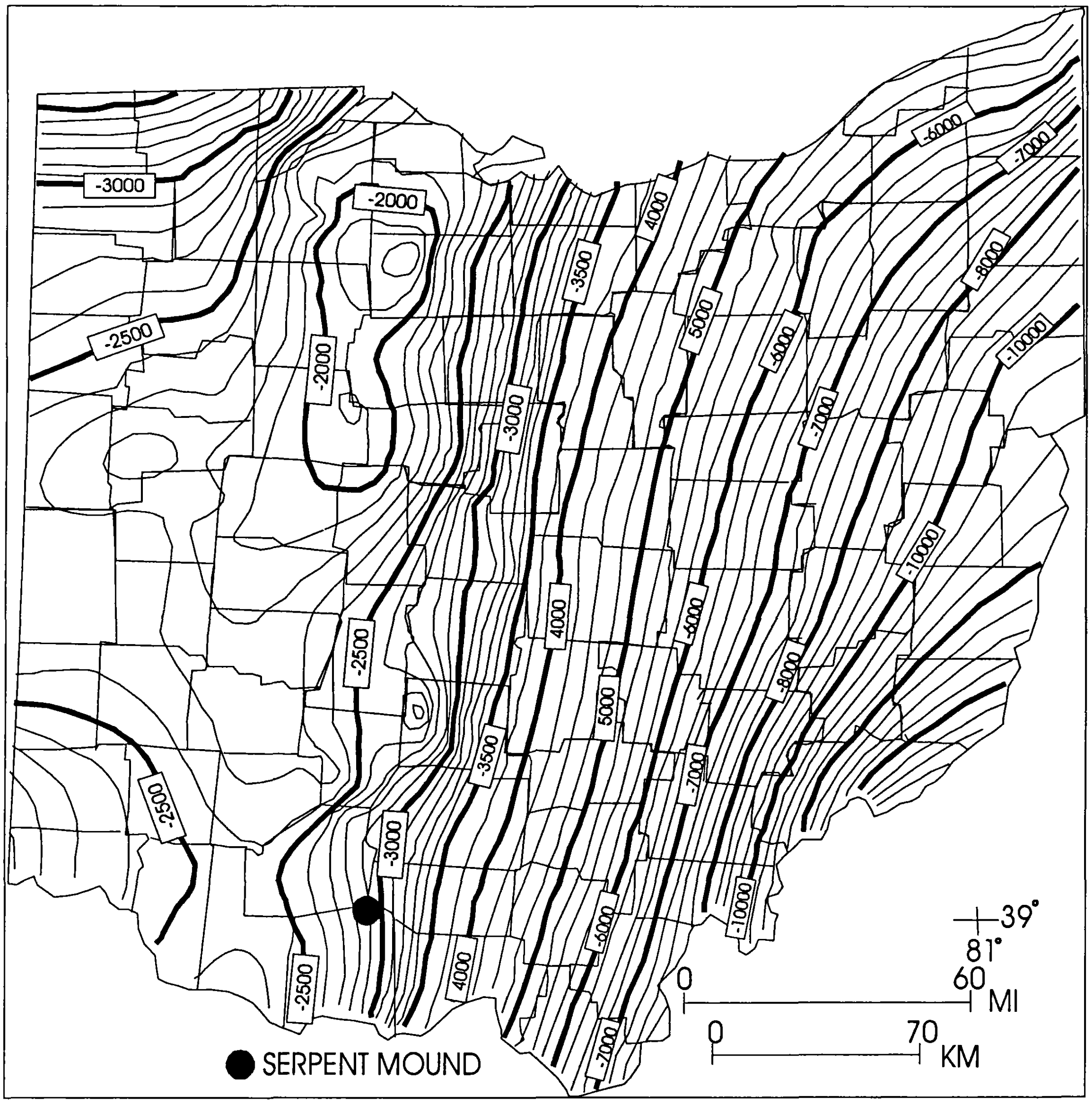

Figure 2.4- Basement map of the State of Ohio
Datum is mean sea level, C.I. 100 ft (30m)

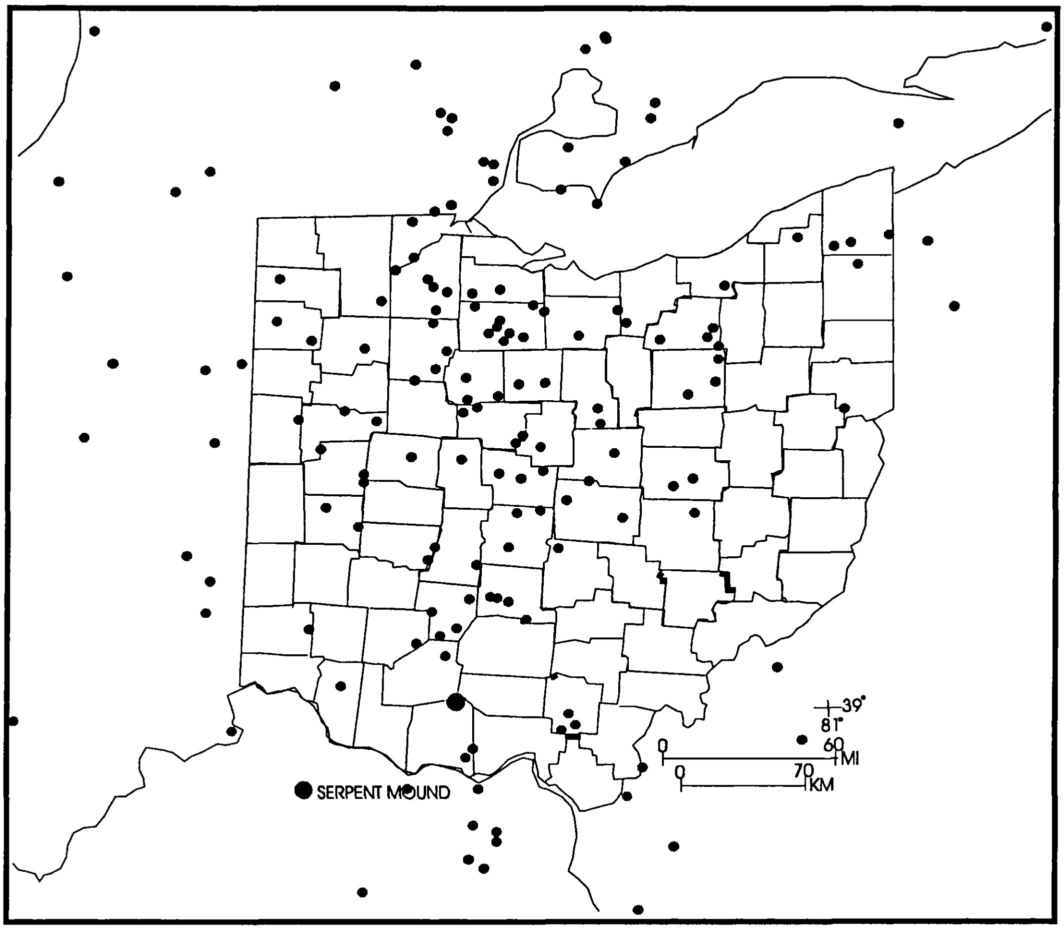

Figure 2.5- Distribution of Deep Wells in Ohio and Surrounding Areas Used to Map the Basement

Figure 2.6- Map of Ohio Showing the Glacial Boundary as a dashed line

2.1.2- Grenville Province

The Grenville Front, a fault zone in Canada represents the boundary between the highly deformed Grenville Province (less than 1000 my. BP) and the older Superior (Central) Province (greater than 1000 my. BP) which lies to the northwest. Movement in the southeast-dipping intensely fractured fault zone thrust the Grenville rocks northwest over rocks of the Superior province. The Grenville Front passes from view beneath the Palaeozoic sediments north of Lake Ontario showing no decrease in deformation intensities of the Grenville orogenic belt. In the central United States (Figure 2.2), the front is delineated by a change in the subsurface Precambrian rocks from medium to high-grade metamorphic rocks in the east to older unmetamorphosed igneous and sedimentary rocks in the west. Figure 2.7 shows some of Ohio deep well locations and basement lithology. Bass (1960), McCormick (1961), Lidiak and others (1966), and Janseens (1973) recognised the two distinct lithologic provinces in the Precambrian rocks of Ohio. Figure 2.8 shows the location of the Grenville front determined by these workers. The basement of the eastern three-quarters of Ohio is the Grenville Province and in the western quarter of Ohio is the Superior (Central) Province (Lidiak, et al. 1985; Lucius, 1985; Lucius and Von Frese, 1988). Both Bass (1961) and McCormick (1961) defined the Grenville Front as a lithologic boundary rather than an age boundary. They based the position of their boundaries on the petrology of the rock samples from deep wells. Both petrology and age determinations were used in the classifications of Lidiak and others (1966). Janssens (1973) has a slightly different trend to the lithologic boundary (Figure 2.8) as it passes through southern Ohio. This line corresponds to the northwest trend of the magnetic anomaly through the area near the Serpent Mound Structure. The Grenville Front Tectonic Zone is a 50 km wide structural zone at the western edge of the Grenville Province (Culotta et al. 1990). The Grenville Front consists of a complex metamorphosed, folded-thrust belt rocks and separates these east and west provinces (Bass, 1960; Rudman et al. 1965; Muehlberger, 1968; Lidiak and Zeitz, 1976). In addition to the Grenville Front, two other major structural features are the Waverly Arch (Woodward, 1961; McGuire and Howell, 1963) about 16 km (10 miles) to the east of the Serpent Mound Structure, and the

Kentucky River Fault System (Ammerman and Keller, 1978), about 96 km (60 miles) to the south of the structure.

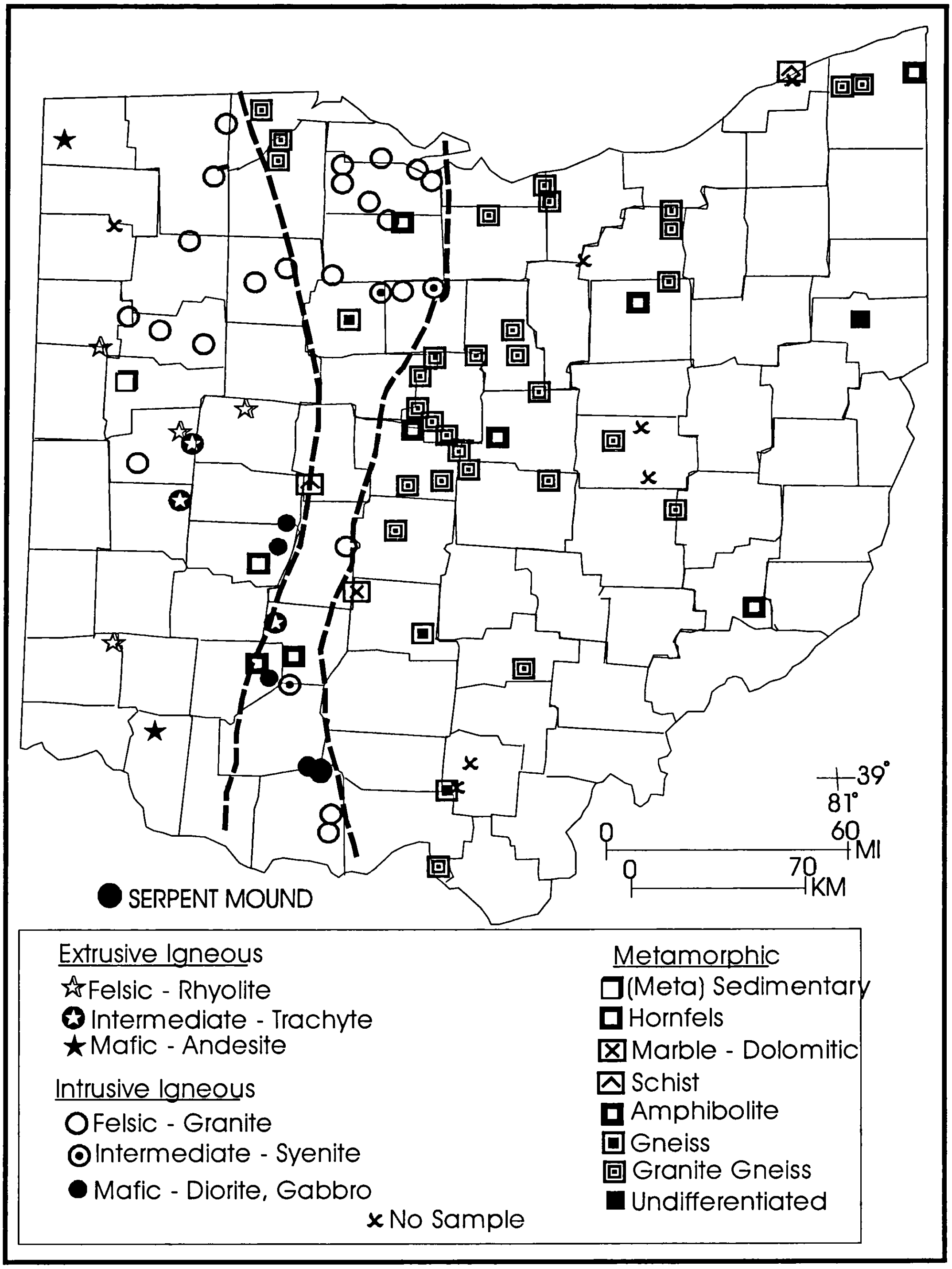

Figure 2.7- Deep Well Locations and Lithology of the Basement

(The dashed line represents the Grenville front zone)

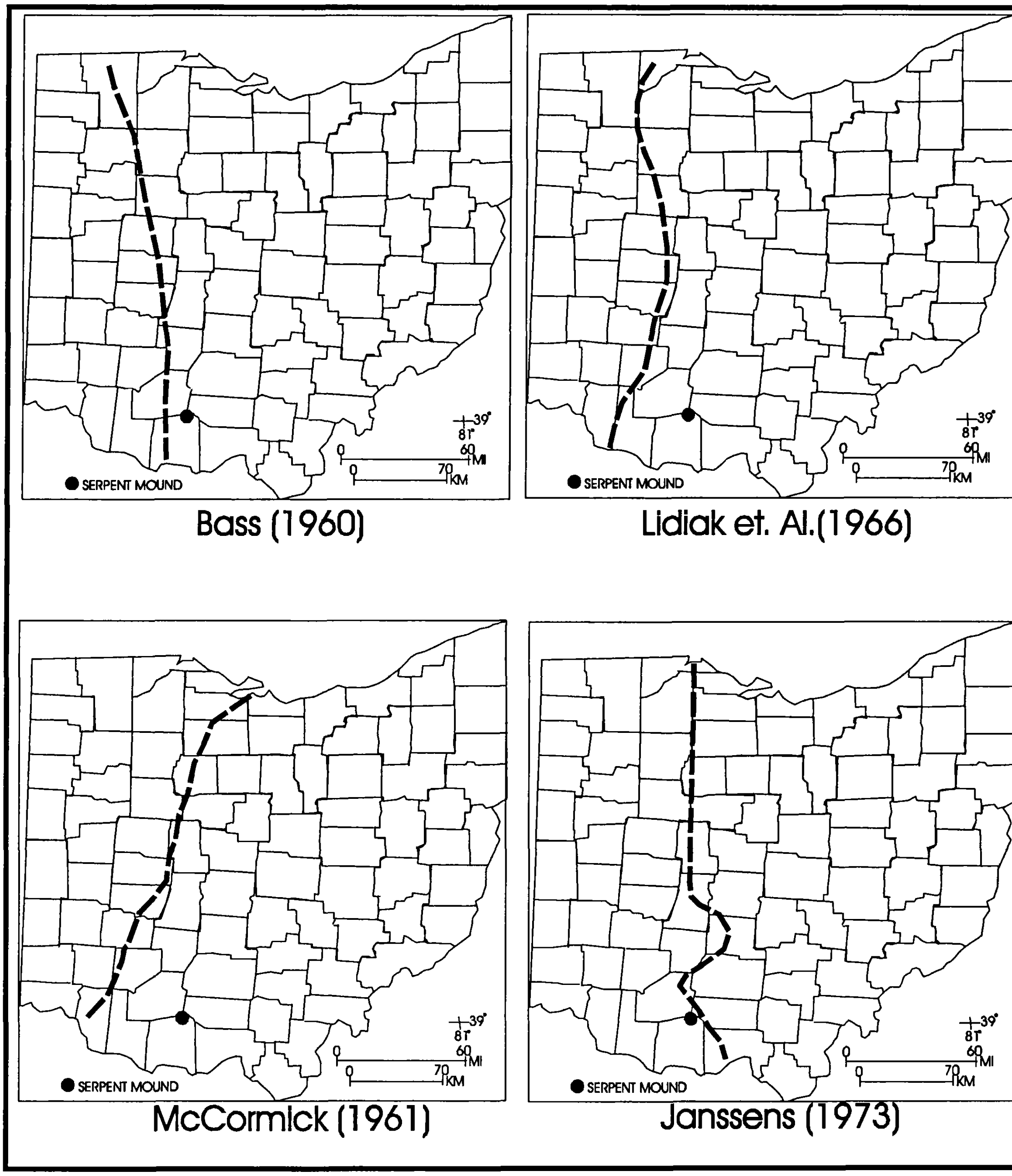

Figure 2.8- Different Interpretations for the Location of the Grenville front (The dashed line represents the edge of the Grenville front)

2.1.3- Cincinnati Arch

The Cincinnati Arch is the dominant structural feature in southern Ohio. The Arch extends from the northern Alabama to just south of Cincinnati, Ohio, where it divides into two branches. The east branch, the Findlay Arch, extends through Cincinnati and Toledo, Ohio, and dies out in southern Canada. The west branch, the Kankakee Arch, extends northwestward through Indiana and fades out near Chicago, Illinois (Figure 2.1).

The Findlay Arch is the structure that most affects the geology in southern Ohio. The crest of the arch dips gently northward at about 10 ft / mile (2 m/km) causing the formations around it to crop out in an arcuate pattern (Kaufmann, 1964). On the east flank of the arch, the strata dip eastward at approximately 15 to 40 ft / mile (2.8 to 7.6 m/km) (Miller, 1955; Kaufmann, 1964). The Findlay Arch as a whole is believed to be the product of differential subsidence rather than uplift. During the period of sediment deposition, subsidence in the Appalachian and Mississippi Basins occurred at a much faster rate than along the crest of the arch. This is illustrated by the lateral differential thickening of some of the formations, particularly the Cincinnatian group of formations and the Ohio Shale (Stout, 1941).

2.1.4- Waverly Arch

The Waverly Arch is a controversial structural feature. Woodward (1961) reported the existence of a broad low concealed arch extending through central Ohio from Lake Erie into eastern Kentucky (Figure 2.9). The Waverly Arch was Woodward's explanation for the thinning of the Cambrian and Lower Ordovician strata in central Ohio, and absence of the Beekmantown Dolomite in certain stratigraphic sections and isopach maps. Woodward (1961) suggested the Waverly Arch was 96 to 128 km (60 to 80 miles) wide, 480 km (300 miles) long and 230 m (750 ft) in amplitude and uplifted during the Cambrian. The axis of the Arch axis trends north-south in central Ohio (Figure 2.9) at the town of Waverly, in Pike County, Ohio, after which it was named.

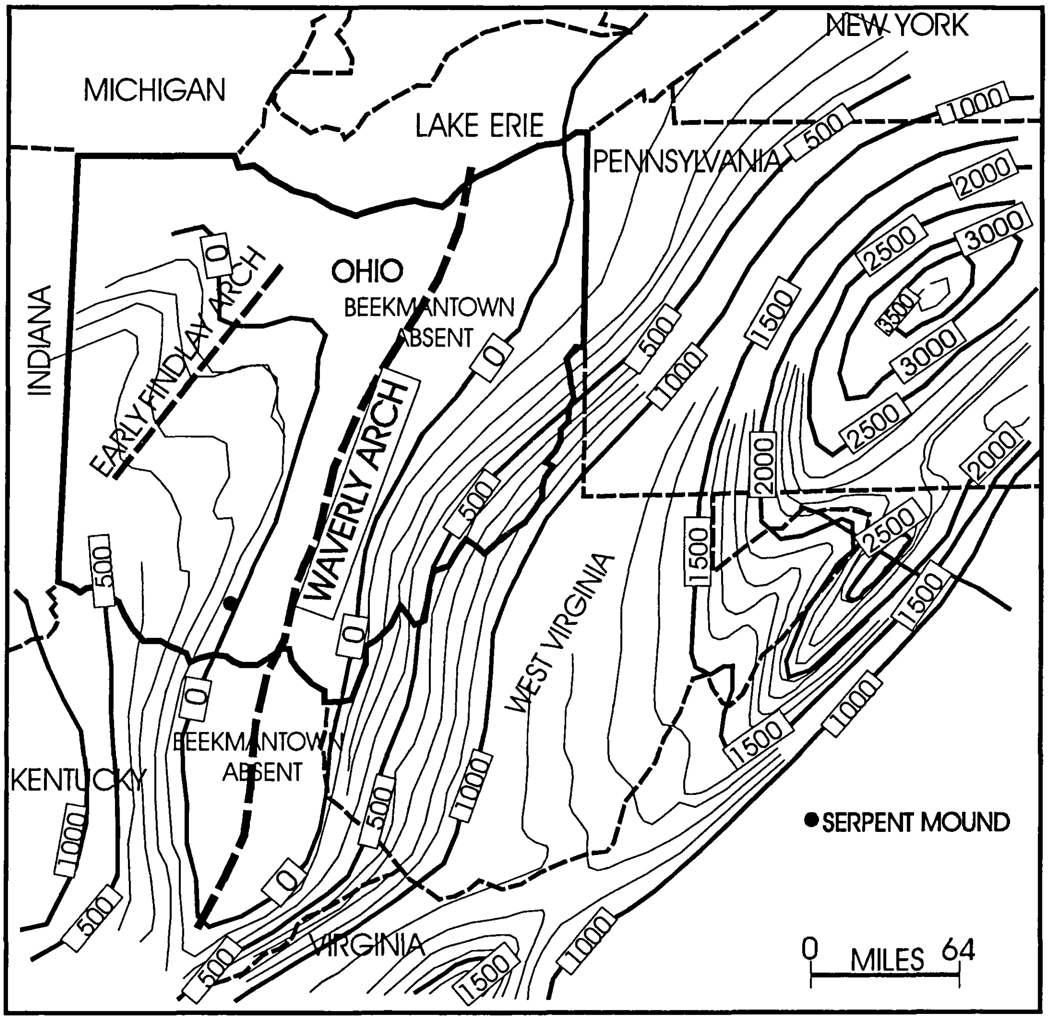

Figure 2.9- Waverly Arch of Central Ohio as proposed by Woodward (after Woodward, 1961)

Sediments of the middle Ordovician age and younger were not affected and no surface expression of the arch was noted. Although Woodward (1961) did not directly implicate the Precambrian basement with the presence of the Arch; Cable and Beardsley (1984); and Riley, et al. (1993) speculated that the Waverly Arch was related to episodic movement of the Precambrian basement. Movement along the Waverly Arch and Kentucky River Fault System was limited primarily to the Cambrian. It has since been suggested by Calvert (1974) that the Waverly Arch may not exist and that no well defined thinning of Cambrian and Lower Ordovician strata occurs along Woodward's Waverly Axis. Calvert attributes the original recognition of the Waverly Arch by Woodward to the latter's use of the Knox Unconformity as the datum surface for the geologic cross sections constructed during the study. Calvert (1974) demonstrates how an erosional valley may be misinterpreted as evidence for arching. An erosional valley filled with shale may be converted into an anticlinal structure capped by shale when the unconformity is used as the datum surface (Figure 2.10). This occurs because of flattening of the erosional surface, when used as a datum, causes depression of the valley walls relative to the valley floor and an apparent arching of the underlying strata. Owens structure map of the Precambrian of Ohio (1967) shows no trace of a large arch other than the Findlay Arch in the northwest section of Ohio. The regional gravity map of Ohio (Heiskanan and Uotila, 1956) shows nothing that would indicate such large displacement. The magnetic anomaly map also shows no evidence for the Waverly Arch in the magnetic basement.

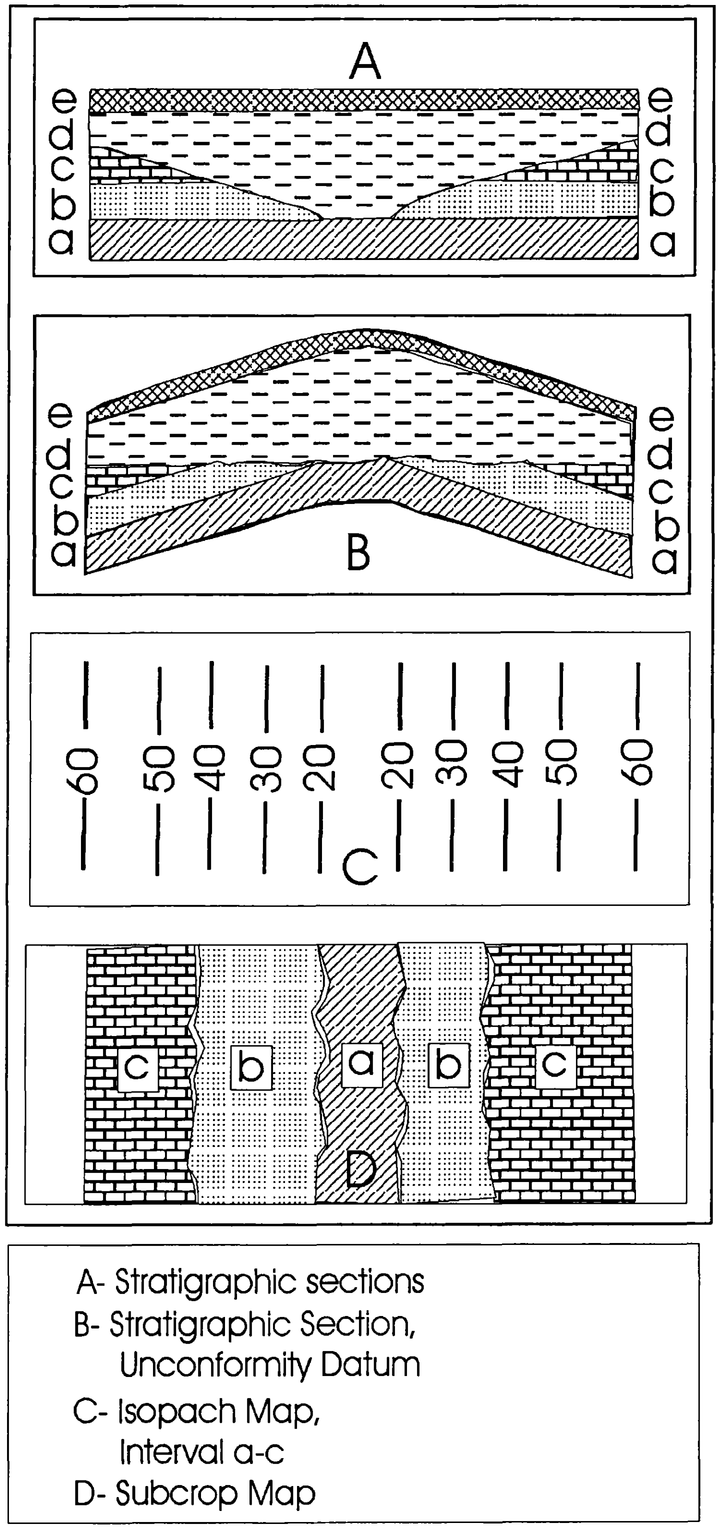

Figure 2.10- Palaeovalley Converted to apparent arch

(after Calvert, 1974)

2.2- Regional Stratigraphy

2.2.1- Introduction

Due to the sparcity of deep wells within the area of the Serpent Mound Structure, little is known about the Precambrian basement. Two deep wells have been drilled a few km south of the structure in Jefferson Township, Adams County, (Figure 2.7). Janssens (1973) mentioned that the upper 60 ft (20 m) of the Precambrian is composed of granitic rocks in these two wells.

Unconformably overlying the Precambrian basement is a thick sequence of Palaeozoic sedimentary rocks. The Palaeozoic rocks of Ohio range in age from Cambrian to Pennsylvanian in the east, and to Silurian in the west, where the Serpent Mound Structure is located (Figure 2.11). Clastic sediments dominate the Palaeozoic of eastern Ohio, while western and central Ohio are dominated by carbonates. During the Palaeozoic the development of the highland to the east was due to continental collision (Acadian, Taconic, and Allegheny Orogenies), and the shedding of clastic detritus westward into the shallow seas that once covered Ohio. The Palaeozoic rocks were exposed to erosion in the Mesozoic and the Cenozoic.

In western Ohio mostly Silurian rocks are exposed. The undeformed bedrock sequence adjacent to the Serpent Mound Structure consists of approximately 3500 ft (1067 m) of Palaeozoic sedimentary rocks. Stratigraphic variations and major unconformities in southern Ohio may be related to the Grenville Front and Waverly Arch, and include facies variations along a north-south trend in the Cambrian Mount Simon Sandstone, Eau Claire and Rome formations, Knox Dolomite (Rose Run Sandstone), and Silurian-Devonian unconformities. The Mount Simon Sandstone changes from dominantly quartz sandstone in the west to the dominantly dolomite of the Rome Formation to the east. The Eau Claire Formation changes from mostly sandstone, siltstone and shale in the west to the dominantly dolomite of the upper part of the Rome Formation and shale, limestone and dolomite of the Conasauga Formation to the east . The Knox Dolomite (Rose Run Sandstone) also changes in this area interfingering with dolomite to the west.

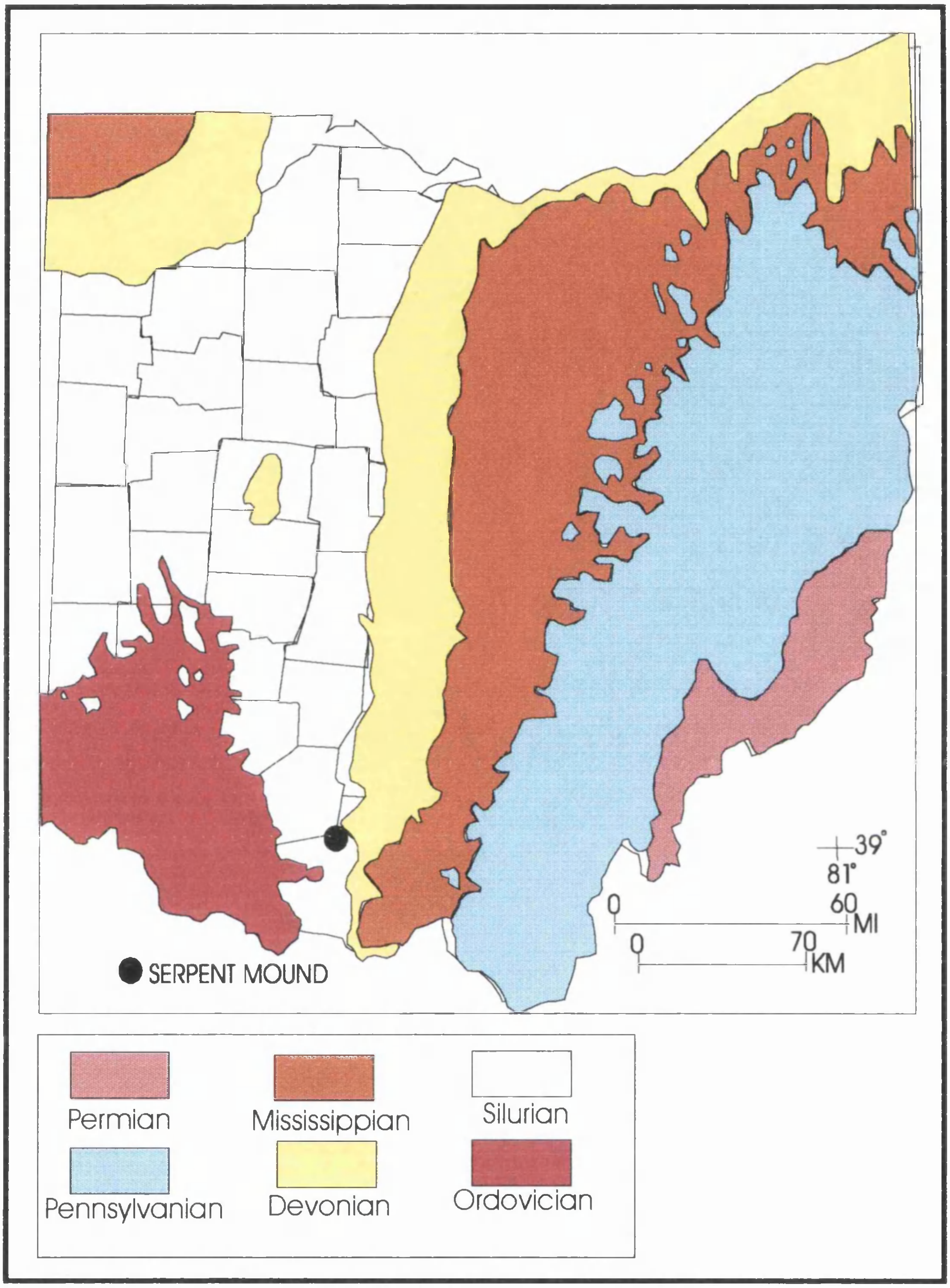

Figure 2.11- Geologic Map of Ohio

2.2.2- Precambrian

Little is known directly about the Precambrian of this part of Ohio, because of the small number of wells drilled that penetrated the Precambrian surface. Historically, the thick cover of sedimentary rocks in Ohio has restricted geologic investigation of the Precambrian crystalline basement complex. Lucius (1985) gave a summary of deep well data (Figure 2.7). The wells are not evenly distributed throughout Ohio. Few wells penetrate more than 100 ft (30 m) into the Precambrian, so that the lithologies encountered may not be indicative of the rocks at depth. Patterson (1980) conducted a low-altitude aeromagnetic survey to investigate the crustal geology of south-central Ohio, Lucius (1985) compiled aeromagnetic anomaly maps and revised gravity anomaly data to present a model of the basement geology of Ohio.

Based on petrologic descriptions, the basement surface of Ohio can be divided into two contrasting lithologic provinces. A transition zone approximately 30 to 50 km wide (Lucius, 1985) separates the provinces extending north-south from Lucas and Sandusky counties in the north to Brown and Adams counties in the south (Figure 2.7). This lithologic transition zone separates rocks to the east that have been subjected to various degrees of metamorphism and deformation from those to the west that are relatively undisturbed igneous and metasedimentary rocks. Precambrian basement rocks in the vicinity of the Serpent Mound Structure consists predominantly of granite gneiss, schist, amphibolite, and marble based on the work of Bass (1960), McCormick (1961), and Gonterman (1973). The depth to the basement surface in the Serpent Mound area ranges from –3400 to –3900 ft (-1036 m to –1189m) below sea level based on the seismic and well control data.

2.2.3- Cambrian

The Cambrian sequence in southern Ohio (Figure 2.12) is divided into the following formations, based on the subsurface geological data and well logs. These formations, from oldest to youngest are the Mt. Simon Sandstone, Rome Formation, the Conasauga Formation, the Kerbel Formation, and the lower part of the Knox Dolomite. Descriptions of the formations follow:

Mt. Simon Formation:

The Mt. Simon Sandstone, unconformably overlying the Grenville granites of the late Precambrian, was first named by Ulrich (Walcott, 1914) for sandstones on Mt. Simon near Eau Claire, Wisconsin. In general, the Mt. Simon Sandstone in Ohio is a fine to coarse-grained sandstone. Locally, the basal portions consist of conglomeratic sandstone, or sandy conglomerate, which grades upward into typical well sorted, pure Mt. Simon Sandstone (Figure 2.12). Colour ranges from colourless at top to colourless, pink, or yellowish at the base. The Mt. Simon Sandstone is mainly poorly consolidated but siliceous cement has been found in a few wells (Janssens, 1973). By definition of the upper boundary, glauconite is absent in the upper portions of the Mt. Simon Sandstone in western Ohio. Glauconite is present in very minor amounts in other areas. Near the study area, the average thickness of the Mt. Simon Sandstone ranges from 100 to 140 ft. (30 to 43 m). This thickness is largely determined by the topography of the underlying Precambrian surface (Janssens, 1973). Density logs from wells near the Serpent Mound structure show the average bulk density for Mt. Simon Sandstone is approximately 2.58 gm/cc.

Rome Formation:

Overlying and in gradational contact with the Mt. Simon Sandstone is the Rome Formation (Figure 2.12), named by Hayes (1891) for sandstone underlying the Conasauga Formation and overlying the Weisner Quartzite in Rome, north-western Georgia. Calvert (1962) first applied the name Rome Formation to strata in Ohio in the Kewanee no.1 Hopkins well in Fayette County. Here, the Rome Formation consists of very fine to coarse grained, poorly sorted, nonglauconitic, dolomitic sandstone interbedded with minor oolitic and pelletal sandy dolomite (Janssens, 1973). Thickness in the study area ranges from 285 to 300 ft. (87 to 91 m). The Rome Formation has an average bulk density of about 2.66 gm/cc. The Rome Formation is dominantly sandstone in south-central Ohio, where a thick north-south trending sandstone facies occurs. East of the disturbed area the Rome Formation is primarily dolomite of the Eau Claire Formation (Janssens, 1973).

Conasauga Formation:

The Conasauga Formation was named by Hayes (1891) for alternating beds of calcareous shale and limestone in the Conasauga Valley in northwestern Georgia. Calvert (1962) was the first to use the name Canasauga in Ohio. He assigned an 87 ft (26.5 m) thick sequence of glauconitic, very fine grained sandstone and green micaceous shale in the no.1 Hopkins well to the Conasauga Formation. The Conasauga Formation of Ohio has three litofacies: A, B, and C (Janssens, 1973). Lithofacies A, the only one present in the study area, is sequence of interbedded red and green shale with minor amounts of partly glauconitic siltstone, very fine grained sandstone, and limestone. The limestone is in part dolomitized. The average thickness of the Conasauga Formation (Figure 2.12) in the study area is about 300 ft. (91.5 m). An average bulk density of 2.70 gm/cc was estimated for this formation from the well logs.

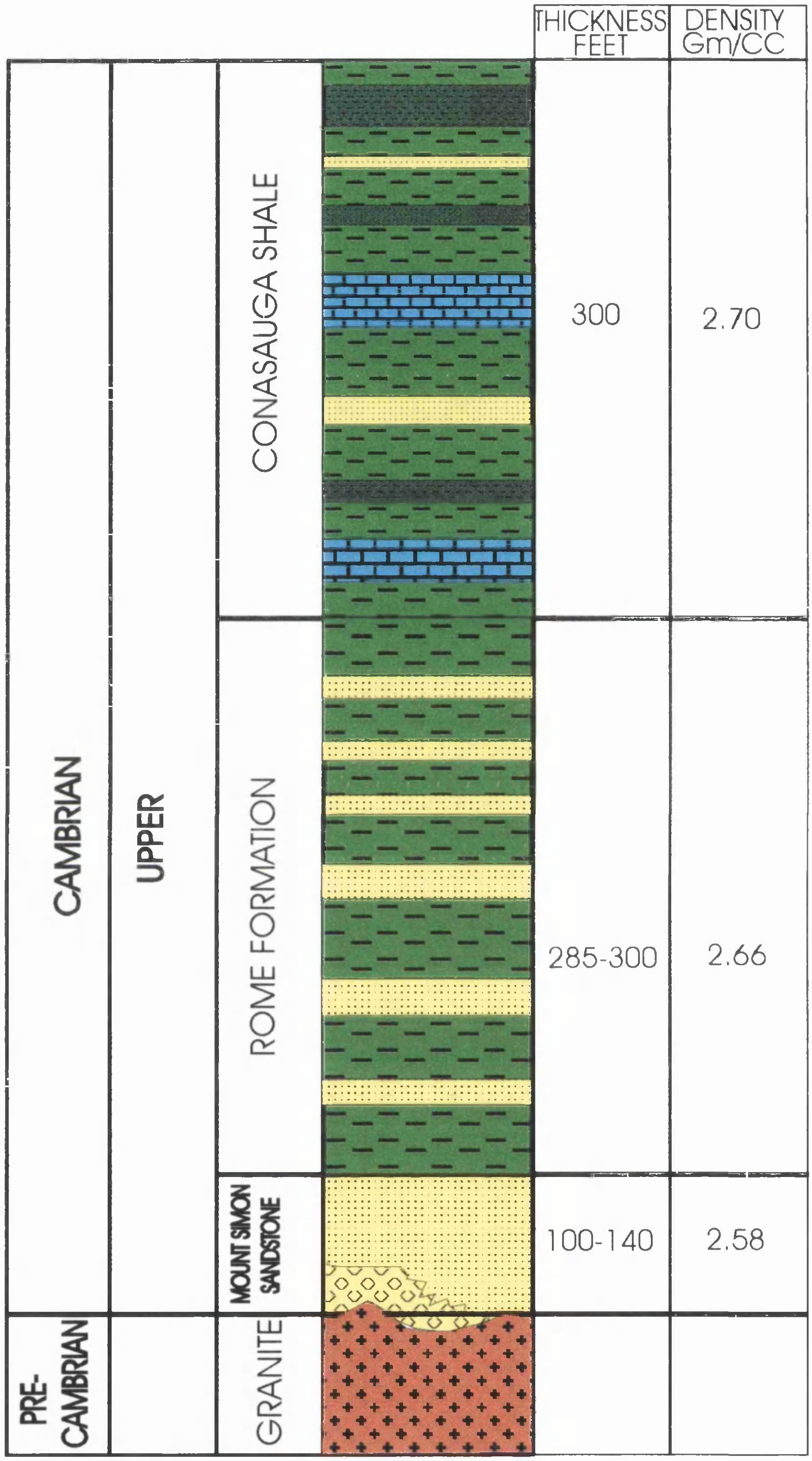

Figure 2.12- Cambrian Stratigraphic Section of Southern Ohio

Kebrel Formation:-

The Kerbel Formation (Figure 2.13) consists of fine to coarse-grained sandstone, siltstone, and dolomite (Janssens, 1973). The Kerbel Formation is interpreted as a deltaic fan related to the underlying marine facies of the Conasauga Formation. The Serpent Mound Structure is located near the southern limit of the Kerbel. To the south and west, the Kerbel intertonges with the basal Knox Dolomite. The Kerbel is 157 ft (48 m) thick, with an average density of 2.69 gm/cc .

2.3.4- Ordovician

Knox Dolomite:-

The Cambro-Ordovician Knox Dolomite (Figure 2.13) is in gradational contact with the underlying Kerbel Formation. The Knox Dolomite in this report refers to the rocks between the top of Kerbel Formation and below the regional Knox unconformity (Janssens, 1973). The Knox consists of dolomite and sandstone with some localised deposits of limestone. Pellets and oolites are common in the dolomite and are frequently found in association with pelletal and oolitic chert. Partial to nearly complete solution of these dolomite and chert pellets is also common and is the most common source of porosity in the formation. The Knox is divided into the Copper Ridge, Rose Run Sandstone, and Beekmantown (Figure 2.13).

The Rose Run Sandstone is the only persistent sandstone throughout the Knox Dolomite The name Rose Run Sandstone was first used by Freeman (1949) for about 70 ft (21.3 m) of sandstone in the Judy and Young no: 1 Rose Run well, Bathe County, Kentucky. The sandstone is poorly consolidated, fine to coarse- grained, slightly dolomatic, in some places glauconitic, and interbedded with sandy dolomites. In the upper portions, sandstone is the dominant lithology, but in the lower portions of the Rose Run, dolomite is more abundant. Baranoski (1993b) and Riley and others (1993) mapped the inferred southern limit of the Rose Run Sandstone subcrop as passing just north of the Serpent Mound disturbance with Beekmantown Dolomite in the vicinity of the disturbance.

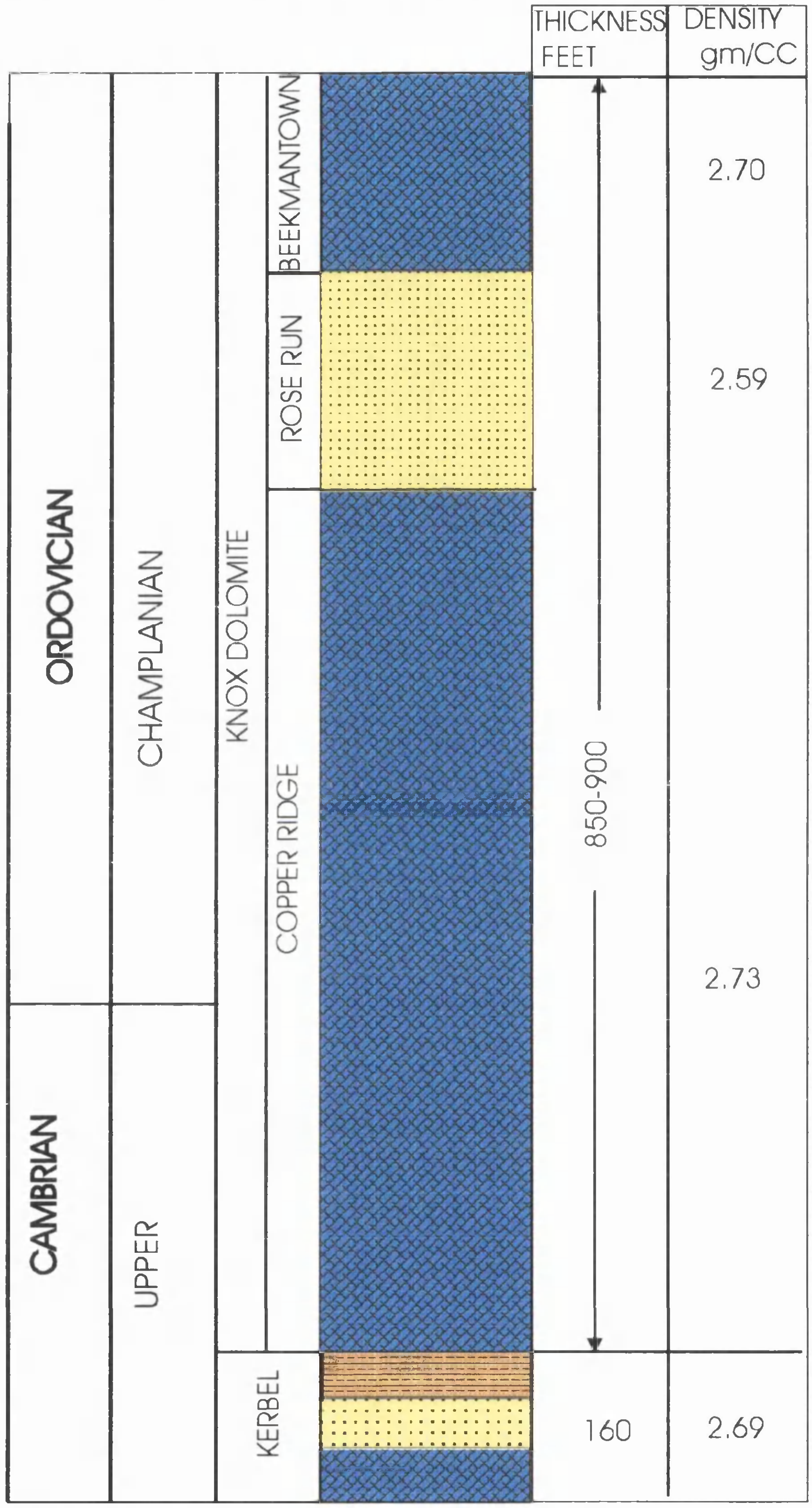

Figure 2.13- Cambro-Ordovician Stratigraphic Section of Southern Ohio

The Rose Run Sandstone apparently changes to a carbonate dominated sandstone west of the Waverly Arch, which would include the area occupied by the Serpent Mound Structure (Riley and others, 1993). The upper part of the Knox Dolomite found in cores DGS 3274 and DGS 3275 may correlate with the Rose Run Sandstone. Total thickness of the Knox Dolomite (Beekmantown, Rose Run, and Copper Ridge) in the study area ranges from 830 to 850 ft. (253 to 259 m). Janssens (1973) found the Knox Dolomite to be much thicker to the south, where it reaches 1100 ft (335 m)at the southern border of Adams County. This large change in thickness can be attributed to three factors: 1-) depositional thinning in the Knox Dolmite; 2-) local relief at the top of the formation caused by erosion prior to middle Ordovician; and 3-) regional truncation to the west due to erosion.

The Knox Dolomite found in the cores DGS 3274 and DGS 3275, correspond to the upper part of this unit and consists of dolomite and sandy dolomite interbedded with quartz sandstone and rare shale. Average densities for the Knox Dolomite units are, 2.7 gm/cc for the Beekmantown , 2.59 gm/cc for the Rose Run Sandstone, and 2.73 gm/cc for the Copper Ridge.

<u>Wells Creek Formation</u>:

Calvin (in Stout, 1941) first named the Glenwood Shale (Wells Creek Formation), which unconformably overlies the Knox Dolomite (Figure 2.14), for deposits in Iowa. In Ohio, a sequence apparently correlative with the Glenwood Formation exists above the Knox unconformity (Stout, 1941). This formation consists of green, grey, and brown shales, siltstone, sandstone, and argillaceous and sandy dolomite (Janssens, 1973). According to Stout (1941), the outstanding feature of the formation is the green colour, primarily caused by the presence of celadonite, sericite, and biotite. These minerals appear to be present as a weathering products of carbonate rocks rather than through direct deposition (Stout, 1941). Thickness of the Formation in the study area is approximately 25 ft. (7.6 m). This Formation have been named Glenwood Shale, Glenwood-St. Peter of drillers, and lower dolomite member of the Chazy Limestone, and the Wells Creek Formation (Janssens, 1973), The name, Wells Creek Formation was preferred by Janssens (1973) and adopted by later workers studying the stratigraphic sequence

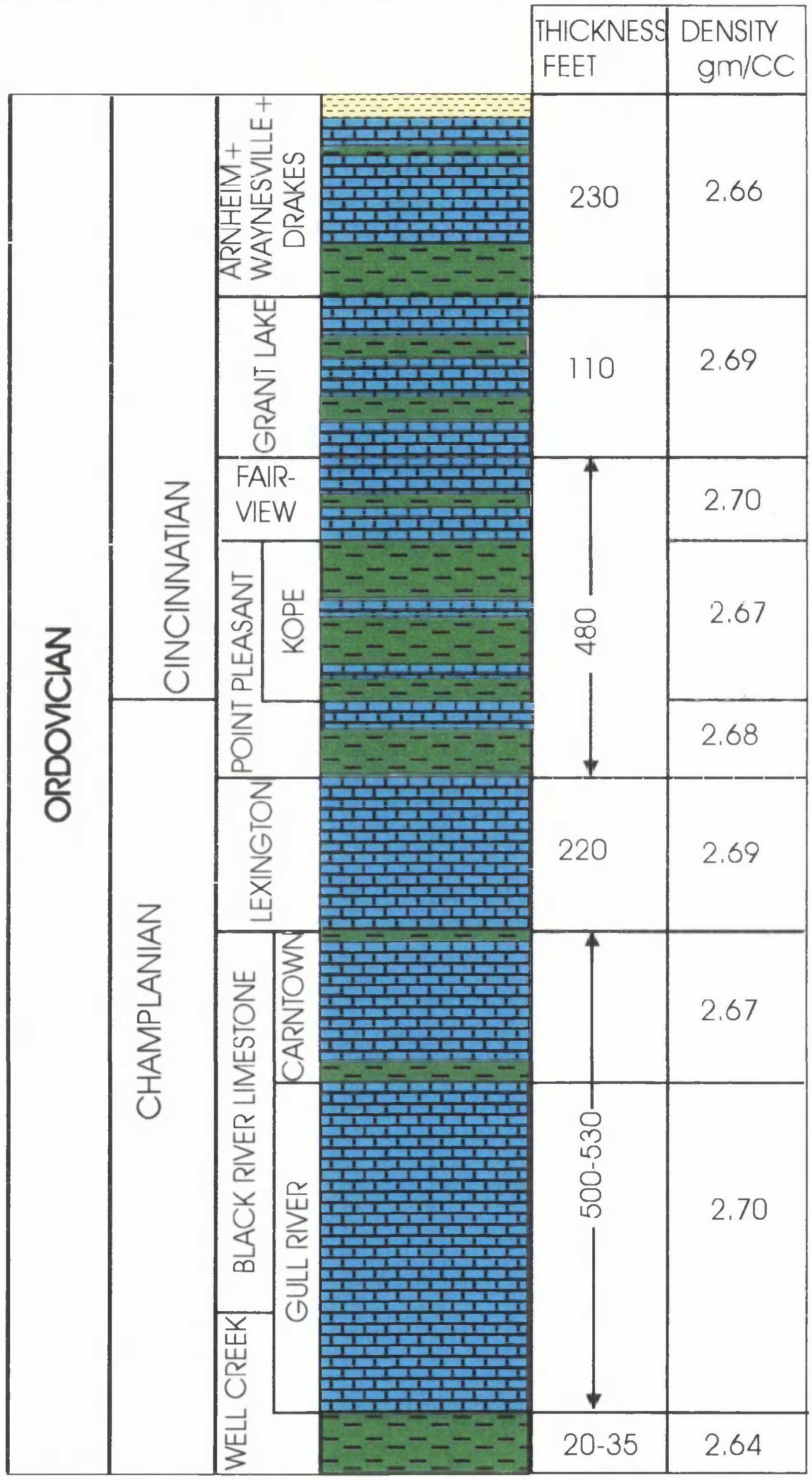

Figure 2.14- continued Ordovician Stratigraphic Section of Southern Ohio

(e.g. Stith,1979, 1986; Riley and others, 1993) and this study. The average bulk density of the Well Creek Formation is 2.64 gm/cc.

Black River Group:-

The Black River Limestone (Figure 2.14) is a finely crystalline, light to light-bluish grey, hard limestone. It is thinly to massively bedded and locally contains some shaley partings. Some layers are cherty and others are oolitic. The thickness of the Black River Limestone in the study area ranges from 500 to 530 ft. (152.4 – 161.5m). It consists of the Carntown, Gull River, and Lower Unit based on geophysical well logs. The average bulk density for the Carntown is 2.67 gm/cc, and for the Gull River is 2.7 gm/cc. Limestone with subordinate dolomitic and skeletal limestone interbedded with minor shale characterise the Black River Group in both cores DGS 3274 and DGS 3275. Burrow mottling, calcite-filled burrows and fractures, and Birdseye structures are common in the Black River Group.

Lexington Group:-

Historically, the rocks of the Lexington Limestone of southern Ohio have been named the Trenton Limestone based on the correlation of Newberry (1870) and Orton (1888) between Ohio and New York. The Trenton Limestone is mostly confined to the subsurface in Ohio, though the Point Pleasant Member (upper Trenton) is exposed on the Ohio River at Point Pleasant, Clermont County, Ohio. Orton (1873) named the Point Pleasant Member for about 50 ft (15.2 m) of limestone with shaly partings quarried at Point Pleasant, Ohio. In general, the Trenton appears as a pure limestone with an average bulk density of 2.66 gm/cc (Zinni, 1982), though in areas it becomes dolomitic. In the early 1960's, the United States Geological Survey revised the lithostratigraphy of the Lexington (Black et al. 1965; Cressman, 1973). The name, Lexington Limestone, has been adopted to replace the Trenton Limestone throughout southwestern Ohio, and the Trenton Limeston is now considered an informal drillers' term (Stith, 1986). The Lexington Limestone consists of the rocks between the top of the Black River and the base of Point Pleasant Formation. In the cores DGS 3274 and DGS 3275, the Lexington Limestone consists of three members: the Curdsville Limestone Member, the Logana Member and the Lexington undifferentiated (Stith, 1986). The Curdsville Limestone Member contains approximately 90 percent brownish gray to gray, fossiliferous limestone and 10 percent grey, sparsely fossiliferous shale. A diagnostic brecciated granular chert within the Curdsville Limestone Member and a zone of brachiopod-rich shales restricted to the lower part of the Logana Member were excellent markers used to recognise and correlate between DGS 3274 and DGS 3275. The brachiopod-rich shale is overlain by interbedded olive grey to black. An average thickness of the Lexington Limestone in the study area is 220 ft (67 m) based on geophysical well logs. It has an average density of 2.69 gm/cc.

Point Pleasant, Kope, and Fairview Formations:-

The Point Pleasant, Kope, and Fairview Formations (Figure 2.14) have been successfully traced by Stith (1986) and Bergstrom (1991) in the subsurface of southwestern Ohio. The undeformed stratigraphic section between the top of the Lexington Limestone and the base of the Grant Lake Limestone is approximately 480 ft (146.3 m) of interbedded shale and limestone which is subdivided into the Point Pleasant, Kope, and Fairview Formations. The diagnostic characteristics which differentiate these units are shale percentage, shale bed thickness, and bedding style. The Point Pleasant and Kope Formations were easily identified in the mildly deformed rocks below 725 ft (221 m) in DGS 3275. However, the Point Pleasant, Kope, and the Fairview Formations could not be identified with confidence in DSG 3274 (Baranoski personal communication) and above 725 ft (221 m) in DGS 3275 because of severe to chaotic deformation. Thus two units combined into thicker undivided sequences. Using biostratigraphic information, the Point Pleasant and Kope Formation (Baranoski, 1997) occurred twice in DGS 3274 and was present in DGS 3275. In DGS 3274, the first drilled interval of the Point Pleasant through the Fairview Formations ranges between 225.3 and 1243.5 ft (68.67 and 379 m) and the second occurs between 1696 and 2030 ft. (516.9 and 618.7 m). Within these intervals, faulted blocks usually separated by breccia zones display abundant internal faulting, folding, and brecciation. The average density of the Point Pleasant Formation based on well logs is 2.68 gm/cc.

The Kope Formation (Weiss and Sweet, 1964; Weiss et al, 1965), is a sequence of blueish-grey to brownish-grey, thin bedded shales alternating with slabby limestones. These limestones, which appear to be concentrated more in the lower portions of the formation (Ali, 1967), occur as discontinuous beds. The thickness of the Kope Formation is more than 200 ft (61m) in the study area with an average density of 2.67 gm/cc.

The Kope Formation grades upwards into the interbedded limestone and shales of the Fairview Formation (Bassler, 1911). Grey, medium to coarse-grained limestone makes up about 60% of the total thickness of the formation. Thirty to thirty five percent of the formation thickness is composed of blue-grey, thin bedded, calcareous shale with some siltstones. The thickness of the Fairview is approximately 40 ft (12.2 m) in the study area and density of 2.70 gm/cc.

Grant Lake Limeston:-

Grant Lake Limestone is conformably overlying the Fairview Formation (Figure 2.14). It is a series of irregularly bedded argillaceous limestones and minor interbedded shales named by (Peck, 1966). Peck proposed the name Grant Lake Limestone as a replacement for McMillan Formation Limestone. Thickness of the Grant Lake Limestone in northeastern Adams County is approximately 100 ft, (30 m) and a density of 2.69 gm/cc (Geophysical well logs). The Grant Lake Limestone has been mapped in outcrop and into the subsurface of Adams, Brown, and Highland Counties, Ohio (Schumacher and others, 1991). Three members are recognised: the Bellevue, Corryville, and Straight Creek. The Grant Lake Limestone is defined by having at least 70 percent irregular to wavy-bedded, fossiliferous limestone, and minor amounts of planar bedded fossiliferous to sparsely fossiliferous limestone and shale. In DGS 3274 and DGS 3275 severe to chaotic deformation has folded, fractured, faulted, and brecciated the strata of Grant Lake Limestone into clasts within breccia zones or into fault blocks generally separated by breccia zones.

Arnheim, Waynesville, and Drakes Formations:-

These formations consist of fine to medium grained limestone and alternating shale beds. The shale in most localities is grey to greyish green and calcareous. Locally, shales grade laterally to calcareous mudstones. Most limestones in the formation are grey, with coarse-grained fossil fragments in a fine grained matrix, and are thin to medium bedded. In core DGS 3275, the Drakes Formation is approximately 80% dolomitic to calcareous shale with minor interbedded limestone. Shale beds are variable in colour from bluish grey to greenish grey to dark reddish grey. The Drakes Formation is distinguished from the underlying Waynesville Formation and the overlying Brassfield Formation by the abundance and colour of the shale beds. The total average thickness of (Drakes, Waynesville, and Arnhiem) in the study area (Figure 2.14) is 230 ft (70.1 m) with an average density of 2.66 gm/cc based on geophysical well logs.

2.2.5- Silurian

The Silurian sequence in southern Ohio (Figure 2.15) is divided into three groups: the Medina Group, Niagara Group, and the Bass Island Group. The Medina Group, the lowermost group in the Silurian section, is represented here by the Brassfield Limestone.

Brassfield Limestone Formation:-

The Brassfield Limestone is hard, dense, fossiliferous, and thin to medium bedded. In Adams County, it usually occurs in one to four layers, is very ferruginous in composition, dark brown to reddish brown in colour, and oolitic in texture. The ferruginous layers usually appear about the middle of the formation. The ferruginous material in these layers, limonite and hematite, appear to be primary in origin (Stout, 1941). In the study area, the Brassfield Limestone has a thickness of approximately 50 ft, (15.2 m); it is a thick-bedded, white limestone with thin shale beds. A prominent hematitic fossil zone near its top is an important stratigraphic marker throughout the area (Reidel, el al, 1982). Some thin beds of the Brassfield Formation are nearly pure hematite (Figure 2.15). The Brassfield generally weathers to a light yellow colour.

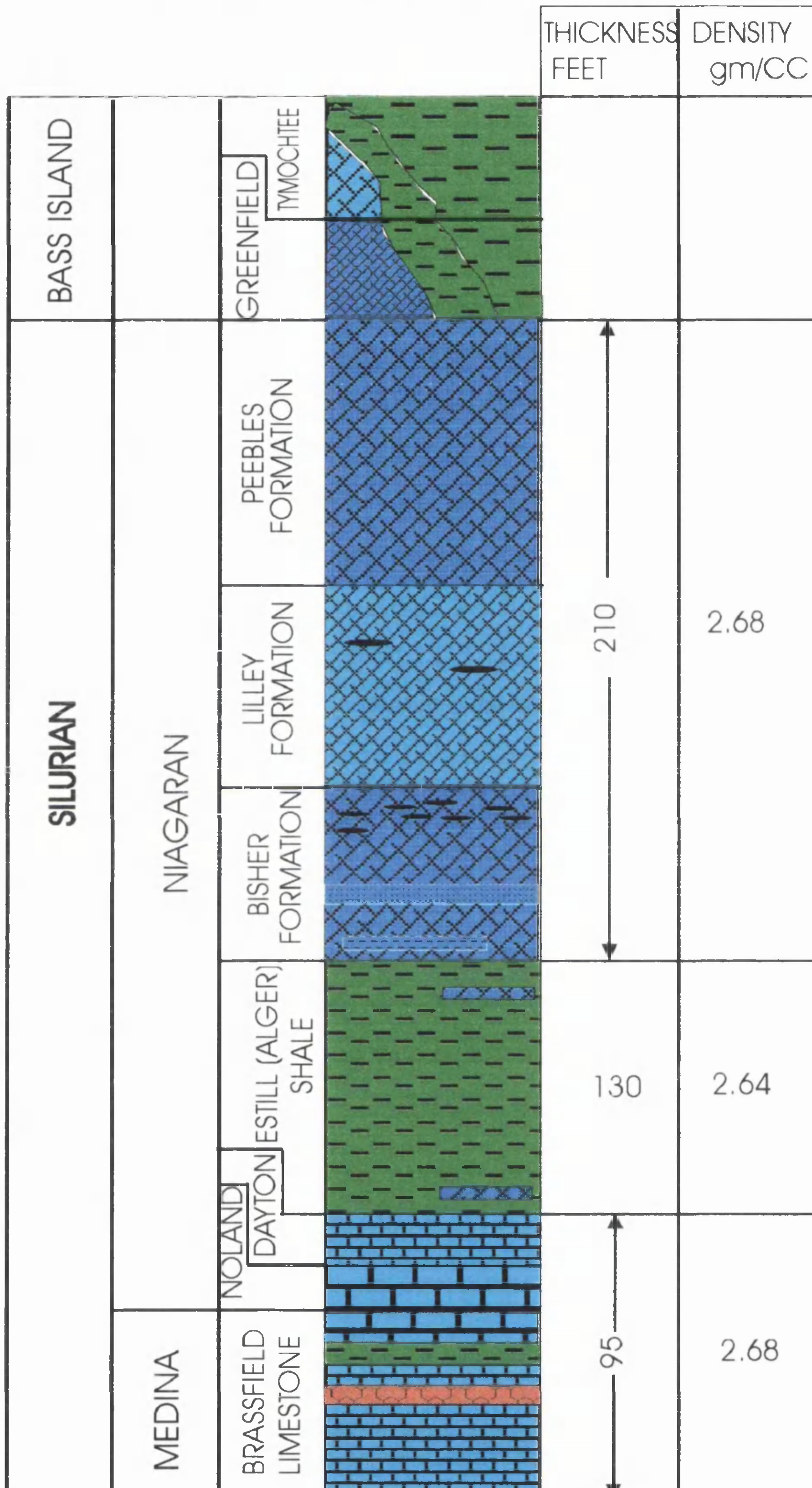

Figure 2.15- Silurian Stratigraphic Section of Southern Ohio

Noland Formation:-

Rexroad et al. (1965) subdivided the lower Silurian rocks of Adams County, Ohio, into the Brassfield Formation overlain by the Noland Formation and Estill Shale of the Crab Orchard Group. The Noland Formation was subdivided into a lower undifferentiated unit overlain by the Dayton Limestone Member. Horvath (1967) observed that the Brassfield Formation thickens to the east and is separated from the Dayton Member of the Noland Formation by an expanding wedge of shale and carbonate units eastward. In the region of the Serpent Mound Structure, he noticed that the undifferentiated unit of the Noland Formation thinned and pinched out in southern Highland County, Ohio. Rexroad et al. (1965) and Swinford (1985) noticed a similar trend in this region northward. In the cores DGS 3274 and DGS3275 the Brassfield and the Noland Formations were undivided because the contact between them could not be picked.

Dayton Limestone:-

The Dayton Limestone belongs to Niagara Group (Figure 2.15), which was named by Vanuxem (1842) for exposures at Niagara Falls, New York, and adopted by Orton (1871) for formations in Adams and Highland Counties, Ohio. The Niagara of southern Ohio consists of the following formations, from oldest to youngest are

Dayton Limestone
Alger Shale (Estill Shale)
Bisher Formation
Lilley Formation
Peebles Dolomite

The Dayton Limestone was named by Orton (1871) for the exposures near Dayton, Ohio. The formation is a siliceous, limey dolomite, changing locally to limestone. Layers are evenly bedded with thickness varying between 3 inches and 2 ft. (0.08 and.0.61 m). The thickness of the formation in Adams County, Ohio reaches a maximum of 6 ft. (1.8 m). Based on the geophysical well logs, the average thickness of

Noland, Dayton, BrassField, and Belfast Member in the study area is 95 ft (29.0 m), with an average bulk density of about 2.68 gm/cc.

Estill (Alger) Shale :-

Regionally, the Alger shale (Orton, 1871) is correlative with the Rochester Shale of New York (Stout, 1941). In general, the Alger is a soft calcareous and ferruginous shale, locally containing dolomite beds. The Rochester Shale formally called the Crab Orchard Shale (Reidel et al. 1982), lies above the Brassfield Limestone and consists of alternating red and green clay shale with rare fossils. Lenses of finely laminated limestone and dolomite are intercalated with the shale near the bottom and the top of the unit (Figure 2.15). In 1897, Foerste divided the Alger into three members: the basal Osgood Member after Osgood, Indiana; the medial Laurel Member after Laurel, Indiana; and the uppermost Massie Member for exposures on Massie Creek, Greene County, Ohio. The Osgood Member is primarily a soft calcareous clay shale with a few thin beds of dolomite. The Laurel Member is a finely crystalline, dense, hard, thin to medium bedded dolomite. The Massie Member is a soft calcareous shale clay shale of about 6 ft (1.82 m) in thickness. Foerste (1906) introduced the Estill Clay Member of the Alger Formation when he described the rocks exposed near Estill Spring located in east-central Kentucky near the town of Irvin. Rexroad and others (1965) proposed that the name of the Alger Formation be abandoned from Ohio and be replaced by the Estill Clay Member evaluated to formational status. Thus the Estill Shale has been adopted by subsequent stratigraphers. Shale interbedded with minor dolomite and limestone characterises the lithology of the Estill Shale. The Estill Shale in DGS 3275 has undergone mild to severe deformation which removed part of the formation. Well logs show an average thickness of Estill Shale of 130 ft (39.6 m), and with average density of 2.64 gm /cc in the study area.

Bisher, Lilley, and Peebles Formations:-

Overlying the Estill (Alger) Shale is the West Union Formation, which Orton (1871) named for exposures near West Union, Adams County, Ohio. In 1917, Foerste divided the West Union into the upper Lilley Formation and the lower Bisher

Formation (Figure 2.15). The Bisher and Lilley Formations lie above the Esill Shale and have a combined thickness of 85 ft (25.9m) (Reidel et al.1982) of silty, grey to blue grey dolomite which weathers to a characteristic red brown colour. The brachiopod *Cryptothyrella cylindrica* is a prominent marker fossil near the base. The Bisher Formation is a massive dolomite, usually impure in composition. Silty to sandy shale and shaley dolomite horizons may occur in any portion of the formation and may make up the bulk of the lower part of the section. Thin, fossiliferous chert layers may be present in the upper Bisher (Figure 2.15), particularly in the area of the Serpent Mound Structure (Stout, 1941).

The Lilley Formation was named for exposures on Lilley Hill near Hillsboro, Highland County, Ohio. It is coarsely to finely crystalline dolomite, light blue in colour, often crinoidal, and locally stained by bituminous impregnation. The thickness in Adams County is approximately 60 ft (18.2 m). The Bisher and Lilley Formations have been subjected to severe deformation in DGS3275. Parts of these units may have been removed by faulting.

The uppermost formation in the Niagara Group is the Peebles Dolomite (Foerste, 1929). This formation was previously named the Cedarville Formation by Orton in 1871. It has a porous structure and a sugary crystalline texture, but is locally dense. Bedding is always massive. Thickness of the Peebles Dolomite varies from 40 to 120 ft 36.6 m), depending in part on the unconformity which is locally present at the top (Stout, 1941). Iron ore deposits may occur in pockets of the upper surface.
Reidel et al. (1982) describe the Peebles Dolomite as a reef dolomite with numerous vugs containing natural asphalt. Average thickness of Peebles, Lilley, and Bisher Formations in the Study area is 210 ft (64.0 m), with average density of 2.68 gm/cc (Well log data).

Greenfield and Tymochtee Dolomites:-

The Bass Island Group, the uppermost group of the Silurian section, was named by Lane, Prosser, Sherzer, and Grabau in 1907. In Adams County, it consists of the Greenfield Dolomite and the Tymochtee Dolomite. The Greenfield Dolomite (Carman, 1927) is fine grained and commonly occurs in beds of 2 to 6 inches with carbonaceous partings. It is often sugary and vesicular in texture. The thickness is stated to range between 75 and 100 ft (22.9 and 30.5m) (Carman, 1927; Stout, 1941) though in a complete section at the Plum Run Stone Quarry just Southeast of Peebles, Adams County, Ohio, only 25 ft (7.6 m) of Greenfield is present (Miller, 1955). The Greenfield is totally absent in parts of Adams County due to the erosion that occurred at the end of the Silurian and beginning of the Devonian, and in these areas the Ohio Shale rests directly on the Peebles Formation (Stout, 1941; Miller, 1955). According to Reidel et al. (1982) the Greenfield Dolomite unconformably overlies the Peebles Formation in the Serpent Mound area, with the contact marked by pockets of clay. The Greenfield Dolomite is tan, well-bedded dolomite with cross bedding and megaripples.

The Tymochtee Formation (Salina) was originally named the Tymochtee Slate (Winchell, 1873) for a section of fine grained (slatey) beds along Tymochtee Creek in Wyandot County, Ohio. In 1907, Lane, Prosser, Sherzer, and Grabau extended the Tymochtee to include all the shales and limestones exposed in the section along Tymochtee Creek. The Tymochtee Formation generally consists of grey-brown to grey, finely crystalline to aphanic, somewhat argillaceous dolomite. Bedding varies from thin to laminated (Figure 2.15). Thickness of the formation varies, depending on the position of the erosion plane. The combined thickness of the Peebles, Greenfield, and Tymochtee Dolomites is between 110 and 150 ft (33.5 and 45.7 m), these three formations were not differentiated on the geologic map of the Serpent Mound Structure (Reidel et al. 1982). All the Silurian formations contain minor amounts of sphalerite.

2.2.6- Devonian

Erosion at the beginning of the Devonian period removed from the sequence in Adams County many of the formations usually present in the typical Devonian section. The only remaining formations are the Olentangy Shale and the Ohio Shale (Figure 2.16).

The Olentangy Shale is a grey, siliceous, calcareous shale with plastic, clay-like properties. It was named for exposures along the Oletangy River at Delaware, Ohio. In Adams County, the thickness of this unit varies from 0 to 20 ft (0 to 6.1 m) (Reidel, 1975).

The Ohio Shale is a dark grey to black fissile shale, oil-bearing shale with a basal unit of sand and clay shale, containing many pyrite concretions in the lower portions. The Ohio Shale was given its name by E. B. Andrews in 1871. Thickness of the Ohio shale in Adams County is approximately 265 ft (80.8 m) (Reidel, 1975).

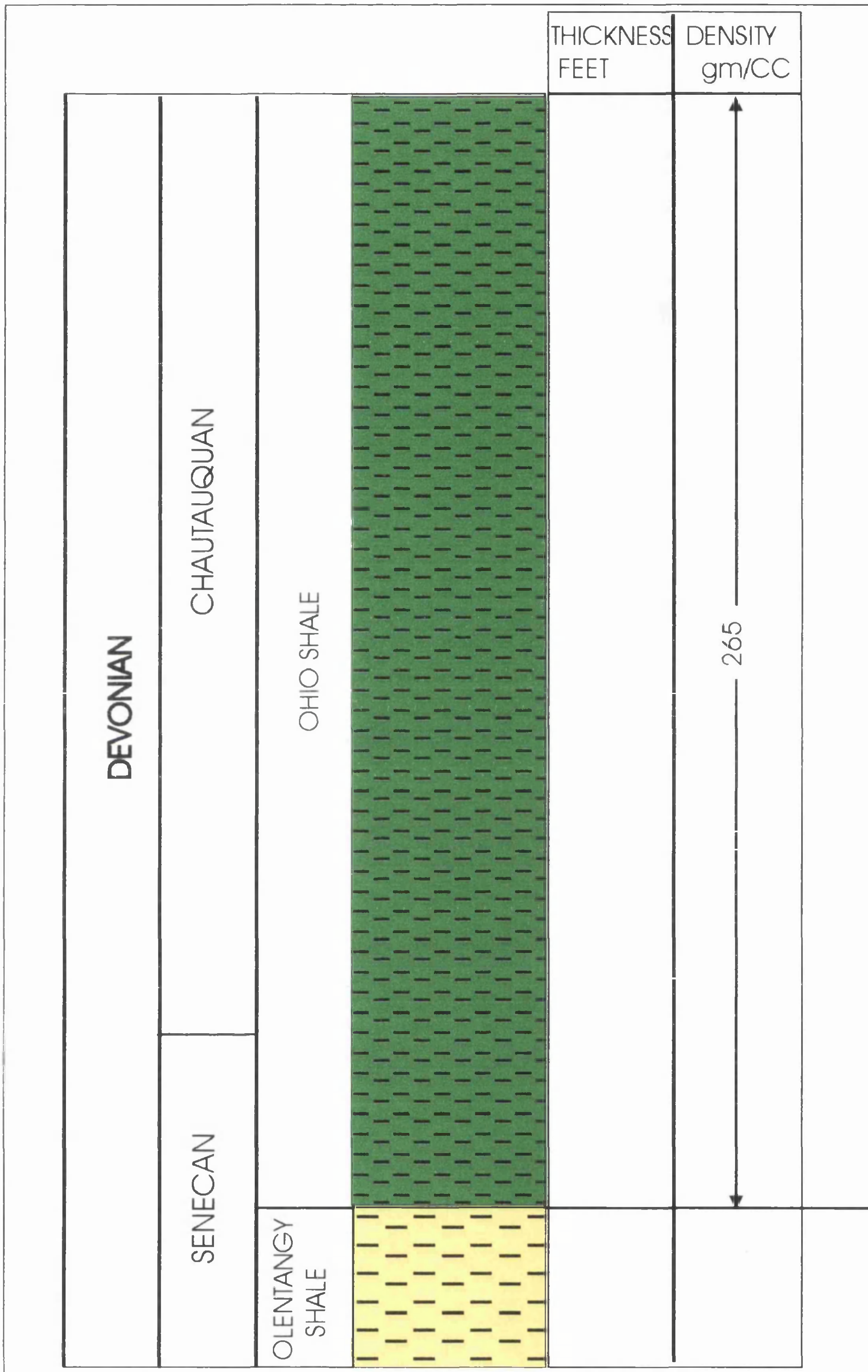

Figure 2.16- Devonian Stratigraphic Section of Southern Ohio

2.2.7- Mississippian

The Mississippian in Adams County (Figure 2.17) may be subdivided, from oldest to youngest (Hyde, 1953) as follows:

Bedford Formation;
Berea Sandstone;
Sunbury Formation;
Cuyahoga Formation;
Logan Formation.

Bedford Formation:-

The contact between the underlying Ohio Shale and the Bedford formation is sharp. According to Hyde (1953), there is some evidence that this contact is disconformable and that, subsequent to the deposition of the basal portions of the Bedford Formation but before the accumulation of the greater thickness, there was movement along the Ohio Shale Bedford Formation contact. This movement was of sufficient character and force to warp the top beds of the Ohio Shale into very low, narrow folds, and to cause the penetration of masses and stringers of each formation into others.

Newberry (1870) named the Bedford Formation for exposures near Bedford, Cuyahoga County, and Ohio. The Bedford in central Ohio is typically shale. In southern Ohio, it ranges in composition from sandstone beds separated by shale partings (Figure 2.17) as found at Buena Vista, Scotia County, Ohio, to very thin platey sandstones with thin shaley partings as it appears in outcrop at Mineral Springs, Adams County, Ohio. Sandstone beds occur more commonly in the upper portions of the Bedford Formation. These strata consist of moderately fine grained, moderately to well sorted, light grey to bluish sandstones and normally occur in beds of 2 to 3 ft (.61 to .91 m) thickness. In many areas, the Lower Bedford consists of sandy shales or thin platey sandstones with thin shale partings. Thickness of the Bedford Formation commonly ranges from 90 to 95 ft (27.4 to 29.0 m).

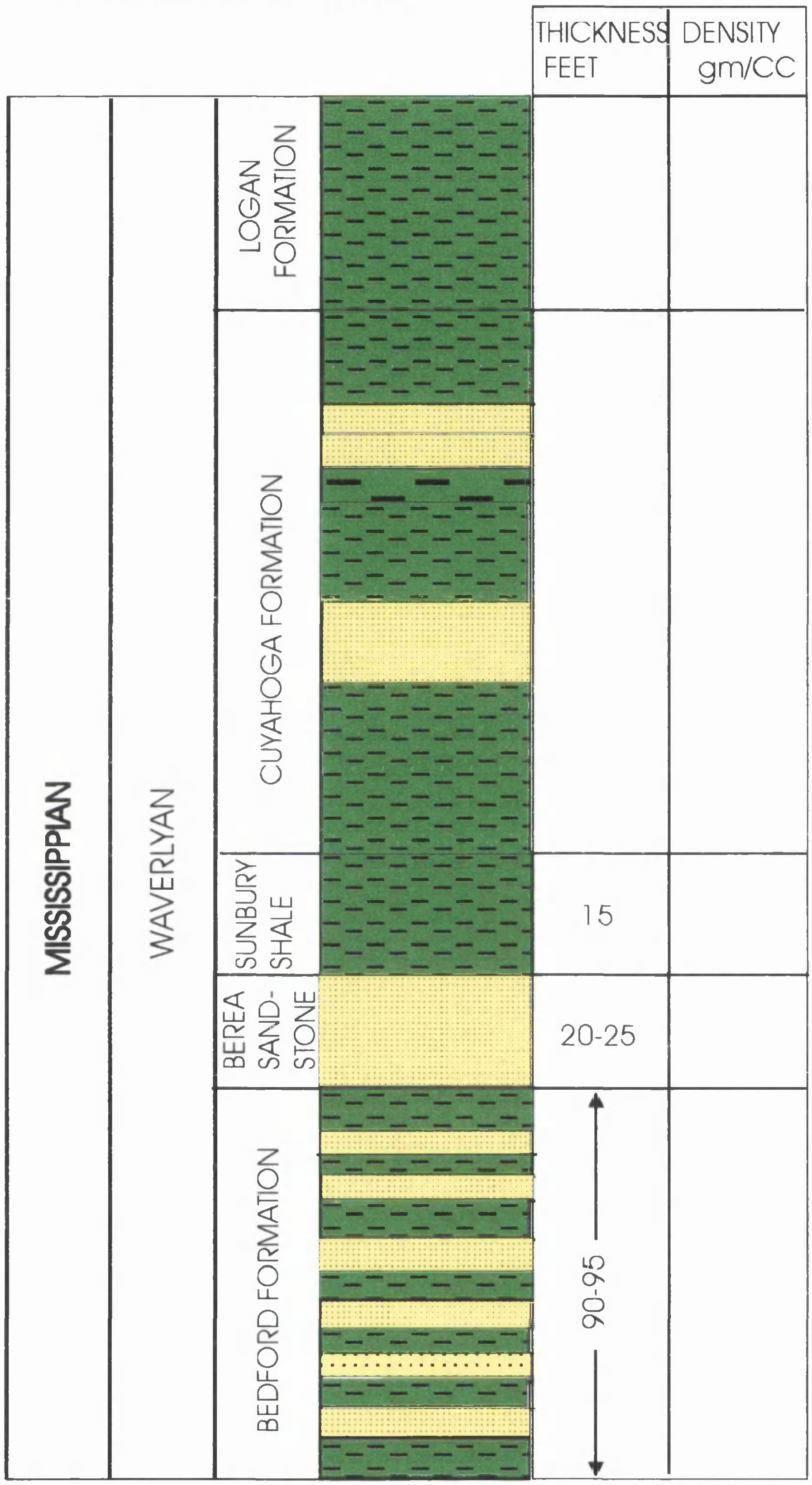

Figure 2.17- Mississippian Stratigraphic Section of Southern Ohio

Berea Sandstone:-

The Berea Sandstone (Figure 2.17) contains moderately coarse to fine grained, grey sandstone beds, in areas separated by thin shale partings. The upper surfaces of these sandstone beds are rippled, as are those of the Bedford Shale. In areas where the upper Bedford contains numerous sandstone beds, it is very difficult to identify the Berea-Bedford contact. However, in many areas the thickness of the transition zone from the Bedford Shale to the Berea Sandstone can vary from zero to 3 ft (.91 m). In most sections, it is impossible to see a horizon above which the sandstone units of the Berea are more numerous than those of the Bedford Shale (Hyde, 1953). The Berea Sandstone is variable in thickness, ranging from about 22 ft (6.7 m) at Rarden, Scioto County, to approximately 35 ft (10.7 m) at Mineral Springs. The thickness may reach 50 ft (15.2 m) or more or may fall as low as 4 ft (1.2 m). Though the thickness has a large range, there is no evidence for an erosional plane between the Bedford and the Berea in Adams County though farther north a disconformable contact does occur (Hyde, 1953).

Sunbury Formation:-

The contact between the Berea Sandstone and the Sunbury Shale (Hicks, 1878) is sharply defined, in many localities appearing as a very thin band of limonite iron produced by oxidation and hydration of a pyrite band which is uniformly present at the contact (Hyde, 1953).

The Sunbury Shale is carbonaceous, tough, fissile, black shale, very similar in appearance to the Ohio Shale. It is frequently more argillaceous toward the top, and in areas of long exposure it may be very difficult to distinguish the Sunburn Shale from the overlying shales of the Cuyahoga Formation. Thickness of the Sunbury Shale is variable, but it generally decreases in thickness to the west. At Rarden, the thickness of the Sunbury is 15 ft (4.6 m) decreasing to 12 ft (3.6 m) at Mineral Springs (Hyde, 1953).

Cuyahoga Formation:-

Hyde (1953) subdivides the Cuyahoga into five members (Figure 2.17) as follows:

1- Henley Member (grey to dark reddish grey shale);
2- Buena Vista Member (hard, moderately coarse, light grey sandstone);
3- Rarden Member (deep red, slightly sand shale);
4- Vanceburg Member (interbedded shales and sandstones overlying a series of sandstone beds separated by thin shale partings);
5- Churn Creek Member (hard, grey, sandy shale).

The Henley Shale Member was named after the town of Henley in Scioto County (Hyde, 1953). It consists of alternating red and grey shales. The red shales disappear to the east along with the sandstones of the Vanceburg Member. The Henley Member increases in thickness both northward and eastward from Henley. The westward thinning of the Henley Member is thought to be indicative of high topographic relief to the west due to the Cincinnati Arch (Hyde, 1953).

The Buena Vista Member was first named by Orton (1874) after a locality near Buena Vista in Scioto County. The Buena Vista member increases in thickness to the east, extending deep into the Scioto Valley Shale Facies, but thins rapidly to the west. and northward, the Buena Vista becomes much more shaley than at its type locality.

The Rarden Shale Member, named after Rarden, Scioto County, (Hyde, 1953) is not recognised outside the limits of the Vanceburg Sandstone Facies, because of the increasing difficulty of the defining its upper boundary with the disappearance of the sandstone facies to the east. The Rarden Member is composed of alternating grey and red shales, thickening to the east and north.

The Vanceburg Member, named after Vanceburg, Kentucky, (Hyde, 1953) is composed of fine-grained sandstones that are typical of the facies. The Vanceburg is about 150 ft (45.7 m) thick at Buena Vista but abruptly disappears into the Scioto Valley Shale Facies to the north and east of Buena Vista.

The Churn Creek Member, named after Churn Creek in Adams County (Hyde, 1953) consists of argillaceous shale with an occasional thin sandstone unit. Thickness ranges from 50 to 100 ft (15.2 to 30.5 m). The Churn Creek Member is only recognised in western Scioto County and eastern Adams County.

Logan Formation

In southern Ohio, the contact between the Logan Formation and the Cuyahoga Formation is transitional. The top 15 ft (4.6 m) of the Cuyahoga Formation contain numerous thin sandstones. Above this interval lies 8 ft (2.4 m) of sandy shale and shaley sandstone overlain by sediments typical of the Logan Formation. The Logan Formation is not present or covered in most of the study area but does occur in outcrop at the head of Churn Creek near the southern perimeter (Hyde, 1953). The Logan Formation, named by Andrews in 1870, is a fine-grained argillaceous sandstone with occasional shale units. It is usually thin bedded but massive bedding does occur. The thickness of this formation near the study area is approximately 60 ft (18.3 m). Due to the poor exposure of the section in Adams County, the Logan Formation cannot be subdivided into members in this area.

Locally, the youngest units of Mississippian involved in the disturbance are the Bedford Shale, Berea Sandstone, Sunbury Shale, and sandstone and shale of the Cuyahoga Formation. The total thickness of the Mississippian strata exposed in the Serpent Mound Structure is 150 ft (45.7 m) (Reidel et al., 1982).

2.2.8- Pleistocene:-

Outwash of the Illinoian glaciation of Pleistocene age lies undisturbed on the northwest edge of the disturbance. Terraces of outwash gravel and recent alluvium in major valleys are primarily derived from the weathered bedrock and glacial till. Figure (2.18) is a generalised stratigraphic nomenclature for the surface and subsurface geology in southern Ohio in the vicinity of the Serpent Mound Structure.

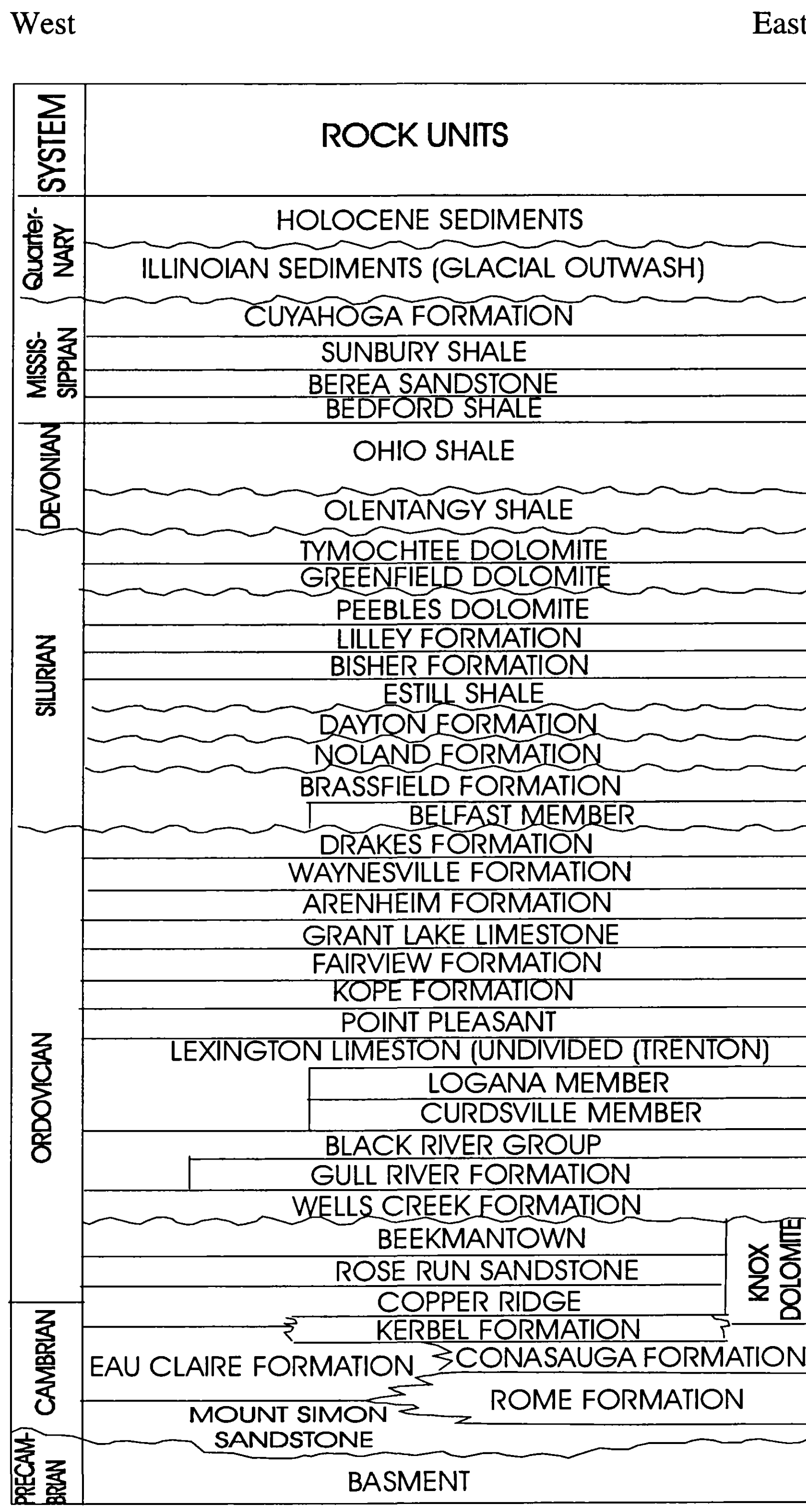

Figure 2.18- Generalised stratigraphy for surface and subsurface geology in southern Ohio (vicinity of the Serpent Mound Structure)

Chapter- 3 IMPACT STRUCTURES

3.1- Introduction

Impact crating is a sudden exogenic process that is violent, relatively rare, unpredictable, and significantly different from those endogenic terrestrial processes, which are generally slow processes leading to gradual changes in the geological record. Impact craters are geologic structures formed when a large meteoroid, asteroid or comet smashes into a planet or a satellite. The phenomena most characteristic of impact are the irreversible changes in the crystal structure of rock-forming minerals as result of the passing shock waves. On the solid surfaces of other planets like Mars and Mercury, and satellites like the Moon, impact cratering is the most important surface-modifying process where other geologic processes stopped millions of years ago. On the planet Earth, impact craters are continually erased, destroyed, or covered by geological processes such as weathering, erosion, redeposition, or by volcanic resurfacing and tectonic activities. Thus to date only about 150 terrestrial impact craters have been recognised, although the Earth must have been subjected to an even larger number of impacts than the Moon because of its larger gravitational cross section. The majority of the Earth's known impact structures are located in the geologically stable cratons of North America, Europe and Australia where most geological exploration has taken place.

Until recently, impacts by extraterrestrial bodies were regarded as, perhaps, an interesting but certainly not an important phenomenon in the spectrum of geological process affecting the Earth. The concept of the importance of impact processes, however, has been changed radically through planetary exploration, which has shown that virtually all planetary surfaces are cratered from the impact of interplanetary bodies. The study of impact craters also gained momentum after the asteroid impact hypothesis for the massive extinction at the Cretaceous-Tertiary boundary introduced by Alvarez et al. (1980). Many geologists now accept that an enormous impact event occurred at the Cretaceous-Tertiary boundary, 66 Ma (Schultz, 1982; Sharpton and Ward, 1990). Recent studies of the Cretaceous-Tertiary boundary, which marks the abrupt demise of a large number of biological species including dinosaurs, revealed unusual enrichments of siderophile elements and shock metamorphic features that are markers of meteorite impact events. Many researchers now believe that a large meteorite hit the Earth at the end of the Cretaceous 66 million years ago, as a result an environmental crisis triggered by the gigantic explosion contributed to the extinction.

Recently many scientists have found what they believe to be the crater of the meteorite. The villain is identified as the buried Chicxulub Structure in the Yucatan Peninsula, Mexico, which has a diameter close to 300 km. NASA scientists believe that an asteroid 10 to 20 kilometres in diameter produced theYucatan impact basin. This basin is characterised by local gravity and magnetic field variations that show a multiringed structure. The impact basin is buried by several hundred metres of sediments, hiding it from view. The asteroid hit a geologically unique, sulphur-rich region of the Yucatan Peninsula and kicked up billions of tons of sulphur and other materials into the atmosphere. Darkness prevailed for about half a year after the collision. This caused global temperatures to plunge to near freezing. Half of most species on Earth became extinct including the dinosaurs (V.L. Sharpton et al.,1992, 1993).

Impacts may also have economic significance. Many buried impact structures are sites of hydrocarbon accumulations. Because the impact cratering results in unique structures with extensive fracturing and brecciation of the target rocks, some structures in sedimentary rocks have provided suitable reservoirs of oil and natural gas deposits (Donofrio, 1981). It is probable that the vast copper-nickel deposits at Sudbury, Canada resulted from a large-scale impact 1850 million years ago.

3.2-Terrestrial Impact Structures

Impact cratering has been recognised as an important geologic process for only the last few decades. As recently as 1950 most astronomers believed that the lunar craters were giant volcanoes, and few geologists derided the idea that the earth's surface has been scarred by impact structures. A vigorous program of planetary exploration in the Apollo era and continued geologic research on earth has changed these views profoundly (Koeberl and Anderson, 1996). It is now recognised that the cratered landscapes of the Moon, Mercury, Mars, and many of the solar system's satellites are sculptured predominantly by repeated impacts of all sizes. On Earth the full connection between meteorites and craters was made in 1906 when Barringer, D. M., demonstrated that the Meteor Crater, Arizona, is of meteoritic origin. Impact craters are becoming the keys to understanding the origin of the Earth. The meteorites that hit the earth contain the basic materials which make up our world and other planets. In 1972 around 50 confirmed terrestrial impact craters were known. By 1994, the number stood close to 150 (Grieve and Shoemaker, 1994). Almost all of these structures are on land, with concentrations in North America, Australia, and Europe. Knowledge of many of the proven terrestrial impact structures is still very limited. Fortunately an improved understanding of impact craters has led to the recognition of many structures in recent times, but detailed studies are not available for the majority of these structures.

Although the number of known impact craters on Earth is relatively small, the preserved sample is an extremely important resource for understanding impact phenomena. They provide the only ground-truth data currently available for extensive geological, geophysical and geochemical study. Earth's impact craters also provide the opportunity to study such features in three dimensions.

3.3- Formation of Impact Structures.

The formation of impact craters is a very rapid process. The initial phases of crater formation are relatively well understood from theoretical and experimental considerations (Gault et al. 1968; Roddy et al. 1977; Melosh, 1989). One of the most unique aspects is the huge kinetic energy that is released with the impact of the meteorite which can hit the earth's surface with a velocity between 10 and 70 km/sec. (Melosh, 1989). Many of the characteristics of the impact crater are the consequence of this enormous kinetic energy, which is released during the impact within seconds. An impact leads to the instantaneous generation of shock waves that penetrate the target area and attenuate in its rocks.

The formation of an impact crater is commonly divided into three stages. These are, the compression stage, the excavation stage, and the post-impact stage. The first stage produces the most important changes in the target rocks, while the final morphology of the crater is in the second and the third stages. The three stages are well described in the literature (Grieve, 1987, 1991; Melosh, 1989). During an impact supersonic shockwaves propagate through the target rocks. The compression of rocks to pressures above their Hugoniot elastic limit leads to irreversible structural changes in the minerals and rocks. The Hugoniot elastic limit (HEL) can generally be described as the maximum stress to which a material can be subjected without plastic, or irreversible, distortions. The value of HEL is about 5-10 Gpa for most minerals and whole rocks (Melosh, 1989). The only known natural process that produces shock pressures exceeding the HEL in rocks is impact cratering.

The conditions for endogenic metamorphism of crustal rocks are distinctly different, rarely exceeding temperature of 1,200 °C and pressures of 2 Gpa. In contrast, shock pressures and temperatures during impact may reach many 100's Gpa and several 1000's C. Considering only the contribution from the impacting body, recent calculations indicate that even relatively small impacting bodies, less than 0.5 km in diameter, can produce impact craters on the scale of 10 km in diameter.

3.4 – Recognition of Impact Craters

Since the 1960s, numerous studies have uncovered physical evident for impact structures, and shock metamorphism. Certain shock metamorphic effects have been shown to be uniquely and unambiguously associated with meteorite impact craters. No other earthly mechanism, including volcanism, produces the extremely high pressure required for the formation of such features. These include shatter cones, multiple sets of microscopic planar features in rock forming minerals such as quartz and feldspar grains, diaplectic glass, and high-pressure mineral phases such as coesite and stishovite. All known terrestrial impact structures exhibit some or all of these shock effects. The following are some of the most important criteria that can be used for the recognition and confirmation of impact structures, these are:

1- Presence of meteorites or geochemical traces of the meteoritic projectile;
2- Evidence for shock metamorphism;
3- Crater morphology;
4-Geophysical anomalies.

Of those criteria mentioned above, the presence of meteorite traces and diagnostic shock metamorphic effects are considered as convincing evidence for an impact. However, geophysical and morphological observations are of great importance in providing additional evidence.

3.4.1- Presence of Meteoritic Projectile

For many years, remnants of meteoritic projectile were the only accepted evidence for impact origin. However, scientists have come to realise that pieces of the impactor often do not survive the tremendous pressures and temperatures it produces. Meteorite fragments are found only at the smallest and youngest craters and they are quickly destroyed in the terrestrial environment. For impact events on Earth that form craters larger than approximately 1 km across, the pressures and temperatures produced upon impact are sufficient to completely melt and even vaporise the impacting body and some of the target rocks. Meteor Crater (also known as Barringer Crater) in Arizona was the first recognised terrestrial impact crater. It was identified in the 1920's on the basis of fragments of meteorite within the crater itself. Several other relatively small and young craters were also found to contain meteorite fragments. However, an improved understanding of these impact craters has recently lead to the recognition of many impact structures.

3.4.2- Shock Metamorphism

Shock effects in minerals and rocks have been studied very thoroughly with a variety of methods over several years (French and Short, 1968; St¬ffler, 1972, 1974; St¬ffler and Langenhorst, 1994). These effects can be classified as either macroscopic deformation features, which include breccia types and shatter cones, or microscopic deformation features, which include planar deformation features (PDF's) and the occurrence of high-pressure polymorphs of quartz (coesite and stishovite).

3.4.2.1- Macroscopic Dynamic Deformation Features

These include autochthonous breccia, allochthonous breccia, and shatter cones. Autochthonous breccia refers to rock material that has been brecciated in place. The brecciation is usually associated with sedimentary rocks with wide range of particle sizes. Allochthonous breccia refers to brecciated material that has been transported over substantial vertical distances. Shatter cones are striated cup-and-cone structures, these complex cones were first described from the Steinheim Basin of Germany (Branca and Frass, 1905) as pressure phenomena. Dietz(1960,1968) concluded that shatter cones have been observed only in hard rocks at cryptoexplosive structures and could only have been reproduced by hypervelocity impact. His interpretation is that shatter cones formed by high-velocity shock waves coming in contact with some inhomogeneity in the rock forming a cone with the apex at that point of inhomogeneity. Shatter cones are believed to point toward the direction from which shock waves came. It is therefore important that their in-place orientation be observed in the field. Figure (3.1) is a sketch showing the formation of the cones. The formation of these features is dependent on the type of target rock, and is thought to take place at pressures in the range of 2 to 30 Gpa Thus is widely believed to be a macroscopic indicator of impact (Dietz, 1968; Milton, 1977). Figure (3.2) shows a piece of shatter cone from the Carswell Impact Structure, Canada.

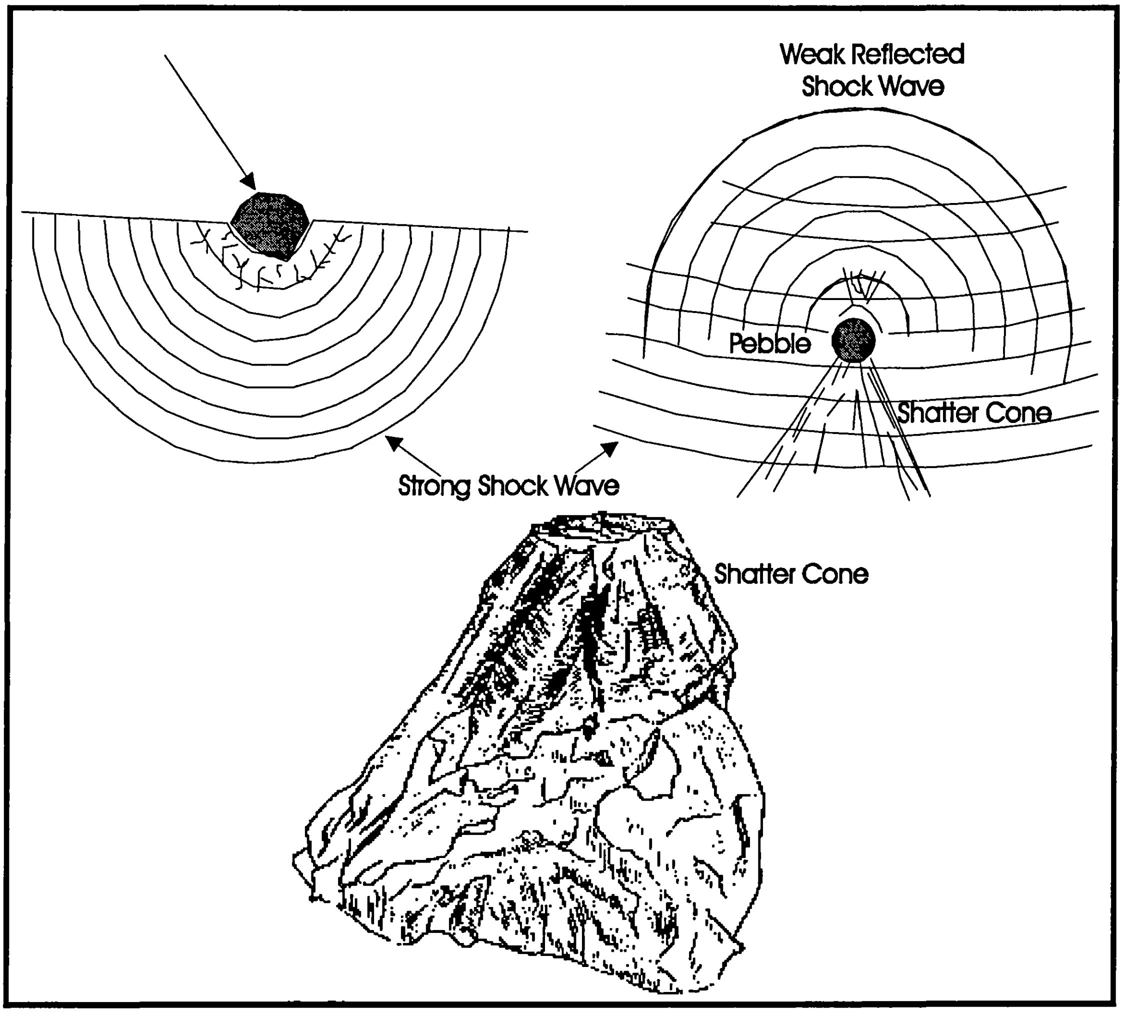

Figure 3.1 - Sketch showing the formation of shatter cones

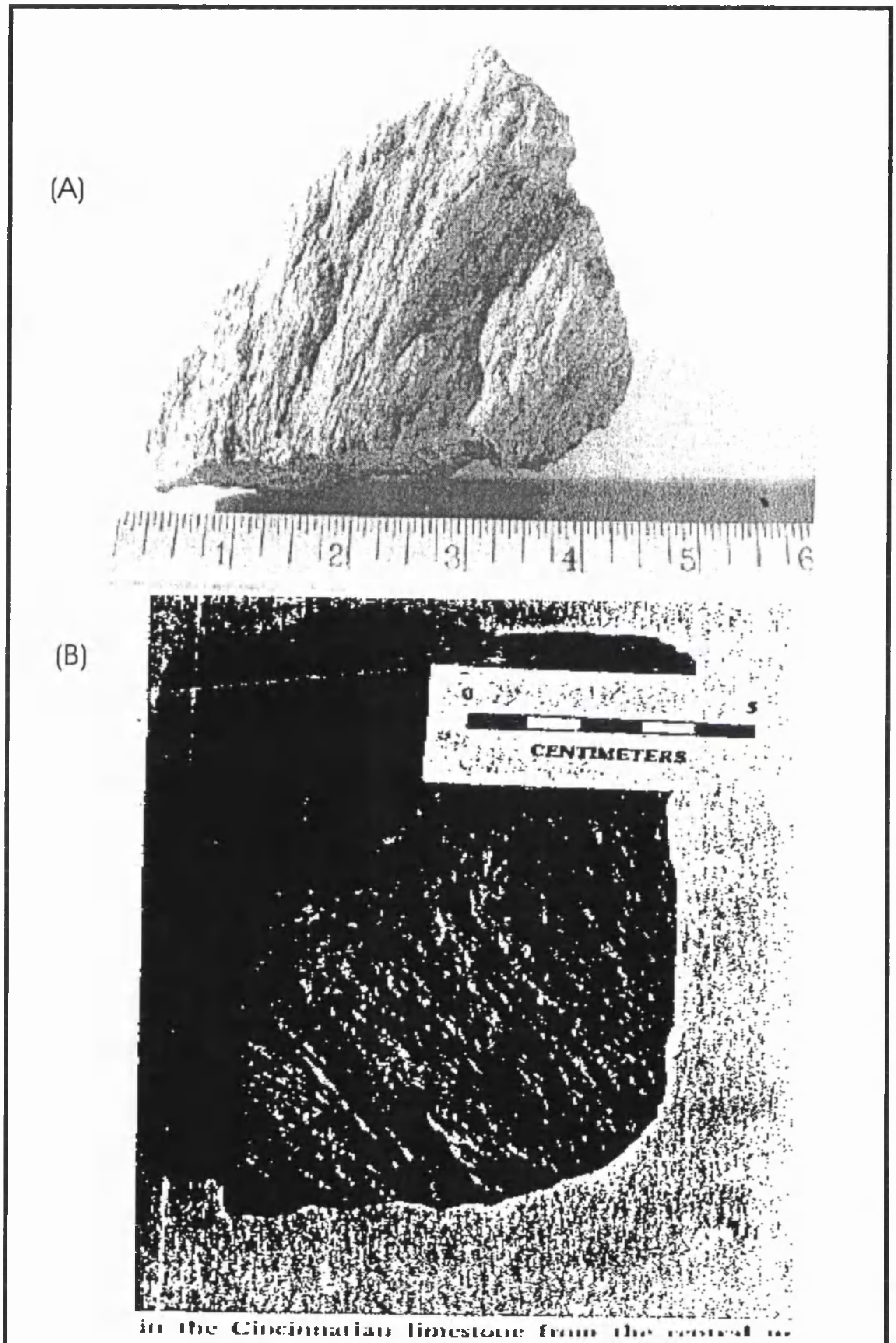

Figure 3.2- Pieces of shatter cones (A) from the Carswell impact structure, Canda (B) from the central uplift of the Serpent Mound (Reldel, et al, 1982)

3.4.2.2. - Microscopic Dynamic Deformation Features

Microstructures induced by shock deformation were studied extensively at many cryptoexplosion structures following the discovery by McIntyre (1962) of shock induced planar deformation features (PDF). The flurry of activity of PDF studies was stimulated initially by the now classic Bucher-Dietz controversy concerning the volcanogenic versus impact origin of cryptoexplosion structures (Officer and Carter, 1991). The studies of shock metamorphism gained momentum after the asteroid impact hypothesis for the massive extinction at the Cretaceous/Tertiary boundary was introduced by Alvarez et al, (1980). Most of the microstructure work has been done on the common target materials, quartz and feldspar.

3.4.2.2.1 Planar Deformation Features

Planar deformation features (PDFs) are parallel zones of microscopic thicknesses which consist of glass. PDFs can be curved as a result of post-impact mineral deformation. Stoffler and Langenhorst (1994) noticed PDFs occur in planes corresponding to specific crystallographic orientations. Table (3.1) shows the microscopic characteristics of planar features in quartz (Stoffler and Langenhorst, 1994). As mentioned above, the effects of shock metamorphism are a consequence of the extremely high pressures and, to a lesser extent, temperatures that the minerals and rocks were subjected to during an impact event. Figure (3.3) shows the pressure-temperature regime of endogenic metamorphism compared to shock metamorphism (Grieve, 1987). Table (3.2) lists a number of typical products of shock metamorphism, as well as the associated diagnostic features. The presence of diagnostic features of shock depends upon the pressure experienced. Observations of naturally and experimentally shocked rocks have enabled calibration of the pressure ranges for the occurrence of different shock features. PDFs in rock forming minerals, such as quartz, feldspar, or olivine are generally accepted to be diagnostic evidence for levels of shock diagnostic of impact (Alexopoulos et al, 1988; Grieve, 1991). Figure (3.4) shows

PDF's in quartz and feldspars from different impact structures; (A) PDFs in quartz from Lac Couture, Quebec; (B) PDFs in plagioclase from Bishop Tuff; (C) PDFs in quartz from the Clearwater Lakes impact site; and (D) in deformed quartz from Dry Creek, Montana.

TABLE 3.1- MICROSCOPIC CHARACTERISTICS OF PLANAR STRUCTURES IN QUARTZ

TERMINOLOGY	1.- PLANAR FEATURES (PF) 2.- PLANAR DEFORMATION FEATURES (PDF) 2.1- NONDECORATED PDFS 2.2- DECORATED PDFS
Crystallographic Orientation	1.- PFs: Usually ‖ to {0001} and $\{10\bar{1}1\}$. 2.- PDFs: Usually ‖ to $\{10\bar{1}3\}$,$\{10\bar{1}2\}$,$\{10\bar{1}1\}$, (001),$\{11\bar{2}2\}$,$\{11\bar{2}1\}$,$\{10\bar{1}0\}$,$\{11\bar{2}0\}$,$\{21\bar{3}1\}$, $\{51\bar{6}1\}$,etc.
Optical microscope Properties	Multiple sets of PFs or PDFs (as much as 15 orientations) per grain. Thickness of PDFs <2 to 3μm. Spacing>15μm (PFs), 2 to 10 μm (PDFs)
TEM Properties (PDFs)	Two types of primary lamellae observed: 1- Amorphous lamellae with a thickness of ca. 30 nm (at pressures <25 Gpa) and ca. 200 nm (at pressures >25 Gpa). 2- Brazil twin lamellae ‖ to (0001).

(After Stoffler and Langenhorst, 1994)

TABLE 3.2- MICROSCOPIC AND MACROSCOPIC FEATURES OF SHOCK METAMORPHISM

PRESSURE RANGE (GPA)	FEATURES	CHARACTERISTICS OF TARGET ROCKS	CHARACTERISTICS OF FEATURES
2-30	Shatter cones	Best developed in homogeneous, fine-grained massive rocks.	Conical fractures; subordinate striations radiating from focal point.
5-45	Planar Features (PF); Planar Deformation Features (PDFs)	Most abundant in crystalline rocks; occur in many rock-forming minerals (quartz, feldspare, olivine, and zircon)	Sets of extremely straight, sharply defined parallel lamellae; having specific crystallographic orientations; often occur in miltiple sets
30-40	Diapletic glass	Common in quartz and feldspar	Solid-state transformation leads to isotropization; crystal habit and primary defects (including PFs) are preserved; refractive index lower than in crystal, but higher than in fusion glass
15-50	High-Pressure Polymorphs	Quartz polymorphs: coesite, stishovite	Characteristic crystal parameters, confirmed usually with XRD or NMR; abundance in a function of post-shock temperature and shock duration; stichovite is

PRESSURE RANGE (GPA)	FEATURES	CHARACTERISTICS OF TARGET ROCKS	CHARACTERISTICS OF FEATURES
			temperature-labile
45->70	Mineral melts	Rock-forming minerals	Complete transformation into glass
> 60	Rock melts	In massive Silicates	Glassy melt or crystalline
35-140	Impact diamond	From carbon present in the form of graphite or coal	Hexagonal form; preserve crystal habite of graphite

(After Koeberl and Anderson, 1996)

3.4.2.2.2 High-pressure Silica Polymorphs

The association of the high-pressure silica polymorphs, such as coesite (dense high-pressure monoclinic polymorph of quartz), with impact sites is widely accepted after the important discovery by Chao and others (1960). Coesite has been found at Barringer Crater, Arizona and in the St. Peter Sandstone from the central uplift of the Kentland Structure, Newton County, Indiana, U.S.A. The presence of impact glass is also a good indicator that the rocks were subjected to high shock pressure levels.

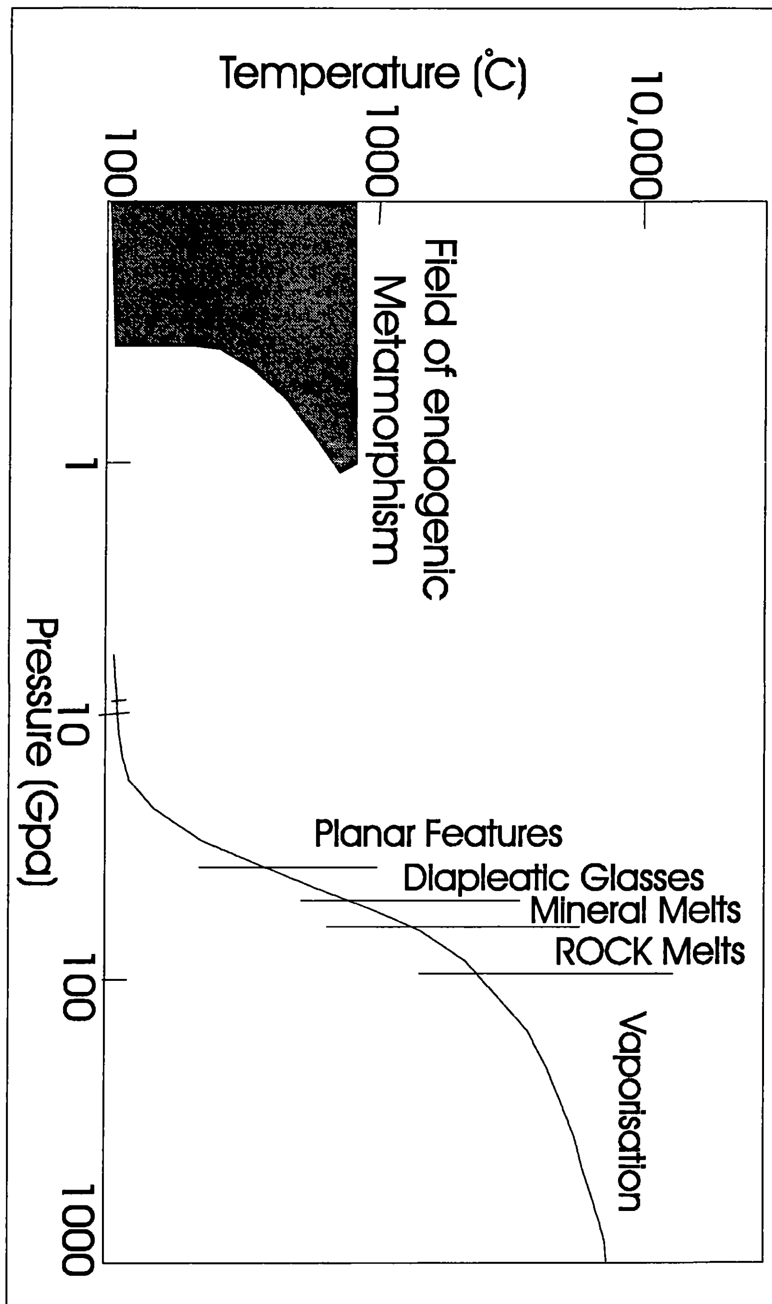

Figure 3.3- Pressure-Temperature regime of endogenic metamorphism compared to shock metamorphism

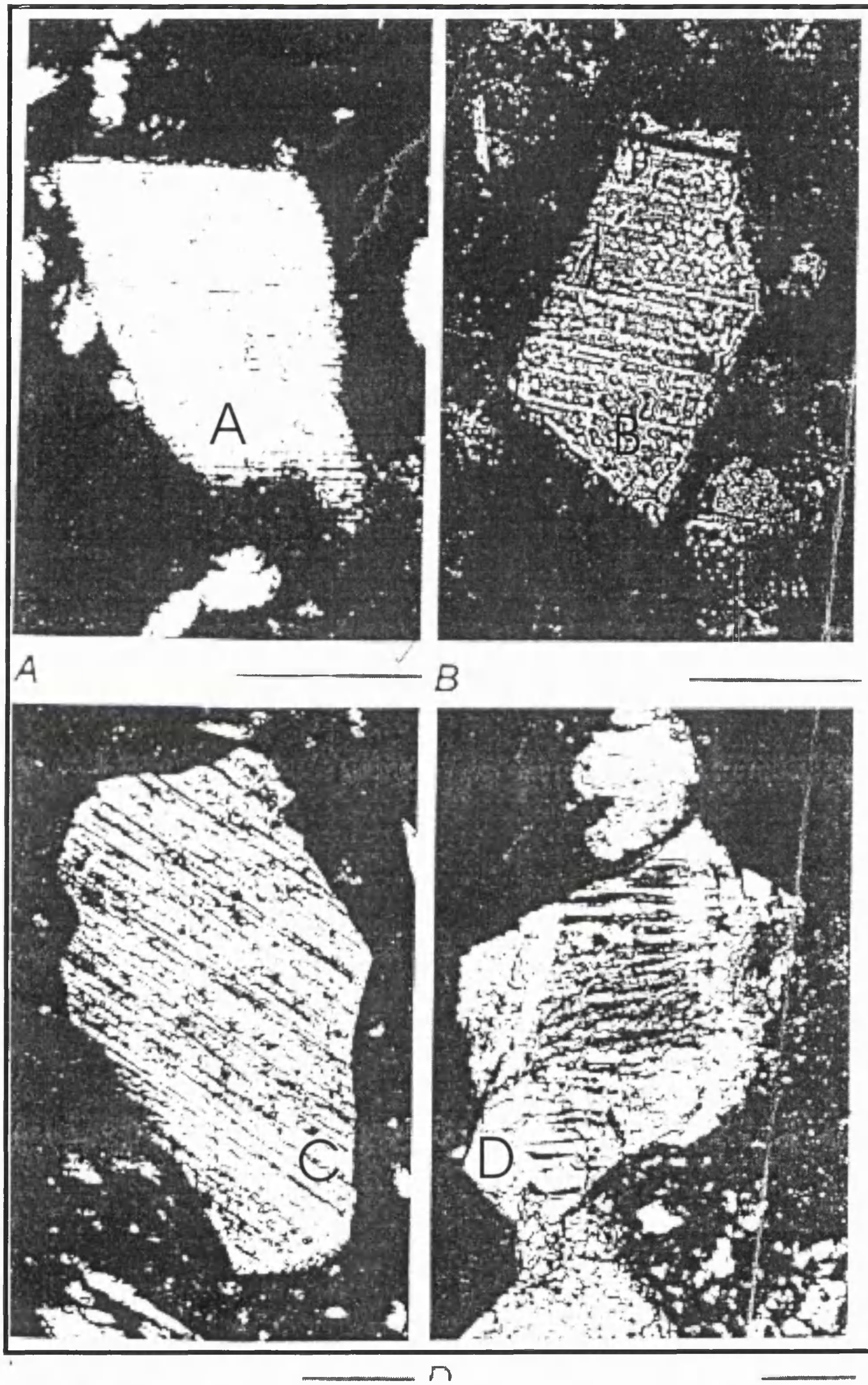

Figure 3.4- Planar Deformation Features (PDFs) in quartz and feldspars

Scale lines beneath photos A-C represent 0.05mm, beneath B-D represents 0.1 mm

3.4.3- Crater Morphology

Impact craters are divided into two groups based on morphology: simple craters and complex craters. Simple structures, up to 4 km in diameter, have uplifted and overturned rim rocks, surrounding a bowl-shaped depression, partially filled by breccia. Figure (3.5) is a schematic cross section of simple craters. In complex craters however, gravity causes the initial steep crater walls to collapse downward and inward, forming a complex structure with a central peak or peak ring and a shallower depth compared to diameter (1:10 to 1:20). Figure (3.6) is a schematic section of complex craters showing idealised form, structure, and distribution of distinct parts. The central peak or peak ring of the complex crater is formed as the initial (transient) deep crater floor rebounds from the compression shock of the impact. Slumping of the rim further modifies and enlarges the final crater. On Earth weathering and erosion of the target rocks quickly alter the surface expression of the structure, obscuring the crater's initial morphology. Ejecta blankets are quickly eroded and concentric ring structures can be produced or enhanced as weaker rocks of the crater floor are removed. More resistant rocks may be left as a plateau overlooking the surrounding structure.

The transition diameter from simple structure to complex structure is a function planet surface gravity and the target rock type (Pike, 1985). On the planet Earth, simple craters occur up to a diameter of 4 km in crystalline rocks and 2 km in sedimentary rocks (Dence, 1972). Above these diameters, terrestrial craters have a complex form.

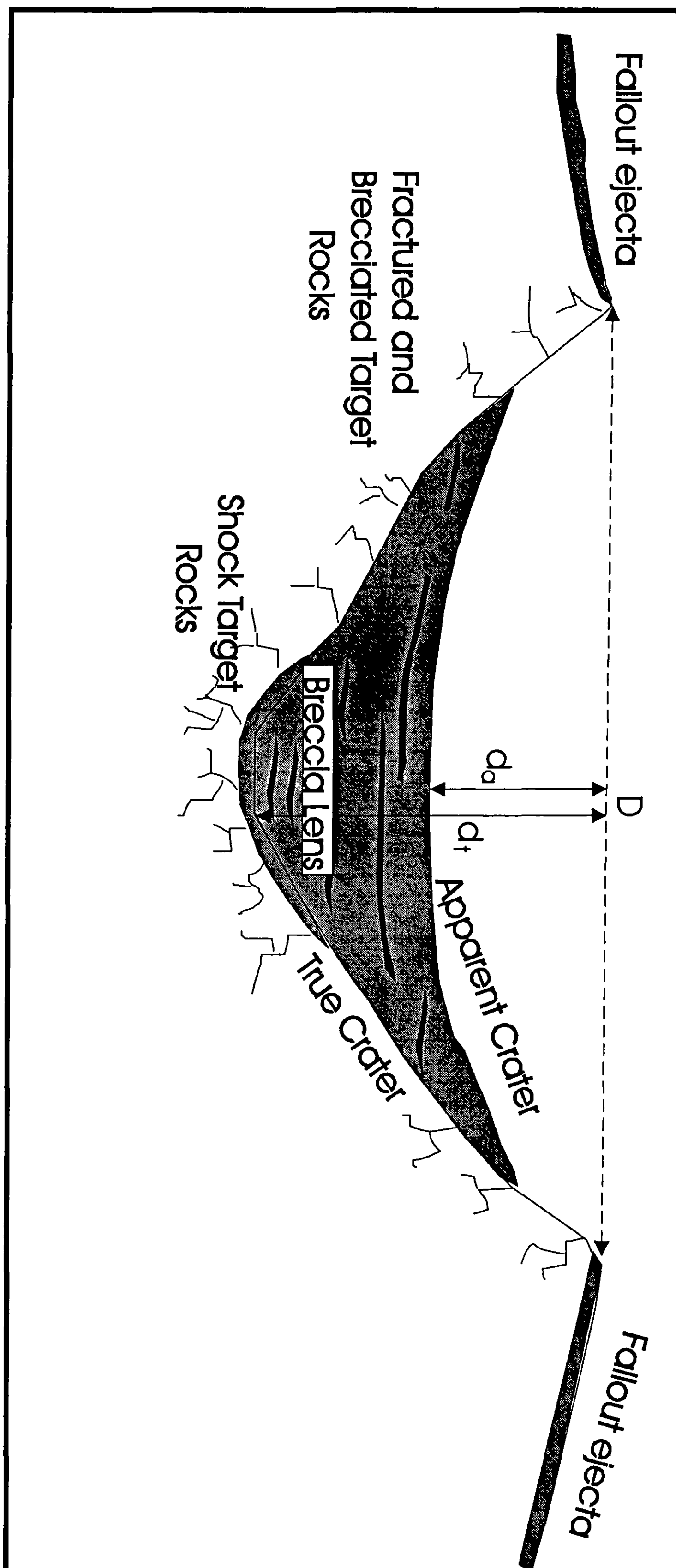

Figure 3.5- Schematic Cross Section of a Simple Crater, d_a is the apparent crater depth, and d_t is the true crater depth

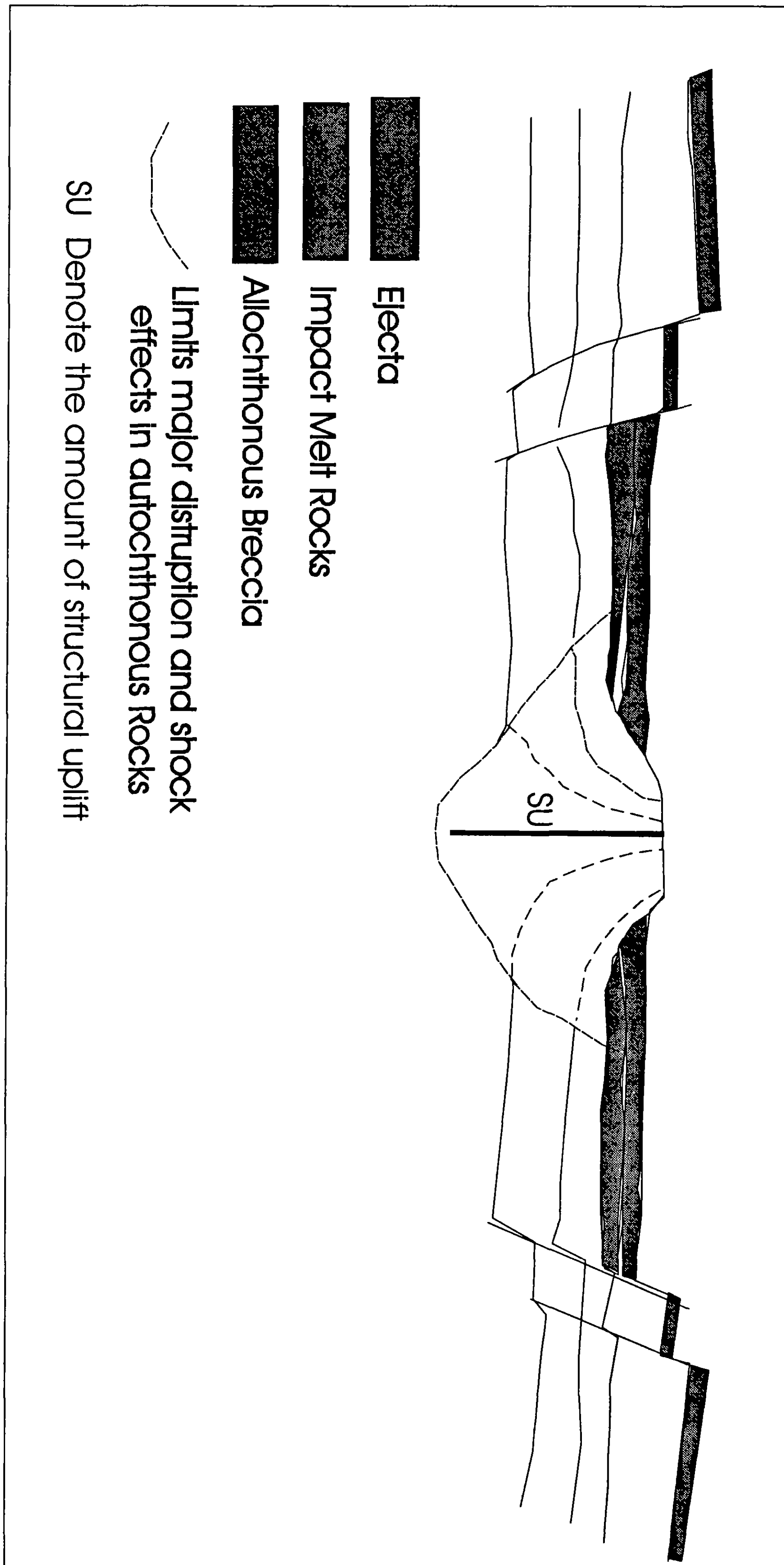

Figure 3.6- Schematic cross section of a complex Crater

3.4.4- Geophysical Signatures

Impact structures reveal that geophysical signatures can result from the induced physical changes in the target rocks due to the impact. The most common and conspicuous geophysical signature of impact structures is a gravity low over the centre of the impact area (Pilkington and Grieve, 1992). The gravity anomaly over simple impact structures is largely due to the presence of an interior allochthonous breccia lens, and in some complex craters the main contribution to the low gravity is from the para-autochthonous target rocks (Pilkington and Grieve, 1992). In general the size of the gravity anomaly increases with the increase in crater diameter (Dabizha and Fedynsky, 1975, 1977). Figure (3.7) shows the relation between gravity anomaly and crater diameter for many terrestrial impacts craters listed in Table (3.3). Also it shows a distinction between craters formed in sedimentary and crystalline lithologies; the later having larger anomalies for given crater diameter (Pilkington and Grieve, 1992). Figure (3.8) shows residual gravity anomaly profiles over some impact craters with different diameters.

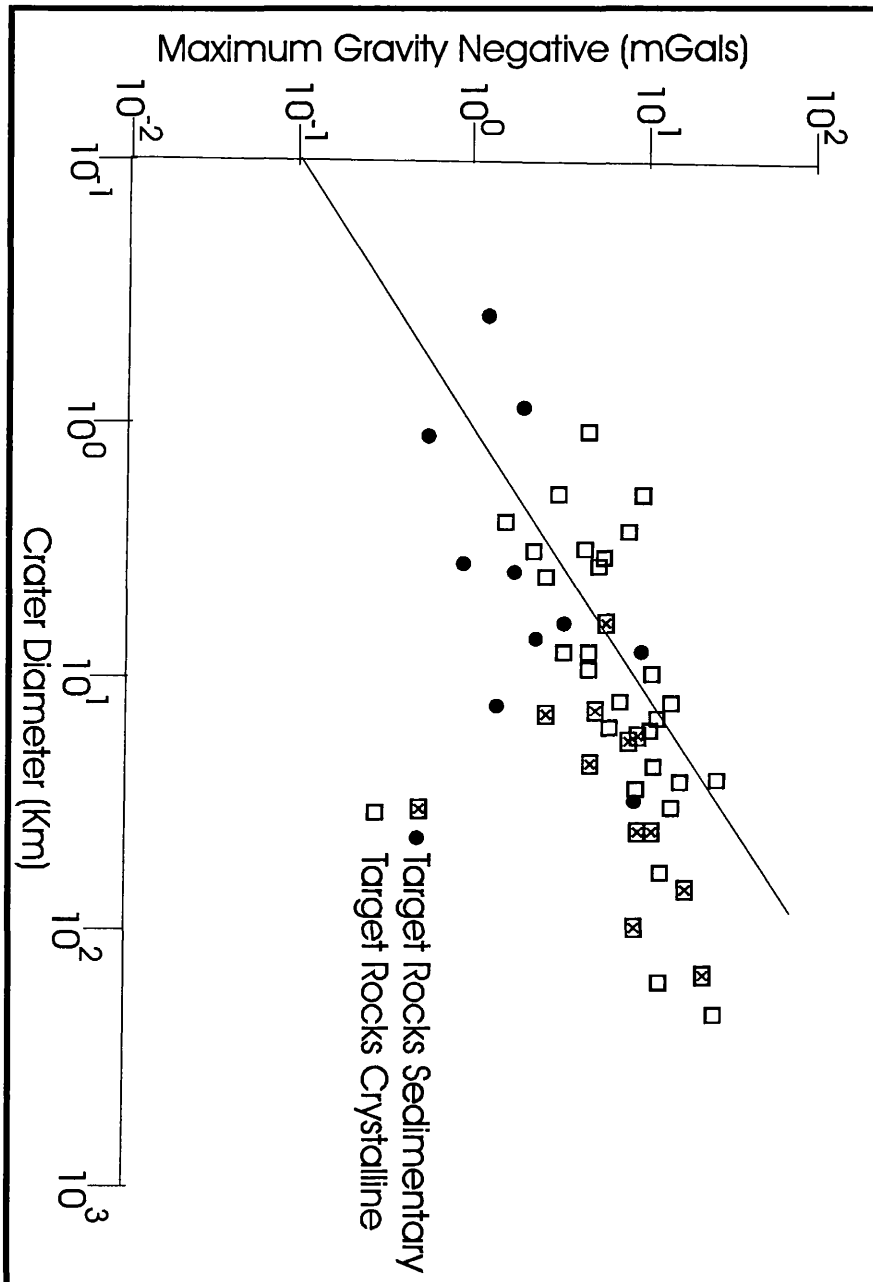

Figure 3.7- Variation in the maximum negative anomaly with crater diameter (Basilevsky et al, 1983)

Table 3.3- Maximum Negative Residual Gravity Anomalies Of Terrestrial Structures (after Pilkington and Grieve, 1992)

CRATER	MGAL	DIAMETER KM	AGE, MY	REFERENCE
1- Acraman, Australia	-14	160	>570	Williams (1990)
2-Aouelloul, Moritania	-1.25	0.39	3.1	Faudi and Cassidy (1972)
3- Barringer, Arizona	-0.6	1.18	0.049	Regan and Hinze (1975)
4- Brent, Canada	-5	3	450	Millman et al, (1960)
5- Carswell, Canada	-11	39	115	Innes (1964)
6-Clearwater West,Can.	-16	32	290	Plante et al, (1990)
7- Crooked Creek, Mi.	-2.5	7	320	Fox (1970)
8- Deep Bay, Canada	-15	13	100	Dent (1973)
9- Kentland, Indiana	-1	13	<300	Tudor (1971)
10- Lappajarvi, Finland	-10	17	77.3	Elo (1976)
11- Manicouagan,Can.	-10	100	212	Sweeney (1978)
12-Middlesboro, Kent.	-3.5	6	<300	Steinemann (1980)
13- New Quebec, Can.	-6	3.44	1.4	Innes (1964)
14- Sierra Madera, Tex.	-1.5	13	<100	Van Lopik and Geyer(63)
15- Siljan, Sweden	-15	55	368	Dyrelius (1988)
16- Steinheim,Germany	-2	3.8	14.8	Ernston (1984)
17- Sudbury, Canada	-30	200	1850	Popelar (1972)
18-Vredefort, South Af.	-25	140	1970	Slawson (1976)
19-WanapiteiLake,Can.	-15	7.5	37	Dence and Popelar(1972)
20- Wells Creek, Tenn.	-3	14	200	Stearns et al. (1968)
21- Wolfe Creek, Aus.	-2	0.875	<0.3	Fudali (1979)

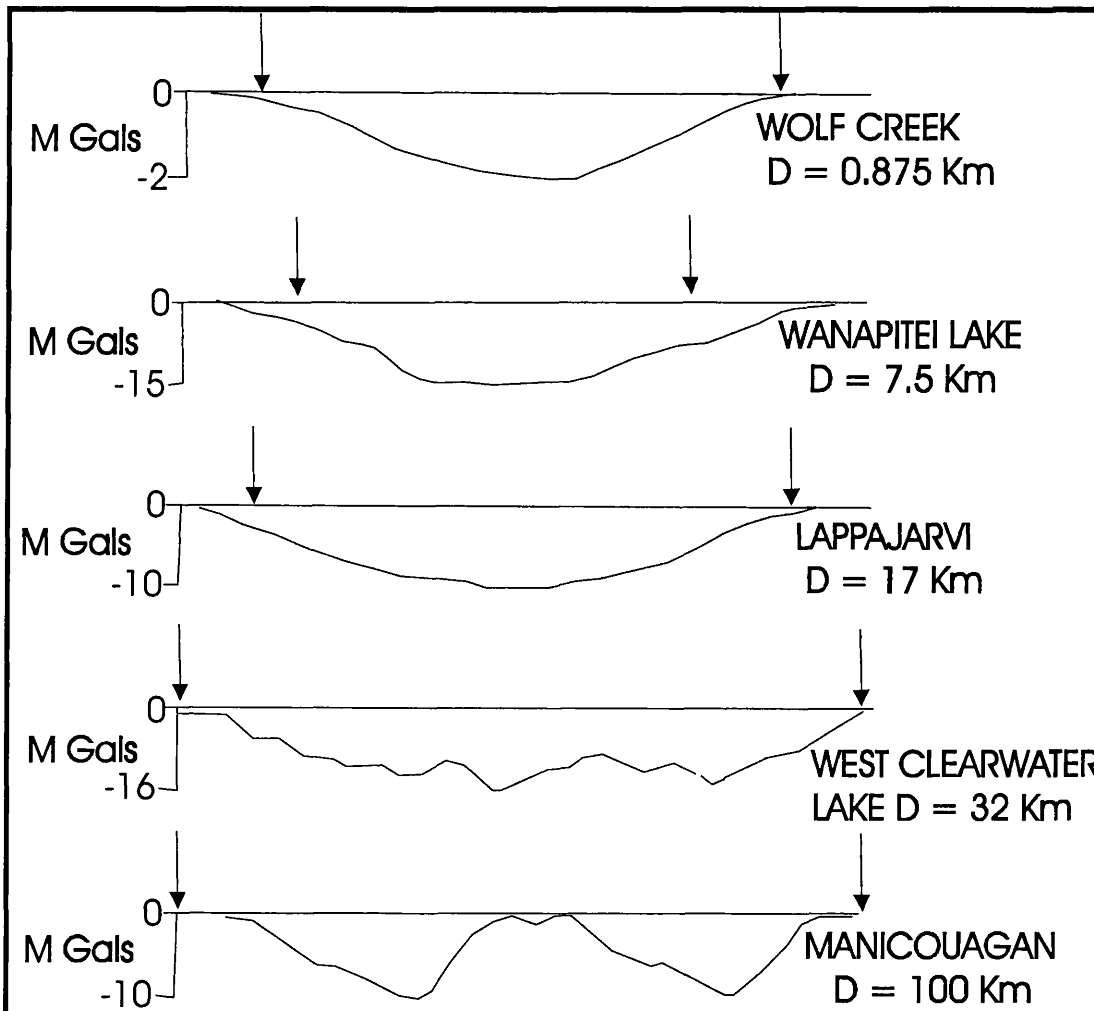

FIGURE 3.8- Residual gravity anomaly profile over impact craters scaled to crater diameter and maximum gravity value

The magnetic signature is varied and more complex than gravity. Some craters show magnetic lows due to the reduction of magnetic susceptibility of the target rocks (Dabizha and Fedynsky, 1975; Clark, 1983). This type of signiture is easily recognised, particularly in crystalline environments by the truncation and disruption of regional magnetic trends. An example is the residual magnetic field intensity mapped over the Deep Bay Structure, Saskatchewan, Canada (Figure 3.9). Other craters tend to exhibit central high amplitude anomalies due to remanently magnetised volumes in the target rocks. The source of these volumes are wide ranging and include the effect of shocks, heat, and chemical alteration. Pilkington and Grieve (1992) summarised the magnetic anomaly characters over 37 cryptoexplosion structures. Shock pressures at target rocks may reach 30 Gpa, which is sufficient to produce shock demagnetisation of the rocks. Hargraves and Perkins (1969); Phol et al. (1985); Cisowski and Fuller (1978), have shown experimentally that shocks pressure of the order of 1 Gpa can remove existing remnant magnetisation. Shock can also aid in the production and modification of magnetic carriers in target rocks. Chao (1968) reported that amphibole and biotite decompose to produce magnetite at pressures around 40 Gpa and temperatures around 1000 $^\circ$ C. At lower pressure, titanomagnetite can result from the breakdown of ilmenite. Thus in addition to demagnetisation, target rocks can also acquire a shock remnant magnetisation (SRM). This magnetisation decreases with distance from the centre of the structure (Phol et al. 1985; Cisowiski and Fuller, 1978). Following an impact, elevated residual temperatures and hydrothermal alteration can produce a chemical remnant magnetisation (CRM), as result of oxidisation due to circulation of meteoric water through cracks and fissures (Elming and Bylund, 1991).

Seismic methods, particularly seismic reflection, provide a detailed image of the subsurface structure of craters. No reflectors would be expected near the centre of the structure due to brecciation and fracturing of the rocks. The degree of the reflection coherency will increase away and below the centre of the structure (Brenan et al, 1975; Jansa et al, 1989; Ezeji-Okoye, 1985). Figure (3.10) shows a seismic section over the

Red Wing Creek Structure of North Dakota. The section delineates the major morphological features expected over the structure. Rim to rim distance is 9 km. Beneath the disturbed zone related to the impact is the reappearance of coherent reflectors. Figure (3.11) is a seismic reflection section over part of Chicxulub impact crater showing deformation of the target stratigraphy.

These geophysical criteria, with other geological evidence can be used to evaluate the hypothesis of the impact origin of any particular structure.

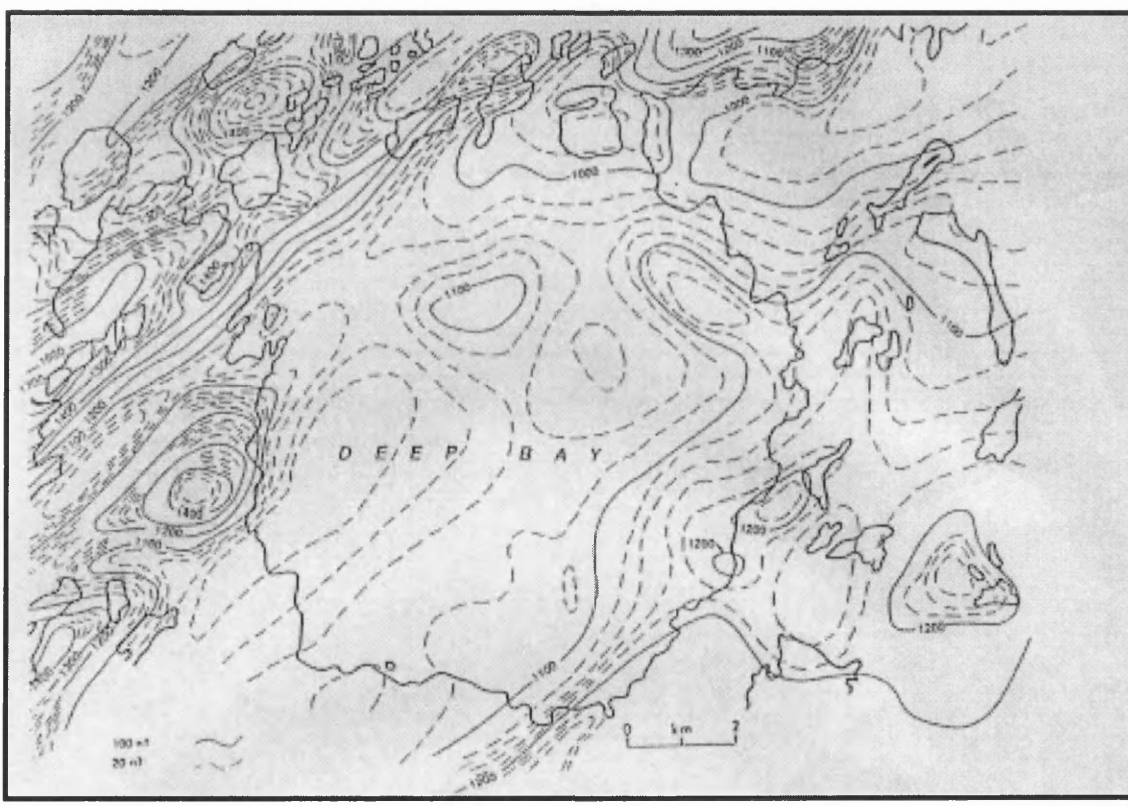

Figure 3.9- Residual magnetic field intensity over Deep Bay, Canada C.I. 20 nT (after Pilkington and Grieve, 1992)

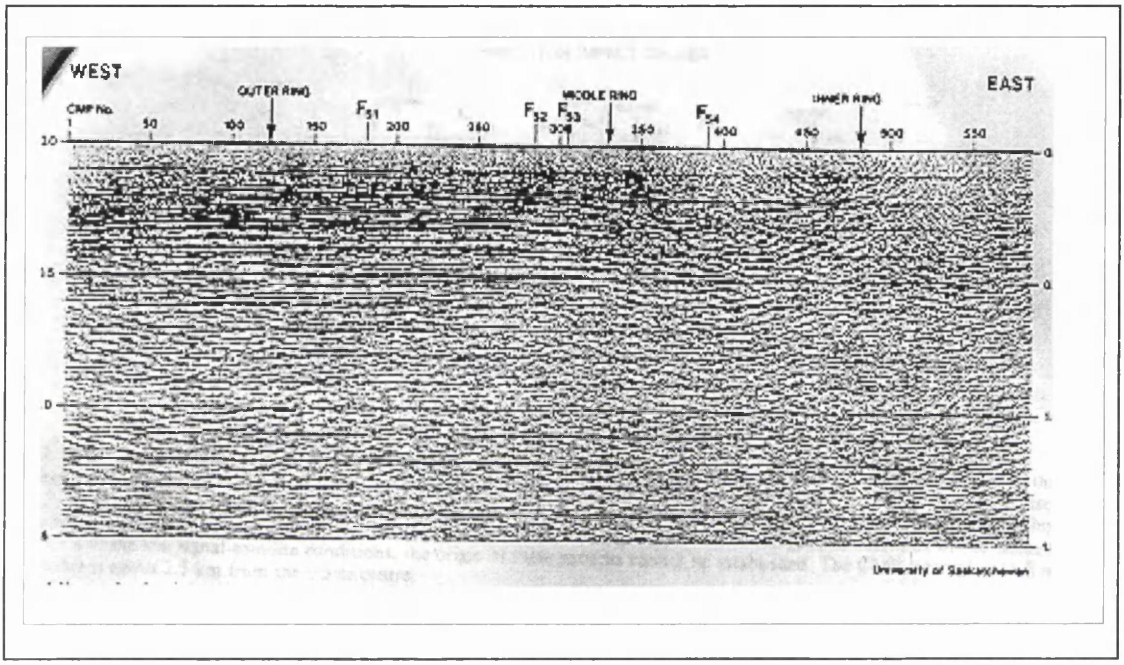

Figure 3.10- Reflection Seismic Section through the Red Wing Creek, N.D. (after Brenan et al., 1975)

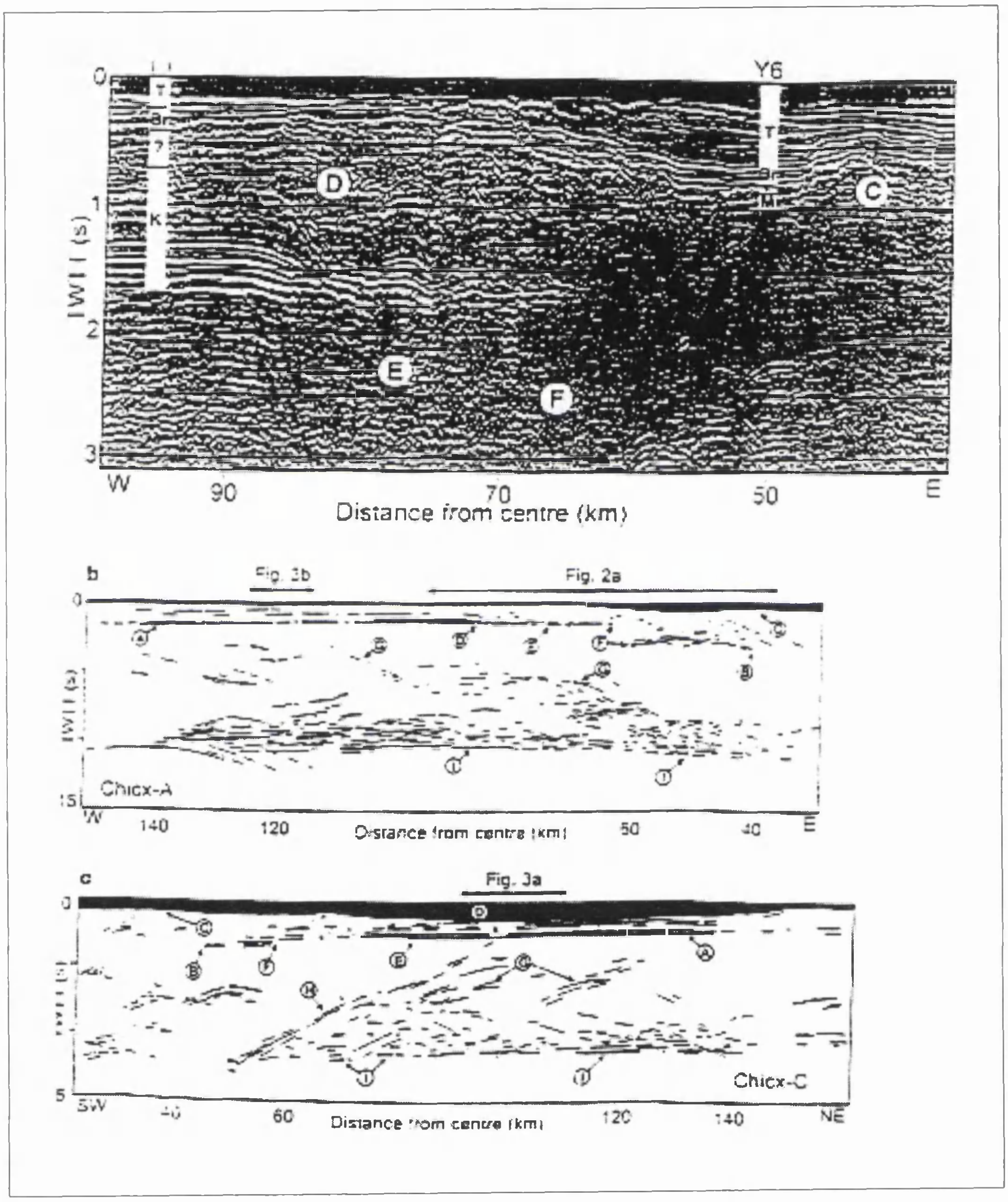

Figure 3.11- Seismic Section of part of the Chicxulub Structure, Mexico showing deformation of target stratigraphy (after Morgan et al, 1997)

Chapter- 4 SEISMIC DATA ACQUISITION AND PROCESSING

4.1- Field Data Acquisition in the vicinity of the Serpent Mound Disturbance

Two seismic lines were acquired in the study area. Seismic line (BV-1-92) is approximately 6 km long beginning at the intersection of Horner Chapel Road and State Route 73 in the outer graben (Figure 4.1). This line crosses the centre of the structure, and ends in the outer graben at the intersection of Parker-Ridge Road with State Route 41. There were 232 recording stations established along this very crooked road. Paragon Geophysical Inc shot this line on the 15 and 16 of April, 1992 for the Ohio Department of Natural Resources (ODNR). The source was an array of three vibroseis trucks generating a linear upsweep. The configuration of the source and receiver arrays is given in Figure 4.2. The recording parameters and general specification of this seismic line are given in Table 4.1. At many of the shotpoints the trucks were operated at 50% power because of the proximity of houses.

The second seismic line (SM-1) is approximately 8.5 km long extending from north to south along State Route 41 (Figure 4.1) and intersects line (BV-1-92) at SP 224 of line SM-1. The Western Geophysical Company (party 717) shot this line from the 7th to the 11th, September 1989 for Columbia Natural Resources Inc. The seismic line comprised 255 stations connected by analog cable to the recording truck. At each station was an array of twenty-four geophones connected in series. The vibroseis array rolled on to the line by first recording 60 channels, switching in channels until 120 channels were recorded with each shot. The vibroseis array then rolled off the line. The source and receiver arrays of seismic line SM-1 are illustrated in Figure (4.3). An array of three vibroseis trucks generated a nonlinear (Figure 4.4) upsweep from 20 Hz to 120 Hz. The vibroseis sweep had a duration of seven seconds and a listening time of five seconds. According to the observer's record, the pilot signal in recording house was 90 degrees out of phase with the signal driving the vibrators for the first 32 shots.

Comparing the two lines, BV-1-92 had the smaller group interval of 82 ft (25.0 m) compared to 110 ft (33.5 m) for SM-1. The sweep for BV-1-92 was a linear sweep from 10 to 110 Hz and the SM-1 line sweep was non-linear with frequencies from 20 to 120 Hz. Both lines were shot with three vibrators though information on the size of the vibrators on either line is not available.

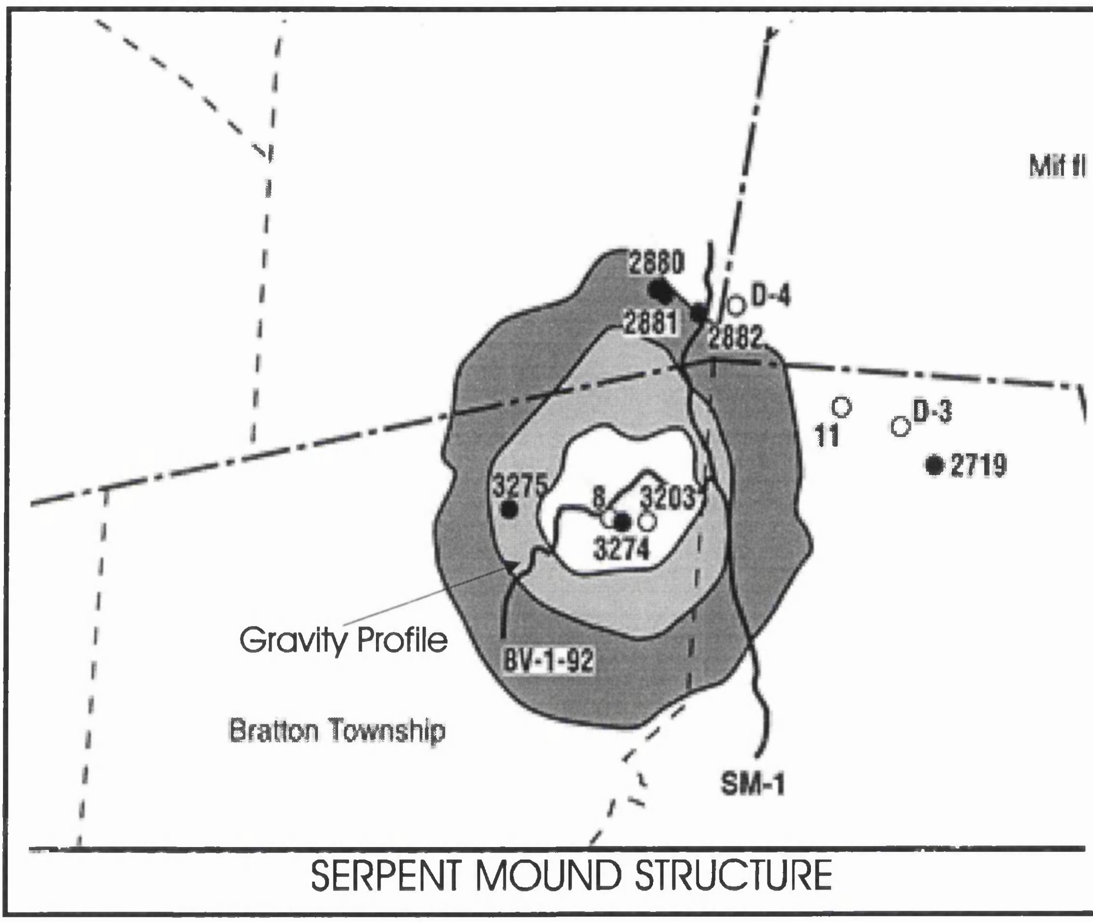

Figure 4.1- Location map of the seismic lines BV-1-92 and SM-1

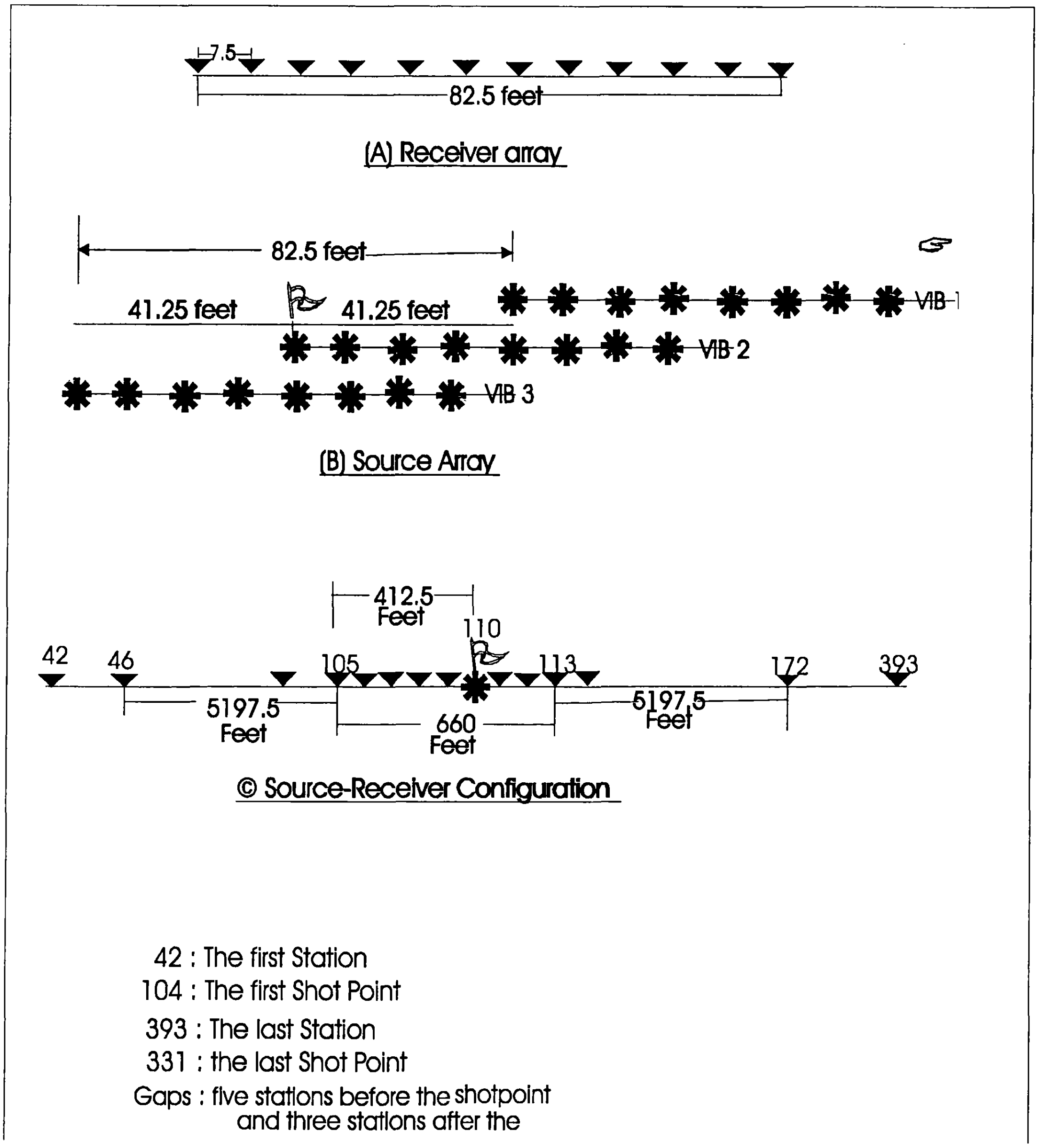

Figure 4.2 Receiver array, Source array, and Source Receiver Configuration of line BV-1-92

Table 4.1: Summary of the recording field parameters for the	
ODNR (BV-1-92) seismic line: -	
SOURCE	
Number of vibrators	3.
Number of sweeps	8.
V.P Interval	82.5/165 ft (25/50 m)
Number of sweeps per V.P	3*8 = 24
Sweep frequency (linear)	20-110 Hz (Upsweep)
Sweep rates	15 Hz/sec.
Sweeplength	6 sec.
Recording length	9 sec
First field file	SP 104
RECORDING	
Recording Instrument	DFS-V
Number of Channels	120
Filters	Low 18 Hz High 128 Hz Notch In
Recording Format	SEGB
Density	1600 bpi
Sample interval	2 ms
First trace-last trace	Southwest - Northeast
Number of reels	3
Nominal Fold of Coverage	60
SPREAD	
Split Spread	5297.5 330 0 330 5297.5 ft
Geophone Natural Frequency	8 Hz
Number of geophones per group	12
. Group interval	82.5 ft (25.1 m)
Geophone spacing	7.5 ft (2.3 m)
Geophone array Diagram	xxxxxx 0 xxxxxx

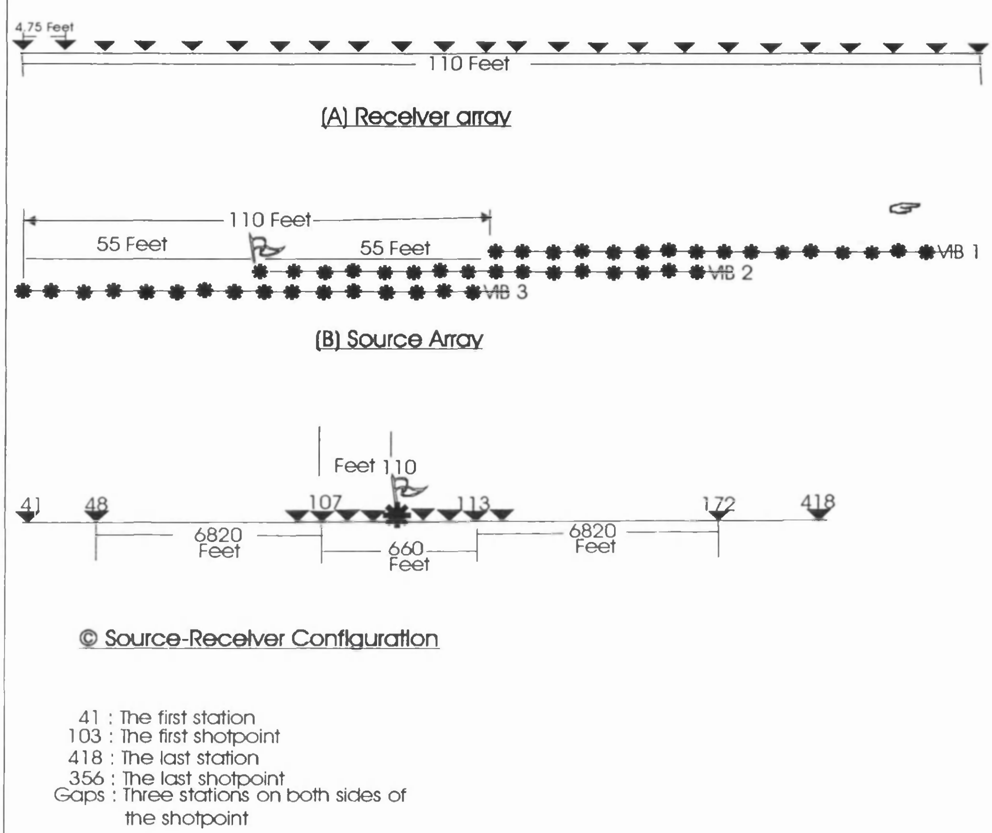

Figure 4.3- Recevier array, Source array, and Source - Recevier Configuration for Columbia line (CNR)

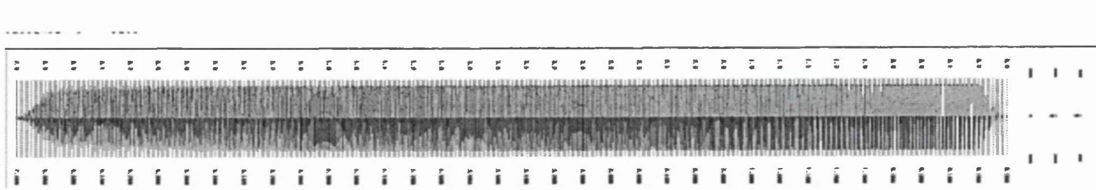

Figure 4.4 Vibroseis nonlinear sweep for seismic line SM-1

Table 4.2: Summary of recording parameters for seismic line SM-1

SOURCE	
Number of vibrators	3.
Number of sweeps	16.
V.P Interval	110 ft (33 m)
Number of sweeps per V.P	3*16 = 48
Sweep frequency (Non-linear)	20-110 Hz (Upsweep)
Sweeplength	7 sec.
Recording length	12 seconds
Taper	0.003 sec.
Sweep channel	aux1
Unsummed sweep channel	aux2
First field file	SP 103
RECORDING	
Recording Instrument	DFS-V
Number of Channels	120
Filters	Low 12 Hz High 128 Hz Notch out
Recording Format	SEGB
Density	1600 bpi
Sample interval	2 ms
First trace-Last trace	North-South
Number of reels	5
Nominal fold of coverage	30
SPREAD	
Spread	6820 330 0 330 6820 ft
Geophone Natural Frequency	8 Hz
Number of geophones per group	24
. Group interval	110 ft (33.5 m)
Geophone spacing	7.5 ft (2.3 m)

4.2- SEISMIC DATA PROCESSING

4.2.1-Introduction

The aim of seismic processing is to extract the seismic signals that are related to the subsurface geologic structure, and to suppress or eliminate all other signals that obscure the seismic section, and to migrate the data to form an image. The results of seismic processing are strongly affected by the field acquisition parameters. The processing is carried out in steps to produce the final seismic sections. These steps include data conditioning, parameter analysis, data enhancement, migration, and depth conversion.

4.2.2 -Data conditioning

4.2.2.1 –Demultiplexing

The seismic data were recorded in a multiplexed SEG B format as a single data stream, in which each recording channel is scanned sequentially. Demultiplexing is the process of recovering the data recorded at each channel as a time series. The trace-sequential (SEG-Y formatted) seismic data were read from ½ inch tapes. In all there were eight reels, of uncorrelated data which led to three reels of correlated data with 147 shot files for seismic line (BV-1-92), and five reels of uncorrelated vibroseis data for the Columbia (SM-1) seismic line (135 shot files). Figure (4.5) shows three uncorrelated shot files from SM-1.

The data were processed using the SierraSEIS 2-D seismic processing software package and PROMAX 2-D software Package mounted on the Sun workstations at the Department of Geology and Applied Geology. I report here the work I did using the SierraSEIS package.

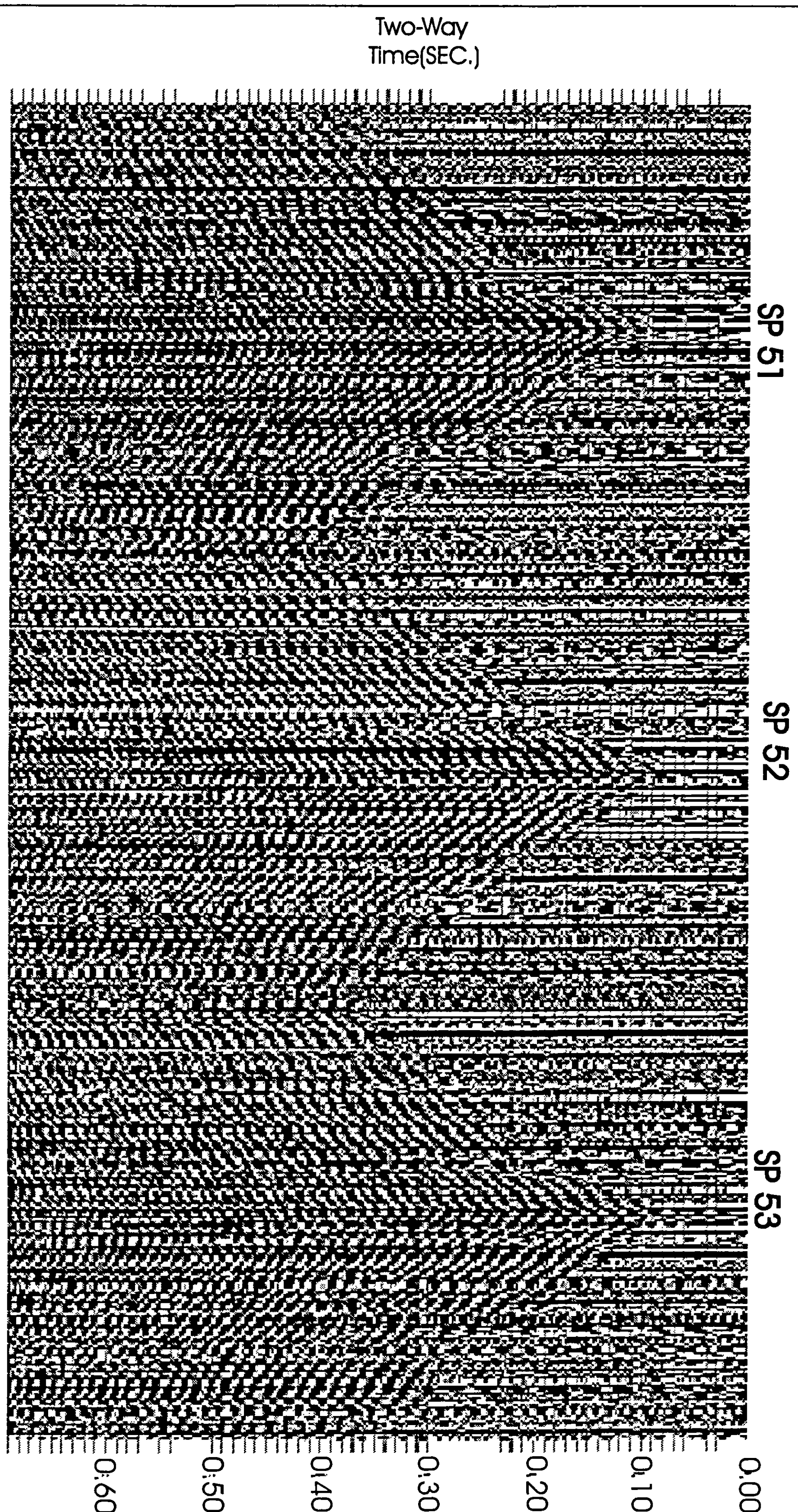

Figure 4.5 Display of Uncorrelated Shot files (raw data)
(from Seismic line SM-1)

4.2.2.2 -Correlation (Vibroseis)

For the vibroseis source, the data have to be correlated with the original pilot signal to produce a set of seismic records with a form equivalent to what would have been observed if the seismic source was an impulse source. For a linear sweep, we can write the vibroseis signal as:

$$S(t) = A \cos 2\pi(f_0 + Qt)\, t \qquad 0 \leq t \leq T, \text{ T (Sweep)} \quad \text{(Equation 4.1)}$$

$$Q = \frac{f_m - f_0}{2T} = \frac{W}{2T}$$

We know that if we correlate S(t) with itself (matched filter), we collapse this long waveform into a compact symmetric pulse:

$$\Phi_{ss}(t) = \int S(\tau)\, S(t+\tau)\, d\tau \quad ,$$

which is the autocorrelation function of S(t). The relation of the peak value of the correlation function to the amplitude of the sweep is illustrated in Figure (4.6). If the amplitude before correlation is A, the amplitude of the wavelet after correlation is A^2 T/2. The improvement of the signal to noise ratios is approximately $= \sqrt{2TW}$, where T is the sweep duration and W is the frequency bandwidth.

The data from line BV-1-92 were supplied to us already correlated in SEG-Y format. The data from SM-1 were supplied to us uncorrelated in the SEG-B format. IMCL geophysics carried out the demultiplexing and correlation for us in the first instance. We later correlated the data from SM-1 ourselves when the ProMAX software became available.

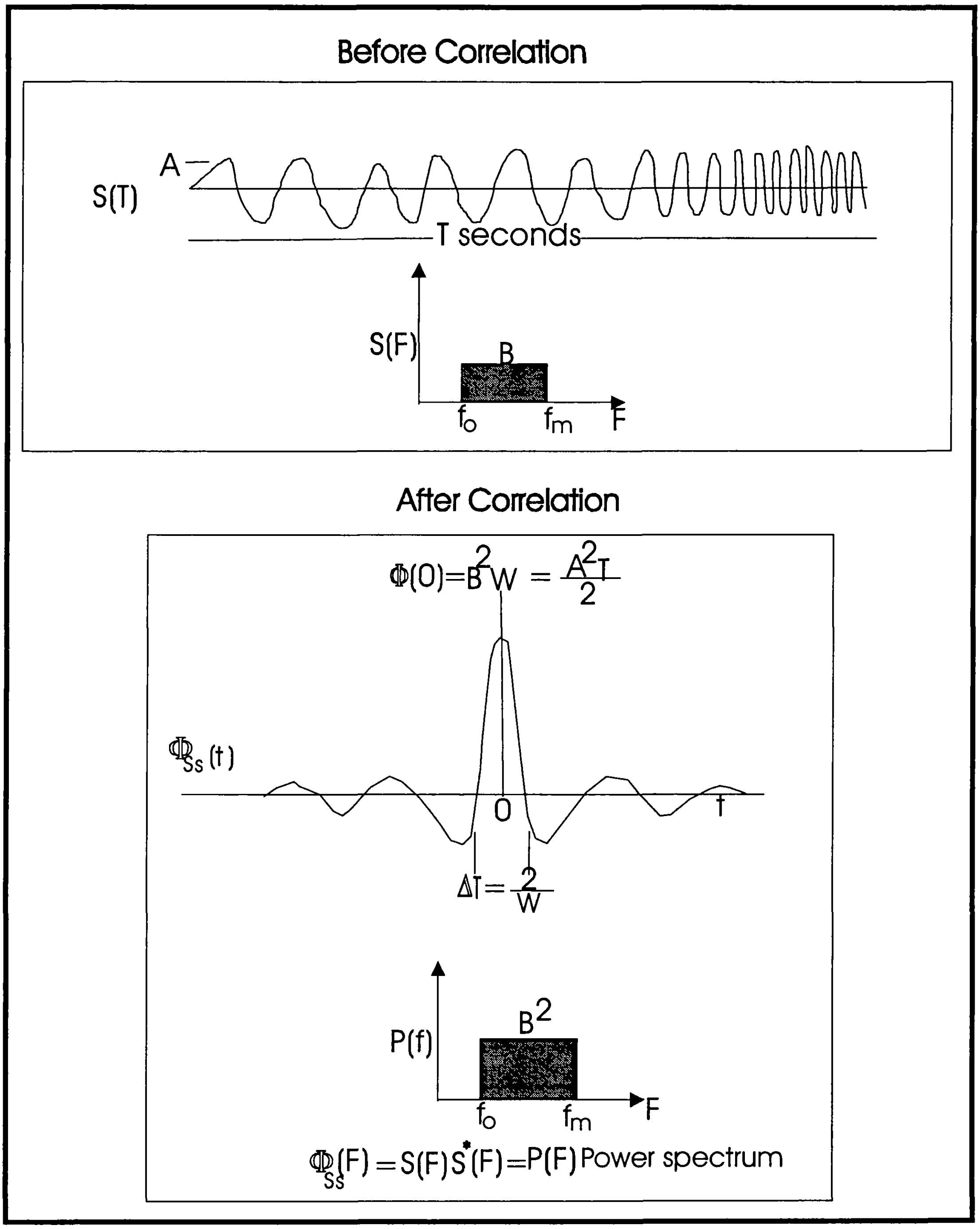

Figure 4.6- Vibroseis sweep with associated wavelet produced by autocorrelation.

4.2.2.3-Seismic Line Geometry

The geometry of the seismic lines was assigned early in the processing sequence, because most processors require the geometry information. Using the geometry information we sorted the seismic data into CMP gathers using binning. Binning is the procedure used for defining common midpoints for seismic lines with a crooked geometry. The survey data outlines the XY coordinates and elevations of all the shot points and the receiver stations. The observer's report identifies every shot point and the relevant spread geometry. We used the SierraSEIS geometry processor (PLGEOM) to store the appropriate information in each trace header, assign traces to CDP bins, and to calculate receiver and source statics. Figures (4.7) and (4.8) are elevation profiles with associated total statics for seismic line BV-1-92 and for seismic line SM-1 respectively. Figure (4.9) is a base map of BV-1-92 showing the X,Y coordinates of the receiver stations and shot points. Figure (4.10) shows the same information for SM-1.

SW NE

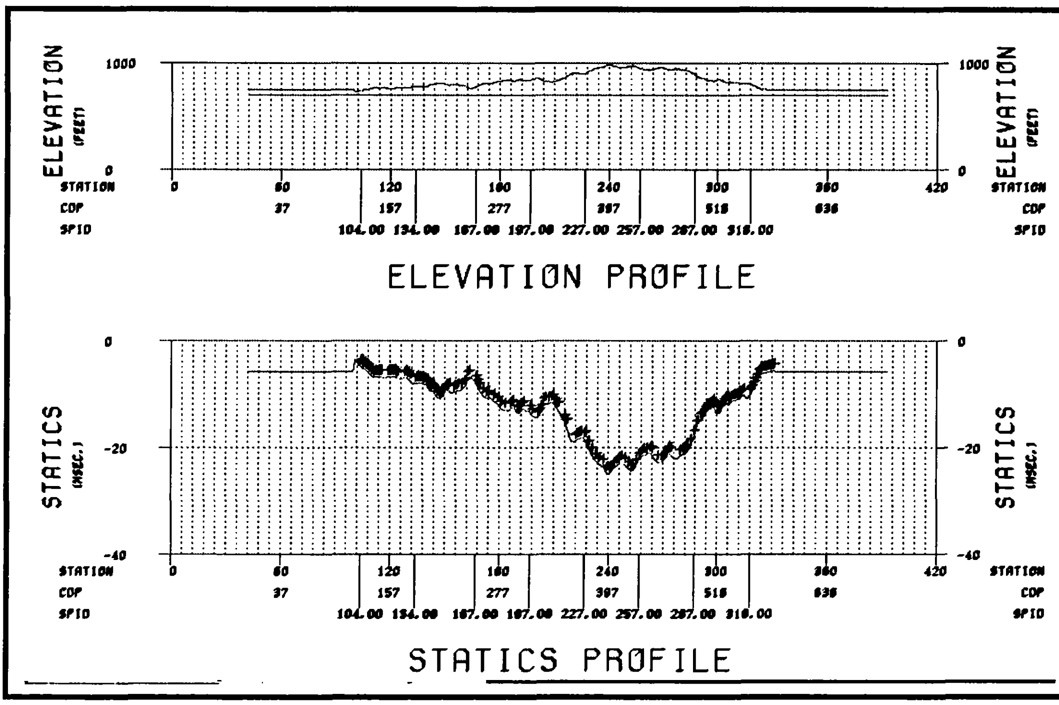

Figure 4.7- Elevation and static profiles of BV-1-92 created by the PLGEOM processor

North South

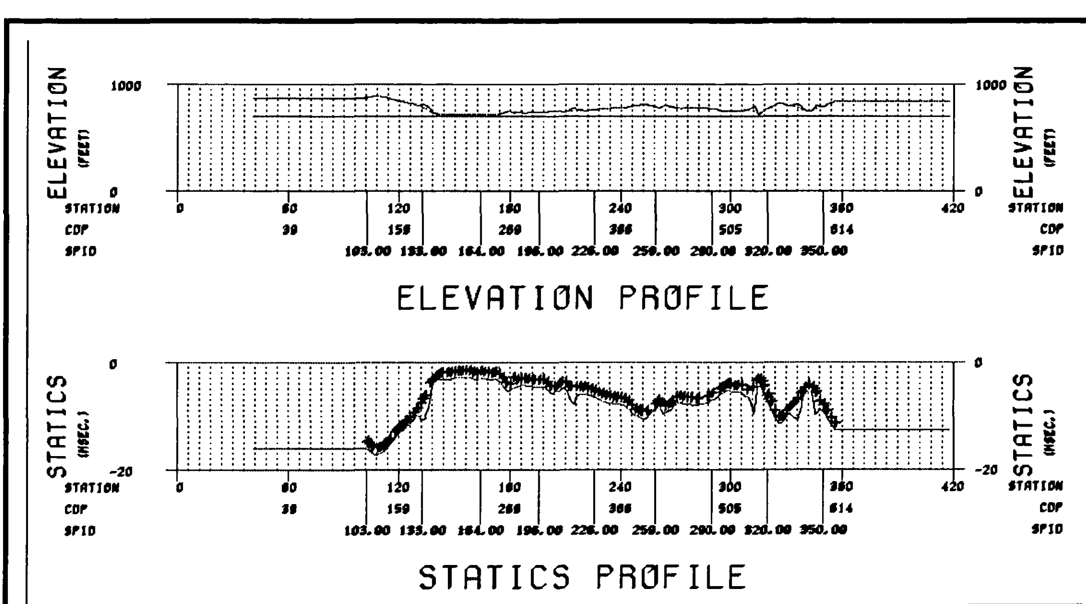

Figure 4.8- Elevation and static profiles of SM-1 created by PLGEOM.

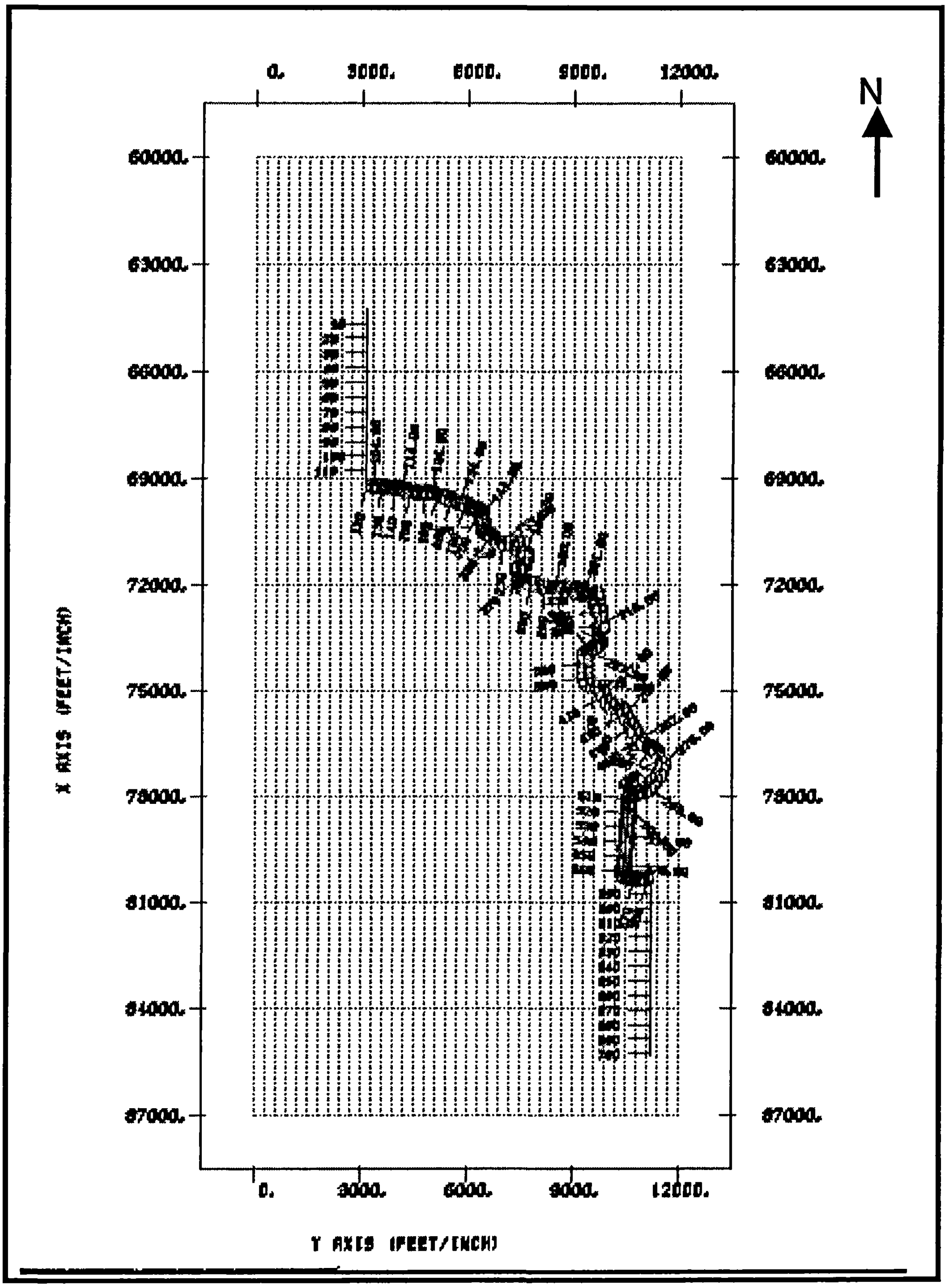

Figure 4.9- Base map of seismic line BV-1-92 (shot points, and CDPs)

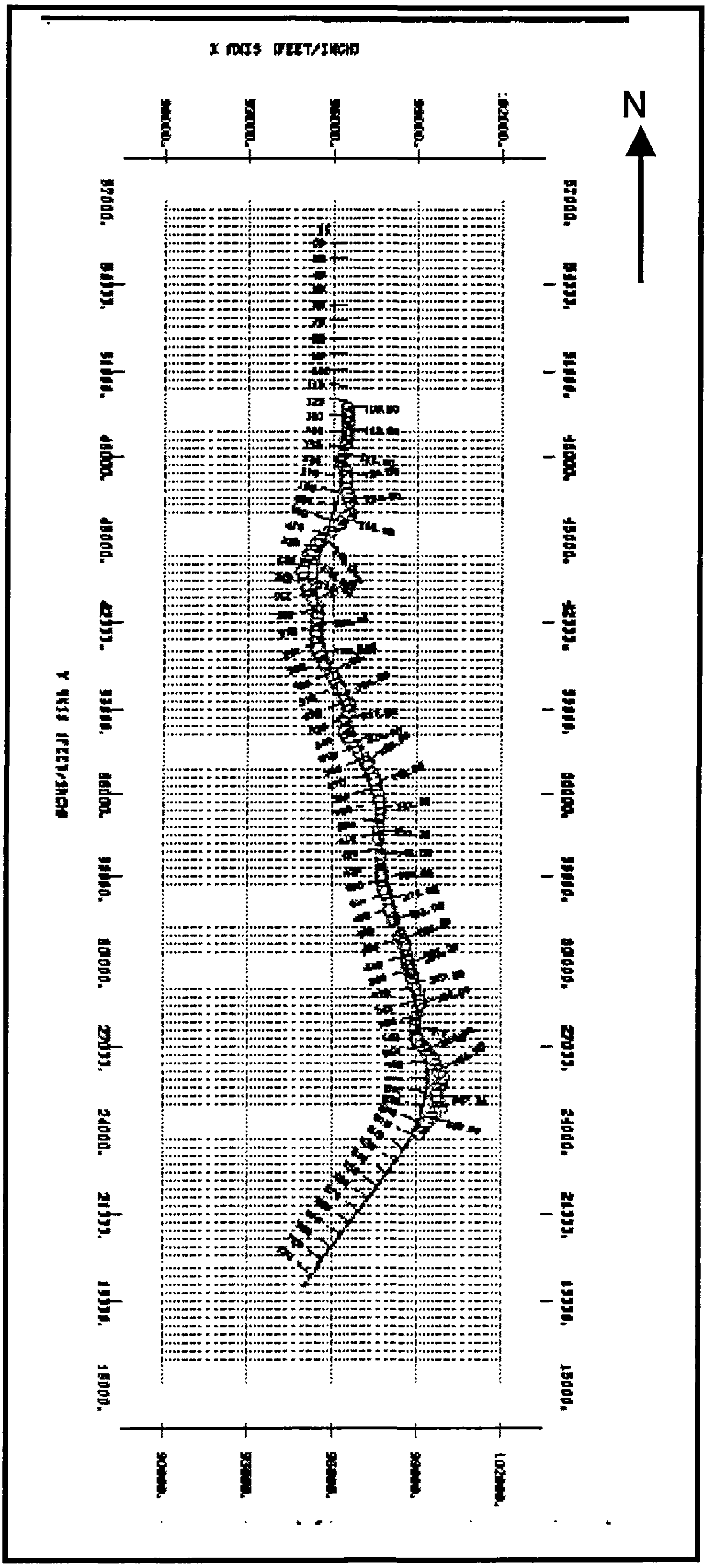

Figure 4.10- Base map of seismic line SM-1 (shot points, and CDPs)

4.2.2.4- Trace Editing and Muting

Trace muting is the process of zeroing the undesired part or parts of the trace with noise. The amplitude of the seismogram is set equal to zero for those parts of the record that contain large amplitude near-surface or other unacceptable noise. This is done to ensure that undesirable data such as first arrivals and refraction arrivals will not be summed with reflection energy to produce the final stacked record. The first part of the trace is normally muted before carrying out any stacking process. This is occasionally referred to as first break suppression. Limits of the trace segments to be muted are decided from the inspection of the shot records.

Part of a trace, a whole trace, and occasionally a whole shotpoint record may be very weak or contain abnormally high amplitude noise events. Data editing involves complete removal of such records before proceeding. Setting to zero all undesired trace-samples effects this.

The polarity of a few traces was inverted. Consequently the peak-trough sense of such traces are reversed with respect to the recording. Finding and inverting the polarity of such traces is an important part of the data editing. Trace editing was preformed on the shot-sequential files of the two seismic lines to remove unwanted data. We used this option to eliminate spikes, apply mutes, and remove bad traces by zeroing such traces. We also corrected the first thirty-nine shots of seismic line SM-1 by correlating with the appropriate pilot. These functions were carried out by the following SierraSEIS processors: DESPK, MUTE, ZERO and RPOL respectively. Figure (4.11) shows several shot files from line BV-1-92 after editing and muting.

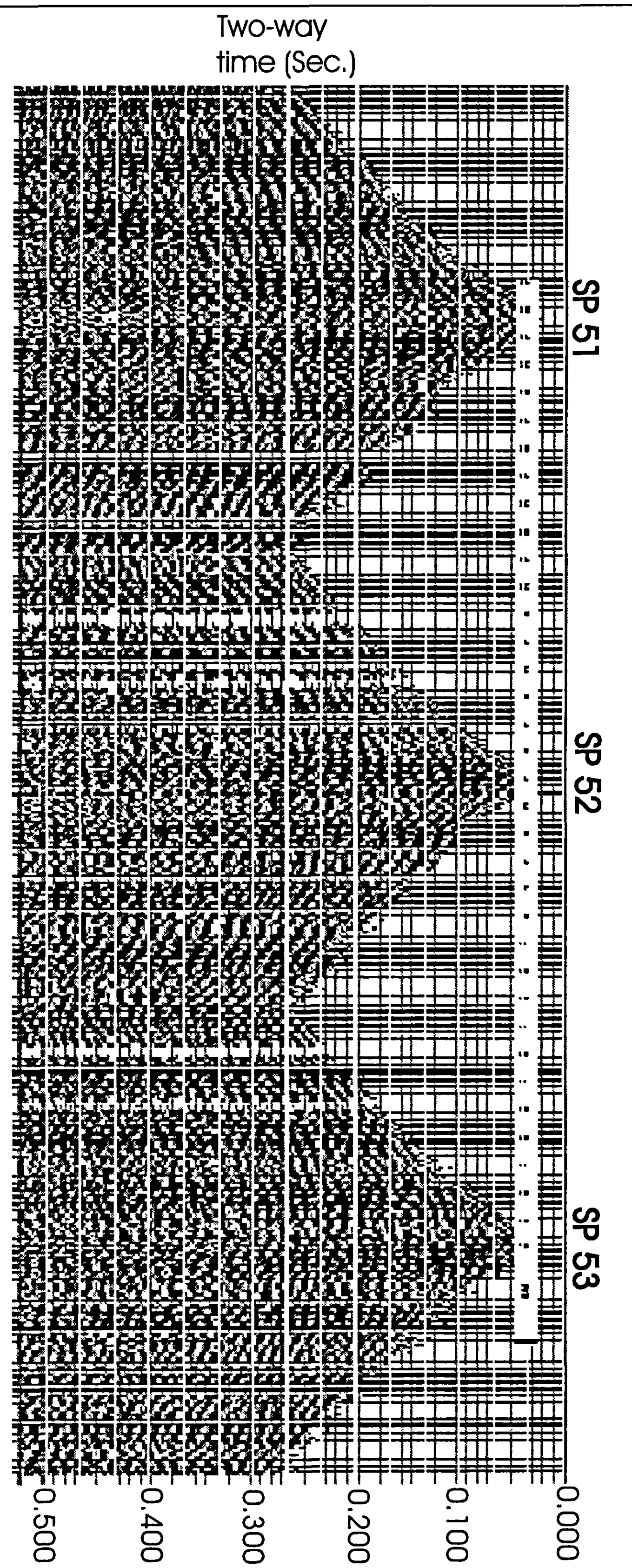

Figure 4.11 - Corrected and Edited Shot files
(compare to Figure 4.5)

4.2.2.5-True Amplitude Recovery

Seismic waves attenuate when traveling in a non-elastic medium. Thus the reflection amplitude recorded on the magnetic tape is the end result of many attenuating factors including, spherical divergence, inelastic attenuation, and a net gain imposed by the recording station. The process of true amplitude recovery involves the removal of all these effects. This is carried out by multiplying the seismic trace by the function F_{TAR} (t) , which is given by

$$F_{TAR}(t) = \frac{C\ V(t)\ t\ e^{\alpha\, v(t)\, t}}{G(t)} \qquad \text{(Equation 4.2)}$$

Where V(t) is the average velocity as a function of the record time t,

α is the absorption coefficient,

G(t) is the time function of the net gain applied by the recording station,

C is a scaling constant.

The factor V(t) t corrects for the spherical divergence (spreading loss), because the source pulse spreads out spherically and the pulse amplitude decays with distance. The exponential factor corrects for the inelastic attenuation (absorption), inelastic friction results in (heat) loss associated with particle motion as the wave passes, and G(t) corrects for station response. The SierraSEIS SPHDIV processor applied time-varying scalars to compensate for the effects of the spherical divergence. For any sample at time T, the magnitude of the scalar is computed and applied to every sample of the trace by

$$\text{Spherical Divergence} = T\left(\frac{V_T}{V_0}\right)^2 \qquad \text{(Equation 4.3)}$$

Where T is the time in seconds

V_T is the RMS velocity at time T

V_0 is the RMS velocity at time 0

The AGC (automatic gain control) processor is used to apply a balancing scalar that equalizes the amplitudes within a trace.

4.2.2.6 -CDP Sorting (Gathering)

The gathering processor sorts the data from one data order to another. After the data are correlated and the geometry information applied the trace –sequential shot files, data were edited. The shot ordered traces are sorted into a common depth point (CDP) gather file using the RASORT processor. Figure (4.12) shows selected CMP gathers. The main objective of common-depth point (CMP) investigation is to sample each subsurface point several times. If the information on each record is then summed after suitable processing, true reflection arrivals will be enhanced and various unwanted signals will tend to be reduced or eliminated, thereby producing superior records. For 120-channels the CMP gathers will typically consist of 30 to 60 traces when spacing between sources is twice the spacing between receivers or if they have the same spacing between receivers respectively. When a shot is missed or rejected after acquisition because of poor data quality, the fold of coverage will drop. At the very beginning and the ending of each line where fold of coverage is gradually built up and drops off, these zones are known as the roll-on and roll-off respectively.

4.2.2.7-Static Corrections

The application of static corrections is a very important step in processing seismic reflection data. Static corrections comprise both a topographic correction and what is called the weathering correction. A static correction is a constant time adjustment, rather than a dynamic time adjustment, applied to seismic trace. Static correction adjusts the trace for travel time anomalies introduced by variations at the near surface. These variations are due to changes in the surface elevation, velocity of the near surface layer, and the thickness of the near surface layer. Unless static corrections are applied, a depth model (Figure 4.13) produces a false subsurface picture due to the variations in travel times caused by the variations in surface elevation. The false reflector is a mirror image of the surface profile.

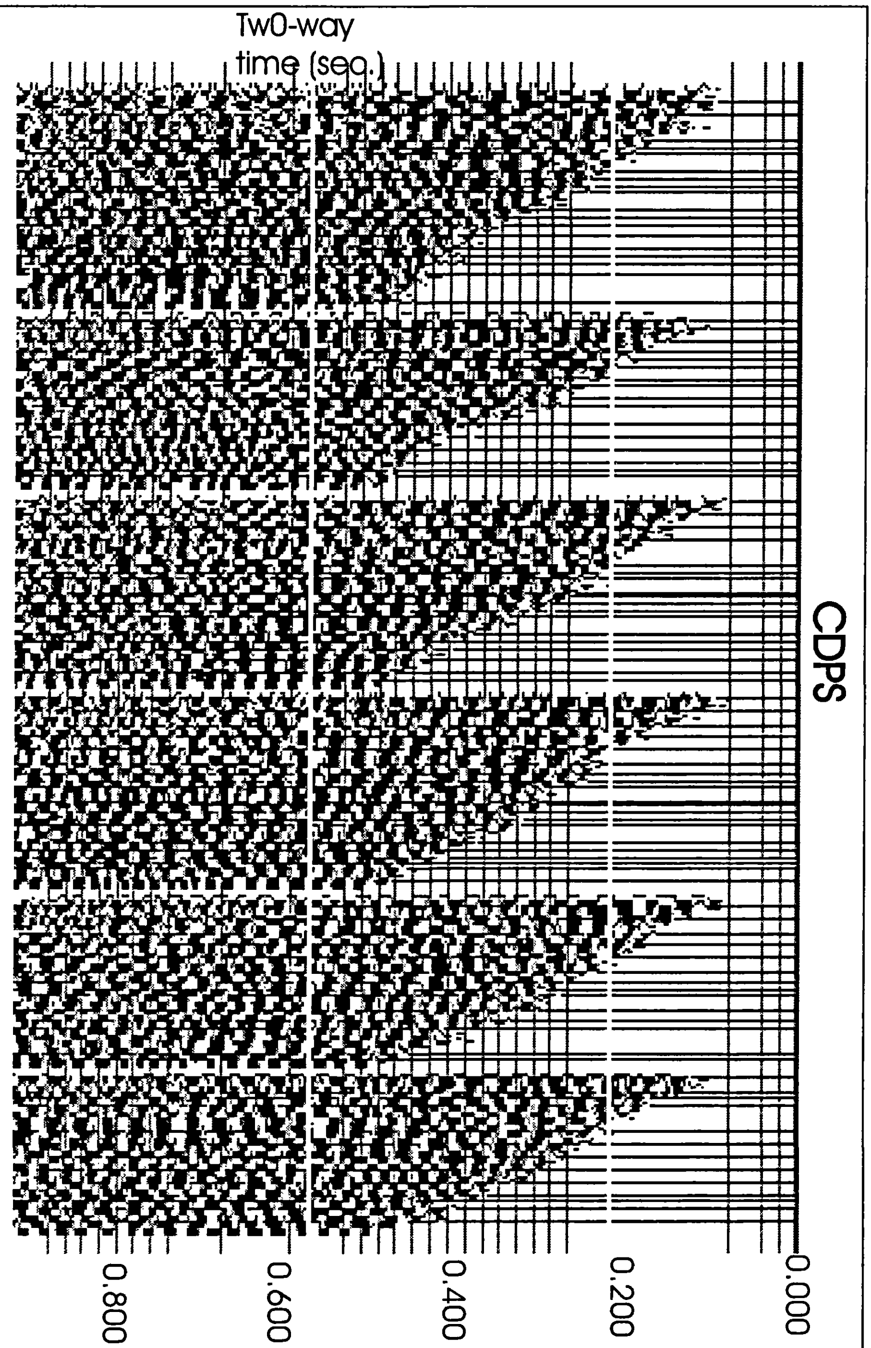

Figure 4.12- Selected CMP gathers

A false structure also can be produced as a result of variable thickness of the low-velocity layer, because travel times in a thick low velocity layer are greater than travel times in thinner material of the same velocity.

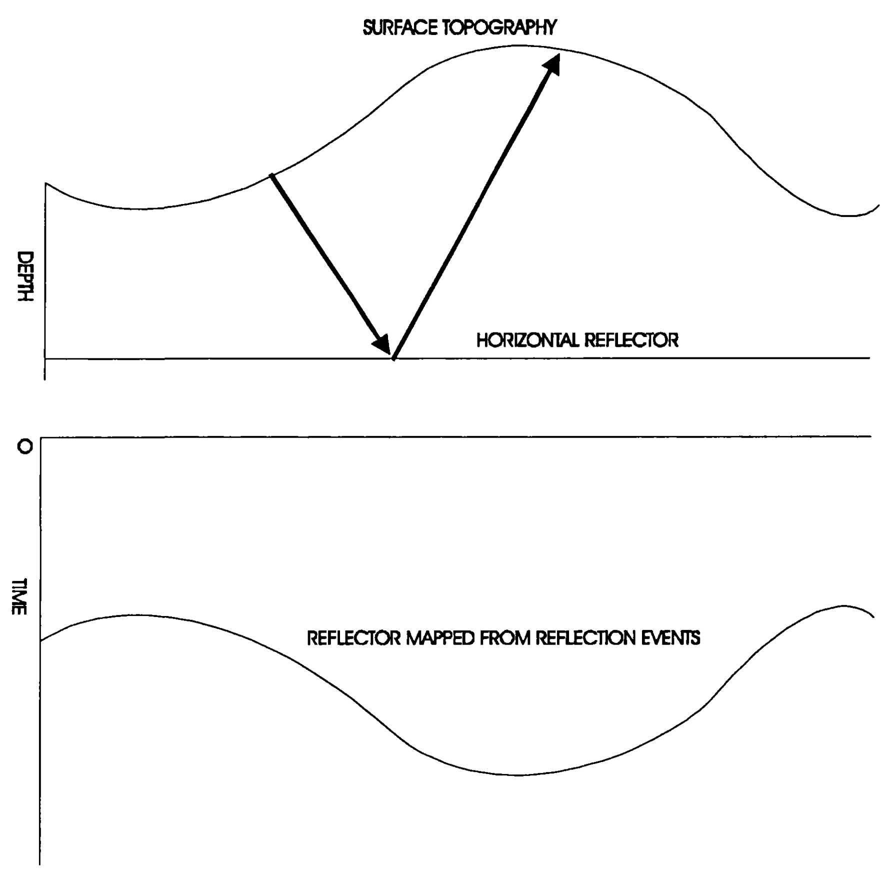

Figure 4.13- Depth Model of a flat Reflector and the effect variable surface elevation

Ideally the computation of static corrections requires the knowledge of the thickness and the velocity of the low-velocity layer. This information can be collected using uphole surveys or refraction surveys. The data must be corrected to a reference surface (Figure 4.13). Thus, the traces are corrected by the amount of time it takes for travel from the source and receiver to the reference surface. This is as if all the sources and the receivers were placed on the reference datum.

This allows us to map the accurate subsurface picture on the corrected time section. Therefore, the static correction is divided into two parts, one for the travel time from the source to the datum (source correction, or source static), and the other is for the travel time from the receiver to the datum (receiver static). In the case where both the source and the receiver are at the surface, the shot static correction is:

$$T_s = \left(\frac{E_S - E_D}{V_W} \right) \quad \text{(Equation 4.4)}$$

The receiver static correction is;

$$T_r = \left(\frac{E_R - E_D}{V_W} \right) \quad \text{(Equation 4.5)}$$

The static correction applied during the processing can be broken into two parts that depend on the sample interval of the data. These two parts are the number of sample periods and the fractional part of a sample period the static correction. The total static correction T_{st} depends on the following factors:

1- The perpendicular distance of the source from the datum plane;
2- The surface topography, or the perpendicular distance of the detector from the datum;
3- The velocity variation of the surface layer along the seismic line;
4- The thickness variation of the surface layer.

In computing $T_{st,}$ it is usually assumed that the reflection raypath in the vicinity of the surface is vertical. As this is usually close to the real situation, this assumption introduces only a negligible error. The total static correction T_{st} is made up of two parts. The source correction T_s and the receiver correction T_r, where

$$T_{st} = T_s + T_r \quad . \quad \text{(Equation 4.6)}$$

Once the total static correction is computed it is then applied to each seismic trace by shifting the whole trace in time by an amount equal to the algebraic sum of the two corrections T_s and $T_{r.}$

The SierraSEIS static correction processors compute nonsurface-consistent residual statics, surface-consistent statics. The STATAPLY processor was used to apply the static shift to the seismic traces, which were computed by the GEOMETRY processor. The elevation of the reference datum was 700 ft (213 m) above sea level and the velocities of the near surface layer and the underlying layer chosen to be 5000 ft/sec. (1524 m/sec). In the first static calculation using the geometry processor. The most negative static correction for the seismic line BV-1-92 seismic line is -49 ms, and the least negative correction for the same line is –8 ms. For the seismic line SM-1 the most negative static correction is -34 ms, and the least negative correction for the same line is –5.5 ms.

4.2.3- Filtering Processors

It is well known that the recorded seismic traces are a mixture of signal and different types of noise. Filtering separates signal and noise. The seismic traces can be high-pass, low-pass, or band-pass frequency filtered to limit the range of frequencies on the record. Application of digital filtering to geophysical data is often done to improve the signal to noise ratio of the data. Filters are normally implemented by transforming the data into a domain in which signal and noise separate. The better the separation in the transformed domain, the more robust the filtering. Thus the filter design is based on the frequency characteristics of the signal and the noise.

A number of filters were applied to the data. Many plots were generated to examine the frequency spectrum of the data to design the proper filters. First, a time-frequency processor TIMFRQ was applied to a number of shot points to examine the amplitude and the frequency content of the vibrator produced signal. Plots of frequency content as a function of time were obtained (for example, Figure 4.14). These plots show that the frequency ranges of the signal as well as the noise frequencies, such as the 60 Hz component on SM-1. This is present because the notch filter was out during the recording. Therefore, the processor NOTCH was applied to these data.

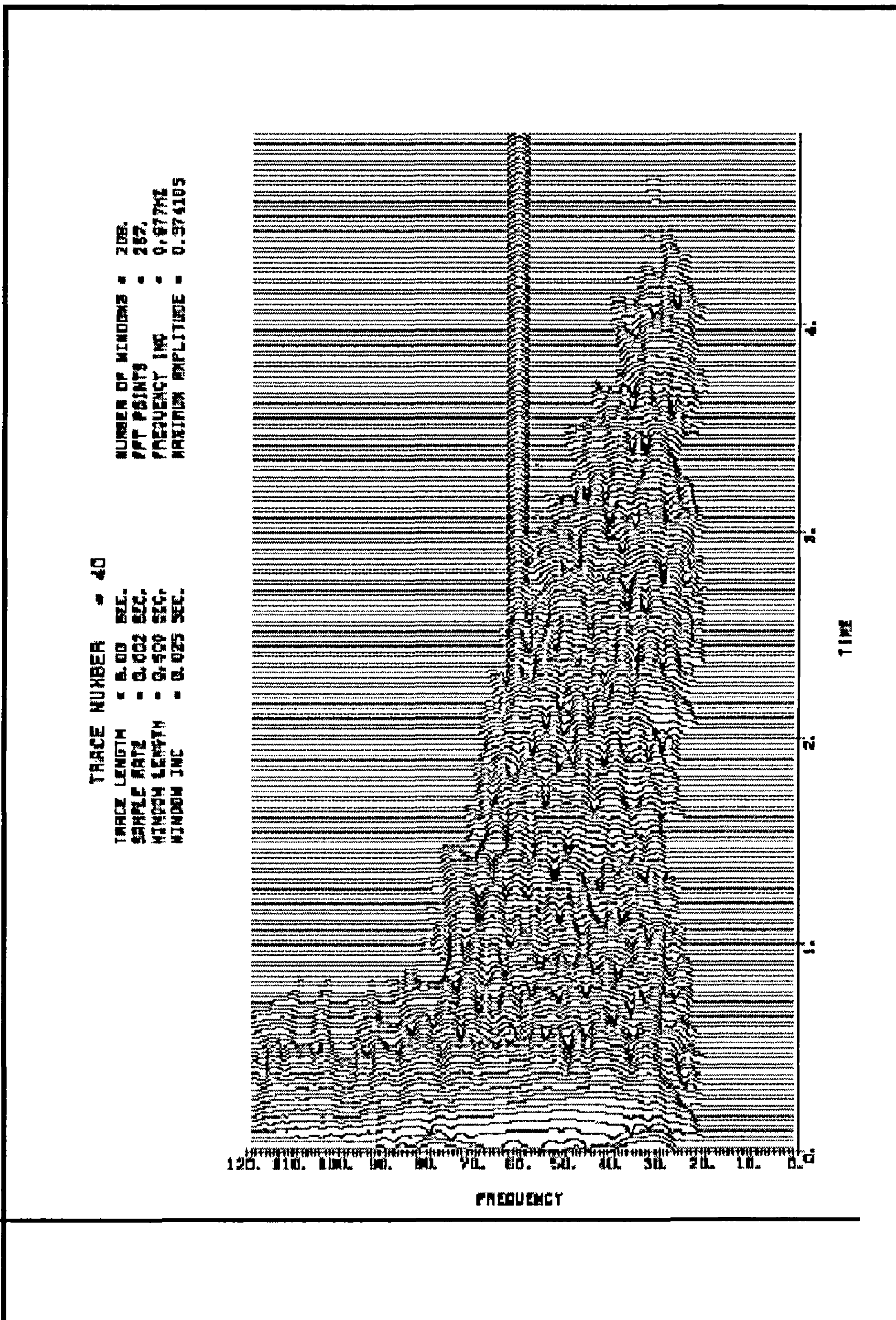

Figure 4.14- Frequency versus time plot of seismic trace

Another frequency analysis processor, FREQAN, was applied to the data. These processors (Figure 4.15) show that the band of useful seismic signal is between 20 Hz and 70 Hz. Thus most of the applied band pass filters used these two limits for the low-pass and high-pass frequencies respectively. This was done using the STVF processor, which applied space and time-varying digital filters across the data.

Frequency-wave number filtering is based on the separation of the seismic data from noise in f-k space. Attempts were made to use the f-k filter but these were not really useful, as the f-k spectra were extremely noisy (Figure 4.16). This is probably due to the irregular spacing of the traces in the space domain as a large number of traces had to be edited from shot records from crooked lines.

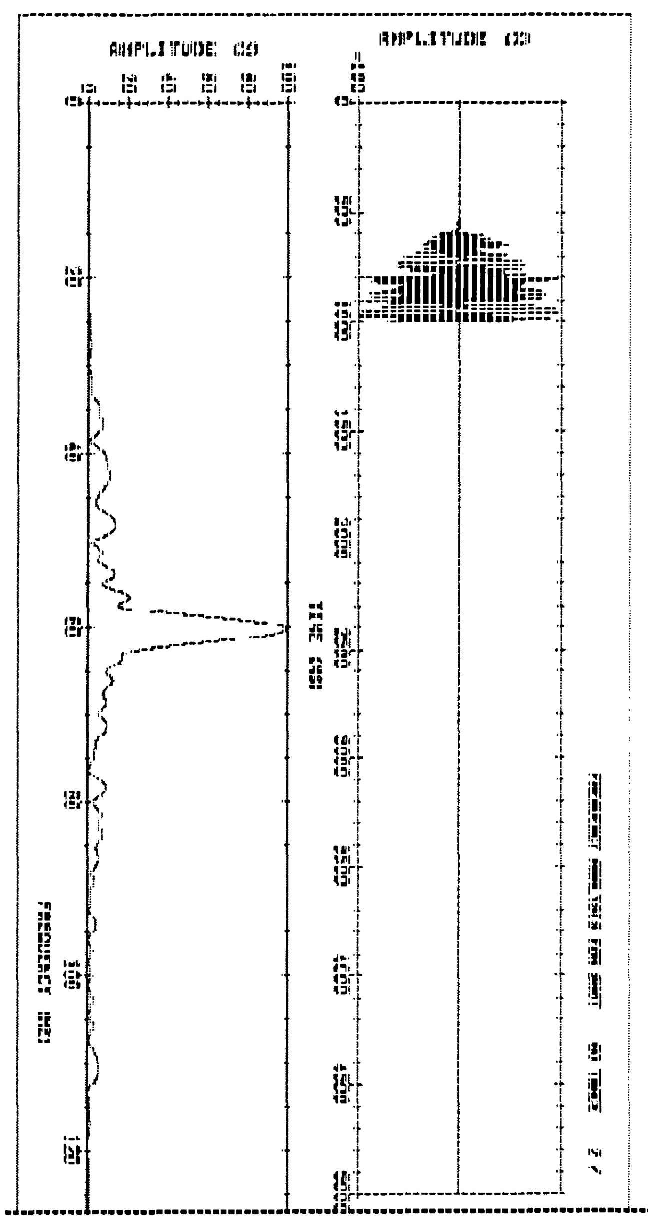

Figure 4.15- Frequency analysis using the FREQAN Processor

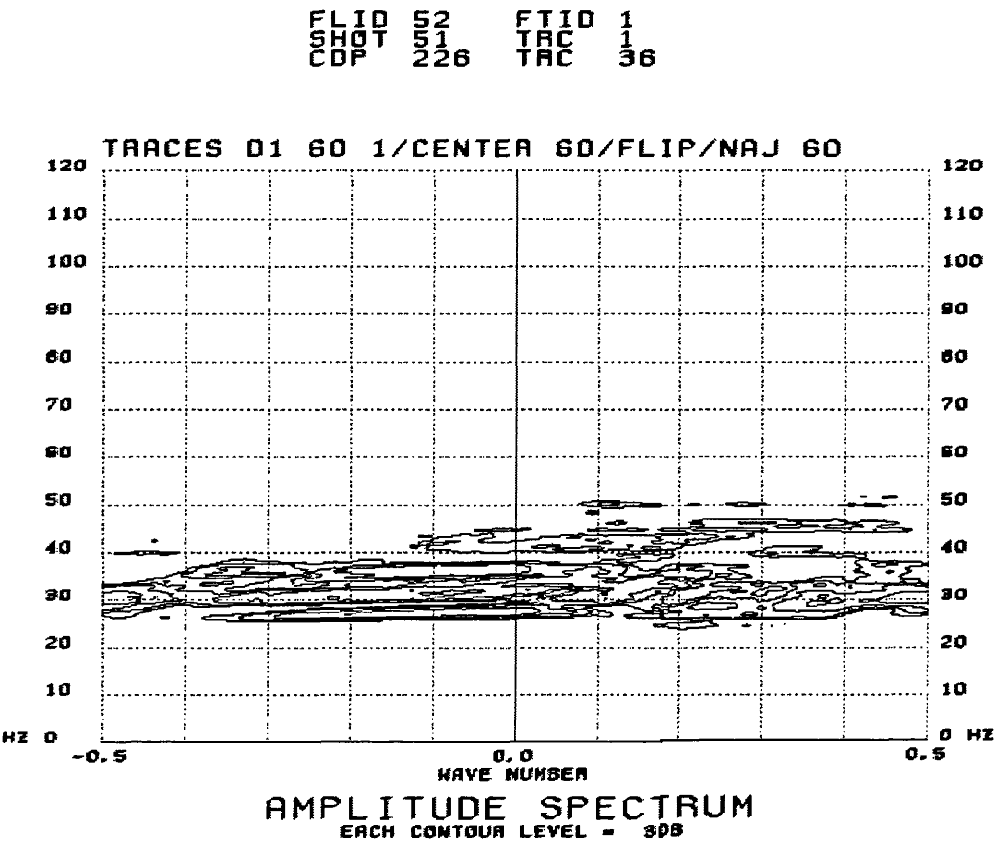

Figure 4.16- Frequency-Wave number (F-K) Analysis

4.2.4- Rawstack

At this stage the processing has reached the CDP-stacking, the reflection record-times are reduced to two-way vertical times measured from a unified datum plane, and each CDP gather now is ready for stacking. This is done by summing together the contributing traces for each CDP and normalizing the sum with respect to the total live traces in each sum. Optimum correction parameters are essential for perfect signal alignment and the subsequent stacking process. After the appropriate adjustment and corrections as outlined, the records are stacked using an estimated velocity function. Generally the stacked section has substantially improved S/N over any of the individual traces. The stacked CMP gather produces a single zero-offset or normal incidence trace, equivalent to a common source and receiver point on the surface.

4.2.5-Stacking Velocity Analysis

From linearity, the individual frequency components are retained under stacking. However, the signal-to-noise ratio (S/N) is enhanced. Assuming optimum static and dynamic corrections, the enhancement of the signal is proportional to the square root of the stack-fold. To obtain perfect dynamic correction, computation must be based on the minimum travel time ray path. This means that the ray path must be determined by applying Snell's law and using the actual velocity distribution in the traversed medium. The apparent velocity that maximises the amplitude or one of various statistical parameters is called the stacking velocity. The stacking velocity depends on the medium, and is not, in practice mathematically defined. Stacking velocity can vary with offset due to the non-linear relation existing between Δt and the trace offset. The dip of the reflector is another important factor that affects the stacking velocity value. Stacking velocity analysis of the CDP gathers is carried out using the CDP gathers. Careful selection of CDP gathers for velocity analysis is important as they must contain reflected energy.

4.2.5.1- Continuous Velocity Estimation

The velocity analysis was carried out on selected CDPs by generating constant velocity panels using the VELPANEL processor. Figure (4.17) shows nine panels from BV-1-92, generated with a velocity increment of 500 ft/sec. (152 m/sec), starting with a velocity of 13000 ft/sec. (3962 m/sec), ending with a velocity of 17000 ft/sec. (5181 m/sec). This analysis shows that, for the shallow part of the data the best stacking velocity is close to 14000 ft/sec. (4267 m/sec). For the strong reflector near 400 ms., approximately 16000 ft/sec (4877 m/sec). is appropriate. A similar analysis for SM-1 shows the same velocity at 400 ms.. The constant velocity stack method is useful for very noisy data. A separate velocity analysis on the data was performed using the VELS processor that plots contours of the semblance parameter as a function of time and velocity. Figure (4.18a) and Figure (4.18b) are semblance plots for CDP's from SM-1 . These are averaged from two adjacent sets of CDP gathers. The stacking velocity varies from 13500 ft/sec (4114 m/sec) at the shallow part to 15600/sec (4755 m/sec) near 430 ms to 16600 ft/sec (5060 m/sec) near 640 ms.

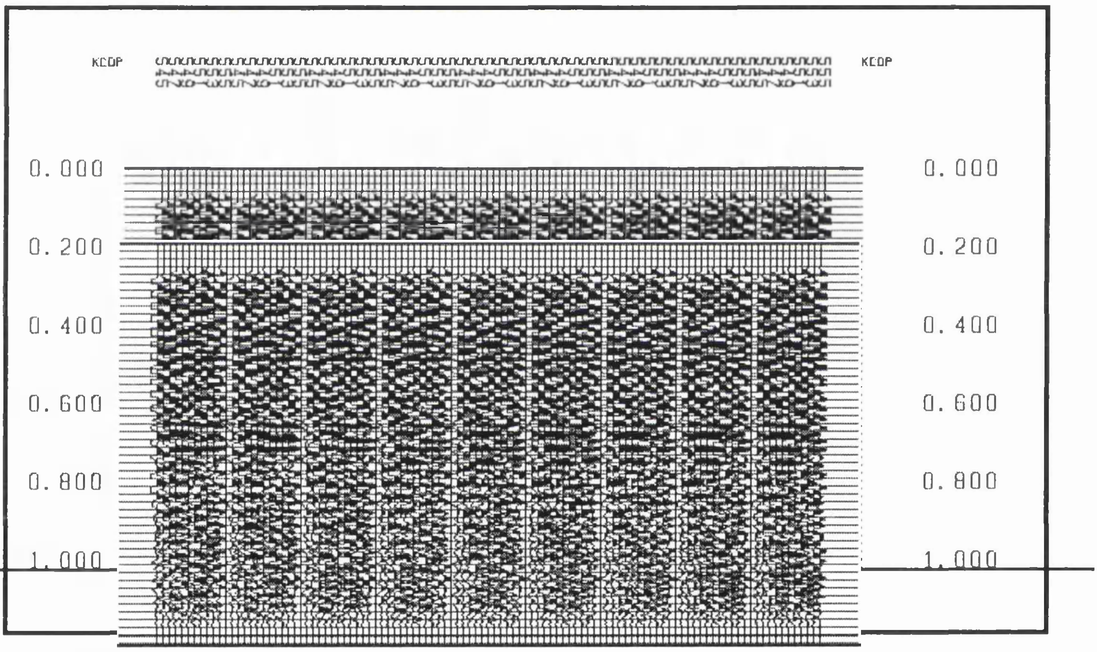

Figure (4.17) Plot of nine panels of stacked CDP gathers with velocity increment of 500 ft/sec (152 m/sec) from 13000 ft/sec (3962 m/sec) Generated by VELPANEL.

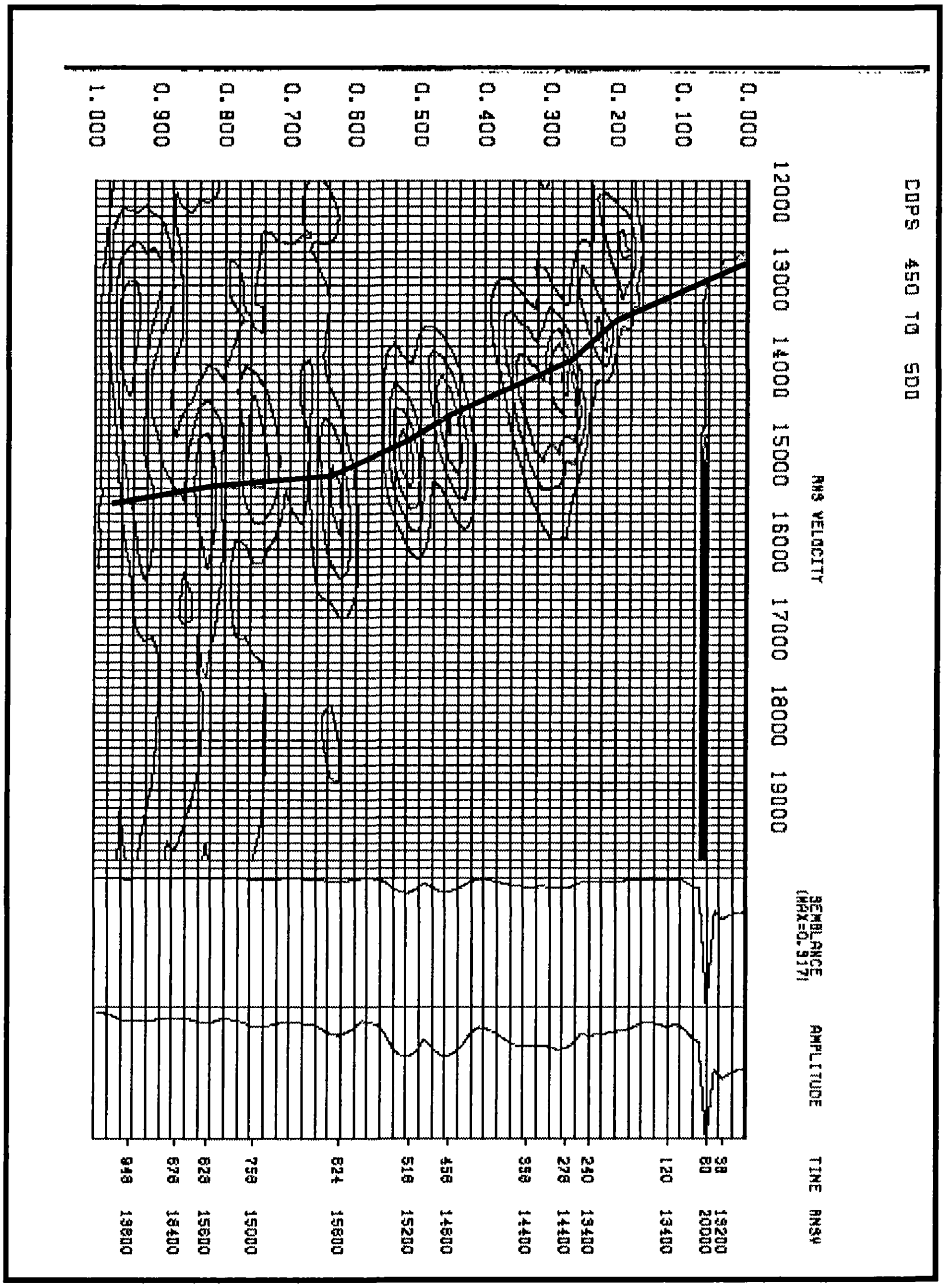

Figure (4.18a)- Velocity spectrum of CDPs (450-500) of seismic line SM-1

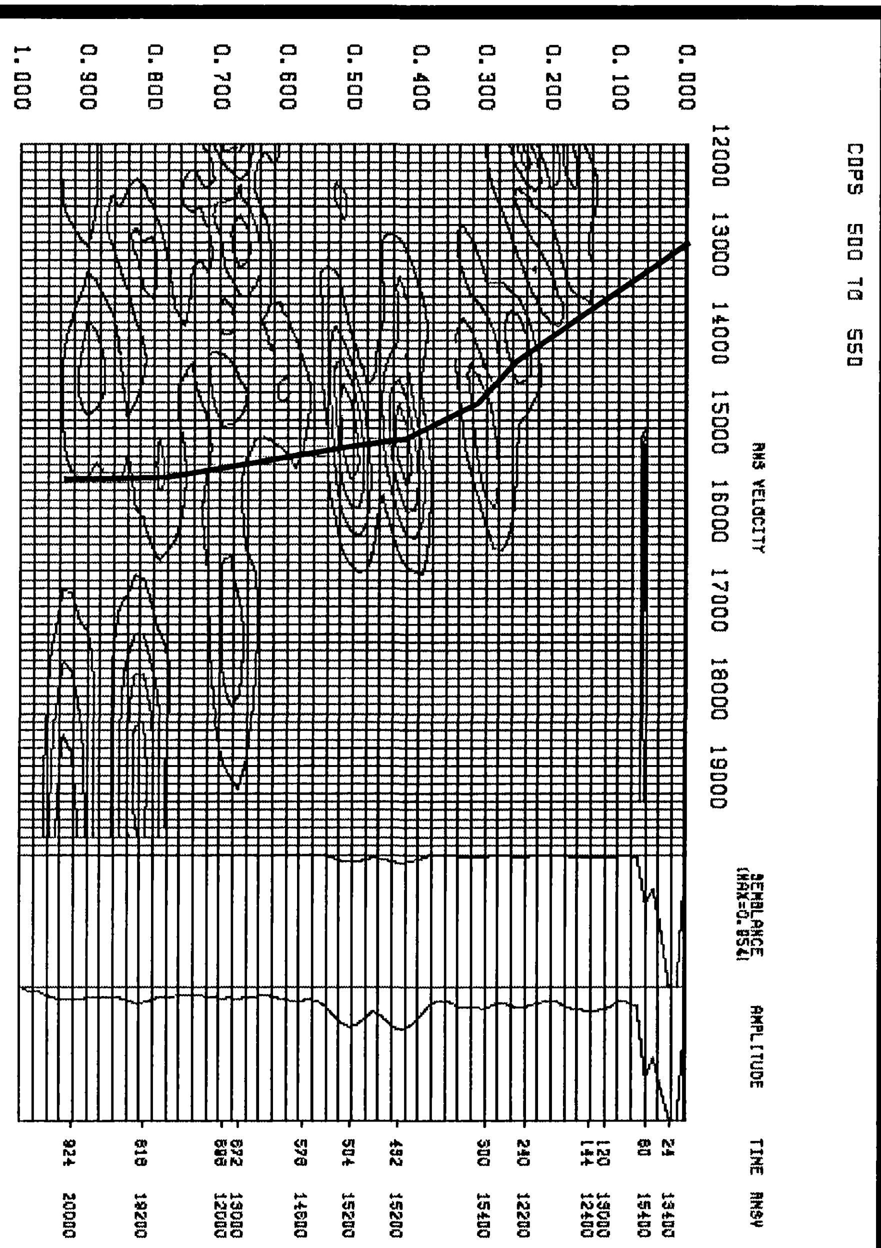

Figure 4.18b- Velocity Spectrum of CDPs 500-550

4.2.6 -Dynamic (NMO) correction

After the application of the static correction the reduced record time represents the two-way slant time where both the source and detector are effectively on the same datum. Now if we examine a reflection-event on all the contributors of one CDP, we find these events falling (in the ideal case) on a hyperbola (Figure 4.19). This is due to the dependence of traveltime on the trace-offset, expressed by the NMO equation

$$T^2 = T_0^2 + \left(\frac{X^2}{V^2}\right) \qquad \text{(Equation 4.7)}$$

Where :

T = The time at offset X

T_0 = The time at zero offset (normal incident time)

X = The offset distance

V = Velocity

The normal moveout correction (NMO) is to correct for the increase in travel time for a reflected wave as the distance increases between the source and the receiver. The correction for source-receiver offset changes with time along the seismogram and is a function of the velocity variation with depth and the length of the raypath. NMO correction, properly applied, aligns the primary reflection events on the traces of CMP gather regardless of the offset distance. Thus reflections will add constructively when the traces are summed, whereas other arrivals on the records should interfere destructively.

When a proper dynamic correction Δt is applied, the reflection travel time is reduced to two-way vertical time for the same CDP. The reflection event will fall along a straight line producing alignment of the phases with the appropriate velocity. The best alignment is achieved by using the result of the velocity analysis mentioned above. The dynamic correction is carried out by computing Δt at each trace-sample. Thus a sample at time T_X will be at time $T_X - \Delta t$ after the correction. Since Δt is a function of time, different parts of the trace will be time-shifted differently. Hence the correction is called dynamic, or time-dependent to distinguish it from the static corrections. The NMO processor applies the normal moveout corrections (Figure 4.19). This correction is carried out after the specification of the RMS velocity distribution as a function of time and CDP locations through the velocity processor VELOCITY.

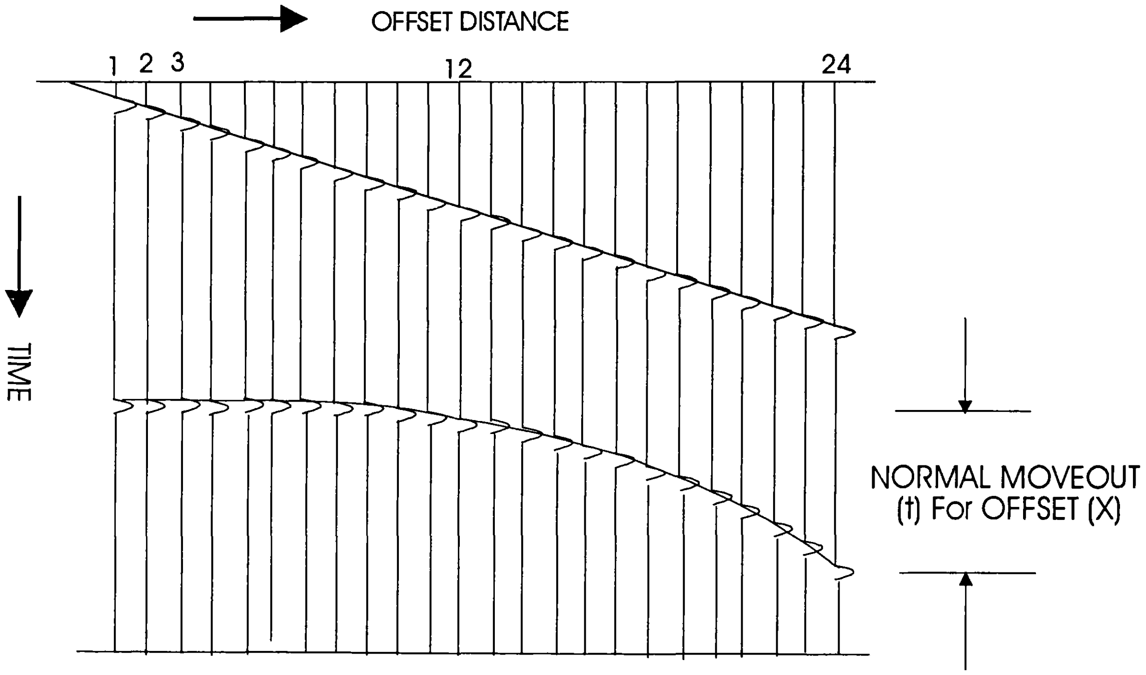

Figure 4.19- Illustration of 24-Fold C.D P. gathers Showing Normal Move Out patterns

4.2.7-Residual Statics Analysis

The field static correction may not be adequate to align the CDP traces to produce a good S/N ratio in the stacked trace. Factors contributing to errors in field statics include incorrect assumptions of the velocity and the thickness of the low-velocity layer from one point to another. The additional correction to align traces to produce a better stack is called residual statics. The residual statics, or surface inconsistent statics are the relative misalignment remaining after the application of field statics calculated from the geometry. Residual statics are calculated by the RSESTIM processor and use the following SierraSEIS common variables: KCDP (CDP number of the current trace), KRCDP (receiver CDP number of the trace), and KSCDP (sequential shot number of the shot file). The reference section of stacked CDP gathered traces is used as input for the calculation of residual statics. Each trace in the reference section is correlated with the corresponding CDP section to find the lag by which each individual trace must be shifted to match the reference. For the correlation we selected the optimum window as 200 ms. to 600 ms. as this is where the most prominent reflectors are found. The velocity analysis was repeated after the application of residual statics to improve the velocity picks. Figure (4.20), and Figure (4.21) show the same section of seismic line SM-1 before and after the residual statics are applied respectively.

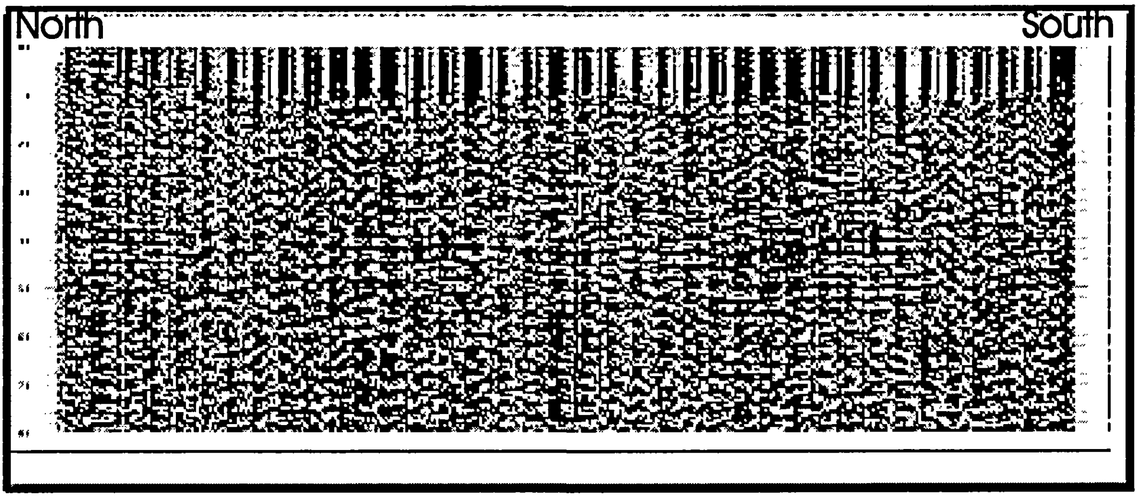

Figure 4.20 Stacked seismic section (SM-1) before residual statics

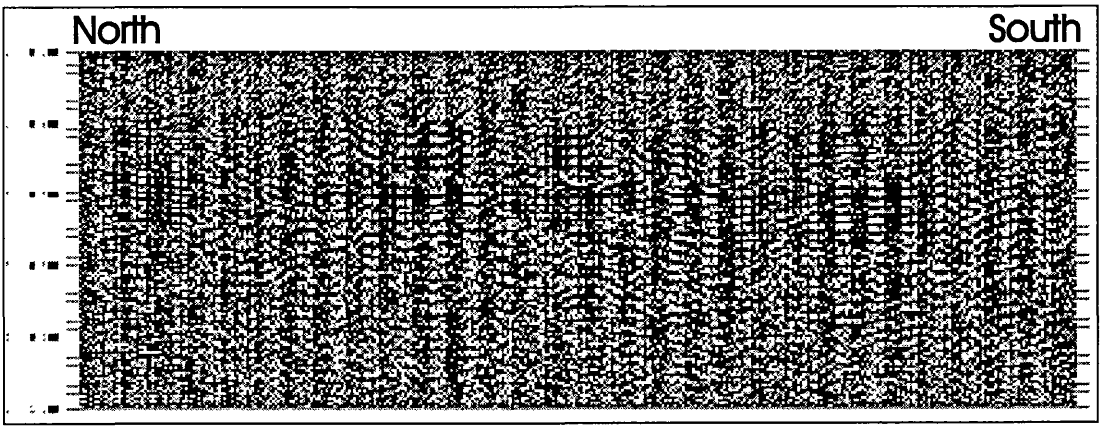

Figure 4.21- Stacked seismic section (SM-1) with residual statics

4.2.8- Migration (Seismic Imagery)/Depth Conversion

Seismic time records are migrated to correct for the fact that a stacked section or zero offset section is not a true image of the subsurface. Migration moves the reflectors to their correct positions in the section and it also collapses diffractions.
Wave equation migration was used to produce migrated sections of BV-1-92, and of SM-1. The migration velocity was chosen to be 15800 ft/sec (4816 m/sec), based on the velocity analysis and well log data.

4.2.8.1-Final Stack Display

The final migrated sections of the BV-1-92 and the SM-1 seismic lines are plotted in Figure (4.22) and Figure (4.23) respectively. Sections with better resolution in the shallow portions were produced by my supervisor, Dr. D. R. Watts, using the ProMAX 2-D processing package. In producing these sections he used the result of my velocity analysis. The major improvement came about as a result of using the POWER AUTOSTATICS processor in ProMAX. Clearly this is a superior method than what is available in SierraSEIS. Comparison between the final sections produced using either the SierraSEIS software package or ProMAX 2-D, show a significant improvement when compared to the previous industry processing.

SW NE

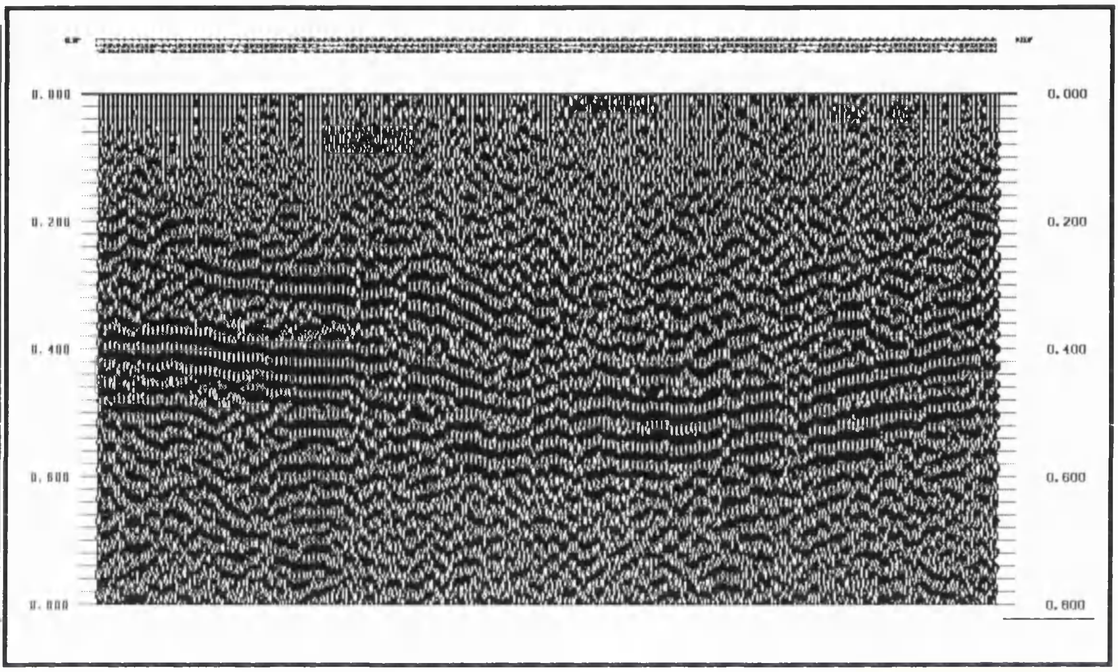

Figure 4.22 Migrated section seismic line BV-1-92

Vertical axis two-way travel time in msec.

N **S**

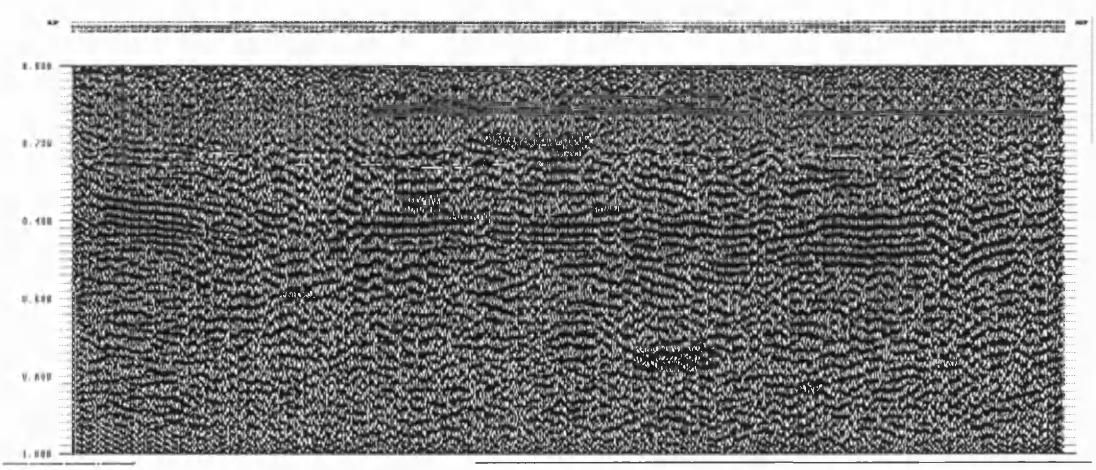

Figure 4.23- Migrated section seismic line SM-1

Vertical axis two-way travel time in msec.

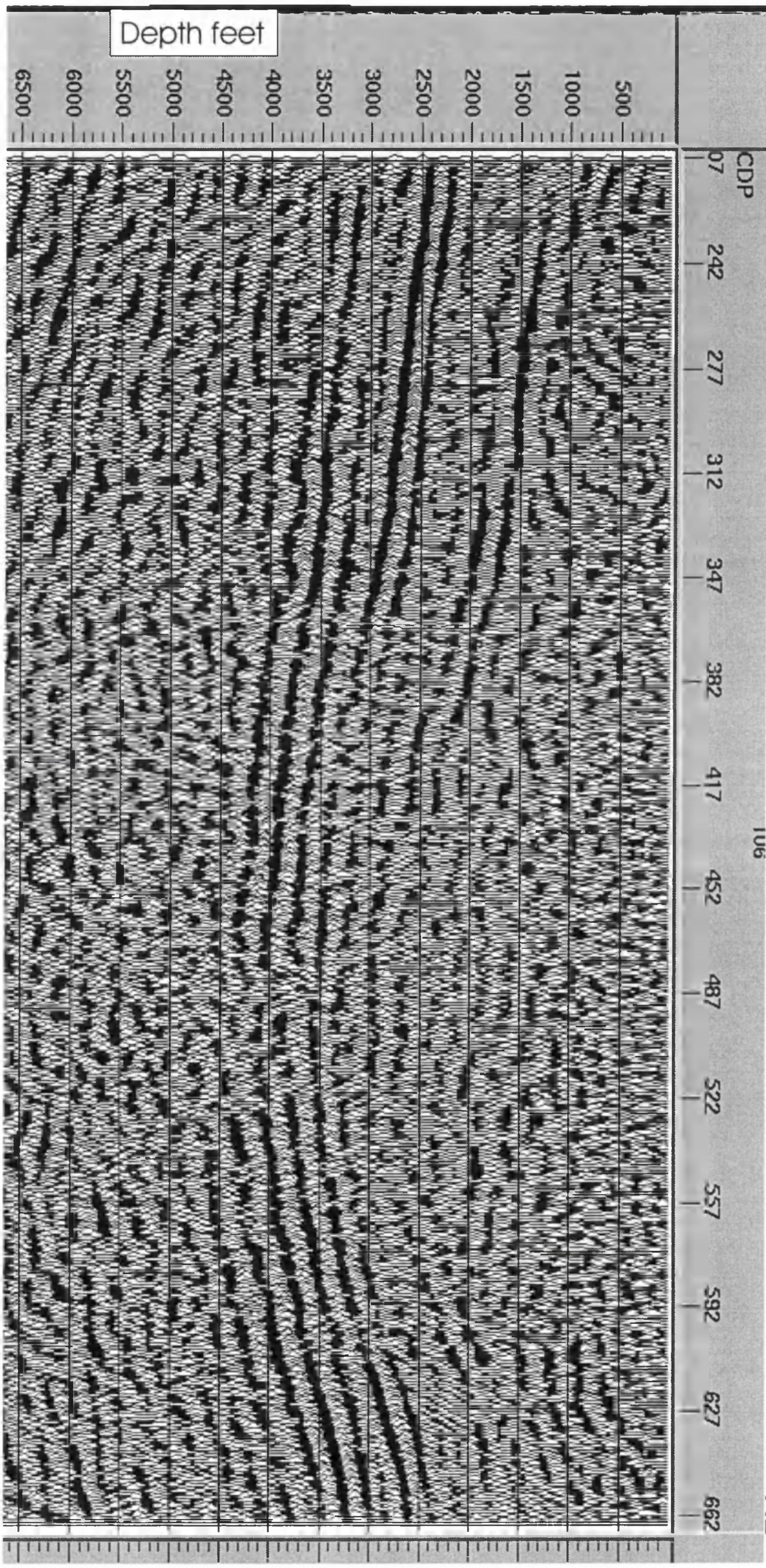

Figure 4.24- Depth-Migrated Seismic Section of the ODNR (BV-1-92) Seismic line

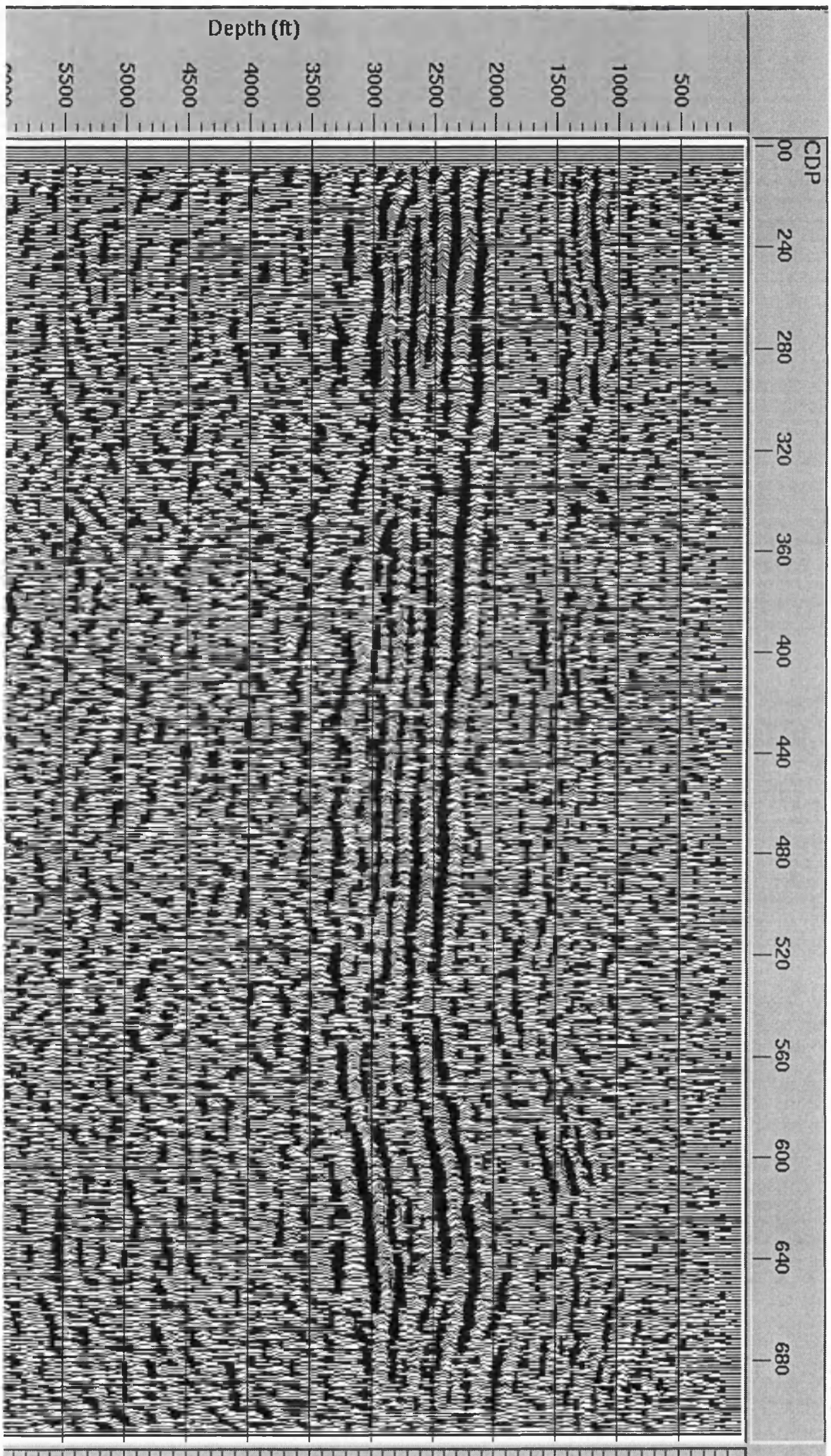

Figure 4.25- Depth-Migrated Seismic Section of the Columbia (SM-1) Seismic line

4.2.9- Summary of Processing

The processing indicates that the sections contain most primary reflectors down to about 600 ms. Velocity analysis shows a gentle velocity gradient with depth. Residual static corrections play a major role in successful processing. The final sections processed by us using both the SierraSEIS software package and the PROMAX 2-D package show significant improvement when compared to earlier processing carried out by industry. The higher frequency contents of the reflectors on the SM-1 section compared to BV-1-92 are likely a result of using a non-linear sweep for the acquisition of SM-1. The continuity of the reflectors allows us to map and correlate those reflectors with synthetic data. Our colleagues in the Ohio Department of Natural Resources informed us they found the interpretation of the seismic data very difficult before our processing. The interpretation of the processed seismic data is discussed in Chapter 5. Appendix (I) represents a typical seismic processing job control file.

CHAPTER-5 SEISMIC MODELING AND INTERPRETATION

5.1- Introduction

In interpreting the seismic data we must make use of all available information in the study area including gravity and magnetic data, cores, well logs, and surface geology. We believe the processed seismic data of the Serpent Mound Structure produced one of the best subsurface images of a mid-continent USA cyrptovolcanic structure to date. Our approach to the interpretation of the seismic data is to identify formation tops from the available well data and correlate these to reflectors on the seismic sections. This was done in two ways. We plotted sonic and density logs beside the seismic data at the same scale. We also compared synthetic seismograms generated from the well data to the seismic sections. The seismograms were generated using wavelets consistent with a vibroseis source. The associated events on the seismic sections were picked through the sections. We looked for faults that displaced the reflectors, changes of reflection character, changes of thickness and facies changes. The interpretation started with the most obvious reflector, associated with the top of the Conasauga Formation, which is generally the strongest reflector in the area. The two sections intersect at s.p. 224 of line SM-1 and show a reasonably tie, given the different frequency content of the two sections.

5.2-Well Logs

The wells drilled in the area provide the tie between the geology of the area and the seismic data. A suite of geophysical logs and continuous cores are available from a number of wells (Figure 5.1) near the study area. The well log data are used to determine the formation tops, lithology, and the expected thickness of units. Specifically sonic and density logs are used to project well information into the seismic data.

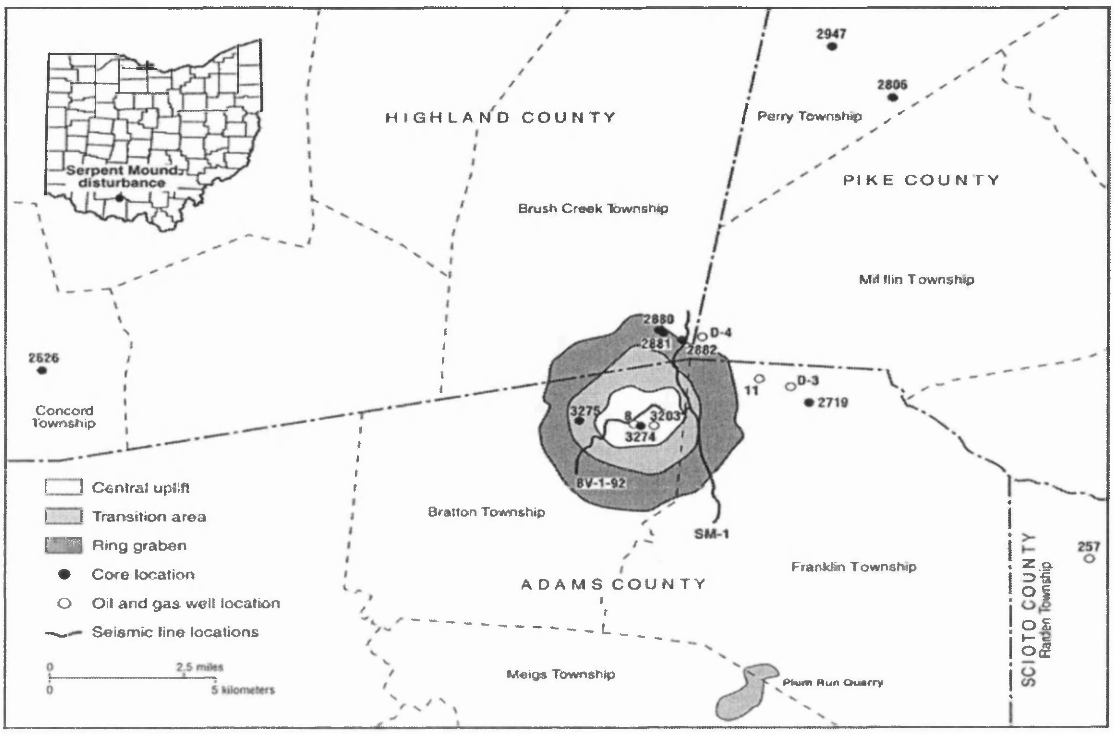

Figure 5.1 Location map showing seismic lines and well locations

5.2.1-Sonic and Density Log model

The best data for modelling the seismic response of the subsurface was from the Smith well (Well 257 on Figure 5.1) as a complete suite of sonic and density logs were available. Measurements of seismic velocity and rock density are required to compute the acoustical impedance which is convolved with a model seismic wavelet. Figure (5.2) shows the sonic and density logs from the Smith well. Driller's records indicate the Smith well penetrated the Lower Mississippian age Cuyahoga Formation through Precambrian granitic gneiss. A number of models were attempted with wavelets of different frequencies. We show the result of convolving with two Ormsby wavelets with different frequency content.

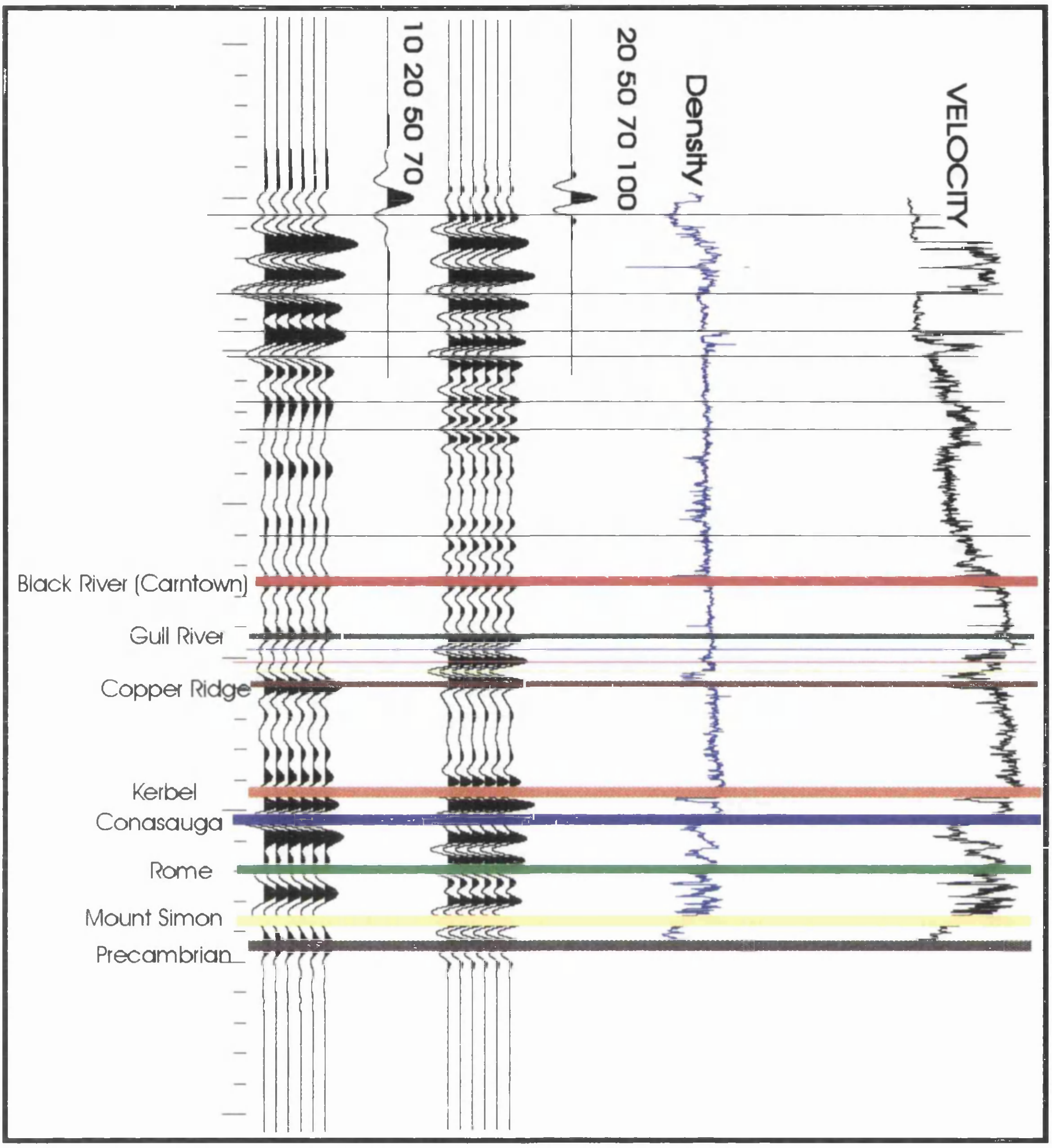

Figure 5.2- Sonic and density logs with corresponding model seismograms From Smith Well no. 257

5.2.2-Density Logs

In 1979, Oxford Oil Company drilled the only well to the Precambrian in the vicinity of the Serpent Mound Structure on the Russell-Tener lease (Figure 5.1 , well no. 11). This well was drilled to a depth of 3,868 ft (1125 m). This well is about one-half mile beyond Reidel's (1975) location of the eastern boundary of the structure. A gas show was reported from the Lexington Limestone (Trenton). No sonic log is available for this well. The paper density log from the Russell-Tener was digitised and compared to the equivalent seismic section. The digitised log was used to estimate the velocity function. This was done using the GMAplus LogM stratigraphic modelling software package, which has the estimated curve option and allows approximations of velocity log curves to be generated if only densities are available. The estimated curves are created using empirical relationships based on various models between density and velocity. The specific formula used here was Gardner's relationship (Gardner, G.H.F.; et al, 1974);

Density $= 0.23 (V)^{0.25}$, where the velocity is in ft/sec.

The estimated sonic and real density logs were used to calculate the acoustic impedance curve to model synthetic seismograms (Figure 5.3). These data were used for the correlation and the determination of the thickness of geological units. The Driller's report, based on the examination of well cuttings, indicates the Precambrian basement consists of granite gneiss. The sub-sea elevation of the Precambrian basement in the well is marked at -3013 ft (-918.4 m).

5.3-Modeling (Synthetic Seismograms)

Once the basic subsurface model is set through the well data (velocity and density logs), these physical parameters are used to synthesise a reliable approximation of a seismic record for the interval where the acoustic log is available.

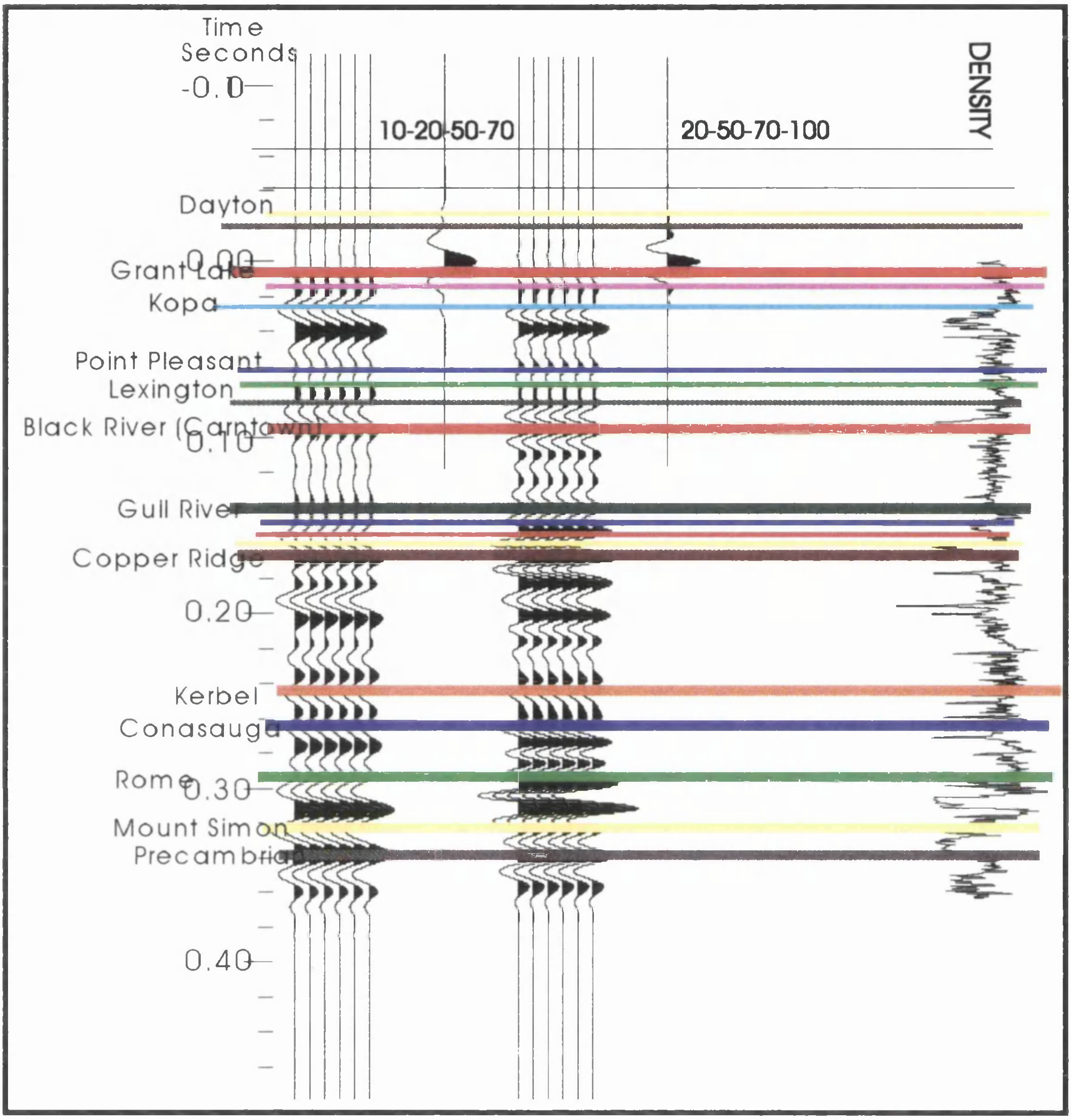

Figure 5.3- Synthetic Seismograms of Russell Tener Well No. 11 Modelled with low and high frequency Ormsby Wavelets

From the acoustic impedance curves the reflection coefficient series is calculated at the boundary between layers of different impedance. These reflection coefficients vary between –1 and +1 based on the impedance contrast. The greater the contrast in the acoustic impedance between the two layers, the stronger the reflection. A small spike at each layer boundary represents the reflection coefficient. Each of these spikes in turn convolves with the input seismic signal and the final result is the synthetic seismogram.

Synthetic seismograms were generated using the GMAplus LogM stratigraphic modelling software package mounted on a Sun workstation at the Department of Geology and Applied Geology compiled for the UNIX operating system. Initially the available well log data were in the LAS (Log ASCII Standard) format. The data were then reformatted to the GMAplus format. The digitised velocity and density data were used to calculate the reflection coefficient (RC) series. Then the RC series were convolved with suitable wavelets with a frequency response and bandwidth similar to the frequency bandwidth of the embedded wavelets of the seismic sections. Correlated vibroseis data theoretically result in zero-phase wavelets. Therefore, the output of the synthetic seismograms should be almost exactly the same as the result of passing the RC series through a zero phase band bass filter having the same bandwidth as the sweep for both seismic lines. Thus the sharp reflection coefficients should be replaced by a zero phase wavelet. Ormsby zero phase wavelets were selected, and were designed from a basic trapezoid bandpass filter with four corner points. The synthetic seismograms were generated using same polarity as the seismic sections (normal polarity). The synthetic seismograms from the Smith and Russell-Tener Wells show very good correlation with either low frequency (Figure 5.4) and high frequency wavelets (Figure 5.5).

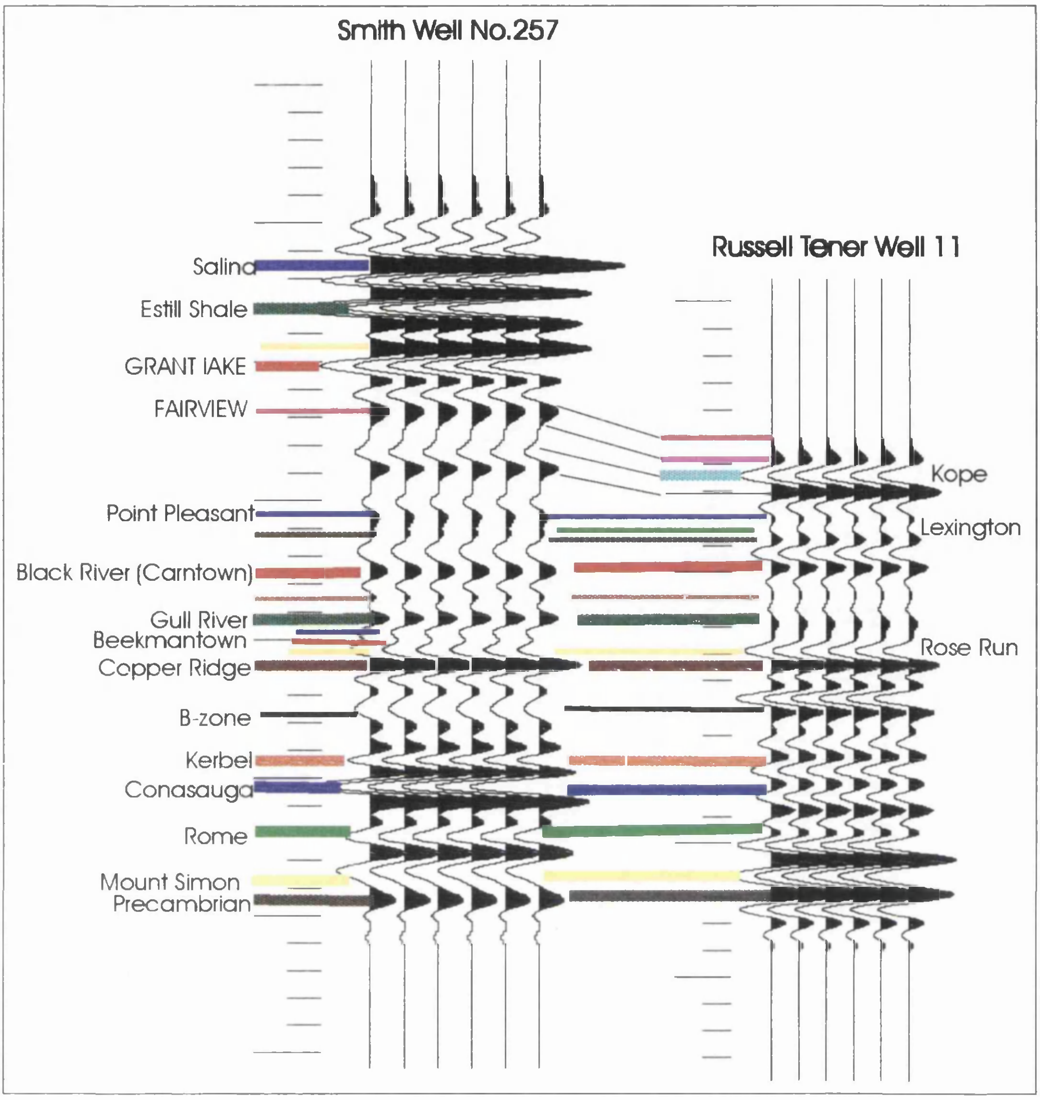

Figure 5.4- Correlation of the Smith Well and Russell Well the synthetic seismograms generated with Low frequency (Ormsby) Wavelet (10-20-50-70) Hz.

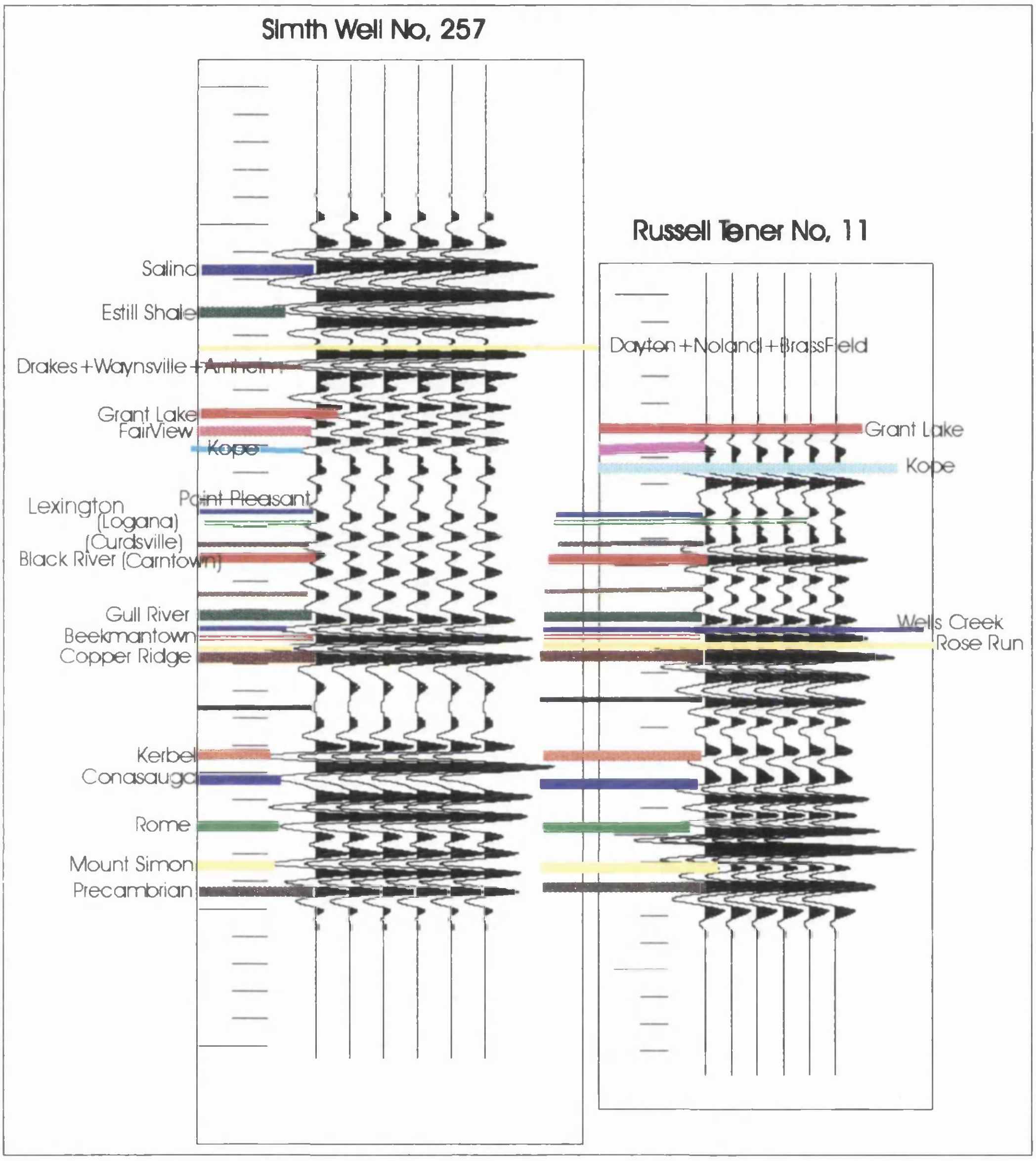

Figure 5.5- Correlation of Smith Well and Russell Tener WellThe Synthetic Seismograms generated with High Frequency (Ormsby) Wavelet (20-50-70-100) Hz

5.4-Interpretation

The definition of the subsurface is now limited to those layer boundaries which are spaced no closer in the section than the period of the highest frequency component present in the returning sweep signal. For our data if the highest frequency is 100 Hz and the lowest velocity of the section 12500 ft/sec (3810 m/sec), the minimum bed separation that could be measured clearly (top and bottom) would be roughly; 12500/2*100 = 62.5 ft (19.0 m). Thus no matter how good the data, we can not resolve strata thinner than this. In practice, the resolution also depends on the bandwidth of the signal.

The approach to reflector identification on seismic sections is based on a good well tie, which is an essential step in the interpretation of the seismic data. In the interpretation procedure we generally assume that the coherent events seen on the seismic sections are reflections from acoustic impedance contrasts in the earth. These contrasts most likely are associated with bedding that represents geologic structure. We also assume that the seismic details of the events, that is the wave-shape, the reflection amplitude, and the frequency are related to geologic details such as the thickness, the lithology and the petrophysical properties of the reflectors.

5.4.1-Correlation of Seismic Data With Synthetic Seismograms

The first task was analysing the effect of the differences in acquisition parameters on both sections. Line SM-1 shows better resolution of some of the shallow reflectors, e.g. the Gull River, Wells Creek, Beekmantown, Rose Run, and the Copper Ridge. On the BV-1-92 seismic line the intermediate reflectors between the Gull River and the Copper Ridge (Wells Creek, Beekmantown, and Rose Run) were not resolved. These formations have a small thickness, and were observed on SM-1 because the non-linear sweep vibroseis source has better resolution in the upper layers, than the linear sweep, which was used for BV-1-92. Thus SM-1 correlates well with the high frequency synthetic seismograms for both wells (Smith Well and Russell-Tener Well).

On the other hand BV-1-92 shows better correlation with the models using the lower frequency wavelet.

5.4.2-Reflections Identification

The tops of formations that correlate with reflectors are marked on the well data. Some reflectors are considered to be of special interest in the interpretation. These reflectors are easily identified by the correlation with well data. Therefore, reflection picking started with these most obvious reflectors, namely the Conasauga, the Copper Ridge, and the Gull River reflectors. These reflectors are characterised by their strong and continuous appearance on the sections. Other reflectors are then identified from the apparent relative position with respect to the most prominent reflectors. The two seismic sections intersected at sp. 224 of line SM-1 and the eastern end of BV-1-92, where both lines tie fairly well. Faults are drawn on the section based on the following criteria:

1- Discontinuities in reflections falling along an essential linear pattern;
2- Divergences in dip not related to stratigraphy;
3- Diffraction patterns, particularly those with vertices;
4- Distortion or disappearance of reflections below suspected fault lines.

5.4.3-Interpretation of Seismic Line SM-1

Columbia Natural Resources seismic line SM-1 was acquired along Rt. 41, beginning just south of Sinking Spring, ending north of Locust Grove (Figure 5.1). It passed through the outer ring graben of the structure as shown by Reidel (1975). Figure (5.6a,b) is the uninterpreted seismic section. Figure (5.7) shows the interpreted seismic line, where both the Smith well and the Russell-Tener well were projected into SM-1 at CDP 710 (SP 350) and CDP 347 (SP 175) respective. The seismic line crosses over the boundary of the structure, passing through the outer graben (Figure 5.7) and coming near the transition zone to the central uplift. The reflectors on SM-1 show the broad faulted depression of the inner graben.

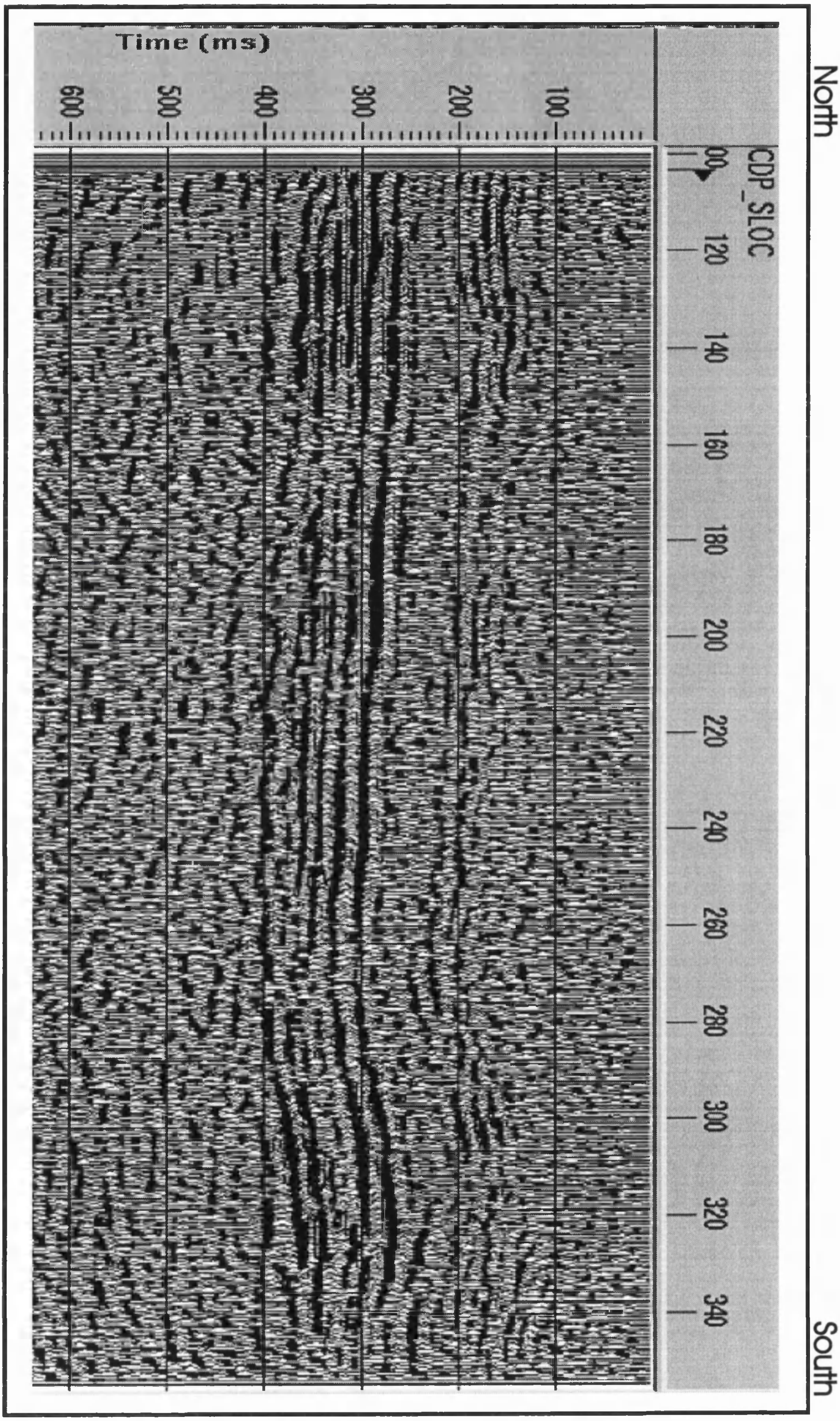

Figure 5.6a- Uninterpreted Time-Migrated Columbia (SM-1) seismic line

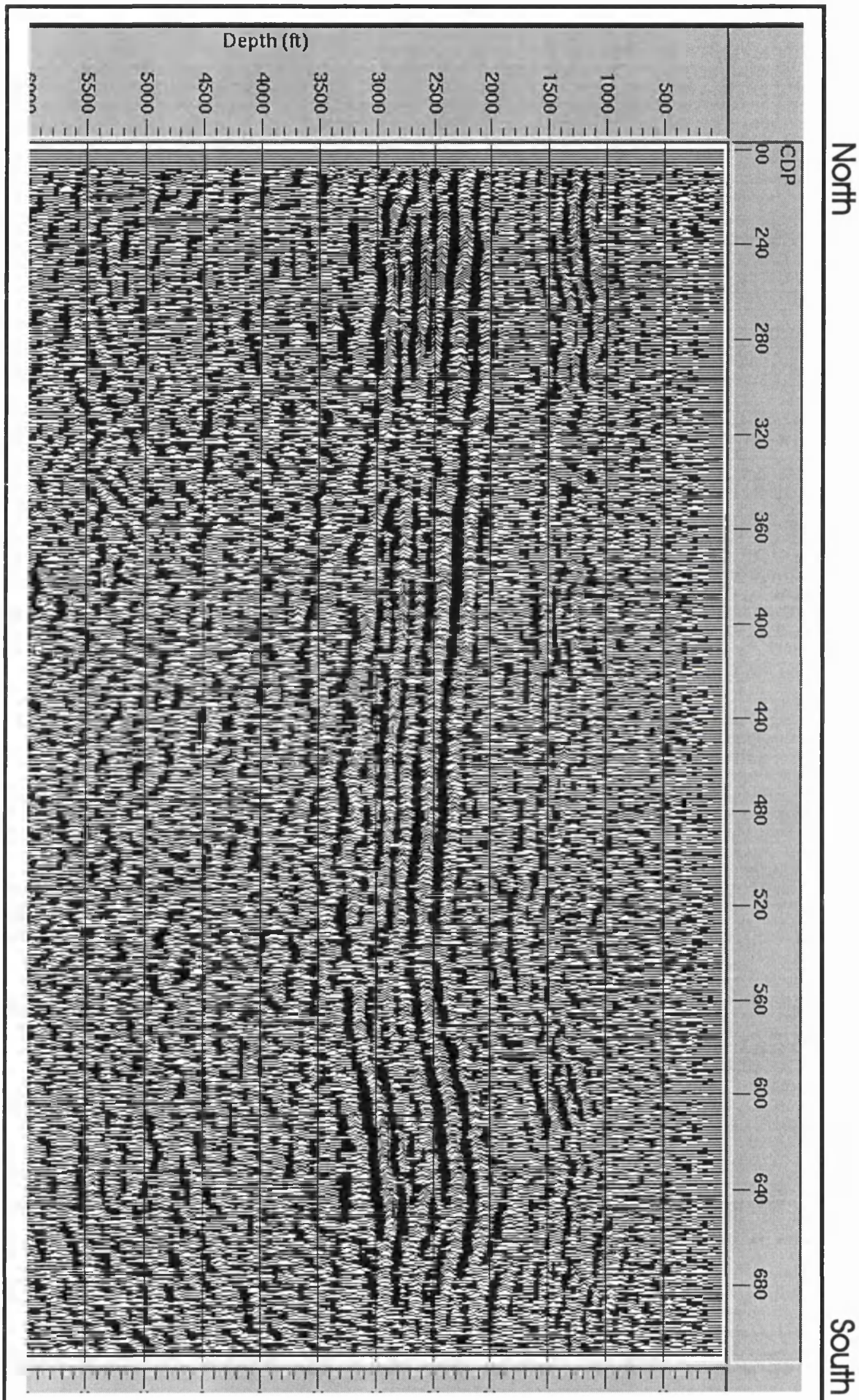

Figure 5.6b- Uninterpretated Depth-Migrated seismic section Columbia (SM-1) seismic line.

Faulted anticlines are seen at both ends of the line, with the most prominent at the south end of the line. The Russell and Tener well, projects into seismic line SM-1 at about shot point 175. The synthetic seismogram correlates well to the Gull River/Knox reflector at 160 milliseconds (ms), the Conasauga at 280 milliseconds, and Precambrian basement at 390ms. Reflectors above the Gull River are very noisy and discontinuous. The Gull River/Knox reflectors are more continuous than the overlying reflectors and are broken by faulting from SP 270 to SP 340 with some of the faults extend into the Precambrian basement. The Conasauga reflector on SM-1 is very well developed along the entire line. The Conasauga (285 ms) at s.p.355 has an estimated subsea value of -2, 300 ft (-699 m). The lowest (300ms) and highest (270ms) points on the Conasauga reflector occur at SP.265 and SP. 322, respectively. The Conasauga to Gull River interval is estimated at to be from 900 to 1,000ft (274 to 304 m) thick. Although variation in this interval occurs, it's slightly thinner in the broad syncline and slightly thickening near faults and anticlines in the outer graben. The deeper Precambrian reflectors are fairly continuous. At the southern part of the line, near Locust Grove a broad anticline is associated with steeply dipping reverse faults, and may involves the basement. Another smaller anticline with less closure seems associated with faulting on the northern end of the line. We speculate these two anticlines may be part of a ring anticline around this structure. Such a structure is associated with the Kentland Structure. Reidel's (1975) surface geologic map indicates a curvilinear anticline crossing Route 41 about 0.6 mile (1 km) south of Sinking Spring. However, his map does not show the anticline on the southern part of SM-1. The suggestion of a ring anticline is a new hypothesis.

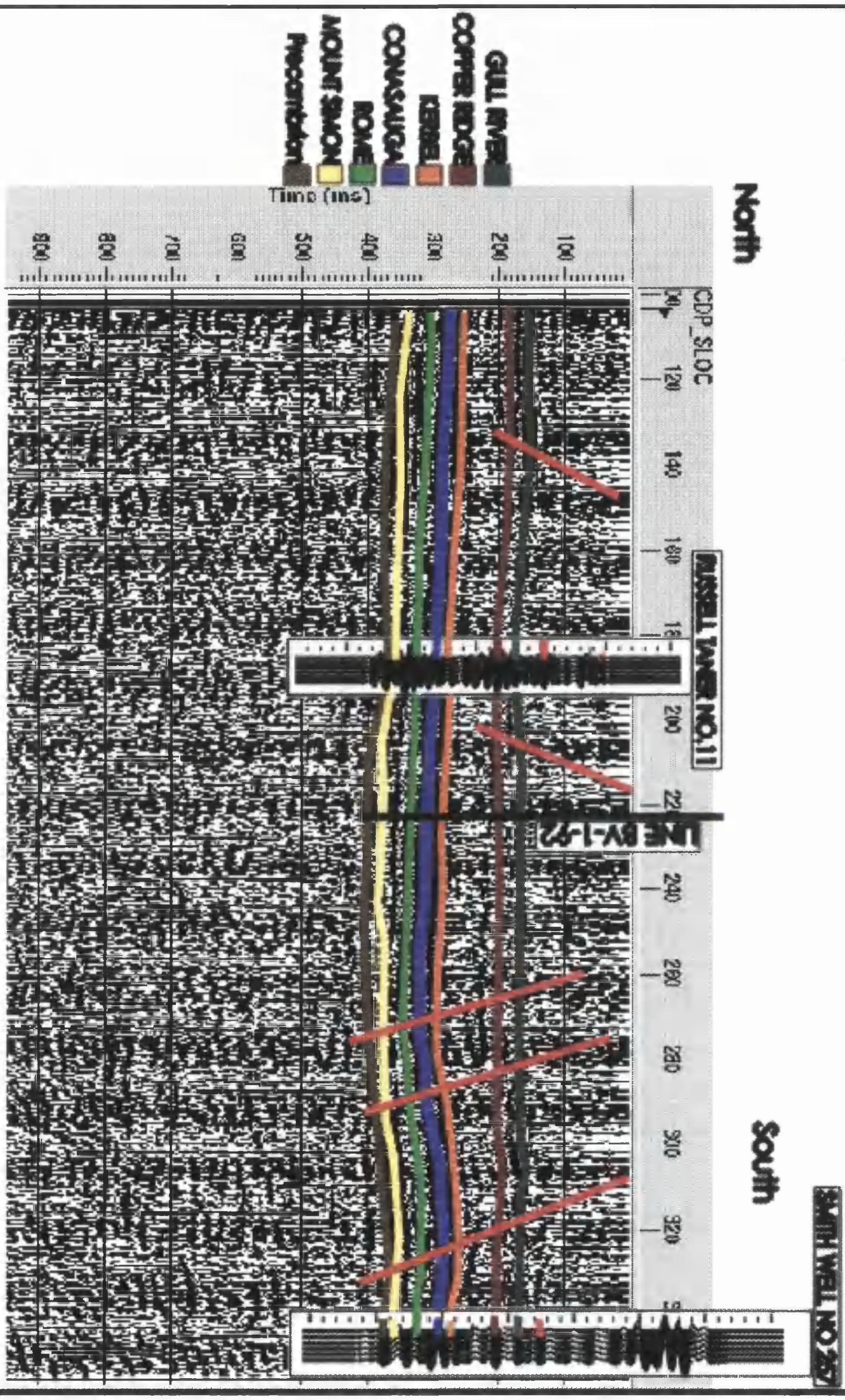

Figure 5.7- Interpreted Seismic Section of Columbia (SM-1) Seismic Line

5. 4.4-Interpretation of Seismic Line-2

Seismic line BV-1-92 (Figure 5.1) began at the intersection of Horner Chapel Road and State Rt. 73, passing through the central uplift area of the structure and ending at the intersection of Parker Ridge Road and State Route, 41, where it ties with seismic line SM-1. Figure (5.8) is the uninterpreted seismic section. On the interpreted seismic section, the two well cores DGS 3274, drilled in the central uplift, and DGS 3275, drilled in the transition zone, project onto BV-1-92 at S.P. 244 and S.P. 135 respectively. Formation tops from the lower parts of both cores correlate well with the interpreted tops on the seismic section. The Gull River reflector at –1800 ft (-548.6 m) correlates very well to the Gull River in DGS 3274 at –1805 ft (550.1 m). The Beekmantown is not evident because of the lower frequency content compared to SM-1. The Kerbel and the Conasauga reflectors are well developed through the entire line, traceable through the central uplift. The Rome Formation below the Conasauga exhibits a facies change toward the centre of the uplift area. Generally the Cambrian reflectors of the migrated BV-1-92 line, may all be traced over through the central uplift and transition area of the structure (Figure 5.9). The general appearance is a broad, highly faulted and structurally complex depression, which appears asymmetrical toward the northeast end of the line. Reflectors above the Gull River are very noisy, discontinuous and difficult to interpret. The Gull River/Knox Dolomite are more continuous than the overlying reflectors, and are traceable even through a series of high angle normal and reverse faults, through the central uplift and the transition zone. The Gull River/Knox Dolomite interval is broken by faulting from SP 195 to SP 315 that extends through the underlying Conasauga developing into the Precambrian basement. The Conasauga reflector is very well developed along the entire seismic line. The lowest point is at 420 ms, and the highest 270 ms points occurring at about SP 260 and 105 respectively. The Conasauga to Gull River interval ranges from 75 ms to 125 ms (600 to 1000 ft, 183 to 305 m). Approximately 50 ms of Knox or an estimated 400 ft (120 m) is missing from SP 230 to SP 270, immediately beneath the central uplift. Reflectors beneath the Conasauga exhibit a fancies change toward the central uplift, where the Conasauga/Precambrian interval becomes slightly thinner.

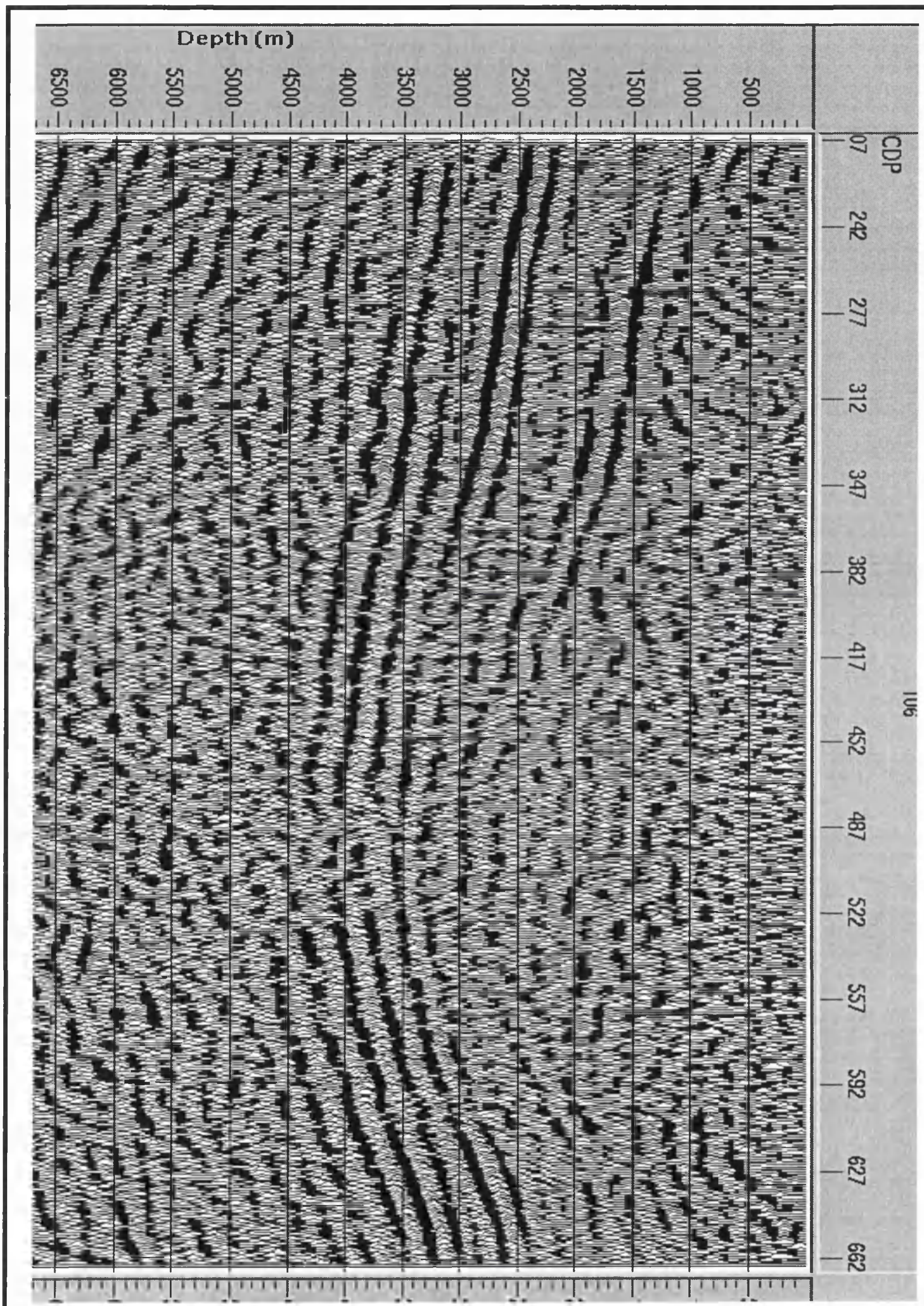

Figure 5.8- Uninterpreted Depth-Migrated ODNR (BV-1-92) Seismic Line

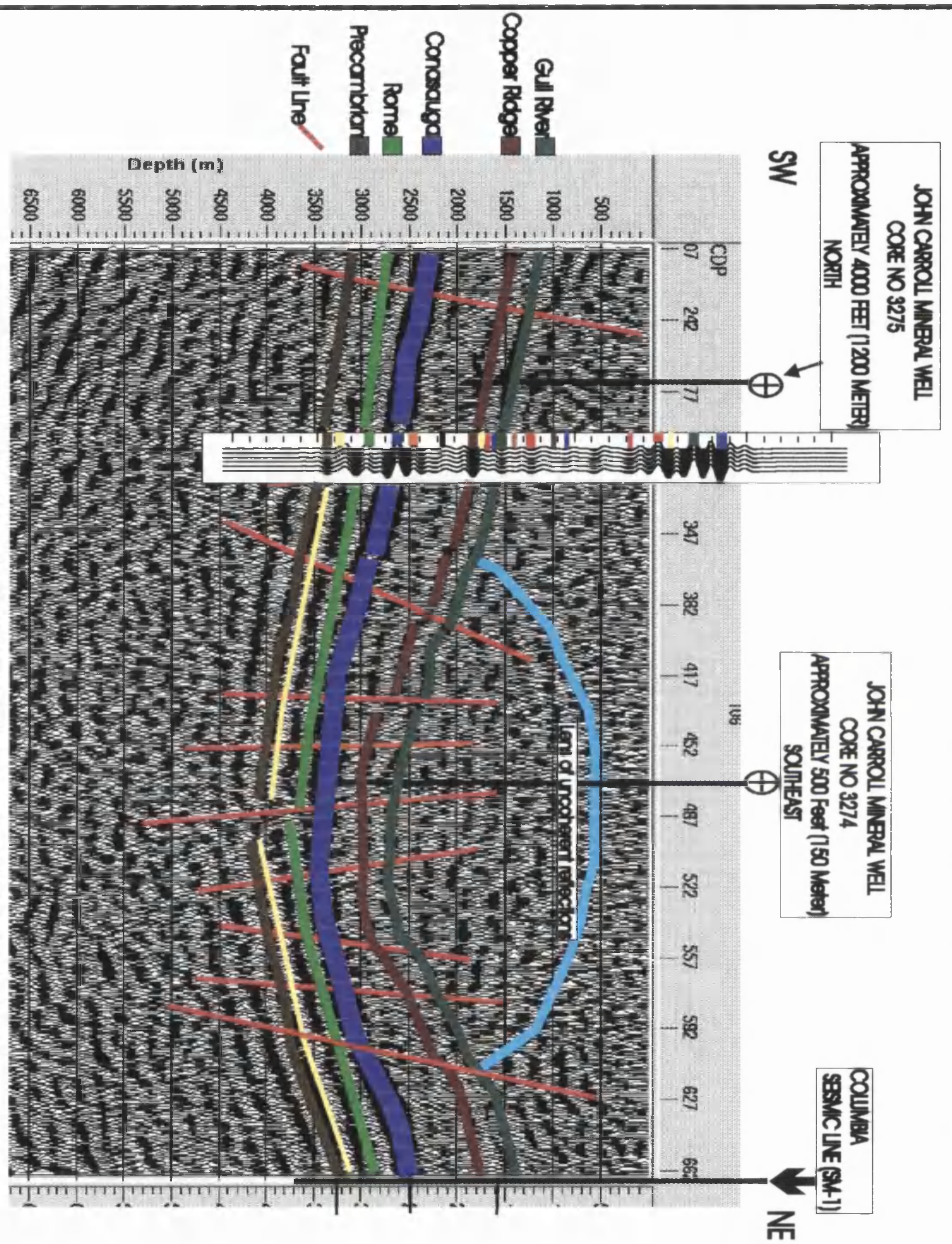

Figure 5.9-Interpreted Seismic Section of ODNR (BV-1-92) Seismic Line

Generally the two seismic sections revealed the three structural zones: the central uplift, the inner ring graben, and the outer ring graben that are shown on Reidel's (1975) surface geologic map of the area. Major faults are shown on the migrated and interpreted seismic sections in Figures 5.7 and 5.9. Some of these faults may be traceable to the surface as mapped by (Reidel, 1975). Our data show many high-angle normal faults on both sides of the depression seen on line BV-1-92, beneath the highly disturbed central uplift. The lower frequency content of BV-1-92 (linear vibroseis data) may result in lower resolution compared to SM-1 and some reflectors such as the Wells Creek, Rose Run, and Beekmantown are not revealed. The eastern end of BV-1-92 does have a suggestion of the Beekmantown reflector. Reflectors on both BV-1-92 and SM-1 beneath the Conasauga exhibit a facies change toward the centre of the line, where some reflectors pinch out and the thickness changes. An anomalous lens-shaped volume of chaotic reflections occurs within the depression beneath the central uplift, but does not continue through the underlying Gull River Reflector.

The structure pattern on the seismic sections supports the impact theorem. Line BV-1-92 shows striking similarity to model studies of impacts conducted by Gault et al.,1968 for NASA. Both his model and the seismic section show a bowl shaped depression under the point of impact and thinning of strata at the greatest depression. Both seismic lines indicate a general decrease in structural complexity with depth. Seismic line BV-1-92 also shows decrease in structural complexity away from the depression of the central uplift area. The type of fault produced by unbalanced stress depends largely on whether the vertical or horizontal stresses are the larger. Most of the faults in the central uplift area are normal faults. Normal faults result when the maximum compressive stress is vertical.

Palinspastic sections or palaeosections are made by time shifting traces to flatten some distinctive horizon. One can assume such horizons were deposited horizontally; The objective is to show relationships that existed at the time of deposition. It seems palaeotopograpy below the Gull River may in part have affected fancies changes of the lower Cambrian strata. The flattening of picked horizon aid in seeing the attitudes of bedding at the time of the picked horizon was deposited.

5.5-Discussion and Conclusions

The seismic study provides new subsurface information of the Serpent Mound Structure. It confirms Reidel's (1975) mapping of the structural zones of the disturbance, in which the structures are more complex in the central uplift area and less complex at the outer graben. The important aspect of the seismic study is the imaging of the subsurface, consistent with cores and log data, providing evidence, which supports the exogenic origin of the structure.

There are possibilities for hydrocarbon traps in the Serpent Mound Structure. These are represented by structural anomalies that may be associated with porosity. Hydrocarbon shows are known in the area from various horizons (Baranoski, ET al, 1998). Our processing of seismic line SM-1 s shows a possible ring anticline that could serve as a structural trap. The deep core from the structure shows asphalt blebs. Asphalt is known to be present in surface breccias. Two wells were drilled in the centre of the structure to test for hydrocarbon. One had a gas show at about 1700 ft (518 m). The wells were drilled in the mistaken concept that the centre represented a dome whereas our seismic image shows it to be a syncline. Our colleagues at the Ohio Department of Natural Resources hope to attract industry sponsorship for further drilling.

CHAPTER-6 GRAVITY METHOD

6.1-Introduction

Gravity surveying measures variations in the Earth's gravitational field caused by differences in the density of sub-surface rocks. Gravity methods have been used extensively in the investigation of impact structures. This gravity survey was conducted in order to gain further information on the origin and deep structure of the Serpent Mound Structure. If the structure is of exogenic origin (Dietz's theory, 1960), one would expect a relatively shallow disturbance that would have lower density brecciated rocks immediately beneath the impact area surrounded by slightly higher density rocks. Such a circumstance may be detected by a microgravity survey passing over the central uplift area of the Serpent Mound Structure itself and not related to regional gravity trends. On the other hand, if the structure was of endogenic origin (Bucher, 1936), one would expect the disturbance to extend into the basement. If the Precambrian were of a higher elevation or an intrusive body present, the density contrast would result in a positive gravity anomaly.

The author, with the help of Dr.Watts, conducted a microgravity across the Serpent Mound Structure during the months of September and October 1996. The survey was conducted along the course of seismic line BV-1-92. The purpose of this study is to conduct a microgravity survey across the Serpent Mound Structure and evaluate the results with respect to the above theories. Previous studies were either on a regional scale or used large station intervals that would not resolve any local anomaly associated with the structure.

6.2- Fundamental Relationships

6.2.1-Theory

The gravity method is based on Newton's universal law of gravitational attraction, and Newton's second law of motion. The first law states that the force of attraction between two masses is directly proportional to the product of the two masses and inversely proportional to the square of the distance between their centres of mass. That is, the greater the distance separating the centres of mass, the smaller is the force of attraction between them.

$$\text{Force} = \text{gravitational constant} \times \frac{mass\ of\ Earth\,(M) \times mass\,(m)}{(distance\ between\ masses)^2}$$

$$F = \frac{G \times M \times m}{R^2} \qquad \text{(Equation 6.1)}$$

Where G is the Universal Gravitation Constant. The value of G was first determined in the laboratory in1798 by Lord Cavendish. The present value of G, which was determined in 1942, is equal to

$G = 6.6732 \times 10^{-11}$ N m^2 kg^{-2} SI units, or

$G = 6.6732$ X 10^{-8} dyne cm^2/g^2 cgs units

Newton's law of motion states that the force (*F*) is equal to mass (m) times acceleration. The vertical acceleration is the gravitational acceleration (g).

Force = mass (m) × acceleration (g)

$$F = m \times g \qquad \text{(Equation 6.2)}$$

From equations (6.1) and (6.2), the acceleration due to gravity on the Earth's surface:

$$g = \frac{G \times M}{R^2} \qquad \text{(Equation 6.3)}$$

Where R is the earth's radius and M is the mass of earth.

In the c.g.s. system the unit for gravity (g) is cm/s^2. Among geophysicists this unit is referred to as the Gal. (in honour of Galileo). The practical unit commonly used in geophysics for the measurement of g is the milligal (mgal). Another unit is the gravity unit (gu) which is 10^{-6} m/ s^2. This is the more modern unit. However we will use the mgal as all the calibration factors and data reduction instruments available to us are for this unit.

6.2.2- Earth's Gravitational Field

If the earth had perfect spherical symmetry and did not rotate, then gravity acceleration at the earth's surface due to its mass would be the same everywhere, disregarding the tidal effects. In reality the earth is a rotating, inhomogeneous, oblate spheroid over which gravitational acceleration varies. Therefore, it is essential to identify the reasons that gravity varies and correct for them in order to determine the density contrasts in the subsurface. The absolute value of gravity at the equator is about 978.0 gal, and at the poles gravity is 983.2 gals. The rotation of the earth produces an outward-directed force that acts in a direction opposite to gravity and, therefore, diminishes the measured value of g. the effect of this centrifugal force is greatest at the equator and diminishes to zero at the poles of the earth's rotational axis. Therefore, it decreases with an increase (north or south) in latitude as a direct consequence of this force; g is greater at the poles than at the equator by 3.4 gals.

The long-term behaviour of the earth is that of a fluid, so the earth's rotation produces centrifugal effects that cause its shape to be an *ellipsoid of revolution.* The fact that the earth is not spherical but is an ellipsoid of revolution means that it is flattened at the poles. Thus the length of the earth's radius is greater at the equator than at the poles. The gravitational acceleration varies as a function of the earth's departure from spherical and the centrifugal force produced by the earth's rotation. The shape of the earth may be well approximated by an oblate spheroid with an eccentricity of 1/298.257 (Bott, 1962). This difference between the mean equatorial radius and the polar radius of $\cong 21$ kilometres causes g to increase from equator to pole by 6.6 Gal. However, since the radial length is greater at the equator, more mass is between the surface and the earth's centre at the equator than at the pole. This mass factor causes g to decrease by 4.8 Gal from equator to pole. The total effect of the above combined with rotation results in a net increase in gravity by 5.2 Gal as one travels from equator to poles. This explains the variation of gravity from 978.0 Gal at the equator to 983.2 Gal at the poles.

In gravity exploration the ultimate goal is to obtain values of gravity for which variations are entirely due to subsurface density distributions. The value of gravity g at any point on the earth's surface is controlled by a number of factors. These include latitude, the elevation of the observation point, the density of the materials between the observation point and the reference datum, the attraction of material surrounding the station, the tidal effect, and density contrasts in the subsurface layers.

6.2.3- Density of Rocks

The total variation of rock densities is quite small relative to the other physical properties of rocks. As in the case of many other physical properties a considerable overlap exists in rock densities and different lithologies. Table (6.1) shows the density range and the average density of older rocks . The average density of the crustal rocks is 2.67 gm/cm^3. This average value is normally used to combine gravity values from different surveys for the production of regional gravity maps, but this value may not suitable for a restricted, local gravity survey. Of course, the best reduction values are determined by sampling rocks from the survey area and determining densities in the laboratory. In some areas like the Serpent Mound, exposures are not sufficiently numerous to permit reliable and representative samples to be collected. Another approach, detailed by Nettelton (1939), requires detailed gravity profiles over topographic features in the study area and finding the density that produces the least correlation between topography and the Bouguer anomaly. The densities for our data reduction and modelling were obtained from the available formation density logs in the vicinity of the Serpent Mound Structure.

Table 6.1 Densities of Rocks

(From Dobrin, 1976; Parasnis, 1972; Clark, 1966)

ROCK TYPES	AGE	DENSITY GM/CC
Sandstones	Pennsylvanian-Cambrian	2.45-2.70
Limestone (compact)	Silurian-Ordovician	2.68-2.80
Shale (older)	Pennsylvanian-Cambrian	2.65-2.75
Dolomite	Silurian-Ordovician	2.72-2.8
Granite		Average 2.67

6.3-Previous Investigations of the Serpent Mound Structure

Early gravity surveys of the area were on a reconnaissance scale (Heiskanen and Uotila, 1956) with one station per tens of square miles, which is appropriate only for regional gravity variations. Rudman et al. (1965) published a regional gravity map of the midwest United States (Figure 6.1) which shows regional gravity anomalies passing through the study area. Zahn (1965) conducted a local gravity survey using a one-quarter mile (400 metre) grid superimposed upon a map of the disturbance, intending to establish a gravity station at each point on the grid. Due to poor access and very rough topography he did not occupy all of the stations. Zahn (1965) found only a regional Bouguer anomaly, which was not associated with the central uplift area of the structure. He concluded that the Bouguer anomaly in the area had no direct relation to the chaotic structure area. Zahn (1965) made several attempts to correlate the gravity data to Bucher's map of the structure. He used the least squares method to generate a second degree surface map (Figure 6.2), subtracted the Bouguer anomaly, and derived a second degree residual map (Figure 6.3). He reached the same conclusion, that there is no relationship between the structure and the gravity data. Bull et al. (1967), Flaugher (1973), and Langford (1984) reported only the regional trends passing through the area.

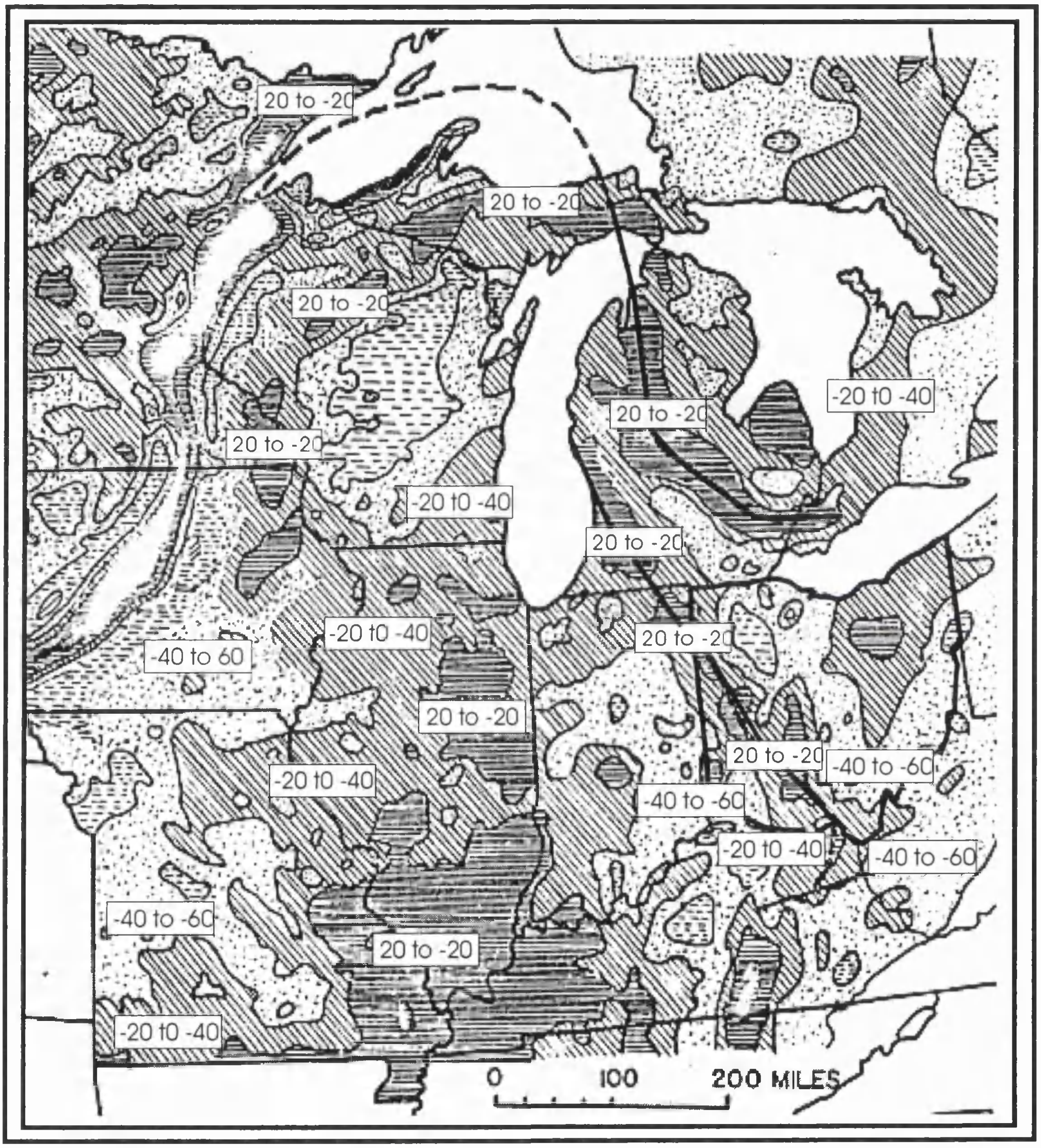

Figure 6.1- Bouguer gravity anomaly map (mgal) of the Midwestern U.S.A. (after Rudman et al. 1965)

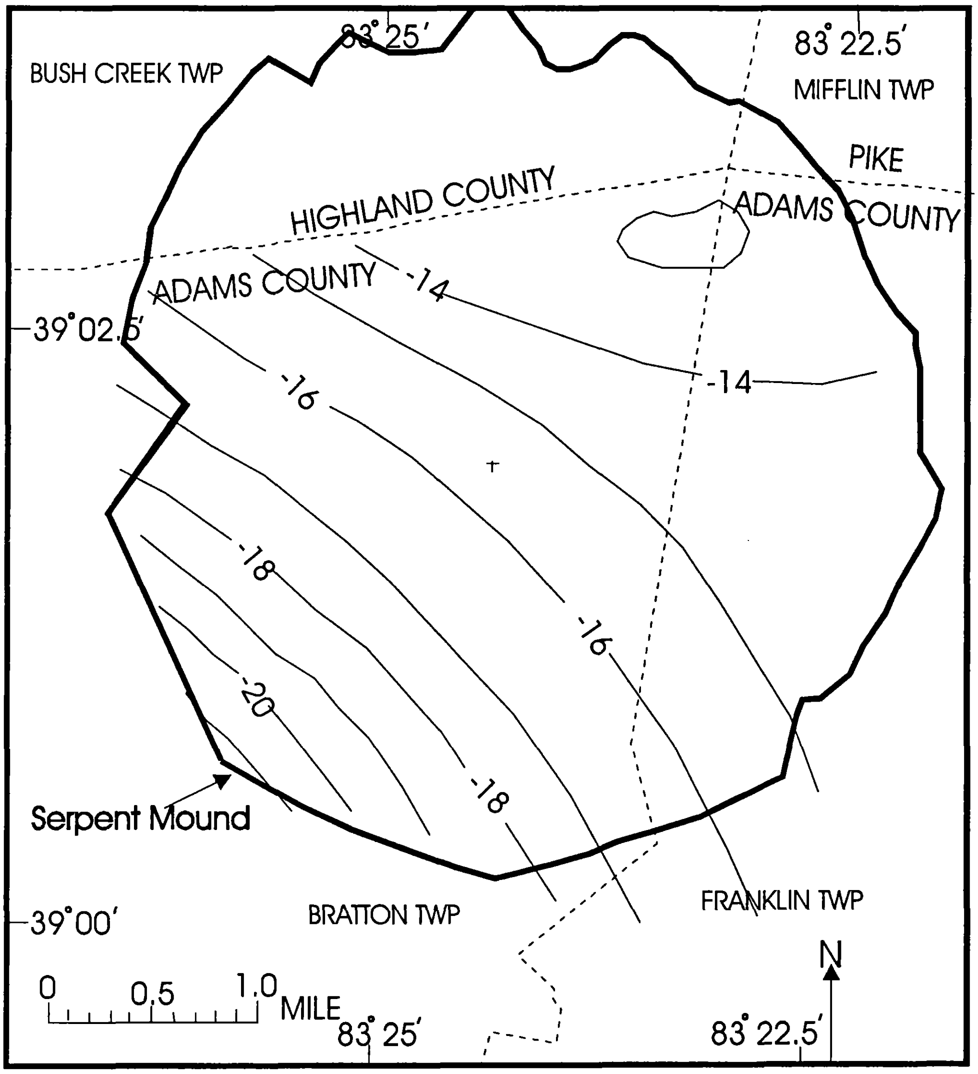

Figure 6.2- Gravity trend surface map (mgal) of the Serpent Mound Structure (after Zahn, 1965)

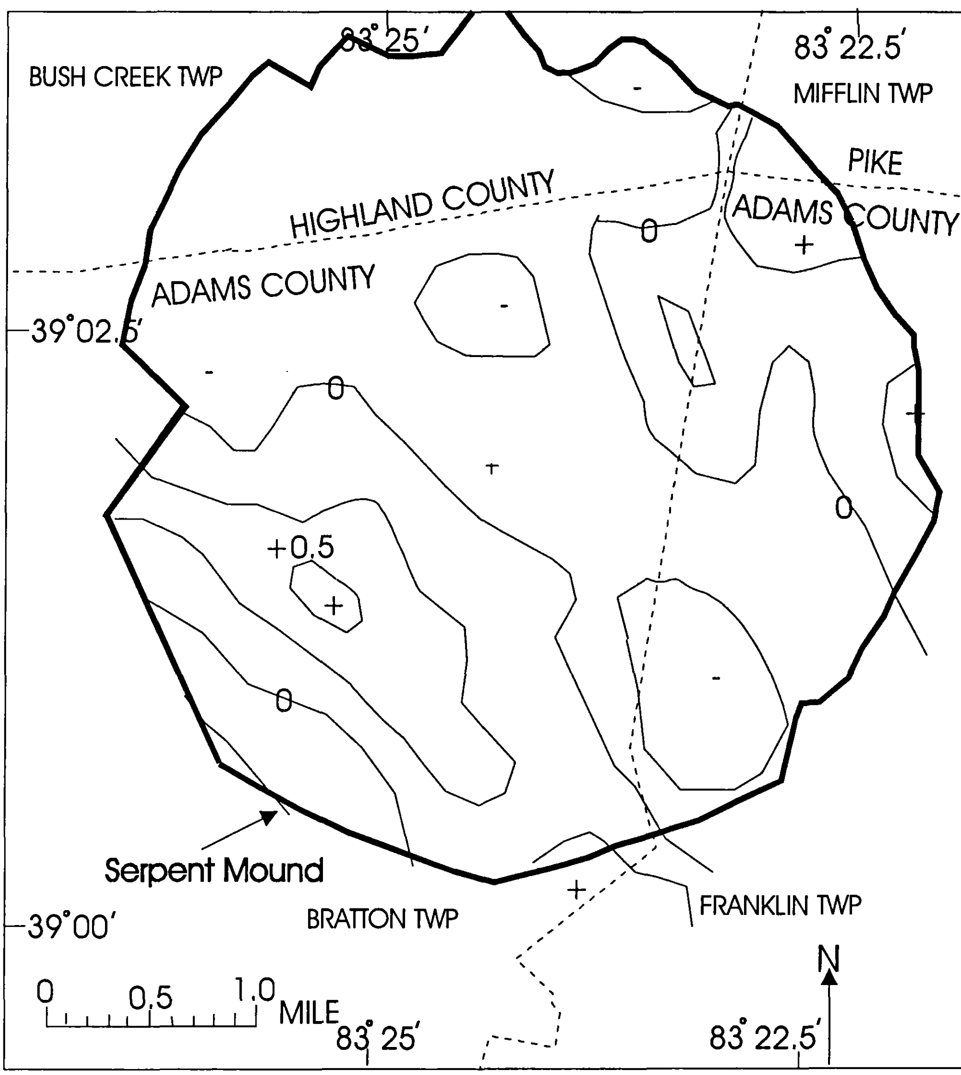

Figure 6.3 – Second degree gravity residual map (mGal) of the Serpent Mound Structure (after Zahn, 1965)

6.4- Gravity Surveying

6.4.1- Introduction

Before the actual surveys were conducted, we spent considerable time introducing ourselves to the local authority and the local people. We obtained the right to enter the survey area from the landowners. We secured their names, addresses, the parcel numbers of their properties, and the extent of those properties from the Court House at West Union, Ohio. We found it very helpful to permit all the land in the study area; even though Dr. Watts and I spent many days explaining to many landowners the purpose of our study and the procedure in carrying out the survey. This was a good rule, because in the past landowners denied geoscientists access to their land for trespassing without consultation.

The discussion of field procedure is to provide additional detail and to give some insight into how certain field requirements and procedures are typically accomplished. For example, if we placed a gravimeter in one position and took readings every hour or so, the values we obtain may vary. This variation is due to two causes. The first is the instrument drift, which is caused by small changes in the physical properties of the gravimeter components. The second is due to tidal effects, which are governed by the position of the sun and the moon relative to the earth. For this reason a gravimeter must be returned to a reference point every so often to establish if drift occurred and by how much. Our strategy in conducting the high-resolution gravity survey is based on the premise that the target is limited in space and has a different density contrast with the surrounding rocks. The problem is to remove all of the other sources of gravity variations.

6.4.2-Gravity Meters

Ultimately in our gravity survey we wish to determine the difference in gravity between the observation points and we measure the change in gravity and not the absolute value. The instruments used in the survey measure the change of gravity from location to location. The principle upon which gravimeter design is based is quite simple. If a mass is placed on a spring and this assembly is moved from one position to another on the earth's surface, the spring will lengthen or shorten a small amount due to the variations in gravity. However, the small changes in gravity from site to site result in only very small displacements of the spring. A critical component of most modern gravimeters is the zero-length spring. Tension is placed on such a spring during manufacture so that the spring is much more sensitive than normal and amplifies the displacements caused by small variations in gravity at the earth's surface. This causes the spring to have effectively 'zero length'. The gravity meters used were a LaCoste-Romberg Model G Gravity meter and a Worden prospector Gravity meter.

6.4.2.1- LaCoste-Romberg Gravity Meter

This device was first developed by LaCoste and Romberg as a long-period seismograph (LaCoste, 1934). The spring is based on the 'zero length' design invented by LaCoste and Rombeg. This type of gravimeter is used extensively in exploration surveys. The Model G gravity meter we used had an average dial constant of 1.0588 milligals per division scale.

6.4.2.2- Worden Gravity Meter

Unlike the Lacoste-Romberg gravimeter, the Worden Gravimeter (made by Texas Instruments) is made entirely of quartz glass springs rods and fibres. The quartz construction makes it much easier to reduce thermal effects. The whole assembly is housed in a glass vacuum flask with an electrical thermostat. The spring and lever are constructed from quartz and placed in a sealed flask to minimise temperature changes, and to maintain constant air pressure. The instrument is easily transported and is lightweight (weight about 6 lbs., 15 lbs. with its tripod and carrying case). Figure (6.4a) is a schematic representation of the interior of one of Worden gravimeters. Figure (6.4b) is a photograph of the actual gravimeter. The Worden gravimeter is sensitive to vibration. Therefore, it must be handled with great care, kept

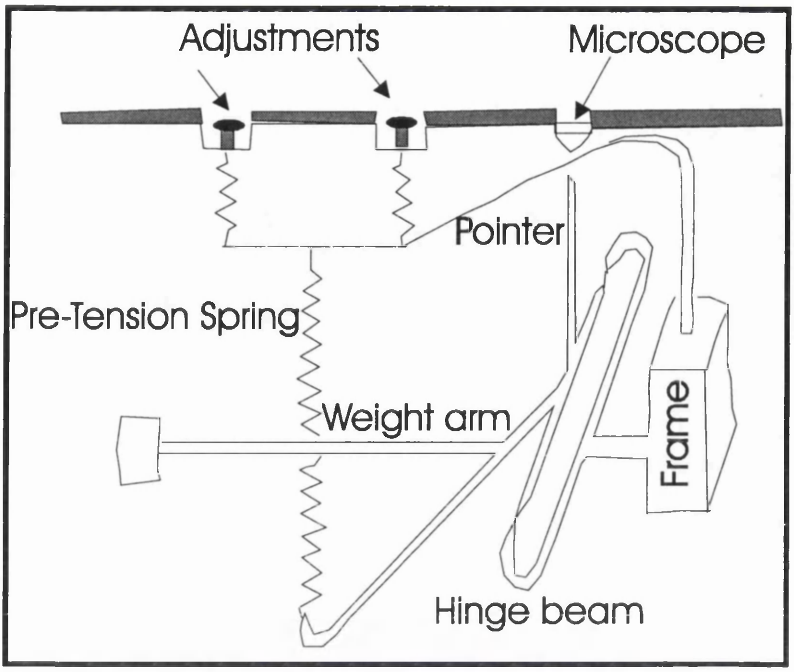

Figure 6.4a- Working Elements of Worden Gravimeter (from Dobrin, 1976)

Figurer 6.4b- Photograph of Worden Gravity Meter

vertical, and must not be subjected to sudden acceleration. The gravimeters are capable of measuring changes in gravity of 1 part in 100,000,000 which is a precision of 0.01 mgal. The gravity meter had a dial constant of 0.0891 milligals per scale division for the range of instrument readings in this gravity survey.

6.4.3- Field Procedure

During the survey two base stations were established. The first base station is at benchmark BM856 (a brass cylinder encased in concrete). This station is described by the National United States Geodetic survey as 0.4 mile north from the post office at Sinking Spring, Highland County, Ohio, along State Highway 41, 15 metres Northwest of the centre of the intersection of Horn street and State Highway 41. The benchmark has a United States Geological Survey Standard Cap, embossed 856 Ohio, and riveted on the top of a 3 ½ inch Iron pipe. It has an absolute gravity value ($g_{abs.}$ = 980.6199 gals), position (Latitude 39° 04'43" N, Longitude 83° 23' 18" W), and elevation 261.753 m (858.760 ft). The other base station (G1) was established using GPS at the intersection of Parker Ridge Road and Route 41 at (Latitude 39° 02 ' 20.8 " N, long 83° 23' 10.2" W), and elevation 229.917 m (754.32 ft). Station (G1) is located at the northeast end of the gravity profile and was used as a reference station in this study.

The gravity profile started at the intersection of State Route 73 and Horner Chapel-Parker Ridge Road. It proceeded along and Horner Chapel-Parker Ridge Road following the same course of the seismic line BV-1-92 (Figure 6.5). A total of 118 observation points (gravity station) were established along this line, and marked using yellow paint and survey flags. The gravity station interval was approximately 50 m (Figure 6.6).

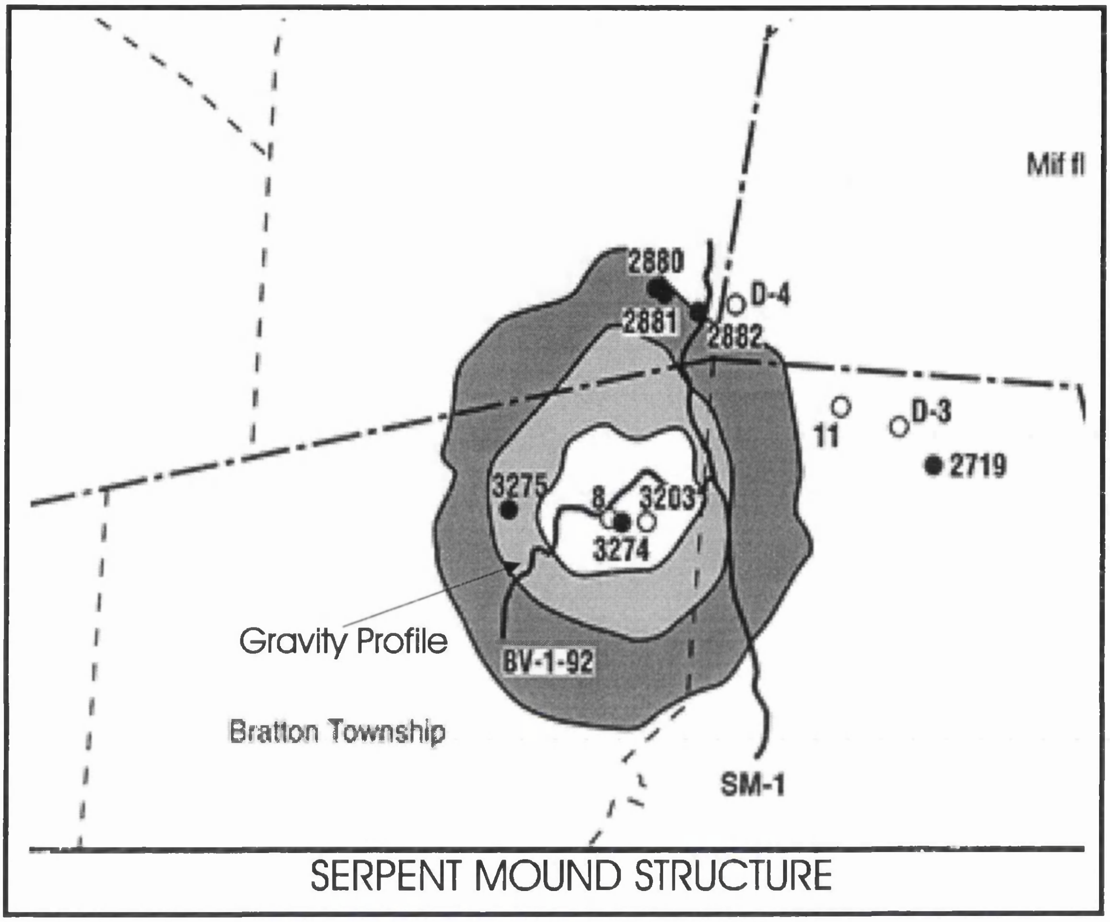

Figure 6.5- Location map of the Serpent Mound Structure
Gravity profile along line BV-1-92

Elevations and locations were determined using an optical theodolite. Elevations and locations of seven gravity stations along the line were determined using the differential Global Positioning System (GPS) The base station BM856 (G0) was used as the survey reference, where elevation and location are known at a high level of precision. GPS surveying uses a constellation of satellites to achieve horizontal and vertical control. Differential GPS is required to measure the change of position and elevation with respect to a reference location. We used two antennas (manufactured by Ashtech, model 'Dimension') to collect the data.

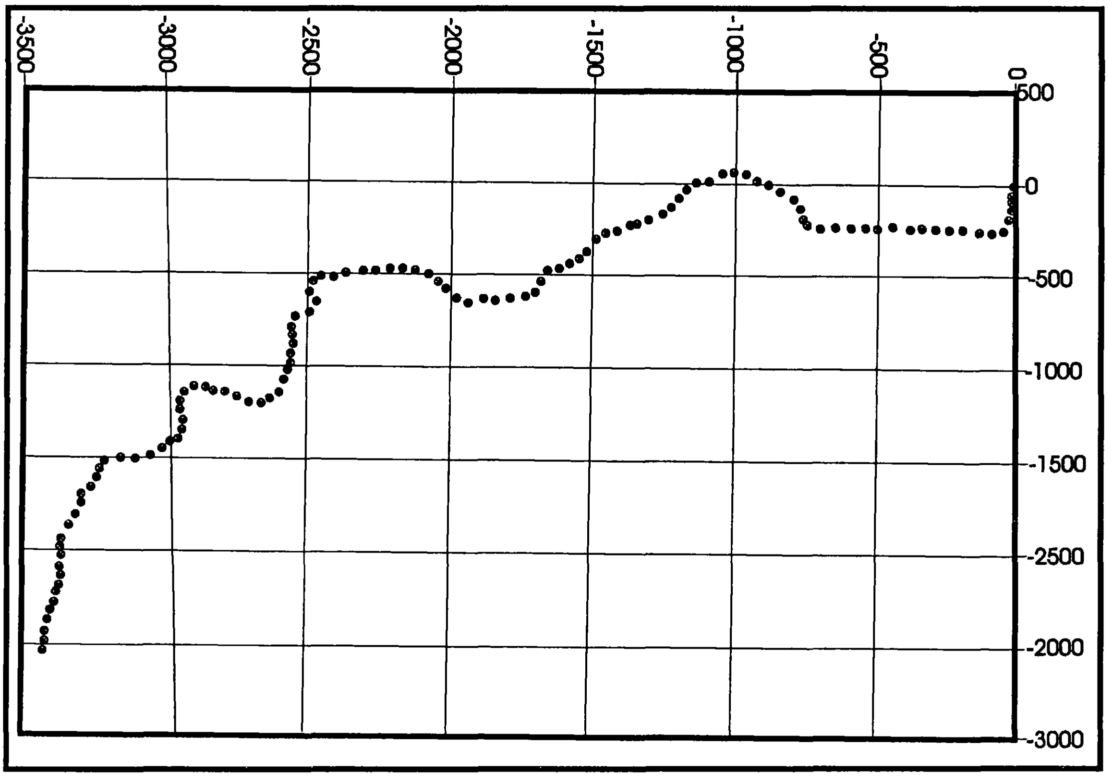

Figure 6.6 Gravity Stations (50 m apart) along Parker Ridge Road

G1 is the reference (0,0)

One antenna was at a known location and the other was a roving antenna. The data are stored in a small computer bundled with the antennas. We found that it was necessary for both antennas to be locked onto at least five satellites for an hour to get a precision of three cm in the elevation difference. The rechargeable batteries last only six hours allowing a maximum of five stations per working day. The data were downloaded each evening and processed using the Prism Version 2.0 software package.

The data collected using GPS (Table 6.2) equipment were used to check the accuracy of the elevations determined by the precise levelling as well as the north-south offset of the observation points with respect to base station G1 (reference datum).

The two gravity meters were simultaneously operated. At each gravity station, the gravimeters were set upon tripods and levelled. The tension in the internal spring was altered by moving the adjustment screw until the reading beam was centred, and the date, time, and dial readings of the gravimeters were recorded.

Table 6.2 – List Global Positioning System (GPS) Survey Data

	STATI ONS	ANTEN. HEIGHT	TIME MIN.	ELEV. METRE	LATITUDE DEGREES	LONGITUDE DEGREES
Known St.	BM856	2.067	56	261.753	N 39 04 43.0	W 83 23 18.0
Unknown	G-1	2.066		229.917	N 39 02 20.83	W 83 23 10.02
Known St.	G-1	2.063	68	229.917	N 39 02 20.83	W 83 23 10.02
Unknown St	G-27	2.046		285.489	N 39 02 22.26	W 83 23 49.39
Known St.	G-1	2.063	62	229.917	N 39 02 20.83	W 83 23 10.02
Unknown	G-32	2.045		287.294	N 39 02 19.63	W 83 23 58.39
Known St.	G-1	2.064	80	229.917	N 39 02 20.83	W 83 23 10.02
Unknown	G-46	2.065		294.930	N 39 02 05.12	W83 24 19.14
Known St.	G-1	2.073	98	229.917	N 39 02 20.83	W 83 23 10.02
Unknown St	G-64	2.047		250.818	N 39 02 04.1	W 83 24 50.40
Known St	G-1	2.063	63	229.917	N 39 02 20.83	W 83 23 10.02
Unknown St	G-92	2.060		242.393	N 39 01 34.64	W 83 25 13.56
Known St	G-1	2.064	67	229.917	N 39 02 20.83	W 83 23 10.02
Unknown St	G-94	2.047		248.095	N 39 01 32.32	W 83 25 16.39
Known St	G-1	2.063	78	229.917	N 39 02 20.83	W 83 23 10.02
Unknown St	G-113	2.062		232.942	N 39 01 6.75	W 83 25 31.11
Known St.	G-1	2.073	94	229.917	N 39 02 20.83	W 83 23 10.02
Unknown St	G-118	2.057		218.912	N 39 00 58.76	W 83 25 32.71

Then the instruments were moved to the next station and levelled. At many stations the internal temperature of the gravimeter was monitored, and the readings were double-checked by both of us to minimise the human error.

During the course of the survey the base stations (G0 and G1) were reoccupied repeatedly. This was done to construct drift curves for both gravimeters.

6.4.4- Density Determination

The most vexing problem in the gravity reduction process is the selection of an appropriate value for density in the Bouguer correction. Many surveys simply select the value of 2.67 gm/cm^3 which is the average density for crustal rocks. In many areas such a value is appropriate and useful if we want to compare gravity values from numerous surveys over an extended area. In this survey, which is of limited extent and has a specific target selecting the best value for density using available formation density data from nearby wells. The density of 2.68 gm/cc used in the Bouguer correction was determined from well logs. This average density was calculated from the available compensated formation density logs namely from well No 11 (J. Russell-Tener permit # 11 R.I. , Adams County, Ohio).

6.5- Gravity Data Reduction

6.5.1- Introduction

The essence of data reduction procedures is to make the measurements appear as if they were all made at the same time, on the same day, at the same latitude, and at the same elevation, on the same convenient reference surface. In gravitational prospecting, observed gravity values are compared from station to station. To maintain relevance between the observations, a reference station (datum surface) is chosen, to which all the data are corrected. The data reductions are accomplished by applying the earth tide and the instrument drift correction, the latitude correction, the free-air correction, the Bouguer correction, and the terrain correction to the data. The resulting value after the correction is the departure from the reference value, which is attributed to density contrasts in the subsurface.

6.5.2.- Instrumental Drift and Tides Correction

The gravimeters are designed to measure changes in the gravity value in the order of 0.005 mgal. Tidal effects due to the movement of the sun and the moon may have amplitudes as large as 0.3 mgal (Telford et al. 1980), must be removed from gravity data. The tidal effects depends on the latitude, time of day, and time of year in which the observation was made (Dobrin, 1976). In this gravity survey base stations (G0 and G1) were reoccupied at least once every two to three hours during the course of the survey, in total they were occupied seventeen times. These readings were taken at the beginning of each field day, at the end of series of measurements (2 to 3 hours later), and at the end of the field day. The drift of gravity readings caused by instrument drift (as a result of elastic creep in the springs of the instrument) and earth tidal effects were treated as a linear function of time. Drift curves were constructed using measurements at BM856 (G0) and G1 by plotting the differences between successive measurements (Figure 6.7) for BM856 and (Figure 6.8) for G1. The drift rate is then simply established by dividing the difference in the initial and the final base values by the elapsed time between base station readings. The remaining stations in the loop are then adjusted using the drift rate. We used two different instruments. From the drift curves shown in Figure 6.7 (Station G0) and Figure 6.8 (Station G1) it is evident that the LaCoste-Romberg gravity meter is an extremely stable instrument shows stable readings, with a drift rate that does not exceed 0.01mgal for a whole day. The drift was small enough to be ignored . On the other hand we note the Worden gravity meter was less stable. We favour the data collected using LaCoste-Romberg gravity meter because the drift rate is much smaller.

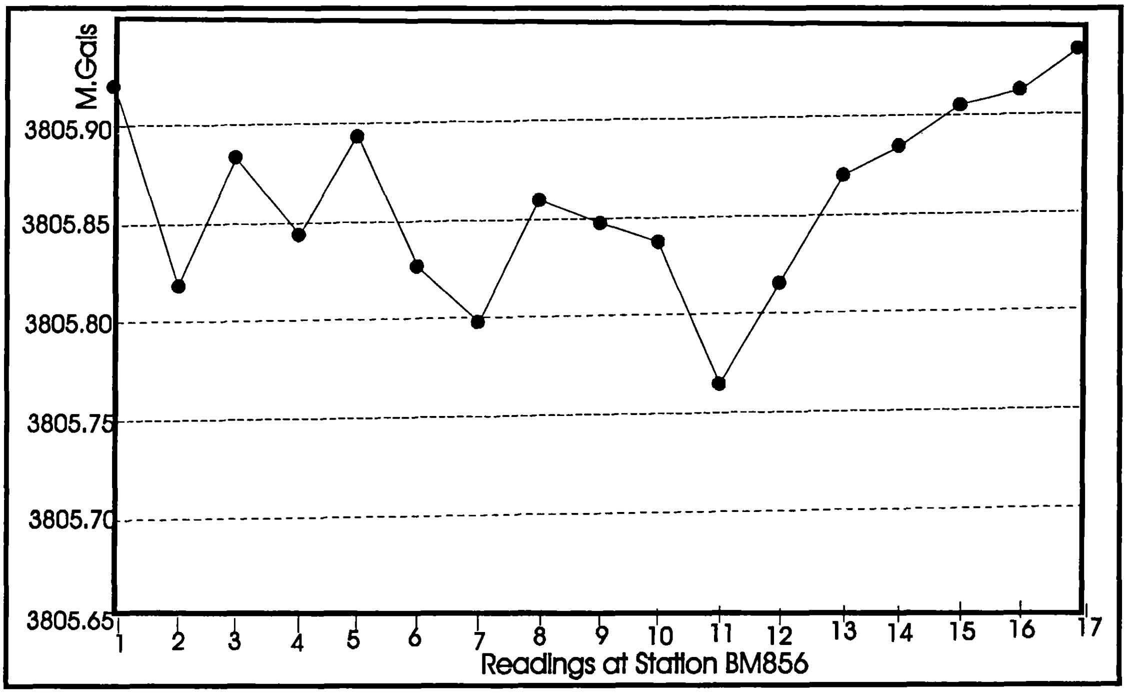

Figure 6.7- LaCoste-Romberg drift curve (30 SEP. to 4 OCT. Appendix II) At Station G0 (BM856)

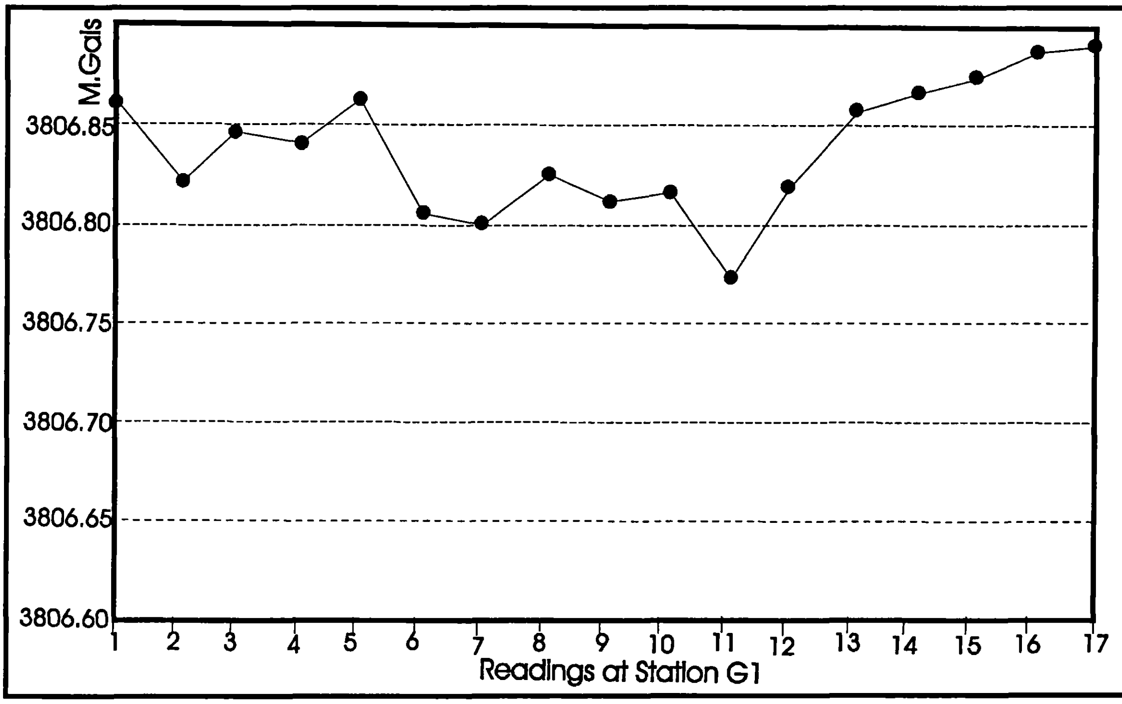

Figure 6.8- LaCoste-Romberg drift curve (30 SEP. to 4 OCT. Appendix II) At Station G-1

6.5.3- Latitude Correction

The equation for latitude correction on the reference ellipsoid is;

$g_n = g_e(1 + A\sin^2 \Phi - B\sin^2 2\Phi)$ Gals. (Equation 6.4)

where g_e represents gravity at the equator at sea level, Φ is latitude and A and B are constants that take into account the Earth's angular velocity of rotation, its size, and its ellipticity. Current values for g_e, A, and B were adopted by the International Association of Geodesy in 1967. The international gravity formula (Equation 6.4) is represented as:

$g_n = 978.03185\,(1 + 0.0053024\sin^2\Phi - 0.0000058\,\sin^2 2\Phi)$ Gals. (Equation 6.5)

Normal gravity g_n (Telford et al. 1976) represents the gravity acceleration that we should observe when measuring gravity at various positions on the earth's surface. Typically, the value of gravity that is measured $g_{obs.}$ (observed gravity) does not match g_n, the difference between the two is thus anomalous and is called the gravity anomaly. Differentiation of the I.G.F. (International Gravity Formula, 1967) with respect to latitude gives the north-south gradient of gravity. This may be expressed as follows:

$$\frac{\partial g}{\partial s} = \frac{1}{R_e}\frac{\partial g}{\partial \Phi} = \frac{1}{R_{eq}}\frac{\partial g}{\partial \Phi} \qquad \text{(Equation 6.6)}$$

$= 90.2739$ mgals/ degree

$= 1.307 \sin 2\Phi$ mgals/mile

$=0.812084 \sin 2\Phi$ mgals/kilometre (Equation 6.6b)

Where ∂s = north-south horizontal distance from the equator, R_e = radius of the earth at latitude Φ, and R_{eq} = equatorial radius which is 6378.140 kilometres (Telford et al. 1976). Equation (6.6), is known as the latitude correction. The latitudinal gravity gradient is zero at the poles and at the equator, and is a maximum of 0.812084 mgals/km at $\pm 45°$ latitude. Figure (6.9) shows gravity gradient changes with latitude.

How accurately do we need to know the position of our observation points along the survey profile? At latitude 38° the variation in normal gravity is 87.5 mgal for a degree of latitude. If we take the length of one degree to be 111 km (it actually varies from about 110.5 km at the equator to 111.5 km at the poles), this variation translates to 1 mgal /1268 m. If we want to maintain an accuracy of 0.01 mgal in our survey, we must be able to locate the station's position within 12.5 metres.

Latitude corrections were applied to each gravity reading using Equation (6.6 b). We corrected all gravity observations (Appendix A) along the profile to appear as if they were made at the latitude of base station (G1). Gravity changes due to latitude increase for observations north of the reference station G1 (latitude), and thus the correction for these observations is negative. For stations with latitudes less than the latitude of the reference station (G1), the correction is added.

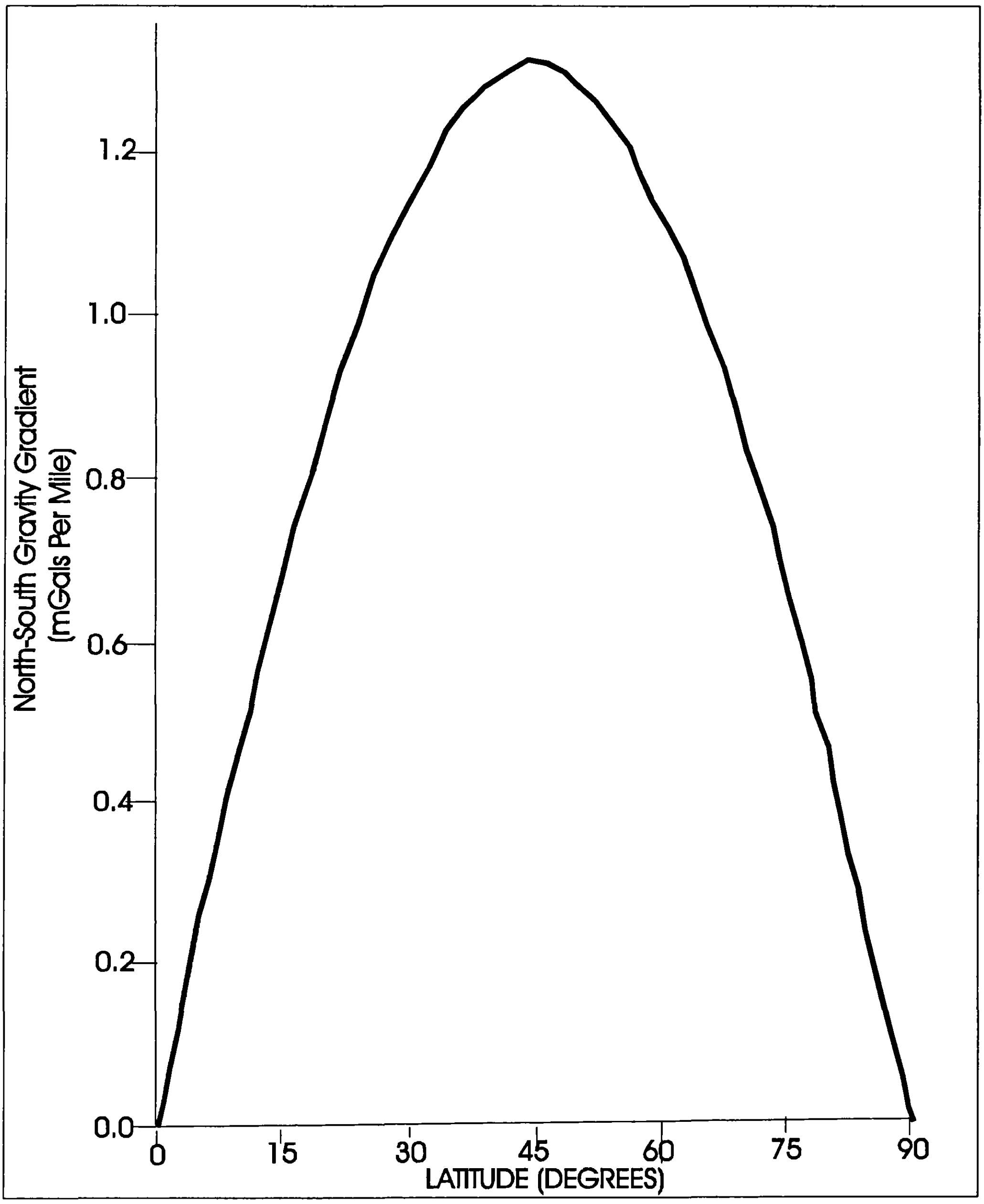

Figure 6.9- Gravity gradient changes with latitude

6.5.4- Elevation Correction

6.5.4.1: The Free-Air Correction

Variation in elevation substantially affects observed gravity. Once again corrections must be applied to observed gravity before such data are useful. Returning to the simple earth model, which is spherical and non-rotating the gravitational acceleration g is;

$$g = \frac{GM}{R^2}$$

To examine how gravity varies with elevation, we can determine the vertical gradient by taking the first derivative of the above equation with respect to R. Thus,

$$\frac{dg}{dR} = -2\frac{GM}{R^3} = -g\frac{2}{R} \qquad \text{(Equation 6.7)}$$

Where R = mean radius of the earth (= 6371.32 kilometres), and g = 981.7855 Gal the acceleration of gravity at the earth's surface at 45 latitude.

If we use the value of g at 45 latitude for gravity at sea level and R, the result is -0.3080 mgal/m. This value tells us what we already know that gravity decrease as the distance increases from the earth's centre, and it tells us of the rate of decrease. As in the case of the latitude correction a more adequate representation of the true character of the earth may be used. This requires the derivative of an equation which includes factors for rotation and ellipsoidal shape (Grant and West, 1965)

$$\frac{dg}{dR} = -0.3086 - 0.00023\cos 2\Phi + 0.00000002\,h \quad \text{mgal/m.} \qquad \text{(Equation 6.8)}$$

Where Φ is latitude and h is elevation. Along the survey profile the latitude is around 39°, thus the second term in Equation (6.8) is .000047 mgal, and the maximum value of the last term in Equation (6.8) is 0.00000014 mgal, since the maximum difference in elevation between the gravity stations is 70 metres. Therefore, in practice both terms are usually ignored, and the value of -0.3086 mgal/m is the only value used for the elevation correction. The elevation correction reduced the gravity readings to a common datum plane, which for our survey was the elevation of base station (G1). This corrects gravity differences between the reference station and the general survey gravity station due to difference in relative elevation. The elevation correction consisted of two parts (1) the free-air correction and (2) the Bouguer correction. The free air correction accounts for the decrease in the pull of gravity with increase in distance from the centre of the earth. This correction added to the gravity stations above the reference datum, and subtracted for stations below the reference datum. Note that this correction considers only the elevation differences relative to the datum and does not consider the material between the observation point and the reference datum, for this reason this correction is known as the *free-air correction.*

Taking into account that the Earth is an oblate spheroid, rather than a sphere, the normally accepted value of the free-air correction is:

$$\Delta g_{fa} = 0.3086\ h \text{ milligals.} \qquad \text{(Equation 6.9)}$$

To maintain a very accurate survey (0.1 mgal), we must know the elevation of an observation point to at least 35 cm. The value remaining after applying both the latitude correction L_{corr} and the free-air correction Fa_{corr}, and subtracting normal gravity from observed gravity is termed the *free-air anomaly,* which can be expressed as the free-air anomaly Δg_{fa} as

$$g_{fa} = g_{obs.} - g_n + Fa_{corr} \qquad \text{(Equation 6.10)}$$

6.5.4.2: Bouguer correction

If a gravity station is at a point on the survey datum, no free-air or Bouguer correction is necessary. If the station is at point above or below the survey datum, a correction is required for the mass lying between station and the datum. The gravity at a point above the datum will be greater due to the presence of the material between the observation point and the reference datum. The usual approach to calculate the effect of this material is to assume an infinite slab of density ρ and thickness h.

The Bouguer correction removes the effect of an assumed infinite slab of material (with uniform thickness and density) between the datum plane and the horizontal plane of each station. The Bouguer correction is named in honour of Pierre

Bouguer (1698-1758), who was the first to attempt measure the horizontal gravitational attraction of mountains. The Bouguer correction calculates the extra gravitational pull exerted by a rock slab equal to $2\pi G\rho h$. Because this correction is supposed to remove the effect of the additional mass above the datum, which adds to observed gravity, correction should be subtracted from the observed gravity value for stations above the datum. If the observation is at a point below the datum, the Bouguer correction must be added to observed gravity. Thus, the Bouguer effect, or g due to a slab of infinite extent and thickness h is

$$B_{corr} = 0.04193\,\rho\,h \;\; \text{mgal/m.} \qquad \text{(Equation 6.11)}$$

For this gravity survey a density of 2.68 gm/cc was assumed for material between the surface and G1 and therefore, the Bouguer correction used was 0.1123157 milligals per metre, that is 0.0342338 milligals per foot. The residual gravity remaining after the Bouguer correction (Appendix II) $B_{corr.}$ is referred to as the *Bouguer Anomaly* (Δg_B) and is equal to

$$\Delta g_B = g_{obs} - g_n + Fa_{corr} - B_{corr} \qquad \text{(Equation 6.12)}$$

$$\Delta g_B = (g_{obs} - g_n + 0.3086h - 0.04193\,\rho\,h) \;\; \text{mgal} \qquad \text{(Equation 6.13)}$$

6.5.5-Terrain Correction

The Bouguer correction is somewhat crude in its assumption of an infinite slab of material between the observation point and the reference datum. In areas of large topographic relief this assumption is not robust. Therefore, the data should be corrected for the topographic effect. If the observation point is near a valley, the Bouguer adjustment is overcorrected, because a mass effect has been subtracted where no mass existed in the first place. Therefore, one must add a small amount to the observed value to adjust for this situation. If the station is near a hill, the mass exerts an upward attraction on the gravimeter. Since the observed gravity is reduced, we must add a small amount to the observed gravity. The corrections which account for the undulation of topography above and below the elevation level of the observation point are referred to as the *terrain correction.* The terrain correction is positive regardless of whether the local topography consists of a hill or a valley. The Bouguer anomaly formula becomes;

$$\Delta g_B = g_{obs} - g_n + FA_{corr} - B_{corr} + TC \qquad \text{(Equation 6.14)}$$

Certainly the most widely used method to carry out terrain correction is the one proposed by Hammer (1939). Hammer's approach considers the gravity effect of topographical features surrounding the observation station as represented by concentric rings having specific thickness as well as inner and outer radii (Figure 6.10) Considering a ring with thickness z, an inner radius R_i, and an outer radius R_o, the equation for the gravitational attraction of the ring at a point at its centre is,

$$g_{ring} = 2\pi G\rho\,[\,R_o - R_i + (R_i^2 + z^2)^{1/2} - (R_o^2 + z^2)^{1/2}\,] \qquad \text{(Equation 6.15)}$$

By dividing the ring in an equal number n of compartment or sectors, the attraction of each sector becomes g_{ring}/n.

Hammer (1939) calculated the sizes of ring radii and sectors that give the most accurate results at increasing distances from the gravity observation point in question. In practice a template consisting of concentric circles is drawn on a clear overlay, each pair of adjacent circles outlines a ring and is referred to as a zone, in turn divided into a number of sectors. In our calculation of the terrain correction, Hammer's template consists of zones D through I at the same scale of the available topographic map (1:24,000). The centre of the circles is located on the station point and the terrain effect calculated using the tables of terrain correction, the maximum terrain correction for the gravity stations is less than 0.1 mgal.

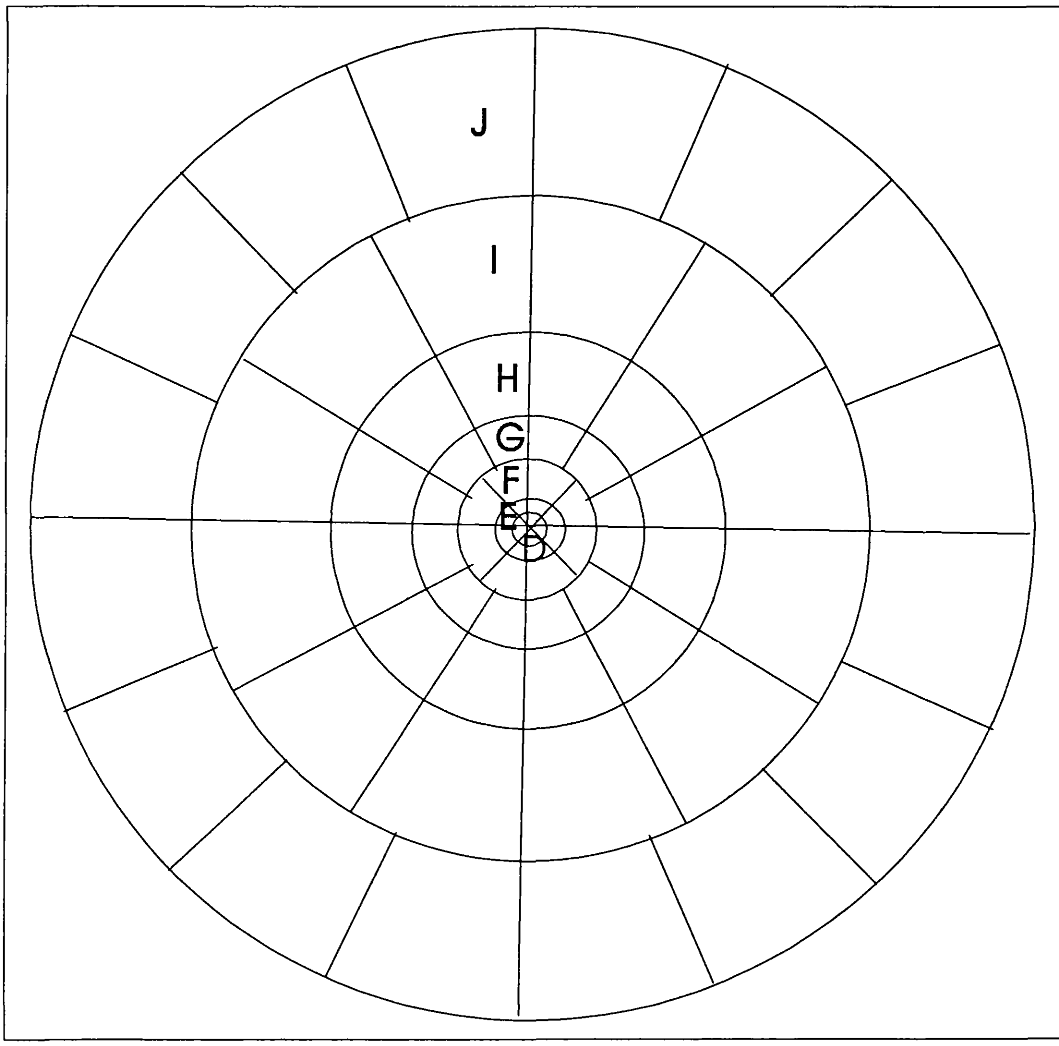

Figure 6.10- Terrain correction-zone chart used for terrian correction

6.6- Modelling and Interpretation

6.6.1-Bouguer Anomaly

After the gravity readings were corrected for drift, latitude, elevation, and terrain effects the remaining value was the Bouguer anomaly value for each station along the profile in reference to base station (G1). Appendix (A) lists the Bouguer anomaly values and correction data for the gravity stations. Figure (6.11) shows the Bouguer anomaly profile across the Serpent Mound Structure. The profile shows a regional anomaly passing through the Serpent Mound area which was well documented by Zahn (1965), Bull and others (1967), and Flaugher (1973). The regional anomaly is sloping from the east towards the west. Superimposed on the regional anomaly is a local negative anomaly with amplitude of about –1.2 mgals. The microgravity profile is shown along with the seismic section BV-1-92 in Figure (6.12). The local gravity anomaly is clearly associated with the central uplift area of the structure.

6.6.2-Regional and Residual Anomalies

The Bouguer profile may be separated into two components based on the wavelength component of the data. The low frequency-long wavelength component is usually caused by broad large structures. The high frequency-short wavelength component is usually due to the localised effect of the lateral density variations in the subsurface. In this study the shorter wavelength anomaly is of primary interest and thus the longer wavelength were removed as the regional effect. Note that the observed gravity profile (Figure 6.11) is dominated by a trend indicating decreasing gravitational acceleration from east to west. These smooth trends usually are referred to as *regional trends.* Smaller, more local sources account for sharper anomaly shapes of more restricted aerial extent.

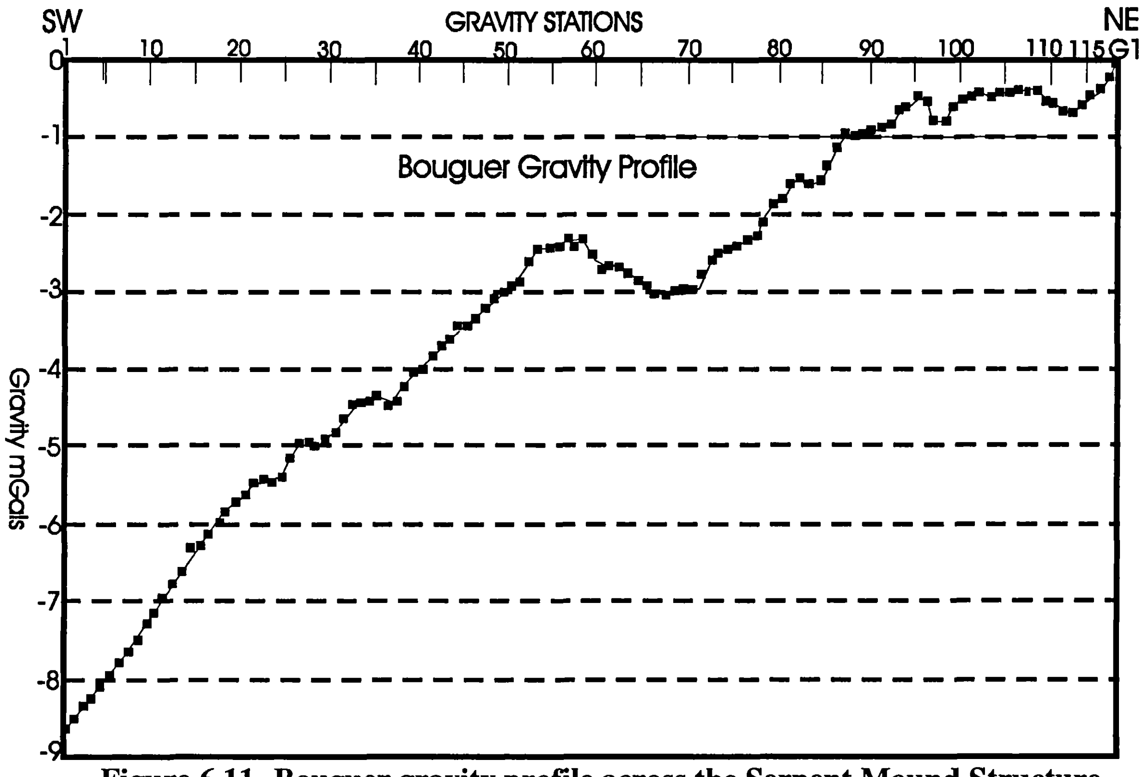

Figure 6.11- Bouguer gravity profile across the Serpent Mound Structure

The target of our survey is the local anomaly, or the small hump at the middle of the gravity profile. If regional anomaly is removed from gravity data, the remaining or residuals values are related to the local disturbance. These are referred to as *residual anomalies*. Thus, to completely define the residual anomaly of a local structure, we must have sufficient station density, and a long enough profile to separate the regional from the residual anomaly. The regional trend is shown as the smooth trend (Figure 6.11). Then the regional field may be subtracted from the Bouguer anomaly values along the same profile.

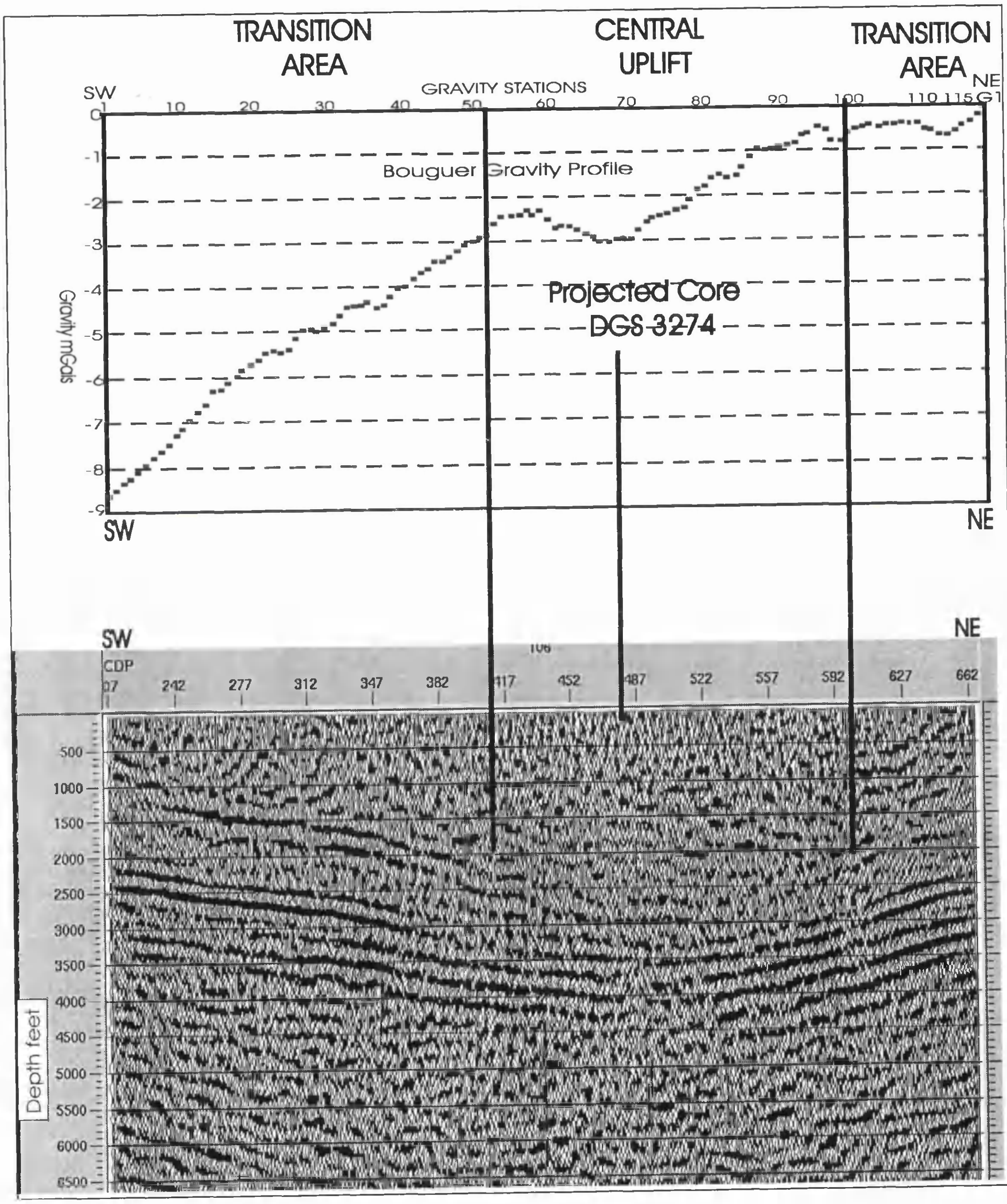

Figure 6.12- The local gravity anomaly with the seismic section BV-1-92

We know how the long-wavelength gravity field varies around the Serpent Mound Area (Zahn, 1965). We may us simple graphical estimates of the regional and subtract it from the total anomaly. A further filter *(wavelength filtering)* is applied to enhance the short wavelength part of the record. This produces the residual anomaly shown in Figure (6.13*)*.

Median filter was conducted using proper frequency cuts. Examining the anomaly shape; comparing its location to the seismic profile and the topographic profile, we conclude that the structure is the source of the local anomaly.

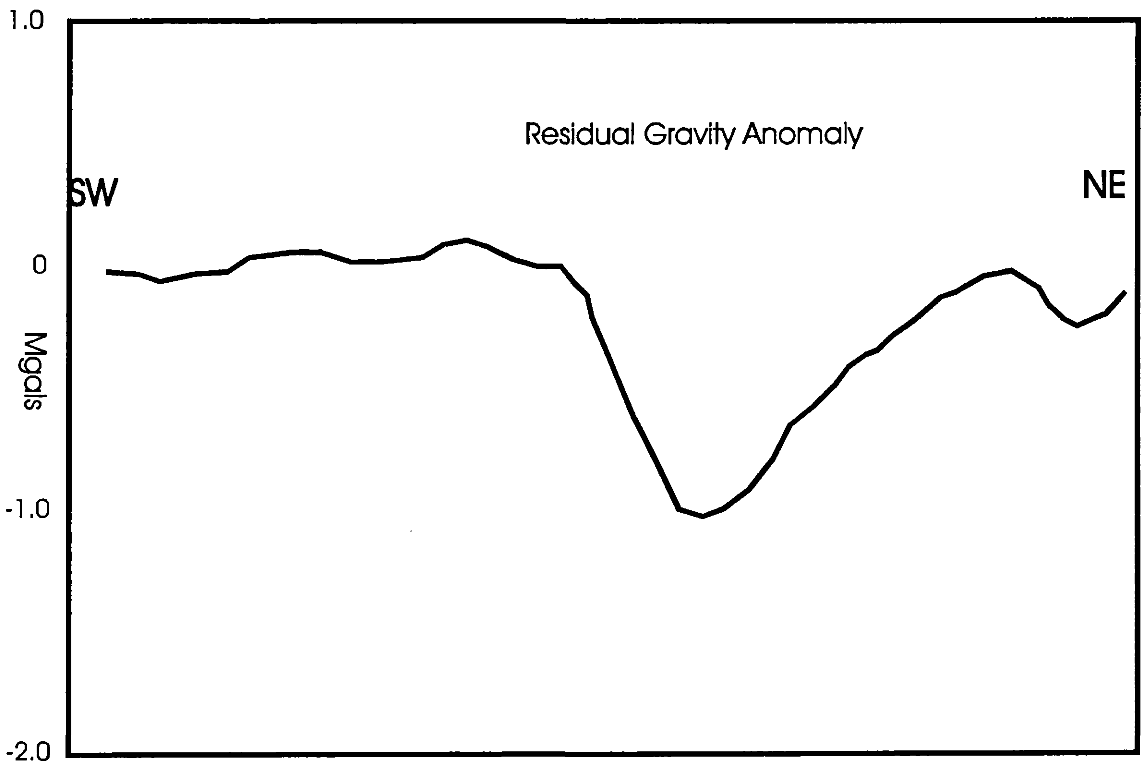

Figure 6.13- Residual gravity anomaly of the Serpent Mound Structure

6.6.3- Modelling

Computer modelling of the gravity profile was conducted using the 2 $^1/_2$ dimensional British Geological Survey gravity modelling program, gravmag (v.1.6). For this model it was assumed that the structure being modelled was laterally continuous for one kilometre for both sides of the profile. The source of the negative anomaly was modelled as a vertical polygon. The density of each layer has been calculated from the Formation density log. The vertical polygon has a density contrast of -0.06 gm/cc.

Gravmag was used to calculate the gravity effect for solids of semi-infinite strike length and polygonal cross section. Because each polygon can have many vertices, and several polygons can comprise a model, a large number of subsurface models are possible. The fundamental equations of the program derived following a procedure much like the procedure to determine the Bouguer correction, the semi-infinite sheet, and the vertical cylinder. If we have a small cell of infinite length in the y-dimension with side length dz and dθ, the gravity effect of such cell is easily determined by integration. Thus we have,

$$G_{cell} = 2\,G\,\rho_c \int_{\theta 1}^{\theta 2} d\theta \int_{z1}^{z2} dz \qquad \text{(Equation 6.16) That is;}$$

$$G_{cell} = 2\,G\,\rho_c (\theta_2 - \theta_1)(Z_2 - Z_1) \qquad \text{(Equation 6.17)}$$

Thus one all he needs is to define polygon such as in Figure (6.14). The polygon consists of an accumulation of cells. If a polygon has n cells, then the gravity effect of the polygon is

$$G_{polygon} = 2\,G\,\rho_c\, n\, \Delta\theta\, \Delta z \quad . \qquad \text{(Equation 6.18)}$$

Given the co-ordinates of the polygon and the density, the summation can be carried out and the gravity effect of the polygon calculated. A solution to this problem was adapted to computer use by Talwani et al. (1959). Dealing with polygonal cross sections of bodies with infinite strike length, one can simulate the geological cross section of the

subsurface based on the seismic sections, well log information, and the data from the cores. The calculated gravity anomaly is compared with the observed anomaly.
The regional field can be determined by the upward continuation of the modelled data
The gravity model gives good agreement to the observed gravity (Figure 6.14), with a low-density vertical polygon. This models the effect of a zone of fractured and brecciated rocks extending to about 2000 ft (610 m) below the centre of the impact. The position and the diameter of the low-density region mimic the Serpent Mound Structure depression seen on the seismic section, and confirmed by the cores (DGS 3274).

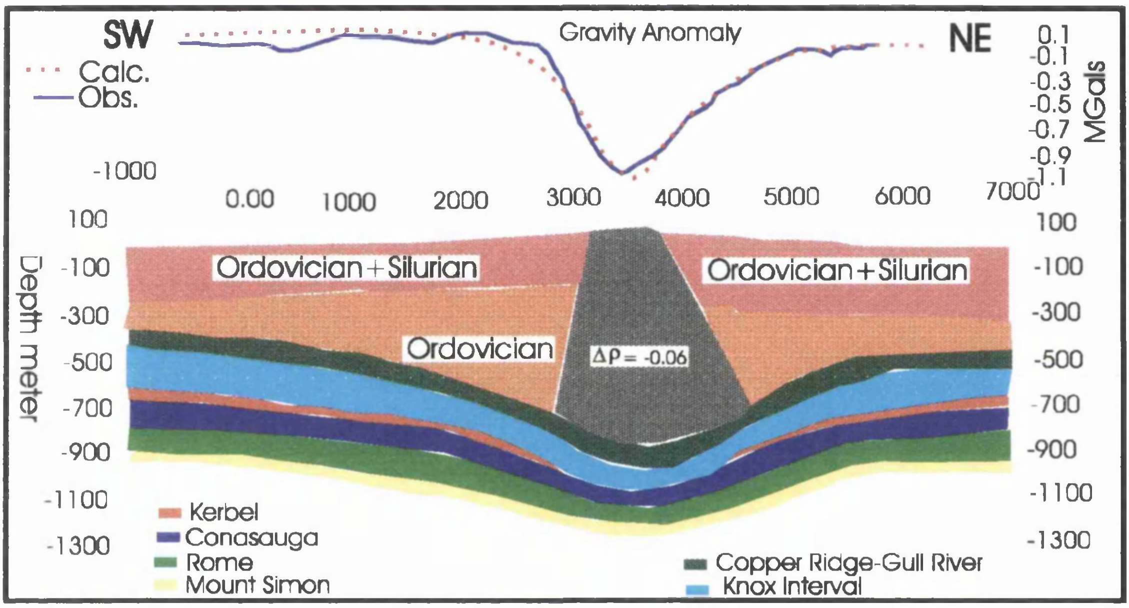

Figure 6.14- Model of the subsurface geology and the gravity anomaly Of the survey profile across the Serpent Mound Structure

6.6.7- Discussion

A microgravity survey of the Serpent Mound reveals a small residual negative gravity anomaly associated with the structure, which was not found by other studies. The gravity anomaly represents evidence for low-density material resulting from the fracturing and the brecciation of the target rocks .

Gravity is an important tool for investigation of about one fifth of the known impact craters on the surface of the earth (Grieve and Pesonen, 1992; Pilkington and Grieve, 1992). The amplitude, shape and character of the residual Bouguer gravity over the Serpent Mound Structure are consistent with observations of other impact structures with similar diameters.

An acceptable fit is achieved between the model curve and the Bouguer anomaly curve (Figure 6.14). This represents one possible geologic configuration. One has to bear in mind that many different models can produce the same gravity profile. There is no unique solution. However, our model is based on seismic and core control. Therefore the final model probably provides a fairly close approximation to the actual subsurface geology as it is consistent with findings from other investigations. These data support the exogenic origin of the Serpent Mound Structure as they show deformation confined to the uppermost levels.

Finally, it always preferable to tie gravity measurements to a location where absolute gravity is known accurately. It is not absolutely necessary for our limited, local survey, as we seek only the variations in gravity across the structure. But this may add to the research base by making our measurements part of the system that everyone else uses. The looping procedure we used between Base station BM856 (G0) and Base station G1 at the beginning of the survey profile provided the relative gravity difference between the two stations after correcting for drift. Because we know the absolute gravity value for G0, we have an absolute gravity value for base station G1. Therefore we know the absolute gravity values of other observation stations along the survey profile by reference to G1 (Appendix II).

CHAPTER-7 MAGNETIC METHOD

7.1- Introduction

Variations in the Earth's magnetic field are caused by differences in the magnetic susceptibility and magnetic remanence of rocks, which are the significant variables in magnetic exploration. Sedimentary rocks exert a small magnetic effect compared to igneous rocks because of their lower magnetic susceptibility. Therefore most variations in the magnetic intensity measurable at the surface result from topographic or lithologic changes within the basement or from igneous rocks, because of the concentration of ferrimagnetic minerals, particularly magnetite. The magnetic method has much in common with the gravity method, but the interpretation of magnetic survey data is generally more complex because the variations in the magnetic field are more erratic and localised. This is due to the variable direction of the ambient magnetic field, whereas the gravitational field is always in the vertical direction, and also due to the time dependence of the earth's magnetic field, compared to very small tidal variations in the gravity field. The magnetic method as used in geophysical exploration is a versatile method, it can be used for both deep and shallow structures. Relative to other geophysical methods, the magnetic method is very rapid and cheap for both local and regional studies.

During the months of September and October 1996, we conducted an extensive ground magnetic survey of the Serpent Mound Structure and its surrounding area. Thirty-one magnetic profiles were completed in an area of approximately 625 square km. Our objective first was to look for any short wavelength anomalies that might be associated with local zones of mineralisation. We thus started the magnetic traverses across the structure with a comparatively short station interval of 10 m. All of the short wavelength anomalies we found were related to cultural features, and the magnetic anomaly over the Serpent Mound Structure is in fact a long wavelength anomaly extending beyond the structure. The magnetic survey resulted in a new magnetic anomaly map of the area, which is a significant revision of the previous map produced by Sappenfield (1951).

7.2- Theoretical Basis

7.2.1 Fundamental Relationships

Each bar magnet has two poles and is referred to as *dipole*. It is convenient to visualise any magnetised body, as if it is composed of a very large number of small dipoles, which are similarly aligned and stacked closely together. The magnetic poles are referred to as positive (+m) and negative (-m). The positive pole (north-seeking pole) of a compass needle points toward the north magnetic pole of the earth.

Coulomb's law states that the force of attraction or repulsion between two poles (m_1 and m_2) is proportional to the product of the poles strength m_1 and m_2 divided by the square of the distance (R) between them.

$$F = \frac{1}{\mu} \frac{m_1 m_2}{R^2} \qquad \text{(Equation 7.1)}$$

Where μ is the magnetic permeability of the medium in which the poles are located. The magnetic permeability is very nearly equal to unity in air and water.

The magnetic field strength **H**, is the force a unit magnetic pole would experience if placed at a point in a magnetic field which is the result of some pole strength *m* and located distance R from *m*, Thus

$$\mathbf{H} = \frac{F}{m} = \frac{1}{\mu} \frac{m}{R^2} \qquad \text{(Equation 7.2)}$$

The magnetic field strength **H** is a vector quantity having magnitude given by (Equation 7.2) and with direction determined by assuming the unit pole is positive. Given the units associated force Newton (N), and magnetic pole (Amp m.), the unit associated with the magnetic field strength is N/Amp m, or Tesla.

The SI unit of the magnetic field strength is the *nanotesla* or simply nT, where the c.g.s unit of the magnetic field strength is the *oersted.* The Oersted is 1 dyne/unit pole strength, and is equal to 10^5 gammas. The gamma is numerically equivalent to the *nanotesla.* Recently nanotesla is the preferred unit employed in geophysics.
If a dipole is placed in a uniform magnetic field, the magnetic dipole will experience a couple: C

$$C = 2\ m\ l\ H \sin\theta \quad . \qquad \text{(Equation 7.3)}$$

A couple (pair) is two forces equal in magnitude and acting parallel to each other but in opposite directions. **H** is a uniform magnetic field, and l is the length of the dipole. The angle θ specifies the original orientation of the magnet in the field. The motion produced by the couple is dependent on the magnitude of H as well as the value of θ (no motion if $\theta = 0$). The other quantity (ml) is the magnetic moment (M).

$$M = m\ l \qquad \text{(equation 7.4)}$$

7.2.1.1-Intensity of magnetisation (I)

A magnetic body possesses a fundamental property per unit volume known as the intensity of magnetisation, I. The magnitude of the intensity I is defined as the magnetic moment M per unit volume

$$I = \frac{M}{volume} \qquad \text{(Equation 7.5)}$$

$$I = \frac{m}{area} \qquad \text{(equation 7.6)}$$

7.2.1.2- Magnetic Potential

Magnetic, gravitational, and electrical fields all are potential fields. The characteristic of such fields is that the work done to move (unit pole strength, or unit mass, or unit charge) from one point to another is independent of the path, that is the potential is zero at infinite distance from the field.

$$V = -\int_{\infty}^{r} \frac{m}{r^2} = \frac{m}{r}$$ (Equation 7.7)

An especially useful feature of the potential is that we can find the magnetic field in a given direction by taking the derivative of the potential in that direction.

7.2.2- Magnetic Properties of Rock

If we place a material that can be magnetised in an external magnetic field H, the intensity of magnetisation (I) will be proportional to the strength of the field. The constant of proportionality generally referred to as the magnetic susceptibility (k).

$$I = k H$$ (Equation 7.8)

Based on the values of magnetic susceptibility materials can classified as diamagnetic or paramagnetic. Diamagnetic materials, such as quartz and feldspar, have negative susceptibilities. Paramagnetic materials have positive susceptibilities, but in general the values are quite low. Examples of paramagnetic materials are the Fe-Mg silicates such as pyroxene, amphibole, and olivine. However, in few paramagnetic materials the magnetic moments imparted to atoms by orbital motion and spin of electrons interact strongly. The result is the alignment of the magnetic moments in small volumes known as magnetic domains (on the order of 10^{-4} cm in magnetite). If these domains are parallel, as they are in iron, nickel, and cobalt, the material is termed ferromagnetic material (Figure 7-1a). Ferromagnetic materials have very high susceptibility and are often present in meteorites. If the domains are parallel and anti-parallel, the net magnet moment is zero, and the material is said to be anti-ferromagnetic (Figure 7-1b), an example is hematite. If the domains are oriented as in anti-ferromagnetic materials, but one direction of orientation is preferred (Figure 7- 1c), the material said to be ferrimagnetic. Examples of such materials are magnetite, ilmenite, and pyrrhoite. These materials have high susceptibilities that depend on temperature and the strength of the inducing field.

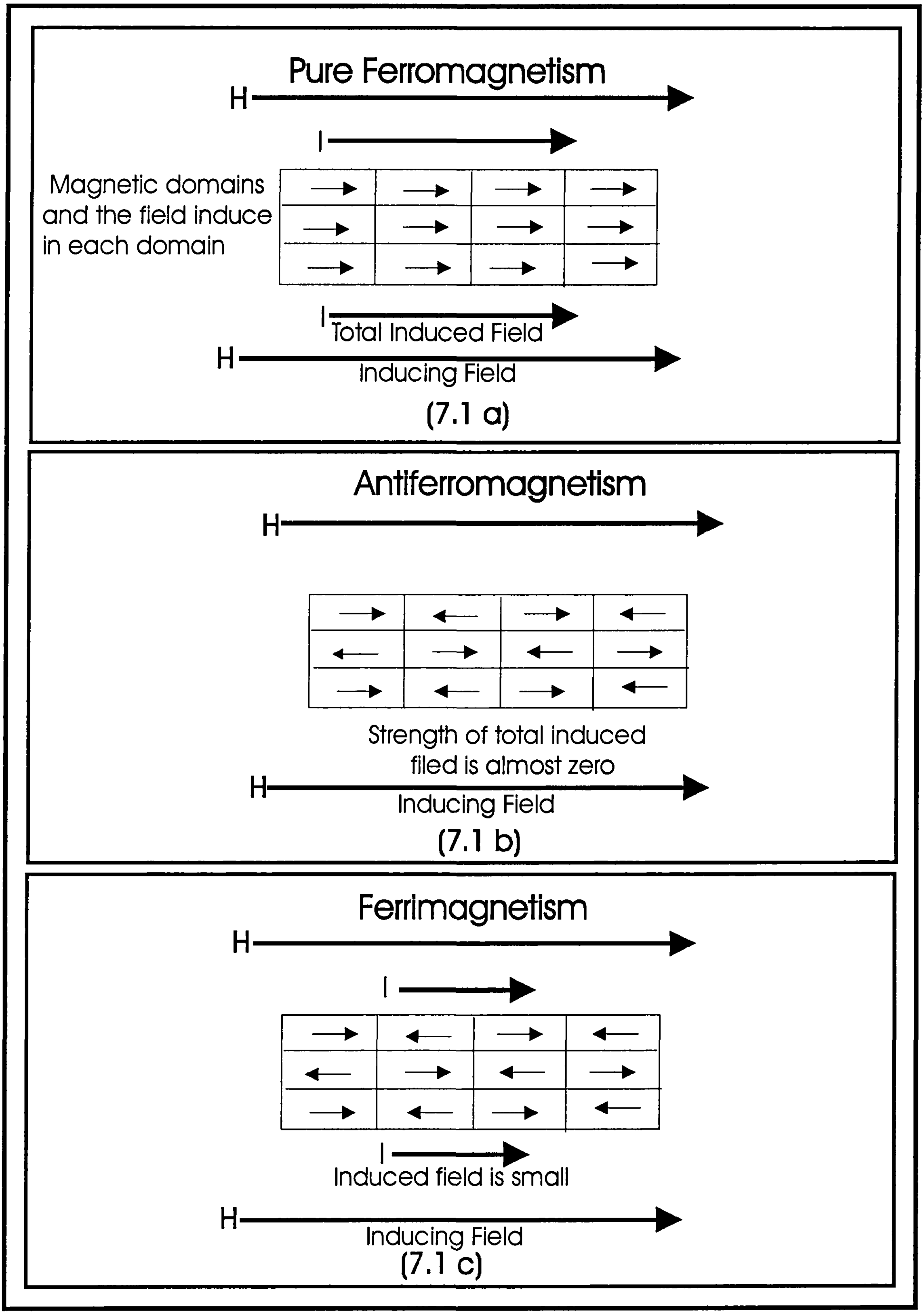

Figure 7.1- Classification of magnetic materials

If a ferrimagnetic material is placed in an external magnetic field, an induced magnetisation is produced, because the external field causes some magnetic domain walls to move. If the external field is weak (as is the earth's magnetic field), only a limited movement of domain walls occurs and no permanent magnetisation remains when the field is removed. If the external field is strong, more domain walls move. Favourably oriented domains increase in volume at the expense of unfavourably oriented domains. Eventually, the induced magnetisation will increase to the saturation level. Further increase in the external field, H, produces no further increase in the induced magnetisation I. If the external field is reduced to zero, the values of I reduce, and do not go back to zero. Instead the magnetization goes to I_r (remnant magnetisation). This is because a large portion of the domain changes are retained during the decrease in the inducing field. The curve of the H-I relation for a magnetic material is known as the hysteresis loop.

When we measure the magnetic effect of geological bodies, any remnant magnetisation with an order of magnitude similar to the induced magnetisation will significantly contribute to the total anomalous field in a manner which depends on the respective orientation of the two magnetisations. Remnant magnetisation in rocks can be produced in a number of natural ways. An important mechanism is thermoremanent magnetisation, which can be produced in ferrimagnetic minerals at high temperature. Even a weak field such as earth's magnetic field can produce preferential alignment of magnetic domains, thus creating a substantial remnant magnetisation (Ir).

Remnant magnetisation may also be caused by the passage of shock waves through a material. Impact sites such as the Kentland structure (Jackson and Van der Voo, 1986), Meteor Crater in Arizona (Cisowski and Fuller, 1978) and the Slate Islands structure (Halls, 1979) have magnetizations that are impact related. Cisowski et al. (1975, 1976) showed by laboratory experiments that the remnant magnetisation of test rock samples are reoriented by the shock produced by impacting projectiles. Crawford and Schulz (1993) showed experimentally that impact-generated plasmas generate magnetic fields. These authors suggest that magnetic fields generated by impacts may be an important component of surface planetary magnetism. Scaling their experiments to dimensions of terrestrial craters (10-100 km) indicates that magnetic fields comparable to that of the Earth may be generated for several minutes or more up to distances of 1-2 crater diameters from the impact point.

Results from magnetic surveying do not normally determine the magnitude and orientation of the remnant magnetisation. Such information more commonly is determined in the laboratory. Typically, survey results are interpreted by assuming the recorded anomalous field is due entirely to induced magnetisation in the causal geological body. Although susceptibility is dimensionless in the SI system, the susceptibility values can be converted from cgs units to SI units by multiplying by 4π. Rock susceptibility is always directly related to the percentage of magnetite present. The true susceptibility of magnetite varies from 0.1 to 1.0 cgs emu. Average susceptibility is quoted in several sources ranges from 0.2 to 0.5 emu (average k = 0.35). The average susceptibilities for ilmenite and pyrrhotite are 0.15 and 0.125 emu, respectively. Table (7-1) gives some representative values of susceptibility for several different kinds of rocks and minerals (Telford et al., 1990). Unlike density, notice the large range of susceptibility variations, not only between varying rocks and minerals, but also within rocks of the same type. The susceptibility is not constant for a magnetic substance; as the inducing field increases. Sedimentary rocks have the lowest average susceptibility and basic igneous rocks have the highest.

Table 7-1 Measured Susceptibilities of rocks and Minerals

TYPE	SUSCEPTIBILITY X 10^3 (SI) RANGE	SUSCEPTIBILITY X 10^3 (SI) AVERAGE
Sedimentary		
Dolomite	0 - 0.9	0.1
Limestones	0 - 3	0.3
Sandstones	0 - 20	0.4
Shales	0.01 - 15	0.6
Average	0 - 18	0.9
Metamorphic		
Amphibolite		0.7
Phyllite	0.3 - 3	1.4
Schist		1.5
Gneiss	0.1 - 25	
Quartzite		4
Serpentine	3 - 17	
Slate	0 - 35	6
Average Meta.	0 - 70	4.2
Igneous		
Granite	0 - 50	2.5
Rhyolite	0.2 - 35	
Dolorite	1 - 35	17
Augite-Syenite	30 - 40	
Olivin-Diabase		25
Diabase	1 - 160	55

Table 7-1 Continues

TYPE	SUSCEPTIBILITY X 10^3 (SI) RANGE	SUSCEPTIBILITY X 10^3 (SI) AVERAGE
Gabbro	1 - 90	70
Basalts	0.2 - 175	70
Diorite	0.6 - 120	85
Pyroxenite		125
Peridotite	90 - 200	150
Andesite		160
Average Acidic Ig.	0 - 80	8
Average Basic Ig.	0.5 - 97	25
Minerals		
Graphite		0.1
Quartz		-0.01
Rock salt		-0.01
Anhydrite, Gypsum		-0.01
Calcite	-0.001 - -0.01	-0.01
Clays		0.02
Chalcopyrite		0.4
Sphalerite		0.7
Siderite	1 - 4	0.9
Pyrite	0.05 - 5	1.5
Limonite		2.5
Hematite	0.5 - 35	6.5
Chromite	3 - 110	7
Pyrrhotite	1 - 6000	1500

Ilmenite	300 - 3500	1800
Magnetite	1200 - 19200	6000

7.2.3-The Earth's Magnetic Field

The earth's magnetic field at any point on the earth's surface is a vector quantity that is defined by its total intensity and direction. Intensity can be measured by any number of instruments. The total field vector is defined by its intensity F_E; its inclination (I), the angle between the field vector and the horizontal plane, and by its declination (D), the angle between the geographic north and the horizontal projection of the field (F). Positive inclinations indicate F is pointed downward, and negative inclinations indicate F is pointed upward. Inclination varies between –90 and 90 degrees.

The total field intensity can be resolved into vertical component Z_E and a horizontal component H_E. The vertical plane containing the total field F_E, the Vertical component Z_E, and the horizontal component H_E, is a magnetic meridian. The Horizontal component H can be resolved into two components, one directed toward the geographic north (X_E), and the other one directed toward the geographic east (Y_E). These elements are related in several ways (Figure 7-2):

$$F = \sqrt{H_E^2 + Z_E^2},$$

$$Z_E = F_E \sin(I), H_E = F_E \cos(I), \text{ and } \tan(I) = \frac{Z_E}{H_E}, \text{ (Equation 7.9)}$$

$$X_E = H_E \cos(D), \text{ and } Y_E = \sin(D).$$

The places where the inclination $I = 90°$ are called the magnetic dip poles.
At the dip poles, $Z_E = F_E$, and the intensity is approximately 60,000 nT. The position where $I = 0°$ is the magnetic equator. At the magnetic equator $H_E = F_E$, and the field intensity is approximately 30,000 nT. This is the portion of the geomagnetic field generated in the earth's core and is referred to as the main field, simply because it is the largest contributor to the total magnetic field.

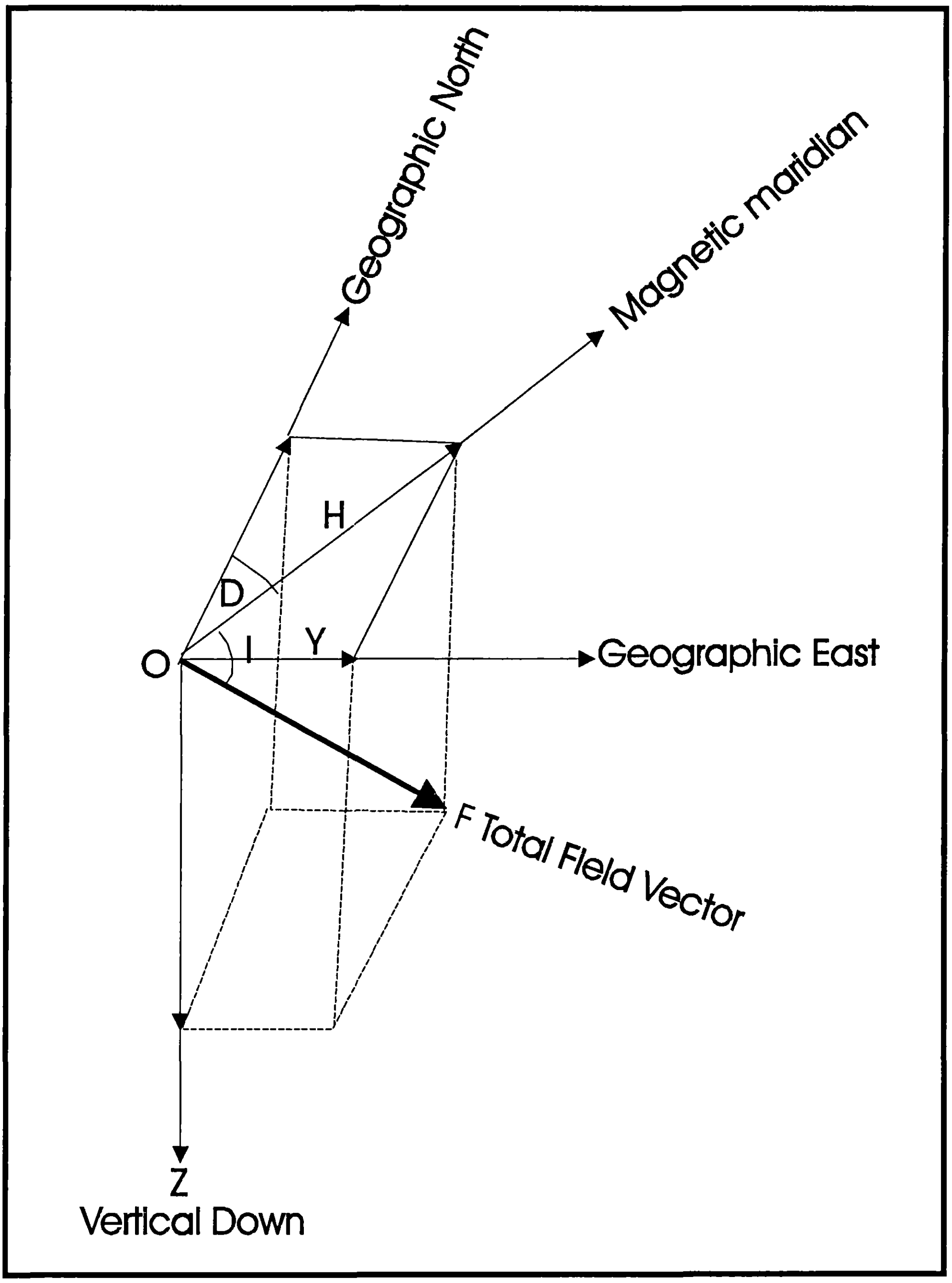

Figure 7.2- The principal components of the Earth's magnetic field

The earth's magnetic field varies by about 200 percent from the equator to the poles, whereas the earth's gravitational varies by less than 0.5 percent.

The magnetic data collected at many points on the earth's surface can be displayed on a map of the world as contours of the magnetic field intensity F_E (Figure 7.3),

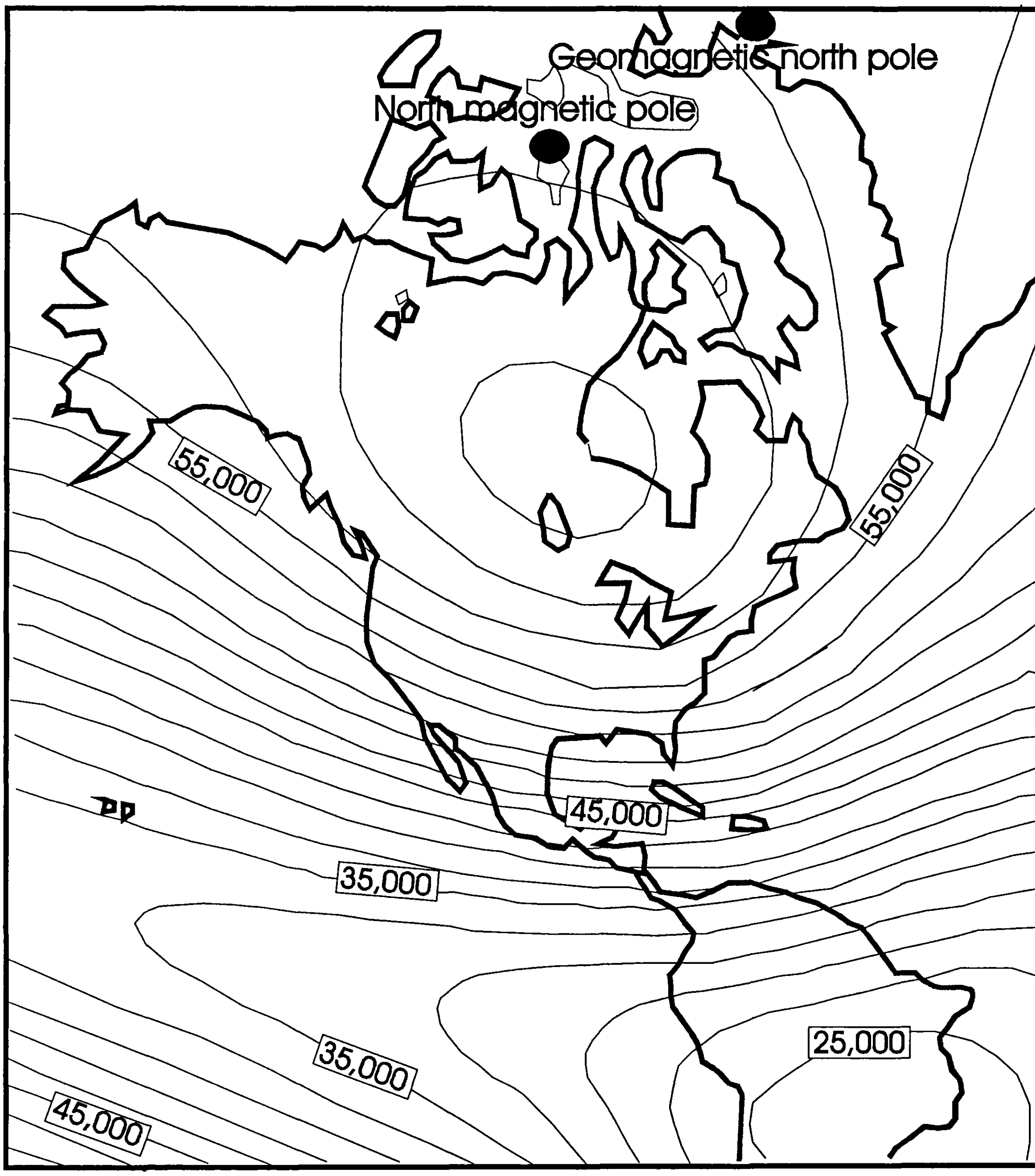

Figure 7.3- Total magnetic field intensity of the Western Hemisphere IGRF epoch (1985)

Inclination (I) (Figure7.4), and declination (D) (Figure 7.5). Those figures illustrate the maps for the Western Hemisphere only. The Earth's field can be quite well approximated by placing a small dipole with large moment at the Earth's centre and tilting the dipole at an angle of about 11.5° to the Earth's axis of rotation (Figure 7.6).

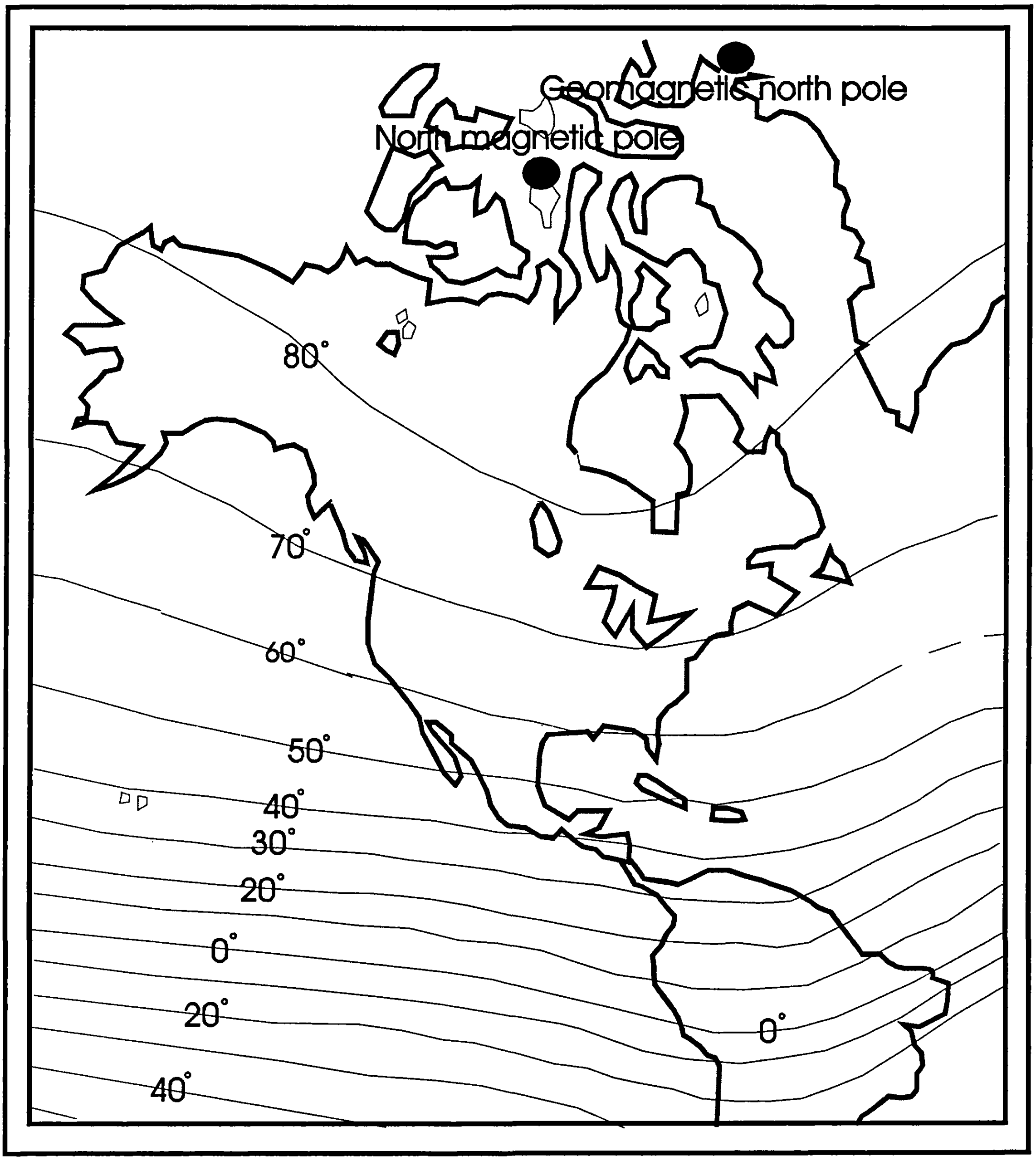

Figure 7.4- Inclination of the Earth's magnetic field (Western Hemisphere) IGRF (1985)

The points where an extension of the axis of this imaginary dipole intersects the earth's surface are referred to as the geomagnetic north and south poles. These do not coincide with the dip poles. Although assuming the earth's field is a dipolar is useful in deriving a number of relationships, the fact that the geomagnetic and dip do not coincide, and the irregularities evident on maps of inclination, declination, and total field intensity demonstrate that this is only an approximation.

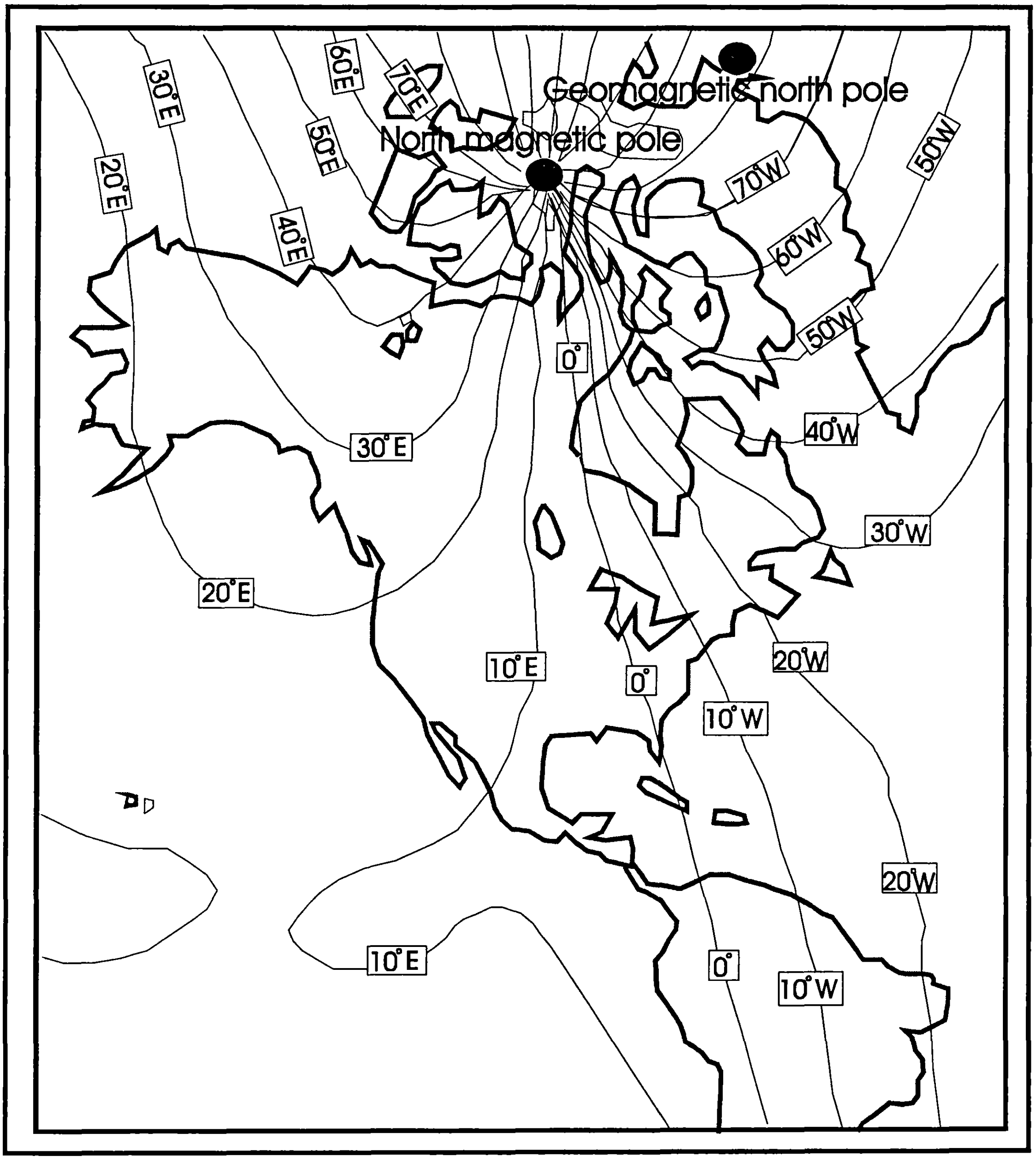

Figure 7.5- Declination of the Earth's magnetic field (Western Hemisphere) IGRF (1985)

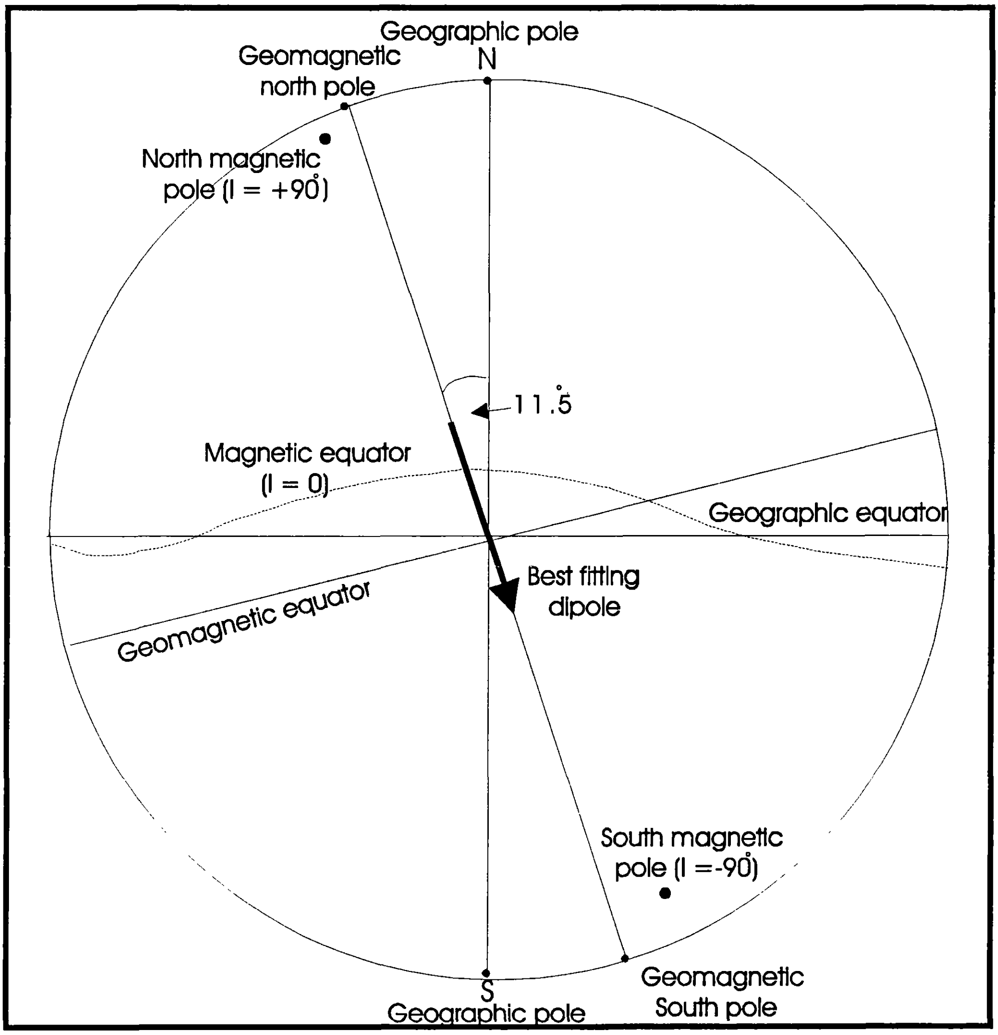

Figure 7.6- Representation of the Earth's magnetic field as an Inclined geocentric dipole

The magnetic potential constitutes a convenient approach to describe the magnetic field at a point (P) due to a dipole. Figure (7-7) illustrates a dipole and the observation point, assuming r is much larger than l.

From equation (7- 7), the potential (V) at point P is

$$V = \frac{m}{r_1} - \frac{m}{r_2} \qquad \text{(Equation 7-10)}$$

Using the assumption $r >>> l$, we have

$$r_1 = r - \frac{l}{2}\cos\theta, \text{ and } \quad r_2 = r + \frac{l}{2}\cos\theta$$

$$V = \frac{ml\cos\theta}{r^2 - \left(\frac{1}{2}\right)^2 \cos^2\theta}$$ and, approximating, this becomes

$$V = \frac{ml\cos\theta}{r^2} = \frac{M\cos\theta}{r^2}$$ (equation 7-11)

To derive the radial H_r and the tangential H_θ components of the field at point P (Figure 7-7), the magnetic field in any direction can be determined by taking the negative of the potential in that direction. Noteing that θ (the co-latitude) is in radians, we get

$$H_r = -\frac{dV}{dr} = \frac{2M\cos\theta}{r^3}$$ (Equation 7-12)

$$H_\theta = -\frac{dV}{d\theta} = \frac{M\cos\theta}{r^3}$$ (Equation 7-13)

Because slightly more than 90 percent of the earth's field can be represented by a dipole at the earth's centre, these equations provide a good approximation of some these properties of this field. From Figure (7-7) the radial field is equivalent to the vertical field ($H_r = Z_E$), and the tangential field is equivalent to the horizontal field ($H_\theta = H_E$). Equations 7-12 and 7-13 are also useful in determining gradients of magnetic field components at various locations on the earth's surface, the vertical gradient of the vertical component of the field is

$$\frac{dZ_E}{dr} = \frac{dH_r}{dr} = -\frac{6M\cos\theta}{r^4} = -\frac{3}{r} H_r = -\frac{3}{r} Z_E$$.(Equation 7-14)

For example the vertical gradient of the vertical component of the earth's field at a point in Ohio, with latitude 39° (Co-latitude 51°) with $Z_E \cong 50750$ nT, $r = 6,370,000$ m

$$\frac{dZ_E}{dr} \cong 0.024 \text{ nT/m}$$

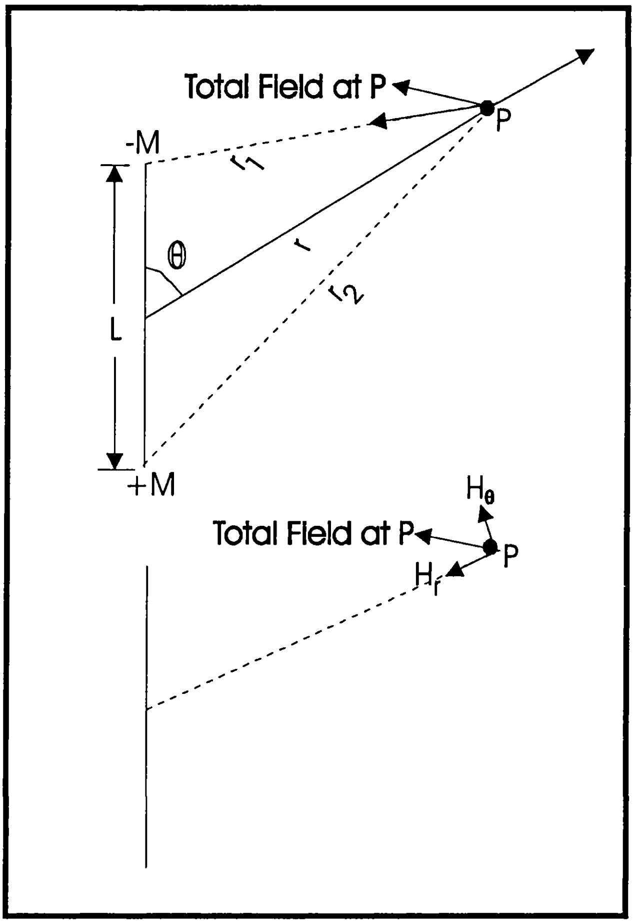

Figure 7.7- The Field of magnetic dipole at a point (Total field, radial component, and tangential component)

7.2.3.1- Secular Variations of the Earth's Magnetic Field

As discussed, the main magnetic field consists of a primary dipole portion and a secondary non-dipole component, which produce variations in the total field vector over the earth's surface. In addition, this main field is not constant but changes slowly in both intensity and direction. These long-term changes in the field, the secular variations, can be ignored when one is conducting an exploration exercise that takes place over a time scale of days or weeks. However, when compiling magnetic data from different years or decades, one should adjust the data for secular variation. This can be achieved by using the geomagnetic reference maps that are normally produced by various agencies at 5-year intervals. These maps are constructed from a network of magnetic observatories from which repeat readings are obtained. Such readings are used in connection with models of the dipolar and non-dipolar components of the geomagnetic field. This results in the International Geomagnetic Reference Field (IGRF), which is presented in the form of maps or data tables through the internet. The direction and intensity of the main field at any position on the earth surface can be obtained once the latitude, longitude, and elevation of the point are known. For example, Figures (7-3), (7-4), and (7-5), are based on information taken from the 1985 calculation of the IGRF.

Also occasionally, and unpredictably, solar activity increases substantially, which leads to an abrupt increase in ionised particles arriving in the ionosphere. These magnetic storms can produce variations of hundreds of nanotesla. Due to this large and erratic variation in magnetic intensities, fieldwork cannot be carried out at such a time. Variations in magnetic susceptibilities of rock lead to local variations in induced magnetisation, which affect total field values. The anomaly field is what we wish to isolate, just as we strive to isolate gravity anomalies by reducing the gravity observations.

7.3- Magnetic Instruments

The most common used instruments for the measurements of the magnetic field are the flux-gate magnetometer, the proton-precession magnetometer and the cesium vapour magnetometer. The flux-gate measures the component of the earth's magnetic field in the direction of the probe. The cesium magnetometer and the proton precession magnetometer both measure the total field. The cesium magnetometer is more sensitive and has a faster measurement time than the proton precession magnetometer. For land-based magnetic surveys, the most commonly used magnetometer is the proton-precession magnetometer because it is considerably less expensive than the cesium magnetometer. The sensor of a proton-precession magnetometer is a cylindrical container filled with a liquid rich in hydrogen atoms and surrounded by a coil.

Commonly used liquids include kerosene, water, and alcohol. The sensor is connected by a cable to a small unit in which is housed the power supply and other necessary electronics such as an amplifier and frequency measuring device. Figure (7.8) is a schematic of the proton precession magnetometer. When power is applied, a DC current is directed through the coil, producing a relatively strong magnetic field in the fluid-filled cylinder. The hydrogen nuclei (protons) behave like minute, dipole magnets and align parallel to the coil axis, in the direction of the applied field. Power is then abruptly removed from the coils. Because the earth's magnetic field generates a torque on the aligned, spinning protons, they precess around the direction of the earth's total magnetic field. This precession induces a small alternating current to flow in the coil at the precession frequency. Because the frequency of precession is proportional to the strength of the total field, and because the constant of proportionality is the well-known gyromagnetic ratio of the proton, the total magnetic field intensity can be determined very accurately.

Important advantages of the proton-precession magnetometer are its ease of use and reliability. Sensor orientation need only to be at a high angle to the Earth's magnetic field. No other levelling or orientation requirements exist. The lack of moving parts ensures generally trouble free operation. Individual readings take about five seconds, with a precision of $\pm$ 1 nT. The proton-precession magnetometer measures only the absolute strength of the earth's total field, giving us the absolute intensity of the Earth's field but not its direction.

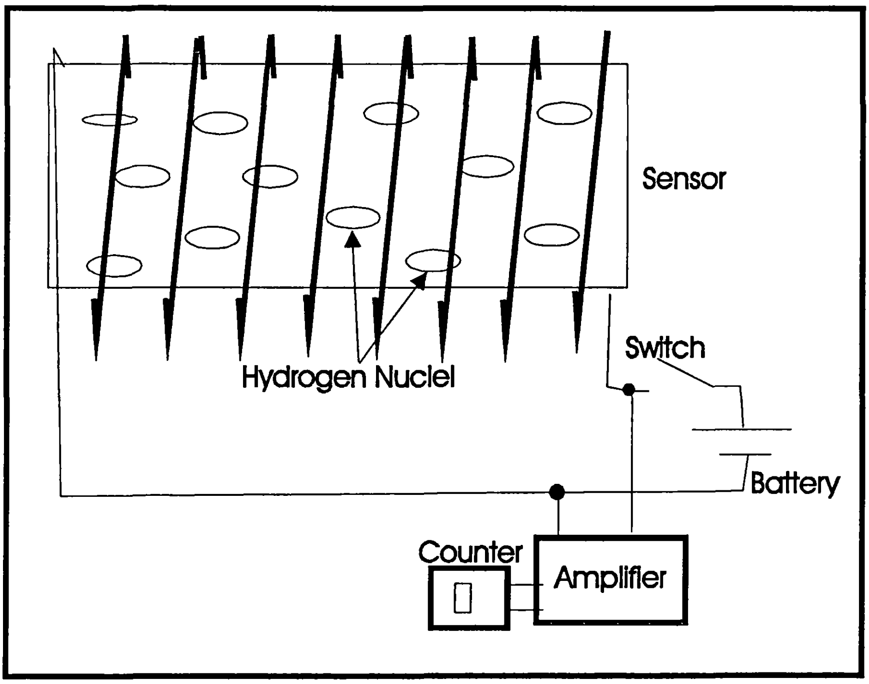

Figure 7.8- Schematic representation of Proton Precession Magnetometer

7.4- Previous Investigations

Hildebrand and Kucks (1984a) produced the total intensity magnetic anomaly map of Ohio from digital data acquired from six different aeromagnetic surveys that were flown at different times, spacing, and elevations. After all the needed corrections, the data were gridded at 1-km grid interval and filtered to remove short wave lengths and contoured. Figure (7.9) is a part of the Ohio State Anomaly Map showing a NW-SE trend of high magnetic anomaly to the west of the Serpent Mound Structure.

(Zietz et al. 1968) suggested the high amplitude magnetic anomalies along a belt between 82° and 84° W as the expression of the Grenville Province in the subsurface. The Grenville Front is coincident with the western margin of this belt. Intriguingly, the Serpent Mound Structure lies near the western margin of this belt, among some of the largest magnetic anomalies in the state.

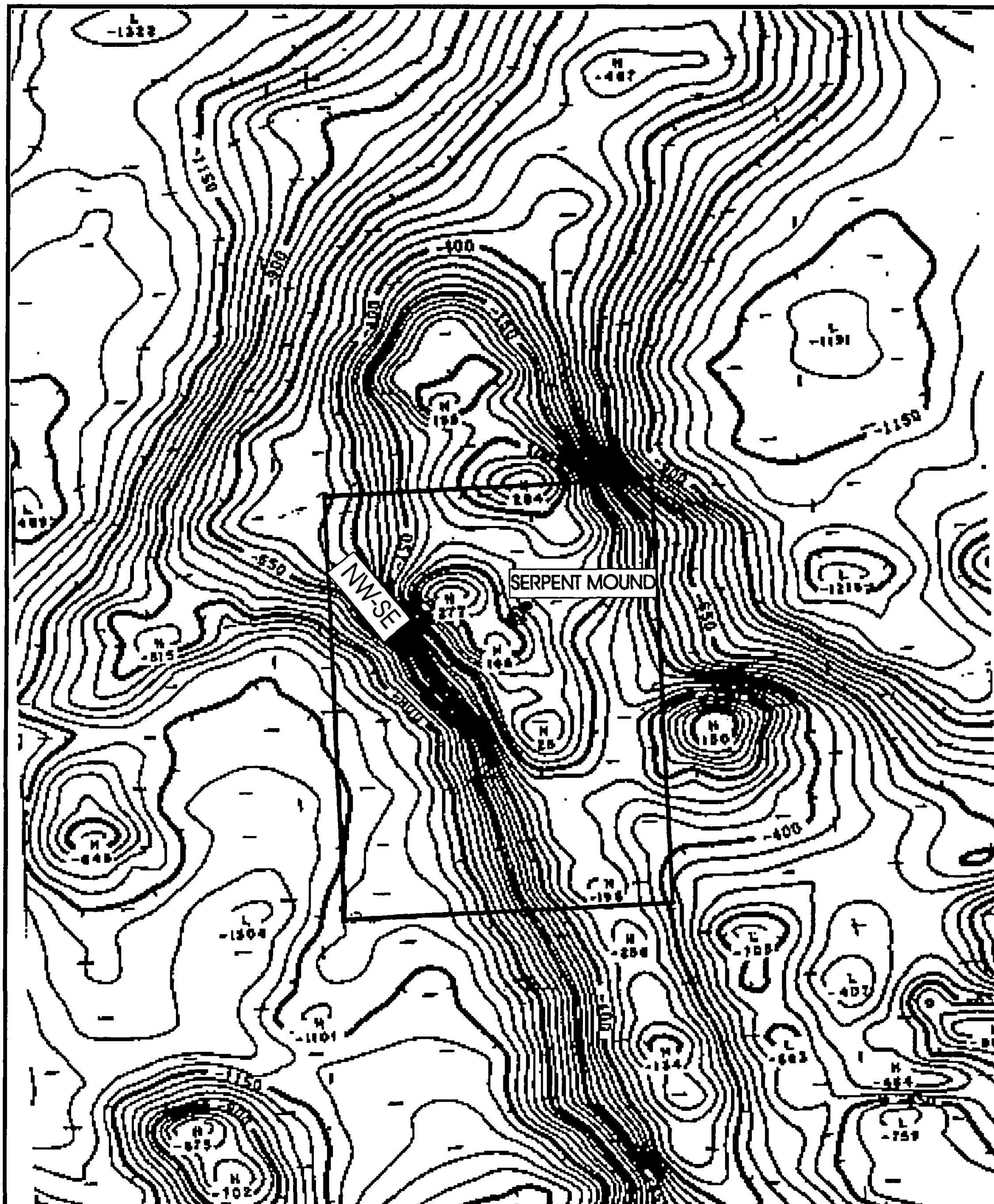

Figure 7.9- Part of the map of Ohio residual magnetic field intensity

Sappenfield (1950) conducted a ground magnetic survey of the Serpent Mound Structure using a Schmidt type vertical magnetometer, with an average of one station every 1.2 square miles over the structure. Sappenfield's map (Figure 7-10) shows an anomaly with an axis striking N25W, through the middle of the structure. The magnetic high, according to his map, is offset from the centre, and is located near the outer, southern boundary of the disturbance. Sappenfield interpreted the anomaly as associated with a basic igneous intrusion in the basement, supporting the endogenic thesis of the origin of the feature.

Memmi and Weaver (1992, personal communication) conducted a magnetic traverse across the centre of the Serpent Mound structure, along Parker Ridge road (Figure 7-11), coincident with the seismic survey line BV-1-92. The figure shows a long wavelength anomaly with superimposed short wavelength features. The short wavelength features undoubtedly correspond to cultural features along the road. The long wavelength anomaly has a maximum that corresponds with the position of the central uplift of the structure.

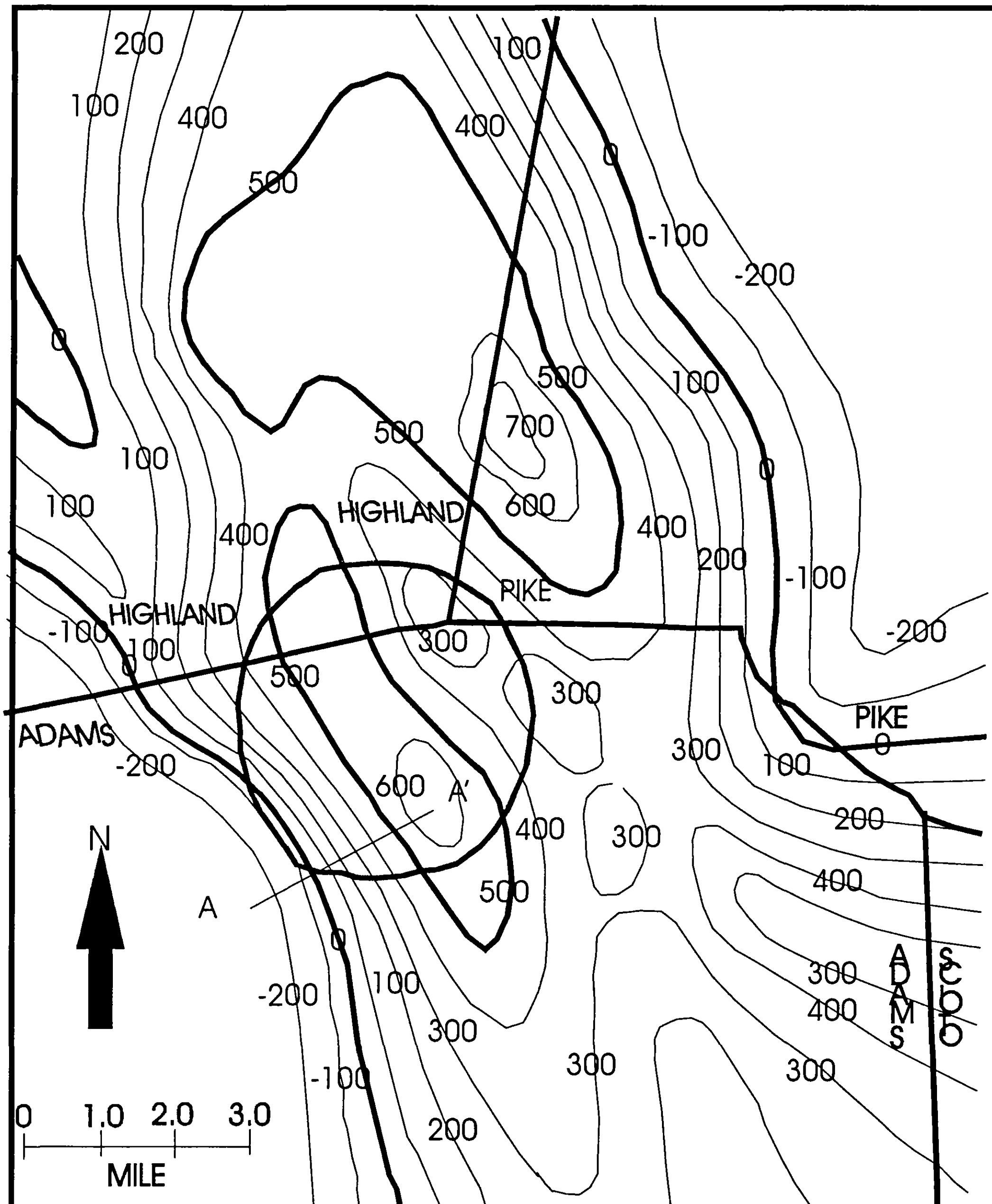

Figure 7.10- Vertical intensity magnetic map (n.T) of the Serpent Mound area (after Sappenfield , 1951)

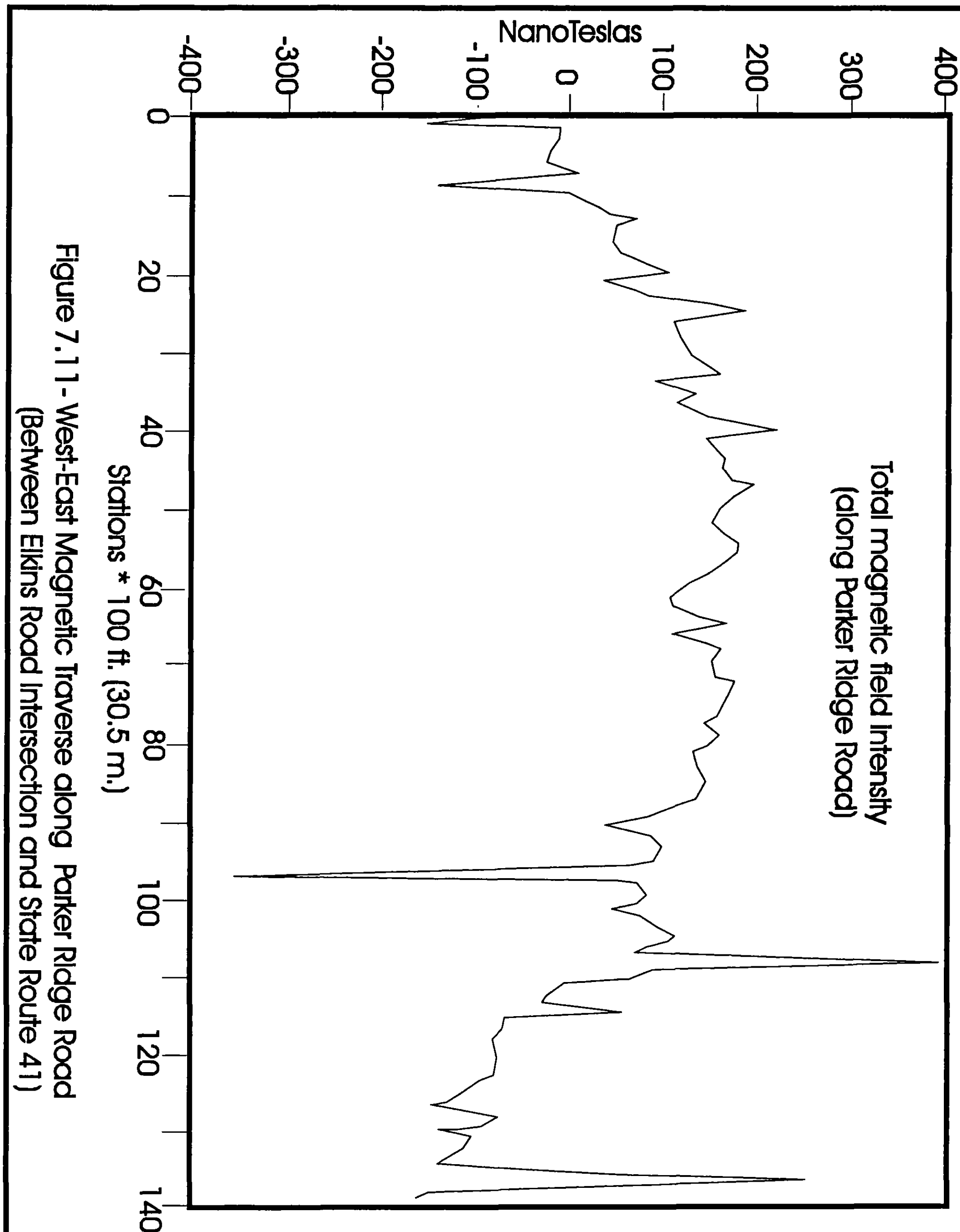

Figure 7.11- West-East traverse along Parker Ridge Road

(Between Horner Chapel Road intersection and State Route 41)

7.5- Field Work

7.5.1- General Procedure

During the survey, a number of simple objects, for example belt buckles, metal eyeglass frames, clipboards, watches, pens, etc. produce strong local magnetic fields and can disrupt readings if they are too close to the instrument. The best rule is for the person operating the instrument or the sensor to divest themselves of all possible magnetic materials. In addition, common cultural objects such as cars, fences, metal poles, a.c. power lines, metal pipes, buildings, beams, and other such magnetic objects should be avoided. In many cases we found it necessary to move 20 m or more from such objects. This was worth the effort for the improvement in the quality of the data. The sensor of the proton-precession magnetometer was on a pole 8 ft (2.4 m) above the ground. This was to ensure that the effects of local magnetic noise due to cultural features are attenuated. Substantial magnetic gradients and time varying fields can degrade proton-precession magnetometer readings. The proton-precession magnetometer then produces erratic readings with small changes in position. The magnetometer we used alerted the user of this circumstance by producing an alarm if such high gradients were present. Normally we would take about three readings at the same position to check for the gradient changes, and reduce the effect of the gradient by averaging the results.

In general the requirements for ground-based magnetic surveying are not as demanding as those requirements related to gravity exploration. Nevertheless, a number of procedures must be followed to compile useful data with accuracy comparable to the instrument used. Two EG&G 856 recording proton precession magnetometers were used to conduct the magnetic survey over the disturbance during a period of 5 weeks in September and October, 1996. A magnetic base station was established in the middle of a large field, away from cultural objects. We placed one magnetometer at the base station in a continuously auto-recording mode, sampling the geomagnetic field every two minutes. We started the magnetometer at the beginning of a magnetic survey day, returning to the base station at the end of the day. We calculated an average value from all of the data gathered by the recording magnetometer for the base station. This was used as the base value of the geomagnetic field, and corrections for diurnal variation were adjusted so the base station field estimate was this average value. Diurnal variations in the geomagnetic field were calculated by subtracting this average value from each day's base station record. Corrections to the roving magnetometer readings consisted of subtracting the measured diurnal variation curve from the results of the roving magnetometer. The typical maximum diurnal variation during the survey was on the order of 20 to 30 nT during a day's work.

7.5.2- Survey Lines

Much of the survey was through difficult topography often covered with impenetrable vegetation. In total, thirty-one (31) magnetic lines were surveyed. At the beginning of the work we were looking for short wavelength anomaly that may be associated with zones of mineralization in the central area of the structure. We wished to determine if any of the short wavelength anomalies that occurred on the Memmi survey were of natural origin. Thus, our initial magnetic traverses started from the central uplift area of the structure and extended in different radial directions. The locations of magnetic stations along these lines were surveyed using optical theodolite, with two control stations established by GPS techniques. The initial lines had very short spacing (10 m) between measurement stations. Along the short spacing traverses, three readings were taken and each station, but only one was stored. We found there are no naturally occurring short wavelength anomalies. Therefore, we extended the survey area beyond the disturbance to map the extent of the anomaly using much larger spacing between stations which varied from 50 m to 160 m (0.1 mile using the odometer on the jeep). On several traverses we had to go through very difficult terrain, such as the High Knob area at the northern edge of the structure. The outermost stations were established at road intersections and easily identified topographic features. On all traverses with station spacing larger than 10 m, between three and five readings were taking at each station. Thus, an area of approximately 625 square km was surveyed in Adams, Highland, and Pike counties of Ohio. The survey is bounded by longitude 83° 15' W on the east and 83° 37' 15" W on the west, latitude 38° 52' 30" N on the south and 39° 07' 30" N on the north. The observation points were plotted on six USGS (7.5 minute) topographic maps, at a scale of 1:24,000. The magnetic stations were digitised in UTM (Universal Transverse Mercator) co-ordinates and are plotted in Figure (7.12) using the GMT (Generic Mapping Tool) package of Weissel and Smith (1995). In total, nearly 1800 stations were occupied with most of the data collected in an area of 11 km (NS) by 9 km (EW) centred on the structure (Figure 7.12).

At each station readings were visually assessed on the meter and stored in the magnetometer memory along with the line number, station number, time, and the Julian day. Multiple readings on lines with station spacing of 50 m or greater were taken and averaged over area of about 10 m^2 to monitor and compensate for any strong local magnetic gradients.

7.6- Magnetic Data Reduction

7.6.1- Noise Correction and Editing

First, the magnetic data were edited to remove any stations at which the magnetometer indicated a high magnetic gradient. Cultural features such as fence lines and power cables were noted and these stations were either not recorded or were removed from the data. Three strong monopole anomalies were recorded and are doubtless associated with iron casing from two oil exploration wells (Parker well, Kaiser well) and DGS3274. The exact location of the Parker well, which was drilled in the 1920's, was not known to the Ohio Geology Survey and they used our results for a more accurate position. These anomalies were also edited from the data. At stations where more than one reading was taken, an average reading was calculated for each station.

7.6.2-Diurnal Correction

The correction for diurnal drift is analogous to the tidal drift correction for gravity data, as it must be measured. One of the magnetometers sampled the earth's magnetic field at a base station every two minutes. This continuously monitors the diurnal variation of the earth's magnetic field. At the end of each field day, diurnal data were downloaded from the base station's magnetometer to our field PC computer.

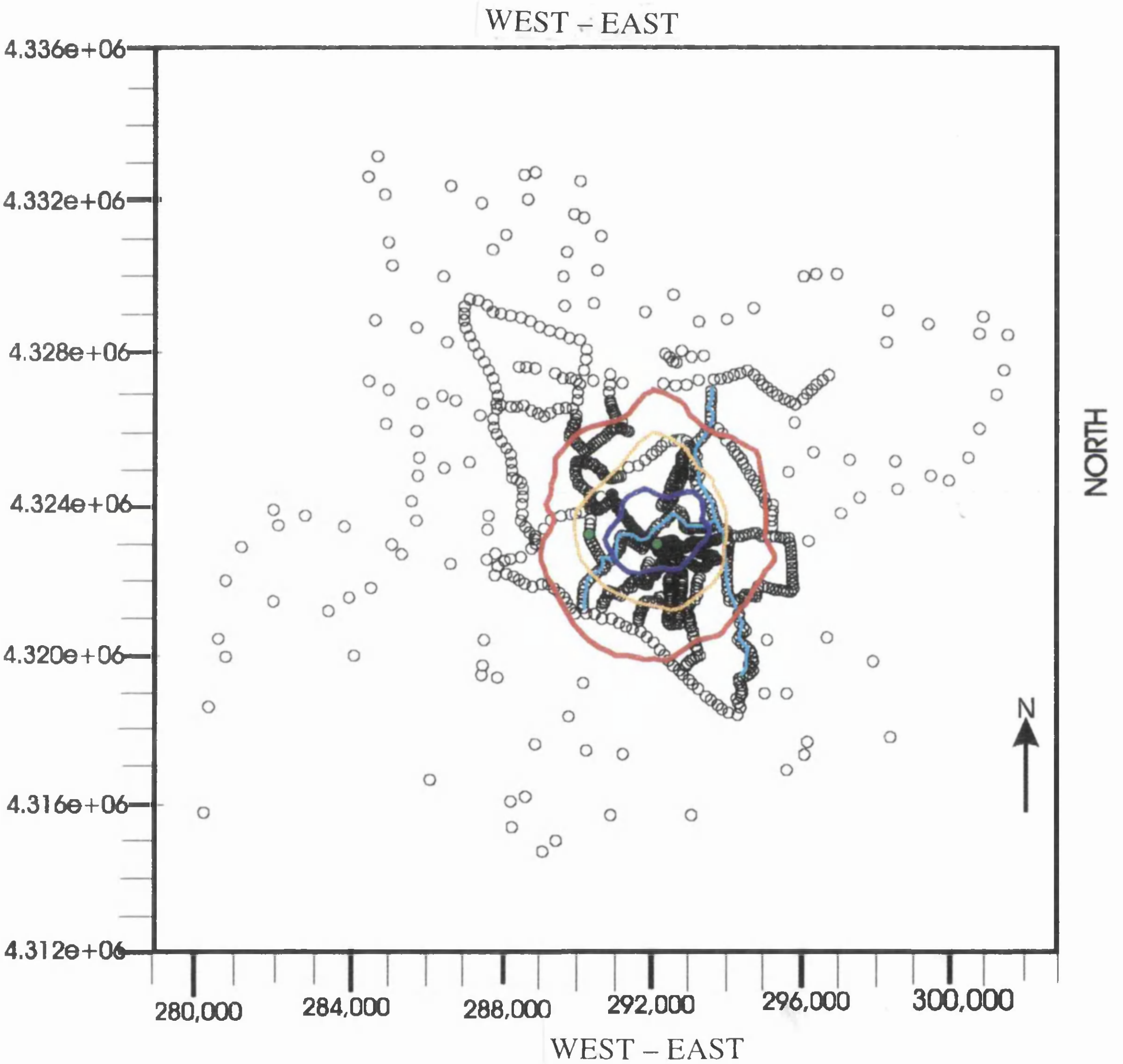

Figure 7.12- Magnetic survey stations of the Serpent Mound area

An average value of the magnetic field at the base station was calculated from all of the base data. The complete magnetic data set of diurnal curves was drawn, and the field data corrected for the diurnal variations. The average variation of the diurnal correction per day was about 20 nT.

7.6.3- Elevation Corrections

Magnetic field data normally are not corrected for elevation differences between recording sites. We have mentioned earlier that the vertical gradient of the vertical magnetic field at 39° N latitude is ≅ 0.024 nT/m, for a change in elevation of 100 m (330 ft), the 50,000 nT field changes by 2 to 3 nT. When the anomalous field changes by hundreds of nanoteslas, this variation is considered small enough to ignore.

7.6.4- Correcting for Horizontal Position (Geomagnetic Corrections)

To examine the change in magnetic field intensity with horizontal position, we once again resort to the dipole equation and take the derivative of the vertical field with respect to the horizontal position θ. Thus,

$$\frac{dZ_E}{d\theta} = \frac{1}{r} \frac{-2M\sin\theta}{r^3} = -2\frac{H_E}{r} \qquad \text{(Equation 7-18)}$$

For appropriate values for 42° N latitude ($r = 6.37 \times 10^6$ m and $H_E = 18{,}200$ nT)
We obtain,

$$\frac{dZ_E}{d\theta} = 0.0057 \text{ nT/m, about 6 nT/Km.}$$

This gradient appears sufficiently large over the survey area to warrant a correction. The best solution to corrections for horizontal position is to calculate the IGRF for the time and area of the survey and subtract it from the data. The IGRF field for this correction was calculated using the USGS Potential-Field geophysical software version 2.0 (Cordell, L., Phillips, J., and Godson, R., 1992). The IGRF models are regularly updated to account for the secular variations. The two programs used are

IGRFPT (component of the geomagnetic reference field (IGRF) at a specified location and date), and IGRFGRID International Geomagnetic Reference Field.

The IGRF was calculated on a constant elevation surface grid. The total magnetic intensity values at four corners of a rectangle bounding the study area were obtained over a computer link to the USGS source for the four specified latitude and longitude co-ordinates. We designate the total field intensity at the south-eastern corner of the study area as the reference value. The north-south gradient between latitude 38.875° N and latitude 39.25° N is approximately 6 nT/km. The east-west gradient between longitude 83.25° W and longitude 83.625° W is approximately1 nT/km. One common used method of applying the main field correction is to linearly interpolate the computed values of the main field at the corners of the survey throughout the survey region. For example, if we have a total field value F = 54700 nT at a site located 10 km north and 15 km west of the corner point. The correction should be

$$F_E = 54700 + 10(6) + 15(1) = 54775 \quad nT$$

Then, if we subtract this value from the total field reading, we have the total field anomaly.

7.7- Modelling and Interpretation

7.7.1- Magnetic Anomaly

' There are more factors that control the morphology of a magnetic anomaly than what control the shape of a gravity anomaly. Magnetic anomalies are a function of the subsurface distribution magnetic susceptibilities, permanent magnetisation, and the orientation of the Earth's main magnetic field. That is the magnetic anomalies over the same susceptibility distribution will be different at different locations. Additionally, the magnetic anomaly over two dimensional body depends on its orientation (east-west or north-south).

After the regional field was subtracted, the digitised data were grided at 700-meter grid using the GMT (The Generic Mapping Tools, Version 3) software (Wessel and Smith, 1995).

A median filter was applied, and the smoothed data were contoured by compute to produce the magnetic anomaly counter map (Figure 7-13).

The magnetic survey of the Serpent Mound Structure shows a well-defined magnetic anomaly indicated by its trend, width, and high amplitude. The final corrected magnetic anomaly map has a contour interval of 50 nT. It shows a single peaked anomaly through the centre of the structure, with an axis approximately N30W. The highest amplitude of the anomaly is ≅ 1000 nT. The highest amplitude of the anomaly is at the northwestern edge of the structure. This is a significant revision of the Sappenfield (1950) result which mapped the largest part of the anomaly at the southeastern edge of the structure. The anomaly falls off sharply to the west. It shows a local low east of the central uplift. Figure (7.14) is an east west cross section of the anomaly. Figure 7.15 is a north-south cross section.

No small amount of basement relief can produce such an anomaly with an amplitude of 1000 nT. There is no evidence of magmatic intrusion in the study area or in the two deep cores examined by colleagues in the Ohio Geological Survey. No feature was observed on the seismic sections that may be interpreted as an igneous intrusive.

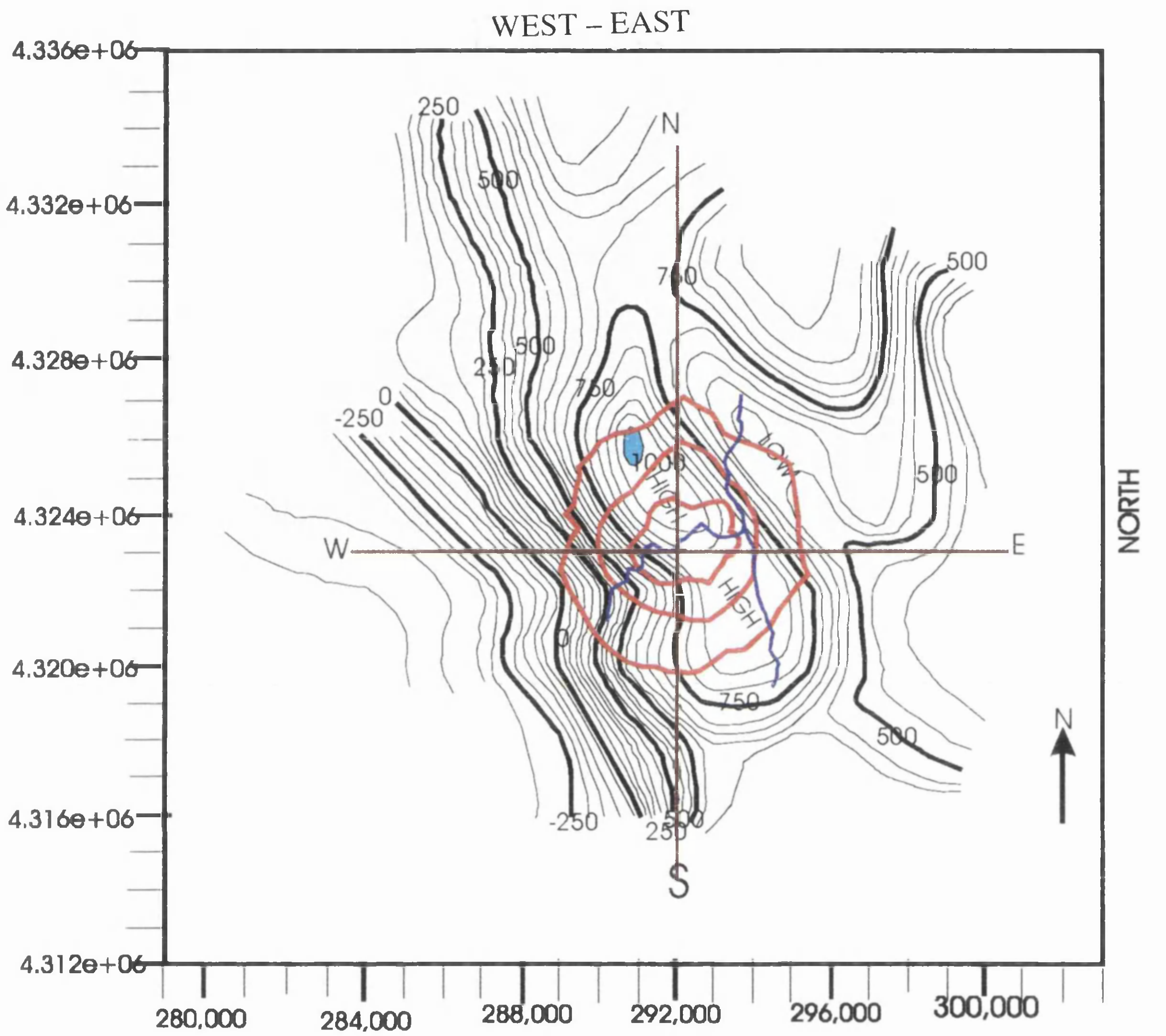

Figure 7.13- Total field magnetic anomaly map of the Serpent Mound Structure (CI 50 nT)

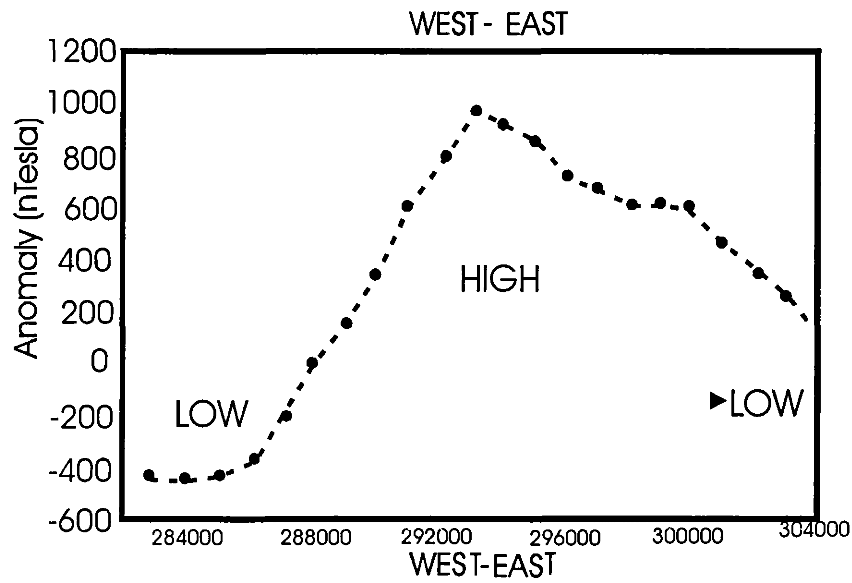

Figure 7.14-W-E Cross Section of the Magnetic Anomaly Map

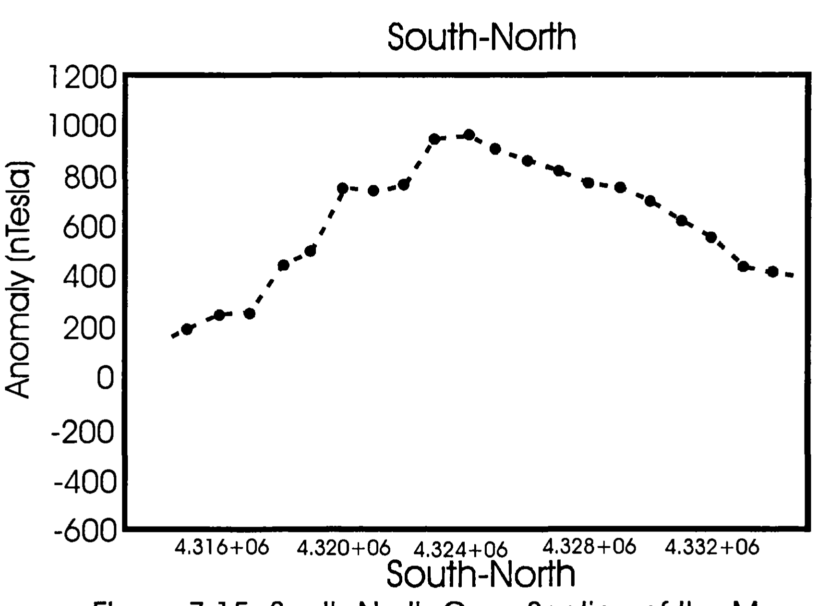

Figure 7.15- South-North Cross Section of the Magnetic Anomaly Map

The main features of the regional anomaly can be explained by a broad zone with high magnetisation in the crystalline rocks beneath the sediments. This may be associated with the Grenville Front. Thus, the regional magnetic anomaly at the Serpent Mound Structure seems to be controlled by the lithology of the basement rather than by its topography. Changes in magnetisation of the basement rocks about 2 km deep may result in anomalies with an amplitude of up to several thousand nT at the surface. At the same depth, structural relief on the basement surface as much as 200 m seldom produces anomalies larger than 50 nT. The impact and subsequent tectonic activities may produce some chemical alteration and increased the susceptibility of the target rocks and the basement underneath compared to the surrounding rocks.

7.7.2- Magnetic Modelling

The association of the magnetic anomaly with the Serpent Mound Structure presents a problem. The anomaly was interpreted by Sappenfield (1951) to be caused by an igneous body directly beneath the structure. We know from other evidence the structure is an impact. Therefore the local anomaly may be somehow related to the impact. We use the BGS software to explore a possible model.

The Serpent Mound structure is located on a major N-S trending anomaly that extends far beyond the structure. This shows that the basement in the area is magnetic. Therefore it is possible that a volume of rock directly beneath the structure was magnetised by the passage of shock waves caused by the impact, or mineralization in impact induced fractures. This idea is illustrated in Figure 7-16, and 7-17. Figure 7-16 shows the basement anomaly before the impact, produced by a magnetic basement (volume 1) with a magnetic contrast of .05 Amp/metre with bodies 3 and 4. The impact needs to add a remanent magnetisation of 2.0 Amp/metre to volume 2 shown in Figure 7-17 to generate the rest of the anomaly, showing what is observed directly on the structure. We do not propose to exhaustively test the model this as it is at present impossible to create an unambiguous model. This model only illustrates the idea of how a magnetic anomaly can be generated by an impact.

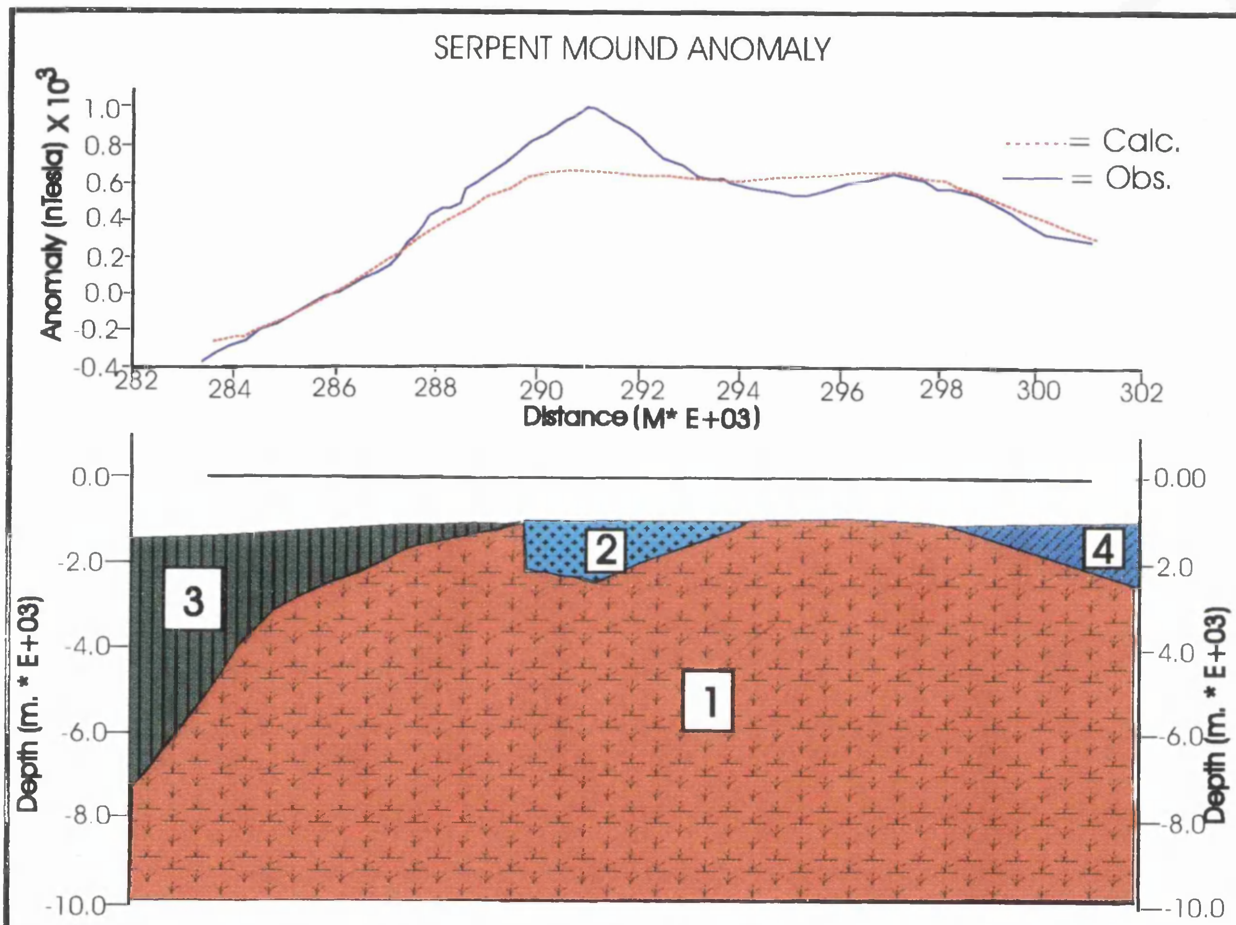

Figure 7.16- Modelled magnetic anomaly prior to impact. Basement units of different magnetic properties are shown. In this model units 1 and 2 have the same properties. Compare with Figure 7.17.

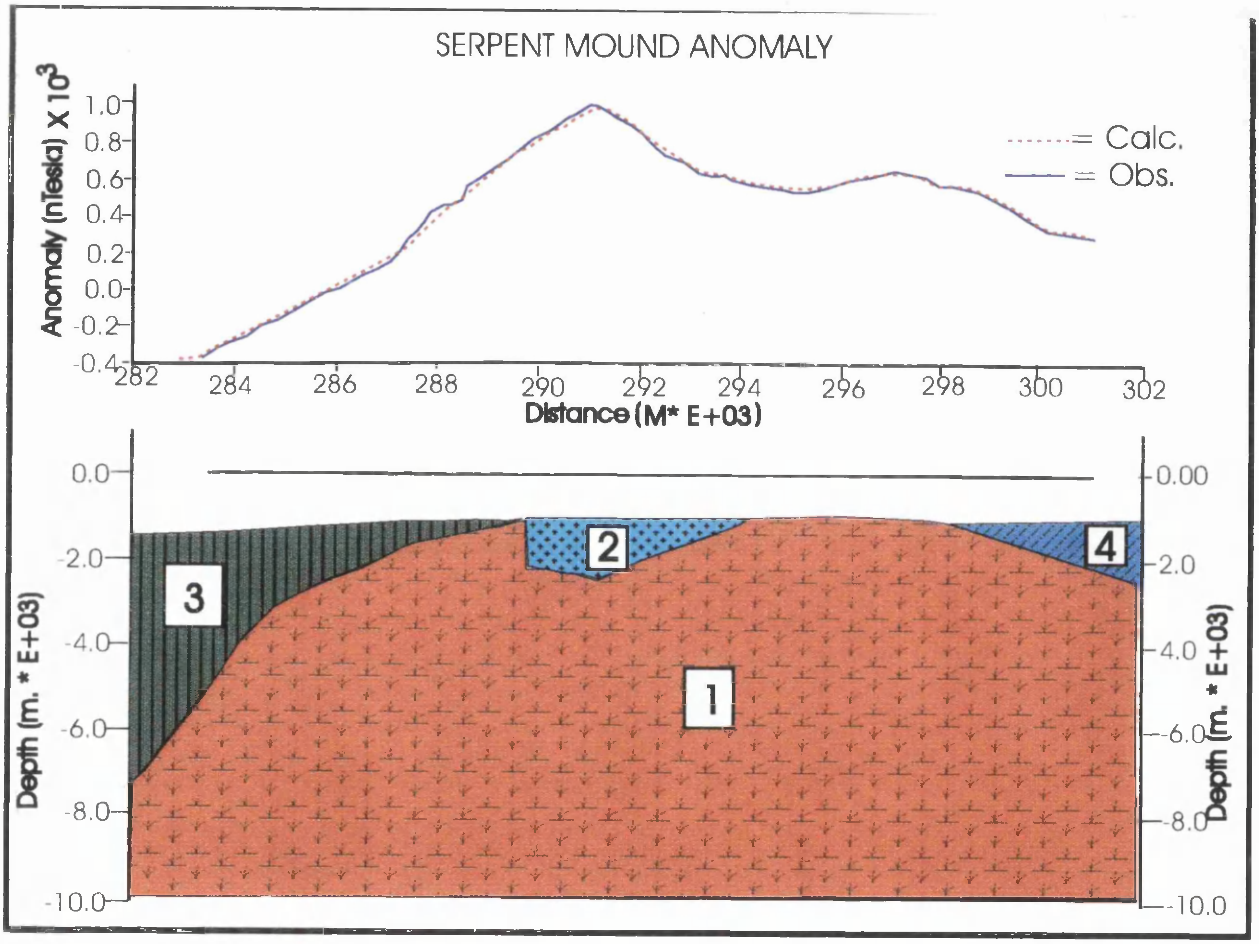

Figure 7.17- Modelled magnetic anomaly after impact. Units 1,3 and 4 are the same as in Figure 7.16. Unit 2 is the location of proposed remagnetisation due to impact.

CHAPTER 8 MINERALOGICAL AND PETROLOGICAL STUDIES

8.1-Introduction

Ohio Division of Geological Survey (DGS) core DGS 3274 was drilled in the central uplift area of the structure to a depth of 2,962 ft (903 m). DGS 3275 was drilled in the transition area of the structure to a depth of 2065 ft (629 m) (Figure 8.1). Samples from these deep cores were studied for their petrographic and geochemical characteristics. The thickness of the lithostratigraphic interval from the undeformed Silurian Peebles formation to Knox Dolomite surrounding the Serpent Mound structure is expected to be approximately 2,100 ft (640 m) (Figure 8.2). As a part of this study our colleagues at the Ohio Department of Natural Resources (ODNR) examined in detail these two cores and another three cores (DGS 2880, 2881, 2882) within the Serpent Mound disturbance. During the work, we visited the core depository in Columbus, Ohio. The two cores show abundant evidence of macroscopic deformation (shatter cones and breccias) to their respective bottoms. The following are brief descriptions of the two deep cores to be reported in our joint publication (Baranoski et al, in preparation).

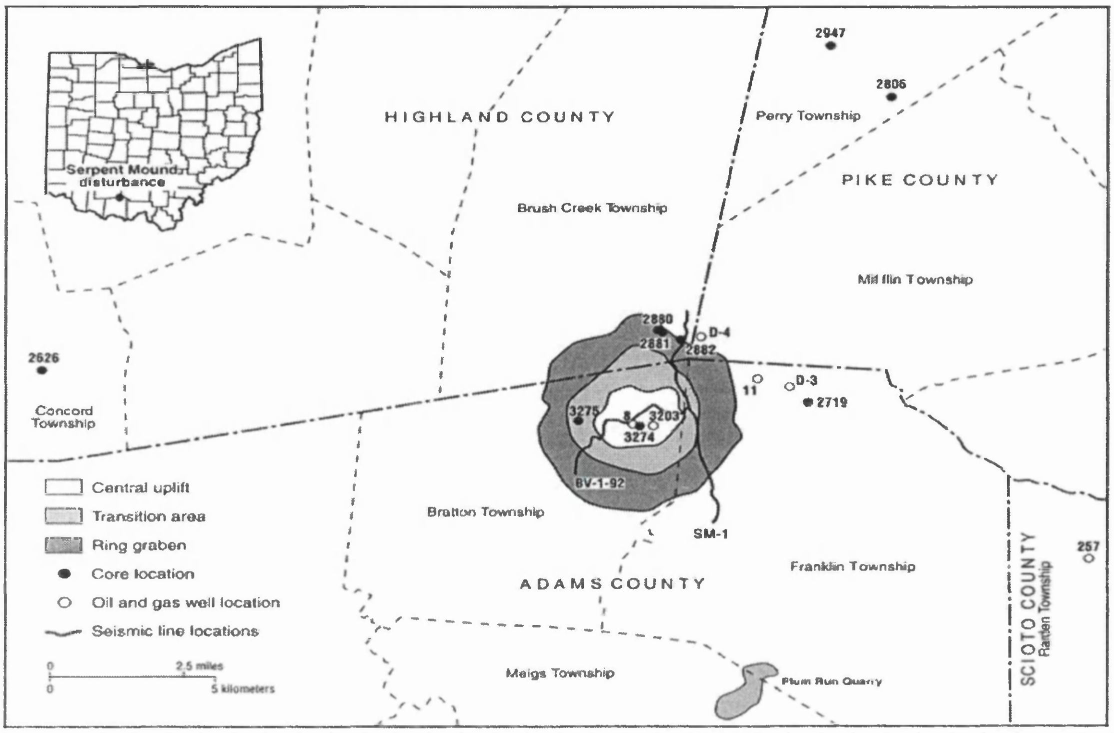

Figure 8.1 Generalised map of the Serpent Mound Structure showing the three structural zones and core locations

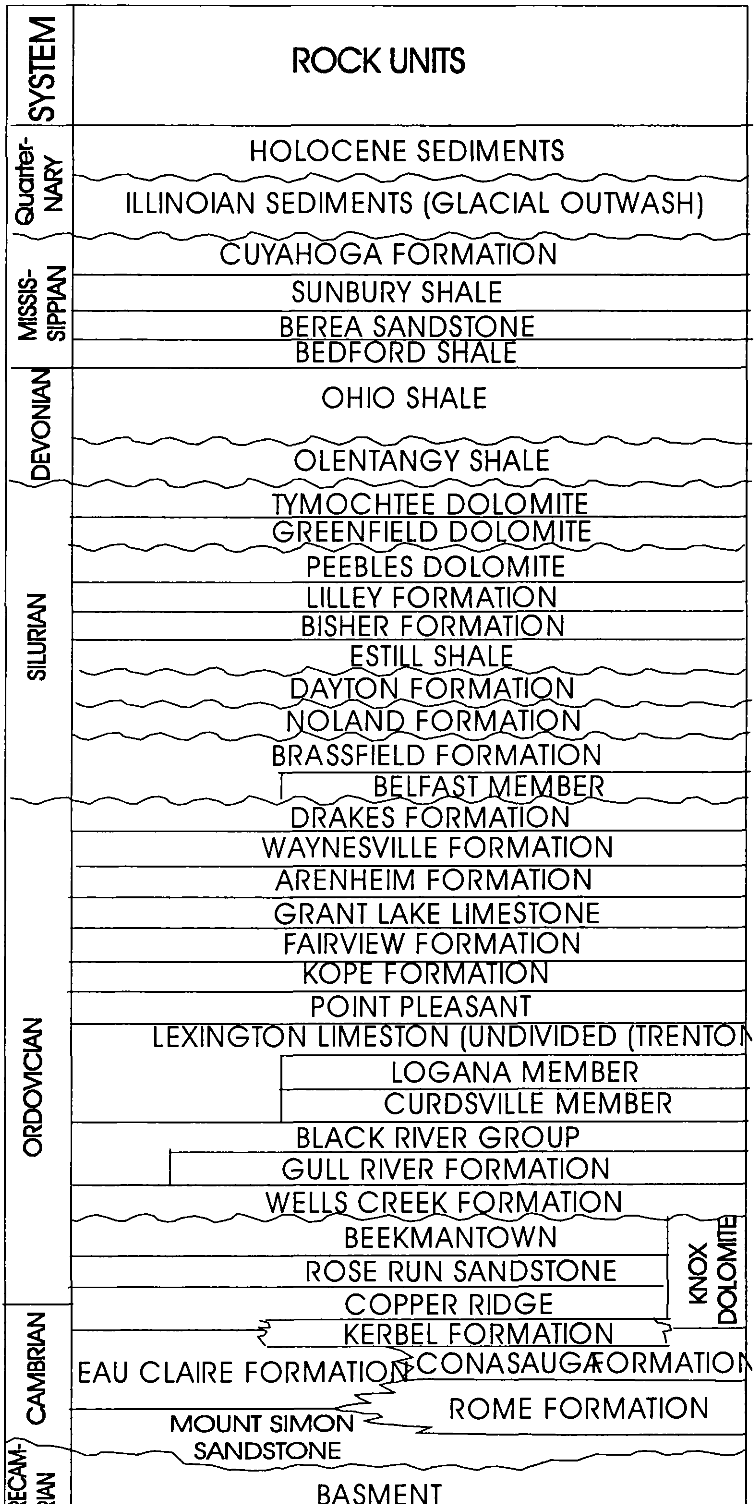

Figure 8.2- Normal Ohio Stratigraphic units in the Vicinity of The Serpent Mound Structure

8.2- Petrogaphical descriptions of Cores

8.2.1-) Core DGS 3274

The bedrock geology (Reidel, 1975) at the drill site location for DGS 3274 indicates undifferentiated Ordovician with the central uplift area. Core 3274 (Figure 8.1) was taken from 2,962 ft (903 m) of fractured, faulted, brecciated, and undeformed to severely deformed upper Cambrian to upper Ordovician limestones, shales, dolomites, and standstones. The middle and lower Silurian and upper Devonian units observed are represented as clasts within faulted, mixed-lithic breccia zones. Discrete fault blocks with discrete strata from these stratigraphically younger units were not observed in the core. Displaced and repeated stratigraphic units along normal and reverse faults occur throughout the core.

The overall core can be generalised into four faulted intervals, separated by major fault contacts or brecciated zones (Figure 8.3). The upper core interval, from 11 to 1417 ft (3.4 to 431.9 m) consists of moderately to highly deformed, folded, faulted, and brecciated Point Pleasant, Kope, and Fairview Formations, and Grant Lake Limestone. Bedding dips in this interval ranges from 0°° to 90°° with some overturned beds. The Grant Lake Limestone occurs as a series of fault blocks between 11 and 225.3 ft (3.4 to 68.7 m) and as isolated blocks within the breccias between 1069.5 to 1126.5 ft (326.0 to 343.4 m). Bedding dips in the fault blocks of the first 214.7 ft (65.4 m) of DGS 3274 range from 80°° to 90°°with some overturned beds. Folded bedding, fractures, bedding plan, normal, and reverse faults, slickenlines, shatter cones, and breccias are common throughout this interval. Small fault planes dip in the range from 25° to 90°, oblique to bedding dip, and generally have very short throws (0.05 to 0.1 ft, 0.015 to 0.030 m). Direction of movement and/or throw along faults may be indeterminate because of the poorly developed slickenlines, or lack of offset information. The dip of fracture planes ranges from 20°° to 70°°. Fractures may be filled with breccia or mineralised with calcite or sulphides. Shatter cones, en echelon tension gashes, and anastomosing fractures are rare. Slickenlines occur along bedding planes and faults. Some fault surfaces have slickenlines with multiple direction of movement. Stylolite seams commonly occur parallel or subparallel to bedding planes. Stylolite seams at oblique angles to bedding are rare. Breccias less than 1 to 57 ft (0.30 to 17.4

m) thick occur in this interval, some zones near high angle faults. The core interval from 1,417 to 1,696.5 ft (431.9 to 517.1 m) consists of faulted, moderately to severely brecciated strata of upper and middle Ordovician, middle and lower Silurian and upper Devonian age. Discrete and complete lithostratigraphic unit are absent from this interval. Rocks of the Curdsville member of the Lexington Limestone (Trenton limestone), Kope, and Fairview Formations, Grant Lake Limestone, and Arnheim Formations were observed as discrete fault blocks, which were undeformed to highly deformed. The Grant Lake Limestone occurs as a series of fault blocks from 1,531 to 1696.5 ft (466.6 to 517.1 m). Breccias dominate the entire interval, separating fault blocks. Folded bedding, overturned strata, and bedding dips ranging from 10°°to 85°° are common throughout the entire interval. Bedding plane, normal, reverse faults, fractures, slickenlines, shatter cones, and brecciation are common. Dips of normal and reverse faults range from 60°° to 70°°.

The interval from 1696.5 to 2851 ft (517.1 to 869.0 m) consists of undeformed to mildly deformed Upper Ordovician Kope and Point Pleasant Formations undifferentiated, Lexington Limestone undifferentiated (with Logana and Curdsville members), Black River Group (with Carntown, Gull River limestone, and lower argillaceous units), and Well Creek Formation. Bedding dips range from 0°° to 50°°. Bedding dip generally diminishes (flattens) with depth below 2150 ft to 2851 ft (655.3 to 869 m), where another major fault and brecciated interval occurs. Folded bedding and bedding plane are rare. Fractures, normal, and reverse faults, shatter cones, and breccias are common. Shatter cones are abundant with apices pointing upward. The lower interval of the core from 2851 to 2962 ft (869 to 902.8 m) consists of moderately to severely deformed, folded, faulted, and brecciated Black River Group, Well Creek Formation, and Knox Dolomite. The Carntown, Gull River, and Lower Unit of the Black River were also identified. TheRose Run Sandstone and Copper Ridge Dolomite were tentatively identified in the Knox Dolomite. The upper contact of the Knox Dolomite is not present in the faulted blocks in this core. The lower contact with the underlying Kerbel/Conasauga was not cored. Breccias dominate the entire interval and separate major fault blocks. Shatter cones are abundant with apices pointing upward.

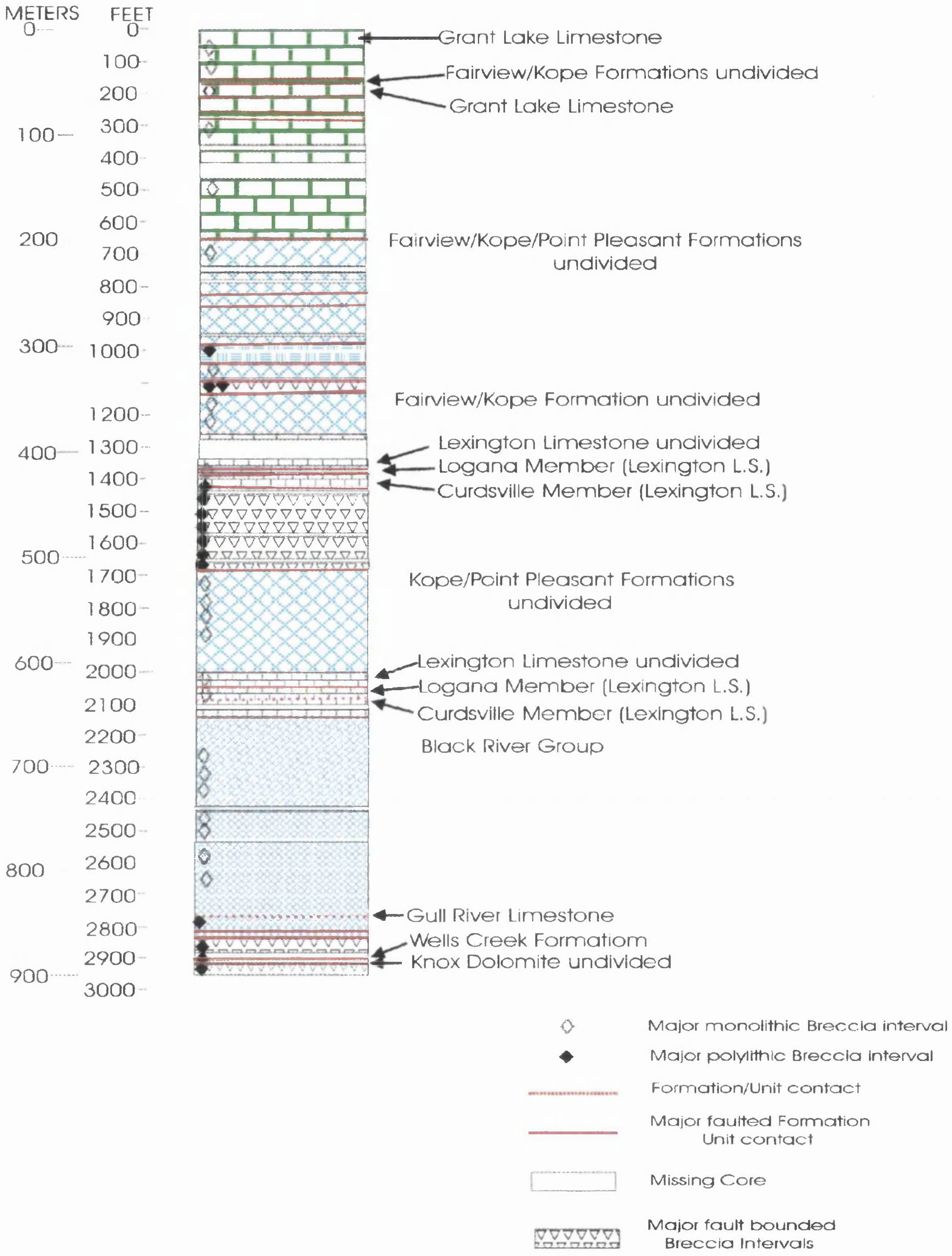

Figure 8.3- DGS Core 3274 (SM 79-1)

Ground elevation 960 ft (293 m)

8.2.2- DGS 3275

The bedrock geology (Reidel, 1975) indicates Silurian age, undifferentiated Tymochtee Formation, Greenfield Dolomite, and Peebles Dolomite in the intermediate transition area at the drill site location for DGS 3275 (Figure 8.1). Reidel's surface map (1975) of the Serpent Mound disturbance indicates three faults within 300 ft (90 m) of the drill site. An extensively brecciated outcrop at an abandoned quarry in possible Silurian age dolomite is located 300 ft (91.4 m) east of the drill site. DGS 3275 (Figure 8.1) has not been examined petrographically but has been logged and described megascopically. DGS 3275 penetrates 2065 ft (629 m) of fractured, faulted, brecciated and undeformed to severely deformed rock strata. The rock ranges in age from Upper Cambrian to Middle Silurian. The core can be divided into three structural intervals separated by major fault contacts. An upper interval from 17 to 415 ft (5.2 to 126.5 m), consists of moderately deformed and brecciated rocks. A middle interval from 415 to 725 ft (126.5 to 221.0 m), consists of moderately to severely deformed, faulted, and brecciated rocks. A lower interval from 725 to 2,065 ft (221.0 to 629.4 m) which is mildly deformed to undeformed, and mildly faulted and brecciated.

Folded strata are rare in the core, and bedding dip diminishes below 725 ft (221 m). Fractures, faulting, brecciated zones, and shatter cones were observed throughout the core. The top interval from 17 to 415 ft (5.2 to 126.5 m) consists of moderately deformed, faulted, and brecciated rocks. The Drakes Formation, Noland and Brassfield Formations, Dayton Limestone, Estill Shale, Bisher and Lilley Formations, and Peebles Dolomite occur in this interval. Minor small-scale faults, fractures, and breccias occur throughout this interval. The middle interval from 415 to 725 ft (126.5 to 221.0 m) contains moderately to severely deformed, faulted, and brecciated rocks. Normal and reverse faults occur throughout this interval. The lower interval from 725 to 2065 ft (221.0 to 629.4 m) is mildly deformed to undeformed. This interval includes Knox Dolomite (Rose Run sandstone and Copper Ridge dolomite), Wells Creek Formation, Black River Group (Carntown unit, Gull River limestone, and lower argillaceous unit), Lexington Limeston (Logana and Curdsville members), and undifferentiated Point Pleasant and Kope Formations. The lower contact of the Knox Dolomite with the underlying Kerbel was not cored.

8.2.3- DGS 2626 and DGS 2719

DGS 2626 and DGS 2719 (Figure 8.1) located near, but outside the structure. These cores used for correlation and thickness determinations of lithostratigraphic units outside the disturbed area. Structural deformation was not observed in either core.

8.3- Shocked Criteria

8.3.1- Macroscopic Deformation Features

8.3.1.1. Breccias

Breccias occur extensively throughout the two cores within the structure the DGS 3274 in the central uplift area and DGS 3275 in the transitional inner graben. Brecciated rocks were observed filling open fractures along faults with coarse-grained, angular to sub-angular clasts held together by fine-grained matrix and cement. Two major types of breccias, monolithic and mixed-lithic, were observed. Monolithic breccias are derived from the adjacent lithostratigraphic unit. Mixed-lithic breccias contain clasts are derived from the adjacent and younger lithostratigraphic units (Figure 8.4). These younger clasts were informally termed 'exotic' because they were, structurally, lower than expected. Neither clasts of older sediments, or Precambrian basement, were observed within these intervals.

8.3.1.2. Shatter cones

Shatter cones were observed throughout DGS 3274 and to lesser extent in DGS 3275. Many of the shatter cones observed appeared fresh and un-weathered. The shatter cones occur in large blocks of carbonate rocks and shale. The observed shatter cones range in height from a few centimetres to about 17 centimetres.

8.3.2- Microscopic Deformation Features

A petrographic study was carried out on some rock samples taken from the DGS 3274 core drilled in the central uplift area of the structure. We were looking for evidence of microscopic shock metamorphism in the form of the presence of highly pressure polymorphs such as the mineral coesite, or the presence of microscopic features such as the plane deformation features (PDFs) in the rock forming minerals. Initially five samples selected from the core DGS 3274 (SM1-05, SM1-22, SM1-25, SM1-27, and SM1-31) brought back to Glasgow University. The samples were thin sectioned for XRD and structural fabric analysis. The XRD results show that the samples are predominantly carbonate-clast breccias (Figure 8.5 and Figure 8.6). These samples also include shale, claystone, sandstone, siltstone, and chert. One sample (SM1-27) consists manly of quartz (Figure 8.7).

Thin sections were examined by optical microscopy (with the help of Dr. A. Hall) for mineral identification and for structural fabrics. Sample SM1-27 shows very compacte quartz grains.

Our Ohio colleagues studied thin sections of 21 samples from core DGS 3274 (Carlton, R.W.; et al. 1998). Most of the breccias examined consisted predominantly of limestone clasts with minor amounts of shale, claystone, sandstone, siltstone, chert, and possible altered impact-melt glass. Three samples of the breccias examined contain more shale or claystone fragments than the carbonate rock clasts (SM1-7,SM1-13, and SM1-4). Two samples (SM1-27 and SM1-28B), from 2,857 ft (870.8 m), were identified as Cambrian Rose Run Sandstone.

A 15-cm section of polymict breccia (SM1-36, Figure 8.4) from a depth of 1437 ft (438 m) was taken for grain-mount studies. The specimen was broken into fragments and placed in HCL solution (10% by volume) for several days to remove the carbonate component of the breccia. The coarse shale and siltstone clasts were removed.

The remainder was sieved and the 37 to 350 μm grain-size fraction used to make three thin sections.

PDFs in quartz were found in seven of the breccias examined. These are SM1-9 (1122 ft, 342 m), SM1-16 (1414 ft, 431 m), SM1-1A (1434 ft, 437 m), SM1-4 (1437 ft, 438 m), SM1-36a,b,c (1437 ft, 438 m), SM1-2 (1624 ft, 495 m), and SM1-28A (2851 ft, 869 m). Two to three intersecting sets of PDFs are abundant (Figure 8.8). The results of analysing the orientations of the crystallographic planes of the PDFs show clear maximum at the shock characteristic orientations of $\{10\bar{1}3\}$ and $\{10\bar{1}2\}$ (Figure 8.9). The distribution of the PDFs suggests that the shock levels experienced by these rocks were relatively high, greater than 10 Gpa (Carlton, R.W.; et al, 1998).

Six of 18 breccias (Figure 8. 4), SM1-33A, SM1-33B, SM1-23, SM1-25, SM1-28A, and SM1-29A contain an estimated 1 to 3% by volume of black aphanitic clasts. These clasts range in length from 1 mm to more than 1 cm (Figure 8.10). These may represent fragments of altered impact-melt rock that have been replaced by calcite and pyrite (Carlton, R.W.; et al, 1998).

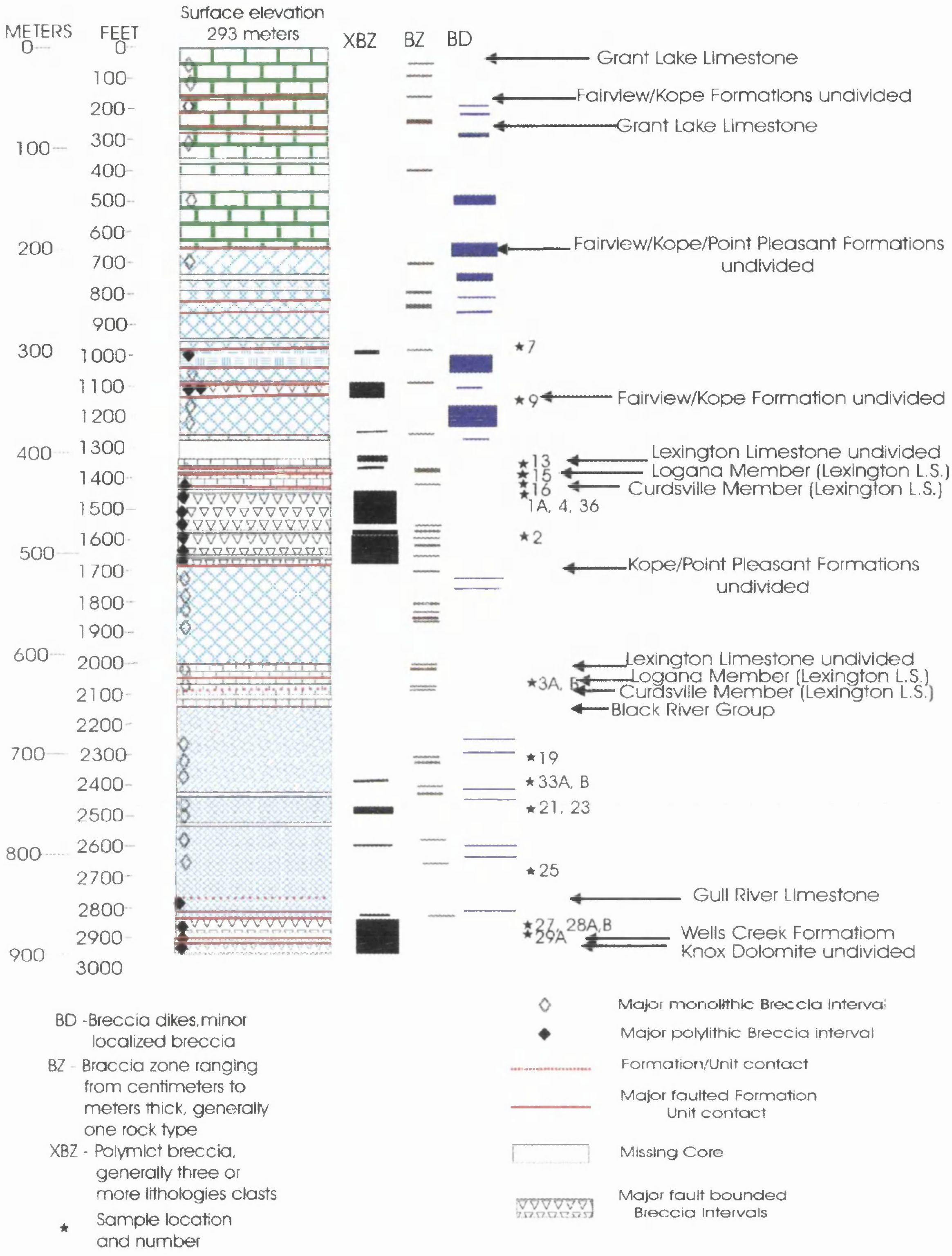

Figure 8.4- Core DGS 3274 showing depths and locations of The rock samples and the breccia zones

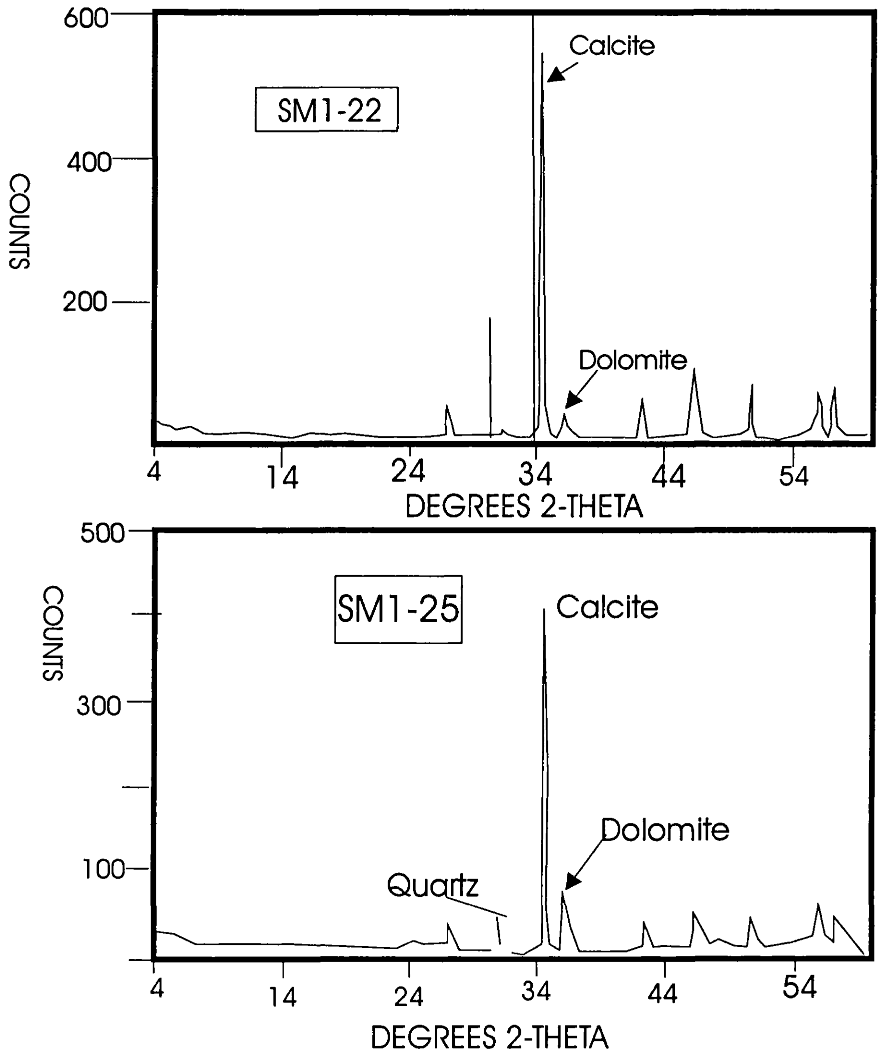

Figure 8.5- Limestone-clast breccias having subordinate amounts Of claystone, sandstone, and dolomite

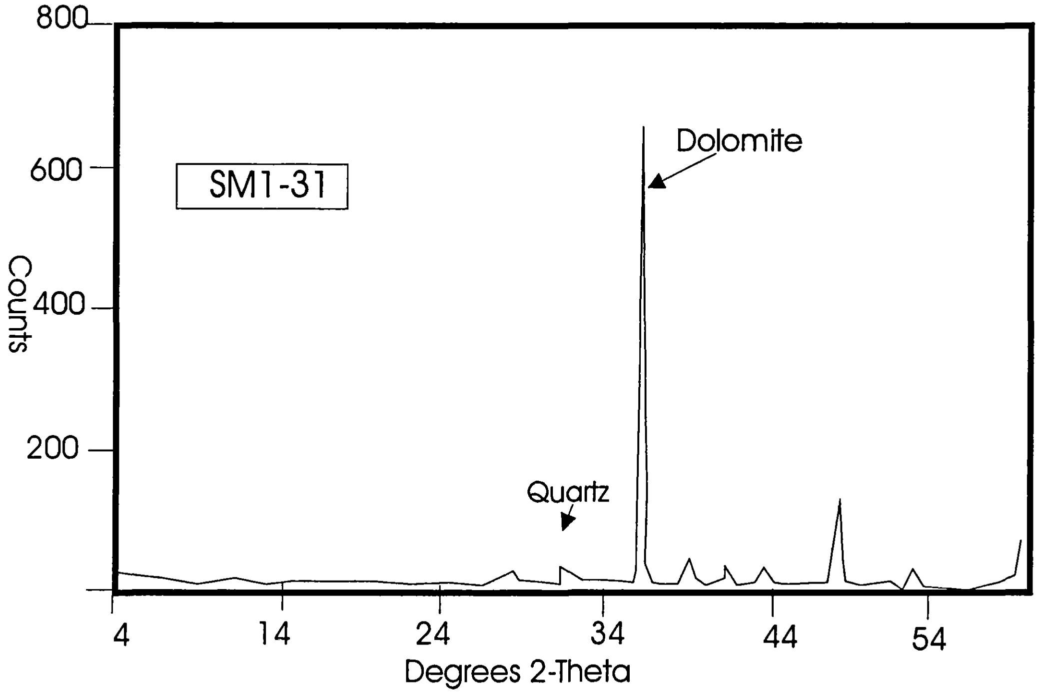

Figure 8.6- predominantly carbonate breccias

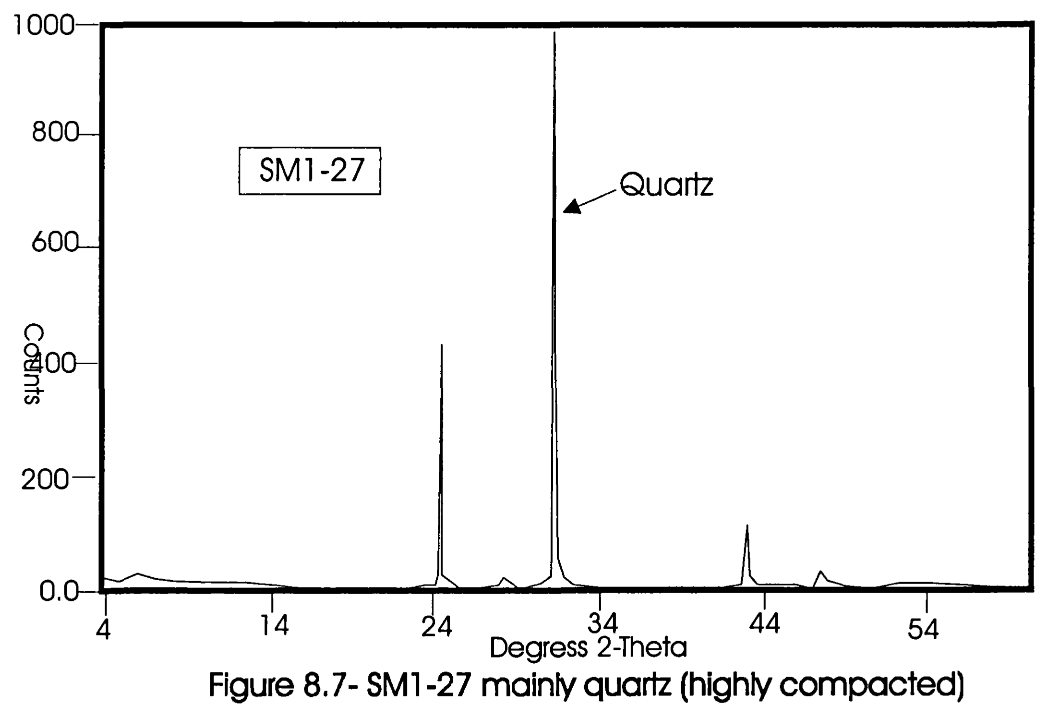

Figure 8.7- SM1-27 mainly quartz (highly compacted)

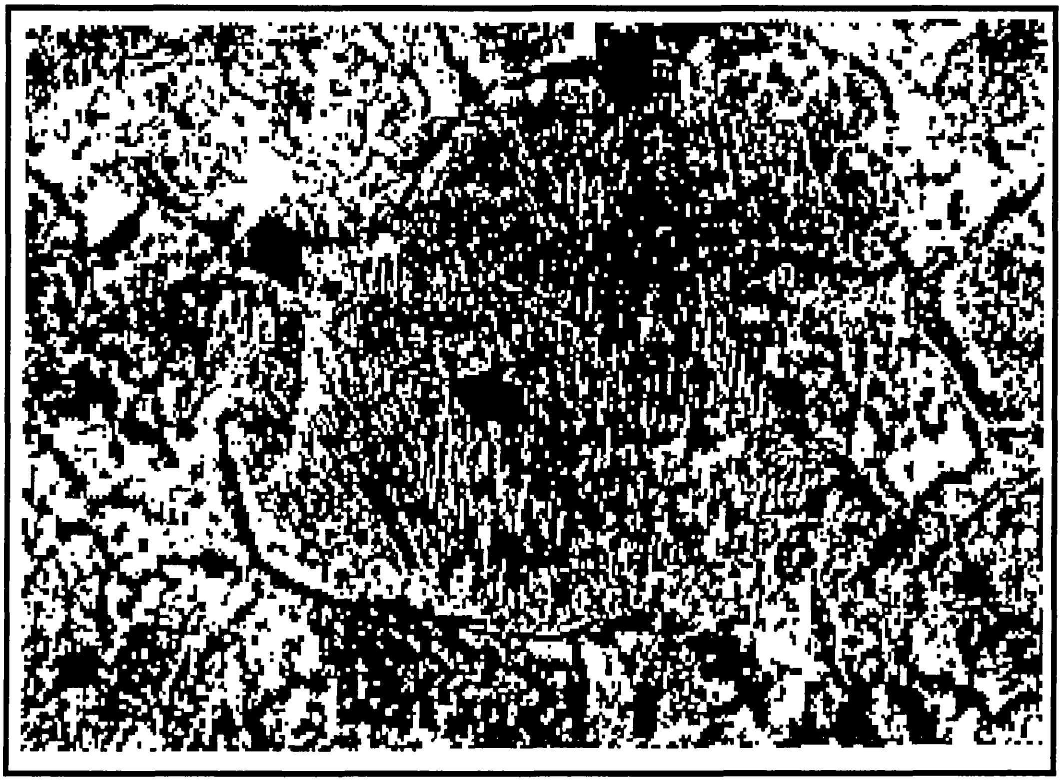

Figure 8.8- Photomicrographs of quartz grains from sample SM1-36a displaying three sets of planar deformation features (PDFs) indicated by arrows. (Width of images: 0.30 mm)

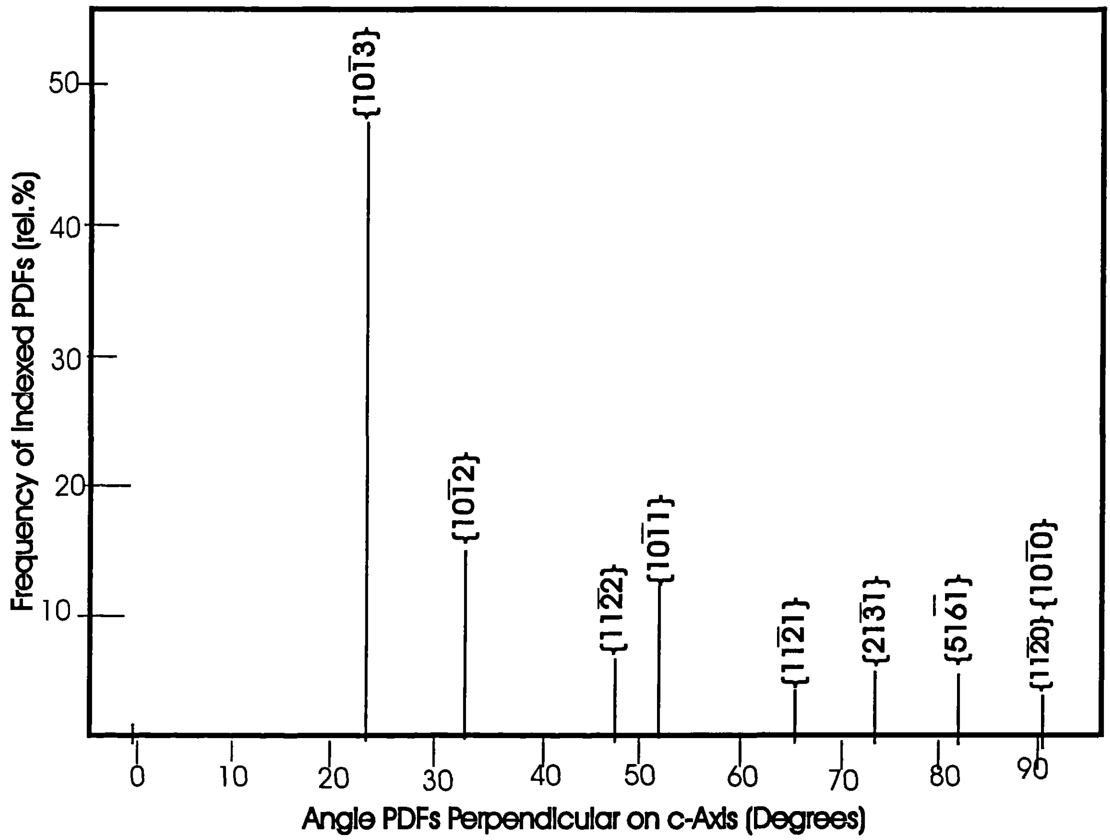

Figure 8.9- Crystallographic orientation of PDFs (Carlton et al, 1998)

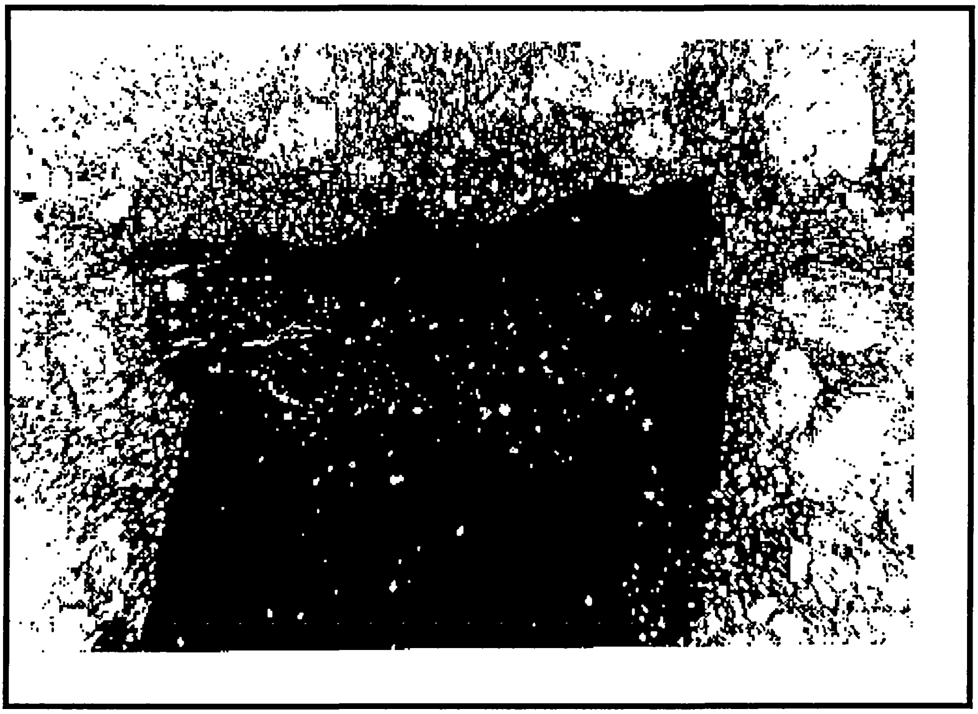

Figure 8.10- Impact-melt, aphanitic clasts having possible flow structure

8.4- Discussion

There is abundant macroscopic evidence for shock metamorphism in the form of intense deformation, brecciation, and shatter cones. Microscopic evidence for shock is found as sets of PDFs in quartz grains and possible impact melt clasts. No coesite was confirmed but the samples containing the quartz with the PDF's have yet to be examined for this or other minerals diagnostic of impacts. The clasts found in the breccias indicate considerable downward movement of rock during the impact. These observations, supported by geophysical observations, confirm that the Serpent Mound Structure is a result of an impact during the Late Paleozoic time.

CHAPTER-9 CONCLUSIONS

9.1- Conclusions

The new data acquired on the Serpent Mound Structure in collaboration with the Ohio Department of Natural Resources (ODNR), resulted in the revision of the magnetic map of the Serpent Mound Structure, and detection of a new gravity anomaly in the course of our high-resolution survey. The reprocessing of the seismic data provided the best image of the subsurface to date. Figures (9.1) and (9.2) show the improvement in the seismic processing which resulted in the Gull River and the Copper Ridge reflectors becoming more smooth and continuous throughout the seismic sections compared to earlier processing carried out by industry. This allows us to correlate the sections through a series of high angle faults and the central uplift (Figure 9.2). Both sections show primary reflectors with maximum tow-way travel time down to 600 ms. The Conasauga reflector is very well developed due to the high impedance contrast with the overlying unit. The seismic data confirm the three structural zones within the disturbance, ranging from the complex central uplift (Figure 9.2) to the least complex outer ring graben.

The structural depression seen on BV-1-92 is confirmed by core DGS 3274 drilled in the central uplift area of the structure, where the Gull River and lower reflectors are 850 to 1000 feet structurally lower than their correlative positions, the consistency of the seismic data and core data negates the possibility that the depression is a result of velocity anomaly.

The seismic data and data from the cores indicate an anomalous lens-shaped area, consisting of thickened and chaotic reflectors occurs above the Gull River at the centre of the complex depression (Figure 9.2). This is also confirmed by the highly deformed and brecciated rocks found in core DGS 3274.

The severely deformed strata observed in core decrease in structural complexity with depth and away from the central uplift area of the structure, suggesting the stresses causing the deformation were directed from above.

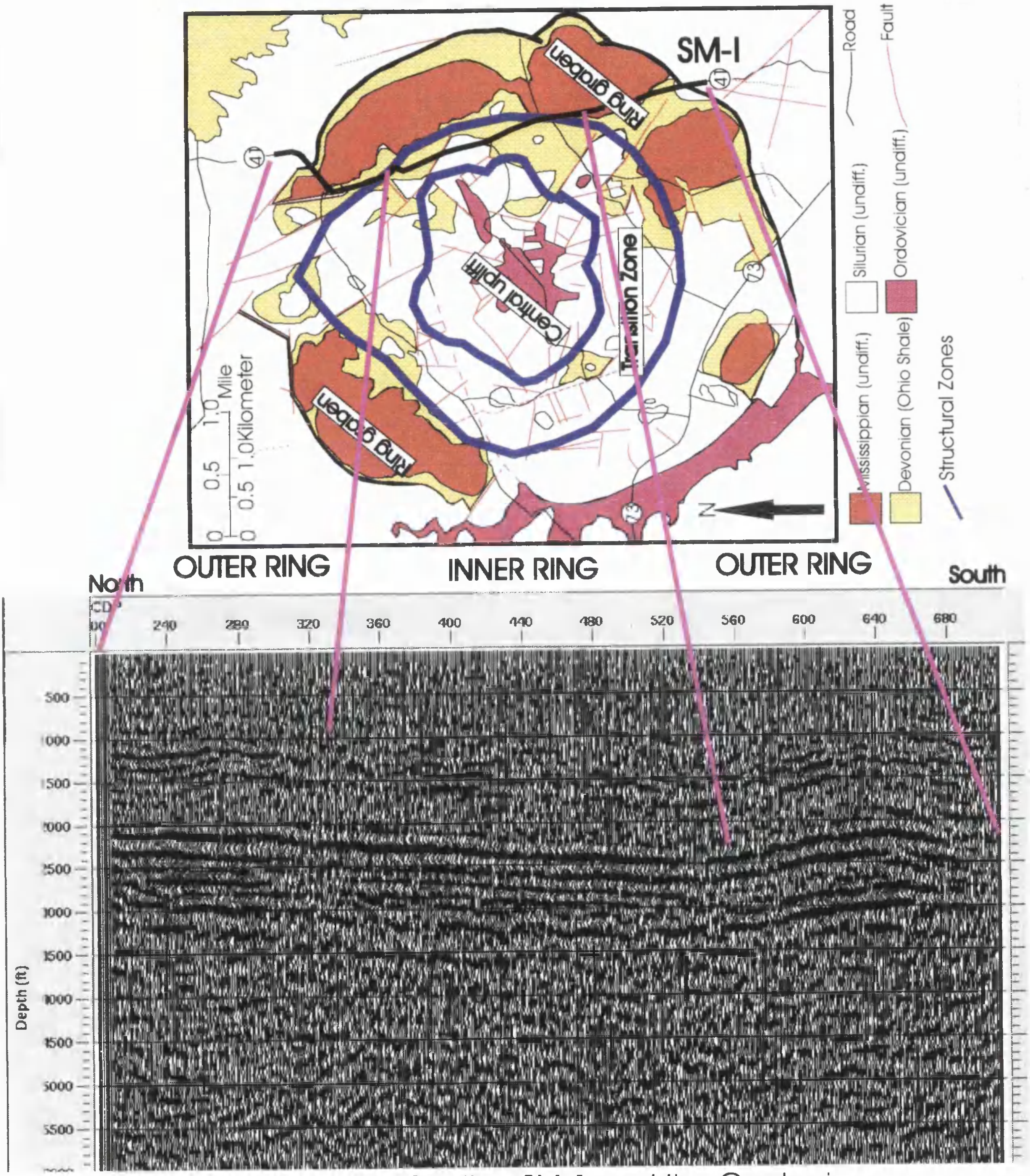

Figure 9.1- Seismic Section SM-1 and the Geologic Map of the Serpent Mound Structure

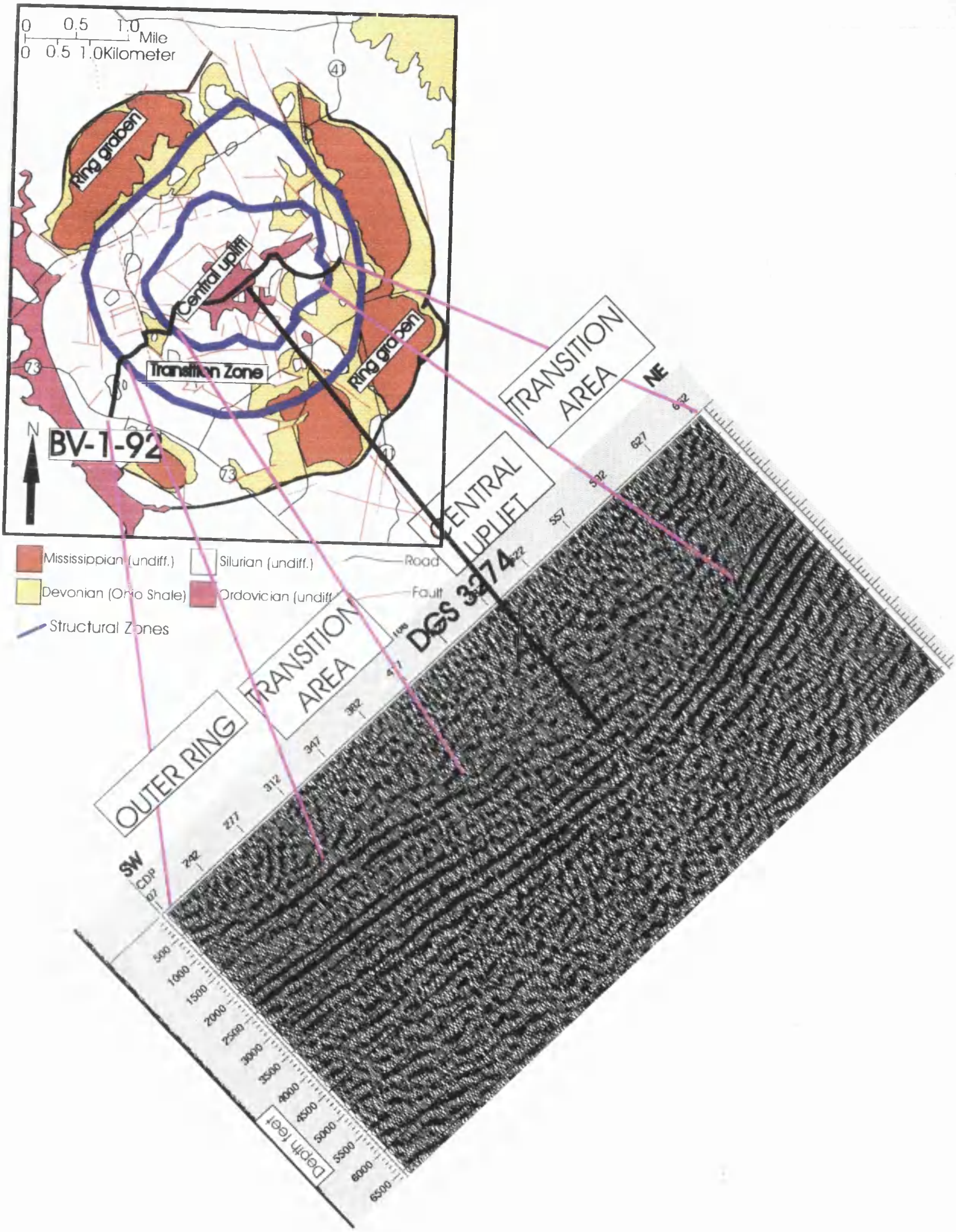

Figure 9.2- Seismic Section BV-1-92 and the Geologic Map of the Serpent Mound Structure

The high-resolution gravity data collected during this study (Figure 9.3) show the regional anomaly passing through the study area, sloping from east to west. Superimposed on the regional anomaly is a local gravity anomaly of about –1.2 mgal mapped as a result of our microgravity survey of the structure. The local anomaly is associated with fractured and intensely brecciated lens at the central uplift area of the structure. The ground magnetic survey of the Serpent Mound area resulted in the revision of Sappenfield's magnetic map of the area (1951). The elongated, closed magnetic high of 1000 nT correlates with the centre of the Serpent Mound Structure (Figure 9.4), and associates with low on the eastern margin of the structure.

The investigations of the Serpent Mound Structure based on gravity, seismic reflection data, petrologic and geochemical studies, make a compelling case for a meteorite impact origin of the structure. The local magnetic anomaly may be a result of the shock-induced magnetisation of the basement rocks beneath the site of impact.

The palaeomagnetic study of hematite rich beds in the Brassfield Formation, suggests the impact happened before the remagnetisation. The palaeomagnetic inclination of the Serpent Mound Structure is 2 ± 3 degrees gives an estimate of the age of magnetisation as approximately 250 ± 15 my. The estimated age of the remagnetisation is Late Permian to Early Triassic.

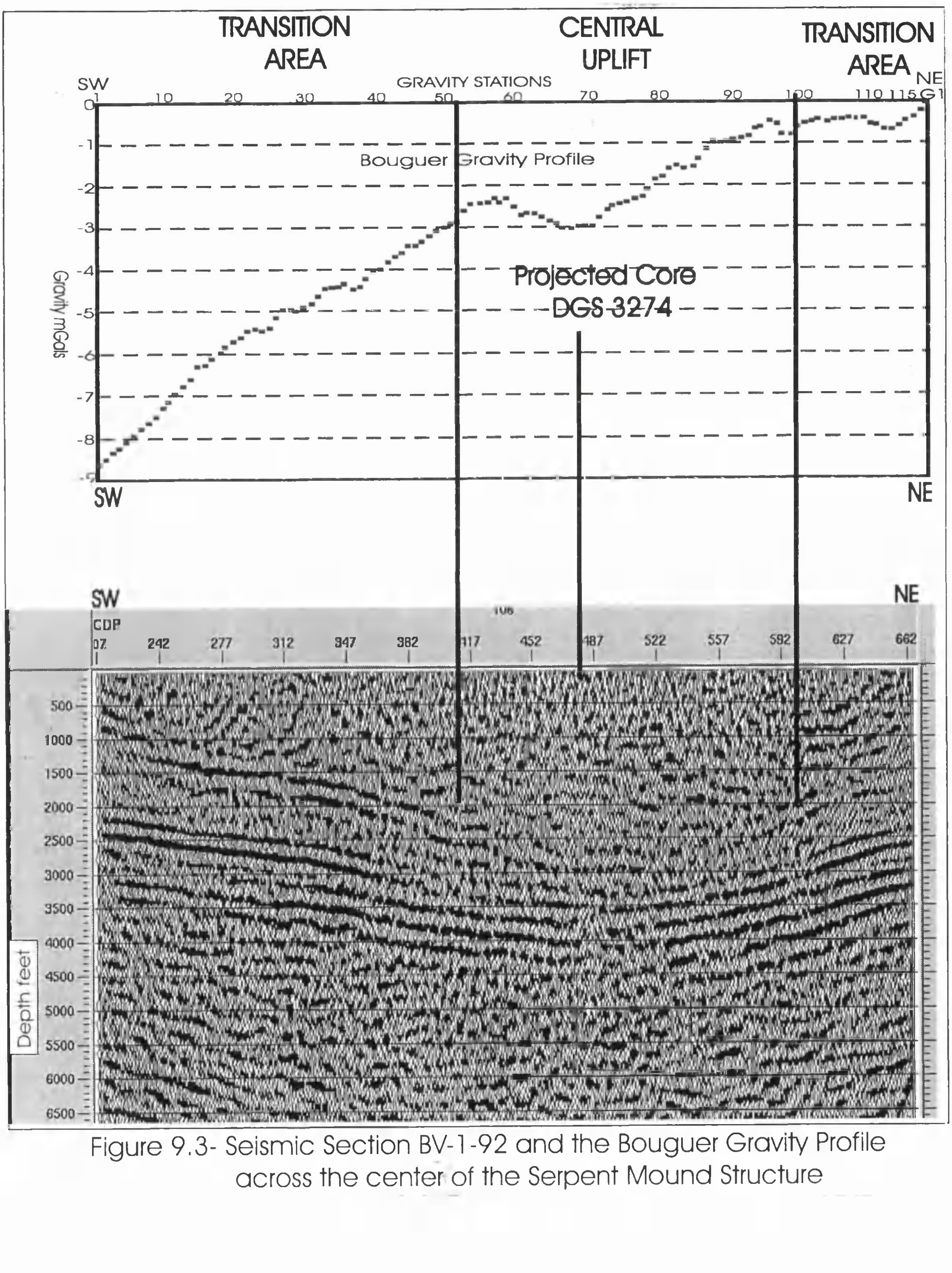

Figure 9.3- Seismic Section BV-1-92 and the Bouguer Gravity Profile across the center of the Serpent Mound Structure

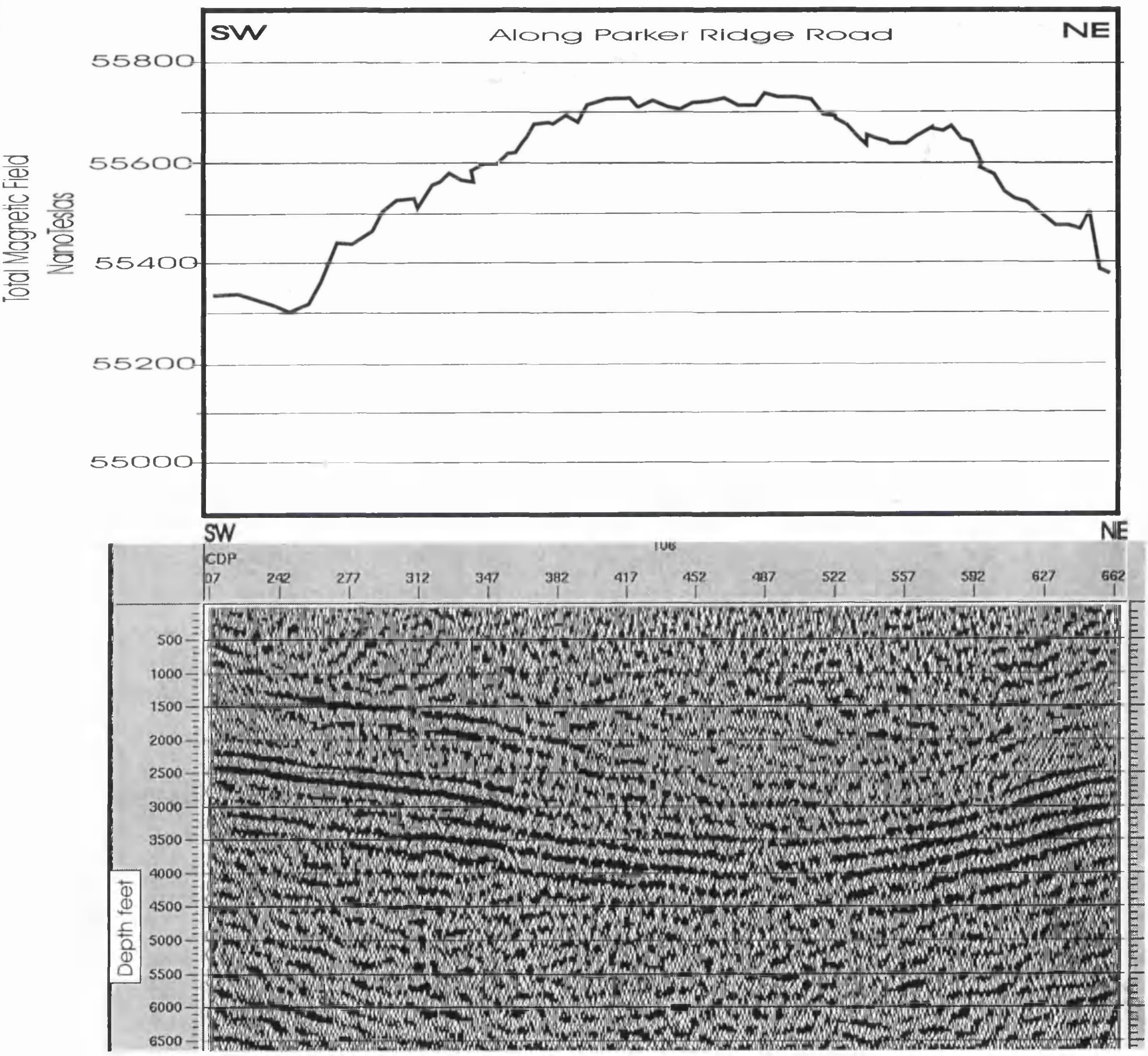

Figure 9.4- Seismic Section and Magnetic Profile across Serpent Mound Structure

REFERENCES CITED

Alexopoulos, J. S., Grieve, R. A. F., and Robertson, P. B., 1988, Microscopic lamellar deformation features in quartz: Discriminative characteristics of shock-generated Varieties: Geology, V. 16, P.796-799.

Ali, S. A., 1967, Kope and Fairview Sedimentary Structures: Brown and Adams Counties, Ohio: unpublished M.S. thesis, the Ohio State University, pp.9-26

Alvarez, L. W., Alvarez, W., Asaro, F., and Michel, H. V., 1980, Extraterrestrial cause for the Cretaceous-Tertiary extinction: Science, V. 208, P. 1095-1108.

Ammerman, M. L., and Keller, G. R., 1979, Delineation of Rome Trough in eastern Kentucky by gravity and deep drilling data: AAPG Bulletin, v. 63, p. 341-353

Anderson, W., 1983, Geology of Iowa: Ames, Iwoa, Iowa State University Press, 268 p.

Andrews, E. B., 1871. Geol. Surv. Of Ohio, Report of progress in 1870, pp. 82-83.

Baranoski, M. T., Schumacher, G. A., Watts, D. R., Carlton, R. W., and Elsaiti, B., 1998, Report on the geology of the Serpent Mound disturbance based upon new core and geophysical data: Ohio Division of Geological Survey Report of Investigation, in press

Baranoski, M. T., Schumacher, G. A., Watts, D. R., Carlton, R. W., and Elsaiti, B., 1997, Hydrocarbon potential beneath the Knox unconformity in the vicinity of the Serpent Mound disturbance based upon new core and geophysical data: Ohio Geological Society Fifth annual Technical Symposium, p. 1-11.

Baranoski, M. T., Watts, D. R., Elsaiti, B., Schumacher, G. A., and Carlton, R. W., 1998a, Interpretation of seismic and gravity data from the Serpent Mound disturbance of south-central Ohio: Geological Society of America Abstracts with programs, v.30, no. 2.

Baranoski, M. T., Schumacher, G. A., Carlton, R. W., Watts, D. R., and Elsaiti, B., 1998b, The Serpent Mound disturbance of south-central Ohio: The ultimate geological lottery: Geological Society of America Abstracts with programs, v.30, no.2.

Baranoski, M. T., 1993b, Regional tectonic features affecting the Knox Group including the Rose Run sandstone in eastern Ohio and adjacent areas [abs.]: west Virginia Geological and Economic Survey.

Baranoski, M. T.,1992, Knox and deeper wells in southern Ohio: Ohio Division Geol. Surv., DCM 1.

Bass, M. N., 1960, The Grenville boundary in Ohio: Journal of Geology, v. 68, p. 673-677

Bassler, R. S., 1911, The stratigraphy of deep well at waverly, Ohio: AM. Jr. Sci., v.31, pp. 19-24.

Bickford, M. E., and Van Schmus, W. R., 1986, Proterozoic history of the mid-continent region of North America: Geology, v.14, p. 492-496.

Black, D., and Scollar, I., 1969, Spatial filtering in the wave-vector domain: Geophysics, v. 34, p. 916-923.

Black, D. F. B., 1986, Basement faulting in Kentucky, International Conference on Basement Tectonics, p.125-139

Blizkovsky, M., 1979, Processing and applications of microgravity surveys: Geophysical prospecting, v. 27, p. 848-861.

Bott, M. H. P., 1959, The use of electronic digital computers for the evaluation of gravimetric terrain corrections: Geophysical Prospecting, v. 5, p. 45-54.

Bott, M. H. P., 1962, A simple criterion for interpreting negative gravity anomalies: Geophysics, v. 27, p. 376-381.

Branco, W., and Fraas, E., 1905, Das Kryptovulkanische Buken von steinheim: Koniglich-Preussische Akademic der wissenschaftes Physikalisch-Mathematische Klasse (Royal Prussian Acadamy of science, Mathematics-Physics section): Abhandlungen, Berlin, p.1-64.

Brenan, R. L., Peterson, B. L., and Smith, H. J., 1975, The Origin of Red Wing Creek Structure, Mckenzie County, North Dakota: Wyoming Geological Association Earth Science Bulletin, v. 8, p. 11-41.

Brigham, E. O., 1974, The Fast Fourier Transform: Prentice-Hall, 252 p.

Bucher, W. H., 1921a, Cryptovolcanic structure in Ohio of the type of the Steinheim Basin [abstract]: Geological Society of America Bulletin, v.32, p.74-75.

Bucher, W. H., 1921b, Cryptovolcanic structure in Ohio of the type of the Steinheim Basin: Geological Society of America Bulletin, v. 2, p. 1060-1064.

Bucher, W. H., 1928, Cryptovolcanic regions [abstract]: Washington D.C. Academy of Science Journal, v.18, p. 521-524.

Bucher, W. H., 1936, Cryptovolcanic Structures in the United States: Sixteenth International Geological Congress, v. 41, p. 1055-1084.

Bucher, W. H., 1963, Cryptoexplosion structure caused from without or within the Earth? (astroblemes or geoblemes): American Journal of Science, v. 261, p. 597-649.

Bull, C., Corbató, C. E., and Zahn, J. C., 1967, Gravity survey of the Serpent Mound area, southern Ohio: Ohio Journal of Science, v.67, p. 359-371.

Cable, M. S., and Beardsley, R. W. , 1984, Structural controls on Late Cambrian and Early Ordovician carbonate sedimentation in eastern Kentucky: American Journal of Science, v. 284, p. 797-823.

Calvert, W. L., 1962, Sub-Trenton rocks from Lee County, Virginia, to Fayette County, Ohio: Ohio Geol. Surv. Report of Inves. No. 45, 57p.

Calvert, W. L., 1974, Sub-Trenton structure of Ohio, with views on isopach maps and stratigraphic sections as basis for structural myths in Ohio, Illinois, New York, Pennsylvania, West Virginia, and Michigan: American Association of Petroleum Geologists Bulletin, v. 58, p. 957-972.

Carlson, E. H., 1991, Serpent Mound Area, Adams County: Ohio Division of Geological Survey Bulletin 69: p. 73-75.

Carlson, E. H., 1994, Geologic, fluid immigration, and isotope studies of the Findlay Arch district, north-western Ohio: Economic Geology, v. 89, p.67-90.

Carlton,R.W., Koeberl C., Baranoski, M. T., and Schumacher, G. A., 1998, Discovery of microscopic evidence for shock metamorphism at the Serpent Mound disturbance, in press.

Carman, J. E., 1927, The Monroe Division of Rocks in Ohio: Jour. Of Geol., v. 35, pp. 481, 506.

Chao, E. C. T., Fahey, J. J., Littler, J., and Milton, D. J., 1962, Stishovite, SiO_2, a very high-pressure mineral from Meteor Crater, Arizona: Journal of Geophysical Research, V. 67, P. 33-40.

Chao, E. C. T., 1968, Pressure and Temperature history of impact metamorphosed rocks based on petrographic observations, in French, B. M. and Short, N. M. eds. Shock metamorphism of natural materials, Baltimore, Mono Book Corp., p.211-218.

Cisowski, S. M., and Fuller, M., 1978, The effect of shock on the magnetism of terrestrial rocks, Journal of Geophysical Research, V.83, p. 3441-3458.

Claerbout, J. F., 1976, Fundamentals of Geophysical Data Processing: New York, McGraw Hill.

Clark, S., 1983, Magnetic Survey Data of meteoritic impact sites in North America. Geomagn. Surv. Coun., p. 1-30.

Clark, S. P., Jr., 1966, Handbook of physical constants: Geol. Soc. Am. Memoir 97, 583.

Cohen, A. J., Bunch, T. E., and Reid, A. M., 1961, Coesite discoveries establish cryptovolcanics as fossil meteorite craters: Science, V. 134, P. 1624-1625.

Cohen, A. J., Reid, A. M., and Bunch, T. E., 1962, Central Uplifts of terrestrial and lunar craters, part 1, Kentland and Serpent Mound Structures [abstract]: Journal of Geophysical Research, V. 67, P. 1632-1633.

Cressman, E., R., 1973, Lithostratigraphy and depositional environments of the Lexington limestone of central Kentucky: USGS prof. Paper 768, 61p.

Culotta, R. C., Pratt, J., and Oliver, J., 1990, a tale of two sutures: COCORP deep seismic survey of the grenville province in the eastern midcontinent USA: GEOL v, 18, p. 646-649.

Dabizha, A. I., and V. V. Fedynsky, 1975, The earth's 'star wounds' and their diagnostic geophysical methods: Zamlya Vselennaya, v.3, p.56-64.

Dabizha, A. I., and V. V. Fedynsky, 1977, Futures of gravitational field of astroblemes: Meteoritica, v. 36, p. 113-120.

Dence, 1972, The nature and signature of terrestrial impact structures Proc. 24th internat: Geol. Sect. 15, p. 77-89.

Denison, R. E., Lidiak, E., Bickford, M. E., and Kisvarsanyl, E. B., 1984, Geology and geochronology of Precambrian rocks of the central Interior region of the United States: U.S.G.S. prof. Paper 20 p.

Dietz, R. S., 1947, Meteorite impact suggested by the orientation of shatter cones at the Kentland, Indiana, disturbance: Science, V. 105, P. 42.

Dietz, R. S., 1959, Shatter cones in cryptoexplosion structures (meteorite impact): J. Geol., v. 67, p. 496-505.

Dietz, R. S., 1960, Meteorite impact suggested by shatter cones in rock: Science, v. 31, p. 1781-1784.

Dietz, R. S., 1961, Astroblemes: Scientific American, v. 205, p. 50-58.

Dietz, R. S., 1966, Shatter cones at the Middlesboro structure, Kentucky: Meteoritic, V. 3 P. 27-29.

Dietz, R. S., 1968, Shatter cones in cryptoexplosion structures, in French, B. M., and Short, N. M. eds., Shock Metamorphism of natural materials: Baltimore, Mono Book Corporation, P. 267-285.

Dietz, R. S., and Lambert, P., 1980, Shock metamorphism at Crooked Creek cryptoexplosition structure: Meteoritics, V. 15, P. 281-282.

Dobrin, M. B., 1976, Introduction to Geophysical Prospecting, 3rd edn: New York, McGraw-Hill

Dobrin, M. B. and Savit, C. H., 1988, Introduction to Geophysical Prospecting, 4th edn.: New York, McGraw-Hill.

Dohr, G., 1981, Applied Geophysics: New York, Halsted Press.

Donofrio, R. R., 1981, Impact craters, Implications of basement hydrocarbon production: J. Petr. Geol. V. 3, p. 279-302.

Drahovzal, J. A., Haarric, D. C., Wickstrom, L. H., Walkers. D., Baranoski, M. T., Keith, B., and Furer, L., 1992, The east continent rift Basin, a new discovery: Ohio Div. Geol. Surv., IC, Lexington, Kentucky, 24 p.

Elming, S. A., and G. Bylund, 1991, Palaemagnetism of the Siljan impact structure, central Sweeden: Geophy. Int., v. 105, p.757-770.

Ezeji-Okoye, S.,1985, The origin of the Eagle Butte Structure, Alberta, Canada: Can. Petro. 75p.

Fagadau, S. P., 1952, Palaeontology and stratigraphy of the Logan Formation of central and southern Ohio: unpublished Ph.D. dissertation, The Ohio State University, pp. 4-6, 88-93.

Faust, L. Y., 1951, Seismic velocity as a function of depth and geologic time: Geophysics, v. 16, p. 192-206.

Flaugher, D. M., 1973, A gravity survey of the Serpent Mound cryptoexplosion structure and surrounding area in southern Ohio: M.Sc. thesis (unpublished), Wright State University, 114 p.

Foerste, A. F., 1897: A report on the Upper and Middle Silurian of Clark, Jefferson, Rippley, Jennings, and southern Decatur Counties, Indiana: Indiana Dept. Nat. Res. Ann. Rep., 21, pp. 213-288.

Foerste, A. F.,1929, The correlation of the Silurian section of Adams and Highland Counties with that of the Springfield area: Ohio Jour. Sci., v.29, p. 168-169.

Freeman, L. B., 1949, Regional aspects of Cambrian and Ordovician subsurface stratigraphy in Kentucky: Am. Assoc. Pet. Geol. Bull., v. 33, pp. 1655-1681.

French, B. M., and Short, N. M., eds., 1968, Shock metamorphism of natural materials: Baltimore, Mono Book Corporation, 644 P.

Galbraith, R. M., IV, 1968, Peripheral deformation of the Serpent Mound cryptoexplosion structure in Adams County, Ohio: M. Sc. Thesis (unpublished), University of Cincinnati, 47 p.

Galbraith, R. M., IV, and Koucky, F. L., 1969, Peripheral deformation of the Serpent Mound cryptoexplosion structure in Adams County, Ohio: Geological Society of America Abstract with Programs, v.1, p. 17.

Gardner, G. H., W. Gardner; and A. R. Gregory, 1974, Formation velocity and density- the rock diagnostic bases for stratigraphic traps: Geophysics v.39, p. 770-780.

Gault, D. E., Quaide, W. L., and Oberbeck, V. R., 1968, Impact cratering mechanics and structures, *in* French, B. M., and Short, N. M., eds., Shock metamorphism of natural materials: Baltimore, Mono Book Corporation, P. 87-99.

Gonterman, J. R., 1973, petrographic study of Precambrian Rocks in Ohio: Columbus, Ohio State University, unpublished M. S. thesis, 132 pp.

Grant, F. S., and West, G. F., 1965, Interpretation theory in Applied Geophysics: McGraw Hill, New York.

Green, D. A., 1957, Trenton structure in Ohio, Indiana and northern Illinois: American Association of Petroleum Geologists Bulletin, v. 14, p. 627-642.

Grieve, R. A. F., 1987, Terrestrial impact structures: Annual Reviews of Earth and Planetary Science, V. 15, P. 245-270.

Grieve, R. A. F., 1991, Terrestrial impact: The record in the rocks: Meteoritics, V. 26, P. 175-194.

Grieve, R. A. F., and C. J. Pesonen, 1992, The terrestrial impact cratering record: Tectonophysics.

Grieve, R. A. F., and Shoemaker, E. M., 1994, Terrestrial impact cratering, *in* Gehre T.eds., Hazards from asteroid impacts: Tucson, University of Arizona Press, P. 417 462.

Halls, H. C., 1979, The Slate Islands meteorite impact site: a study of rock remnant magnetization, Geophys. J. R. Astron. Soc., v.59, p. 553-591.

Hammer, S., 1939, Terrain corrections for gravimeter stations: Geophysics, v. 4, p. 184-194.

Hansen, M. C., 1994, Return to Sunken Mountain: The Serpent Mound cryptoexplosion structure: Ohio Geology Newsletter, v. 1994-Winter issue, p. 1-17.

Hargraves, R. B., and N. E. Perkins, 1969, Investigations of the effect of shock on natural remnant magnetisation: J. Geoph. Res., v. 74, p. 2576-2589.

Hayes, C. W., 1891, The overthrust faults of the southern appalachian: Geol Soc. Am. Bull., v. 2, pp. 141-154.

Heiskanen, W. A. and Uotila, U. A., 1956, Gravity Survey of the State of Ohio: Ohio Geological Survey Report Inv. No. 30, 34 p.

Heyl, A. V., and Brock, M. R., 1962, Zinc occurrence in the Serpent Mound structure of southern Ohio: U. S. Geological Survey Professional Paper 450-D, p. 95-97.

Hicks, L. E., 1878, The Waverly Group in central Ohio: Am Jour. Sci, v. 16, pp. 216-224.

Hildenbrand, T. G. and Kucks, R. P., 1984a, Residual total intensity magnetic map of Ohio: U. S. Geological Survey, Geophys. Inv. Map GP-961, scale 1:500,000.

Hildenbrand, T. G. and Kucks, R. P., 1984b, Complete Bouguer gravity anomaly map of Ohio: U. S. Geological Survey, Geophys. Inv. Map GP-962, scale 1:500,000.

Hyde, J. E., 1953, The Mississippian formations of central and southern Ohio: Geol. Surv. Ohio., Bull. 51, pp. 1-61, 169-213.

IAGA Division I Working Group, 1987, The International Geomagnetic Reference Field revision 1987: Journal of Geomagnetism and Geoelectricity, v. 39, p. 773-779.

Istok, J. D., 1978, Palaeomagnetism at Serpent Mound: B. S. thesis (unpublished), the Ohio State University, 13 pp.

Jackson, M., and Van der Voo, R., 1986, A palaeomagnetic estimate of the age and thermal history of the Kentland, Indiana cryptoexplosion structure, Journal of Geology, v. 94, p. 713-723.

Jansa, L. F., P. Pipa, P.B. Robeston, and O. Freidenrecith, Montagnais, 1989, A submarine impact Structure of the Scotian self, eastern Canada: Geol. Soc. Am. Bull., p. 450-463.

Janssens, Adriaan, 1973, Stratigraphy of the Cambrian and Lower Ordovician rocks in Ohio: Ohio Division of Geological Survey Bulletin 64, 197 pp.

Kaufmann, R. F., 1964, The stratigraphy of northwestern Adams and northeastern Brown counties, Ohio: unpublished thesis M. S. thesis, The Ohio State University, 184 pp.

Keller, G. R., Lidiak, E., Hinze, W., and Brail, L., 1983, The tectonic development of the midcontinent U.S.A., in Morgan, P. and Baker, B. eds., Processes of continental rifting: Tectonophysics, v. 14, p. 319-412.

Kieffer, S. W., 1971, Shock metamorphism of the Coconino Sandstone at Meteor Crater, Arizona: Journal of Geophysical Research, v. 76, p. 5449-5473.

LaCoste, L. J. B., 1934, A new type of long period vertical seismograph: Physics, v. 5, p. 178-180.

Lane, A. C., Prosser, C. S., Sherzer, W. H., and Grabau, A. W., 1908, Nomenclature and subdivision of the Upper Silurian strata of Michigan, Ohio, and Western New York: Bull. G. S. A., v. 19, pp. 553-556.

Langford, C. S., 1984, A gravity survey of northeastern Adams County, Ohio: M. S. thesis (unpublished), The Ohio State University, 170 pp.

Lidiak, E. G., Marvin, R. F., Thomas, H. H., and Bass, M. N., 1966, Geochronology of the mid-continent region, United States, Part 4, Eastern area: Journal of Geophysical Research, v. 71, p. 5427-5438.

Lidiak, E. G., and Zietz, I., 1976, Interpretation of aeromagnetic anomalies between latitude 37 N and 38 N in the eastern and central United States, 167 {uof} Geological Society of America Special Paper: 37 pp.

Lidiak, E. G., Hinze, W. J., Keller, G. R., Reed, J. E., Braile, L. W., and Johnson, R. W., 1985, Geologic significance of regional gravity and magnetic anomalies in the east central mid-continent, in Hinze, W. J., ed., The utility of regional gravity and magnetic anomaly maps: Society of Exploration Geophysicists Special Publication, p. 287-307.

Lidiak, E. G. and Hinze, W. J., 1988, Subsurface Grenville age rocks between the Adirondack Massif and the Black warrior Basin, in Proterozoic rocks east and southeast of the Grenville Front: Geological Society of America DNAG Volume E.

Locke, J., 1838, Geological report (on southwestern Ohio): Ohio Division of Geological Survey Second annual Report, p. 201-286.

Lucius, J. E., 1985, Crustal Geology of Ohio inferred from aeromagnetic and gravity anomaly analysis: M. S. Thesis (unpub.), The Department of Geology and Mineralogy, The Ohio State University, Columbus, Ohio, 131 p.

Lucius, J. E., and Von Frese, R. R. B., 1988, Aeromagnetic and gravity anomaly constraints of the crustal geology of Ohio: Geological Society of America Bulletin, v.100, no. 1, p. 104-116

McCormick, G. R., 1961, Petrology of the Precambrian rocks of Ohio: Ohio Geological Survey, Report of Investigation 41, 60 pp.

McFadden, P. L., and Reid, A. B., 1982, Analysis of palaeomagnetic inclination data, Geophys J.R. Astron. Soc., v.69, p. 307-319

McFarland, B. P., McMasters, P. C., Sanfrey, S. L., Damato, E. J., Miller, T. L., and Carlson, E. H., 1993, Trace metal patterns in stream sediments and panned concentrates, Serpent Mound disturbance, southwest Ohio: Geological Society of America Abstracts with programs, v. 25, no. 7, p.278.

McFarland, B. P., and Carlson, E. H., 1994, Sulfur isotope investigation of the Serpent Mound district, southwest Ohio: American Geophysical Union, EOS, Abstracts with programs, p. 356.

McFarland, B. P., Carlson, E. H., and Talnagi, J. W., Jr., 1994, Mineralogical and trace element studies from the Serpent Mound district, southwest, Ohio: Geological Society of America, Abstracts with programs, v. 26, no. 7, p. 500.

McFarland, B. P., and Carlson, E. H., 1995a, The Serpent Mound disturbance, southwest Ohio: A new model based on mineralogy, sulfur isotopes, and trace element geochemistry (extended abstract): International field conference on carbonate-hosted lead-zinc deposits, St. Louis, Proceedings Volume, P. 204-206.

McFarland, B. P., and Carlson, E. H., 1995b, unravelling the enigma of the Serpent Mound Cryptoexplosion structure: Fifth V. M. Goldschmidt Conference, University Park. Pennsylvanian, Program and Abstracts, p. 71.

McFarland, B. P., and Carlson, E. H., 1996, Evidence for Late Palaeozoic brine migration in the Serpent Mound district, southwestern Ohio: Geological Society of America Abstracts with programs, v.28. no. 3, p. 79.

McGuire, W. H., and Howell P., 1963, oil and gas possibilities of the Cambrian and Ordovician in Kentucky: Lexington commerce commonwealth of Kentucky, 134 p.

Melosh, H. J., 1989, Impact cratering, a geologic process: New York, Oxford University Press, 245 p.

Miller, P. M., 1955, Stratigraphy and petrography of the Greenfield and Tymochtee Formations of southern Ohio: unpublished M. S. thesis, The Ohio State University, pp58.

Milton, D. J., 1977, Shatter cones- An outstanding problem in shock mechanics in Roddy, D. J., Pepin, R., and Merrill, R., eds., Impact and explosion cratering: New York Pergamn press, p. 703-714.

Morgan, J., Warner M., and the Chicxulub Working Group, 1997, Size and morphology of the Chicxulub Impact crater: Nature, v. 4, p 472-476.

Muehlberger, 1968, Basement rock in the central interior of the United States: AAPG Bull,

v. 51, p. 2351-2380.

Nettelton, L. L., 1939, Determination of density for reduction of gravimeter observations: Geophysics, v. 4, p. 176-183.

Newberry, J. S., 1870, Report of progress in 1869: Geol. Surv. Ohio, p.21.

Officer, C. B., and Carter, N. L., 1991, A review of the Structure, petrology, and dynamic deformation characteristics of some engmatic terrestrial structures: Earth Sci, Rev. ,p. 1-49.

Orton, E., Sr., 1871, The Cliff Limestone of Adams and Highland Counties: Geol. Surv. Ohio, Rept. Of progress in 1870, pp. 296-298.

Orton, E., Sr., 1873, The geological relations of Ohio: Ohio Div. Geol. Surv., v. 1, Geology and paleontology, p. 1-167.

Orton, E., Sr., 1888, The Geology of Ohio considered in the relation to petroleum an natural gas: Ohio Div. Of Geol. Surv., v.6, p. 1-59.

Owens, G. L., 1967, The Precambrian Surface of Ohio: Ohio Geological Survey, Report of Investigation, no. 64, 8 pp. plus map.

Parasnis, D. S., 1972, Principle of Applied Geophysics, 2nd eds. : Chapman and Hall, London

Patterson, R. L., 1980, Low-altitude aeromagnetic survey of south-central Ohio: unpublished M. S. thesis, The Ohio State University, pp 1-55.

Parés, J. M., Van der Voo, R. , Stamatakos, J., and Pérez-Estau's, A., 1994, Remagnetization and post-folding oroclinal rotations in the Cantabrian/Asturian arc, northern Spain: Tectonics, v.13, p. 1461-1471

Peck, J. H., 1966, Upper Ordovician formations in the Maysville, Kentucky, area: U. S. Geol. Surv. Bull.1244-B, 30p.

Phol, J., U. Bleil, and U. Hornemann, 1985, Skock magnetisation and demagnetisation of basalt by transient stress to 10 kbar; J Geophy., v. 41, p. 23-41.

Pike, R. J., 1985, Some morphologic systematics of complex impact Structures: Meteoritics, v.20, p. 49-68.

Pilkington, M., and Grieve, R. A. F., 1992, The geophysical signature of terrestrial impact craters: Review of Geophysics, v. 30, p. 161-181.

Reidel, S. P., 1975, Bedrock geology of the Serpent Mound cryptoexplosion structure, Adams, Highland, and Pike Counties, Ohio: Ohio Division of Geological Survey Report of Investigations 95, colour map, scale 1:12 000, one sheet with text.

Reidel, S. P., Koucky, F. L., and Stryker, J. R., 1982, The Serpent Mound disturbance, southwestern Ohio: American Journal of Science, v. 282, p. 1343-1377.

Riley, R. A.,, Harper, J., Baranoski, M T, Laughery, C., and Carlton, R., 1993, Reservoirhetrogenety in measuring and predicting complex deposystems the late Cambrian Rose Run sandstone of eastern Ohio and western Pennsylvania: Report of U.S. Dept. of Energy, 257 p.

Roddy, D. J., 1977, Pre-impact conditions and cratering processes at the Flynn Cree Crater, Tennessee, in Roddy, D. J., Pepin, R. O., and Merrill, R. B., eds, Impact and explosion cratering, New York, Pergaman Press. P.277-308.

Rudman, A. J. and Blakely, R. F., 1965, A geophysical study of a basement anomaly in Indiana: Geophysics, v. 30, p. 740-761.

Rudman, A. J., Summerson, C. H., and Hinze, W. J., 1965, Geology of basement in the midwestern United States: American Association of Petroleum Geologists Bulletin, V. 49, no 7, p. 894-904.

Sappenfield, L. W., 1950, A Magnetic Survey of the Adams County Cryptovolcanic Structure: Unpublished Master Thesis, The University of Cincinnati, 27 p.

Sappenfield, L. W., 1951, A magnetic Survey of the Adams County, Ohio cryptovolcanic structure: Compass, v. 28, p. 115-124.

Schumaker, G. A., and Carlton, R. W., 1991, Impure K-bentonite beds from the Lexington limestone and Point Pleasant for Middle Ordovician of northern Kentucky and southwestern Ohio: Ohio Geol., v. 32, p. 83-105.

Sharpton, V. L., and Ward, P. D., 1990, eds, Global catastrophes in Earth history, an Interdisciplinary conference on impacts, volcanism, and mass mortality: Geol. Soc. Am., special paper, 247p.

Sharpton, V. L.,Dalrymple, G. B., Marin, L. E., Ryder, G., Schuraviz, B. C., and Uriutia Fucugauchi, J., 1992, New links between the Chixulub impact structure and the Cretaceous/Tertiary boundary: Nature, v. 359, p. 819-821.

Sharpton, V. L. and others, 1993, Chicxulub multiring impact basin: Size and other characteristics derived from gravity analysis: Sciences, v. 261, p. 1564- 1567.

Short, N. M., 1970, Anatomy of a meteorite impact crater: West Hawk Lake, Manitoba, Canada: Geological Society of America Bulletin, V.81, P.609-648.

Stith, D. A., 1979, Chemical composition, stratigraphy, and depositional environments of theBlack River Group (Middle Ordovician), southwestern Ohio: Ohio Division of Geological Survey Report of Investigation 113, 36 p.

Stith, D. A., 1986, Supplemental core investigations for high-calcium limestones in western Ohio and discussion of natural gas and stratigraphic relationships in the Middle and Upper Ordovician rocks of southwestern Ohio: Ohio Division of Geological Survey Report of Investigations 132, 16p.

Stöffler, D., 1972, Deformation and transformation of rockforming minerals by natural and experimental shock pressures: fortschnie der mineralogica, v. 49, p. 50-113.

Stöffler, D., 1974, Deformation and transformation of rock forming minerals by natural and experimental processes: 2 physical properties of shocked minerals: Fortschritte der Mineralogie, v. 51, p. 256-289.

Stöffler, D., and Langenhorst, F., 1994, Shock metamorphism of quartz and experiment: I. Basic observations and theory: Meteoritics, V.29, P.155-181.

Stout, W., 1941, Dolomite and Limestones of western Ohio: Ohio Division of Geological Survey, Fourth series Bulletin 42, 468 pp.

Stryker, J., R., 1971, Geologic and geochemical survey of the area south of Sinking Springs, Highland County, Ohio: B. S. thesis (unpublished), University of Cincinnati, 25 p.

Summerson, C. H., 1963, Serpent Mound Structure, Adams County, Ohio: A Summary 1 11 p.

Sverjensky, D. A., 1984, Oilfield brines as ore forming solutions: Economic Geology, v. 79, p. 23-37.

Swinford, E. M., 1985, Geology of the Peebles quadrangle, Adams County, Ohio: Ohio Journal of Science, V.85, P. 218-230.

Talwani, M., Worzel, J. L., and Lundisman, M., 1959, Rapid gravity computations for two dimensional bodies: J. Geophys. Res., v. 64, p. 49-59.

Telford, W. M., Geldart, L. P., Sheriff, R. E., Keys, D. A., 1980, Applied Geophysics: Cambridge University press.

Walcott, C. D., 1914, Cambrian geology and paleontology: smithsonian Misc. coll., v. 57, p. 345-412.

Watts, D. R., Elsaiti, B., Baranoski, M. T., and Schumacher, G. A., 1998, Palaeomagnetic constraints on the age of the Serpent Mound disturbance: Geological Society of America abstracts with programs, v.30, no.2.

Watts, D. R., Elsaiti, B., Memmi, J. M., Weaver, J., and Baranoski, M. B., 1998, The Serpent Mound Magnetic Anomaly: Fingerprint of a Meteorite Impact, in press.

Weiss, M. P., and Sweet, W. C., 1964. Kope Formation (Upper Ordovician): Ohio and Kentucky: Science, v. 145, no., 3638, pp. 1296-1302.

Weiss, M. P., Edwards, W. R., Norman, C. E., and Sharp, E. R., 1965, The American Upper Ordovician Standard VIII, stratigraphy and petrography of the Cynthiana and Eden Formations of the Ohio valley: Geol Soc. AM. Special paper 81, 76 p.

Wessel, P., and Walter, H. S., 1995, The generic Mapping Tools (GMT), technical reference and cook book.

Winchell, N. H., 1873, Geology of Wyandot County: Geol. Surv. Ohio, v.1, part 1, p. 633.

Woodward, H. P., 1961, Preliminary subsurface study of south-eastern Appalachian Interior Plateau: American Association of Petroleum Geologists Bulletin, v. 45, p. 1634-1655.

Zahn, J. C., 1965, Subsurface Structure of the Serpent Mound Area in southeastern ,Ohio: Unpublished Master thesis, The Ohio State University.

Zeitz, I., King, E. R., Geddes, W. and Likiak, E. G., 1966. Crustal study of the continental strip from the Atlantic Ocean to the Rocky Mountains: Geol. Soc. America Bull., v. 77, p. 1427-1448.

Zeitz, I., Stockkards, H., and Kirby, J., 1968, Transconetenintal Survey Geophysical survey: United States Geol. Surv. Miscellameous, Geol Invs. Maps.

Zijderveld, J. D. A., 1967, A. C. demagnetisation of rocks: analysis of results, in Methods in Palaeomagnetic, Collision, D. W., Runcorn, S. K., and Crier, K. M. Des, Ellesmere, New York, pp 254-286.

Zinni, E. V., 1982. Gravity survey of southeastern Guernsey County, Ohio: unpublished M. S. thesis, The Ohio State University, pp. 1-79.

APPENDIX I

TYPICAL SEISMIC PROCESSING JOB COTROL FILES

```
/JOB ACCT 'B. M. EL-SAITI' FEET

(1)    SEGYDIN to read seismic data from SEGY files from disk
       Files into the processing buffer for use by subsequent
       processors.

!/SEGYDIN FILENAME 'ODNR'
/SEGYDIN FILENAME 'COLUMBIA'

(2)    Write the data to  SierraSEIS House formatted Disk file

/HOUSDOUT FILENAME 'MAR' DELETE

(3)    Read the from the file apply filter, correlate the shot files
       With the recorded pilot signal and create the file of correlated
       data

/HOUSDIN FILENAME 'MAR'
SORTKEY 'KSHOT'
START 79 END 79
/AUX  IKEYA 'KTRC'
  TRACES D1, 121, 1
/RESAMP   SR 1

/QSFUNON
 NOTCH
 SWEEP 20. 120.  7.
 SCAN  1 .46 .10
      60 .001 .12
     120 .40 .08
/RESAMP   SR 2

/VCORR
 SWEEP 20 10 7000
 TAPER 2 300 300
 TAPESWP
 DATASWP 1
 BADSWEEP 100
/HOUSDOUT   FILENAME 'COR1'  DELETE

(4)    Geometry Processor to define the geometry information nedded to
       Process the seismic data
/GEOMETRY
PRINTALL
GEOMFILE 'SERPENT'
SURVEY
STBASE 42
SPLIST
D104,115,1 D119,124,1 D128,131,1 D134,152,1 D155,163,2 167 168 169 171
173 174
```

```
D177,183,2 186 187 190 191 193 197 198 201 202 D203,211,2 212 216 217
D222,225,1
D227,263,2 264 D267,271,2 D272,274,1 D279,291,2 D292,314,1 D318,331,1
XYBASE 32130.3 1544.4

STATION
42 32130.3 1544.4, 43 32212.8 1544.4, 44 32295.3 1544.4,
45 32377.8 1544.4, 46 32460.3 1544.4, 47 32542.8 1544.4,
48 32625.3 1544.4, 49 32707.8 1544.4, 50 32790.3 1544.4,
51 32872.8 1544.4, 52 32955.3 1544.4, 53 33037.8 1544.4,
54 33120.3 1544.4, 55 33202.8 1544.4, 56 33285.3 1544.4,
57 33367.8 1544.4, 58 33450.3 1544.4, 59 33532.8 1544.4,
60 33615.3 1544.4, 61 33697.8 1544.4, 62 33780.3 1544.4,
63 33862.8 1544.4, 64 33945.3 1544.4, 65 34027.8 1544.4,
66 34110.3 1544.4, 67 34192.8 1544.4, 68 34275.3 1544.4,
69 34357.8 1544.4, 70 34440.3 1544.4, 71 34522.8 1544.4,
72 34605.3 1544.4, 73 34687.8 1544.4, 74 34770.3 1544.4,
75 34852.8 1544.4, 76 34935.3 1544.4, 77 35017.8 1544.4,
78 35100.3 1544.4, 79 35182.8 1544.4, 80 35265.3 1544.4,
81 35347.8 1544.4, 82 35430.3 1544.4, 83 35512.8 1544.4,
84 35595.3 1544.4, 85 35677.8 1544.4, 86 35760.3 1544.4,
87 35842.8 1544.4, 88 35925.3 1544.4, 89 36007.8 1544.4,
90 36090.3 1544.4, 91 36172.8 1544.4, 92 36255.3 1544.4,
93 36337.8 1544.4, 94 36420.3 1544.4, 95 36502.8 1544.4,
96 36585.3 1544.4, 97 36667.8 1544.4, 98 36750.3 1544.4,
99 36832.8 1544.4, 100 36915.3 1544.4,
101 36997.8 1544.4, 102 37009.0 1626.0, 103 37020.2 1707.6,
104 37031.6 1789.3, 105 37042.9 1871.0, 106 37054.2 1952.7,
107 37065.6 2034.4, 108 37076.9 2116.2, 109 37088.2 2197.8,
110 37099.6 2279.5, 111 37110.9 2360.7, 112 37125.0 2441.8,
113 37139.0 2523.0, 114 37153.0 2604.1, 115 37167.0 2685.3,
116 37181.1 2766.4, 117 37195.1 2847.5, 118 37209.1 2928.7,
119 37223.1 3009.8, 120 37228.6 3091.8, 121 37234.2 3173.8,
122 37239.8 3255.8, 123 37245.2 3337.7, 124 37250.8 3419.7,
125 37256.2 3501.7, 126 37282.6 3579.1, 127 37313.6 3655.7,
128 37344.5 3732.3, 129 37375.5 3808.8, 130 37406.4 3885.4,
131 37437.4 3962.0, 132 37468.2 4038.5, 133 37499.2 4115.1,
134 37530.2 4191.7, 135 37561.2 4268.3, 136 37592.1 4344.9,
137 37623.1 4421.5, 138 37654.0 4498.1, 139 37685.0 4574.7,
140 37715.9 4651.2, 141 37746.8 4727.8, 142 37785.6 4800.2,
143 37863.2 4828.8, 144 37946.2 4839.9, 145 38029.4 4850.9,
146 38112.5 4862.0, 147 38195.8 4873.1, 148 38274.2 4895.3,
149 38347.8 4935.8, 150 38402.6 4997.4, 151 38451.5 5063.6,
152 38500.5 5129.9, 153 38549.4 5196.1, 154 38598.2 5262.4,
155 38647.2 5328.5, 156 38674.2 5405.8, 157 38680.2 5488.4,
158 38670.6 5570.2, 159 38651.2 5650.6, 160 38639.8 5731.5,
161 38641.6 5813.5, 162 38648.8 5896.1, 163 38649.8 5977.6,
164 38693.2 6048.1, 165 38774.0 6064.6, 166 38856.0 6064.9,
167 38938.0 6065.1, 168 39019.6 6065.4, 169 39101.5 6065.7,
170 39183.2 6055.5, 171 39256.5 6019.0, 172 39312.8 5958.6,
173 39366.9 5896.7, 174 39432.8 5846.8, 175 39510.4 5819.1,
176 39587.1 5848.5, 177 39647.4 5905.7, 178 39696.6 5972.5,
179 39741.5 6041.6, 180 39776.9 6115.8, 181 39799.9 6195.3,
182 39819.4 6275.9, 183 39834.5 6357.0, 184 39849.8 6438.1,
185 39864.9 6519.4, 186 39880.1 6600.5, 187 39889.2 6683.1,
188 39891.8 6765.3, 189 39894.1 6847.6, 190 39896.6 6929.7,
```

```
191 39899.1 7012.0, 192 39901.5 7094.3, 193 39904.0 7176.5,
194 39906.4 7258.8, 195 39918.0 7339.4, 196 39936.8 7420.5,
197 39993.8 7479.6, 198 40064.1 7523.6, 199 40124.8 7580.8,
200 40136.4 7664.4, 201 40125.2 7744.6, 202 40105.9 7823.7,
203 40086.8 7902.7, 204 40083.8 7983.8, 205 40093.8 8065.9,
206 40163.1 8110.6, 207 40246.0 8112.3, 208 40328.8 8114.0,
209 40407.6 8138.2, 210 40486.5 8162.5, 211 40565.2 8186.7,
212 40647.2 8192.7, 213 40729.5 8198.6, 214 40811.6 8204.6,
215 40893.5 8210.5, 216 40975.6 8216.5, 217 41057.5 8222.4,
218 41138.8 8228.3, 219 41220.4 8234.2, 220 41302.4 8240.1,
221 41383.6 8222.3, 222 41455.6 8183.6, 223 41516.6 8128.3,
224 41572.8 8067.4, 225 41620.2 7999.2, 226 41673.2 7936.5,
227 41722.8 7870.6, 228 41781.2 7810.7, 229 41844.2 7760.8,
230 41923.2 7733.6, 231 42006.2 7742.2, 232 42087.4 7753.8,
233 42169.6 7758.8, 234 42252.1 7758.0, 235 42334.5 7755.3,
236 42417.2 7756.7, 237 42498.8 7769.5, 238 42579.4 7791.8,
239 42646.2 7841.1, 240 42686.4 7913.2, 241 42719.1 7988.8,
242 42729.5 8070.6, 243 42737.8 8152.7, 244 42792.9 8211.7,
245 42865.6 8250.5, 246 42938.4 8289.3, 247 43011.1 8328.1,
248 43083.9 8366.9, 249 43156.5 8405.7, 250 43224.4 8451.9,
251 43275.1 8517.2, 252 43294.8 8597.9, 253 43305.1 8678.9,
254 43325.5 8758.1, 255 43378.2 8820.5, 256 43449.8 8860.1,
257 43521.8 8899.9, 258 43593.8 8939.7, 259 43665.9 8979.6,
260 43738.0 9019.5, 261 43806.8 9065.2, 262 43875.6 9110.9,
263 43944.4 9156.7, 264 44013.2 9202.4, 265 44082.1 9248.1,
266 44150.8 9293.8, 267 44219.6 9339.5, 268 44288.4 9385.2,
269 44338.5 9451.2, 270 44376.8 9524.2, 271 44408.8 9600.5,
272 44454.9 9668.5, 273 44509.8 9730.5, 274 44566.8 9789.6,
275 44636.5 9833.5, 276 44706.2 9877.5, 277 44776.1 9921.5,
278 44853.0 9952.2, 279 44934.9 9961.4, 280 45017.1 9955.8,
281 45097.9 9940.6, 282 45177.6 9919.2, 283 45244.8 9870.0,
284 45306.6 9816.0, 285 45368.1 9762.2, 286 45429.6 9708.5,
287 45491.0 9654.8, 288 45552.4 9601.1, 289 45613.8 9547.5,
290 45674.9 9494.0, 291 45713.0 9422.2, 292 45727.1 9341.2,
293 45741.2 9260.5, 294 45755.4 9179.8, 295 45769.5 9099.0,
296 45839.5 9058.7, 297 45920.0 9051.0, 298 46000.4 9043.2,
299 46080.8 9035.4, 300 46161.2 9027.6, 301 46241.9 9019.8,
302 46323.5 9011.9, 303 46405.2 9005.0, 304 46486.9 8998.0,
305 46568.6 8991.1, 306 46650.8 8984.2, 307 46732.9 8977.2,
308 46814.8 8970.3, 309 46896.6 8963.3, 310 46978.6 8956.4,
311 47060.5 8949.4, 312 47142.4 8942.5, 313 47224.4 8935.5,
314 47306.2 8928.6, 315 47388.1 8921.7, 316 47470.2 8914.7,
317 47552.2 8907.7, 318 47634.4 8900.7, 319 47716.4 8893.7,
320 47798.1 8886.7, 321 47879.8 8879.7, 322 47961.8 8872.7,
323 48043.2 8865.8, 324 48111.5 8917.2, 325 48131.5 8997.7,
326 48151.6 9078.1, 327 48171.6 9158.7, 328 48191.6 9239.2,
329 48186.2 9321.7, 330 48178.0 9404.5, 331 48178.4 9486.8,
332 48202.8 9564.8, 333 48242.6 9637.1,
334 48325.1 9637.1, 335 48407.6 9637.1, 336 48490.1 9637.1,
337 48572.6 9637.1, 338 48655.1 9637.1, 339 48737.6 9637.1,
340 48820.1 9637.1, 341 48902.6 9637.1, 342 48985.1 9637.1,
343 49067.6 9637.1, 344 49150.1 9637.1, 345 49232.6 9637.1,
346 49315.1 9637.1, 347 49397.6 9637.1, 348 49480.1 9637.1,
349 49562.6 9637.1, 350 49645.1 9637.1, 351 49727.6 9637.1,
352 49810.1 9637.1, 353 49892.6 9637.1, 354 49975.1 9637.1,
355 50057.6 9637.1, 356 50140.1 9637.1, 357 50222.6 9637.1,
```

```
358 50305.1 9637.1, 359 50387.6 9637.1, 360 50470.1 9637.1,
361 50552.6 9637.1, 362 50635.1 9637.1, 363 50717.6 9637.1,
364 50800.1 9637.1, 365 50882.6 9637.1, 366 50965.1 9637.1,
367 51047.6 9637.1, 368 51130.1 9637.1, 369 51212.6 9637.1,
370 51295.1 9637.1, 371 51377.6 9637.1, 372 51460.1 9637.1,
373 51542.6 9637.1, 374 51625.1 9637.1, 375 51707.6 9637.1,
376 51790.1 9637.1, 377 51872.6 9637.1, 378 51955.1 9637.1,
379 52037.6 9637.1, 380 52120.1 9637.1, 381 52202.6 9637.1,
382 52285.1 9637.1, 383 52367.6 9637.1, 384 52450.1 9637.1,
385 52532.6 9637.1, 386 52615.1 9637.1, 387 52697.6 9637.1,
388 52780.1 9637.1, 389 52862.6 9637.1, 390 52945.1 9637.1,
391 53027.6 9637.1, 392 53110.1 9637.1, 393 53192.6 9637.1,

SHOT 104 AT 104 INTO D42,101,1 D107,166,1
SHOT 105 AT 105 INTO D42,101,1 D108,167,1
SHOT 106 AT 106 INTO D42,101,1 D109,168,1
SHOT 107 AT 107 INTO D43,102,1 D110,169,1
SHOT 108 AT 108 INTO D44,103,1 D111,170,1
SHOT 109 AT 109 INTO D45,104,1 D112,171,1
SHOT 110 AT 110 INTO D46,105,1 D113,172,1
SHOT 111 AT 111 INTO D47,106,1 D114,173,1
SHOT 112 AT 112 INTO D48,107,1 D115,174,1
SHOT 113 AT 113 INTO D49,108,1 D116,175,1
SHOT 114 AT 114 INTO D50,109,1 D117,176,1
SHOT 115 AT 115 INTO D51,110,1 D118,177,1
SHOT 119 AT 119 INTO D55,114,1 D122,181,1
SHOT 120 AT 120 INTO D56,115,1 D123,182,1
SHOT 121 AT 121 INTO D57,116,1 D124,183,1
SHOT 122 AT 122 INTO D58,117,1 D125,184,1
SHOT 123 AT 123 INTO D59,118,1 D126,185,1
SHOT 124 AT 124 INTO D60,119,1 D127,186,1
SHOT 128 AT 128 INTO D64,123,1 D131,190,1
SHOT 129 AT 129 INTO D65,124,1 D132,191,1
SHOT 130 AT 130 INTO D66,125,1 D133,192,1
SHOT 131 AT 131 INTO D67,126,1 D134,193,1
SHOT 134 AT 134 INTO D70,129,1 D137,196,1
SHOT 135 AT 135 INTO D71,130,1 D138,197,1
SHOT 136 AT 136 INTO D72,131,1 D139,198,1
SHOT 137 AT 137 INTO D73,132,1 D140,199,1
SHOT 138 AT 138 INTO D74,133,1 D141,200,1
SHOT 139 AT 139 INTO D75,134,1 D142,201,1
SHOT 140 AT 140 INTO D76,135,1 D143,202,1
SHOT 141 AT 141 INTO D77,136,1 D144,203,1
SHOT 142 AT 142 INTO D78,137,1 D145,204,1
SHOT 143 AT 143 INTO D79,138,1 D146,205,1
SHOT 144 AT 144 INTO D80,139,1 D147,206,1
SHOT 145 AT 145 INTO D81,140,1 D148,207,1
SHOT 146 AT 146 INTO D82,141,1 D149,208,1
SHOT 147 AT 147 INTO D83,142,1 D150,209,1
SHOT 148 AT 148 INTO D84,143,1 D151,210,1
SHOT 149 AT 149 INTO D85,144,1 D152,211,1
SHOT 150 AT 150 INTO D86,145,1 D153,212,1
SHOT 151 AT 151 INTO D87,146,1 D154,213,1
SHOT 152 AT 152 INTO D88,147,1 D155,214,1
SHOT 155 AT 155 INTO D91,150,1 D158,217,1
SHOT 157 AT 157 INTO D93,152,1 D160,219,1
```

```
SHOT 159 AT 159 INTO D95,154,1 D162,221,1
SHOT 161 AT 161 INTO D97,156,1 D164,223,1
SHOT 163 AT 163 INTO D99,158,1 D166,225,1
SHOT 167 AT 167 INTO D103,162,1 D170,229,1
SHOT 168 AT 168 INTO D104,163,1 D171,230,1
SHOT 169 AT 169 INTO D105,164,1 D172,231,1
SHOT 171 AT 171 INTO D107,166,1 D174,233,1
SHOT 173 AT 173 INTO D109,168,1 D176,235,1
SHOT 174 AT 174 INTO D110,169,1 D177,236,1
SHOT 177 AT 177 INTO D113,172,1 D180,239,1
SHOT 179 AT 179 INTO D115,174,1 D182,241,1
SHOT 181 AT 181 INTO D117,176,1 D184,243,1
SHOT 183 AT 183 INTO D119,178,1 D186,245,1
SHOT 186 AT 186 INTO D122,181,1 D189,248,1
SHOT 187 AT 187 INTO D123,182,1 D190,249,1
SHOT 190 AT 190 INTO D126,185,1 D193,252,1
SHOT 191 AT 191 INTO D127,186,1 D194,253,1
SHOT 193 AT 193 INTO D129,188,1 D196,255,1
SHOT 197 AT 197 INTO D133,192,1 D200,259,1
SHOT 198 AT 198 INTO D134,193,1 D201,260,1
SHOT 201 AT 201 INTO D137,196,1 D204,263,1
SHOT 202 AT 202 INTO D138,197,1 D205,264,1
SHOT 203 AT 203 INTO D139,198,1 D206,265,1
SHOT 205 AT 205 INTO D141,200,1 D208,267,1
SHOT 207 AT 207 INTO D143,202,1 D210,269,1
SHOT 209 AT 209 INTO D145,204,1 D212,271,1
SHOT 211 AT 211 INTO D147,206,1 D214,273,1
SHOT 212 AT 212 INTO D148,207,1 D215,274,1
SHOT 216 AT 216 INTO D152,211,1 D219,278,1
SHOT 217 AT 217 INTO D153,212,1 D220,279,1
SHOT 222 AT 222 INTO D158,217,1 D225,284,1
SHOT 223 AT 223 INTO D159,218,1 D226,285,1
SHOT 224 AT 224 INTO D160,219,1 D227,286,1
SHOT 225 AT 225 INTO D161,220,1 D228,287,1
SHOT 227 AT 227 INTO D163,222,1 D230,289,1
SHOT 229 AT 229 INTO D165,224,1 D232,291,1
SHOT 231 AT 231 INTO D167,226,1 D234,293,1
SHOT 233 AT 233 INTO D169,228,1 D236,295,1
SHOT 235 AT 235 INTO D171,230,1 D238,297,1
SHOT 237 AT 237 INTO D173,232,1 D240,299,1
SHOT 239 AT 239 INTO D175,234,1 D242,301,1
SHOT 241 AT 241 INTO D177,236,1 D244,303,1
SHOT 243 AT 243 INTO D179,238,1 D246,305,1
SHOT 245 AT 245 INTO D181,240,1 D248,307,1
SHOT 247 AT 247 INTO D183,242,1 D250,309,1
SHOT 249 AT 249 INTO D185,244,1 D252,311,1
SHOT 251 AT 251 INTO D187,246,1 D254,313,1
SHOT 253 AT 253 INTO D189,248,1 D256,315,1
SHOT 255 AT 255 INTO D191,250,1 D258,317,1
SHOT 257 AT 257 INTO D193,252,1 D260,319,1
SHOT 259 AT 259 INTO D195,254,1 D262,321,1
SHOT 261 AT 261 INTO D197,256,1 D264,323,1
SHOT 263 AT 263 INTO D199,258,1 D266,325,1
SHOT 264 AT 264 INTO D200,259,1 D267,326,1
SHOT 267 AT 267 INTO D203,262,1 D270,329,1
SHOT 269 AT 269 INTO D205,264,1 D272,331,1
```

```
SHOT 271 AT 271 INTO D207,266,1 D274,333,1
SHOT 272 AT 272 INTO D208,267,1 D275,334,1
SHOT 273 AT 273 INTO D209,268,1 D276,335,1
SHOT 274 AT 274 INTO D210,269,1 D277,336,1
SHOT 279 AT 279 INTO D215,274,1 D282,341,1
SHOT 281 AT 281 INTO D217,276,1 D284,343,1
SHOT 283 AT 283 INTO D219,278,1 D286,345,1
SHOT 285 AT 285 INTO D221,280,1 D288,347,1
SHOT 287 AT 287 INTO D223,282,1 D290,349,1
SHOT 289 AT 289 INTO D225,284,1 D292,351,1
SHOT 291 AT 291 INTO D227,286,1 D294,353,1
SHOT 292 AT 292 INTO D228,287,1 D295,354,1
SHOT 293 AT 293 INTO D229,288,1 D296,355,1
SHOT 294 AT 294 INTO D230,289,1 D297,356,1
SHOT 295 AT 295 INTO D231,290,1 D298,357,1
SHOT 296 AT 296 INTO D232,291,1 D299,358,1
SHOT 297 AT 297 INTO D233,292,1 D300,359,1
SHOT 298 AT 298 INTO D234,293,1 D301,360,1
SHOT 299 AT 299 INTO D235,294,1 D302,361,1
SHOT 300 AT 300 INTO D236,295,1 D303,362,1
SHOT 301 AT 301 INTO D237,296,1 D304,363,1
SHOT 302 AT 302 INTO D238,297,1 D305,364,1
SHOT 303 AT 303 INTO D239,298,1 D306,365,1
SHOT 304 AT 304 INTO D240,299,1 D307,366,1
SHOT 305 AT 305 INTO D241,300,1 D308,367,1
SHOT 306 AT 306 INTO D242,301,1 D309,368,1
SHOT 307 AT 307 INTO D243,302,1 D310,369,1
SHOT 308 AT 308 INTO D244,303,1 D311,370,1
SHOT 309 AT 309 INTO D245,304,1 D312,371,1
SHOT 310 AT 310 INTO D246,305,1 D313,372,1
SHOT 311 AT 311 INTO D247,306,1 D314,373,1
SHOT 312 AT 312 INTO D248,307,1 D315,374,1
SHOT 313 AT 313 INTO D249,308,1 D316,375,1
SHOT 314 AT 314 INTO D250,309,1 D317,376,1
SHOT 318 AT 318 INTO D254,313,1 D321,380,1
SHOT 319 AT 319 INTO D255,314,1 D322,381,1
SHOT 320 AT 320 INTO D256,315,1 D323,382,1
SHOT 321 AT 321 INTO D257,316,1 D324,383,1
SHOT 322 AT 322 INTO D258,317,1 D325,384,1
SHOT 323 AT 323 INTO D259,318,1 D326,385,1
SHOT 324 AT 324 INTO D260,319,1 D327,386,1
SHOT 325 AT 325 INTO D261,320,1 D328,387,1
SHOT 326 AT 326 INTO D262,321,1 D329,388,1
SHOT 327 AT 327 INTO D263,322,1 D330,389,1
SHOT 328 AT 328 INTO D264,323,1 D331,390,1
SHOT 329 AT 329 INTO D265,324,1 D332,391,1
SHOT 330 AT 330 INTO D266,325,1 D333,392,1
SHOT 331 AT 331 INTO D267,326,1 D334,393,1


PROF
DATUM 700
DVEL 12000
SPD R0, 147
WVEL 5000
WDEPTH 10
```

```
SPELX

104 744.0, 105 747.2, 106 749.8, 107 753.3,
108 756.2, 109 760.2, 110 765.1, 111 768.5,
112 767.9, 113 767.5, 114 767.3, 115 767.3,
119 767.4, 120 766.8, 121 766.7, 122 766.9,
123 768.2, 124 769.5, 128 769.4, 129 768.7,
130 770.9, 131 776.2, 134 781.5, 135 781.2,
136 782.2, 137 782.6, 138 782.5, 139 783.9,
140 787.1, 141 792.4, 142 798.1, 143 800.3,
144 802.2, 145 807.5, 146 813.8, 147 816.2,
148 817.3, 149 811.0, 150 803.3, 151 798.6,
152 797.1, 155 801.5, 157 797.5, 159 797.0,
161 788.0, 163 768.4, 167 780.0, 168 789.7,
169 796.8, 171 808.8, 173 814.7, 174 814.3,
177 821.9, 179 827.9, 181 837.1, 183 840.9,
186 840.0, 187 836.4, 190 846.3, 191 847.6,
193 838.5, 197 847.3, 198 854.0, 201 860.5,
202 855.6, 203 845.3, 205 828.8, 207 828.5,
209 823.9, 211 833.4, 212 840.0, 216 868.7,
217 877.5, 222 911.0, 223 907.9, 224 906.2,
225 904.5, 227 905.9, 229 925.9, 231 941.2,
233 954.7, 235 962.6, 237 966.8, 239 983.0,
241 983.7, 243 973.0, 245 965.8, 247 959.9,
249 963.5, 251 973.0, 253 978.1, 255 967.3,
257 952.3, 259 944.4, 261 941.1, 263 937.9,
264 941.5, 267 957.7, 269 957.8, 271 951.4,
272 944.8, 273 939.7, 274 940.2, 279 944.8,
281 940.3, 283 935.8, 285 921.2, 287 901.7,
289 880.9, 291 863.9, 292 861.0, 293 855.2,
294 847.8, 295 842.1, 296 839.3, 297 838.4,
298 833.5, 299 838.5, 300 847.5, 301 849.8,
302 846.2, 303 837.6, 304 831.2, 305 824.9,
306 825.5, 307 829.4, 308 822.3, 309 819.9,
310 820.7, 311 818.5, 312 813.9, 313 815.2,
314 809.7, 318 809.6, 319 802.0, 320 793.2,
321 784.6, 322 776.4, 323 764.9, 324 761.2,
325 759.1, 326 757.7, 327 756.6, 328 755.4,
329 754.6, 330 753.8, 331 753.6,

GPELX
42 754.1, 43 754.1, 44 754.1,
45 754.1, 46 754.1, 47 754.1,
48 754.1, 49 754.1, 50 754.1,
51 754.1, 52 754.1, 53 754.1,
54 754.1, 55 754.1, 56 754.1,
57 754.1, 58 754.1, 59 754.1,
60 754.1, 61 754.1, 62 754.1,
63 754.1, 64 754.1, 65 754.1,
66 754.1, 67 754.1, 68 754.1,
69 754.1, 70 754.1, 71 754.1,
72 754.1, 73 754.1, 74 754.1,
75 754.1, 76 754.1, 77 754.1,
```

```
78 754.1, 79 754.1, 80 754.1,
81 754.1, 82 754.1, 83 754.1,
84 754.1, 85 754.1, 86 754.1,
87 754.1, 88 754.1, 89 754.1,
90 754.1, 91 754.1, 92 754.1,
93 754.1, 94 754.1, 95 754.1,
96 754.1, 97 754.1, 98 754.1,
99 754.1, 100 754.1,
101 727.6, 102 733.5, 103 739.5, 104 744.0,
105 747.2, 106 749.8, 107 753.3, 108 756.2,
109 760.2, 110 765.1, 111 768.5, 112 767.9,
113 767.5, 114 767.3, 115 767.3, 116 768.3,
117 769.2, 118 768.5, 119 767.4, 120 766.8,
121 766.7, 122 766.9, 123 768.2, 124 769.5,
125 770.9, 126 771.5, 127 771.3, 128 769.4,
129 768.7, 130 770.9, 131 776.2, 132 781.1,
133 782.7, 134 781.5, 135 781.2, 136 782.2,
137 782.6, 138 782.5, 139 783.9, 140 787.1,
141 792.4, 142 798.1, 143 800.3, 144 802.2,
145 807.5, 146 813.8, 147 816.2, 148 817.3,
149 811.0, 150 803.3, 151 798.6, 152 797.1,
153 801.8, 154 803.7, 155 801.5, 156 801.4,
157 797.5, 158 797.4, 159 797.0, 160 793.4,
161 788.0, 162 780.4, 163 768.4, 164 766.8,
165 770.4, 166 774.1, 167 780.0, 168 789.7,
169 796.8, 170 803.3, 171 808.8, 172 813.0,
173 814.7, 174 814.3, 175 812.9, 176 817.4,
177 821.9, 178 823.6, 179 827.9, 180 832.0,
181 837.1, 182 840.3, 183 840.9, 184 841.5,
185 843.0, 186 840.0, 187 836.4, 188 835.6,
189 841.0, 190 846.3, 191 847.6, 192 843.3,
193 838.5, 194 840.0, 195 844.0, 196 843.0,
197 847.3, 198 854.0, 199 855.3, 200 858.0,
201 860.5, 202 855.6, 203 845.3, 204 834.3,
205 828.8, 206 828.1, 207 828.5, 208 826.9,
209 823.9, 210 828.7, 211 833.4, 212 840.0,
213 846.2, 214 852.5, 215 861.7, 216 868.7,
217 877.5, 218 890.6, 219 902.9, 220 911.1,
221 913.3, 222 911.0, 223 907.9, 224 906.2,
225 904.5, 226 903.2, 227 905.9, 228 914.8,
229 925.9, 230 933.0, 231 941.2, 232 949.1,
233 954.7, 234 959.0, 235 962.6, 236 964.1,
237 966.8, 238 974.2, 239 983.0, 240 986.1,
241 983.7, 242 977.2, 243 973.0, 244 970.5,
245 965.8, 246 961.7, 247 959.9, 248 960.7,
249 963.5, 250 968.1, 251 973.0, 252 976.6,
253 978.1, 254 975.5, 255 967.3, 256 958.4,
257 952.3, 258 947.6, 259 944.4, 260 942.8,
261 941.1, 262 937.0, 263 937.9, 264 941.5,
265 947.8, 266 953.8, 267 957.7, 268 960.2,
269 957.8, 270 954.6, 271 951.4, 272 944.8,
273 939.7, 274 940.2, 275 945.0, 276 948.8,
277 950.3, 278 948.5, 279 944.8, 280 941.8,
281 940.3, 282 939.4, 283 935.8, 284 929.8,
285 921.2, 286 911.9, 287 901.7, 288 891.6,
289 880.9, 290 868.5, 291 863.9, 292 861.0,
```

```
293 855.2, 294 847.8, 295 842.1, 296 839.3,
297 838.4, 298 833.5, 299 838.5, 300 847.5,
301 849.8, 302 846.2, 303 837.6, 304 831.2,
305 824.9, 306 825.5, 307 829.4, 308 822.3,
309 819.9, 310 820.7, 311 818.5, 312 813.9,
313 815.2, 314 809.7, 315 809.0, 316 816.1,
317 814.2, 318 809.6, 319 802.0, 320 793.2,
321 784.6, 322 776.4, 323 764.9, 324 761.2,
325 759.1, 326 757.7, 327 756.6, 328 755.4,
329 754.6, 330 753.8, 331 753.6, 332 754.1,
333 754.1,
334 754.1, 335 754.1, 336 754.1,
337 754.1, 338 754.1, 339 754.1,
340 754.1, 341 754.1, 342 754.1,
343 754.1, 344 754.1, 345 754.1,
346 754.1, 347 754.1, 348 754.1,
349 754.1, 350 754.1, 351 754.1,
352 754.1, 353 754.1, 354 754.1,
355 754.1, 356 754.1, 357 754.1,
358 754.1, 359 754.1, 360 754.1,
361 754.1, 362 754.1, 363 754.1,
364 754.1, 365 754.1, 366 754.1,
367 754.1, 368 754.1, 369 754.1,
370 754.1, 371 754.1, 372 754.1,
373 754.1, 374 754.1, 375 754.1,
376 754.1, 377 754.1, 378 754.1,
379 754.1, 380 754.1, 381 754.1,
382 754.1, 383 754.1, 384 754.1,
385 754.1, 386 754.1, 387 754.1,
388 754.1, 389 754.1, 390 754.1,
391 754.1, 392 754.1, 393 754.1,
```

(5) PLGEOM to generate plots, diagrams for the verification of Geometry Information

```
/PLGEOM
 DESC 'GEOMETRY SERPENT MOUND LINE BV1 OHIO DEPT NATURAL RESOURCES'
 GEOMFILE 'SERPENT'
 PROF
 XSCL 60
 BASE
 ALLCDPS
 !CDPT
 CDPL
 CDPDOC 10
 SP
```

(6) Apply trace Editing, select traces to zero and apply Mute to traces

```
/GEOMETRY
 GEOMFILE 'SERPENT'
 USE

/ZERO IKEYA 'KSHOT' IVAL 1
      IKEYB 'KTRC ' IVAL D1,60,1 72 73 80 81 86 D96,101,1,D107,110,1
```

```
/ZERO IKEYA 'KSHOT' IVAL 2
      IKEYB 'KTRC ' IVAL D1,59,1 D73,80,1 108 109 110 112 113 114 115
116 117
/ZERO IKEYA 'KSHOT' IVAL 3
      IKEYB 'KTRC ' IVAL D1,58,1 73 74 84 95 96 102 109 110 111
D116,120,1
/ZERO IKEYA 'KSHOT' IVAL 4
      IKEYB 'KTRC ' IVAL D1,57,1 D71,74,1 82 83 91 D97,101,1
 D105,110,1 D114,118,1
/ZERO IKEYA 'KSHOT' IVAL 5
      IKEYB 'KTRC ' IVAL D1,56,1 79 80 D92,96,1 110 111 112 113 117
120
/ZERO IKEYA 'KSHOT' IVAL 6
      IKEYB 'KTRC ' IVAL D1,56,1 73 79 80 D102,105,1 109 110 116 120
/ZERO IKEYA 'KSHOT' IVAL 7
      IKEYB 'KTRC ' IVAL D1,52,1 D76,78,1 102 104 105 D109,112,1 118
119
/ZERO IKEYA 'KSHOT' IVAL 8
      IKEYB 'KTRC ' IVAL D1,54,1, 85 86 D103,105,1 D109,111,1 116 117
120
/ZERO IKEYA 'KSHOT' IVAL 9
      IKEYB 'KTRC ' IVAL D1,52,1 83 95 102 103 107 108 109 112 113 118
119
/ZERO IKEYA 'KSHOT' IVAL 10
      IKEYB 'KTRC ' IVAL D1,52,1 70 71 83 97 D102,107,1 109 116 118
/ZERO IKEYA 'KSHOT' IVAL 11
      IKEYB 'KTRC ' IVAL D1,50,1 64 91 92 106 108 109 118 119
/ZERO IKEYA 'KSHOT' IVAL 12
      IKEYB 'KTRC ' IVAL D1,45,1 70 84 85 86 D93,96,1 D102,108,1 112
113 117
118 120
/ZERO IKEYA 'KSHOT' IVAL 13
      IKEYB 'KTRC ' IVAL D1,44,1 46 47 48 90 96 D101,104,1 D109,112,1
119 120
/ZERO IKEYA 'KSHOT' IVAL 14
      IKEYB 'KTRC ' IVAL D1,43,1 58 D78,81,1 D93,97,1 D100,102,1 104
D110,113,1
   D117,119,1
/ZERO IKEYA 'KSHOT' IVAL 15
      IKEYB 'KTRC ' IVAL D1,42,1 D82,85,1 D92,105,1 110 111 120
/ZERO IKEYA 'KSHOT' IVAL 16
      IKEYB 'KTRC ' IVAL D1,42,1 D90,94,1 D97,102,1 D106,109,1 120
/ZERO IKEYA 'KSHOT' IVAL 17
      IKEYB 'KTRC ' IVAL D1,40,1 50 51 85 86 91 92 93 94 98 107 112
113
/ZERO IKEYA 'KSHOT' IVAL 18
      IKEYB 'KTRC ' IVAL D1,39,1 41 43 47 51 52 74 75 D81,83,1
D89,92,1 D95,99,1
 D104,106,1 D115,117,1
/ZERO IKEYA 'KSHOT' IVAL 19
      IKEYB 'KTRC ' IVAL D1,37,1 44 66 67 76 87 88 D92,95,1 D102,104,1
112 113
  119 120
/ZERO IKEYA 'KSHOT' IVAL 20
      IKEYB 'KTRC ' IVAL D1,35,1 D38,40,1 64 65 77 78 D92,94,1
D100,103,1
```

```
 D109,111,1 D118,120,1
/ZERO IKEYA 'KSHOT' IVAL 21
      IKEYB 'KTRC ' IVAL D1,34,1 D46,48,1 D82,85,1 D90,92,1 D100,102,1
 D108,110,1 D114,118,1
/ZERO IKEYA 'KSHOT' IVAL 22
      IKEYB 'KTRC ' IVAL D1,32,1 39 40 41 66 82 94 100 102 107 108 115
116
/ZERO IKEYA 'KSHOT' IVAL 23
      IKEYB 'KTRC ' IVAL D1,32,1 42 52 72 87 88 100 D104,107,1
D111,116,1
/ZERO IKEYA 'KSHOT' IVAL 24
      IKEYB 'KTRC ' IVAL D1,30,1 36 D87,89,1 96 100 101 102 105 106
D110,112,1
116 120
/ZERO IKEYA 'KSHOT' IVAL 25
      IKEYB 'KTRC ' IVAL D1,28,1 36 48 49 72 D83,85,1 D90,94,1 96 98
103 111 118
/ZERO IKEYA 'KSHOT' IVAL 26
      IKEYB 'KTRC ' IVAL D1,31,1 D45,47,1 74 75 83 D91,94,1 102 108
109
/ZERO IKEYA 'KSHOT' IVAL 27
      IKEYB 'KTRC ' IVAL D1,27,1 41 45 46 49 81 82 90 D96,98,1
D104,106,1
 D112,114,1
/ZERO IKEYA 'KSHOT' IVAL 28
      IKEYB 'KTRC ' IVAL
D1,26,1,D41,43,1,D78,80,1,83,D87,91,1,D104,107,1
 D115,118,1
/ZERO IKEYA 'KSHOT' IVAL 29
      IKEYB 'KTRC ' IVAL D1,24,1 30 31 41 42 72 78 79 87 88 D101,103,1
113
/ZERO IKEYA 'KSHOT' IVAL 30
      IKEYB 'KTRC ' IVAL D1,17,1 21 26 D37,39,1 75 86 87 93 101 102
103 111 112

/ZERO IKEYA 'KSHOT' IVAL 31
      IKEYB 'KTRC ' IVAL D1,16,1 19 20 24 32 39 40 73 D89,91,1 99 102
106
109 D115,117,1 119 120
/ZERO IKEYA 'KSHOT' IVAL 32
      IKEYB 'KTRC ' IVAL D1,17,1 26 33 71 82 91 93 106 119
/ZERO IKEYA 'KSHOT' IVAL 33
      IKEYB 'KTRC ' IVAL D1,16,1 26 27 32 38 39 69 72 89 92 99 100
D111,114,1
/ZERO IKEYA 'KSHOT' IVAL 34
      IKEYB 'KTRC ' IVAL D1,14,1 27 28 66 67 75 76 89 91 93 94 107 112
/ZERO IKEYA 'KSHOT' IVAL 35
      IKEYB 'KTRC ' IVAL D1,11,1 15 16 21 27 37 65 74 75 80 88 89 100
109 110 111
/ZERO IKEYA 'KSHOT' IVAL 36
      IKEYB 'KTRC ' IVAL D1,9,1  24 25 27 28 63 80 84 85 94 95
D99,102,1 105 113 119
/ZERO IKEYA 'KSHOT' IVAL 37
      IKEYB 'KTRC ' IVAL D1,8,1 11 12 16 24 25 26 47 D70,72,1 78 84 85
88 89 90 94
D100,103,1 113 114 115 116 117
```

```
/ZERO IKEYA 'KSHOT' IVAL 38
      IKEYB 'KTRC ' IVAL D1,5,1 8 9 15 16 23 26 82 85 92 D100,103,1
107 110 111 117
/ZERO IKEYA 'KSHOT' IVAL 39
      IKEYB 'KTRC ' IVAL D1,3,1 15 16 D19,26,1 83 90 93  95 101 102
109 113 116 120

/ZERO IKEYA 'KSHOT' IVAL 40
      IKEYB 'KTRC ' IVAL 1 7 D17,21,1 36 37 88 89 98 99 110 120

/ZERO IKEYA 'KSHOT' IVAL 41
      IKEYB 'KTRC ' IVAL 21 22 46 58 59 82 88 89 90 D104,107,1 112 113
/ZERO IKEYA 'KSHOT' IVAL 42
      IKEYB 'KTRC ' IVAL 7 19 57 80 86 87 88 90 D102,106,1
/ZERO IKEYA 'KSHOT' IVAL 43
      IKEYB 'KTRC ' IVAL D11,14,1 17 34 54 56 D86,89,1 94 99 100 101
113 114
/ZERO IKEYA 'KSHOT' IVAL 44
      IKEYB 'KTRC ' IVAL D13,16,1 45 46 52 76 84 92 93 101 106 107
/ZERO IKEYA 'KSHOT' IVAL 45
      IKEYB 'KTRC ' IVAL 8 12 35 36 D44,46,1 50 56 97 98 99 104 105
/ZERO IKEYA 'KSHOT' IVAL 46
      IKEYB 'KTRC ' IVAL 5 9 11 12 27 36 37 38 80 89 94 95 96 97 116
/ZERO IKEYA 'KSHOT' IVAL 47
      IKEYB 'KTRC ' IVAL 4 8 9 10 27 28 31 35 36 39 78 86 94 95 96 97
102 110 111 120
/ZERO IKEYA 'KSHOT' IVAL 48
      IKEYB 'KTRC ' IVAL 1 5 6 10 12 16 17 23 24 26 28 30 34 37 38 76
77 80 83 84
85 D91,95,1 D98,101,1 120
/ZERO IKEYA 'KSHOT' IVAL 49
      IKEYB 'KTRC ' IVAL 3 4 22 23 D31,34,1 36 74 75 76 D81,84,1
D89,91,1 98 106 114 118
/ZERO IKEYA 'KSHOT' IVAL 50
      IKEYB 'KTRC ' IVAL 3 87 D95,98,1 112 113 115 116
/ZERO IKEYA 'KSHOT' IVAL 51
      IKEYB 'KTRC ' IVAL 1 14 17 18 19 24 25 D28,30,1 34 35 43 45 46
78 85 86
94D103,105,1 D110,112,1 114 115
/ZERO IKEYA 'KSHOT' IVAL 52
      IKEYB 'KTRC ' IVAL 2 10 11 12 15 16 24 25 75 82 83 91 93 97 98
99 107 108 110
111 112 120
/ZERO IKEYA 'KSHOT' IVAL 53
      IKEYB 'KTRC ' IVAL 10 11 16 17 24 25 34 41 45 67 74 75 82 83 84
90 91 105 106 110
/ZERO IKEYA 'KSHOT' IVAL 54
      IKEYB 'KTRC ' IVAL 4 13 14 15 16 24 38 41 42 65 73 74 81 82 88
89 90 98 105 106
/ZERO IKEYA 'KSHOT' IVAL 55
      IKEYB 'KTRC ' IVAL 11 39 40 70 71 77 78 79 84 85 86 95 96 102
103 104 110
/ZERO IKEYA 'KSHOT' IVAL 56
      IKEYB 'KTRC ' IVAL 3 8 9 16 24 25 32 68 76 77 78 82 83 84 90 99
100 101 108 109
110 111 114 117 118
```

```
/ZERO IKEYA 'KSHOT' IVAL 57
      IKEYB 'KTRC ' IVAL 7 8 21 23 39 66 74 75 D80,83,1 85 87 88 93 94
95 98 115 119
/ZERO IKEYA 'KSHOT' IVAL 58
      IKEYB 'KTRC ' IVAL D1,37,1 64 D71,73,1 D78,80,1 D97,120,1
/ZERO IKEYA 'KSHOT' IVAL 59
      IKEYB 'KTRC ' IVAL 6 24 D26,28,1 31 34 39 40 42 61 62 70 71 76
78 81 89
90 94 97
 98 100 101 102 111
/ZERO IKEYA 'KSHOT' IVAL 60
      IKEYB 'KTRC ' IVAL 1 10 11 15 22 23 27 39 40 68 69 D74,77,1 92
94 97 107
110 111 112
/ZERO IKEYA 'KSHOT' IVAL 61
      IKEYB 'KTRC ' IVAL D1,35,1 D42,44,1 73 77 78 D88,120,1
/ZERO IKEYA 'KSHOT' IVAL 62
      IKEYB 'KTRC ' IVAL D1,28,1 41 42 74 D76,78,1 D88,120,1
/ZERO IKEYA 'KSHOT' IVAL 63
      IKEYB 'KTRC ' IVAL D1,17,1 35 39 44 45 73 74 86 87 94 102 103
110 111 119
/ZERO IKEYA 'KSHOT' IVAL 64
      IKEYB 'KTRC ' IVAL D1,33,1 38 39 50 51 72 73 82 83 90 94 95
D101,120,1
/ZERO IKEYA 'KSHOT' IVAL 65
      IKEYB 'KTRC ' IVAL D1,9,1 16 17 20 24 31 32 39 40 41 69 70 71 72
      IKEYB 'KTRC ' IVAL 80 81 83 84 D103,120,1
/ZERO IKEYA 'KSHOT' IVAL 66
      IKEYB 'KTRC ' IVAL 9 17 18 26 27 33 34 81 82 87 88 89 94 97 98
99
      IKEYB 'KTRC ' IVAL D106,120,1
/ZERO IKEYA 'KSHOT' IVAL 67
      IKEYB 'KTRC ' IVAL D1,6,1 26 27 42 43 79 D94,98,1 D106,111,1
/ZERO IKEYA 'KSHOT' IVAL 68
      IKEYB 'KTRC ' IVAL 11 13 27 28 36 82 85 95 106 107 108
/ZERO IKEYA 'KSHOT' IVAL 69
      IKEYB 'KTRC ' IVAL 8 14 17 18 22 99 106 107 119 120
/ZERO IKEYA 'KSHOT' IVAL 70
      IKEYB 'KTRC ' IVAL D2,4,1 12 13 19 20 75 83 84 85 93 98
D102,104,1 113 115
/ZERO IKEYA 'KSHOT' IVAL 71
      IKEYB 'KTRC ' IVAL 9 10 37 D44,47,1 73 79 80 89 92 94 98 102 103
105 114 118
119 120/ZERO IKEYA 'KSHOT' IVAL 72
      IKEYB 'KTRC ' IVAL 5 6 12 22 29 31 34 37 40 51 97 113 118
/ZERO IKEYA 'KSHOT' IVAL 73
      IKEYB 'KTRC ' IVAL 8 10 20 26 32 36 41 49 82 83 90 97 105 106
D112,120,1
/ZERO IKEYA 'KSHOT' IVAL 74
      IKEYB 'KTRC ' IVAL 1 2 14 24 28 29 30 37 47 48 74 93 114 115
/ZERO IKEYA 'KSHOT' IVAL 75
      IKEYB 'KTRC ' IVAL 5 13 14 20 21 22 28 29 31 32 39 40 41 45 71
77 78
/ZERO IKEYA 'KSHOT' IVAL 76
      IKEYB 'KTRC ' IVAL 17 20 24 25 26 27 29 37 43 89 92 93 94 95 104
105 120
```

```
/ZERO IKEYA 'KSHOT' IVAL 77
      IKEYB 'KTRC ' IVAL 5 6 8 11 12 17 D23,28,1 41 42 48 87 89 91 110
113 117
/ZERO IKEYA 'KSHOT' IVAL 78
      IKEYB 'KTRC ' IVAL 12 13 18 20 21 25 26 31 39 40 46 47 D75,80,1
92 105 106
111 D117,120,1
/ZERO IKEYA 'KSHOT' IVAL 79
      IKEYB 'KTRC ' IVAL 10 14 15 17 20 37 38 48 49 D74,76,1 84
D103,107,1
      IKEYB 'KTRC ' IVAL D116,118,1
/ZERO IKEYA 'KSHOT' IVAL 80
      IKEYB 'KTRC ' IVAL 1 11 12 13 17 18 19 22 D34,36,1 41 42 50 76
81 82
      IKEYB 'KTRC ' IVAL 92 D103,108,1 D112,120,1
/ZERO IKEYA 'KSHOT' IVAL 81
      IKEYB 'KTRC ' IVAL 13 23 24 33 34 71 D78,80,1 101 105 106 108
D112,120,1
/ZERO IKEYA 'KSHOT' IVAL 82
      IKEYB 'KTRC ' IVAL 7 8 15 23 24 25 31 32 38 39 71 77 78
D98,103,1 111 113
114 115 120
/ZERO IKEYA 'KSHOT' IVAL 83
      IKEYB 'KTRC ' IVAL D1,49,1 56 77 78 79 86 87 D95,120,1
/ZERO IKEYA 'KSHOT' IVAL 84
      IKEYB 'KTRC ' IVAL 1 4 9 24 26 28 30 38 39 40 74 75 76 87 88 96
100
      IKEYB 'KTRC ' IVAL D103,107,1 114,117
/ZERO IKEYA 'KSHOT' IVAL 85
      IKEYB 'KTRC ' IVAL D1,4,1 17 18 21 25 26 48 49 81 87 95 96 101
104 110

/ZERO IKEYA 'KSHOT' IVAL 86
      IKEYB 'KTRC ' IVAL 8 9 20 24 82 D91,93,1 102 107 108 117
/ZERO IKEYA 'KSHOT' IVAL 87
      IKEYB 'KTRC ' IVAL 113 114
/ZERO IKEYA 'KSHOT' IVAL 88
      IKEYB 'KTRC ' IVAL 1 9 10 11 16 19 20 43 96 97 D111,114,1 120
/ZERO IKEYA 'KSHOT' IVAL 89
      IKEYB 'KTRC ' IVAL 2 6 7 14 18 21 31 87 98 119 120
/ZERO IKEYA 'KSHOT' IVAL 90
      IKEYB 'KTRC ' IVAL 6 12 16 21 23 24 39 80 D116,120,1
/ZERO IKEYA 'KSHOT' IVAL 91
      IKEYB 'KTRC ' IVAL 4 8 10 11 14 15 22 27 36 37 92 93
/ZERO IKEYA 'KSHOT' IVAL 92
      IKEYB 'KTRC ' IVAL 1 2 8 12 21 35 46 78 92
/ZERO IKEYA 'KSHOT' IVAL 93
      IKEYB 'KTRC ' IVAL 1 2 3 10 18 33 36 110 111 112 113
/ZERO IKEYA 'KSHOT' IVAL 94
 IKEYB 'KTRC ' IVAL D1,4,1 8 11 14 31 34 48 D108,110,1
/ZERO IKEYA 'KSHOT' IVAL 95
      IKEYB 'KTRC ' IVAL 1 2 6 7 11 18 19 D27,29,1 32 86 93 95
D99,102,1 120
/ZERO IKEYA 'KSHOT' IVAL 96
      IKEYB 'KTRC ' IVAL D1,15,1 23 24 26 29 30 53 54 95 101 102 120
/ZERO IKEYA 'KSHOT' IVAL 97
```

```
      IKEYB 'KTRC ' IVAL 7 16 D25,28,1 D51,53,1 98 99 D118,120,1
/ZERO IKEYA 'KSHOT' IVAL 98
      IKEYB 'KTRC ' IVAL 4 15 20 21 23 24 44 47 48 82 83 89 98 110 111
/ZERO IKEYA 'KSHOT' IVAL 99
      IKEYB 'KTRC ' IVAL 1 2 9 10 19 22 46 47 91 92 110 113
/ZERO IKEYA 'KSHOT' IVAL 100
      IKEYB 'KTRC ' IVAL 7 16 20 23 24 29 D44,46,1 73 79 D90,94,1 108
D116,120,1
/ZERO IKEYA 'KSHOT' IVAL 101
      IKEYB 'KTRC ' IVAL D1,27,1 46 47 50 83 D87,103,1 D112,120,1
/ZERO IKEYA 'KSHOT' IVAL 102
      IKEYB 'KTRC ' IVAL D1,19,1 D23,26,1 35 36 50 82 91 96 D100,104,1
113
      IKEYB 'KTRC ' IVAL D118,120,1
/ZERO IKEYA 'KSHOT' IVAL 103
      IKEYB 'KTRC ' IVAL D1,4,1 7 11 23 24 38 39 49 D86,89,1 99 105
110 111
IKEYB 'KTRC ' IVAL D116,120,1
/ZERO IKEYA 'KSHOT' IVAL 104
      IKEYB 'KTRC ' IVAL D1,3,1 7 10 11 D20,23,1 37 38 48 88 89 101
102 103
      IKEYB 'KTRC ' IVAL D117,120,1
/ZERO IKEYA 'KSHOT' IVAL 105
      IKEYB 'KTRC ' IVAL 1 8 9 10 20 22 36 37 47 83 84 91 92
D111,120,1
/ZERO IKEYA 'KSHOT' IVAL 106
      IKEYB 'KTRC ' IVAL 1 7 8 18 21 22 35 36 46 47 87 88 101 110 111
112 113
      IKEYB 'KTRC ' IVAL D116,120,1
/ZERO IKEYA 'KSHOT' IVAL 107
      IKEYB 'KTRC ' IVAL 1 5 6 7 14 34 45 78 D83,87,1 98 99 111
D115,120,1
/ZERO IKEYA 'KSHOT' IVAL 108
      IKEYB 'KTRC ' IVAL D1,7,1 17 18 21 32 43 44 83 84 D112,120,1
/ZERO IKEYA 'KSHOT' IVAL 109
      IKEYB 'KTRC ' IVAL D1,4,1 15 21 22 30 41 78 82 89 90 95 96 101
102 103
      IKEYB 'KTRC ' IVAL D107,120,1
/ZERO IKEYA 'KSHOT' IVAL 110
      IKEYB 'KTRC ' IVAL D1,6,1 8 9 16 23 27 28 35 39 40 67 73 74 81
103
      IKEYB 'KTRC ' IVAL D107,120,1
/ZERO IKEYA 'KSHOT' IVAL 111
      IKEYB 'KTRC ' IVAL 7 8 16 17 25 35 36 84 91 92 D103,120,1
/ZERO IKEYA 'KSHOT' IVAL 112
      IKEYB 'KTRC ' IVAL 1 6 7 17 18 22 23 26 27 33 74 81 82
D100,120,1
/ZERO IKEYA 'KSHOT' IVAL 113
      IKEYB 'KTRC ' IVAL 3 6 7 14 19 31 69 70 84 D99,120,1
/ZERO IKEYA 'KSHOT' IVAL 114
      IKEYB 'KTRC ' IVAL 5 9 10 13 18 19 29 30 69 72 77 D96,120,1
/ZERO IKEYA 'KSHOT' IVAL 115
      IKEYB 'KTRC ' IVAL 1 2 3 75 D96,120,1
/ZERO IKEYA 'KSHOT' IVAL 116
      IKEYB 'KTRC ' IVAL 20 21 D94,120,1
/ZERO IKEYA 'KSHOT' IVAL 117
```

```
      IKEYB 'KTRC ' IVAL 13 14 24 87 D90,120,1
/ZERO IKEYA 'KSHOT' IVAL 118
      IKEYB 'KTRC ' IVAL 12 13 23 D91 120,1

/ZERO IKEYA 'KSHOT' IVAL 119
      IKEYB 'KTRC ' IVAL 1 10 19 36 74 75 76 D89,120,1
/ZERO IKEYA 'KSHOT' IVAL 120
      IKEYB 'KTRC ' IVAL 3 6 8 9 15 73 D85,120,1
/ZERO IKEYA 'KSHOT' IVAL 121
      IKEYB 'KTRC ' IVAL 1 6 10 11 18 40 70 71 D83,120,1
/ZERO IKEYA 'KSHOT' IVAL 122
      IKEYB 'KTRC ' IVAL 3 4 17 D83,120,1
/ZERO IKEYA 'KSHOT' IVAL 123
      IKEYB 'KTRC ' IVAL 2 12 13 25 26 D80,120,1
/ZERO IKEYA 'KSHOT' IVAL 124
      IKEYB 'KTRC ' IVAL 77 D80,120,1
/ZERO IKEYA 'KSHOT' IVAL 125
      IKEYB 'KTRC ' IVAL 6 7 8 11 19 D78,120,1
/ZERO IKEYA 'KSHOT' IVAL 126
      IKEYB 'KTRC ' IVAL 5 7 D77,120,1
/ZERO IKEYA 'KSHOT' IVAL 127
      IKEYB 'KTRC ' IVAL D1,5,1 12 13 52 D72,120,1
/ZERO IKEYA 'KSHOT' IVAL 128
      IKEYB 'KTRC ' IVAL D1,4,1 41 49 D72,120,1
/ZERO IKEYA 'KSHOT' IVAL 129
      IKEYB 'KTRC ' IVAL4 13 14 17 37 D71,120,1
/ZERO IKEYA 'KSHOT' IVAL 130
      IKEYB 'KTRC ' IVAL 1 11 14 15 23 D69,120,1
/ZERO IKEYA 'KSHOT' IVAL 131
      IKEYB 'KTRC ' IVAL 13 14 21 23 D67,120,1
/ZERO IKEYA 'KSHOT' IVAL 132
      IKEYB 'KTRC ' IVAL 4 13 14 39 40 D64,120,1
/ZERO IKEYA 'KSHOT' IVAL 133
/ZERO IKEYA 'KSHOT' IVAL 133
      IKEYB 'KTRC ' IVAL 11 12 15 D62,120,1
/ZERO IKEYA 'KSHOT' IVAL 134
      IKEYB 'KTRC ' IVAL 9 10 15 D61,120,1
/ZERO IKEYA 'KSHOT' IVAL 135
      IKEYB 'KTRC ' IVAL 4 5 D61,120,1
/DESPK

/MUTE
  FIRSTID 'KSHOT'
  SECONDID 'KTRC'
    FMUTE 1, 61 40, 120 440
    FMUTE 2, 61 30, 120 450
    FMUTE 3, 61 30, 120 460
    FMUTE 4, 61 40, 120 480
    FMUTE 5, 61 40, 120 470
    FMUTE 6, 57 60, 61 40,   120 480
    FMUTE 7, 53 90,  61 40,  120 460
    FMUTE 8, 51 110, 61 40,  120 470
    FMUTE 9, 50 110, 61 40,  120 470
    FMUTE 10,51 110, 61 40,  120 460
    FMUTE 11,47 130, 61 40,  120 460
    FMUTE 12,46 150, 61 40,  120 470
```

```
FMUTE 13,45 180, 61 40,  120 470
FMUTE 14,45 180, 61 40,  120 480
FMUTE 15,43 200, 61 50,  120 480
FMUTE 16,42 190, 61 40,  120 470
FMUTE 17,41 200, 61 40,  120 470
FMUTE 18,40 210, 61 40,  120 470
FMUTE 19,38 230, 61 40,  120 480
FMUTE 20,36 240, 61 40,  120 480
FMUTE 21,35 250, 61 40,  120 470
FMUTE 22,33 280, 61 40,  120 480
FMUTE 23,31 280, 61 40,  120 480
FMUTE 24,29 280, 61 40,  120 470
FMUTE 25,28 310, 61 50,  120 460
FMUTE 26,26 330, 61 50,  120 460
FMUTE 27,25 340, 61 40,  120 470
FMUTE 28,26 320, 61 40,  120 470
FMUTE 29,24 330, 61 50,  120 470
FMUTE 30,18 400, 61 40,  120 480
FMUTE 31,17 400, 61 40,  120 470
FMUTE 32,14 410, 61 40,  120 470
FMUTE 33,12 430, 61 40,  120 480
FMUTE 34,11 440, 61 40,  120 480
FMUTE 35,9 460,  61 40,  120 480
FMUTE 36,7 470,  61 40,  120 480
FMUTE 37,8 470,  61 40,  120 480
FMUTE 38,4 480,  61 40,  120 460
FMUTE 39,1 480,  61 40,  120 460
FMUTE 40,1 480,  61 40,  120 480
FMUTE 41,1 490,  61 40,  120 490
FMUTE 42,1 480,  61 40,  120 500
FMUTE 43,1 480,  61 30,  120 480
FMUTE 44,1 470,  61 20,  120 480
FMUTE 45,1 480,  61 30,  120 470
FMUTE 46,1 460,  61 30,  120 470
FMUTE 47,1 480,  61 20,  120 470
FMUTE 48,1 490,  61 40,  120 500
FMUTE 49,1 470,  61 20,  120 480
FMUTE 50,1 480,  61 20,  120 460
FMUTE 51,1 480,  61 40,  120 460
FMUTE 52,1 460,  61 30,  120 480
FMUTE 53,1 460,  61 40,  120 500
FMUTE 54,1 460,  61 40,  120 500
FMUTE 55,1 480,  61 30,  120 510
FMUTE 56,1 470,  61 40,  120 480
FMUTE 57,1 460,  61 40,  120 500
FMUTE 58,1 500,  61 40,  120 500
FMUTE 59,1 500,  61 40,  120 500
FMUTE 60,1 480,  61 30,  120 510
FMUTE 61,35 260, 61 30,  87 290, 120 490
FMUTE 62,1 500,  61 40,  87 270, 120 500
FMUTE 63,1 520,  61 40,  120 520
FMUTE 64,1 520,  61 40,  120 520
FMUTE 65,1 520,  61 40,  120 540
FMUTE 66,1 500,  61 40,  120 530
FMUTE 67,1 500,  61 40,  87 280, 120 530
FMUTE 68,1 500,  61 50,  120 500
```

```
FMUTE 69,1 500,  61 40,  120 500
FMUTE 70,1 500,  61 40,  120 500
FMUTE 71,1 490,  61 40,  120 500
FMUTE 72,1 500,  61 40,  120 480
FMUTE 73,1 520,  61 60,  120 490
FMUTE 74,1 520,  61 60,  120 500
FMUTE 75,1 510,  61 50,  120 500
FMUTE 76,1 490,  61 60,  120 470
FMUTE 77,1 470,  61 40,  120 500
FMUTE 78,1 520,  61 60,  120 500
FMUTE 79,1 510,  61 30,  120 500
FMUTE 80,1 510,  61 40,  120 510
FMUTE 81,1 520,  61 40,  120 500
FMUTE 82,1 510,  61 50,  120 480
FMUTE 83,1 500,  61 40,  120 500
FMUTE 84,1 510,  61 40,  120 500
FMUTE 85,1 510,  61 45,  120 510
FMUTE 86,1 510,  61 40,  120 510
FMUTE 87,1 510,  61 45,  120 510
FMUTE 88,1 520,  61 45,  120 500
FMUTE 89,1 510,  61 45,  120 500
FMUTE 90,1 510,  61 45,  120 500
FMUTE 91,1 520,  61 50,  120 500
FMUTE 92,1 520,  61 50,  120 500
FMUTE 93,1 520,  61 50,  120 500
FMUTE 94,1 510,  61 40,  120 500
FMUTE 95,1 510,  61 40,  120 500
FMUTE 96,1 520,  61 40,  120 480
FMUTE 97,1 510,  61 40,  120 470
FMUTE 98,1 500,  61 30,  120 470
FMUTE 99,1 500,  61 30,  120 480
FMUTE 100,1 510,  61 40, 120 470
FMUTE 101,1 510,  61 40, 120 460
FMUTE 102,1 510,  61 30, 120 470
FMUTE 103,1 510,  61 30, 120 460
FMUTE 104,1 510,  61 40, 120 460
FMUTE 105,1 510,  61 40, 120 440
FMUTE 106,1 510,  61 45, 120 450
FMUTE 107,1 510,  61 45, 120 450
FMUTE 108,1 510,  61 45, 120 460
FMUTE 109,1 510,  61 45, 120 460
FMUTE 110,1 510,  61 45, 120 460
FMUTE 111,1 510,  61 45, 120 460
FMUTE 112,1 510,  61 45, 100 320
FMUTE 113,1 505,  61 50, 98  320
FMUTE 114,1 500,  61 50, 96  300
FMUTE 115,1 490,  61 45, 95  290
FMUTE 116,1 490,  61 45, 95  260
FMUTE 117,1 480,  61 45, 93  270
FMUTE 118,1 480,  61 45, 94  270
FMUTE 119,1 480,  61 45, 91  260
FMUTE 120,1 480,  61 45, 89  260
FMUTE 121,1 500,  61 45, 86  240
FMUTE 122,1 500,  61 45, 85  230
FMUTE 123,1 480,  61 45, 82  220
FMUTE 124,1 480,  61 45, 80  200
```

```
    FMUTE 125,1 480,  61 40, 76  150
    FMUTE 126,1 470,  61 40, 75  150
    FMUTE 127,1 480,  61 30, 72  120
    FMUTE 128,1 480,  61 40, 72  130
    FMUTE 129,1 480,  61 45, 70  110
    FMUTE 130,1 500,  61 40, 68  100
    FMUTE 131,1 480,  61 45, 66  70
    FMUTE 132,1 480,  61 40, 64  40
    FMUTE 133,1 480,  61 40, 63  35
    FMUTE 134,1 450,  61 40,
    FMUTE 135,1 480,  61 40
```

(7) AGC Processor to apply balancing Scalers to the seismic trace to equalise the amplitude within the trace

```
/AGC WINDOW 400
```

(8) Gather the data into CDP Gathers and create CDP file

```
/RASORT
  FIRSTID 'KCDP'
/HOUSDOUT FILENAME 'SERPENT CDP'
 DELETE
```

(9) STATAPLY to apply a static field corrections

```
/HOUSDIN FILENAME 'SERPENT CDP'
/RASORT
 FIRSTID 'KCDP'

/STATAPLY
```

(10) Apply initial velocity values for RawStack

```
/VELOCITY
  VEL 1 63 6 112 6000 212 13000 312 14400 382 15000 432 15600 744
18000
```

(11) STVF Processor to compute and apply space and time-varing digital filters to seismic data

```
/STVF
 BANDPASS ZERO
  FILT 1 10 80 110 80
  FILT 2 20 70 80 70
  FILT 3 20 50 60 50
  FILT 4 20 40 45 40
  FILT 5 10 30 40 30
 APPLY 1 2 63 0 600 0
 APPLY 2 2 63 110 600 110
 APPLY 3 2 63 220 600 220
 APPLY 4 2 63 450 600 450
 APPLY 5 2 63 560 600 560
```

(12) FKFILT transforms the data to the f-k domain, examine the plots, and remove some selected areas

```
/RASORT
 FIRSTID 'KSHOT'
/FKFILT
REGION 0.20 0 0.5 0 0.5 125 0.2 125
/FKFILT
 REGION -0.20 0 -0.5 0 -0.5 125 -0.2 125
/FKFILT
REGION .115 0 0.30 0 0.30 62.5 0.115 62.5
/FKFILT
REGION -0.115 0 -0.30 0 -0.30 62.5 -0.115 62.5

/RASORT
 FIRSTID 'KCDP'
/NOTCH


/TIMFRQ
    TRLIST 1 10 20 30 40 50 60 70 80 90 100 120
    FLDFILE 51
    SWEEP 20 120
    WINDOW 300
    INC 25
    MAXFREQ 120
    LINEPLOT

(13)  SPHDIV compensates for the effects of spherical divergence

/SPHDIV
/HOUSDOUT FILENAME 'CDP2' DELETE

/HOUSDIN FILENAME 'CDP2'

(14)  Apply NMO correction on the CDP file  and stack the data

/NMO
/STACK
/HOUSDOUT FILENAME 'RAWSTACK' DELETE

(15) Apply different methods of velocity analysis

/HOUSDIN FILENAME 'CDP2'

/RASORT
 FIRSTID 'KCDP'

/VELOCITY
 VEL 1 125 1 12500 17500

/SPHDIV

/VELPANEL IKEYA 'KCDP' IVAL D545 555 1

 PANELS 11
 VELINC 500
 NCDP 11
 NLOC 1
```

```
 FMUTE 10 1 50

/VELS
 IKEYA 'KCDP' IVAL D130,135,1 D150,159,1  D200,209,1 D250,259,1
  D300,309,1 D340,349,1  D400,409,1 D430,440,1 D490,500,1 D550,560,1
 NTMAX 2000
 HILBFILT 'ON'
 BALANCE 'ON'
 LEVEL 10 60 12
 VELRANGE 200 5000 20000
 VELINC 100
 HORZ 1000
 VERT 10
 NSPECT 7

/HOUSDIN FILENAME 'CDP2'
```

(15) Velocity processor to specify the RMS velocity and final stack

```
 /VELOCITY
 CMP 124 0 12900 408 15400 744 16600
 CMP 170 0 13200 216 13200 336 14200 456 18600 624 20000
 CMP 255 0 13200 312 14100 576 14900 816 18800
 CMP 275 0 13200 312 15200 432 15300 888 16400
 CMP 295 0 13200 240 13200 288 13700 432 14200 504 14300 506 14600 936
17300
 CMP 410 0 13000 264 13100 336 14400 432 14500 552 16300 672 16300 936
17200
 CMP 505 0 13200 192 13500 312 14500 408 14600 504 14700 840 20000
 CMP 570 0 12500 312 15000 432 15100 792 16900

/NMO
/STACK
/HOUSDIN FILENAME 'FSTACK1'
```

(16) RSESTIM Processor to compute nonsurface-consistent residual
      statics

```
/RSESTIM
 FILENAME'FSTACK1'
 WINDOW 114 200 600 614 200 600

/RSSAVE STATFILE 'FSTACK2' DELETE
        DESC 'FIRST PASS'
/STACK
/HOUSDOUT FILENAME 'FSTACK3'
```

(17) FKMIG to migrate Stacked data using FK migration algorithm

```
/FKMIG
SPACING 41.5
MAXTRC 128
VELOCITY 15600
WFAC -10.0
/HOUSDIN FILENAME 'STACKED'
```

(18) DISPLAY Processor to create plots of the seismic data

```
/DISPLAY
 WINDOW 0 1500
 TIMELINE 20 100 500
 HORZ 25 VERT 8
 ANNOTATE 'KCDP'
 ANNOTATE 'KFLDFN'
$EOJ
```

APPENDIX II
(GRAVITY DATA)

1-) Survey Data

STN	BS/FS	ELEV	ROD	ELEVA.	DIFF
G1	BS	1.041	1.6	229.917	0
G2	FS	0.113	1.6	228.987	-0.93
G3	FS	0.199	1.6	229.072	-0.845
G4	FS	0.706	1.6	229.577	-0.34
G5	BS	-1.28	1.6	230.334	0.417
G6	BS	-0.174	1.6	231.448	1.531
G7	FS	4.617	1.6	236.233	6.316
G8	BS	-5.852	1.6	241.343	11.426
G9	BS	-0.99	1.6	246.199	16.282
G10	FS	0.664	1.6	247.854	17.937
G11	BS	-2.872	1.6	246.224	16.307
G12	BS	-1.722	1.6	247.366	17.449
G13	FS	0.363	1.6	249.453	19.536
G14	BS	-8.465	1.6	249.958	20.041
G15	BS	-7.602	1.6	250.788	20.871
G16	FS	-5.785	1.6	252.625	22.708
G17	FS	-1.526	1.6	256.882	26.965
G18	FS	-0.904	1.6	257.503	27.586
G19	FS	-5.002	1.6	253.403	23.486
G20	FS	-3.28	1.6	255.124	25.207
G21	FS	2.11	1.6	257.934	28.017
G22	FS	5.853	1.6	261.676	31.759
G23	FS	1.265	1.6	264.283	34.366
G24	FS	8.138	1.6	271.155	41.238
G25	FS	14.21	1.6	277.225	47.308
G26	FS	-1.709	1.6	282.75	52.833
G27	FS	1.03	1.6	285.489	55.572
G28	FS	0.5	1.6	286.295	56.378
G29	FS	2.516	1.6	288.311	58.394
G30	FS	-0.487	1.6	288.304	58.387
G31	FS	-2.898	1.6	285.893	55.976
G32	FS	-0.369	1.6	287.295	57.378
G33	FS	2.713	1.6	290.237	60.32
G34	FS	-0.614	1.6	291.799	61.882
G35	FS	-2.489	1.6	289.924	60.007
G36	FS	0.097	1.6	286.144	56.227
G37	FS	-1.104	1.6	284.943	55.026
G38	FS	0.361	1.6	286.408	56.491
G39	FS	2.012	1.6	288.063	58.146
G40	FS	5.17	1.6	291.082	61.165
G41	FS	10.436	1.6	296.358	66.441

G42	FS	-0.588	1.6	296.785	66.868
G43	FS	-1.628	1.6	294.348	64.431
G44	FS	-4.004	1.6	291.972	62.055
G45	FS	-3.785	1.6	292.194	62.277
G46	FS	-0.693	1.6	294.927	65.01
G47	FS	1.499	1.6	297.101	67.184
G48	FS	0.329	1.6	299.751	69.834
G49	FS	-0.04	1.6	296.123	66.206
G50	FS	-3.182	1.6	292.981	63.064
G51	FS	-4.606	1.6	291.557	61.64
G52	FS	-7.614	1.6	288.549	58.632
G53	FS	1.356	1.6	283.817	53.9
G54	FS	-3.486	1.6	278.795	48.878
G55	FS	-7.479	1.6	274.802	44.885
G56	FS	-2.012	1.6	275.359	45.442
G57	FS	-0.674	1.6	276.697	46.78
G58	FS	-0.249	1.6	277.122	47.205
G59	FS	-5.19	2.5	271.281	41.364
G60	FS	5.314	1.6	264.372	34.455
G61	FS	0.466	1.6	259.524	29.607
G62	FS	-3.404	1.6	255.654	25.737
G63	FS	-6.956	1.6	252.102	22.185
G64	FS	-8.272	1.6	250.832	20.915
G65	FS	-7.325	1.6	251.773	21.856
G66	FS	-2.999	1.7	253.921	24.004
G67	FS	3.42	1.7	260.331	30.414
G68	FS	5.612	3.5	260.723	30.806
G69	FS	-0.632	1.7	259.592	29.675
G70	FS	-2.42	3	256.504	26.587
G71	FS	-1.34	1.7	255.352	25.435
G72	FS	-0.351	1.7	256.341	26.424
G73	FS	0.567	1.7	257.259	27.342
G74	FS	-0.464	1.7	254.179	24.262
G75	FS	0.632	1.7	255.275	25.358
G76	FS	-0.002	1.7	255.823	25.906
G77	FS	-0.419	1.7	255.406	25.489
G78	FS	-2.74	1.7	253.085	23.168
G79	FS	0.056	1.7	250.449	20.532
G80	FS	-1.703	1.7	248.69	18.773
G81	FS	0.209	1.7	247.466	17.549
G82	FS	0.08	1.7	247.337	17.42
G83	FS	-2.208	2.2	244.549	14.632
G84	FS	0.269	1.7	240.432	10.515
G85	FS	-4.703	1.7	235.46	5.543
G86	FS	-1.449	1.7	233.501	3.584
G87	FS	1.355	1.7	236.305	6.388
G88	FS	6.018	1.7	240.968	11.051
G89	FS	-1.35	1.7	242.318	12.401
G90	FS	-0.121	1.7	243.547	13.63
G91	FS	0.652	1.7	244.32	14.403
G92	FS	-0.478	2.5	242.387	12.47

G93	FS	-3.566	1.7	243.836	13.919
G94	FS	0.722	1.7	248.089	18.172
G95	FS	0.026	1.7	247.428	17.511
G96	FS	1.643	1.7	243.949	14.032
G97	FS	0.41	1.7	242.716	12.799
G98	FS	-2.894	1.7	239.412	9.495
G99	FS	-4.518	1.7	237.788	7.871
G100	FS	-4.615	1.7	237.671	7.754
G101	FS	0.059	1.7	237.341	7.424
G102	FS	0.189	1.7	237.471	7.554
G103	FS	-2.718	1.7	234.564	4.647
G104	FS	-3.678	1.7	233.604	3.687
G105	FS	-2.84	1.7	234.442	4.525
G106	FS	0.926	1.7	234.221	4.304
G107	FS	0.056	1.7	233.351	3.434
G108	FS	-0.092	1.7	233.013	3.096
G109	FS	0.036	1.7	233.433	3.516
G110	FS	0.227	1.7	233.624	3.707
G111	FS	-0.262	1.7	233.135	3.218
G112	FS	-0.104	1.7	233.184	3.267
G113	FS	-0.353	1.7	232.938	3.021
G114	FS	1.741	1.7	230.093	0.176
G115	FS	-0.134	1.7	228.218	-1.699
G116	FS	-1.838	1.7	226.514	-3.403
G117	FS	-4.573	1.7	225.479	-4.438
G118	FS	-8.891	2.2	218.902	-11.015

2- Gravity Data

STN	LACOSTE	WODREN	MGAL W	
G1	36022.66	1249.1	111.2948	3806.859
G2	36022.03	1251.3	111.4908	3806.792
G3	36020.67	1252.5	111.5977	3806.648
G4	36019.05	1250.6	111.4284	3806.477
G5	36016.83	1253.7	111.7046	3806.241
G6	36014.13	1246.2	111.0364	3805.956
G7	36005.35	1238.3	110.3325	3805.026
G8	35996.59	1226.7	109.2989	3804.098
G9	35988.2	1221.9	108.8712	3803.210
G10	35986.45	1217.3	108.4614	3803.025
G11	35999.73	1220.5	108.7465	3804.431
G12	35986.85	1215.8	108.3277	3803.067
G13	35983.26	1212.9	108.0693	3802.687
G14	35982.04	1209.1	107.7308	3802.558
G15	35980.1	1210.3	107.8377	3802.352
G16	35977	1188.2	105.8686	3802.024
G17	35968.65	1180.1	105.1469	3801.140

G18	35967	1178.2	104.9776	3800.965
G19	35974.02	1188.5	105.8953	3801.709
G20	35969.17	1182.7	105.3785	3801.195
G21	35963.84	1176.7	104.8439	3800.631
G22	35959.03	1169.6	104.2113	3800.122
G23	35954.72	1166.4	103.9262	3799.665
G24	35940.51	1158.5	103.2223	3798.161
G25	35928.61	1145.4	102.0551	3796.901
G26	35916.5	1127.4	100.4513	3795.619
G27	35910.95	1122.1	99.97911	3795.031
G28	35909.45	1122	99.9702	3794.872
G29	35905.12	1115.1	99.35541	3794.414
G30	35904.83	1116.4	99.47124	3794.383
G31	35909.63	1122.5	100.0147	3794.891
G32	35905.55	1117.3	99.55143	3794.459
G33	35898.23	1108.4	98.75844	3793.684
G34	35893.6	1102.8	98.25948	3793.194
G35	35896.84	1105.7	98.51787	3793.537
G36	35904.68	1104.7	98.42877	3794.367
G37	35906.1	1105.6	98.50896	3794.517
G38	35901.86	1101.9	98.17929	3794.068
G39	35898.17	1098.4	97.86744	3793.678
G40	35890.63	1091.4	97.24374	3792.879
G41	35879.1	1075.5	95.82705	3791.659
G42	35887.63	1074.6	95.74686	3792.562
G43	35882.04	1079.8	96.21018	3791.970
G44	35886.18	1085.3	96.70023	3792.408
G45	35885.43	1084.8	96.65568	3792.329
G46	35879.5	1084.6	96.63786	3791.701
G47	35873.91	1080.1	96.23691	3791.109
G48	35867.25	1070.1	95.34591	3790.404
G49	35874.3	1081.2	96.33492	3791.150
G50	35889.95	1087.4	96.88734	3792.807
G51	35882.25	1090.3	97.14573	3791.992
G52	35888	1095.6	97.61796	3792.601
G53	35897.94	1108.5	98.76735	3793.653
G54	35907.33	1119.3	99.72963	3794.648
G55	35915.63	1128.7	100.5671	3795.526
G56	35915.26	1127.9	100.4958	3795.487
G57	35912.7	1127.1	100.4246	3795.216
G58	35911.4	1119.8	99.77418	3795.079
G59	35924.05	1131.8	100.8433	3796.418
G60	35938.93	1156.7	103.0619	3797.993
G61	35947.18	1164.9	103.7925	3798.867
G62	35955.17	1176.1	104.7905	3799.713
G63	35960.6	1182.7	105.3785	3800.288
G64	35963.06	1184.6	105.5478	3800.548
G65	35960.91	1190.7	106.0913	3800.321

G66	35955.73	1161.6	103.4985	3799.772
G67	35941.6	1145.9	102.0996	3798.276
G68	35940.65	1143.2	101.8591	3798.176
G69	35941.93	1145.4	102.0551	3798.311
G70	35947.18	1151.3	102.5808	3798.867
G71	35948.37	1153.2	102.7501	3798.993
G72	35945.36	1147.1	102.2066	3798.674
G73	35942.94	1143.6	101.8947	3798.418
G74	35948.65	1157.4	103.1243	3799.023
G75	35945.3	1151.6	102.6075	3798.668
G76	35943.5	1156.3	103.0263	3798.477
G77	35943.25	1156.5	103.0441	3798.451
G78	35946.36	1161.1	103.4540	3798.780
G79	35950.87	1165.3	103.8282	3799.258
G80	35952.64	1166.4	103.9262	3799.445
G81	35953.02	1167.8	104.0509	3799.485
G82	35952.83	1167.2	103.9975	3799.465
G83	35959.03	1174.4	104.6390	3800.122
G84	35965.85	1176.5	104.8261	3800.844
G85	35974.78	1181.8	105.2983	3801.789
G86	35978.32	1196.1	106.5725	3802.164
G87	35971.98	1191.3	106.1448	3801.493
G88	35961.46	1177.7	104.9330	3800.379
G89	35958.35	1173	104.5143	3800.050
G90	35955.53	1168.1	104.0777	3799.751
G91	35954.51	1167.8	104.0509	3799.643
G92	35958.19	1174.1	104.6123	3800.033
G93	35953.5	1166.1	103.8995	3799.536
G94	35943.6	1155.7	102.9728	3798.488
G95	35944.32	1155.4	102.9461	3798.564
G96	35951.1	1163.6	103.6767	3799.282
G97	35953.03	1168.5	104.1133	3799.486
G98	35957.94	1174.5	104.6479	3800.006
G99	35960.35	1178.6	105.0132	3800.261
G100	35959.3	1178.2	104.9776	3800.150
G101	35959.03	1177.1	104.8796	3800.122
G102	35957.18	1179.6	105.1023	3799.926
G103	35961.43	1180.3	105.1647	3800.376
G104	35962.94	1180.7	105.2003	3800.536
G105	35958.65	1178.8	105.0310	3800.081
G106	35957.59	1178.3	104.9865	3799.969
G107	35957.9	1179.1	105.0578	3800.002
G108	35956.9	1176.2	104.7994	3799.896
G109	35955	1172.9	104.5053	3799.695
G110	35953.01	1170.9	104.3271	3799.484
G111	35952.62	1169.8	104.2291	3799.443
G112	35951.1	1168.5	104.1133	3799.282
G113	35950.09	1167.5	104.0242	3799.175

G114	35954.38	1171.8	104.4073	3799.629
G115	35957.06	1173.4	104.5499	3799.913
G116	35959.05	1176.9	104.8617	3800.124
G117	35962.58	1178.9	105.0399	3800.497
G118	35970.61	1190.4	106.0646	3801.348

3-) Drift Calculation

READINGS	B.STN	G.MGALS	DRIFT	G1.STN	G.MGALS	DRIFT
1	36013.8	3805.921	0.060944	36022.66	3806.859	0.021040
2	36012.83	3805.818	-0.041759	36022.33	3806.824	-0.013899
3	36013.45	3805.884	0.023886	36022.56	3806.848	0.010452
4	36013.06	3805.842	-0.017407	36022.53	3806.845	0.007276
5	36013.54	3805.893	0.033415	36022.68	3806.861	0.023158
6	36012.9	3805.825	-0.034348	36022.13	3806.803	-0.035075
7	36012.63	3805.797	-0.062935	36022.1	3806.799	-0.038252
8	36013.21	3805.858	-0.001525	36022.35	3806.826	-0.011782
9	36013.12	3805.849	-0.011054	36022.23	3806.813	-0.024487
10	36013.03	3805.839	-0.020583	36022.26	3806.816	-0.021311
11	36012.33	3805.765	-0.094699	36021.78	3806.766	-0.072133
12	36012.82	3805.817	-0.042818	36022.29	3806.820	-0.018134
13	36013.32	3805.870	0.010121	36022.6	3806.852	0.014688
14	36013.45	3805.884	0.023886	36022.71	3806.864	0.026334
15	36013.66	3805.906	0.046120	36022.79	3806.873	0.034805
16	36013.73	3805.913	0.053532	36022.92	3806.886	0.048569
17	36013.93	3805.934	0.074708	36022.93	3806.887	0.049628

4-) Data Reduction (Elevation correction)

STN	ELE.M.	M.GALS.	STN-G1	FAC+BC2 .68	EAST G1	NORTH G1
118	-11.015	3801.348	-5.511	-2.16233	-3422.18	-2521.95
117	-4.438	3800.498	-6.361	-0.87121	-3418.14	-2472.42
116	-3.403	3800.124	-6.735	-0.66804	-3412.54	-2423.02
115	-1.699	3799.914	-6.945	-0.33353	-3407.14	-2373.53
114	0.176	3799.63	-7.229	0.03455	-3401.77	-2323.74
113	3.021	3799.176	-7.683	0.593046	-3396.92	-2274.38
112	3.267	3799.282	-7.577	0.641338	-3390.69	-2224.86
111	3.218	3799.443	-7.416	0.631719	-3383.68	-2175.53
110	3.707	3799.485	-7.374	0.727714	-3372.68	-2125.82
109	3.516	3799.695	-7.164	0.690219	-3370.2	-2076.81
108	3.096	3799.897	-6.962	0.60777	-3367.95	-2027.07
107	3.434	3800.002	-6.857	0.674122	-3365.32	-1977.25
106	4.304	3799.97	-6.889	0.84491	-3363.86	-1927.56
105	4.525	3800.082	-6.777	0.888294	-3350.8	-1879.39
104	3.687	3800.536	-6.323	0.723788	-3332.23	-1833.24
103	4.647	3800.376	-6.483	0.912243	-3313.66	-1787.01
102	7.554	3799.926	-6.933	1.482911	-3295.57	-1740.79
101	7.424	3800.122	-6.737	1.457391	-3277.48	-1694.27
100	7.754	3800.151	-6.708	1.522172	-3259.31	-1647.83
99	7.871	3800.262	-6.597	1.54514	-3240.87	-1601.53
98	9.495	3800.007	-6.852	1.863944	-3223.18	-1554.93
97	12.799	3799.487	-7.372	2.512546	-3198.18	-1512
96	14.032	3799.282	-7.577	2.754594	-3149.58	-1499.81
95	17.511	3798.565	-8.294	3.437549	-3100.07	-1494.37
94	18.172	3798.488	-8.371	3.567309	-3051.47	-1483.96
93	13.919	3799.537	-7.322	2.732411	-3013.86	-1451.85
92	12.47	3800.033	-6.826	2.447961	-2983.09	-1412.67
91	14.403	3799.644	-7.215	2.827424	-2952.02	-1373.64
90	13.63	3799.752	-7.107	2.675678	-2930.99	-1328.66
89	12.401	3800.05	-6.809	2.434416	-2932.95	-1279.04
88	11.051	3800.379	-6.48	2.1694	-2943.09	-1230.02
87	6.388	3801.493	-5.366	1.254016	-2938.3	-1180.69
86	3.584	3802.165	-4.694	0.703568	-2921.71	-1134.38
85	5.543	3801.79	-5.069	1.088135	-2871.55	-1128.5
84	10.515	3800.844	-6.015	2.064179	-2821.74	-1130.94
83	14.632	3800.122	-6.737	2.872379	-2772.24	-1134.97
82	17.42	3799.466	-7.393	3.419685	-2734.63	-1167.57
81	17.549	3799.486	-7.373	3.445009	-2697.88	-1201.17
80	18.773	3799.446	-7.413	3.68529	-2650.71	-1196.6
79	20.532	3799.258	-7.601	4.030596	-2617.81	-1159.09
78	23.168	3798.781	-8.078	4.548064	-2593.71	-1115.57
77	25.489	3798.451	-8.408	5.003695	-2581.63	-1067.02
76	25.906	3798.478	-8.381	5.085555	-2572.04	-1017.99
75	25.358	3798.668	-8.191	4.977978	-2561.15	-969.251
74	24.262	3799.023	-7.836	4.762825	-2557.25	-919.519
73	27.342	3798.418	-8.441	5.367453	-2556.27	-869.556

72	26.424	3798.675	-8.184	5.187243	-2555.98	-819.63
71	25.435	3798.993	-7.866	4.993094	-2550.52	-770.143
70	26.587	3798.867	-7.992	5.219241	-2539.67	-721.525
69	29.675	3798.312	-8.547	5.82544	-2500.97	-690.16
68	30.806	3798.176	-8.683	6.047464	-2477.52	-648.244
67	30.414	3798.277	-8.582	5.970512	-2491.34	-600.47
66	24.004	3799.773	-7.086	4.712177	-2493.95	-550.945
65	21.856	3800.321	-6.538	4.290508	-2463.99	-511.89
64	20.915	3800.549	-6.31	4.105782	-2414.27	-508.583
63	22.185	3800.288	-6.571	4.355093	-2366.7	-493.515
62	25.737	3799.713	-7.146	5.052379	-2317.66	-485.708
61	29.607	3798.867	-7.992	5.812091	-2267.91	-482.431
60	34.455	3797.994	-8.865	6.763792	-2218.57	-477.302
59	41.364	3796.418	-10.441	8.120084	-2169.03	-474.373
58	47.205	3795.079	-11.78	9.266719	-2119.6	-475.225
57	46.78	3795.217	-11.642	9.183288	-2073.37	-494.129
56	45.442	3795.488	-11.371	8.920628	-2039.49	-530.94
55	44.885	3795.527	-11.332	8.811285	-2009.73	-571.132
54	48.878	3794.648	-12.211	9.595142	-1977.36	-609.205
53	53.9	3793.654	-13.205	10.581	-1932.16	-629.144
52	58.632	3792.601	-14.258	11.50993	-1882.96	-623.338
51	61.64	3791.993	-14.866	12.10043	-1832.75	-622.261
50	63.064	3792.808	-14.051	12.37997	-1782.86	-623.34
49	66.206	3791.151	-15.708	12.99677	-1734.12	-612.946
48	69.834	3790.404	-16.455	13.70897	-1700.75	-576.87
47	67.184	3791.11	-15.749	13.18876	-1688.79	-529.041
46	65.01	3791.701	-15.158	12.76198	-1667.56	-483.806
45	62.277	3792.329	-14.53	12.22547	-1624.4	-458.802
44	62.055	3792.409	-14.45	12.18189	-1579.56	-436.616
43	64.431	3791.97	-14.889	12.64832	-1536.62	-411.226
42	66.868	3792.562	-14.297	13.12672	-1516.76	-366.381
41	66.441	3791.659	-15.2	13.0429	-1507.08	-317.433
40	61.165	3792.88	-13.979	12.00718	-1467.85	-286.951
39	58.146	3793.678	-13.181	11.41452	-1422.97	-264.971
38	56.491	3794.069	-12.79	11.08964	-1381.79	-236.855
37	55.026	3794.518	-12.341	10.80204	-1340.9	-208.149
36	56.227	3794.368	-12.491	11.03781	-1298.88	-181.169
35	60.007	3793.537	-13.322	11.77985	-1257.02	-154.24
34	61.882	3793.194	-13.665	12.14793	-1217.03	-124.367
33	60.32	3793.685	-13.174	11.8413	-1189.41	-83.0342
32	57.378	3794.46	-12.399	11.26376	-1165.93	-39.1199
31	55.976	3794.892	-11.967	10.98854	-1133.36	-1.50574
30	58.387	3794.383	-12.476	11.46184	-1092.49	26.99633
29	58.394	3794.414	-12.445	11.46321	-1048.43	50.44799
28	56.378	3794.873	-11.986	11.06745	-998.554	52.64847
27	55.572	3795.031	-11.828	10.90923	-949.838	42.3979
26	52.833	3795.619	-11.24	10.37154	-908.855	14.11625
25	47.308	3796.901	-9.958	9.286939	-869.768	-16.4054
24	41.238	3798.161	-8.698	8.095349	-830.423	-46.3789
23	34.366	3799.666	-7.193	6.746321	-794.668	-80.6487
22	31.759	3800.122	-6.737	6.234546	-773.434	-125.736

21	28.017	3800.631	-6.228	5.499961	-766.241	-174.992
20	25.207	3801.196	-5.663	4.948336	-740.804	-212.523
19	23.486	3801.709	-5.15	4.61049	-690.987	-215.911
18	27.586	3800.966	-5.893	5.415352	-641.24	-218.705
17	26.965	3801.141	-5.718	5.293445	-591.129	-220.76
16	22.708	3802.025	-4.834	4.457762	-541.723	-223.48
15	20.871	3802.353	-4.506	4.097144	-491.913	-226.363
14	20.041	3802.558	-4.301	3.934209	-442.126	-228.724
13	19.536	3802.688	-4.171	3.835073	-392.303	-231.6
12	17.449	3803.068	-3.791	3.425378	-342.506	-234.91
11	16.307	3804.431	-2.428	3.201195	-292.746	-238.249
10	17.937	3803.025	-3.834	3.521177	-242.816	-241.011
9	16.282	3803.211	-3.648	3.196287	-192.95	-244.046
8	11.426	3804.099	-2.76	2.243015	-143.353	-247.502
7	6.316	3805.026	-1.833	1.239881	-93.064	-250.337
6	1.531	3805.956	-0.903	0.300548	-47.5327	-240.39
5	0.417	3806.242	-0.617	0.08186	-34.7827	-192.156
4	-0.34	3806.477	-0.382	-0.06674	-24.3223	-143.457
3	-0.845	3806.649	-0.21	-0.16588	-27.1586	-93.6414
2	-0.93	3806.793	-0.066	-0.18257	-23.7122	-43.8731
1	0	3806.859	0	0	0	0

Absolute Gravity at BM856 and at G1

GR.AV B+	GR.AV.G1	ABS.GR.B	ABS.G.G1
3805.86	3806.838	980023.8	980024.8

READINGS	B.STN	G.MGALS	DRIFT	G1.STN	G.MGALS	DRIFT
1	36013.8	3805.921	0.060944	36022.66	3806.859	0.021041
2	36012.83	3805.818	-0.04176	36022.33	3806.824	-0.0139
3	36013.45	3805.884	0.023886	36022.56	3806.849	0.010453
4	36013.06	3805.843	-0.01741	36022.53	3806.845	0.007276
5	36013.54	3805.894	0.033415	36022.68	3806.861	0.023158
6	36012.9	3805.826	-0.03435	36022.13	3806.803	-0.03508
7	36012.63	3805.797	-0.06294	36022.1	3806.8	-0.03825
8	36013.21	3805.859	-0.00153	36022.35	3806.826	-0.01178
9	36013.12	3805.849	-0.01105	36022.23	3806.814	-0.02449
10	36013.03	3805.84	-0.02058	36022.26	3806.817	-0.02131
11	36012.33	3805.766	-0.0947	36021.78	3806.766	-0.07213
12	36012.82	3805.817	-0.04282	36022.29	3806.82	-0.01813
13	36013.32	3805.87	0.010122	36022.6	3806.853	0.014688
14	36013.45	3805.884	0.023886	36022.71	3806.865	0.026335
15	36013.66	3805.906	0.046121	36022.79	3806.873	0.034805
16	36013.73	3805.914	0.053532	36022.92	3806.887	0.04857

17	36013.93	3805.935	0.074708	36022.93	3806.888	0.049628

5-) Residual Gravity and Absolute gravity

STN	L.C	FA-BC+LC	BOUG.PR	EST.REG.	RES.	ABS.GRA
118	0.912198	-1.25013	-6.76113	-6.76113	-4.2E-06	980019.3
117	0.894283	0.023068	-6.64388	-6.64173	-0.00215	980018.4
116	0.876415	0.208379	-6.52662	-6.52233	-0.00429	980018.1
115	0.858514	0.524987	-6.42001	-6.40293	-0.01709	980017.9
114	0.840505	0.875055	-6.35394	-6.28353	-0.07042	980017.6
113	0.822651	1.415698	-6.2673	-6.16413	-0.10318	980017.1
112	0.80474	1.446078	-6.13092	-6.04473	-0.0862	980017.2
111	0.786897	1.418616	-5.99738	-5.92532	-0.07206	980017.4
110	0.768917	1.496631	-5.87737	-5.80592	-0.07145	980017.4
109	0.75119	1.441409	-5.72259	-5.68652	-0.03607	980017.6
108	0.733199	1.340968	-5.62103	-5.56712	-0.05391	980017.8
107	0.715178	1.3893	-5.4677	-5.44772	-0.01998	980017.9
106	0.697205	1.542115	-5.34688	-5.32832	-0.01856	980017.9
105	0.679782	1.568076	-5.20892	-5.20892	-4.1E-06	980018
104	0.66309	1.386877	-4.93612	-4.93612	-2.8E-06	980018.5
103	0.646368	1.558611	-4.92439	-4.86555	-0.05884	980018.3
102	0.62965	2.112561	-4.82044	-4.79498	-0.02546	980017.9
101	0.612824	2.070214	-4.66679	-4.7244	0.057617	980018.1
100	0.596026	2.118198	-4.5898	-4.65383	0.064029	980018.1
99	0.579279	2.124419	-4.47258	-4.58326	0.110678	980018.2
98	0.562424	2.426368	-4.42563	-4.51269	0.087054	980017.9
97	0.546896	3.059442	-4.31256	-4.44211	0.129555	980017.4
96	0.542487	3.297081	-4.27992	-4.37154	0.091622	980017.2
95	0.540519	3.978068	-4.31593	-4.30097	-0.01496	980016.5
94	0.536754	4.104063	-4.26694	-4.2304	-0.03654	980016.4
93	0.525139	3.25755	-4.06445	-4.15982	0.095374	980017.5
92	0.510968	2.958929	-3.86707	-4.08925	0.22218	980018
91	0.496851	3.324275	-3.89073	-4.01868	0.127954	980017.6
90	0.480581	3.156259	-3.95074	-3.94811	-0.00263	980017.7
89	0.462633	2.897049	-3.91195	-3.87753	-0.03442	980018
88	0.444903	2.614302	-3.8657	-3.80696	-0.05874	980018.3
87	0.42706	1.681075	-3.68492	-3.73639	0.051465	980019.4
86	0.410309	1.113877	-3.58012	-3.66582	0.085694	980020.1
85	0.408183	1.496318	-3.57268	-3.59524	0.022563	980019.7
84	0.409065	2.473244	-3.54176	-3.52467	-0.01708	980018.8
83	0.410523	3.282901	-3.4541	-3.4541	1.42E-06	980018.1
82	0.422314	3.842	-3.551	-3.551	-3.4E-07	980017.4
81	0.434468	3.879477	-3.49352	-3.46935	-0.02418	980017.4
80	0.432815	4.118105	-3.2949	-3.38769	0.092799	980017.4
79	0.419247	4.449843	-3.15116	-3.30604	0.154884	980017.2
78	0.403506	4.951569	-3.12643	-3.22439	0.097957	980016.7
77	0.385945	5.38964	-3.01836	-3.14274	0.124375	980016.4
76	0.368211	5.453766	-2.92723	-3.06108	0.133848	980016.4
75	0.350582	5.32856	-2.86244	-2.97943	0.116989	980016.6

74	0.332593	5.095418	-2.74058	-2.89778	0.157194	980017
73	0.314522	5.681975	-2.75903	-2.81612	0.057098	980016.4
72	0.296463	5.483706	-2.70029	-2.73447	0.034176	980016.6
71	0.278564	5.271657	-2.59434	-2.65282	0.058474	980016.9
70	0.260978	5.480219	-2.51178	-2.57116	0.059383	980016.8
69	0.249633	6.075073	-2.47193	-2.48951	0.017584	980016.3
68	0.234472	6.281936	-2.40106	-2.40786	0.006794	980016.1
67	0.217192	6.187704	-2.3943	-2.32621	-0.06809	980016.2
66	0.199279	4.911456	-2.17454	-2.24455	0.070008	980017.7
65	0.185152	4.47566	-2.06234	-2.1629	0.100559	980018.3
64	0.183956	4.289738	-2.02026	-2.08125	0.060984	980018.5
63	0.178506	4.533599	-2.0374	-1.99959	-0.03781	980018.2
62	0.175682	5.228061	-1.91794	-1.91794	1.34E-06	980017.7
61	0.174497	5.986588	-2.00541	-1.87936	-0.12605	980016.8
60	0.172642	6.936434	-1.92857	-1.84079	-0.08778	980015.9
59	0.171582	8.291667	-2.14933	-1.80221	-0.34712	980014.4
58	0.171891	9.43861	-2.34139	-1.76364	-0.57775	980013
57	0.178728	9.362016	-2.27998	-1.72506	-0.55492	980013.2
56	0.192043	9.112671	-2.25833	-1.68649	-0.57184	980013.4
55	0.206581	9.017865	-2.31413	-1.64791	-0.66622	980013.5
54	0.220352	9.815494	-2.39551	-1.60934	-0.78617	980012.6
53	0.227564	10.80856	-2.39644	-1.57076	-0.82567	980011.6
52	0.225464	11.73539	-2.52261	-1.53219	-0.99042	980010.5
51	0.225074	12.3255	-2.5405	-1.49361	-1.04689	980009.9
50	0.225464	12.60543	-2.51501	-1.45504	-1.05998	980010.7
49	0.221705	13.21847	-2.48953	-1.41646	-1.07306	980009.1
48	0.208656	13.91763	-2.53737	-1.37789	-1.15948	980008.3
47	0.191356	13.38011	-2.36889	-1.33931	-1.02957	980009.1
46	0.174994	12.93698	-2.22102	-1.30074	-0.92028	980009.6
45	0.16595	12.39142	-2.13858	-1.26216	-0.87641	980010.3
44	0.157926	12.33982	-2.11018	-1.22359	-0.88659	980010.4
43	0.148742	12.79706	-2.09194	-1.18501	-0.90692	980009.9
42	0.132521	13.25924	-2.06711	-1.14644	-0.92067	980010.5
41	0.114817	13.15772	-2.04228	-1.10786	-0.93442	980009.6
40	0.103791	12.11097	-1.86803	-1.06929	-0.79874	980010.8
39	0.095841	11.51037	-1.67063	-1.03071	-0.63992	980011.6
38	0.085671	11.17531	-1.61469	-0.99214	-0.62256	980012
37	0.075288	10.87733	-1.46367	-0.95356	-0.51011	980012.5
36	0.065529	11.10334	-1.38766	-0.91499	-0.47267	980012.3
35	0.055789	11.83564	-1.48636	-0.87641	-0.60995	980011.5
34	0.044984	12.19292	-1.47208	-0.83784	-0.63425	980011.1
33	0.030034	11.87133	-1.30267	-0.79926	-0.50341	980011.6
32	0.01415	11.27791	-1.12109	-0.76069	-0.3604	980012.4
31	0.000545	10.98908	-0.97792	-0.72211	-0.25581	980012.8
30	-0.00976	11.45207	-1.02393	-0.68354	-0.34039	980012.3
29	-0.01825	11.44496	-1.00004	-0.64496	-0.35508	980012.4
28	-0.01904	11.04841	-0.93759	-0.60639	-0.33121	980012.8
27	-0.01534	10.89389	-0.93411	-0.56781	-0.3663	980013
26	-0.00511	10.36643	-0.87357	-0.52924	-0.34433	980013.6
25	0.005934	9.292873	-0.66513	-0.49066	-0.17447	980014.8
24	0.016775	8.112125	-0.58588	-0.45209	-0.13379	980016.1

23	0.029171	6.775492	-0.41751	-0.41351	-0.004	980017.6
22	0.045479	6.280025	-0.45698	-0.45698	4.94E-06	980018.1
21	0.063295	5.563256	-0.66474	-0.43522	-0.22952	980018.6
20	0.07687	5.025206	-0.63779	-0.41346	-0.22434	980019.1
19	0.078096	4.688585	-0.46141	-0.3917	-0.06972	980019.7
18	0.079106	5.494459	-0.39854	-0.36994	-0.0286	980018.9
17	0.07985	5.373295	-0.34471	-0.34818	0.00347	980019.1
16	0.080834	4.538596	-0.2954	-0.32641	0.03101	980020
15	0.081876	4.179021	-0.32698	-0.30465	-0.02233	980020.3
14	0.08273	4.016939	-0.28406	-0.28289	-0.00117	980020.5
13	0.083771	3.918844	-0.25216	-0.26113	0.008975	980020.6
12	0.084968	3.510346	-0.28065	-0.23937	-0.04128	980021
11	0.086176	3.28737	-0.25315	-0.21761	-0.03554	980022.4
10	0.087175	3.608351	-0.22565	-0.19585	-0.0298	980021
9	0.088272	3.284559	-0.36344	-0.17409	-0.18935	980021.2
8	0.089522	2.332538	-0.42746	-0.15233	-0.27514	980022
7	0.090548	1.330429	-0.50257	-0.13057	-0.37201	980023
6	0.08695	0.387497	-0.5155	-0.1088	-0.4067	980023.9
5	0.069504	0.151364	-0.46564	-0.08704	-0.37859	980024.2
4	0.051889	-0.01486	-0.39686	-0.06528	-0.33157	980024.4
3	0.03387	-0.13201	-0.34201	-0.04352	-0.29849	980024.6
2	0.015869	-0.1667	-0.2327	-0.02176	-0.21094	980024.7
1	-0	0	0	0	0	980024.8

APPENDIX III (MAGNETIC DATA)

LINE (0) JULIAN DAY (264) 1996

STN. INT.	EAST G1	North G1	UTM E-W	UTM N-S	MAG. FIELD
0.1	308.198	-898.899	293791.4	4322928	554277.
0.2	299.346	-904.448	293782.6	4322923	554004.3
0.3	290.494	-909.997	293773.7	4322917	554949
0.4	281.642	-915.546	293764.9	4322911	556314
0.6	263.938	-926.644	293747.2	4322900	554380.3
0.7	255.086	-932.193	293738.3	4322895	555987.7
0.8	246.234	-937.742	293729.5	4322889	555229
0.9	237.382	-943.291	293720.6	4322884	555400.7
1	228.53	-948.84	293711.8	4322878	555409.7
1.1	220.893	-953.279	293704.1	4322874	555465.3
1.2	213.256	-957.718	293696.5	4322869	555379
1.3	205.619	-962.157	293688.9	4322865	555421.7
1.4	197.982	-966.596	293681.2	4322860	555533
1.5	190.345	-971.035	293673.6	4322856	555628
1.6	182.708	-975.474	293665.9	4322852	555642
1.7	175.071	-979.913	293658.3	4322847	555610
1.8	167.434	-984.352	293650.7	4322843	555549.7
1.9	159.797	-988.791	293643	4322838	555520
2	152.16	-993.23	293635.4	4322834	555606
2.1	143.482	-998.446	293626.7	4322829	555680.7
2.2	134.804	-1003.66	293618	4322823	555616
2.3	126.126	-1008.88	293609.4	4322818	555557
2.4	117.448	-1014.09	293600.7	4322813	555571.3
2.5	108.77	-1019.31	293592	4322808	555418.7
2.6	100.092	-1024.53	293583.3	4322802	555483.7
2.7	91.414	-1029.74	293574.7	4322797	555529
2.8	82.736	-1034.96	293566	4322792	555473.3
2.9	74.058	-1040.17	293557.3	4322787	555581
3	65.38	-1045.39	293548.6	4322782	555910.3
3.1	57.136	-1051.61	293540.4	4322775	556133.3
3.2	48.892	-1057.82	293532.1	4322769	556056
3.3	40.648	-1064.04	293523.9	4322763	556206.7
3.4	32.404	-1070.25	293515.6	4322757	556204
3.5	24.16	-1076.47	293507.4	4322751	556163.3
3.6	15.916	-1082.68	293499.2	4322744	556246.7
3.7	7.672	-1088.9	293490.9	4322738	556100.3
3.8	-0.572	-1095.11	293482.7	4322732	555626.3
4	-17.06	-1107.54	293466.2	4322719	556557
4.1	-24.611	-1113.64	293458.6	4322713	556441.7
4.2	-32.162	-1119.75	293451.1	4322707	556514.7
4.3	-39.713	-1125.85	293443.5	4322701	556544.7
4.4	-47.264	-1131.95	293436	4322695	556508.7
4.5	-54.815	-1138.06	293428.4	4322689	556557.7
4.6	-62.366	-1144.16	293420.9	4322683	556553
4.7	-69.917	-1150.26	293413.3	4322677	556589
4.8	-77.468	-1156.36	293405.8	4322671	556646

4.9	-85.019	-1162.47	293398.2	4322665	556645
5.1	-101.508	-1175.12	293381.7	4322652	556849.3
5.2	-110.446	-1181.67	293372.8	4322645	557148.3
5.3	-119.384	-1188.21	293363.9	4322639	556839
5.4	-128.322	-1194.76	293354.9	4322632	556858
5.5	-137.26	-1201.31	293346	4322626	557001.7
5.6	-146.198	-1207.86	293337	4322619	556949.7
5.7	-155.136	-1214.41	293328.1	4322613	556882.3
5.8	-164.074	-1220.95	293319.2	4322606	557168.3
5.9	-173.012	-1227.5	293310.2	4322599	556884.7
6	-181.95	-1234.05	293301.3	4322593	556857.3
6.1	-190.368	-1239.38	293292.9	4322588	556800
6.2	-198.786	-1244.7	293284.5	4322582	556692.7
6.6	-232.458	-1266.01	293250.8	4322561	555670.3
6.7	-240.876	-1271.34	293242.4	4322556	556302.3
6.8	-249.294	-1276.67	293233.9	4322550	556618.7
6.9	-257.712	-1281.99	293225.5	4322545	556570.7
7	-266.13	-1287.32	293217.1	4322540	556755.7
7.1	-274.375	-1293.09	293208.9	4322534	556984.3
7.2	-282.62	-1298.86	293200.6	4322528	557247.7
7.3	-290.865	-1304.63	293192.4	4322522	557206.7
7.4	-299.11	-1310.4	293184.1	4322517	557068.3
7.6	-315.6	-1321.95	293167.6	4322505	556702.3
7.7	-323.845	-1327.72	293159.4	4322499	557099.3
7.8	-332.09	-1333.49	293151.2	4322493	556822.3
7.9	-340.335	-1339.26	293142.9	4322488	556981
264-8	-348.58	-1345.03	293134.7	4322482	557092.3

LINE (1) JULIAN DAY (265) 1996

STN.	EAST G1	North G1	UT E-W	UT N-S	MAG. FIELD INT.
M1-0	205.08	-763.63	293688.321	4323063.34	555512
M1-.1	195.0279	-764.028	293678.269	4323062.95	555405
M1-.2	185.0357	-764.423	293668.277	4323062.55	555412
M1-.3	175.0435	-764.818	293658.285	4323062.16	555466
M1-.4	165.0513	-765.214	293648.293	4323061.76	555533
M1-.5	155.0591	-765.609	293638.3	4323061.36	555595
M1-.6	145.067	-766.004	293628.308	4323060.97	555644
M1-.7	135.0748	-766.4	293618.316	4323060.57	555670
M1-.8	125.0826	-766.795	293608.324	4323060.18	555695
M1-.9	115.0904	-767.19	293598.332	4323059.78	555658
M1-1	105.0982	-767.586	293588.34	4323059.39	555775
M1-1.1	95.10604	-767.981	293578.347	4323058.99	555801
M1-1.2	85.11386	-768.377	293568.355	4323058.6	555842
M1-1.3	75.12168	-768.772	293558.363	4323058.2	555873
M1-1.4	65.1295	-769.167	293548.371	4323057.81	555894
M1-1.5	55.13732	-769.563	293538.379	4323057.41	555948
M1-1.6	45.14513	-769.958	293528.387	4323057.02	555997
M1-1.7	35.15295	-770.353	293518.394	4323056.62	555999
M1-1.8	25.16077	-770.749	293508.402	4323056.22	556185
M1-1.9	15.1486	-771.145	293498.39	4323055.83	556050
M1-2.0	5.156422	-771.54	293488.398	4323055.43	556068
M1-2.1	-4.83576	-771.935	293478.406	4323055.04	556112
M1-2.2	-14.8279	-772.331	293468.413	4323054.64	556116
M1-2.3	-24.8201	-772.726	293458.421	4323054.25	556167

M1-2.4	-34.8123	-773.121	293448.429	4323053.85	556185
M1-02.5	-44.8045	-773.517	293438.437	4323053.46	556260
M1-02.6	-54.7967	-773.912	293428.445	4323053.06	556253
M1-02.7	-64.7889	-774.308	293418.452	4323052.67	556251
M1-02.8	-74.781	-774.703	293408.46	4323052.27	556322
M1-02.9	-84.9131	-775.104	293398.328	4323051.87	556265
M1-03.0	-94.9053	-775.499	293388.336	4323051.47	556314
M1-03.1	-104.897	-775.894	293378.344	4323051.08	556413
M1-03.2	-114.89	-776.29	293368.351	4323050.68	556818
M1-03.3	-124.882	-776.685	293358.359	4323050.29	556429
M1-03.4	-134.874	-777.08	293348.367	4323049.89	556409
M1-03.5	-144.866	-777.476	293338.375	4323049.5	556471
M1-03.6	-154.858	-777.871	293328.383	4323049.1	556508
M1-03.7	-164.851	-778.266	293318.39	4323048.71	556533
M1-03.8	-174.843	-778.662	293308.398	4323048.31	556523
M1-03.9	-184.835	-779.057	293298.406	4323047.92	556491
M1-04.0	-194.887	-779.455	293288.354	4323047.52	556591
M1-04.1	-204.879	-779.85	293278.362	4323047.12	556617
M1-04.2	-214.871	-780.246	293268.37	4323046.73	556641
M1-04.3	-224.864	-780.641	293258.377	4323046.33	556651
M1-04.4	-234.856	-781.036	293248.385	4323045.94	556769
M1-04.5	-244.848	-781.432	293238.393	4323045.54	556753
M1-04.6	-254.84	-781.827	293228.401	4323045.15	556727
M1-04.7	-264.832	-782.222	293218.409	4323044.75	556740
M1-04.8	-274.825	-782.618	293208.416	4323044.36	556778
M1-04.9	-284.853	-783.014	293198.388	4323043.96	556697
M1-05.0	-294.845	-783.41	293188.396	4323043.56	556600
M1-05.1	-304.837	-783.805	293178.404	4323043.17	556771

M1-05.2	-314.829	-784.2	293168.412	4323042.77	556815
M1-05.3	-324.821	-784.596	293158.42	4323042.38	556887
M1-05.4	-334.814	-784.991	293148.427	4323041.98	556866
M1-05.5	-344.806	-785.387	293138.435	4323041.59	556997
M1-05.6	-354.798	-785.782	293128.443	4323041.19	556947
M1-05.7	-364.79	-786.177	293118.451	4323040.8	557007
M1-05.8	-374.782	-786.573	293108.459	4323040.4	557015
M1-05.9	-384.774	-786.968	293098.467	4323040.01	557027
M1-06.0	-394.767	-787.363	293088.474	4323039.61	557058
M1-06.1	-404.759	-787.759	293078.482	4323039.21	557056
M1-06.2	-414.751	-788.154	293068.49	4323038.82	557093
M1-06.3	-424.743	-788.549	293058.498	4323038.42	557099
M1-06.4	-434.735	-788.945	293048.506	4323038.03	557122
M1-06.5	-444.728	-789.34	293038.513	4323037.63	557125
M1-06.6	-454.72	-789.735	293028.521	4323037.24	557146
M1-06.7	-464.712	-790.131	293018.529	4323036.84	557236
M1-06.8	-474.704	-790.526	293008.537	4323036.45	557169
M1-06.9	-484.736	-790.923	292998.505	4323036.05	557232
M1-07.0	-494.728	-791.318	292988.513	4323035.66	557208
M1-07.1	-494.333	-801.31	292988.908	4323025.66	557267
M1-07.2	-493.938	-811.303	292989.303	4323015.67	557242
M1-07.3	-493.542	-821.295	292989.699	4323005.68	557249
M1-07.4	-493.147	-831.287	292990.094	4322995.69	557267
M1-07.5	-492.752	-841.279	292990.489	4322985.69	557307
M1-07.6	-492.356	-851.271	292990.885	4322975.7	557305
M1-07.7	-491.961	-861.264	292991.28	4322965.71	557300
M1-07.8	-491.566	-871.256	292991.675	4322955.72	557293
M1-07.9	-491.169	-881.278	292992.072	4322945.7	557255

M1-08.0	-490.774	-891.27	292992.467	4322935.7	557259
M1-08.1	-500.766	-891.665	292982.475	4322935.31	557424
M1-08.2	-510.758	-892.061	292972.483	4322934.91	557521
M1-08.3	-520.75	-892.456	292962.491	4322934.52	557317
M1-08.4	-530.743	-892.851	292952.498	4322934.12	557333
M1-08.5	-540.735	-893.247	292942.506	4322933.73	557394
M1-08.6	-550.727	-893.642	292932.514	4322933.33	557413
M1-08.7	-560.719	-894.038	292922.522	4322932.94	557418
M1-08.8	-570.711	-894.433	292912.53	4322932.54	557427
M1-08.9	-580.723	-894.829	292902.518	4322932.14	557460
M1-09.0	-590.716	-895.224	292892.525	4322931.75	557442
M1-09A.0	-600.708	-895.62	292882.533	4322931.35	557437
M1-09A.1	-610.7	-896.015	292872.541	4322930.96	557443
M1-09A.2	-620.692	-896.41	292862.549	4322930.56	557469
M1-09A.3	-630.684	-896.806	292852.557	4322930.17	557503
M1-09A.4	-640.677	-897.201	292842.564	4322929.77	557553
M1-09A.5	-650.669	-897.596	292832.572	4322929.38	557516
M1-09A.6	-660.661	-897.992	292822.58	4322928.98	557381
M1-09A.7	-670.653	-898.387	292812.588	4322928.59	557170
M1-09A.8	-680.655	-898.783	292802.586	4322928.19	557105
M1-09A.9	-690.647	-899.178	292792.594	4322927.8	557253
M1-09.1	-698.556	-893.058	292784.685	4322933.92	557411
M1-09.2	-706.465	-886.938	292776.776	4322940.04	557490
M1-09.3	-714.373	-880.818	292768.868	4322946.16	557492
M1-09.4	-722.282	-874.698	292760.959	4322952.28	557485
M1-09.5	-730.19	-868.578	292753.051	4322958.4	557496
M1-09.6	-738.099	-862.458	292745.142	4322964.52	557534
M1-09.7	-746.007	-856.338	292737.234	4322970.64	557545

M1-09.8	-753.916	-850.218	292729.325	4322976.76	557537
M1-09.9	-761.825	-844.098	292721.416	4322982.88	557535
M1-10.0	-769.789	-837.935	292713.452	4322989.04	557490
M1-10.1	-777.697	-831.815	292705.544	4322995.16	557537
M1-10.2	-785.606	-825.695	292697.635	4323001.28	557538
M1-10.3	-793.514	-819.575	292689.727	4323007.4	557506
M1-10.4	-801.423	-813.455	292681.818	4323013.52	557474
M1-10.5	-809.331	-807.335	292673.91	4323019.64	557274
M1-10.7	-825.149	-795.095	292658.092	4323031.88	557491
M1-10.8	-833.057	-788.975	292650.184	4323038	557477
M1-10.9	-840.934	-782.88	292642.307	4323044.09	557514
M1-11.0	-848.843	-776.76	292634.398	4323050.21	557488
M1-11.1	-856.751	-770.64	292626.49	4323056.33	557496
M1-11.2	-864.66	-764.52	292618.581	4323062.45	557496
M1-11.3	-872.568	-758.4	292610.673	4323068.57	557527
M1-11.4	-880.477	-752.28	292602.764	4323074.69	557538
M1-11.5	-888.386	-746.16	292594.855	4323080.81	557555
M1-11.6	-896.294	-740.04	292586.947	4323086.93	557533
M1-11.7	-904.203	-733.92	292579.038	4323093.05	557514
M1-11.8	-912.111	-727.8	292571.13	4323099.17	557516
M1-11.9	-920.052	-721.655	292563.189	4323105.32	557502
M1-12.0	-927.96	-715.535	292555.281	4323111.44	557487
M1-12.1	-935.869	-709.415	292547.372	4323117.56	557484
M1-12.2	-943.777	-703.295	292539.464	4323123.68	557477
M1-12.3	-951.686	-697.175	292531.555	4323129.8	557495
M1-12.4	-959.594	-691.055	292523.647	4323135.92	557492
M1-12.5	-967.503	-684.935	292515.738	4323142.04	557500
M1-12.6	-975.412	-678.815	292507.829	4323148.16	557529

M1-12.7	-983.32	-672.695	292499.921	4323154.28	557534
M1-12.8	-991.229	-666.575	292492.012	4323160.4	557585
M1-13.0	-1007.06	-654.321	292476.181	4323172.65	557436
M1-13.1	-1014.97	-648.201	292468.271	4323178.77	557451
M1-13.2	-1022.88	-642.081	292460.361	4323184.89	557446
M1-13.3	-1030.79	-635.961	292452.451	4323191.01	557445
M1-13.4	-1038.7	-629.841	292444.541	4323197.13	557432
M1-13.5	-1046.61	-623.721	292436.631	4323203.25	557429
M1-13.6	-1054.52	-617.601	292428.721	4323209.37	557418
M1-13.7	-1062.47	-611.446	292420.771	4323215.53	557359
M1-13.8	-1070.99	-616.678	292412.251	4323210.3	557401
M1-13.9	-1079.51	-621.91	292403.731	4323205.06	557411
M1-14.0	-1088.04	-627.141	292395.201	4323199.83	557404
M1-14.1	-1096.56	-632.373	292386.681	4323194.6	557386
M1-14.2	-1105.08	-637.605	292378.161	4323189.37	557366
M1-14.3	-1113.6	-642.837	292369.641	4323184.14	557362
M1-15.15	-1186.1	-687.347	292297.141	4323139.63	557618
M1-15.2	-1190.37	-689.963	292292.871	4323137.01	557583
M1-15.25	-1194.63	-692.579	292288.611	4323134.39	557557
M1-15.3	-1198.89	-695.195	292284.351	4323131.78	557549
M1-15.35	-1203.15	-697.811	292280.091	4323129.16	557541
M1-15.4	-1207.41	-700.426	292275.831	4323126.55	557535
M1-15.45	-1211.67	-703.042	292271.571	4323123.93	557537
M1-15.5	-1215.93	-705.658	292267.311	4323121.32	557536
M1-15.55	-1220.19	-708.274	292263.051	4323118.7	557533
M1-15.6	-1224.45	-710.89	292258.791	4323116.08	557537
M1-15.65	-1228.72	-713.506	292254.521	4323113.47	557560
M1-15.7	-1232.98	-716.122	292250.261	4323110.85	557484

M1-15.8	-1241.5	-721.354	292241.741	4323105.62	557481
M1-15.9	-1250.02	-726.586	292233.221	4323100.39	557413
M1-16.0	-1258.54	-731.818	292224.701	4323095.16	557498
M1-16.1	-1267.07	-737.05	292216.171	4323089.92	557498
M1-16.2	-1275.59	-742.281	292207.651	4323084.69	557517
M1-16.3	-1284.11	-747.513	292199.131	4323079.46	557492
M1-16.4	-1292.63	-752.745	292190.611	4323074.23	557495
M1-16.5	-1301.15	-757.977	292182.091	4323069	557484
M1-16.6	-1309.68	-763.209	292173.561	4323063.76	557481
M1-16.7	-1318.1	-768.38	292165.141	4323058.59	557529
M1-16.8	-1326.62	-773.612	292156.621	4323053.36	557453
M1-16.9	-1335.14	-778.844	292148.101	4323048.13	557458
M1-17.0	-1343.67	-784.076	292139.571	4323042.9	557474
M1-17.1	-1352.19	-789.308	292131.051	4323037.67	557471
M1-17.2	-1360.71	-794.54	292122.531	4323032.43	557520
M1-17.3	-1369.31	-799.82	292113.931	4323027.15	557550

LINE (2)

STN.	**EAST G1**	**North G1**	**UTM E-W**	**UTM N-S**	**MAG. FIELD INT.**
M2--01.0	297.0949	-559.833	293780.336	4323267.14	554811 〃
M2--00.9	287.1027	-560.228	293770.344	4323266.75	554873
M2--00.8	277.1105	-560.624	293760.352	4323266.35	554928
M2--00.7	267.1184	-561.019	293750.36	4323265.95	554959
M2--00.6	257.1262	-561.414	293740.368	4323265.56	554951
M2--00.5	247.134	-561.81	293730.375	4323265.16	555006
M2--00.4	237.1418	-562.205	293720.383	4323264.77	555002
M2--00.3	227.1496	-562.6	293710.391	4323264.37	555011
M2--00.2	217.1574	-562.996	293700.399	4323263.98	555065

M2--00.1	207.1653	-563.391	293690.407	4323263.58	554993
M2-00.0	197.1731	-563.786	293680.414	4323263.19	555133
M2-00.1	187.1809	-564.182	293670.422	4323262.79	555187
M2-00.2	177.1887	-564.577	293660.43	4323262.4	555169
M2-00.3	167.1965	-564.972	293650.438	4323262	555173
M2-00.4	157.2044	-565.368	293640.446	4323261.61	555045
M2-00.5	147.2122	-565.763	293630.454	4323261.21	555181
M2-00.6	137.22	-566.158	293620.461	4323260.82	555250
M2-00.7	127.2278	-566.554	293610.469	4323260.42	555255
M2-00.8	117.2356	-566.949	293600.477	4323260.02	555637
M2-00.9	107.2434	-567.344	293590.485	4323259.63	555409
M2-01.0	97.25126	-567.74	293580.493	4323259.23	555487
M2-01.1	87.25908	-568.135	293570.5	4323258.84	555372
M2-01.2	77.2669	-568.531	293560.508	4323258.44	555470
M2-01.3	67.27472	-568.926	293550.516	4323258.05	555461
M2-01.4	57.28253	-569.321	293540.524	4323257.65	555570
M2-01.5	47.29035	-569.717	293530.532	4323257.26	555607
M2-01.6	37.29817	-570.112	293520.54	4323256.86	555603
M2-01.7	27.30599	-570.507	293510.547	4323256.47	555619
M2-01.8	17.31381	-570.903	293500.555	4323256.07	555637
M2-01.9	7.321623	-571.298	293490.563	4323255.68	555662
M2-02.0	-2.67056	-571.693	293480.571	4323255.28	555682
M2-02.1	-2.27521	-581.685	293480.966	4323245.29	555736
M2-02.2	-1.87987	-591.678	293481.362	4323235.3	555720
M2-02.3	-1.48452	-601.67	293481.757	4323225.3	555782
M2-02.4	-1.08918	-611.662	293482.152	4323215.31	555843
M2-02.5	-0.69383	-621.654	293482.548	4323205.32	555829
M2-02.6	-0.29848	-631.646	293482.943	4323195.33	555816

M2-02.7	0.096863	-641.639	293483.338	4323185.33	555837
M2-02.8	0.492209	-651.631	293483.734	4323175.34	555860
M2-02.9	0.887554	-661.623	293484.129	4323165.35	555863
M2-03.0	1.2829	-671.615	293484.524	4323155.36	555934
M2-03.1	-8.70928	-672.01	293474.532	4323154.96	555918
M2-03.2	-18.7015	-672.406	293464.54	4323154.57	555938
M2-03.3	-28.6936	-672.801	293454.548	4323154.17	555971
M2-03.4	-38.6858	-673.196	293444.556	4323153.78	556015
M2-03.5	-48.678	-673.592	293434.563	4323153.38	556032
M2-03.6	-58.6702	-673.987	293424.571	4323152.99	556067
M2-03.7	-68.6624	-674.383	293414.579	4323152.59	556074
M2-03.8	-78.6546	-674.778	293404.587	4323152.2	556074
M2-03.9	-88.6467	-675.173	293394.595	4323151.8	556278
M2-04.0	-98.6389	-675.569	293384.602	4323151.4	556101
M2-04.1	-108.631	-675.964	293374.61	4323151.01	556155
M2-04.2	-118.623	-676.359	293364.618	4323150.61	556181
M2-04.3	-128.615	-676.755	293354.626	4323150.22	556248
M2-04.4	-138.608	-677.15	293344.633	4323149.82	556257
M2-04.5	-148.6	-677.545	293334.641	4323149.43	556254
M2-04.6	-158.592	-677.941	293324.649	4323149.03	556291
M2-04.7	-168.584	-678.336	293314.657	4323148.64	556345
M2-04.8	-178.576	-678.731	293304.665	4323148.24	556342
M2-04.9	-188.569	-679.127	293294.672	4323147.85	556340
M2-05.0	-198.561	-679.522	293284.68	4323147.45	556407
M2-05.1	-208.553	-679.917	293274.688	4323147.06	556417
M2-05.2	-218.545	-680.313	293264.696	4323146.66	556424
M2-05.3	-228.537	-680.708	293254.704	4323146.27	556548
M2-05.4	-238.529	-681.103	293244.712	4323145.87	556493

M2-05.5	-248.522	-681.499	293234.719	4323145.47	556499
M2-05.6	-258.514	-681.894	293224.727	4323145.08	556479
M2-05.7	-268.506	-682.289	293214.735	4323144.68	556463
M2-05.8	-278.498	-682.685	293204.743	4323144.29	556472
M2-05.9	-288.49	-683.08	293194.751	4323143.89	556555
M2-06.0	-298.483	-683.475	293184.758	4323143.5	556563
M2-06.1	-308.475	-683.871	293174.766	4323143.1	556658
M2-06.2	-318.467	-684.266	293164.774	4323142.71	556720
M2-06.3	-328.459	-684.662	293154.782	4323142.31	556723
M2-06.4	-338.451	-685.057	293144.79	4323141.92	556752
M2-06.5	-348.443	-685.452	293134.798	4323141.52	556757
M2-06.6	-358.436	-685.848	293124.805	4323141.13	556767
M2-06.7	-368.428	-686.243	293114.813	4323140.73	556951
M2-06.8	-378.42	-686.638	293104.821	4323140.34	556848
M2-06.9	-388.412	-687.034	293094.829	4323139.94	556795
M2-07.0	-398.404	-687.429	293084.837	4323139.54	557057
M2-07.1	-408.397	-687.824	293074.844	4323139.15	556984
M2-07.2	-418.389	-688.22	293064.852	4323138.75	556962
M2-07.3	-428.381	-688.615	293054.86	4323138.36	556982
M2-07.4	-438.373	-689.01	293044.868	4323137.96	557005
M2-07.5	-448.365	-689.406	293034.876	4323137.57	557002
M2-07.6	-458.357	-689.801	293024.884	4323137.17	557055
M2-07.7	-468.35	-690.196	293014.891	4323136.78	557211
M2-07.8	-478.342	-690.592	293004.899	4323136.38	557047
M2-07.9	-488.334	-690.987	292994.907	4323135.99	557050
M2-08.0	-498.326	-691.382	292984.915	4323135.59	557049
M2-08.1	-508.318	-691.778	292974.923	4323135.2	557069
M2-08.2	-518.311	-692.173	292964.93	4323134.8	557119

M2-08.3	-528.303	-692.568	292954.938	4323134.41	557182

LINE (3)

STN. INT.	EAST G1	North G1	UTM E-W	UTM N-S	MAG. FIELD
3-2.9	-1394.33	-874.49	292088.911	4322952.48	557465
4.7	-1534.92	-1124.18	291948.321	4322702.79	557260
6	-1667.7	-1235.16	291815.541	4322591.81	557247
7	-1689.39	-1285.1	291793.851	4322541.87	557364
8	-1698.07	-1362.78	291785.171	4322464.19	557186
9	-19821.2	-1705.7	273662.041	4322121.27	557011
10	-1787.46	-1600.27	291695.781	4322226.7	556930
11	-1765.76	-1692.38	291717.481	4322134.59	556963
11.7	-1739.73	-1766.73	291743.511	4322060.24	556882
12	-1767.5	-1781.16	291715.741	4322045.81	556880
13	-1838.66	-1775.61	291644.581	4322051.36	556791
14	-1897.67	-1714.58	291585.571	4322112.39	556747
15	-1988.8	-1705.7	291494.441	4322121.27	556602
16	-2060.83	-1756.75	291422.411	4322070.22	556417
17	-2118.97	-1812.23	291364.271	4322014.74	556130
18	-2175.38	-1866.61	291307.861	4321960.36	555991
19	-2236.13	-1917.66	291247.111	4321909.31	555788
20	-2286.47	-1989.8	291196.771	4321837.17	555641
20.5	-2334.2	-2016.43	291149.041	4321810.54	555528
21	-2372.38	-2039.74	291110.861	4321787.23	555407
22	-2468.71	-2067.48	291014.531	4321759.49	555212
23	-2537.27	-2036.41	290945.971	4321790.56	555009
24	-2609.3	-2084.13	290873.941	4321742.84	554769
25	-2667.45	-2134.06	290815.791	4321692.91	554713
26	-2739.48	-2197.32	290743.761	4321629.65	554285
27	-2782.87	-2255.03	290700.371	4321571.94	553985
28	-2826.26	-2328.27	290656.981	4321498.7	553653
29	-2854.9	-2411.5	290628.341	4321415.47	553385
30	-2913.05	-2521.37	290570.191	4321305.6	552991
31	-2956.44	-2593.51	290526.801	4321233.46	552637
3-31.8	-2913.05	-2650.1	290570.191	4321176.87	551471

LINE (4)

STN. INT.	EAST G1	North G1	UTM E-W	UTM N-S	MAG. FIELD
4-00.0	-1388.25	-865.61	292095	4322961	557490
″					
4-00.1	-1377.34	-869.097	292105.9	4322958	557440
″					
4-00.2	-1366.43	-872.584	292116.8	4322954	557441
4-00.3	-1355.52	-876.071	292127.7	4322951	557446
4-00.4	-1344.61	-879.559	292138.6	4322947	557433

4-00.5	-1333.7	-883.046	292149.5	4322944	557444
4-00.6	-1322.79	-886.533	292160.5	4322940	557444
4-00.7	-1311.88	-890.02	292171.4	4322937	557505
4-00.8	-1301.9	-886.136	292181.3	4322941	557453
4-00.9	-1291.92	-882.252	292191.3	4322945	557455
4-01.0	-1281.94	-878.368	292201.3	4322949	557480
4-01.1	-1271.96	-874.484	292211.3	4322952	557484
4-01.2	-1261.98	-870.6	292221.3	4322956	557505
4-01.3	-1252	-866.716	292231.2	4322960	557484
4-01.4	-1242.02	-862.832	292241.2	4322964	557501
4-01.5	-1232.04	-858.948	292251.2	4322968	557508
4-01.6	-1222.06	-855.064	292261.2	4322972	557510
4-01.7	-1212.08	-851.18	292271.2	4322976	557573
4-01.8	-1201.84	-853.4	292281.4	4322974	557564
4-01.9	-1191.6	-855.62	292291.6	4322971	557534
4-02.0	-1181.36	-857.84	292301.9	4322969	557570
4-02.1	-1171.12	-860.06	292312.1	4322967	557591
4-02.2	-1160.88	-862.28	292322.4	4322965	557580
4-02.3	-1150.63	-864.5	292332.6	4322962	557561
4-02.4	-1140.39	-866.72	292342.8	4322960	557530
4-02.5	-1130.15	-868.94	292353.1	4322958	557547
4-02.6	-1119.91	-871.16	292363.3	4322956	557560
4-02.7	-1109.67	-873.38	292373.6	4322954	557607
4-02.8	-1100.56	-879.04	292382.7	4322948	557564
4-02.9	-1091.45	-884.7	292391.8	4322942	557631
4-03.0	-1082.33	-890.36	292400.9	4322937	557609
4-03.1	-1073.22	-896.02	292410	4322931	557626
4-03.2	-1064.11	-901.68	292419.1	4322925	557651
4-03.3	-1055	-907.34	292428.2	4322920	557669

4-03.4	-1045.89	-913	292437.4	4322914	557678
4-03.5	-1036.77	-918.66	292446.5	4322908	557678
4-03.6	-1027.66	-924.32	292455.6	4322903	557675
4-03.7	-1018.55	-929.98	292464.7	4322897	557587
4-03.8	-1010.57	-935.195	292472.7	4322892	557705
4-03.9	-1002.58	-940.41	292480.7	4322887	557678
4-04.0	-994.598	-945.625	292488.6	4322881	557654
4-04.1	-986.614	-950.84	292496.6	4322876	557770
4-04.2	-978.63	-956.055	292504.6	4322871	557675
4-04.3	-970.646	-961.27	292512.6	4322866	557693
4-04.4	-962.662	-966.485	292520.6	4322860	557684
4-04.5	-954.678	-971.7	292528.6	4322855	557719
4-04.6	-946.694	-976.915	292536.5	4322850	557728
4-04.7	-938.71	-982.13	292544.5	4322845	557667
4-04.8	-932.201	-987.346	292551	4322840	557736
4-04.9	-925.692	-992.562	292557.5	4322834	557731
4-05.0	-919.183	-997.778	292564.1	4322829	557711
4-05.1	-912.674	-1002.99	292570.6	4322824	557688
4-05.2	-906.165	-1008.21	292577.1	4322819	557547
4-05.3	-899.656	-1013.43	292583.6	4322814	557057
4-05.4	-893.147	-1018.64	292590.1	4322808	557853
4-05.5	-886.638	-1023.86	292596.6	4322803	557696
4-05.6	-880.129	-1029.07	292603.1	4322798	557688
4-05.7	-873.62	-1034.29	292609.6	4322793	557739
4-05.8	-866.938	-1040.17	292616.3	4322787	557741
4-05.9	-860.256	-1046.05	292623	4322781	557768
4-06.0	-853.574	-1051.94	292629.7	4322775	557759
4-06.1	-846.892	-1057.82	292636.3	4322769	557747

4-06.2	-840.21	-1063.7	292643	4322763	557690
4-06.3	-833.528	-1069.58	292649.7	4322757	557663
4-06.5	-820.164	-1081.35	292663.1	4322746	557618
4-06.7	-806.8	-1093.11	292676.4	4322734	557215
4-06.8	-794.65	-1098.18	292688.6	4322729	557958
4-06.9	-782.5	-1103.26	292700.7	4322724	557705
4-07.0	-770.35	-1108.33	292712.9	4322719	557719
4.07.1	-758.2	-1113.4	292725	4322714	557719
4-07.2	-746.05	-1118.47	292737.2	4322709	557701
4-07.3	-733.9	-1123.55	292749.3	4322703	557665
4-07.4	-721.75	-1128.62	292761.5	4322698	557705
4-07.5	-713.506	-1133.61	292769.7	4322693	557710
4-07.6	-705.262	-1138.61	292778	4322688	557748
4-07.7	-697.018	-1143.6	292786.2	4322683	557705
4-07.8	-688.774	-1148.6	292794.5	4322678	557742
4-07.9	-680.53	-1153.59	292802.7	4322673	557756
4-08.0	-672.286	-1158.58	292811	4322668	557752
4-08.1	-664.042	-1163.58	292819.2	4322663	557759
4-08.2	-655.798	-1168.57	292827.4	4322658	557745
4-08.3	-647.554	-1173.57	292835.7	4322653	557800
4-08.4	-639.31	-1178.56	292843.9	4322648	557727
4-08.5	-632.106	-1185.22	292851.1	4322642	557714
4-08.6	-624.902	-1191.88	292858.3	4322635	557690
4-08.7	-617.698	-1198.54	292865.5	4322628	557667
4-08.8	-610.494	-1205.2	292872.7	4322622	557611
4-08.9	-603.29	-1211.86	292880	4322615	558013
4-09.0	-596.086	-1218.51	292887.2	4322608	557594
4-09.1	-588.882	-1225.17	292894.4	4322602	557688

4-09.2	-581.678	-1231.83	292901.6	4322595	557722
4-09.3	-574.474	-1238.49	292908.8	4322588	557740
4-09.4	-567.27	-1245.15	292916	4322582	557728
4-09.5	-559.286	-1249.92	292924	4322577	557705
4-09.6	-551.302	-1254.69	292931.9	4322572	557733
4-09.7	-543.318	-1259.47	292939.9	4322568	557696
4-09.8	-535.334	-1264.24	292947.9	4322563	557700
4-09.9	-527.35	-1269.01	292955.9	4322558	557702
4-10.0	-519.366	-1273.78	292963.9	4322553	557692
4-10.1	-511.382	-1278.55	292971.9	4322548	557683
4-10.2	-503.398	-1283.33	292979.8	4322544	557698
4-10.3	-495.414	-1288.1	292987.8	4322539	557676
4-10.4	-487.43	-1292.87	292995.8	4322534	557701
4-10.5	-481.645	-1298.42	293001.6	4322529	557645
4-10.6	-475.86	-1303.97	293007.4	4322523	557607
4-10.7	-470.075	-1309.51	293013.2	4322517	557716
4-10.8	-464.29	-1315.06	293019	4322512	557656
4-10.9	-458.505	-1320.61	293024.7	4322506	557579
4-11.0	-452.72	-1326.16	293030.5	4322501	557516

LINE (5)

STN. INT.	**EAST G1**	**North G1**	**UTM E-W**	**UTM N-S**	**MAG. FIELD**
ln-5					
"					
Readings	EAST G1	NORTH G1			
"					
1.8	-1287.58	-991.01	292195.661	4322835.96	557529
"					
1.9	-1285.65	-998.039	292197.59	4322828.93	557529
"					
2	-1283.72	-1005.07	292199.519	4322821.91	557538
"					
2.1	-1281.79	-1012.1	292201.448	4322814.88	557538
2.2	-1279.86	-1019.13	292203.377	4322807.85	557532
2.3	-1277.94	-1026.15	292205.306	4322800.82	557544

2.4	-1276.01	-1033.18	292207.235	4322793.79	557558
2.5	-1274.08	-1040.21	292209.164	4322786.76	557554
2.6	-1272.15	-1047.24	292211.092	4322779.73	557542
2.7	-1270.22	-1054.27	292213.021	4322772.7	557504
2.8	-1261.67	-1065.37	292221.576	4322761.61	557423
3	-1244.56	-1087.56	292238.684	4322739.41	557483
3.1	-1236	-1098.66	292247.239	4322728.31	557530
3.2	-1227.45	-1109.76	292255.793	4322717.22	557622
3.3	-1218.89	-1120.85	292264.347	4322706.12	557615
3.4	-1210.34	-1131.95	292272.901	4322695.02	557647
3.5	-1200.27	-1142.38	292282.967	4322684.59	557599
3.6	-1190.21	-1152.81	292293.033	4322674.16	557603
3.7	-1180.14	-1163.25	292303.099	4322663.73	557616
3.8	-1170.08	-1173.68	292313.165	4322653.3	557622
3.9	-1160.01	-1184.11	292323.231	4322642.86	557700
4	-1155.15	-1192.99	292328.091	4322633.99	557658
4.1	-1150.29	-1201.87	292332.951	4322625.11	557705
4.2	-1145.43	-1210.74	292337.811	4322616.23	557648
4.3	-1140.57	-1219.62	292342.671	4322607.35	557674
4.4	-1135.71	-1228.5	292347.531	4322598.47	557727
4.5	-1130.5	-1236.49	292352.739	4322590.48	557697
4.6	-1125.29	-1244.48	292357.947	4322582.49	557723
4.7	-1120.09	-1252.47	292363.155	4322574.5	557734
4.8	-1114.88	-1260.46	292368.363	4322566.51	557760
4.9	-1109.67	-1268.45	292373.571	4322558.52	557817
5	-1104.98	-1278.22	292378.257	4322548.76	557757
5.1	-1100.3	-1287.98	292382.943	4322538.99	557770
5.2	-1095.61	-1297.75	292387.629	4322529.23	557771
5.3	-1090.93	-1307.51	292392.315	4322519.46	557788
5.4	-1086.24	-1317.28	292397.001	4322509.69	557743
5.5	-1079.64	-1323.49	292403.597	4322503.48	557829
5.6	-1073.05	-1329.71	292410.193	4322497.27	557797
5.7	-1066.45	-1335.92	292416.789	4322491.05	557909
5.8	-1059.86	-1342.14	292423.385	4322484.84	557935
5.9	-1053.26	-1348.35	292429.981	4322478.62	557844
6	-1049.96	-1356.56	292433.277	4322470.41	557861
6.1	-1046.67	-1364.78	292436.573	4322462.2	557840
6.2	-1043.37	-1372.99	292439.869	4322453.98	557826
6.3	-1040.08	-1381.21	292443.165	4322445.77	557901
6.4	-1036.78	-1389.42	292446.461	4322437.55	558025
6.5	-1033.65	-1396.74	292449.587	4322430.23	557893
6.6	-1030.53	-1404.07	292452.713	4322422.91	557910
6.7	-1027.4	-1411.39	292455.839	4322415.58	557805
6.8	-1024.28	-1418.72	292458.965	4322408.26	557911
6.9	-1021.15	-1426.04	292462.091	4322400.93	557948
7	-1014.73	-1434.25	292468.513	4322392.72	557841
7.1	-1008.31	-1442.46	292474.935	4322384.51	557820
7.2	-1001.88	-1450.68	292481.357	4322376.3	557722
7.3	-995.462	-1458.89	292487.779	4322368.09	557500
7.4	-989.04	-1467.1	292494.201	4322359.87	557619
7.5	-982.792	-1477.31	292500.449	4322349.66	557922
7.6	-976.544	-1487.52	292506.697	4322339.45	557866
7.7	-970.296	-1497.73	292512.945	4322329.24	557804
7.8	-964.048	-1507.94	292519.193	4322319.03	557781
7.9	-957.8	-1518.15	292525.441	4322308.82	557821
8	-953.462	-1525.25	292529.779	4322301.72	557763

8.1	-949.124	-1532.35	292534.117	4322294.62	557777
8.2	-944.786	-1539.46	292538.455	4322287.52	557842
8.3	-940.448	-1546.56	292542.793	4322280.42	557829
8.4	-936.11	-1553.66	292547.131	4322273.31	557820
8.5	-930.556	-1563.2	292552.685	4322263.77	557780
8.6	-925.002	-1572.75	292558.239	4322254.23	557773
8.7	-919.448	-1582.29	292563.793	4322244.68	557861
8.8	-913.894	-1591.84	292569.347	4322235.14	557840
8.9	-908.34	-1601.38	292574.901	4322225.59	557844
9	-905.388	-1611.37	292577.853	4322215.61	557873
9.1	-902.436	-1621.36	292580.805	4322205.62	557855
9.2	-899.484	-1631.34	292583.757	4322195.63	557850
9.3	-896.532	-1641.33	292586.709	4322185.64	557830
9.4	-893.58	-1651.32	292589.661	4322175.65	557856
9.5	-887.852	-1659.53	292595.389	4322167.44	557871
9.6	-882.124	-1667.74	292601.117	4322159.23	557839
9.7	-876.396	-1675.96	292606.845	4322151.02	557839
9.8	-870.668	-1684.17	292612.573	4322142.81	557845
9.9	-864.94	-1692.38	292618.301	4322134.59	557891
10	-860.08	-1705.6	292623.161	4322121.38	557863
10.1	-855.22	-1718.82	292628.021	4322108.16	557877
10.2	-850.36	-1732.03	292632.881	4322094.94	557877
10.3	-845.5	-1745.25	292637.741	4322081.72	557871
10.4	-840.64	-1758.97	292642.601	4322068	557908

LINE (6)

STN. INT.	EAST G1	North G1	UTM E-W	UTM N-S	MAG. FIELD
M6-00.1	-1378.31	-795.463	292104.931	4323031.51	557421
″					
M6-00.2	-1387.31	-791.106	292095.931	4323035.87	557409
″					
M6-00.3	-1396.31	-786.749	292086.931	4323040.22	557395
″					
M6-00.4	-1405.31	-782.392	292077.931	4323044.58	557390
M6-00.5	-1414.31	-778.035	292068.931	4323048.94	557384
M6-00.6	-1423.32	-773.678	292059.921	4323053.3	557373
M6-00.7	-1432.32	-769.321	292050.921	4323057.65	557368
M6-00.8	-1441.37	-764.937	292041.871	4323062.04	557432
M6-00.9	-1446.2	-756.179	292037.041	4323070.79	557379
M6-01	-1451.02	-747.422	292032.221	4323079.55	557399
M6-01.1	-1455.85	-738.664	292027.391	4323088.31	557424
M6-01.9	-1493.16	-721.8	291990.081	4323105.17	557205

M6-02	-1497.55	-730.788	291985.691	4323096.19	557250
M6-02.1	-1501.93	-739.776	291981.311	4323087.2	557292

LINE (7)

STN.	EAST G1	North G1	UTM E-W	UTM N-S	MAG. FIELD INT.
"					
M7-00.1	-1269.61	-1008.62	292213.631	4322818.35	557512
"					
M7-00.2	-1270.31	-1018.59	292212.931	4322808.38	557436
M7-00.3	-1273.73	-1027.99	292209.511	4322798.98	557471
M7-00.4	-1277.15	-1037.39	292206.091	4322789.58	557481
M7-00.5	-1280.57	-1046.78	292202.671	4322780.19	557494
M7-00.6	-1283.99	-1056.18	292199.251	4322770.79	557554
M7-00.7	-1287.41	-1065.58	292195.831	4322761.39	557472
M7-00.8	-1290.17	-1075.19	292193.071	4322751.78	557541
M7-00.9	-1292.92	-1084.8	292190.321	4322742.17	557542
M7-01	-1295.68	-1094.41	292187.561	4322732.56	557568
M7-01.1	-1298.44	-1104.03	292184.801	4322722.94	557559
M7-01.2	-1301.19	-1113.64	292182.051	4322713.33	557596
M7-01.3	-1304.94	-1122.91	292178.301	4322704.06	557550
M7-01.4	-1308.68	-1132.18	292174.561	4322694.79	557541
M7-01.5	-1312.43	-1141.46	292170.811	4322685.51	557483
M7-01.6	-1316.18	-1150.73	292167.061	4322676.24	557490
M7-01.7	-1319.92	-1160	292163.321	4322666.97	557458
M7-01.8	-1328.58	-1165	292154.661	4322661.97	557536
M7-01.9	-1337.24	-1170	292146.001	4322656.97	557510
M7-02	-1345.9	-1175	292137.341	4322651.97	557457
M7-02.1	-1354.56	-1180	292128.681	4322646.97	557476
M7-02.2	-1363.22	-1185	292120.021	4322641.97	557553
M7-02.3	-1373.1	-1186.56	292110.141	4322640.41	557514
M7-02.4	-1382.98	-1188.13	292100.261	4322638.84	557512
M7-02.5	-1392.85	-1189.69	292090.391	4322637.28	557529
M7-02.6	-1399.67	-1197.01	292083.571	4322629.96	557451

M7-02.7	-1406.49	-1204.32	292076.751	4322622.65	557497
M7-02.8	-1413.31	-1211.63	292069.931	4322615.34	557459
M7-02.9	-1422.59	-1215.38	292060.651	4322611.59	557441
M7-03	-1431.86	-1219.12	292051.381	4322607.85	557455
M7-03.1	-1441.13	-1222.87	292042.111	4322604.1	557463
M7-03.2	-1450.4	-1226.62	292032.841	4322600.35	557464
M7-03.3	-1459.67	-1230.36	292023.571	4322596.61	557455
M7-03.4	-1468.15	-1235.66	292015.091	4322591.31	557455
M7-03.5	-1476.63	-1240.96	292006.611	4322586.01	557457
M7-03.6	-1485.11	-1246.26	291998.131	4322580.71	557383
M7-03.7	-1492.66	-1252.82	291990.581	4322574.15	557432
M7-03.8	-1500.21	-1259.38	291983.031	4322567.59	557413
M7-03.9	-1507.76	-1265.94	291975.481	4322561.03	557403
M7-04.0	-1515.3	-1272.5	291967.941	4322554.47	557417
M7-04.1	-1522.85	-1279.06	291960.391	4322547.91	557466
M7-04.2	-1527.08	-1288.13	291956.161	4322538.84	557411
M7-04.3	-1531.3	-1297.19	291951.941	4322529.78	557421
M7-04.4	-1535.21	-1306.39	291948.031	4322520.58	557378
M7-04.475	-1538.14	-1313.3	291945.101	4322513.67	557363

LINE (8)

STN. INT.	EAST G1	North G1	UTM E-W	UTM N-S	MAG. FIELD
M8-00.0	-1700.95	-576.87	291782.291	4323250.1	557274
M8-00.1	-1695.36	-585.16	291787.881	4323241.81	557204
M8-00.2	-1689.77	-593.451	291793.471	4323233.52	557175
M8-00.3	-1684.17	-601.741	291799.071	4323225.23	557029
M8-00.4	-1678.58	-610.032	291804.661	4323216.94	557091
M8-00.5	-1672.99	-618.322	291810.251	4323208.65	557163
M8-00.6	-1666.17	-625.635	291817.071	4323201.34	557159

M8-00.7	-1659.35	-632.949	291823.891	4323194.02	557119
M8-00.8	-1652.53	-640.262	291830.711	4323186.71	557098
M8-01.3	-1619.61	-677.871	291863.631	4323149.1	558075
M8-01.35	-1614.63	-678.307	291868.611	4323148.67	557763
M8-01.4	-1609.64	-678.742	291873.601	4323148.23	557538
M8-01.45	-1604.66	-679.178	291878.581	4323147.8	557409
M8-01.5	-1599.68	-679.614	291883.561	4323147.36	557388
M8-01.55	-1594.7	-680.05	291888.541	4323146.92	557349
M8-01.6	-1589.72	-680.486	291893.521	4323146.49	557270
M8-01.65	-1584.74	-680.921	291898.501	4323146.05	557228
M8-01.7	-1579.76	-681.357	291903.481	4323145.62	557276
M8-01.75	-1574.78	-681.793	291908.461	4323145.18	557351
M8-01.8	-1569.8	-682.229	291913.441	4323144.74	557320
M8-01.9	-1559.8	-682.229	291923.441	4323144.74	557325
M8-02	-1549.8	-682.229	291933.441	4323144.74	557332
M8-02.1	-1539.8	-682.229	291943.441	4323144.74	557329
M8-02.2	-1529.8	-682.229	291953.441	4323144.74	557320
M8-02.3	-1519.8	-682.229	291963.441	4323144.74	557318
M8-02.4	-1510.73	-686.455	291972.511	4323140.52	557273
M8-02.5	-1501.67	-690.681	291981.571	4323136.29	557156

LINE (9)

STN.	EAST G1	North G1	UTM E-W	UTM N-S	MAG. FIELD INT.
″					
M9-01.1	-1772.86	-623.34	291710.381	4323203.63	556616
″					
M9-01.2	-1779.29	-615.68	291703.951	4323211.29	557159
″					
M9-01.3	-1785.72	-608.019	291697.521	4323218.95	557226
″					

M9-01.4	-1792.14	-600.359	291691.101	4323226.61	557279
M9-01.5	-1798.57	-592.698	291684.671	4323234.28	557295
M9-01.6	-1805	-585.038	291678.241	4323241.94	557338
M9-01.7	-1812.07	-577.967	291671.171	4323249.01	557355
M9-01.8	-1819.14	-570.896	291664.101	4323256.08	557340
M9-01.9	-1826.21	-563.825	291657.031	4323263.15	557335
M9-02	-1833.28	-556.754	291649.961	4323270.22	557344
M9-02.1	-1840.35	-549.682	291642.891	4323277.29	557327
M9-02.2	-1847.3	-542.489	291635.941	4323284.48	557347
M9-02.3	-1854.25	-535.296	291628.991	4323291.68	557349
M9-02.4	-1861.19	-528.102	291622.051	4323298.87	557340
M9-02.5	-1868.14	-520.909	291615.101	4323306.06	557335
M9-02.6	-1875.09	-513.715	291608.151	4323313.26	557337
M9-02.7	-1881.91	-506.402	291601.331	4323320.57	557345
M9-02.8	-1888.73	-499.088	291594.511	4323327.89	557334
M9-02.9	-1895.55	-491.775	291587.691	4323335.2	557310
M9-03	-1902.37	-484.461	291580.871	4323342.51	557322
M9-03.1	-1909.19	-477.148	291574.051	4323349.83	557330
M9-03.2	-1916.13	-469.954	291567.111	4323357.02	557367
M9-03.3	-1923.08	-462.761	291560.161	4323364.21	557368
M9-03.4	-1930.03	-455.568	291553.211	4323371.41	557341
M9-03.5	-1936.97	-448.374	291546.271	4323378.6	557337
M9-03.6	-1943.92	-441.181	291539.321	4323385.79	557356
M9-03.7	-1949.51	-432.89	291533.731	4323394.08	557390
M9-03.8	-1955.1	-424.6	291528.141	4323402.37	557379
M9-03.9	-1960.7	-416.31	291522.541	4323410.66	557377
M9-04	-1966.29	-408.019	291516.951	4323418.95	557424
M9-04.1	-1971.88	-399.729	291511.361	4323427.24	557422
M9-04.2	-1977.62	-391.537	291505.621	4323435.44	557422
M9-04.3	-1983.35	-383.346	291499.891	4323443.63	557432

M9-04.4	-1989.09	-375.154	291494.151	4323451.82	557439
M9-04.5	-1994.82	-366.963	291488.421	4323460.01	557441
M9-04.6	-2000.56	-358.771	291482.681	4323468.2	557496
M9-04.7	-2006.99	-351.111	291476.251	4323475.86	557472
M9-04.8	-2013.41	-343.45	291469.831	4323483.52	557487
M9-04.9	-2019.84	-335.79	291463.401	4323491.18	557467
M9-05	-2026.27	-328.13	291456.971	4323498.84	557560
M9-05.1	-2032.7	-320.469	291450.541	4323506.5	557349
M9-05.2	-2040.36	-314.041	291442.881	4323512.93	557480
M9-05.3	-2048.02	-307.613	291435.221	4323519.36	557526
M9-05.4	-2055.68	-301.185	291427.561	4323525.79	557539
M9-05.5	-2063.34	-294.758	291419.901	4323532.22	557520
M9-05.6	-2071	-288.33	291412.241	4323538.64	557522
M9-05.7	-2079.75	-283.482	291403.491	4323543.49	557522
M9-05.8	-2088.49	-278.633	291394.751	4323548.34	557471
M9-05.9	-2097.24	-273.785	291386.001	4323553.19	557474
M9-06	-2105.99	-268.937	291377.251	4323558.04	557470
M9-06.1	-2114.73	-264.089	291368.511	4323562.88	557486
M9-06.2	-2120.03	-255.609	291363.211	4323571.36	557468
M9-06.3	-2125.33	-247.128	291357.911	4323579.85	557475
M9-06.4	-2130.63	-238.648	291352.611	4323588.33	557478
M9-06.5	-2135.93	-230.167	291347.311	4323596.81	557499
M9-06.6	-2141.23	-221.687	291342.011	4323605.29	557496
M9-06.7	-2146.67	-213.3	291336.571	4323613.67	557848
M9-06.8	-2152.12	-204.913	291331.121	4323622.06	557516
M9-06.9	-2157.57	-196.527	291325.671	4323630.45	557527
M9-07	-2163.01	-188.14	291320.231	4323638.83	557538
M9-07.1	-2168.46	-179.753	291314.781	4323647.22	557547
M9-07.2	-2174.05	-171.463	291309.191	4323655.51	557555
M9-07.3	-2179.64	-163.173	291303.601	4323663.8	557572

M9-07.4	-2185.24	-154.882	291298.001	4323672.09	557588
M9-07.5	-2190.83	-146.592	291292.411	4323680.38	557589
M9-07.6	-2196.42	-138.301	291286.821	4323688.67	557594
M9-07.7	-2202.3	-130.211	291280.941	4323696.76	557614
M9-07.8	-2208.17	-122.121	291275.071	4323704.85	557634
M9-07.9	-2214.05	-114.031	291269.191	4323712.94	557652
M9-08	-2219.93	-105.941	291263.311	4323721.03	557643
M9-08.1	-2225.81	-97.8505	291257.431	4323729.12	557662
M9-08.2	-2232.24	-90.1901	291251.001	4323736.78	557664
M9-08.3	-2238.66	-82.5297	291244.581	4323744.44	557708
M9-08.4	-2245.09	-74.8692	291238.151	4323752.1	557729
M9-08.5	-2251.52	-67.2088	291231.721	4323759.76	557722
M9-08.6	-2257.95	-59.5483	291225.291	4323767.42	557630
M9-08.7	-2263.97	-51.562	291219.271	4323775.41	557677
M9-08.8	-2269.98	-43.5756	291213.261	4323783.4	557735
M9-08.9	-2276	-35.5893	291207.241	4323791.38	557757
M9-09	-2282.02	-27.6029	291201.221	4323799.37	557759
M9-09.1	-2288.04	-19.6165	291195.201	4323807.36	557756
M9-09.2	-2294.2	-11.7364	291189.041	4323815.24	557767
M9-09.3	-2300.35	-3.85633	291182.891	4323823.12	557777
M9-09.4	-2306.51	4.023773	291176.731	4323831	557835
M9-09.5	-2312.66	11.90388	291170.581	4323838.88	557826
M9-09.6	-2318.82	19.78399	291164.421	4323846.76	557801
M9-09.7	-2324.84	27.77034	291158.401	4323854.74	557705
M9-09.8	-2330.86	35.7567	291152.381	4323862.73	557756
M9-08.9	-2336.88	43.74305	291146.361	4323870.72	557769
M9-10	-2342.89	51.72941	291140.351	4323878.7	557780
M9-10.1	-2348.91	59.71576	291134.331	4323886.69	557820
M9-10.2	-2355.07	67.59587	291128.171	4323894.57	557831
M9-10.3	-2361.23	75.47598	291122.011	4323902.45	557797

M9-10.4	-2367.38	83.35609	291115.861	4323910.33	557903
M9-10.5	-2373.54	91.23619	291109.701	4323918.21	557890
M9-10.6	-2379.7	99.1163	291103.541	4323926.09	557849
M9-10.7	-2385.99	106.8878	291097.251	4323933.86	557861
M9-10.8	-2392.28	114.6592	291090.961	4323941.63	557911
M9-10.9	-2398.57	122.4307	291084.671	4323949.4	557884
M9-11	-2404.87	130.2021	291078.371	4323957.18	557896
M9-11.1	-2411.16	137.9736	291072.081	4323964.95	557899
M9-11.2	-2417.59	145.634	291065.651	4323972.61	557873
M9-11.3	-2424.02	153.2945	291059.221	4323980.27	557903
M9-11.4	-2430.45	160.9549	291052.791	4323987.93	557881
M9-11.5	-2436.87	168.6154	291046.371	4323995.59	557895
M9-11.6	-2443.3	176.2758	291039.941	4324003.25	557880
M9-11.7	-2449.59	184.0473	291033.651	4324011.02	557915
M9-11.8	-2455.89	191.8187	291027.351	4324018.79	557901
M9-11.9	-2462.18	199.5902	291021.061	4324026.56	557851
M9-12	-2468.47	207.3617	291014.771	4324034.33	557900
M9-12.1	-2474.77	215.1331	291008.471	4324042.11	557862
M9-12.2	-2481.59	222.4467	291001.651	4324049.42	557928
M9-12.3	-2488.41	229.7602	290994.831	4324056.73	557945
M9-12.4	-2495.23	237.0737	290988.011	4324064.05	557955
M9-12.5	-2502.05	244.3873	290981.191	4324071.36	557943
M9-12.6	-2508.87	251.7008	290974.371	4324078.67	557961
M9-12.7	-2516.53	258.1287	290966.711	4324085.1	558018
M9-12.8	-2524.19	264.5566	290959.051	4324091.53	557953
M9-12.9	-2531.85	270.9844	290951.391	4324097.96	557987
M9-13	-2539.51	277.4123	290943.731	4324104.39	557992
M9-13.1	-2547.17	283.8402	290936.071	4324110.81	558011
M9-13.2	-2540.1	290.9113	290943.141	4324117.88	558063

M9-13.3	-2533.03	297.9823	290950.211	4324124.96	558033
M9-13.4	-2525.96	305.0534	290957.281	4324132.03	558023
M9-13.5	-2518.88	312.1245	290964.361	4324139.1	558019
M9-13.6	-2511.81	319.1955	290971.431	4324146.17	557998
M9-13.7	-2514.4	328.8548	290968.841	4324155.83	558083
M9-13.8	-2516.99	338.514	290966.251	4324165.49	558129
M9-13.9	-2519.58	348.1733	290963.661	4324175.15	558058
M9-14	-2522.17	357.8326	290961.071	4324184.81	558216
M9-14.1	-2524.75	367.4918	290958.491	4324194.47	558179
M9-14.2	-2527.34	377.1511	290955.901	4324204.12	558390
M9-14.3	-2529.93	386.8103	290953.311	4324213.78	557967
M9-14.4	-2532.52	396.4696	290950.721	4324223.44	558083
M9-14.5	-2535.11	406.1288	290948.131	4324233.1	558193
M9-14.6	-2537.7	415.7881	290945.541	4324242.76	558305
M9-14.7	-2540.28	425.4474	290942.961	4324252.42	558248
M9-14.8	-2542.87	435.1066	290940.371	4324262.08	558200
M9-14.9	-2545.46	444.7659	290937.781	4324271.74	558231
M9-15	-2548.05	454.4251	290935.191	4324281.4	558214
M9-15.1	-2550.64	464.0844	290932.601	4324291.06	558227

LINE (10)

STN.	EAST G1	North G1	UTM E-W	UTM N-S	MAG. FIELD INT.
〃					
10-0.0	-4663.19	-678.8	288820.051	4323148.17	552342
〃					
1	-4547.48	-455	288935.761	4323371.97	554276
2	-4272.66	-209	289210.581	4323617.97	555670
3	-3997.85	-25.89	289485.391	4323801.08	556575
4	-3679.64	20.35	289803.601	4323847.32	557318
5	-3535	64.74	289948.241	4323891.71	557856
6	-3404.82	175.72	290078.421	4324002.69	558025
7	-3245.72	242.3	290237.521	4324069.27	560576
8	-3158.93	395.82	290324.311	4324222.79	557869
9	-3043.22	506.79	290440.021	4324333.76	556721
10	-2855.19	765.74	290628.051	4324592.71	557939

11	-2522.52	1061.67	290960.721	4324888.64	557484
12	-2314.24	1320.62	291169.001	4325147.59	557684
14	-2010.49	1413.1	291472.751	4325240.07	557021
15	-1897.67	1505.58	291585.571	4325332.55	556229
16	-1773.28	1616.55	291709.961	4325443.52	556190
17	-1648.89	1727.53	291834.351	4325554.5	555556
18	-1527.39	1820.01	291955.851	4325646.98	554953
19	-1417.47	1912.49	292065.771	4325739.46	554612
20	-1261.26	2004.97	292221.981	4325831.94	554182
21	-1090.58	2041.96	292392.661	4325868.93	552998
22	-931.48	2041.96	292551.761	4325868.93	553468
23	-804.19	2060.46	292679.051	4325887.43	552576
24	-665.34	1986.47	292817.901	4325813.44	553053
10-25.0	-522.15	1930.99	292961.091	4325757.96	552301
26	-461.4	3706.6	293021.841	4327533.57	552301
27	-601.99	3614.49	292881.251	4327441.46	554339
28	-727.82	3540.14	292755.421	4327367.11	553720
29	-1041.12	3465.78	292442.121	4327292.75	553625
30	-1216.42	3465.78	292266.821	4327292.75	553238
31	-1381.31	3503.52	292101.931	4327330.49	553746
34	-2476.52	3559	291006.721	4327385.97	554996
41	-3289.11	3632.62	290194.131	4327459.59	555317
45	-3751.96	3632.62	289731.281	4327459.59	554095
46	-3911.06	3651.11	289572.181	4327478.08	554693
47	-4055.7	3688.11	289427.541	4327515.08	554726
48	-4229.27	3725.1	289253.971	4327552.07	554628
52	-4865.69	3854.57	288617.551	4327681.54	553133
53	-5010.33	3891.56	288472.911	4327718.53	553432
54	-5183.89	3928.55	288299.351	4327755.52	552603

LINE (11)

STN. INT.	EAST G1	North G1	UTM E-W	UTM N-S	MAG. FIELD
〃					
M11-00	-496.11	1949.48	292987.131	4325776.45	552691
M11-02	-561.2	1764.52	292922.041	4325591.49	552152.3
M11-03	-545.29	1653.55	292937.951	4325480.52	552913.3
M11-04	-506.24	1561.07	292977.001	4325388.04	552973
M11-05	-455.61	1468.59	293027.631	4325295.56	553002
M11-06	-397.76	1394.6	293085.481	4325221.57	553126.3
M11-07	-389.08	1302.12	293094.161	4325129.09	553098.3
M11-08	-391.97	1209.64	293091.271	4325036.61	552874.3
M11-09	-390.52	1117.16	293092.721	4324944.13	553240.7

M11-10	-397.76	1006.19	293085.481	4324833.16	552702
M11-11	-360.15	913.71	293123.091	4324740.68	553494.3
M11-12	-305.19	821.23	293178.051	4324648.2	553622
M11-13	-266.13	747.24	293217.111	4324574.21	553532
M11-14	-212.62	654.76	293270.621	4324481.73	553711.3
M11-15	-148.98	580.78	293334.261	4324407.75	553123.7
M11-16	-111.37	488.3	293371.871	4324315.27	553593.3
M11-17	-63.64	395.82	293419.601	4324222.79	553713.3
M11-18	-18.8	327.38	293464.441	4324154.35	554061
M11-19	-49.17	223.81	293434.071	4324050.78	553994.7
M11-20	-69.42	129.48	293413.821	4323956.45	554168.7
M11-21	-21.69	18.5	293461.551	4323845.47	554359.3
M11-22	36.16	-66.58	293519.401	4323760.39	554522
M11-23	96.91	-160.91	293580.151	4323666.06	554425
M11-24	166.34	-242.29	293649.581	4323584.68	554325.3
M11-25	225.64	-323.68	293708.881	4323503.29	554549.3
M11-26	270.48	-429.1	293753.721	4323397.87	554482.7
M11-27	305.19	-512.34	293788.431	4323314.63	554759.7
M11-28	326.89	-615.91	293810.131	4323211.06	554729.7
M11-29	350.03	-710.24	293833.271	4323116.73	554670.3
M11-30	354.37	-804.57	293837.611	4323022.4	554929
M11-31	357.26	-906.3	293840.501	4322920.67	555003
M11-32	350.03	-1002.48	293833.271	4322824.49	555032.3
M11-33	357.26	-1098.66	293840.501	4322728.31	555103.3
M11-34	365.94	-1205.94	293849.181	4322621.03	555333.3
M11-36	381.85	-1413.09	293865.091	4322413.88	555644.7
M11-37	389.09	-1507.42	293872.331	4322319.55	555998.7
M11-38	402.1	-1612.85	293885.341	4322214.12	556081.3
M11-39	429.58	-1710.88	293912.821	4322116.09	556009
M11-40	457.07	-1794.11	293940.311	4322032.86	556343.3
M11-42	530.83	-1973.52	294014.071	4321853.45	556228.7

M11-43	577.12	-2060.45	294060.361	4321766.52	556217.3
M11-44	607.49	-2151.08	294090.731	4321675.89	556074.3
M11-48	730.44	-2535.8	294213.681	4321291.17	556320.7
M11-49	765.15	-2624.58	294248.391	4321202.39	556498.7
M11-50	801.31	-2704.11	294284.551	4321122.86	555867.3
M11-51	838.92	-2805.84	294322.161	4321021.13	556006.7
M11-52	857.72	-2918.67	294340.961	4320908.3	556237
M11-53	807.09	-3001.9	294290.331	4320825.07	556766.7
M11-54	809.99	-3101.78	294293.231	4320725.19	556905
M11-55	795.52	-3207.2	294278.761	4320619.77	556430.3
M11-56	856.27	-3284.89	294339.511	4320542.08	556196.3
M11-57	921.36	-3362.57	294404.601	4320464.4	555927
M11-58	982.11	-3442.1	294465.351	4320384.87	556135

LINE (12)

STN. INT.	EAST G1	North G1	UTM E-W	UTM N-S	MAG. FIELD
12-0.0	-322.54	-1333.93	293160.701	4322493.04	557069.3
"					
1	-374.61	-1429.37	293108.631	4322397.6	556955
"					
2	-381.56	-1533.68	293101.681	4322293.29	557542.3
3	-387.63	-1633.56	293095.611	4322193.41	557341.7
4	-400.65	-1733.44	293082.591	4322093.53	557319.3
5	-407.59	-1823.33	293075.651	4322003.64	557276
6	-389.37	-7124.66	293093.871	4316702.31	557063
7	-442.31	-2014.21	293040.931	4321812.76	558280
8	-471.81	-2119.64	293011.431	4321707.33	558217.3
9	-491.77	-2213.97	292991.471	4321613	558398.7
10	-507.39	-2319.39	292975.851	4321507.58	557978.7
11	-554.26	-2404.85	292928.981	4321422.12	557904
12	-601.99	-2489.19	292881.251	4321337.78	557600.7
13	-613.27	-2593.51	292869.971	4321233.46	557598
14	-606.33	-2694.49	292876.911	4321132.48	557248
15	-585.5	-2776.62	292897.741	4321050.35	556977.3
16	-571.61	-2885.37	292911.631	4320941.6	555914
17	-549.92	-2988.58	292933.321	4320838.39	557012.7
18	-524.75	-3070.7	292958.491	4320756.27	556804.3
19	-503.05	-3179.46	292980.191	4320647.51	556955
20	-467.47	-3277.12	293015.771	4320549.85	559260
21	-433.63	-3370.34	293049.611	4320456.63	557000

22	-409.33	-3459.12	293073.911	4320367.85	557388
23	-380.69	-3559	293102.551	4320267.97	556964.3
24	-361.6	-3648.89	293121.641	4320178.08	557108.3
25	-433.63	-3721.02	293049.611	4320105.95	556746.7
27	-584.63	-3845.31	292898.611	4319981.66	556424.7
28	-649.72	-3911.9	292833.521	4319915.07	556177.7
29	-732.16	-3975.16	292751.081	4319851.81	556029.3
12-30.0	-815.48	-4030.64	292667.761	4319796.33	556199.3

LINE (13)

STN. INT.	EAST G1	North G1	UTM E-W	UTM N-S	MAG. FIELD
13-0.0	-318.2	-1322.83	293165.041	4322504.14	556985.7
1	-450.12	-1353.9	293033.121	4322473.07	557215.7
2	-541.24	-1414.94	292942.001	4322412.03	556904.3
3	-611.53	-1467.1	292871.711	4322359.87	557518
4	-695.71	-1462.66	292787.531	4322364.31	557584
5	-720.01	-1561.43	292763.231	4322265.54	557705.3
6	-713.07	-1650.21	292770.171	4322176.76	557774.3
7	-726.09	-1755.64	292757.151	4322071.33	556951.7
8	-798.12	-1803.36	292685.121	4322023.61	557878.7
9	-908.34	-1814.45	292574.901	4322012.52	557860.3
10	-999.46	-1845.53	292483.781	4321981.44	557859.7
11	-1057.6	-1928.76	292425.641	4321898.21	557786.3
12	-1144.39	-1983.14	292338.851	4321843.83	557360.7
13	-1213.82	-2055.27	292269.421	4321771.7	557535
14	-1278.9	-2134.06	292204.341	4321692.91	557217.7
15	-1340.52	-2210.64	292142.721	4321616.33	557156
16	-1440.32	-2227.28	292042.921	4321599.69	556971.7
17	-1527.11	-2275	291956.131	4321551.97	556772.3
18	-1613.89	-2293.87	291869.351	4321533.1	556573.7
19	-1686.79	-2360.46	291796.451	4321466.51	556074
20	-1787.46	-2343.81	291695.781	4321483.16	555970
21	-1826.51	-2419.27	291656.731	4321407.7	555017
22	-1852.55	-2513.6	291630.691	4321313.37	555637.7
23	-1888.99	-2604.6	291594.251	4321222.37	555407
24	-1917.63	-2691.16	291565.611	4321135.81	555040.7
25	-1964.5	-2776.62	291518.741	4321050.35	553964.7
26	-2013.1	-2872.06	291470.141	4320954.91	554202.3
13-27.0	-2046.94	-2949.74	291436.301	4320877.23	553779.7

LINE (14)

STN. INT.	EAST G1	North G1	UTM E-W	UTM N-S	MAG. FIELD
″					
14-0.0	-3448.5	-2644.55	290034.741	4321182.42	550229.3
″					
1	-3433.75	-2560.21	290049.491	4321266.76	550960
″					

2	-3433.75	-2450.35	290049.491	4321376.62	550699.7
″					
3	-3419	-2354.91	290064.241	4321472.06	551777.3
″					
4	-3405.11	-2256.14	290078.131	4321570.83	552262.3
5	-3390.36	-2166.25	290092.881	4321660.72	553400
6	-3390.36	-2058.6	290092.881	4321768.37	552589.3
7	-3361.72	-1967.6	290121.521	4321859.37	553165
8	-3332.21	-1872.16	290151.031	4321954.81	553075.7
9	-3288.82	-1790.04	290194.421	4322036.93	553160.3
10	-3245.43	-1686.83	290237.811	4322140.14	553627.7
11	-3173.4	-1623.58	290309.841	4322203.39	554430.7
12	-3086.61	-1618.03	290396.631	4322208.94	554230.7
13	-3014.58	-1540.34	290468.661	4322286.63	554643.3
14	-2956.44	-1451.56	290526.801	4322375.41	555023
15	-2971.19	-1359.45	290512.051	4322467.52	555228
16	-2999.83	-1265.12	290483.411	4322561.85	554675.7
17	-3028.47	-1170.79	290454.771	4322656.18	555559
18	-3071.86	-1085.34	290411.381	4322741.63	555587.7
19	-3086.61	-987.68	290396.631	4322839.29	555473.3
20	-3101.37	-904.45	290381.871	4322922.52	556113.3
21	-3158.64	-832.32	290324.601	4322994.65	556049.7
22	-3231.54	-765.73	290251.701	4323061.24	556349.7
23	-3288.82	-680.28	290194.421	4323146.69	556120
24	-3346.97	-604.82	290136.271	4323222.15	556328.3
25	-3332.21	-502.72	290151.031	4323324.25	556766.3
26	-3318.33	-397.29	290164.911	4323429.68	557054.7
27	-3303.57	-301.85	290179.671	4323525.12	557205.3
28	-3303.57	-194.2	290179.671	4323632.77	557441.7
29	-3260.18	-99.87	290223.061	4323727.1	557788.3
30	-3245.43	-3.33	290237.811	4323823.64	557997.3
31	-3188.15	94.33	290295.091	4323921.3	558155.7
14-32.0	-3245.43	174.24	290237.811	4324001.21	558218.7

LINE (15)

STN. INT.	EAST G1	North G1	UTM E-W	UTM N-S	MAG. FIELD
″					
15-0	710.1824	-5114.14	294193.424	4318712.83	556448
″					
15-1	585.792	-5103.04	294069.033	4318723.93	556304.3
″					
15-2	488.8832	-5106.74	293972.125	4318720.23	556318
″					
15-3	397.76	-5077.15	293881.001	4318749.82	556596.3
15-4	319.6544	-5019.81	293802.896	4318807.16	556499.7
15-5	242.9952	-4947.68	293726.237	4318879.29	556418.7
15-6	170.6752	-4888.49	293653.917	4318938.48	556625.7
15-7	95.4624	-4812.66	293578.704	4319014.31	556776.7
15-8	23.1424	-4755.32	293506.384	4319071.65	556676.3
15-9	-57.856	-4690.58	293425.385	4319136.39	556465.3
15-10	-133.069	-4627.7	293350.172	4319199.27	556304.7
15-11	-224.192	-4562.96	293259.049	4319264.01	555565.7

15-12	-300.851	-4505.62	293182.39	4319321.35	556433.7
15-13	-384.742	-4455.68	293098.499	4319371.29	556128
15-14	-464.294	-4392.8	293018.947	4319434.17	555856.7
15-15	-533.722	-4311.41	292949.519	4319515.56	556234.7
15-16	-650.88	-4257.78	292832.4	4319569	556362.7
15-17	-718.86	-4189.34	292764.4	4319638	556008.3
15-18	-792.62	-4120.91	292690.6	4319706	555618.3
15-19	-856.27	-4045.07	292627	4319782	556025.3
15-20	-927.14	-3991.43	292556.1	4319836	556007.3
15-21	-1005.24	-3923	292478	4319904	555689.3
15-22	-1081.9	-3860.11	292401.3	4319967	555560.3
15-23	-1146.99	-3782.43	292336.3	4320045	555480.7
15-24	-1212.08	-3715.84	292271.2	4320111	555468.3
15-25	-1291.63	-3636.31	292191.6	4320191	555149
15-26	-1359.61	-3573.42	292123.6	4320254	555136
15-27	-1430.49	-3506.84	292052.8	4320320	555123
15-28	-1492.68	-3432.85	291990.6	4320394	555145
15-29	-1567.89	-3364.42	291915.4	4320463	555345.3
15-30	-1647.45	-3305.23	291835.8	4320522	554888
15-31	-1724.11	-3242.35	291759.1	4320585	554076.7
15-32	-1794.98	-3179.46	291688.3	4320648	554414.7
15-33	-1880.32	-3129.52	291602.9	4320697	554467.3
15-34	-1978.67	-3072.18	291504.6	4320755	553498.7
15-35	-2058.22	-3016.69	291425	4320810	553962.7
15-36	-2145.01	-2976	291338.2	4320851	553945.3
15-37	-2239.02	-2937.16	291244.2	4320890	553494.7
15-38	-2325.81	-2885.37	291157.4	4320942	553569.7
15-39	-2419.82	-2840.98	291063.4	4320986	553290
15-40	-2463.22	-2824.34	291020	4321003	552962.3
15-42	-2609.3	-2755.9	290873.9	4321071	552483.7
15-43	-2696.09	-2722.61	290787.2	4321104	552950.3
15-44	-2782.87	-2693.01	290700.4	4321134	552134.3
15-45	-2884.12	-2694.86	290599.1	4321132	552271
15-45.5	-2941.97	-2678.22	290541.3	4321149	552113
15-46	-3028.76	-2650.47	290454.5	4321177	552196.3
15-47	-3086.61	-2663.42	290396.6	4321164	551836.7
15-48	-3187.86	-2657.87	290295.4	4321169	551693.7
15-49	-3289.11	-2646.77	290194.1	4321180	551324.3
15-50	-3404.82	-2652.32	290078.4	4321175	550844
15-52	-3506.07	-2622.73	289977.2	4321204	550896.3
15-53	-3592.85	-2593.14	289890.4	4321234	550751
15-54	-3679.64	-2561.69	289803.6	4321265	549720.3
15-55	-3780.89	-2485.86	289702.4	4321341	550257.3
15-56	-3809.81	-2410.03	289673.4	4321417	550629
15-57	-3853.21	-2321.24	289630	4321506	550766.7
15-58	-3896.6	-2230.61	289586.6	4321596	550694.3
15-59	-3939.99	-2119.64	289543.3	4321707	550875.7
15-60	-3997.85	-2075.25	289485.4	4321752	550848
15-61	-4070.17	-2008.66	289413.1	4321818	551005.7
15-62	-4171.41	-1956.87	289311.8	4321870	550637.3
15-63	-4258.2	-1921.73	289225	4321905	550488
15-64	-4446.23	-1849.6	289037	4321977	550132.3
15-65	-4547.48	-1818.15	288935.8	4322009	549938.3
15-66	-4634.26	-1829.25	288849	4321998	549617.3
15-67	-4721.05	-1877.34	288762.2	4321950	549198

15-68	-4822.29	-1923.58	288661	4321903	548570.3
15-69	-4909.08	-1914.33	288574.2	4321913	548522.3
15-70	-4995.86	-1866.24	288487.4	4321961	548114.3
15-71	-5082.65	-1818.15	288400.6	4322009	547951
15-72	-5169.43	-1758.97	288313.8	4322068	547654
15-73	-5227.29	-1679.43	288256	4322148	547916.7
15-74	-5314.07	-1620.25	288169.2	4322207	547796.3
15-75	-5415.32	-1585.1	288067.9	4322242	547673
15-76	-5502.1	-1562.91	287981.1	4322264	547415
15-77	-5603.35	-1542.56	287879.9	4322284	547451.3

LINE (16)

STN. INT.	EAST G1	North G1	UTM E-W	UTM N-S	MAG. FIELD
〃					
16-0	-6948.5	-1362.78	286534.7	4322464	545570
〃					
16-1	-8438.58	-893.35	285044.7	4322934	544417
〃					
16-2	-9827.13	-366.22	283656.1	4323461	543984
〃					
16-13	-9407.09	-3952.96	284076.2	4319874	542843
〃					
16-15	-9696.95	-2333.82	283786.3	4321493	543020
16-16	-9103.35	-2025.31	284379.9	4321802	543237
16-17	-8278.9	-1020.98	285204.3	4322806	543943
16-18	-7844.98	-194.2	285638.3	4323633	545618
16-19	-8048.06	358.46	285435.2	4324185	546049
16-20	-7917.88	1043.18	285565.4	4324870	547175
16-21	-5791.67	2855.42	287691.6	4326682	551168
16-22	-4431.77	2652.33	289051.5	4326479	555132
16-23	-3752.25	2910.9	289731	4326738	555840

LINE (17)

STN. INT.	EAST G1	North G1	UTM E-W	UTM N-S	MAG. FIELD
17-0	342.8	-599.27	293826	4323228	554596
17-1	433.92	-593.72	293917.2	4323233	553732
17-2	545.3	-571.52	294028.5	4323255	553811
17-3	630.63	-553.03	294113.9	4323274	553999
17-4	733.33	-532.68	294216.6	4323294	553927
17-5	814.33	-480.89	294297.6	4323346	553647
17-6	906.9	-447.6	294390.1	4323379	553388
17-7	1770.394	51.7924	295253.6	4323879	553238.3
17-8	1871.642	57.3412	295354.9	4323884	553065.3
17-9	1975.782	55.4916	295459	4323882	553123
17-10	2069.798	35.146	295553	4323862	552821
17-11	2178.278	14.8004	295661.5	4323842	553074.3
17-12	2276.634	-7.3948	295759.9	4323820	553044.3
17-13	2369.203	-25.8908	295852.4	4323801	552888.3
17-14	2476.237	-38.838	295959.5	4323788	552592.7
17-15	2576.038	-53.6348	296059.3	4323773	551875.7
17-16	2667.162	-64.7324	296150.4	4323762	551158.7

17-17	2897.139	4723.882	296380.4	4328551	552354.3
17-18	2787.213	-184.956	296270.5	4323642	552726.7
17-19	2803.123	-282.985	296286.4	4323544	550674
17-20	2837.837	-375.465	296321.1	4323452	552662.7
17-21	2852.301	-477.193	296335.5	4323350	553120
17-22	2868.211	-586.32	296351.5	4323241	552804.3
17-23	2866.765	-676.95	296350	4323150	552408.7
17-24	2860.979	-769.43	296344.2	4323058	552722.3
17-25	2843.622	-873.008	296326.9	4322954	552680.7
17-26	2833.498	-971.036	296316.7	4322856	552873.3
17-27	2820.48	-1065.37	296303.7	4322762	552739.7
17-28	2813.248	-1159.7	296296.5	4322667	552317
17-29	2816.141	-1255.87	296299.4	4322571	552368
17-30	2816.141	-1355.75	296299.4	4322471	552616.7
17-31	2807.462	-1450.08	296290.7	4322377	552083.3
17-32	2701.875	-1437.14	296185.1	4322390	552938
17-33	2602.074	-1427.89	296085.3	4322399	552981.3
17-34	2513.843	-1411.24	295997.1	4322416	553005.7
17-35	2409.702	-1405.69	295892.9	4322421	553471.7
17-36	2298.33	-1390.9	295781.6	4322436	553279
17-37	2215.885	-1377.95	295699.1	4322449	552846.7
17-38	2107.405	-1363.15	295590.6	4322464	553000.3
17-39	2001.818	-1342.81	295485.1	4322484	553389
17-40	1913.587	-1337.26	295396.8	4322490	552817.3
17-41	1899.123	-1426.04	295382.4	4322401	554284
17-42	1877.427	-1520.37	295360.7	4322307	554292.7
17-43	1766.054	-1520.37	295249.3	4322307	554551.3
17-44	1666.253	-1514.82	295149.5	4322312	554728
17-45	928.59	-2025.31	294411.8	4321802	555479
17-46	833.13	-2053.05	294316.4	4321774	555683
17-47	743.45	-2086.35	294226.7	4321741	555719
17-48	658.12	-2121.86	294141.4	4321705	555845
17-48.4	627.74	-2136.28	294111	4321691	555993

LINE (18)

STN. INT.	EAST G1	North G1	UTM E-W	UTM N-S	MAG. FIELD
18-0	2356.186	-27.7404	295839.4	4323799	551574.3
18-1	2382.221	133.1748	295865.5	4323960	552487.7
18-2	2416.934	295.9396	295900.2	4324123	552596.7
18-3	2428.506	469.802	295911.7	4324297	552859
18-4	2453.094	617.77	295936.3	4324445	552788.7
18-5	2482.022	802.73	295965.3	4324630	553508.3
18-6	2359.078	895.21	295842.3	4324722	552711
18-7	2254.938	1006.186	295738.2	4324833	552787.7
18-8	2186.957	1154.154	295670.2	4324981	552552.7
18-9	2113.19	1302.122	295596.4	4325129	552084
18-10	2037.978	1431.594	295521.2	4325259	552344.7
18-11	1952.64	1579.562	295435.9	4325407	552632.7

18-12	1862.963	1727.53	295346.2	4325555	552726.7
18-13	836.02	1339.48	294319.3	4325166	552850.7
18-14	736.22	1468.22	294219.5	4325295	552681.3
18-15	632.08	1579.19	294115.3	4325406	553082.7
18-16	571.33	1709.03	294054.6	4325536	552710
18-17	456.78	1838.88	293940	4325666	552771.7
18-18	345.69	1949.85	293828.9	4325777	552837
18-19	267.59	2078.58	293750.8	4325906	552584.3
18-20	195.56	2208.43	293678.8	4326035	552937.7
18-21	76.66	2319.4	293559.9	4326146	552779
18-22	-57.85	2319.4	293425.4	4326146	552664.7
18-23	-81.28	2393.76	293402	4326221	553449.7

LINE (19)

STN. INT.	**EAST G1**	**North G1**	**UTM E-W**	**UTM N-S**	**MAG. FIELD**
19-0	-269.03	4409.45	293214.2	4328236	555317.8
19-1	-441.152	4446.442	293042.1	4328273	555041.7
19-2	-552.525	4316.97	292930.7	4328144	554918
19-3	-621.952	4316.97	292861.3	4328144	554797
19-4	-762.253	4390.954	292721	4328218	554398.3
19-5	-809.984	4409.45	292673.3	4328236	554728.5
19-6	205.3888	4446.442	293688.6	4328273	556160.3
19-7	-6080.67	6074.09	287402.6	4329901	549921.3
19-8	-5921.56	6037.098	287561.7	4329864	551022.3
19-9	-5776.92	6000.106	287706.3	4329827	551132.3
19-10	-5617.82	5981.61	287865.4	4329809	551941.7
19-11	-5516.57	5852.138	287966.7	4329679	552205.7
19-12	-5429.79	5722.666	288053.5	4329550	552020.3
19-13	-5270.68	5667.178	288212.6	4329494	552684
19-14	-5126.04	5630.186	288357.2	4329457	552901.7
19-15	-4952.47	5593.194	288530.8	4329420	553158.7
19-16	-4807.83	5537.706	288675.4	4329365	553427.3
19-17	-4663.19	5519.21	288820.1	4329346	551374.3
19-18	-4504.09	5463.722	288979.2	4329291	554162.3
19-19	-4344.99	5371.242	289138.3	4329198	554143.3
19-20	-4214.81	5278.762	289268.4	4329106	554622.7
19-21	-4055.71	5241.77	289427.5	4329069	555281.3
19-22	-3911.07	5186.282	289572.2	4329013	555147.7
19-23	-3766.43	5075.306	289716.8	4328902	555403.3
19-24	-3636.25	5001.322	289847	4328828	555334.7
19-25	-3462.68	4964.33	290020.6	4328791	555507
19-26	-3318.04	4927.338	290165.2	4328754	555575
19-27	-3173.4	4890.346	290309.8	4328717	555263.7
19-28	-3014.3	4853.354	290468.9	4328680	555208.7
19-29	-2855.19	4797.866	290628.1	4328625	554940.3
19-30	-2913.05	4649.898	290570.2	4328477	555234.7
19-31	-2956.44	4483.434	290526.8	4328310	555335.3
19-32	-2999.83	4316.97	290483.4	4328144	555090
19-33	-3028.76	4187.498	290454.5	4328014	555141
19-34	-3072.15	4002.538	290411.1	4327830	555349.3
19-35	-3101.08	3854.57	290382.2	4327682	555643
19-36	-3130.01	3688.106	290353.2	4327515	555320.7
19-37	-3173.4	3540.138	290309.8	4327367	555627

19-38	-3216.79	3392.17	290266.5	4327219	555718.3
19-39	-3260.19	3225.706	290223.1	4327053	555795.7
19-40	-3346.97	3151.722	290136.3	4326979	555914
19-41	-3477.15	3133.226	290006.1	4326960	555753
19-42	-3636.25	3096.234	289847	4326923	555550.7
19-43	-3795.35	3059.242	289687.9	4326886	555549
19-44	-3954.46	3003.754	289528.8	4326831	555296.3
19-45	-4070.17	2948.266	289413.1	4326775	554903.7
19-46	-4214.81	3003.754	289268.4	4326831	554594.3
19-47	-4373.91	3059.242	289109.3	4326886	553917.3
19-48	-4518.55	3114.73	288964.7	4326942	553706
19-49	-4721.05	-6342.27	288762.2	4317485	551533.7
19-50	-4807.83	3188.714	288675.4	4327016	552880
19-51	-4952.47	3170.218	288530.8	4326997	552486
19-52	-5111.58	3207.21	288371.7	4327034	552057.3
19-53	-5270.68	3207.21	288212.6	4327034	551247
19-54	-2334.49	3799.082	291148.8	4327626	555128.3
19-55	-2361.97	3651.114	291121.3	4327478	555587.3
19-56	-2389.45	3484.65	291093.8	4327312	555753
19-57	-2418.38	3336.682	291064.9	4327164	555735.7
19-60	1657.574	-3223.85	295140.8	4320603	553750.7
19-64	2114.637	-2715.21	295597.9	4321112	551996
19-65	3723.034	-2768.85	297206.3	4321058	550999.3

LINE (20)

STN. INT.	EAST G1	North G1	UTM E-W	UTM N-S	MAG. FIELD
20-00	-2659.2	3043.2	290824.041	4326870.17	555801
20-00.5	-2660.07	2993.208	290823.171	4326820.18	556026
20-01	-2660.95	2943.215	290822.291	4326770.19	556144
20-01.5	-2648	2894.919	290835.241	4326721.89	555341.7
20-03.5	-2569.91	2710.944	290913.331	4326537.92	556276.3
20-04	-2574.27	2661.134	290908.971	4326488.11	556315.7
20-04.5	-2574.27	2611.134	290908.971	4326438.11	556397.3
20-05	-2574.27	2561.134	290908.971	4326388.11	556662
20-05.5	-2528.59	2540.798	290954.651	4326367.77	556420.3
20-06	-2482.91	2520.461	291000.331	4326347.43	556365.7
20-06.2	-2464.64	2512.326	291018.601	4326339.3	556336.3
20-06.5	-2437.68	2499.175	291045.561	4326326.15	556312.7
20-07	-2397.06	2477.579	291086.181	4326304.55	556263
20-07.5	-2380.58	2434.634	291102.661	4326261.61	556566.7
20-08	-2424.57	2421.185	291058.671	4326248.16	556491.7
20-08.5	-2468.56	2407.736	291014.681	4326234.71	556554.7
20-09	-2514.38	2403.727	290968.861	4326230.7	557251
20-09.5	-2560.04	2398.121	290923.201	4326225.09	556548

20-10	-2603.27	2382.388	290879.971	4326209.36	556597.3
20-10.5	-2642.28	2358.012	290840.961	4326184.99	556676.7
20-11	-2679.96	2331.627	290803.281	4326158.6	556745.7
20-11.5	-2719.39	2307.936	290763.851	4326134.91	556789.7
20-12.0	-2759.62	2285.634	290723.621	4326112.61	556815.7
20-12.5	-2797.3	2259.25	290685.941	4326086.22	556867.7
20-13	-2834.98	2232.865	290648.261	4326059.84	556894.3
20-13.5	-2873.56	2207.812	290609.681	4326034.79	556966.7
20-14	-2911.24	2181.427	290572.001	4326008.4	557004.3
20-14.5	-2948.92	2155.043	290534.321	4325982.02	556999
20-15	-2987.06	2129.32	290496.181	4325956.29	557073.7
20-15.5	-3024.74	2102.936	290458.501	4325929.91	557131
20-16	-3062.42	2076.551	290420.821	4325903.52	557167.7
20-16.5	-3100.1	2050.167	290383.141	4325877.14	557221
20-17	-3137.78	2023.782	290345.461	4325850.76	557239.3
20-17.5	-3175.46	1997.397	290307.781	4325824.37	557220.3
20-18	-3213.15	1971.013	290270.091	4325797.99	557220
20-18.5	-3250.83	1944.628	290232.411	4325771.6	557226
20-19	-3290.66	1921.628	290192.581	4325748.6	557264.3
20-19.5	-3333.89	1905.896	290149.351	4325732.87	557260.7
20-20	-3371.57	1879.511	290111.671	4325706.48	557260.3
20-20.5	-3409.25	1853.126	290073.991	4325680.1	557230.7
20-21	-3424.98	1809.901	290058.261	4325636.87	557275.7
20-21.5*	-3440.72	1853.126	290042.521	4325680.1	557236.3
20-22	-3456.45	1896.352	290026.791	4325723.33	557238.3
20-22.5	-3472.18	1939.578	290011.061	4325766.55	557203.7
20-23	-3487.92	1982.804	289995.321	4325809.78	557203.3
20-23.5	-3520.44	2015.331	289962.801	4325842.3	557190.7
20-24	-3560.28	2038.331	289922.961	4325865.3	557257.3
20-24.5	-3603.51	2054.064	289879.731	4325881.04	557153.3
20-25	-3646.73	2069.797	289836.511	4325896.77	556569.7
20-25.5	-3689.96	2085.53	289793.281	4325912.5	556397.7
20-26	-3726.7	2113.213	289756.541	4325940.19	557082.3
20-26.5	-3753.08	2150.894	289730.161	4325977.87	556879.7
20-27	-3779.46	2188.575	289703.781	4326015.55	556864.7
20-27.5	-3809.03	2223.813	289674.211	4326050.79	556836.3
20-28	-3784.66	2262.823	289698.581	4326089.8	556699.3

20-28.5	-3758.16	2305.226	289725.081	4326132.2	556595
20-29	-3740.24	2351.905	289743.001	4326178.88	555845.3
20-29.5	-3724.79	2399.458	289758.451	4326226.43	556161.7
20-30	-3709.34	2447.011	289773.901	4326273.98	556247.3
20-31.5	-3662.99	2589.669	289820.251	4326416.64	556347.3
20-32.5	-3632.09	2684.775	289851.151	4326511.75	555401.3
20-33	-3630.34	2734.744	289852.901	4326561.72	555185.3
20-33.5	-3628.6	2784.714	289854.641	4326611.69	555294.3
20-34	-3626.85	2834.683	289856.391	4326661.66	556186.3
20-34.5	-3625.11	2884.653	289858.131	4326711.63	555977
20-35	-3623.36	2934.622	289859.881	4326761.6	555991.7
20-35.5	-3621.62	2984.592	289861.621	4326811.57	555751

LINE (21)

STN.	EAST G1	North G1	UTM E-W	UTM N-S	MAG. FIELD INT.
21-00	-2724	614.4	290759.241	4324441.37	558298.7
21-00.5	-2766.4	587.904	290716.841	4324414.88	558295.3
21-01	-2804.7	555.7647	290678.541	4324382.74	558346
21-01.5	-2840.06	520.4093	290643.181	4324347.38	558382.7
21-02	-2875.42	485.054	290607.821	4324312.03	558299
21-02.5	-2910.77	449.6986	290572.471	4324276.67	558204
21-03	-2944.87	413.131	290538.371	4324240.1	557675.7
21-03.5	-2982.03	379.6744	290501.211	4324206.65	558217.3
21-04	-3017.38	344.3191	290465.861	4324171.29	558234.7
21-04.5	-3039.3	299.3794	290443.941	4324126.35	558247.7
21-05	-3061.22	254.4397	290422.021	4324081.41	558175
21-05.5	-3111.03	250.0819	290372.211	4324077.06	558229.7
21-06	-3160.84	245.7241	290322.401	4324072.7	558186.3
21-07	-3120	504	290363.241	4324330.97	558305.7
21-07.5	-3157.16	537.4565	290326.081	4324364.43	558167.3
21-08	-3187.94	576.8571	290295.301	4324403.83	558157.7
21-08.5	-3221.4	614.0143	290261.841	4324440.99	558334
21-09	-3251.49	653.9461	290231.751	4324480.92	558385.3
21-09.5	-3278.72	695.8796	290204.521	4324522.85	558330
21-10	-3295.82	742.8642	290187.421	4324569.84	558336
21-10.5	-3316.95	788.1796	290166.291	4324615.15	558146.7

21-11	-3355.25	820.319	290127.991	4324647.29	557795.7
21-11.5	-3391.22	855.0519	290092.021	4324682.03	558214.3
21-12	-3430.62	885.835	290052.621	4324712.81	558275.3
21-12.5	-3451.75	931.1504	290031.491	4324758.12	558188
21-13	-3476.75	974.4517	290006.491	4324801.42	558155.3
21-13.5	-3501.75	1017.753	289981.491	4324844.73	558104.7
21-14	-3526.75	1061.054	289956.491	4324888.03	557993.7
21-14.5	-3558.89	1099.356	289924.351	4324926.33	558016
21-15	-3582.37	1143.504	289900.871	4324970.48	557971.3
21-15.5	-3599.47	1190.488	289883.771	4325017.46	557838.7
21-16	-3608.15	1239.729	289875.091	4325066.7	557881.7
21-16.5	-3621.93	1287.792	289861.311	4325114.77	557845.7
21-17	-3634.03	1336.307	289849.211	4325163.28	557748
21-17.5	-3636.64	1386.238	289846.601	4325213.21	557684.3
21-18	-3619.54	1433.223	289863.701	4325260.2	557609.7
21-18.5	-3595.3	1476.954	289887.941	4325303.93	557570.7
21-19	-3552	1451.954	289931.241	4325278.93	557610.7
21-19.5	-3538.22	1500.017	289945.021	4325326.99	557563.7
21-20	-3509.54	1540.974	289973.701	4325367.95	557575.3
21-20.5	-3462.56	1523.873	290020.681	4325350.85	557596
21-21	-3415.57	1506.772	290067.671	4325333.75	557634.7
21-21.5	-3368.59	1489.671	290114.651	4325316.64	557650.3
21-22	-3321.6	1472.57	290161.641	4325299.54	557667.3
21-22.5	-3274.62	1455.469	290208.621	4325282.44	557681.7
21-23	-3227.63	1438.368	290255.611	4325265.34	557847
21-23.5	-3180.65	1421.267	290302.591	4325248.24	557800.7
21-24	-3133.66	1404.166	290349.581	4325231.14	557858.3
21-24.5	-3086.68	1387.065	290396.561	4325214.04	557852.7
21-25	-3039.69	1369.964	290443.551	4325196.94	558064.3
21-25.5	-3001.39	1337.825	290481.851	4325164.8	557902.3
21-26	-2972.71	1296.867	290510.531	4325123.84	557890
21-26.5	-2944.03	1255.91	290539.211	4325082.88	558022.3
21-27	-2895.74	1242.969	290587.501	4325069.94	557607
21-27.5	-2857.44	1210.829	290625.801	4325037.8	557998
21-28	-2828.76	1169.872	290654.481	4324996.85	558003.3
21-28.5	-2800.08	1128.914	290683.161	4324955.89	558100.7
21-29	-2771.4	1087.957	290711.841	4324914.93	558229.3

21-29.5	-2742.72	1046.999	290740.521	4324873.97	558100

LINE (22)

STN. INT.	EAST G1	North G1	UTM E-W	UTM N-S	MAG. FIELD
22-00	-470	1944	293013.241	4325770.97	552765.7
22-00.5	-505.967	1909.267	292977.274	4325736.24	552905
22-01	-541.322	1873.912	292941.919	4325700.89	552965.3
22-01.5	-576.678	1838.556	292906.563	4325665.53	553076.3
22-02	-614.413	1805.753	292868.828	4325632.73	553075.3
22-02.5	-652.149	1772.951	292831.092	4325599.92	553041
22-03	-689.884	1740.148	292793.357	4325567.12	553226.7
22-03.5	-727.62	1707.345	292755.621	4325534.32	553406.7
22-04	-765.355	1674.542	292717.886	4325501.52	553569.7
22-04.5	-803.091	1641.739	292680.15	4325468.71	553640.3
22-05	-829.587	1599.336	292653.654	4325426.31	553844
22-05.5	-853.06	1555.189	292630.181	4325382.16	553937.3
22-06	-878.812	1512.331	292604.429	4325339.3	554087
22-06.5	-881.429	1462.399	292601.812	4325289.37	554285
22-07	-884.046	1412.468	292599.195	4325239.44	554420.6
22-07.5	-886.662	1362.536	292596.579	4325189.51	554297.7
22-08	-889.279	1312.605	292593.962	4325139.58	554448.3
22-08.5	-891.896	1262.673	292591.345	4325089.65	554556
22-09	-894.513	1212.742	292588.728	4325039.72	554564.3
22-09.5	-917.986	1168.594	292565.255	4324995.57	554798.7
22-10	-935.087	1121.61	292548.154	4324948.58	554918.3
22-10.5	-967.227	1083.307	292516.014	4324910.28	555093
22-11	-1004.38	1049.851	292478.861	4324876.82	555499
22-11.5	-1027.86	1005.704	292455.381	4324832.68	555377.3
22-12	-1051.33	961.5562	292431.911	4324788.53	555507.3
22-12.5	-1078.56	919.6226	292404.681	4324746.6	555655.7
22-13	-1102.04	875.4753	292381.201	4324702.45	555822
22-13.5	-1125.51	831.3279	292357.731	4324658.3	555984.7
22-14	-1148.21	786.7775	292335.031	4324613.75	556013.3
22-14.5	-1171.68	742.6302	292311.561	4324569.6	556070.3
22-15	-1195.16	698.4828	292288.081	4324525.46	556291.7
22-15.5	-1217.08	653.5431	292266.161	4324480.52	556559

22-16	-1240.55	609.3957	292242.691	4324436.37	556534.3
22-16.5	-1264.02	565.2483	292219.221	4324392.22	556682.7
22-17	-1287.5	521.1009	292195.741	4324348.07	556746.3
22-17.5	-1310.97	476.9536	292172.271	4324303.93	556887
22-18	-1334.44	432.8062	292148.801	4324259.78	556955
22-18.5	-1357.92	388.6588	292125.321	4324215.63	556952.7
22-19	-1357.92	338.6588	292125.321	4324165.63	557056.7
22-19.5	-1307.92	388.6588	292175.321	4324215.63	557235.7
22-20	-1272.56	424.0141	292210.681	4324250.99	556765.7
22-20.5	-1246.81	466.8725	292236.431	4324293.85	556777.3
22-21	-1203.51	491.8725	292279.731	4324318.85	556500
22-21.5	-1160.21	516.8725	292323.031	4324343.85	556423
22-22	-1116.91	541.8725	292366.331	4324368.85	556293
22-22.5	-1073.6	566.8725	292409.641	4324393.85	556227
22-23	-1030.3	591.8725	292452.941	4324418.85	555983.3
22-23.5	-1023.34	641.3859	292459.901	4324468.36	555892.7
22-24	-1012.95	690.2933	292470.291	4324517.27	555891.3
22-24.5	-1002.55	739.2007	292480.691	4324566.17	555771.7
22-25	-992.158	788.1081	292491.083	4324615.08	555639
22-25.5	-981.762	837.0154	292501.479	4324663.99	555703.7
22-26	-964.661	884.0001	292518.58	4324710.97	555145.7
22-26.5	-947.56	930.9847	292535.681	4324757.96	555497
22-27	-930.459	977.9693	292552.782	4324804.94	555142
22-27.5	-913.358	1024.954	292569.883	4324851.93	555037.3
22-28	-896.257	1071.939	292586.984	4324898.91	554891
22-28.5	-879.156	1118.923	292604.085	4324945.9	554777.3
22-29	-862.055	1165.908	292621.186	4324992.88	554579
22-29.5	-815.071	1183.009	292668.17	4325009.98	554519
22-30	-765.83	1191.691	292717.411	4325018.66	554321.3
22-30.5	-716.59	1200.374	292766.651	4325027.35	554139
22-31	-666.598	1201.246	292816.643	4325028.22	554084.7
22-31.5	-616.598	1201.246	292866.643	4325028.22	553833.3
22-32	-566.598	1201.246	292916.643	4325028.22	553822.3
22-32.5	-516.598	1201.246	292966.643	4325028.22	553454
22-33	-466.598	1201.246	293016.643	4325028.22	553515.3
22-33.5	-416.598	1201.246	293066.643	4325028.22	553290

LINE (23)

STN. INT.	EAST G1	North G1	UTM E-W	UTM N-S	MAG. FIELD
23-00	-1123	-1680	292360.241	4322146.97	556105.7
23-00.5	-1123	-1730	292360.241	4322096.97	557583
23-01	-1123	-1780	292360.241	4322046.97	557570.7
23-01.5	-1123	-1830	292360.241	4321996.97	557560
23-02	-1123	-1880	292360.241	4321946.97	557541.3
23-02.5	-1123	-1930	292360.241	4321896.97	557480
23-03	-1123	-1980	292360.241	4321846.97	557482.3
23-03.5	-1123	-2030	292360.241	4321796.97	557483
23-04	-1123	-2080	292360.241	4321746.97	557442.3
23-04.5	-1123	-2130	292360.241	4321696.97	557357.7
23-05	-1123	-2180	292360.241	4321646.97	557283.3
23-05.5	-1123	-2230	292360.241	4321596.97	557242.7
23-06	-1123	-2280	292360.241	4321546.97	557223.3
23-06.5	-1123	-2330	292360.241	4321496.97	557199.7
23-07	-1123	-2380	292360.241	4321446.97	557170.3
23-07.5	-1123	-2430	292360.241	4321396.97	557142.7
23-08	-1123	-2480	292360.241	4321346.97	557071.3
23-08.5	-1123	-2530	292360.241	4321296.97	556990.7
23-09	-1123	-2580	292360.241	4321246.97	556955.3
23-09.5	-1123	-2630	292360.241	4321196.97	557007
23-10	-1123	-2680	292360.241	4321146.97	556914.3
23-10.5	-1123	-2730	292360.241	4321096.97	556808.3
23-11	-1073	-2730	292410.241	4321096.97	556992.3
23-11.5	-1023	-2730	292460.241	4321096.97	557063.7
23-12	-973	-2730	292510.241	4321096.97	557125
23-12.5	-923	-2730	292560.241	4321096.97	557265
23-13	-873	-2730	292610.241	4321096.97	557514
23-13.5	-823	-2730	292660.241	4321096.97	557459.7
23-14	-773	-2730	292710.241	4321096.97	557531
23-14.5	-873	-2680	292610.241	4321146.97	557435.3
23-15	-873	-2630	292610.241	4321196.97	557411.3
23-15.5	-873	-2580	292610.241	4321246.97	557468
23-16	-873	-2530	292610.241	4321296.97	557477.3
23-16.5	-873	-2480	292610.241	4321346.97	557486.7
23-17	-873	-2430	292610.241	4321396.97	557607.7
23-17.5	-873	-2380	292610.241	4321446.97	557640.7
23-18	-873	-2330	292610.241	4321496.97	557633
23-18.5	-873	-2280	292610.241	4321546.97	557650.3
23-19	-873	-2230	292610.241	4321596.97	557657
23-19.5	-873	-2180	292610.241	4321646.97	557703.3
23-20	-873	-2130	292610.241	4321696.97	557684.3
23-20.5	-873	-2080	292610.241	4321746.97	557700.3
23-21	-873	-2030	292610.241	4321796.97	557741.3
23-21.5	-873	-1980	292610.241	4321846.97	557776.3
23-22	-873	-1930	292610.241	4321896.97	557744
23-22.5	-873	-1880	292610.241	4321946.97	557751.3
23-23	-873	-1830	292610.241	4321996.97	557869.3

LINE (24)

STN. INT.	EAST G1	North G1	UTM E-W	UTM N-S	MAG. FIELD

24-0	-5805.85	-1507.42	287677.391	4322319.55	546059.7
24-1	-5762.46	-1355.75	287720.781	4322471.22	547945.7
24-2	-5617.82	-1255.87	287865.421	4322571.1	547298.7
24-3	-5458.71	-1209.63	288024.531	4322617.34	548455
24-4	-5299.61	-1176.34	288183.631	4322650.63	549291
24-5	-5140.51	-1126.4	288342.731	4322700.57	549955
24-6	-4995.87	-1069.07	288487.371	4322757.9	550725
24-7	-4851.23	-1017.28	288632.011	4322809.69	551881.7
24-8	-4749.98	-889.654	288733.261	4322937.32	551944
24-9	-4634.27	-756.483	288848.971	4323070.49	552818
24-10	-4721.05	-610.364	288762.191	4323216.61	552727.7
24-11	-4851.23	-521.584	288632.011	4323305.39	552826
24-12	-4966.94	-418.006	288516.301	4323408.97	552601.7
24-13	-5024.79	-277.436	288458.451	4323549.54	552917.3
24-14	-5082.65	-116.521	288400.591	4323710.45	553310.3
24-15	-5097.11	51.7924	288386.131	4323878.77	553738.7
24-16	-5082.65	216.4068	288400.591	4324043.38	554275.7
24-17	-5068.19	377.322	288415.051	4324204.3	554194.7
24-18	-5082.65	543.786	288400.591	4324370.76	554411.7
24-19	-5039.26	691.754	288443.981	4324518.73	554899.7
24-20	-5111.58	839.722	288371.661	4324666.7	554563.7
24-21	-5227.29	932.202	288255.951	4324759.18	554738.7
24-22	-5328.54	1043.178	288154.701	4324870.15	554529
24-23	-5386.39	1191.146	288096.851	4325018.12	554364.7
24-24	-5400.86	1357.61	288082.381	4325184.58	554275.7
24-25	-5386.39	1524.074	288096.851	4325351.05	554107
24-26	-5458.71	1672.042	288024.531	4325499.02	554016
24-27	-5559.96	1801.514	287923.281	4325628.49	553505.7
24-28	-5661.21	1930.986	287822.031	4325757.96	553087.7
24-29	-5776.92	2041.962	287706.321	4325868.94	552789
24-30	-5878.17	2171.434	287605.071	4325998.41	552355
24-31	-5892.63	2337.898	287590.611	4326164.87	554242.3
24-32	-5892.63	2504.362	287590.611	4326331.34	551574.7
24-33	-5849.24	2652.33	287634.001	4326479.3	551121.3
24-34	-5805.85	2818.794	287677.391	4326645.77	551334
24-35	-5805.85	2966.762	287677.391	4326793.74	552086.3
24-36	-5820.31	3133.226	287662.931	4326960.2	550617.7
24-37	-5849.24	3281.194	287634.001	4327108.17	550570.3
24-38	-5878.17	3429.162	287605.071	4327256.14	549944.7
24-39	-5921.56	3577.13	287561.681	4327404.1	550870.3
24-40	-5993.88	3743.594	287489.361	4327570.57	551000
24-41	-6051.74	3873.066	287431.501	4327700.04	549315.7
24-42	-6138.52	4021.034	287344.721	4327848.01	550209.7
24-43	-6225.31	4150.506	287257.931	4327977.48	550563.3
24-44	-6297.63	4298.474	287185.611	4328125.45	550455
24-45	-6384.41	4427.946	287098.831	4328254.92	550449
24-46	-6485.66	4557.418	286997.581	4328384.39	549521.3
24-47	-6557.98	4705.386	286925.261	4328532.36	550453.3
24-48	-6615.83	4834.858	286867.411	4328661.83	550220
24-49	-6688.15	5001.322	286795.091	4328828.3	550198
24-50	-6731.55	5149.29	286751.691	4328976.26	550172
24-51	-6760.47	5315.754	286722.771	4329142.73	550343.3
24-52	-6717.08	5463.722	286766.161	4329290.7	549042.7
24-53	-6673.69	5648.682	286809.551	4329475.66	550380.7
24-54	-6659.23	5722.666	286824.011	4329549.64	548907.3

LINE (25)

STN. INT.	EAST G1	North G1	UTM E-W	UTM N-S	MAG. FIELD
25-0	-28.928	3725.098	293454.313	4327552.07	554808.3
25-1	133.0688	3706.602	293616.31	4327533.58	555172.7
25-2	296.512	3706.602	293779.753	4327533.58	555758.7
25-3	436.8128	4242.986	293920.054	4328069.96	555587
25-4	559.7568	3854.57	294042.998	4327681.54	556036.7
25-5	713.0752	3947.05	294196.317	4327774.02	556922.7
25-6	2027.853	4372.458	295511.094	4328199.43	557121.3
25-7	2168.154	4372.458	295651.395	4328199.43	557464.7
25-8	2292.544	4261.482	295775.785	4328088.46	557409
25-9	2344.614	4113.514	295827.855	4327940.49	556979
25-10	2463.219	4002.538	295946.46	4327829.51	557129.7
25-11	2591.949	3910.058	296075.19	4327737.03	557211
25-12	2709.107	3799.082	296192.348	4327626.06	557309.7
25-13	2827.712	3688.106	296310.953	4327515.08	556180.3
25-14	2950.656	3577.13	296433.897	4327404.1	557027
25-15	3103.974	3521.642	296587.215	4327348.62	556691.7
25-16	3268.864	3521.642	296752.105	4327348.62	557059.3
25-17	3425.075	3558.634	296908.316	4327385.61	557352
25-18	3540.787	3669.61	297024.028	4327496.58	557276.7
25-19	3642.035	3780.586	297125.276	4327607.56	557265.3
25-20	3762.086	3891.562	297245.327	4327718.54	557665.7
25-21	3896.602	4002.538	297379.843	4327829.51	557046
25-22	4031.117	4076.522	297514.358	4327903.5	556874.3
25-23	4178.65	4132.01	297661.891	4327958.98	556983.7

LINE (26)

STN. INT.	EAST G1	North G1	UTM E-W	UTM N-S	MAG. FIELD
G1	0	0	293483.241	4323826.97	553867
G2	-23.7122	-43.8731	293459.529	4323783.1	555052.7
G3	-27.1586	-93.6414	293456.083	4323733.33	554504
G4	-24.3223	-143.457	293458.919	4323683.52	554537.3
G5	-34.7827	-192.156	293448.459	4323634.82	554766.3
G6	-47.5327	-240.39	293435.709	4323586.58	554767.7
G7	-93.064	-250.337	293390.177	4323576.64	554709.3
G8	-143.353	-247.502	293339.888	4323579.47	554935
G9	-192.95	-244.046	293290.291	4323582.93	555065.3
G10	-242.816	-241.011	293240.425	4323585.96	555245.3
G11	-292.746	-238.249	293190.495	4323588.72	555308
G12	-342.506	-234.91	293140.735	4323592.06	555360.3
G13	-392.303	-231.6	293090.938	4323595.37	555162.7
G14	-442.126	-228.724	293041.115	4323598.25	555771.3
G15	-491.913	-226.363	292991.328	4323600.61	555959
G16	-541.723	-223.48	292941.518	4323603.49	555856.3
G17	-591.129	-220.76	292892.112	4323606.21	556364.7
G18	-641.24	-218.705	292842.001	4323608.27	556416.3
G19	-690.987	-215.911	292792.254	4323611.06	556671.3
G20	-740.804	-212.523	292742.437	4323614.45	556625
G21	-766.241	-174.992	292717	4323651.98	556650.7
G22	-773.434	-125.736	292709.807	4323701.24	557023
G23	-794.668	-80.6487	292688.573	4323746.32	556500.3

G24	-830.423	-46.3789	292652.818	4323780.59	556393
G25	-869.768	-16.4054	292613.473	4323810.57	556418
G26	-908.855	14.11625	292574.386	4323841.09	556411.7
G27	-949.838	42.3979	292533.403	4323869.37	556070
G28	-998.554	52.64847	292484.687	4323879.62	556494
G29	-1048.43	50.44799	292434.811	4323877.42	556207.7
G30	-1092.49	26.99633	292390.751	4323853.97	556231.7
G31	-1133.36	-1.50574	292349.881	4323825.47	556503.7
G32	-1165.93	-39.1199	292317.311	4323787.85	556771.7
G33	-1189.41	-83.0342	292293.831	4323743.94	556888
G34	-1217.03	-124.367	292266.211	4323702.61	556799
G35	-1257.02	-154.24	292226.221	4323672.73	556749.3
G36	-1298.88	-181.169	292184.361	4323645.8	556900.3
G37	-1340.9	-208.149	292142.341	4323618.82	558112
G38	-1381.79	-236.855	292101.451	4323590.12	557285.7
G39	-1422.97	-264.971	292060.271	4323562	557272.3
G40	-1467.85	-286.951	292015.391	4323540.02	557307
G41	-1507.08	-317.433	291976.161	4323509.54	557083.3
G42	-1516.76	-366.381	291966.481	4323460.59	557409.3
G43	-1536.62	-411.226	291946.621	4323415.75	557163
G44	-1579.56	-436.616	291903.681	4323390.36	557128
G45	-1624.4	-458.802	291858.841	4323368.17	557121
G46	-1667.56	-483.806	291815.681	4323343.17	557125.3
G47	-1688.79	-529.041	291794.451	4323297.93	557261.7
G48	-1700.95	-576.87	291782.291	4323250.1	557237.3
G49	-1734.12	-612.946	291749.121	4323214.03	557195.3
G50	-1782.86	-623.34	291700.381	4323203.63	556759
G51	-1832.75	-622.261	291650.491	4323204.71	557214.3
G52	-1882.96	-623.338	291600.281	4323203.64	557072
G53	-1932.16	-629.144	291551.081	4323197.83	556901
G54	-1977.36	-609.205	291505.881	4323217.77	557139.3
G55	-2009.73	-571.132	291473.511	4323255.84	557239.3
G56	-2039.49	-530.94	291443.751	4323296.03	557174.7
G57	-2073.37	-494.129	291409.871	4323332.84	557120.3
G58	-2119.6	-475.225	291363.641	4323351.75	556891.3
G59	-2169.03	-474.373	291314.211	4323352.6	557234
G60	-2218.57	-477.302	291264.671	4323349.67	557193
G61	-2267.91	-482.431	291215.331	4323344.54	557232
G62	-2317.66	-485.708	291165.581	4323341.27	557166.3
G63	-2366.7	-493.515	291116.541	4323333.46	557208.3
G64	-2414.27	-508.583	291068.971	4323318.39	557116.3
G65	-2463.99	-511.89	291019.251	4323315.08	556652
G66	-2493.95	-550.945	290989.291	4323276.03	556841
G67	-2491.34	-600.47	290991.901	4323226.5	556853.7
G68	-2477.52	-648.244	291005.721	4323178.73	556755.7
G69	-2500.97	-690.16	290982.271	4323136.81	556748.3
G70	-2539.67	-721.525	290943.571	4323105.45	556709
G71	-2550.52	-770.143	290932.721	4323056.83	556387
G72	-2555.98	-819.63	290927.261	4323007.34	556406
G73	-2556.27	-869.556	290926.971	4322957.42	556055.3
G74	-2557.25	-919.519	290925.991	4322907.45	556864.7
G75	-2561.15	-969.251	290922.091	4322857.72	556215.7
G76	-2572.04	-1017.99	290911.201	4322808.98	555939.3
G77	-2581.63	-1067.02	290901.611	4322759.95	555907.3
G78	-2593.71	-1115.57	290889.531	4322711.4	555988
G79	-2617.81	-1159.09	290865.431	4322667.88	555477

G80	-2650.71	-1196.6	290832.531	4322630.37	555152
G81	-2697.88	-1201.17	290785.361	4322625.8	555663
G82	-2734.63	-1167.57	290748.611	4322659.4	555827
G83	-2772.24	-1134.97	290711.001	4322692	555624.7
G84	-2821.74	-1130.94	290661.501	4322696.03	555562.7
G85	-2871.55	-1128.5	290611.691	4322698.47	554486.3
G86	-2921.71	-1134.38	290561.531	4322692.59	555055.3

LINE (27)

STN. INT.	EAST G1	North G1	UTM E-W	UTM N-S	MAG. FIELD
27-0	-524.75	5204.78	292958.5	4329032	557137
27-1	-1168.69	5889.5	292314.6	4329716	557076.7
27-2	-1906.35	5463.35	291576.9	4329290	556073.3
27-3	-3188.15	6536.49	290295.1	4330363	555746.3
27-4	-3216.79	5685.3	290266.5	4329512	555731
27-5	-3144.76	7443.16	290338.5	4331270	554539
27-6	-3607.32	7904.82	289875.9	4331732	553912.7
27-7	-3722.74	8922.47	289760.5	4332749	556574.7
27-8	-3795.64	8015.8	289687.6	4331843	554447
27-9	-3997.85	6999.26	289485.4	4330826	553837.7
27-10	-4069.88	5574.33	289413.4	4329401	555743.3
27-11	-4026.48	6406.65	289456.8	4330234	554815
27-12	-5646.74	7479.79	287836.5	4331307	552717
27-13	-5965.24	7017.02	287518	4330844	552003.3
27-14	-5126.04	8404.22	288357.2	4332231	555077.7
27-15	-5111.28	8959.1	288372	4332786	555694
27-16	-4981.11	9329.76	288502.1	4333157	556447.7
27-17	-6384.41	8293.24	287098.8	4332120	552642.7
27-18	-7122.07	8663.9	286361.2	4332491	551913.7
27-19	-9089.46	9385.24	284393.8	4333212	548280.7
27-20	-9320.31	8848.12	284162.9	4332675	548845
27-21	-8915.9	8386.46	284567.3	4332213	549029.7
27-22	-8785.72	7146.86	284697.5	4330974	548699
27-23	-8626.04	6573.11	284857.2	4330400	548305.3
27-24	-7223.61	6240.18	286259.6	4330067	549230.3
27-25	-9146.74	5149.29	284336.5	4328976	548970
27-26	-8061.94	4835.23	285421.3	4328662	549012
27-27	-7165.46	4520.06	286317.8	4328347	549836.3
27-28	-9248.28	3465.78	284235	4327293	549479.3
27-29	-8655.54	3337.05	284827.7	4327164	549572.7
27-30	-8843	2411.51	284640.2	4326238	549166.3
27-31	-7844.98	2948.64	285638.3	4326776	550002.3
27-32	-7280.88	3096.23	286202.4	4326923	549386.7
27-33	-6905.11	2985.26	286578.1	4326812	549314.3
27-34	-6138.81	2577.98	287344.4	4326405	550942
27-35	-7975.16	2208.43	285508.1	4326035	549504.7
27-36	-7874.49	1450.46	285608.8	4325277	547927.3
27-37	-7194.1	1173.02	286289.1	4325000	548912
27-38	-6529.34	1301.75	286953.9	4325129	549777.3
27-39	-5935.73	-52.16	287547.5	4323775	550243
27-40	-5979.12	-418.38	287504.1	4323409	549916.7
27-41	-5835.06	-1045.39	287648.2	4322782	547870.7
27-42	-5993.88	-1148.6	287489.4	4322678	547523
27-43	228.53	5371.24	293711.8	4329198	558708.3

27-44	2270.848	6166.57	295754.1	4329994	560443.7
27-45	3704.23	6795.434	297187.5	4330622	559331
27-46	4012.314	6887.914	297495.6	4330715	556099
27-47	4520	6795.434	298003.2	4330622	554493.7
27-48	5815.974	5759.658	299299.2	4329587	552157.7
27-49	6951.398	5297.258	300434.6	4329124	549687
27-50	8418.048	5278.762	301901.3	4329106	556260

LINE (28)

STN. INT.	EAST G1	North G1	UTM E-W	UTM N-S	MAG. FIELD
28-0.0	-516.07	1949.85	292967.171	4325776.82	552859.7
1	-454.46	2023.1	293028.781	4325850.07	553828.7
2	-394.57	2097.45	293088.671	4325924.42	552725
3	-341.64	2171.8	293141.601	4325998.77	552831
4	-257.46	2245.05	293225.781	4326072.02	552417.7
5	-177.61	2319.4	293305.631	4326146.37	552788.3
6	-101.24	2374.89	293382.001	4326201.86	553054.7
7	-82.15	2485.87	293401.091	4326312.84	552843
8	-94.3	2577.98	293388.941	4326404.95	552906.7
9	-129.88	2671.2	293353.361	4326498.17	553059.3
10	-116	2763.31	293367.241	4326590.28	553039.3
11	-129.88	2855.42	293353.361	4326682.39	553300.7
12	-176.75	2948.64	293306.491	4326775.61	553476.3
13	-194.1	3040.75	293289.141	4326867.72	552728
14	-155.92	3132.86	293327.321	4326959.83	553058.3
15	-137.69	3226.08	293345.551	4327053.05	553125.7
16	-131.62	3337.05	293351.621	4327164.02	553603
28-17.0	-138.56	3448.03	293344.681	4327275	553999.7

LINE (29)

STN. INT.	EAST G1	North G1	UTM E-W	UTM N-S	MAG. FIELD
29-0	1582.362	-3016.69	295065.6	4320810	555456.3
29-1	1604.058	-3099.93	295087.3	4320727	555772
29-2	1638.771	-3185.01	295122	4320642	555441.7
29-3	1582.362	-3270.09	295065.6	4320557	555559.7
29-4	1562.112	-3349.62	295045.4	4320477	556161
29-5	1595.379	-3453.2	295078.6	4320374	556362
29-6	1565.005	-3525.33	295048.2	4320302	555592
29-7	984.9984	-4122.75	294468.2	4319704	556151
29-8	927.1424	-4196.74	294410.4	4319630	556081.3
29-9	872.1792	-4278.12	294355.4	4319549	556125.3
29-10	1217.869	-4370.6	294701.1	4319456	556522
29-11	1219.315	-4464.93	294702.6	4319362	556514
29-12	1217.869	-4564.81	294701.1	4319262	556257.7

29-13	1207.744	-4666.54	294691	4319160	556329.3
29-14	1201.958	-4762.72	294685.2	4319064	556412.7
29-15	1190.387	-4860.75	294673.6	4318966	557442.7
29-16	1188.941	-4949.53	294672.2	4318877	556136.3
29-17	1175.923	-5056.8	294659.2	4318770	556260

LINE (30)

STN. INT.	EAST G1	North G1	UTM E-W	UTM N-S	MAG. FIELD
30-0	3370.112	-188.656	296853.353	4323638.32	552978.3
30-1	4258.202	451.306	297741.443	4324278.28	553749
30-2	4774.566	802.73	298257.807	4324629.7	554117.3
30-3	5758.118	1024.682	299241.359	4324851.66	552835.4
30-4	5817.421	1635.05	299300.662	4325462.02	552411.3
30-5	6696.832	1357.61	300180.073	4325184.58	550015
30-6	7203.072	1172.65	300686.313	4324999.62	548317.3
30-7	7777.293	1746.026	301260.534	4325573	548225.7
30-8	8059.341	2522.858	301542.582	4326349.83	548717
30-9	8590.17	3262.698	302073.411	4327089.67	549003
30-10	8824.486	4039.53	302307.727	4327866.5	546846.7
30-11	8987.93	4779.37	302471.171	4328606.34	545881
30-12	8176.499	5019.818	301659.74	4328846.79	546059.3
30-13	5727.744	4945.834	299210.985	4328772.81	551071
30-14	4107.776	4113.514	297591.017	4327940.49	556751
30-15	3144.474	2966.762	296627.715	4326793.74	556194.3
30-16	3620.339	2152.938	297103.58	4325979.91	555408.3
30-17	4592.32	1857.002	298075.561	4325683.98	554374.7
30-18	2917.389	1653.546	296400.63	4325480.52	554042.3

APPENDIX IV

PALAEOMAGNETIC METHOD

1- Introduction

Palaeomagnetism is primarily concerned with the study of the natural remnant magnetisation (NRM) of rocks in order to provide information on the earth's magnetic field in geological times. Most natural remnant magnetisation (NRM) of thermal origin is acquired in a temperature interval of $100^{\circ}C$ to $150^{\circ}C$ below the Curie point (T_c) in the presence of the ambient magnetic field H_a. The distinct blocking temperatures $T_B < T_C$, depend on the composition and size of the magnetic grains present. Generally the higher the blocking temperature T_B the greater the stability of the NRM. NRM may also result from chemical reactions that produce magnetite and hematite. Although produced at low temperatures, such magnetisation also has fairly high blocking temperatures in a similar range as magnetisation of thermal origin. The NRM of rock samples is often the resultant of more than one magnetisation component. Individual components may be acquired at different stages in the history of the sample. Components acquired at the time of formation of the rock are referred to as primary magnetisation, and those associated with later geological events such as diagenesis, deformation, thermal alteration, or effects of weathering are referred to as secondary magnetisation. The stability and strength of the NRM with respect to demagnetisation permits separation of different components of magnetisation. This allows the use of paleomagnetism as a dating tool for such as mineralisation, structural deformation, and impacts. Sites such as the Kentland structure (Jackson and Van der Voo, 1986), Meteor Crater in Arizona (Cisowski and Fuller, 1978) and the Slate Islands structure (Halls, 1979) have magnetisation that are impact related, or generated by the passage of shock waves through magnetic material.

Based on stratigraphic relationships, the age of the Serpent Mound Structure postdates the Early Mississippian Cuyahoga Formation and predates Illinoisian glacial deposits (Bucher, 1921). The aim of this paleomagnetic study is to constrain the age of the structure more precisely through the use of relative dating methods such as the fold test of the stability of the remanence and to provide a new upper limit to the age of the structure.

2- Sampling

The first requirement of the paleomagnetic studies of rocks is the collection of a set of oriented samples. If the rock formation has undergone a deformation the horizontal plane as indicated by the bedding is determined. The samples for this study were collected from deep and shallow drill cores within and near the Serpent Mound Structure. The cores are not oriented in azimuth and we assume they do not systematically deviate from vertical. Therefore, we are able to measure average paleomagnetic inclinations, either with respect to the vertical axis or with respect to observed bedding planes. The sampled units include hematite rich beds in the Early Silurian Brassfield Formation, Silurian carbonates and Ordovician carbonates. The carbonates are from core DGS 3274SM79-1 (903 m), drilled in the central uplift and DGS 3275SM79-2 (629 m), drilled in the transition zone between the uplift and the outer graben (Figure 1). The Brassfield was sampled from DGS 3275SM79-2 in which bedding dips ~35°, three shallow cores (DGS 2880, 2881, 2882) drilled in the periphery of the structure (Figure 1) where bedding dips ~15°, and one deep core (DGS 2626), not involved in the structure. The samples were selected on the basis of magnetic susceptibility measurements carried out using a hand held kappa meter. The hematite rich beds of the Brassfield Formation have susceptibilities ranging from 0.7 x 10^{-3} SI units to 0.3 x 10^{-3} SI units, whereas the carbonates range from 0.1 x 10^{-3} SI units to values which were below the sensitivity of the meter. We selected carbonates that had susceptibilities in the upper part of this range, the cores were drilled and cut to standard 2.3 cm x 2.54-cm cylinders. The reference mark started at the top of the core and proceeded along the 'V' formed by the intersection of the bedding planes with the core. This was done so a structural correction could be applied by rotating about the strike of the bedding plane in each core to determine the inclination of the magnetisation with respect to bedding. Every effort was made to ensure the core was right side up as stratigraphic and lithological continuity were continuously monitored during the logging process and core depth markers were checked for consistency.

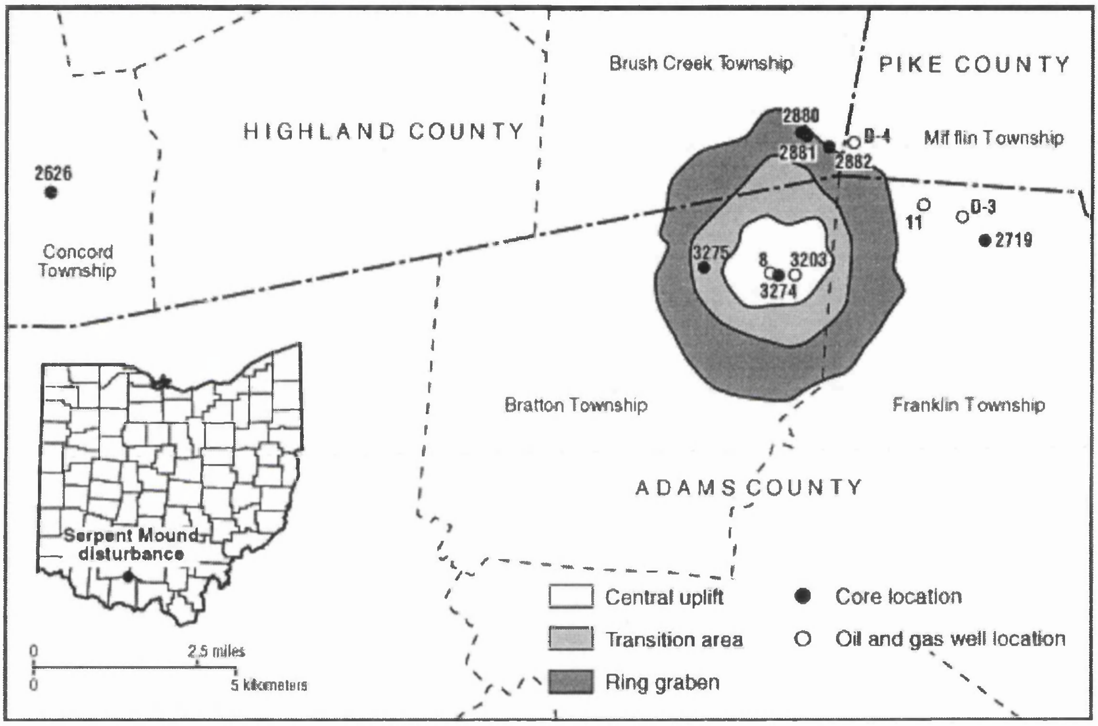

Figure 1- Map of Serpent Mound Structure with borehole locations.

3- Demagnetisation and Measurements

For the measurement of natural remnant magnetisation (NRM) of the samples in terms of the intensity of magnetisation and the direction of the ancient magnetic field can be measured by the use of a number of instruments such as the Astatic magnetometer, Spinner magnetometer, and Superconducting magnetometer (SQUID), which is very sensitive and used to measure NRM of weakly magnetisation.

Samples were measured by Dr. Watts using a 2-G cryogenic magnetometer at the University of Michigan (Laboratory facilities of Professor Rob Van der Voo), and a JR5A spinner magnetometer at Ohio State University (Laboratory of Dr. Anne Grunow of the Byrd Polar Centre). The cryogenic magnetometer, where the pick-up coils and SQUID sensors operate at liquid helium temperature, measures the intensity of the sample magnetic field simultaneously in three orthogonal directions. This allows the calculation of the total moment of the sample as well as the declination and the inclination of the magnetisation relative to the orientation of the sample. The magnetisation of the sample is then rotated into geographic co-ordinates, and rotate again about the strike of the bedding to account for bedding tilt. The standard procedure for determining the component content of the NRM is by using thermal and alternating field demagnetisation characteristics indicate the blocking temperature and coercively spectra respectively. Only two samples of carbonate and one Brassfield sample were subjected to alternating field demagnetisation in a Schonstedt SM-1 A.F. demagnetiser. The rest were analysed thermally, the cleaning of the rock specimens thermally by heating and cooling in a field-free space (step-wise thermal demagnetisation in an MMTD60 oven). As a specimen is heated, the magnetisations of grains tend to become randomly oriented, depending on the blocking temperatures of the magnetisation components. Thus the blocking temperature spectrum of a specimen can be determined by its thermal demagnetisation behaviour and the stable component of the NRM can be isolated by the destruction of other components of relatively low thermal stability.

4-Statistical Analysis

We monitored orthogonal projections (Zijderveld, 1967) of the demagnetisation results during the process, and identified characteristic magnetisations, which were isolated using the IAPD program of Torsvik, Briden, and Smethurst (Program available at: /http://www.ngu.no.geophysics/).

As these are inclination-only data, we used the statistical methods outlined by McFadden and Reid (1982) to determine the mean inclination, the estimate of the precision parameter (k), and α_{95}. This was done for the Brassfield results after structural correction with 10% tilt increments.

In general the statistical analysis of paleomagnetic data to estimate the mean direction of N samples is determined using the direction cosines of the individual unit vectors. An individual component combined with others of the same horizon, these vectors represented as unit vectors and displayed as point on an equal area stereographic projection. The parameter (k) is a measure of the dispersion of the points. If k=0 then the points are distributed evenly over the sphere and the directions are random. If the values of k are large, the points are clustered tightly about the true mean direction. If a group of points representing directions of magnetisation are distributed on a sphere, the best estimate of the mean direction of magnetisation (the centre of these points) can be found by the vector addition of all directions. Therefore, in general the direction of magnetisation of a sample is given in terms of the declination (D) measured over 360° clockwise from true north and the inclination (I) measured positive or negative downward or upward from the horizontal respectively. The unit vector can be determined by its three direction cosines:

North component l = CosD CosI

East component m = SinD CosI

Down (Up) component n = SinI

The resultant direction of N such directions determined by the summing of the direction cosines, and is given by:

$$X = \frac{1}{R}\sum_{i=1}^{N} l_i$$

$$Y = \frac{1}{R}\sum_{i=1}^{N} m_i$$

$$Z = \frac{1}{R}\sum_{i=1}^{N} n_i$$

The vector sum will have a length R;

$$R^2 = (\sum_{i}^{N} l_i)^2 + (\sum_{i=1}^{N} m_i)^2 + (\sum_{i=1}^{N} n_i)^2$$

The declination and inclination of the vector mean direction R are given by;

$$Tan\,D_R = \frac{\sum_{i=1}^{N} m_i}{\sum_{i=1}^{N} n_i}$$

$$Sin I_R = \frac{1}{R}\sum_{i=1}^{N} n_i$$

The best estimate of k is

$$K = \frac{N-1}{N-R}$$

And the angle α_{95} is given by

$$\alpha_{95} = \frac{140}{\sqrt{K N}} \;.$$

Figure (2) shows the result of typical stepwise thermal demagnetisation of the carbonates from DGS 3274SM79-1 and DGS 3275SM79-2. These are the orthogonal projections of the magnetisation vector displayed after each step. The open characters denote projection on a vertical plane and the closed characters denote projection on the horizontal plane. The magnetisation is thermally distributed, decaying towards or near the origin, with multivector or curved trajectories before a major alteration of the magnetic minerals cause a sudden increase in the magnetisation at around 400°C. A.f demagnetisation at 50 mT reduced the intensity of the magnetisation by 95%.

The inclinations were highly variable and included a number of negative inclinations. We have no reason to believe the core is upside down where we found the negative inclinations. Our geological colleagues who logged the core checked this. The highly variable inclination that includes those near the present field, combined with the presence of reversals implies this secondary magnetisation was acquired over a considerable time and could not be related to an impact.

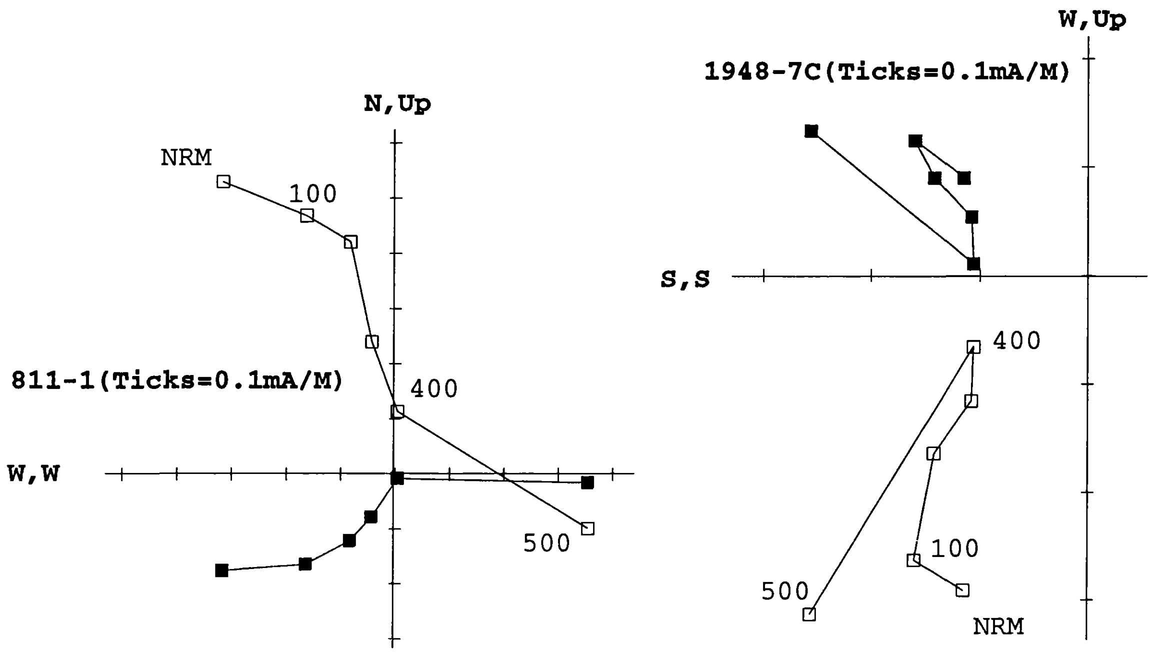

Figure 2- Orthogonal projections of demagnetisation results from Silurian and Ordovician carbonates. Open symbols denote projection on the vertical Plane. Closed symbols denote projection on the horizontal plane

Figure (3) shows orthogonal projections of thermal demagnetisation results from the hematite rich beds of the Brassfield Formation. A steep, positive inclination secondary magnetisation was removed at the first stages of thermal demagnetisation to reveal a high blocking temperature thermally discrete magnetisation. The high blocking temperature magnetisation did not decay perfectly to the origin of the demagnetisation plots but it was impossible to isolate a further magnetisation due to the rapid acquisition of viscous magnetisation at the highest steps. This was in spite of doing the demagnetisation and the measurements in a shielded room at the University of Michigan that reduced the ambient magnetic field to levels of 200 nT, and storing samples in mu-metal boxes in the shielded room.

Assuming the low blocking temperature magnetisation is a present day overprint, we assume the declination of this magnetisation indicates magnetic north. We can therefore find an estimate of the declination of the high-blocking temperature magnetisation by the angle its declination makes with respect to the low blocking temperature magnetisation. Examination of Figures (3 a,b,d) indeed shows that the declination of the secondary magnetisation is nearly opposite (~180°) that of the high temperature magnetisation.

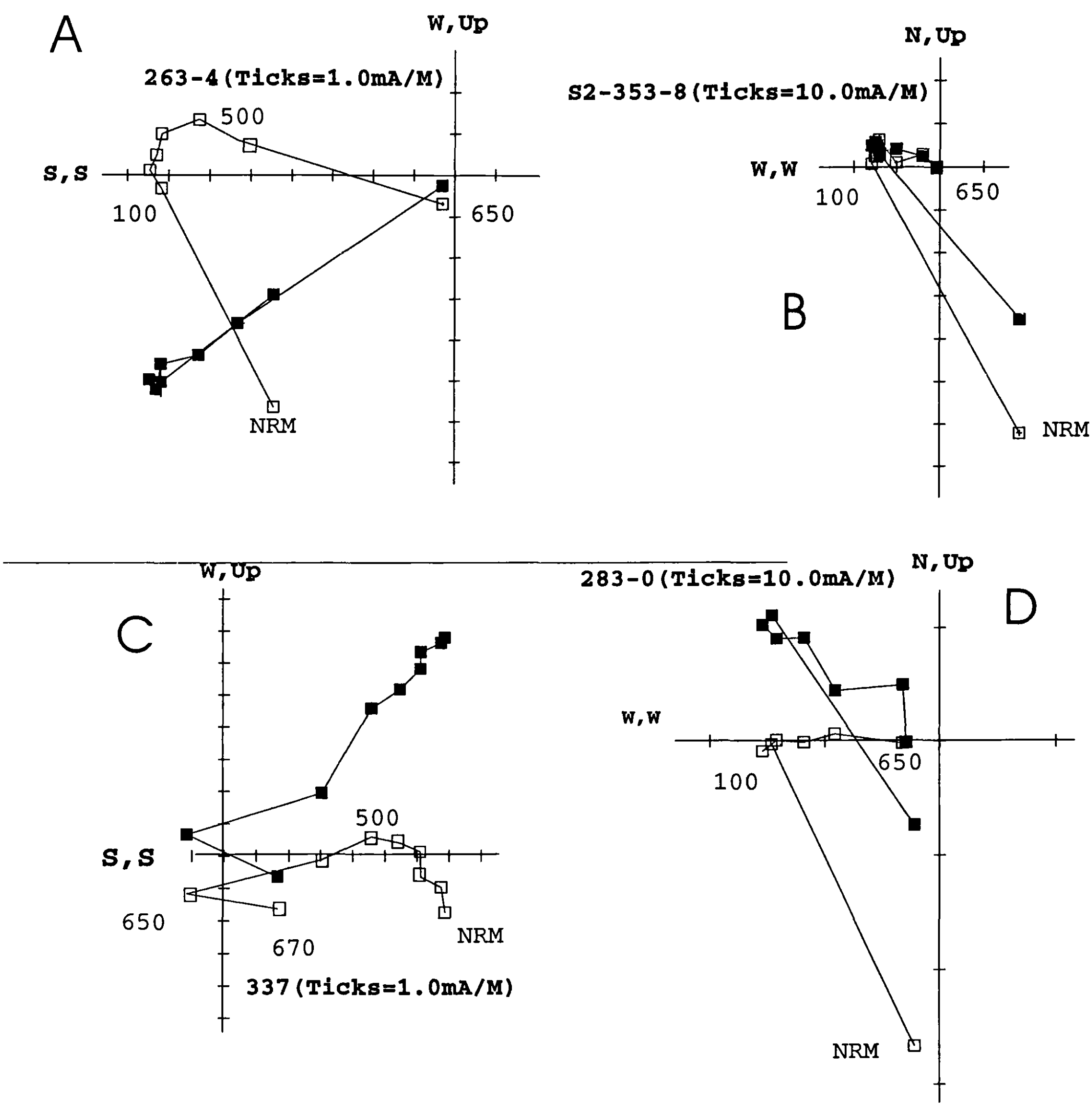

Figure 3- Orthogonal projections of demagnetisation results from the Brassfield Formation. Convention as in Figure (2)

An equal area projection of the high blocking temperature magnetisation with the declination estimated by rotating the secondary magnetisation to the north, is shown in Figure 4. Only a subset of specimens had both a low and high blocking temperature magnetisation. The distribution shows this high blocking temperature magnetisation to be of reversed polarisation. Although some of the declinations are found in northern quadrants, none of them are clearly antipodal to the mean southeast direction. We therefore proceed to analyse the data by the inclination only method described by McFadden and Reid (1982). We are confident we do not have to deal with mixed polarities if we deal with this subset of the data. We do not regard the estimates of the declinations accurate enough to carry out statistical analysis of the vector data and considered only the inclinations. We analyse the complete data set, and those data that are shown to be from reversed polarity magnetisation.

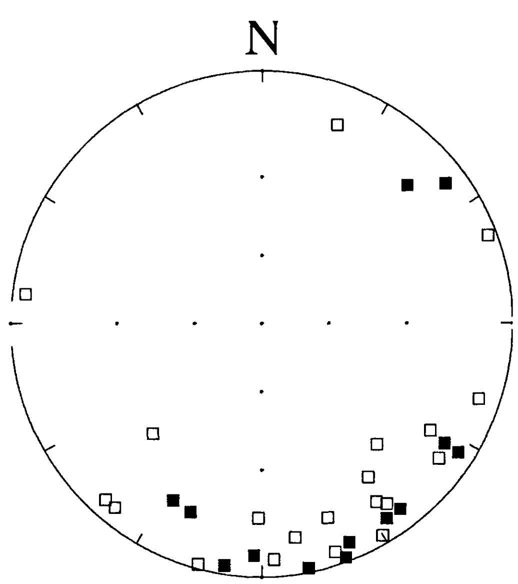

Figure 4- Equal area projection of high blocking temperature magnetisation of the Brassfield Formation with declinations estimated using secondary magnetisation. Open symbols denote negative (up) inclination; closed symbols denote positive (down) inclination.

The result of stepwise structural correction is shown in Figure (5a). The value of the precision parameter, k, attains its maximum value at a 30% structural correction, with an average inclination of -2° and α_{95} of 3°. From this point k decreases steadily to the full 100% correction to where it obviously fails the fold test with k a factor of ~3 smaller than the maximum. Figure (5b) shows the results of the inclination only statistical analysis for the subset of magnetisation known to be of reversed polarity. The average inclination is also -2° corresponding to a maximum k of 50.5 at a tilt correction of 20%.

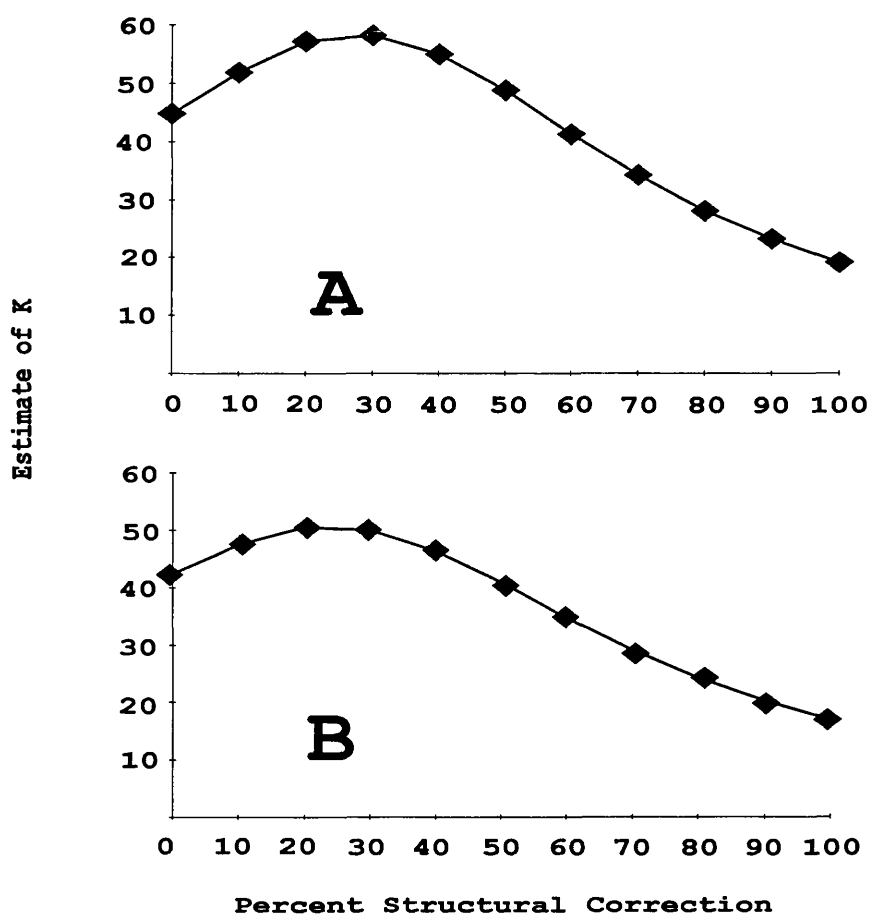

Figure 5- Estimate of precision parameter, k, plotted against percent of structural correction; (a) all data; (b) subset of data

McFadden and Reid (1982) also discuss the polarity ambiguity for shallow inclination data and suggest that histograms of the inclinations be examined to evaluate the probable polarity structure. A single polarity will show a unimodal distribution, and a mixed polarity will show a bimodal distribution. Figure (6) shows histograms from the complete set of data of the distribution of the inclinations before structural correction (Figure 6a), at 30% correction (Figure 6b) and at 100% correction (Figure 6c). We note that before correction, and at 30% correction the distribution is distinctly unimodal. At 100% correction, the inclinations are clearly dispersed. Parés et al. (1994) lament the lack of a statistical significance test for the inclination only fold test, and so do we. We cannot assign statistical levels of significance to the fold test. However, the drop in k by a factor of 3 after 100% tilt correction and the histogram in Figure (6c) indicate to us the magnetisation was acquired after the major tilting event. It is more difficult to evaluate the statistical significance of the increase in k up to 30% tilt correction. We use the inclination of -2. degrees, with associated α_{95} of 3 degrees, as the estimate of the average inclination with reversed polarity at the time the Brassfield Formation acquired its magnetisation. We note this is not significantly different for the average inclination and α_{95} at 0% tilt correction.

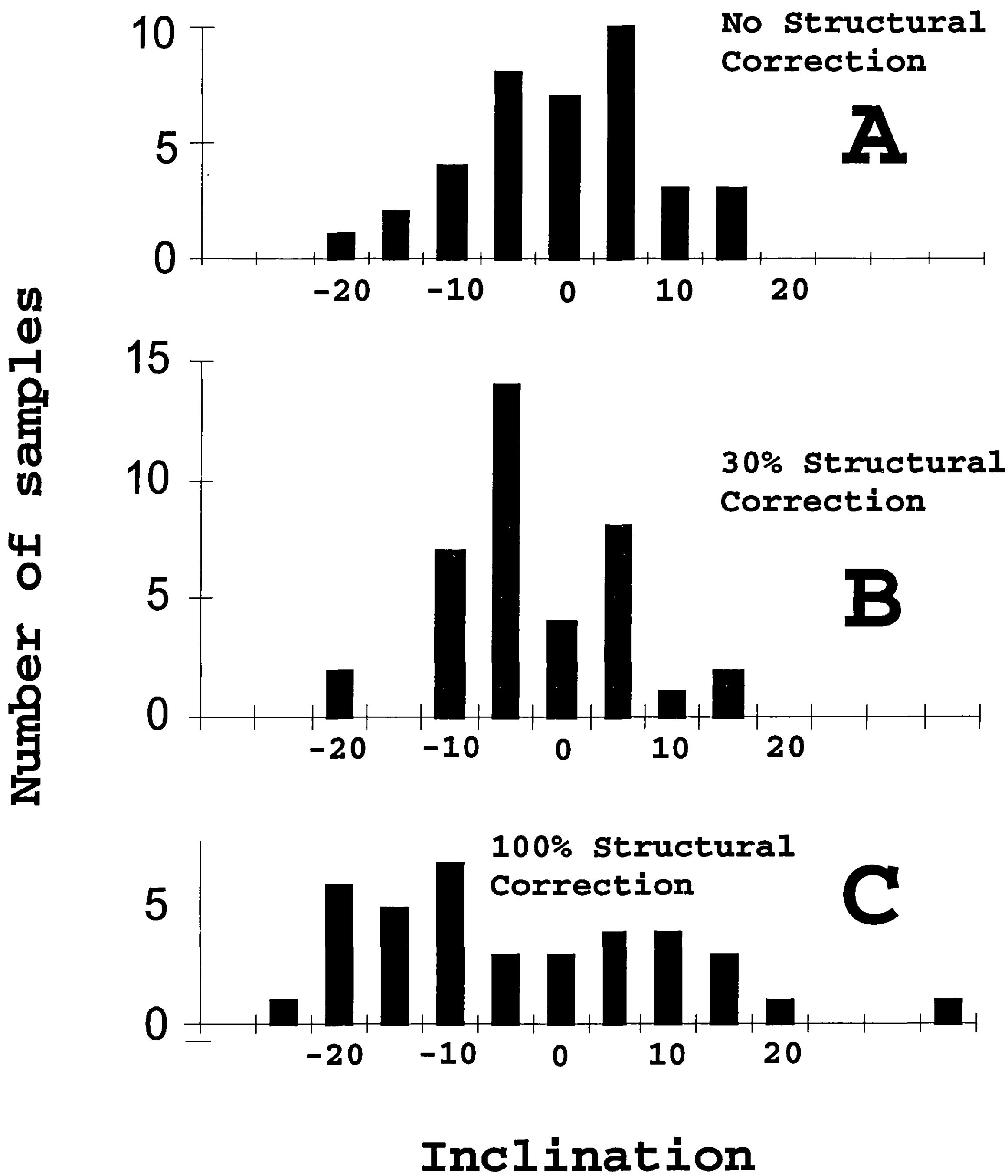

Figure 6- Histogram showing distribution of magnetic inclinations of Brassfield Formation at (a) no structural correction, (b) 30% and (c) 100% structural correction.

8.5- Discussion and Conclusions

The carbonates have low blocking temperature (~400° C), dispersed inclination, mixed polarity magnetisation. The Brassfield Formation retains a low blocking temperature (~200° C), secondary magnetisation with steep positive inclinations, and a high blocking temperature (~670° C), thermally discrete magnetisation that has the lowest dispersion (k=58.1, mean inclination = -2. degrees) after 30% tilt correction, and greatest dispersion at 100% tilt correction. The very high blocking temperature of this magnetisation, and its presence in core DGS 2626 precludes an impact origin. Using the secondary magnetisation as an indicator of north, we find the high temperature magnetisation is of reversed polarity. The magnetisation was therefore probably acquired during the widespread Permian re-magnetisation that affected much of the mid-continent North America. The Serpent Mound Structure therefore pre-dates this event.

Reidel et al. (1982) present evidence for multiple episodes of deformation within the Serpent Mound Structure, relative to the mineralization. We speculate that the maximum k at 30% correction suggests post impact structure adjustments by normal faulting which would explain mineralised fabrics showing episodic deformation. Indeed, local inhabitants report present-day seismic activity in the vicinity of the structure.

Figure (7) shows the average normal polarity paleomagnetic inclination for the Serpent Mound Structure location as a function of age, calculated using the polar wander path of Stamatakos et al. (1996) . The inclination slowly increases from negative to positive representing the slow drift of the site from the Southern to Northern Hemisphere during this time. If the average normal polarity inclination is 2. ± 3 . degrees, one may estimate the age of magnetisation from Figure (7) as approximately 250 ± 15 my, i.e. Late Permian to Early Triassic. The magnetisation was probably acquired during the widespread reversed polarity remagnetisation event that affected much of the North American craton. The age of the Brassfield magnetisation is therefore Late Permian, though the remagnetisation no doubt occurred over a considerable time scale, affecting different locations with different intensities at different times. This represents the best constraint of the upper age of the Serpent Mound Structure to date; certainly better than afforded by the geology. It does raise the possibility that ejecta from the impact may be preserved in Carboniferous to Permian rocks, which crop out within 100 km of the site. The identification of microfossils or lithologies from the allocthonous breccias preserved within the structure and the deep core may yield information more diagnostic of the age of formation of the feature.

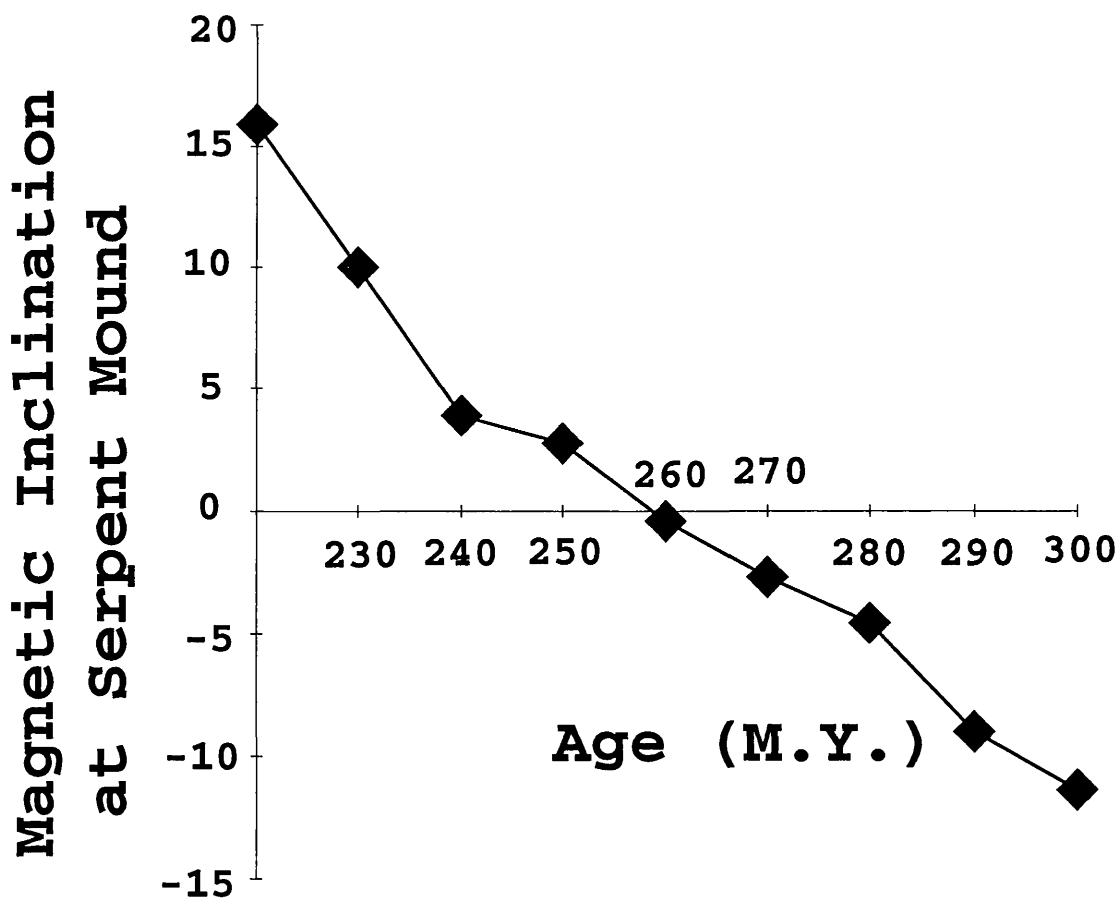

Figure 7- Magnetic inclination plotted against geological age at the site of The Serpent Mound Structure.